Hadis Morkoç and Ümit Özgür

WILEY-VCH

Zinc Oxide

Fundamentals, Materials and Device Technology

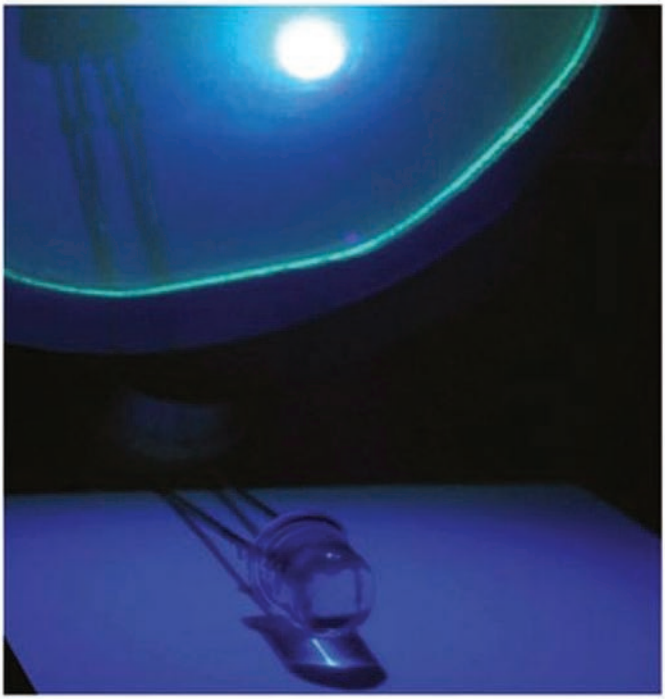

Hadis Morkoç and Ümit Özgür
Zinc Oxide

Related Titles

Neumark, G. F., Kuskovsky, I. L., Jiang, H. (eds.)

Wide Bandgap Light Emitting Materials And Devices

2007
ISBN: 978-3-527-40331-8

Capper, P., Mauk, M. (eds.)

Liquid Phase Epitaxy of Electronic, Optical and Optoelectronic Materials

2007
ISBN: 978-0-470-85290-3

Hadis Morkoç and Ümit Özgür

Zinc Oxide

Fundamentals, Materials and Device Technology

WILEY-VCH Verlag GmbH & Co. KGaA

The Authors

Prof. Dr. Hadis Morkoç
Virginia Commonwealth University
Dept. of Electrical Engineering
Richmond, VA
USA

Ümit Özgür
Virginia Commonwealth University
Dept. of Electrical Engineering
Richmond, VA
USA

Library of Congress Card No.: applied for

British Library Cataloguing-in-Publication Data
A catalogue record for this book is available from the British Library.

Bibliographic information published by the Deutsche Nationalbibliothek
The Deutsche Nationalbibliothek lists this publication in the Deutsche Nationalbibliografie; detailed bibliographic data are available on the Internet at http://dnb.d-nb.de.

Typesetting Thomson Digital, Noida, India
Printing betz-druck GmbH, Darmstadt
Binding Litges & Dopf GmbH, Heppenheim

Printed in the Federal Republic of Germany
Printed on acid-free paper

ISBN: 978-3-527-40813-9

Preface

The semiconductor ZnO has gained substantial interest in the research community in part because of its large exciton binding energy (60 meV) that could lead to lasing action based on exciton recombination and possibly polariton/exciton interaction even above room temperature. The motivation for this book stems from the applications of ZnO in potential optical devices, transparent ohmic contacts, light extraction enhancement structures for GaN-based light-emitting diodes (LEDs), transparent thin-film transistors, transducers, and so on, for which ZnO is well suited.

We should mention that even though research focusing on ZnO goes back to many decades, the renewed interest is fuelled by the availability of high-quality substrates and reports of p-type conduction and ferromagnetic behavior when doped with transition metals, both of which remain controversial. The lattice parameter studies date back to 1935 [1], vibrational properties were studied by Raman scattering in 1966 [2], detailed optical properties were investigated in 1954 [3], and its growth by chemical vapor transport was attained in 1970 [4]. In terms of devices, Au Schottky barriers were formed in 1965 [5], LEDs were demonstrated in 1967 [6] wherein Cu2O was used as the p-type material, metal insulator semiconductor (MIS) structures were reported in 1974 [7], ZnO/ZnTe n–p junctions were accomplished in 1975 [8], and Al/Au ohmic contacts were reported in 1978 [9]. Very high quality what used to be called whiskers and platelets, the nomenclature that gave way to nanostructure, of late, have been prepared early on and used to deduce much of the principal properties of this material, particularly the optical properties, albeit with a healthy debate about the valence band ordering and assignment of some of the peaks appearing in optical excitation measurements. In addition to the requisite direct bandgap, the attraction to ZnO can simply be attributed to its large exciton binding energy of 60 meV, which might potentially pave the way for efficient room-temperature exciton-based and/or polariton/exciton interaction-based lasers with very low-threshold currents. The field is also fuelled by theoretical predictions and perhaps experimental confirmation of ferromagnetism at room temperature for potential spintronics applications. Of paramount importance is the transparency of ZnO to visible light that is in part responsible for exploring this material for applications such as transparent ohmic contacts for light emitters based on GaN, solar cells that have been gaining considerable interest, transparent thin-film transistors, and nanostructures that can be used to extract light from LEDs such as those

Contents

based on GaN. Furthermore, highly piezoelectric nature of ZnO and its favorable electromechanical coupling coefficient are very attractive for devices such as surface acoustic waves.

This book is unique in the sense that it represents the first cohesive treatment of the entire field of ZnO and related materials and devices under one cover. As such, much needed continuity and smooth flow are provided without duplications. The aspects of ZnO forming the basis for this book are presented in eight chapters, the contents of which are elaborated on below.

Chapter 1 treats the mechanical–thermal, chemical, and electrical properties of ZnO. Low-field as well as high-field transport is discussed. Chapter 2 discusses the growth of ZnO and heterostructures by popular techniques such as sputtering, molecular beam epitaxy, pulsed laser deposition, and chemical vapor deposition. Substrates on which ZnO is deposited along with resultant properties of the material are also discussed. Chapter 3 provides the most comprehensive treatment of optical properties of ZnO that are rich not only in terms of linear processes but also in terms of nonlinear processes. In this vein, following an introduction to optical processes in semiconductors, the specifics of optical transitions related to free excitons and polaritons, bound excitons, two-electron satellite transitions are treated in detail. This segues into the discussion of defect-related transitions such as the celebrated green, yellow, and red transitions. After discussing the refractive index of ZnO and its ternary ZnMgO, a detailed discussion of stimulated emission in ZnO is given, including single-crystal and polycrystal forms and quantum wells. The treatment then moves on to the discussion of recombination dynamics looking at the recombination lifetimes. The attention is then turned onto nonlinear optical properties including second- and third-order harmonic generation, intensity-dependent refractive index, and two-photon absorption.

Chapter 4 discusses the all-important doping in ZnO, in particular p-type doping. Details and motivations for approaches taken for attaining p-type conductivity inclusive of codoping methods and characterization schemes are provided. Chapter 5 deals with doping ZnO with magnetic ions in the context of dilute magnetic semiconductors. A sufficient amount of the theory of magnetization, classification of magnetic materials, measurement techniques, and theoretical and experimental investigations of magnetic ion-doped ZnO such as Mn and Co, among others, are discussed.

Chapter 6 discusses bandgap engineering that forms the basis for many of the high-performance electrical and optical devices based on semiconductors. ZnO alloyed with Mg and Be for increasing its bandgap and alloyed with Cd for decreasing its bandgap is discussed with the accompanying issues with regard to changes in the lattice constant and of course the bandgap. Chapter 7 paves the way for nanostructures based on ZnO. After the discussion of most popular nanostructure fabrication techniques, the application of these techniques to ZnO nanostructures such as nanorods (nanowires), nanobelts, and polypod systems is discussed.

The book ends with the discussion of ZnO processing needed for devices, metal semiconductors contacts and their current–voltage relationships including the fundamentals of current conduction mechanisms in various regimes, etching of

ZnO, and heterostructure devices. Among the devices, light emitters, microcavities, optically pumped lasers, photodiodes, metal–insulator–semiconductor diodes, field-effect transistors, transparent conducting oxides, and transparent thin-film transistors based on ZnO, piezoelectric devices in the form of surface acoustic wave devices, and gas and biosensor followed by solar cells cap the discussion.

It is not only fair but gratifying to state that we owe so much to so many including our family members, friends, coworkers, colleagues, and those who contributed to the field of semiconductors in general and ZnO in particular in our efforts to bring this manuscript to the service of readers. To this end, HM would like to thank his wife Amy and son Erol for at least their understanding why he was not really there for them fully during the preparation of this manuscript, which took longer than most could ever realize. UO wants to thank his parents and his sister for their continuing support throughout his career. Also, without the support of VCU, our past Dean R.J. Mattauch and current Dean R.D. Jamison, past assistant Dean Susan Younce, Department Chair A. Iyer, and our coworkers and students, it would not have been possible to pursue this endeavor.

Special recognitions also go to our coworkers Dr Y.I. Alivov, Dr V. Avrutin, Dr N. Izyumskaya, and Professor M. Reshchikov for their contributions to the research that made possible the discussions on growth, devices, and point defects a much more manageable task.

Special thanks go to J.M. Recio, S. Desgreiners, J. Pollmann, J.E. Jaffe, F. Decremps, M. Schubert, C. Bundesmann, N. Ashkenov, T. Sekiguchi, T. Fukuda, J.-J. Song, J. Nause, P. Ruterana, Q. Wang, Y. Chen, T. Yao, K. Thonke, C. G. van de Walle, P. Dahan, B. Meyer, S.-J. Park, A. Krost, X. Feng, T. Fukumura, Y.-H. Jeong, G. Lawes, I. Tanaka, D.P. Norton, N.H. Hong, J.M.D. Coey, M.H. Kane, T.-S. Chin, Y. Ishida, K. Ando, A. Ohtomo, T. Makino, P. Yang, Z.L. Wang, A.B. Djurišić, G.-C. Yi, B.P. Zhang, M. Kawasaki, R. Shimada, D. Hofstetter, Y. Lu, S. Fujita, N.H. Nickel, B. Gil, R.L. Hoffman, J. Fallert, and C.K. Klingshirn for willingly devoting considerable time and effort to provide us with digital copies of figures and high-quality images. They are also acknowledged in conjunction with the figures.

Richmond, VA, June 2008 *Hadis Morkoç and Ümit Özgür*

References

1 Bunn, C.W. (1935) *Proceedings of the Physical Society*, **47**, 835.
2 Damen, T.C., Porto, S.P.S. and Tell, B. (1966) *Physical Review*, **142**, 570.
3 Mollwo, E. (1954) *Zeitschrift fur Angewandte Physik*, **6**, 257.
4 Galli, G. and Coker, J.E. (1970) *Applied Physics Letters*, **16**, 439.
5 Mead, C.A. (1965) *Physics Letters*, **18**, 218.
6 Drapak, I.T. (1968) *Semiconductors*, **2**, 624.
7 Minami, T., Tanigava, M., Yamanishi, M. and Kawamura, T. (1974) *Japanese Journal of Applied Physics*, **13**, 1475.
8 Tsurkan, A.E., Fedotova, N.D., Kicherman, L.V. and Pas'ko, P.G. (1975) *Semiconductors*, **6**, 1183.
9 Brillson, L.J. (1978) *Journal of Vacuum Science & Technology*, **15**, 1378.

1
General Properties of ZnO

In this chapter, crystal structure of ZnO encompassing lattice parameters, electronic band structure, mechanical properties, including elastic constants and piezoelectric constants, lattice dynamics, and vibrational processes, thermal properties, electrical properties, and low-field and high-field carrier transport is treated.

1.1
Crystal Structure

Most of the group II–VI binary compound semiconductors crystallize in either cubic zinc blende or hexagonal wurtzite (Wz) structure where each anion is surrounded by four cations at the corners of a tetrahedron, and vice versa. This tetrahedral coordination is typical of sp^3 covalent bonding nature, but these materials also have a substantial ionic character that tends to increase the bandgap beyond the one expected from the covalent bonding. ZnO is a II–VI compound semiconductor whose ionicity resides at the borderline between the covalent and ionic semiconductors. The crystal structures shared by ZnO are *wurtzite* (B4), *zinc blende*[1] (B3), and *rocksalt* (or Rochelle salt)[2] (B1) as schematically shown in Figure 1.1. B1, B3, and B4 denote the *Strukturbericht*[3] designations for the three phases. Under ambient conditions, the thermodynamically stable phase is that of wurtzite symmetry. The zinc blende ZnO structure can be stabilized only by growth on cubic substrates, and

1) The term zinc blende originated from compounds such as ZnS, which could be in cubic or hexagonal phase. But the term has been used ubiquitously for compound semiconductors with cubic symmetry. The correct term that should be used for the cubic phase of ZnO GaN is actually *sphalerite*. To be consistent with the diction throughout the literature even at the expense of bordering inaccuracy, the term zinc blende is used throughout this book.

2) Also called Seignette salt – named after Pier Seignette from La Rochelle, France, who first prepared potassium sodium tartrate tetrahydrate ($KNaC_4H_4O_6{\cdot}4H_2O$) in 1675 and determined its structure.

3) *Strukturbericht*, the original crystallographic reports. From 1919 to 1939 (Vols 1–8), they were published in Germany. Since then, they have been published in the United States under the name *Structure Reports*, *Acta Crystallographica Section E*, by the International Union of Crystallography.

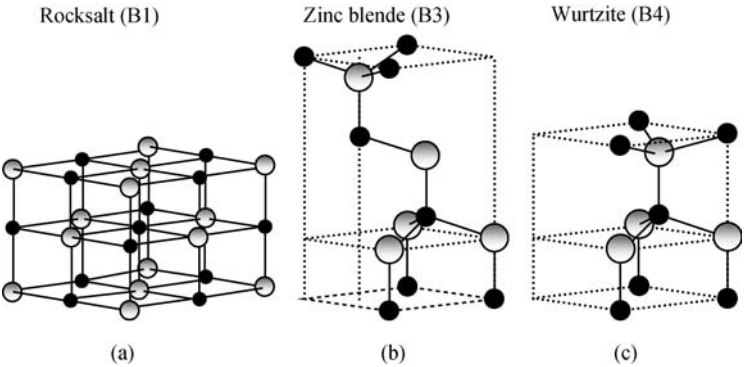

Figure 1.1 Stick-and-ball representation of ZnO crystal structures: (a) cubic rocksalt (B1), (b) cubic zinc blende (B3), and (c) hexagonal wurtzite (B4). Shaded gray and black spheres denote Zn and O atoms, respectively.

the rocksalt or Rochelle salt (NaCl) structure may be obtained at relatively high pressures, as in the case of GaN.

The *wurtzite* structure has a hexagonal unit cell with two lattice parameters a and c in the ratio of $c/a = \sqrt{8/3} = 1.633$ (in an ideal wurtzite structure) and belongs to the space group C_{6v}^4 in the Schoenflies notation and $P6_3mc$ in the Hermann–Mauguin notation. A schematic representation of the wurtzitic ZnO structure is shown in Figure 1.2. The structure is composed of two interpenetrating hexagonal close-packed (hcp) sublattices, each of which consists of one type of atom displaced with respect to each other along the threefold c-axis by the amount of $u = 3/8 = 0.375$ (in an ideal wurtzite structure) in fractional coordinates. The internal parameter u is defined as the length of the bond parallel to the c-axis (anion–cation bond length or the

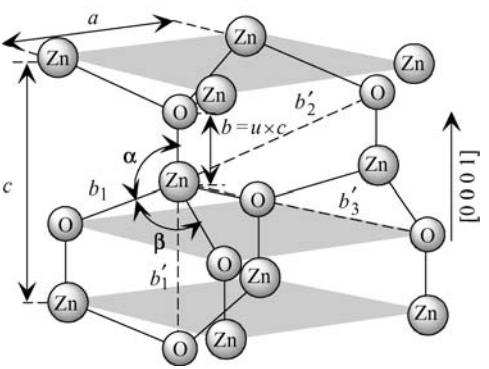

Figure 1.2 Schematic representation of a wurtzitic ZnO structure with lattice constants a in the basal plane and c in the basal direction, u parameter, which is expressed as the bond length or the nearest-neighbor distance b divided by c (0.375 in ideal crystal), α and β (109.47° in ideal crystal) bond angles, and three types of second-nearest-neighbor distances b'_1, b'_2, and b'_3.

nearest-neighbor distance) divided by the c lattice parameter. The basal plane lattice parameter (the edge length of the basal plane hexagon) is universally depicted by a; the axial lattice parameter (unit cell height), perpendicular to the basal plane, is universally described by c. Each sublattice includes four atoms per unit cell, and every atom of one kind (group II atom) is surrounded by four atoms of the other kind (group VI), or vice versa, which are coordinated at the edges of a tetrahedron. The crystallographic vectors of wurtzite are $\vec{a} = a(1/2, \sqrt{3}/2, 0), \vec{b} = a(1/2, -\sqrt{3}/2, 0)$, and $\vec{c} = a(0, 0, c/a)$. In Cartesian coordinates, the basis atoms are (0, 0, 0), (0, 0, uc), $a(1/2, \sqrt{3}/6, c/2a)$, and $a(1/2, \sqrt{3}/6, [u+1/2]c/a)$.

In a real ZnO crystal, the wurtzite structure deviates from the ideal arrangement, by changing the c/a ratio or the u value. The experimentally observed c/a ratios are smaller than ideal, as in the case of GaN, where it has been postulated that not being so would lead to zinc blende phase [1]. It should be pointed out that a strong correlation exists between the c/a ratio and the u parameter in that when the c/a ratio decreases, the u parameter increases in such a way that those four tetrahedral distances remain nearly constant through a distortion of tetrahedral angles due to long-range polar interactions. These two slightly different bond lengths will be equal if the following relation holds:

$$u = \left(\frac{1}{3}\right)\left(\frac{a^2}{c^2}\right) + \frac{1}{4}. \tag{1.1}$$

The nearest-neighbor bond lengths along the c-direction (expressed as b) and off c-axis (expressed as b_1) can be calculated as

$$b = cu \quad \text{and} \quad b_1 = \sqrt{\frac{1}{3}a^2 + \left(\frac{1}{2} - u\right)^2 c^2}. \tag{1.2}$$

In addition to the nearest neighbors, there are three types of second-nearest neighbors designated as b'_1 (one along the c-direction), b'_2 (six of them), and b'_3 (three of them) with the bond lengths [2]

$$b'_1 = c(1-u), \quad b'_2 = \sqrt{a^2 + (uc)^2}, \quad \text{and} \quad b'_3 = \sqrt{\frac{4}{3}a^2 + c^2\left(\frac{1}{2} - u\right)^2}. \tag{1.3}$$

The bond angles, α and β, are given by [2]

$$\begin{aligned} \alpha &= \pi/2 + \arccos\left[\left(\sqrt{1 + 3(c/a)^2(-u+1/2)^2}\right)^{-1}\right], \\ \beta &= 2\arcsin\left[\left(\sqrt{4/3 + 4(c/a)^2(-u+1/2)^2}\right)^{-1}\right]. \end{aligned} \tag{1.4}$$

The lattice parameters are commonly measured at room temperature by X-ray diffraction (XRD), which happens to be the most accurate one, using the Bragg law. In ternary compounds, the technique is also used for determining the composition;

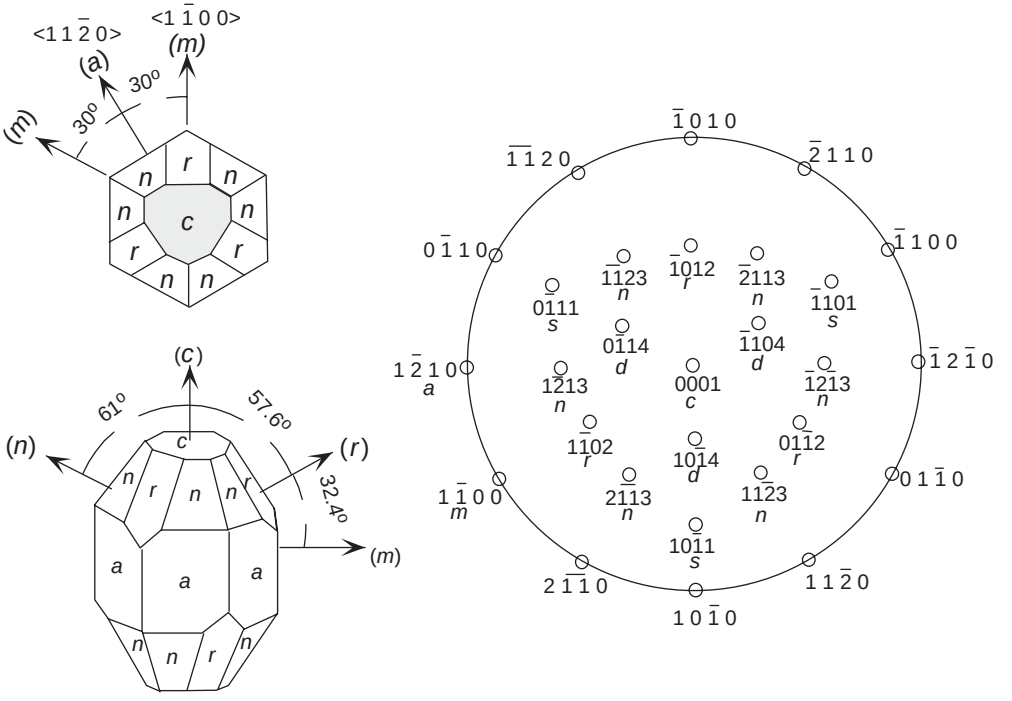

Common crystallographic planes in sapphire

Plane name	Miller index	*d* spacing
a	$(11\bar{2}0)$	2.379 Å
m	$(10\bar{1}0)$	1.375 Å
c	(0001)	2.165 Å
r	$(1\bar{1}02)$	1.740 Å
n	$(11\bar{2}3)$	1.147 Å
s	$(10\bar{1}1)$	1.961 Å

Angles between common planes

(0001) ^ $(1\bar{1}02)$	*c* ^ *r*	57° 35′
(0001) ^ $(11\bar{2}3)$	*c* ^ *n*	61° 11′
(0001) ^ $(10\bar{1}1)$	*c* ^ *s*	72° 23′
(0001) ^ $(11\bar{2}1)$	*c* ^	79° 37′
(0001) ^ $(11\bar{2}0)$	*c* ^ *a*	90° 00′
(0001) ^ $(10\bar{1}0)$	*c* ^ *m*	90° 00′
$(11\bar{2}0)$ ^ $(10\bar{1}0)$	*c* ^ *m*	30° 00′

Figure 1.3 Labeling of planes in hexagonal symmetry (for sapphire).

however, strain and relevant issues must be taken into consideration as the samples are in the form of epitaxial layers on foreign substrates. The accuracy of the X-ray diffraction and less than accurate knowledge of elastic parameters together allow determination of the composition to only within about 1% molar fraction. In addition to composition, the lattice parameter can be affected by free charge, impurities, stress, and temperature [3]. Because the *c*/*a* ratio also correlates with the difference of the electronegativities of the two constituents, components with the greatest differences show largest departure from the ideal *c*/*a* ratio [4].

The nomenclature for various commonly used planes of hexagonal semiconductors in two- and three-dimensional versions is presented in Figures 1.3 and 1.4. The Wz ZnO lacks an inversion plane perpendicular to the *c*-axis; thus, surfaces have either a group II element (Zn, Cd, or Mg) polarity (referred to as Zn polarity) with a

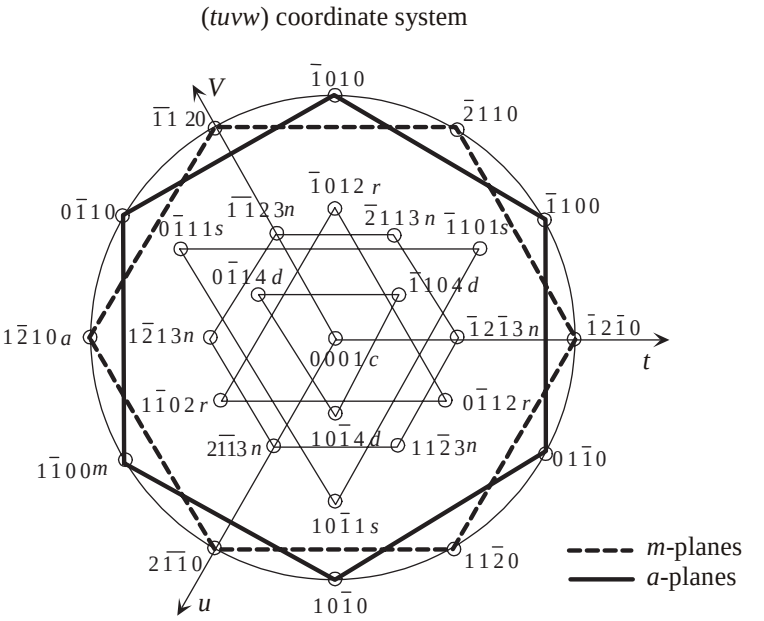

Figure 1.4 A magnified view of labeling of planes in hexagonal symmetry in the (*tuvw*) coordinate system with *w* representing the unit vector in the *c*-direction. The lines simply show the symmetry only. If the lines connecting *m*-points among each other and *a*-points among each other were to be interpreted as the projection of those planes on the *c*-plane, the roles would be switched in that the lines connecting the *m*-points would actually represent the *a*-planes and lines connecting the *a*-points would actually represent the *m*-planes, which are normal to the plane of the page.

designation of $(0\,0\,0\,1)$ or $(0\,0\,0\,1)A$ plane or an O polarity with a designation of $(0\,0\,0\,\bar{1})$ or $(0\,0\,0\,\bar{1})B$ plane. The distinction between these two directions is essential due to polarization charge. Three surfaces and directions are of special importance, which are $(0\,0\,0\,1)$, $(1\,1\,\bar{2}\,0)$, and $(1\,\bar{1}\,0\,0)$ planes and the directions associated with them, $\langle 0\,0\,0\,1\rangle$, $\langle 1\,1\,\bar{2}\,0\rangle$, and $\langle 1\,\bar{1}\,0\,0\rangle$, as shown in Figure 1.5. The $(0\,0\,0\,1)$, or the basal plane, is the most commonly used surface for growth. The other two are important in that they represent the primary directions employed in reflection high-energy electron diffraction (RHEED) observations in MBE growth, apart from being perpendicular to one another.

The *zinc blende* ZnO structure is metastable and can be stabilized only by heteroepitaxial growth on cubic substrates, such as ZnS [5], GaAs/ZnS [6], and $Pt/Ti/SiO_2/Si$ [7], reflecting topological compatibility to overcome the intrinsic tendency of forming wurtzite phase. In the case of highly mismatched substrates, there is usually a certain amount of zinc blende phase of ZnO separated by crystallographic defects from the wurtzite phase. The symmetry of the zinc blende structure is given by space group $F\bar{4}3m$ in the Hermann–Mauguin notation and T_d^2 in the Schoenflies notation and is composed of two interpenetrating face-centered cubic (fcc) sublattices shifted along the body diagonal by one-quarter of the length of

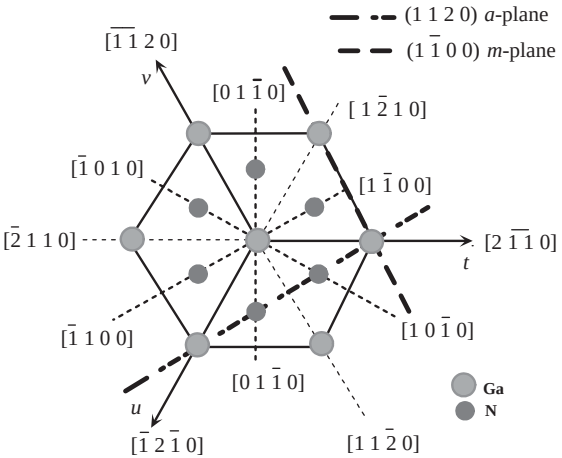

Figure 1.5 Orientations that are commonly used in wurtzite phase, namely, the $(1\,1\,\bar{2}\,0)$ and $(1\,\bar{1}\,0\,0)$ planes and associated directions are shown as projections on the (0 0 0 1) basal plane.

the body diagonal. There are four atoms per unit cell and every atom of one type (group II) is tetrahedrally coordinated with four atoms of other type (group VI), and vice versa.

Because of the tetrahedral coordination of wurtzite and zinc blende structures, the 4 nearest neighbors and 12 next-nearest neighbors have the same bond distance in both structures. Stick-and-ball stacking models for 2H wurtzitic and 3C zinc blende polytypes of ZnO crystals are shown in Figure 1.6. The wurtzite and zinc blende structures differ only in the bond angle of the second-nearest neighbors and, therefore, in the stacking sequence of close-packed diatomic planes. The wurtzite structure consists of triangularly arranged alternating biatomic close-packed (0 0 0 1) planes, for example, Zn and O pairs; thus, the stacking sequence of the (0 0 0 1) plane is AaBbAaBb. . . in the $\langle 0\,0\,0\,1\rangle$ direction, meaning a mirror image but no in-plane rotation with the bond angles. In contrast, the zinc blende structure along the [1 1 1] direction exhibits a 60° rotation and, therefore, consists of triangularly arranged atoms in the close-packed (1 1 1) planes along the $\langle 1\,1\,1\rangle$ direction that causes a stacking order of AaBbCcAaBbCc. . .. The point with regard to rotation is very well illustrated in Figure 1.6b. Upper and lower case letters in the stacking sequences stand for the two different kinds of constituents.

Like other II–VI semiconductors, wurtzite ZnO can be transformed to the *rocksalt* (NaCl) structure at relatively modest external hydrostatic pressures. The reason for this is that the reduction of the lattice dimensions causes the interionic Coulomb interaction to favor the ionicity more over the covalent nature. The space group symmetry of the rocksalt type of structure is $Fm3m$ in the Hermann–Mauguin notation and O_h^5 in the Schoenflies notation, and the structure is sixfold coordinated. However, the rocksalt structure cannot be stabilized by the epitaxial growth. In ZnO, the pressure-induced phase transition from the wurtzite (B4) to the rocksalt (B1)

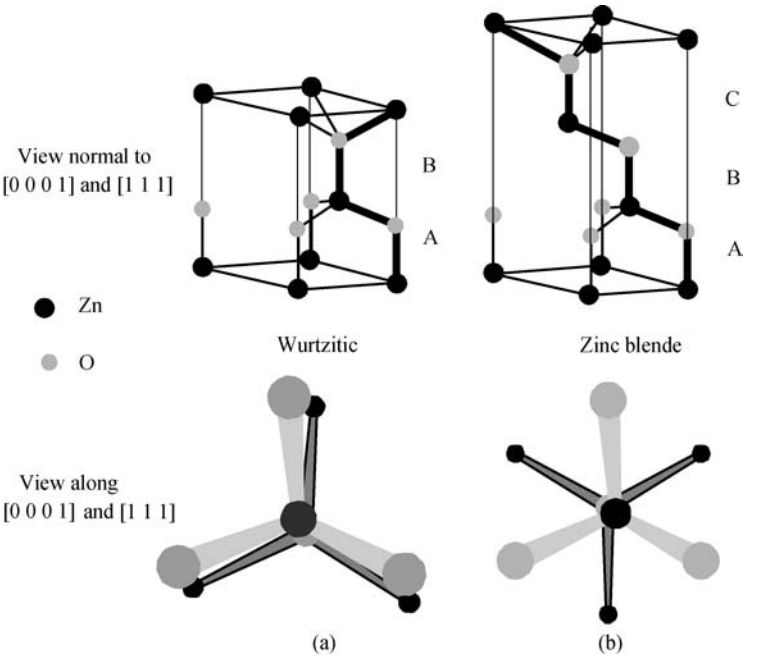

Figure 1.6 Stick-and-ball stacking model of crystals with (a, both top and bottom) 2H wurtzitic and (b, both top and bottom) 3C zinc blende polytypes. The bonds in an *A*-plane $(1\,1\,\bar{2}\,0)$ are indicated with heavier lines to accentuate the stacking sequence. The figures on top depict the three-dimensional view. The figures at the bottom indicate the projections on the (0 0 0 1) and (1 1 1) planes for wurtzitic and cubic phases, respectively. Note the rotation in the case of zinc blende along the $\langle 1\,1\,1 \rangle$ direction.

phase occurs in the range of 10 GPa associated with a large decrease in volume of about 17% [8]. High-pressure cubic phase has been found to be metastable for long periods of time even at ambient pressure and above 100 °C [8]. Energy-dispersive X-ray diffraction (EDXD) measurements using synchrotron radiation have shown that the hexagonal wurtzite structure of ZnO undergoes a structural phase transformation with a transition pressure $p_T = 10$ GPa and completed at about 15 GPa [9, 10]. The measured lattice-plane spacings as a function of pressure for the B1 phase are shown in Figure 1.7. Accordingly, a large fraction of the B1 phase is retained when the pressure is released indicating the metastable state of the rocksalt phase of ZnO even at zero pressure.

In contrast, using *in situ* X-ray diffraction [11], and later EDXD [12], this transition was reported to be reversible at room temperature. EDXD spectra recorded at pressures ranging from 0.1 MPa to 56 ± 1 GPa at room temperature with increasing and decreasing pressures show a clear wurtzite-to-rocksalt transition starting at 9.1 ± 0.2 GPa with increasing pressure. The two phases coexist over a pressure range of 9.1–9.6 GPa, as shown in Figure 1.8. The structural transition is complete at 9.6 GPa resulting in a 16.7% change in the unit cell volume. Upon decompression, it was observed that ZnO reverts to the wurtzite structure beginning at 1.9 ± 0.2 GPa,

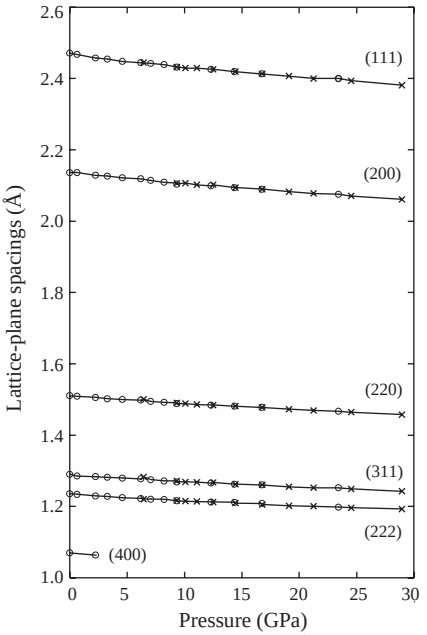

Figure 1.7 Lattice-plane spacing as functions of pressure for the ZnO B1 phase. Crosses denote increasing pressure and circles decreasing pressure. Miller indices *hkl* are indicated for each set of data. (Courtesy of J.M. Recio [10].)

below which only a single wurtzite phase is present. Consequently, the phase hysteresis is substantial. Similar hysteresis was also reported for this transition using X-ray diffraction and Zn Mössbauer spectroscopy [13]. The transition pressure was measured to be 8.7 GPa for increasing pressure whereas it was 2.0 GPa for decreasing pressure.

On the theoretical side, there have been several first-principles studies of compressive parameters of dense ZnO, such as the linear combination of Gaussian-type orbitals (LCGTO), the Hartree–Fock (HF) method [20], the full-potential linear muffin-tin orbital (FP-LMTO) approach to density functional theory (DFT) within the local density approximation (LDA) and generalized gradient approximation (GGA) [14], linear augmented plane wave (LAPW) LDA [13], HF [15], correlated HF perturbed ion (HF-PI) models [10], LCGTO-LDA and GGA methods [10], and the extended ionic model [16]. A critical comparison between experimental and theoretical results can be made for ZnO as the structural and compressive parameters are measured because the dense solid adopts simple structures. These calculations have mostly been limited to the same pressure range as the experiments, and reasonable agreements are realized. Both experimental and theoretical results are summarized in Table 1.1 for comparison.

In addition to the commonly observed and calculated phase transition of ZnO from B4 to B1 at moderate pressures (maximum pressure attained in any experiment on

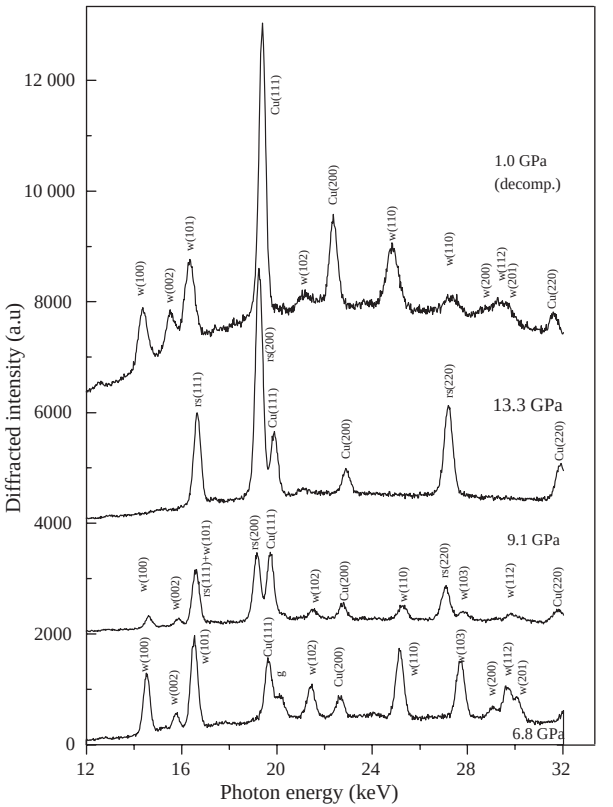

Figure 1.8 Examples of EDXD spectra indicating the coexistence of the wurtzite and rocksalt phases around 9.1 ± 0.2 GPa (increasing pressure) and the emergence of the wurtzite phase $P < 1.9 \pm 0.2$ GPa upon decompression. Spectra are presented in cascade for clarity. Labels w and rs refer to wurtzite and rocksalt, respectively. X-ray diffraction lines from the Cu pressure gauge and the gasket material are labeled as Cu and g, respectively. (Courtesy of S. Desgreniers [12].)

ZnO to date is 56 GPa where the B1 phase remained stable), it has been suggested [17] that at sufficiently high pressures ZnO would undergo a phase transformation from the sixfold-coordinated B1 (cubic NaCl) to the eightfold-coordinated B2 (cubic CsCl) structure, in analogy to the alkali halides and alkaline earth oxides. The transition pressure from B1 phase to B2 phase was predicted at $p_{T2} = 260$ and 256 GPa by employing local density approximation and generalized gradient – corrected local density – approximation, respectively [18], whereas atomistic calculations based on an interatomic pair potential within the shell model approach resulted in a higher value of $p_{T2} = 352$ GPa [19]. However, these theoretical predictions are still awaiting experimental confirmation.

The ground-state total energy of ZnO in wurtzite, zinc blende, and rocksalt structures has been calculated as a function of the unit cell volume using first-principles periodic Hartree–Fock linear combination of atomic orbitals (LCAO)

Table 1.1 Theoretical and experimental compressive parameters of ZnO.

	Experimental results					Theoretical calculations				
	Ref. [8]	**Ref. [9]**	**Ref. [11]**	**Ref. [12]**	**Ref. [13]**	**Ref. [13]**	**Ref. [14]**	**Ref. [17]**	**Ref. [19]**	**Ref. [20]**
Volume, wurtzite ($Å^3$)	23.829	23.785		23.81	23.796		23.62	23.346	23.839	24.570
Volume, rocksalt ($Å^3$)	19.60	19.60	19.40	19.60	19.484		19.08	19.515	19.041	19.799
Volume change, $\Delta V/V$ (%)	16.7	18.0		17.68	18.13	17.9	18.8	16.41	20.3	19.42
Transition pressure, p_T (GPa)	9.5	10.0	9.0	9.1	8.7	14.5	8.0	9.32	10.45	8.57

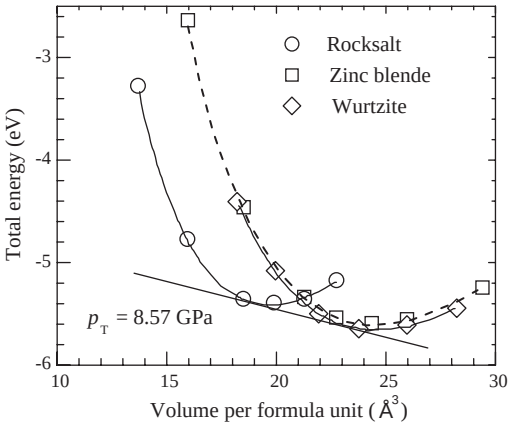

Figure 1.9 Total energy versus volume (both per ZnO formula unit) for the three phases: zinc blende (squares), wurtzite (diamonds), and rocksalt (circles). The zero of energy is the sum of the total energies of an isolated Zn and an isolated O atom. The hexagonal/cubic phase transition occurs at $p_T = 8.57$ GPa. (After Ref. [20].)

theory [20]. The total energy data versus volume for the three phases are shown in Figure 1.9 along with the fits to the empirical functional form of the third-order Murnaghan equation, which is used to calculate the derived structural properties:

$$E(V) = E_0 - \frac{B_0 V_0}{B' - 1} + \frac{B_0 V}{B'}\left[\frac{(V_0/V)^{B'}}{B' - 1} + 1\right], \tag{1.5}$$

where E_0, V_0, and B_0 are the total energy, volume per ZnO formula unit, and bulk modulus at zero pressure (P), respectively, and $B' = \mathrm{d}B/\mathrm{d}P$ is assumed to be constant.

In this calculation, although E_0 represents the sum of the total energies of isolated neutral Zn and O atoms, the absolute value of the energy at the minimum of each curve was considered as a rough estimate of the equilibrium cohesive energy of the corresponding ZnO phases. The total energy (or roughly the cohesive energy per bond) in wurtzite variety was calculated to be -5.658 eV for wurtzite, -5.606 eV for zinc blende, and -5.416 eV for rocksalt phases. The density functional theory using two different approximations, namely, the local density and the generalized gradient approximations, in the exchange correlation function was also employed to calculate the total energy and electronic structure of ZnO [18]. In these calculations, cohesive energies were obtained by subtracting the total energy per ZnO formula unit of the solid at its equilibrium lattice constant from the energy of the corresponding isolated atoms. The cohesive energies of ZnO obtained by using the LDA are -9.769, -9.754, and -9.611 eV for wurtzite, zinc blende, and rocksalt structures, respectively. The best agreement with the experimental value of -7.52 eV, which is deduced from experimental Zn heat vaporization, ZnO enthalpy of formation, and O_2 binding energy for the wurtzite phase [21], was achieved using the GGA technique. The GGA

gives −7.692, −7.679, and −7.455 eV cohesive energies for wurtzite, zinc blende, and rocksalt phases, respectively. In these two techniques, although the calculated energy difference ΔE_{W-ZB} between wurtzite and zinc blende lattice is small (about −15 and −13 meV atom^{-1} for LDA and GGA, respectively), whereas it is relatively large, ∼50 meV atom^{-1}, for Hartree–Fock approximation, the wurtzite form is energetically favorable compared to zinc blende and rocksalt forms.

Because none of the three structures described above possesses inversion symmetry, the crystal exhibits crystallographic polarity, which indicates the direction of the bonds; that is, close-packed (1 1 1) planes in zinc blende and rocksalt (Rochelle salt) structures and corresponding (0 0 0 1) basal planes in the wurtzite structure differ from $(\bar{1}\ \bar{1}\ \bar{1})$ and $(0\,0\,0\,\bar{1})$ planes, respectively. The convention is that the [0 0 0 1] axis points from the face of the O plane to the Zn plane and is the positive *z*-direction. In other words, when the bonds along the *c*-direction are from cation (Zn) to anion (O), the polarity is referred to as Zn polarity. By the same argument, when the bonds along the *c*-direction are from anion (O) to cation (Zn), the polarity is referred to as O polarity. Many properties of the material depend also on its polarity, for example, growth, etching, defect generation and plasticity, spontaneous polarization, and piezoelectricity. In wurtzite ZnO, besides the primary polar plane (0 0 0 1) and associated direction ⟨0 0 0 1⟩, which is the most commonly used surface and direction for growth, many other secondary planes and directions exist in the crystal structure.

1.2 Lattice Parameters

Lattice parameters of ZnO have been investigated over many decades [22–30]. The lattice parameters of a semiconductor usually depend on the following factors: (i) free electron concentration acting via deformation potential of a conduction band minimum occupied by these electrons, (ii) concentration of foreign atoms and defects and their difference of ionic radii with respect to the substituted matrix ion, (iii) external strains (e.g., those induced by substrate), and (iv) temperature. The lattice parameters of any crystalline material are commonly and most accurately measured by high-resolution X-ray diffraction (HRXRD) using the Bond method [31] for a set of symmetrical and asymmetrical reflections. Table 1.2 tabulates measured and calculated lattice parameters, c/a ratio, and u parameter reported by several groups for ZnO crystallized in wurtzite, zinc blende, and rocksalt structures for comparison.

The room-temperature lattice constants determined by various experimental measurements and theoretical calculations for the wurtzite ZnO are in good agreement with each other. The lattice constants mostly range from 3.2475 to 3.2501 Å for the *a*-parameter and from 5.2042 to 5.2075 Å for the *c*-parameter. The data produced in earlier investigations, reviewed by Reeber [30], are also consistent with the values given in Table 1.2. The c/a ratio and u parameter vary in a slightly wider range, from 1.593 to 1.6035 and 0.383 to 0.3856, respectively. The deviation from that of the ideal wurtzite crystal is probably due to lattice stability and ionicity. It has been reported that free charge is the dominant factor responsible for expanding

Table 1.2 Measured and calculated lattice constants and the *u* parameter of ZnO.

Wurtzite				
***a* (Å)**	***c* (Å)**	***c*/*a***	***u***	**Reference**
		1.633	0.375	Ideal
3.2496	5.2042	1.6018	0.3819	[a]
3.2501	5.2071	1.6021	0.3817	[b]
3.286	5.241	1.595	0.383	[c]
3.2498	5.2066	1.6021		[d]
3.2475	5.2075	1.6035		[e]
3.2497	5.206	1.602		[f]
		1.593	0.3856	[g]
		1.600	0.383	[h]

Zinc blende (sphalerite actually)
4.619[c], 4.60[g], 4.463[i], 4.37[i], 4.47[i]

Rocksalt (Rochelle salt)
4.271[a], 4.283[d], 4.294[e], 4.30[g], 4.280[j], 4.275[k], 4.058[k], 4.316[k], 4.207[k], 4.225[l]

[a]Measured by using XRD [13].
[b]Measured by using XRD [4].
[c]Calculated by using *ab initio* periodic LCAO method, based mainly on the Hartree–Fock Hamiltonian, with an all-electron Gaussian-type basis set [32].
[d]Measured by using EDXD [12].
[e]Measured by using XRD [9].
[f]Measured by using XRD [30].
[g]Calculated by using first-principles periodic Hartree–Fock LCOAO program [20].
[h]Calculated by using *ab initio* quantum mechanical level through the Berry phase scheme applied to delocalized crystalline orbitals and through the definition of well-localized Wannier functions [33].
[i]Measured by using RHEED, XRD, and TEM [6].
[j]Measured by using XRD [8].
[k]Measured by using EDXD and calculated by using Coulomb Hartree–Fock perturbed ion, GGA, and LDA methods [10].
[l]Calculated by using first-principles periodic Hartree–Fock [15].

the lattice proportional to the deformation potential of the conduction band minimum and inversely proportional to the carrier density and bulk modulus. The point defects such as zinc antisites, oxygen vacancies, and extended defects, such as threading dislocations, also increase the lattice constant, albeit to a lesser extent in the heteroepitaxial layers.

For the zinc blende polytype of ZnO, the calculated lattice constants based on modern *ab initio* technique are predicted to be 4.60 and 4.619 Å. Zinc blende ZnO films have been grown by using ZnS buffer layers [6]. The lattice constant was estimated to be 4.463, 4.37, and 4.47 Å by using the spacing of RHEED pattern, albeit spotty, comparing the XRD peak position, and examining the transmission electron microscopy (TEM) images, respectively. These values are far from wurtzite phase indicating the formation of zinc blende ZnO. The lattice constant measured with the RHEED technique is in very good agreement with the theoretical predictions.

High-pressure phase transition from the wurtzite to the rocksalt structure decreases the lattice constant down to the range of 4.271–4.294 Å. The experimental values obtained by X-ray diffraction are in close agreement. The predicted lattice parameters of 4.058–4.316 Å, using various calculation techniques such as the HF-PI, GGA, and HF, are about 5% smaller or larger than the experimental values. The dispersion in the calculated values is larger than the measured ones.

The ideal relationship between the c/a axial ratio and the u oxygen positional parameter is preserved as the wurtzite ZnO lattice becomes denser while approaching the structural transition pressure [12]. The change in the c/a axial ratio was measured up to $\sim$10 GPa, and a pressure coefficient of $\mathrm{d}(c/a)/\mathrm{d}P = -0.0005$ $0.0001\,\mathrm{GPa}^{-1}$ was obtained from a linear fit (giving $c/a = 1.6021$ at atmospheric pressure) to the experimental data. Even though the variation with pressure seems within the experimental error, this pressure coefficient is in agreement with the previously published experimental ($-0.0007\,\mathrm{GPa}^{-1}$) [13] and predicted ($-0.0005$ GPa^{-1}) [20] values. The effect of pressure-induced change in the axial ratio on the u parameter against a possible breakdown of the ideal relationship between the axial ratio and u was isolated by recording pressure dependence variation of X-ray diffraction intensity.

1.3 Electronic Band Structure

The band structure of a given semiconductor is pivotal in determining its potential utility. Consequently, an accurate knowledge of the band structure is critical if the semiconductor in question is to be incorporated in the family of materials considered for device applications. Several theoretical approaches with varying degrees of complexity have been employed to calculate the band structure of ZnO for its wurtzite, zinc blende, and rocksalt polytypes. Besides, a number of experimental data have been published regarding the band structure of the electronic states of wurtzite ZnO. X-ray or UV reflection/absorption or emission techniques have conventionally been used to measure the electronic core levels in solids. These methods basically measure the energy difference by inducing transitions between electronic levels (e.g., transitions from the upper valence band states to the upper conduction band states and from the lower valence band states) or by exciting collective modes (e.g., the upper core states to the lower edge of the conduction band and to excitations of plasmons). Another important method for the investigation of the energy region is based on the photoelectric effect extended to the X-ray region, namely, photoelectron spectroscopy (PES). The peaks in emission spectrum correspond to electron emission from a core level without inelastic scattering, which is usually accompanied by a far less intense tail region in the spectrum. Additionally, angle-resolved photoelectron spectroscopy (ARPES) technique together with synchrotron radiation excitation have been recognized as a powerful tool that enables the determination of experimental bulk and surface electronic band structures under the assumptions of k-conservation and single

nearly free-electron-like final band [34]. After the first theoretical work on band structure calculation of ZnO proposed by Rössler using Green's function (Korringa–Kohn–Rostoker (KKR) method) [35] in 1969, several experimental works [36–39] have been performed on the wurtzite ZnO, which proved Rössler's predicted bulk electronic structure to be far from satisfactory. The first experimental data related to the energy levels of core electrons in ZnO were obtained by using X-ray induced photoemission spectroscopy [36]. Consequently, the location of the Zn 3d level in ZnO was unambiguously determined and the discrepancy between the measured values and the theoretically determined energy values was found to be dependent on angular momentum. UV photoemission measurements on hexagonal ZnO cleaved in vacuum showed the Zn 3d core level at about 7.5 eV below the valence band maximum [37, 38], which is 3 eV lower than the value predicted by Rössler's band calculation. This assignment is in good agreement with X-ray photoemission measurements that produced 8.5 eV [40] and 8.81 eV [39]. In the ensuing years, local density approximation and tight-binding methods were carried out [41–44] by considering the Zn 3d states as core levels to simplify calculations. Satisfactory agreement with qualitative valence band dispersions was achieved with this assumption. However, quantitative disagreements remained and the location of the Zn 3d states could not be predicted. With the advent of new computer capabilities, theoretical works began to include the effect of Zn 3d level in the calculations and thus considering them as valence band states [45–48]. These methods enable an estimation of the position of the Zn 3d states and also take into account their non-negligible influence on the s- and p-derived valence bands.

Angle-resolved photoelectron spectroscopy has been employed to study the electronic structure of the ZnO (0 0 0 1) [49]. Recording both normal and off-normal emission spectra gives valuable information about bulk and surface states as well as the Zn 3d states. Figure 1.10 shows some of the normal emission spectra recorded at photon energies ranging from 20 to 50 eV and the information extracted from these data for bulk band structure. In these measurements, the binding energies were referred to the Fermi level and the intensities were normalized to the photon flux. Among all the spectra displayed, seven features were observed, labeled from A to G. The dispersions of the four valence bands observed in the (0 0 0 1) direction were compared with theory based on LDA calculations, which consider the Zn 3d electrons as part of the valence band [45] and good agreement was realized. It should also be noted that the Zn 3d states were observed to separate into two groups of four and six bands, which show dispersion with k, which is in agreement with theoretical results, but the locations of these states (about 10.5 eV below Fermi level) were not accurately predicted.

The polar (0 0 0 1)-Zn and $(0\,0\,0\,\bar{1})$-O surfaces and the nonpolar $(1\,0\,\bar{1}\,0)$ surface (m-plane) have also been the object of experimental and theoretical investigations. Of these surfaces, the nonpolar $(1\,0\,\bar{1}\,0)$ surface is of particular interest from the viewpoint of surface chemistry, because the surface is terminated with the same number of O and Zn atoms. The low-energy electron diffraction (LEED) studies have revealed that the surface undergoes relaxation, which is characterized by downward shift (spatially) of both surface Zn and O atoms, with a greater shift for the Zn atom

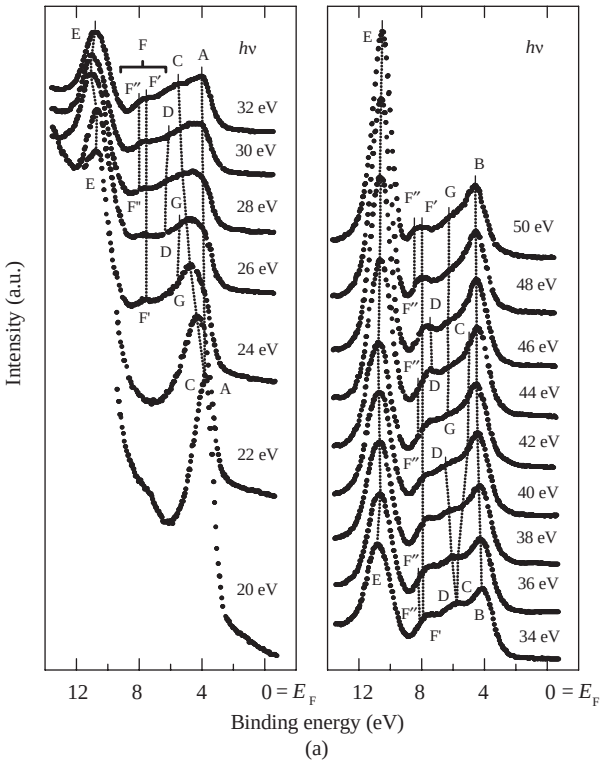

Figure 1.10 (a) Normal emission spectra for photon energies ranging between 20 and 50 eV. The spectra were normalized with respect to the photon flux. (b) Bulk band structure of ZnO, Γ*A* corresponding to 0.6 $Å^{-1}$. (After Ref. [49].) The dashed lines are the LDA calculation results reproduced from Schröer *et al.* [45].

than the O atom, resulting in the Zn−O bond rotation by 6.2° [50] or 11.5° [51] with respect to the ideal surface plane. Such a surface relaxation should influence the energetic position as well as the dispersion width of the surface dangling bond bands of the occupied O 2p and unoccupied Zn 4s states. Besides, several theoretical studies have indicated that, upon relaxation, the O 2p dangling bond state is stabilized while the Zn 4s dangling bond state shifts up in energy [43, 47, 52]. The theoretically determined position of these dangling bond bands, especially the occupied O 2p dangling bond band, relative to the bulk bands projected onto the $(1\,0\,\bar{1}\,0)$ surface varies depending on the method employed in the calculations.

Surface states have been revealed in ARPES studies of both polar and nonpolar ZnO surfaces. In one particular study [53], two surface-induced features at the Γ, *M*, and *X* points of the surface Brillouin zone (BZ) have been identified and assigned to the O 2p-derived dangling bond state and the Zn–O backbond state. Similarly, the

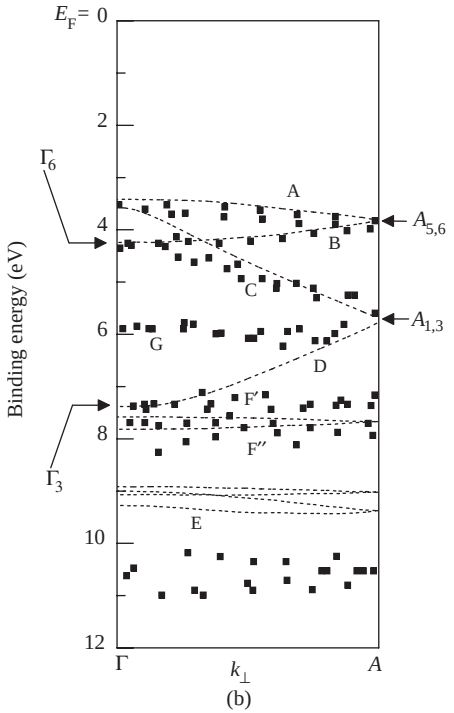

Figure 1.10 (*Continued*)

off-normal ARPES spectra recorded in the $\bar{\Gamma}\bar{M}$, $\bar{\Gamma}\bar{K}$, and $\bar{K}\bar{M}$ directions, for 20, 34, and 44 eV photon energies and emission angles ranging between 0 and 30° revealed two surface states on the (0 0 0 1) surface [49]. One of these states, with a 7.5 eV binding energy as predicted by theory, was interpreted as arising from the "backbondings" of the Zn 4s–O 2p mixed bulk states. The other state at 4.5 eV below the Fermi level, which was not predicted by theoretical calculations, was related to Zn 4p–O 2p-derived states. However, in another ARPES study on ZnO $(1\,0\,\bar{1}\,0)$ surface [54], where the valence band structure along the ΓM axis of the bulk BZ was revealed, no surface-related states were identified and all the observed peaks were attributed to the bulk band transitions.

Detailed ARPES study has been performed to investigate the two-dimensional band structure of the O 2p dangling bond state on the ZnO $(1\,0\,\bar{1}\,0)$ surface along the selected high-symmetry axes of the surface BZ, that is, the $\bar{\Gamma}\bar{X}$ and $\bar{\Gamma}\bar{X}'$ axes [55]. The energetic position relative to the projected bulk bands and the dispersion of the dangling bond band were determined and compared well with the calculated band structures [47, 52]. Figure 1.11 shows off-normal emission spectra taken at various detection angles along the $[1\,\bar{2}\,1\,0](\bar{\Gamma}\bar{X})$ and $[0\,0\,0\,1]$ $(\bar{\Gamma}\bar{X}')$ azimuths and measured dispersion of the O 2p dangling bond state and the bulk band related states along the $\bar{\Gamma}\bar{X}$ and $\bar{\Gamma}\bar{X}'$ axes together with theoretical calculations for comparison.

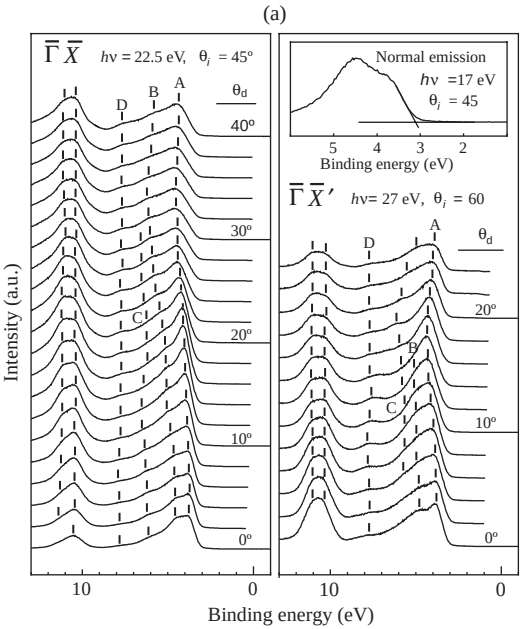

Figure 1.11 (a) Off-normal emission spectra of the clean surface recorded at $h\nu = 22.5$ eV and $\theta_i = 45^\circ$ along the $[1\ \bar{2}\ 1\ 0]$($\bar{\Gamma}\bar{X}$) direction and at $h\nu = 27$ eV and $\theta_i = 60^\circ$ along the [0 0 0 1] ($\bar{\Gamma}\bar{X}'$)direction. The incidence plane of the light was parallel to the $[1\ \bar{2}\ 1\ 0]$ direction for both detection directions. The spectra are shown with a 2° interval. Peak positions, indicated by vertical bars, were determined from the second derivative of the spectra. The position of the valence band maximum was determined from the normal emission spectrum taken at $h\nu = 17$ eV by extrapolating the onset of the valence band emission as shown in the inset of the right panel. (Courtesy of K. Ozawa [55].) (b) Measured dispersion of the O 2p dangling bond state (open circles) and the bulk band related states (filled circles) along the $\bar{\Gamma}\bar{X}$ and $\bar{\Gamma}\bar{X}'$ axes. (Courtesy of K. Ozawa [55].) Hatched area corresponds to the projected bulk band region and a bold dashed line indicates the O 2p dangling bond bands, both of which have been calculated by using the sp^3 model by Wang and Duke [52]. Thin dashed lines located above the projected bulk bands are the dangling bond bands obtained from the LDA calculations [47].

From photon energy dependent measurements and K and O_2 adsorption studies, it has been found that the surface-localized O 2p dangling bond state exists at 3.7 eV below the Fermi level at the $\bar{\Gamma}$ point in the surface Brillouin zone and shifts to the higher binding energy side by 0.8 and 0.5 eV along the $\bar{\Gamma}\bar{X}$ and $\bar{\Gamma}\bar{X}'$ axes, respectively. Measurements on K and O_2 exposed ZnO $(1\ 0\ \bar{1}\ 0)$ surfaces helped to identify which peaks in the angle-resolved photoelectron spectra were associated with the states localized at the surface. The O 2p dangling bond band was found located below the upper edge of the projected bulk bands along these two high-symmetry axes. The empirical tight-binding calculations, which emphasize the ionic [43] and covalent [52] characters of the Zn–O bonds, predict that the gap state by the O 2p dangling bond is not formed at least along the $\bar{\Gamma}\bar{X}$ and $\bar{\Gamma}\bar{X}'$ axes. On the contrary, calculations using LDA [47] indicate that the dangling bond band is formed within the gap above the

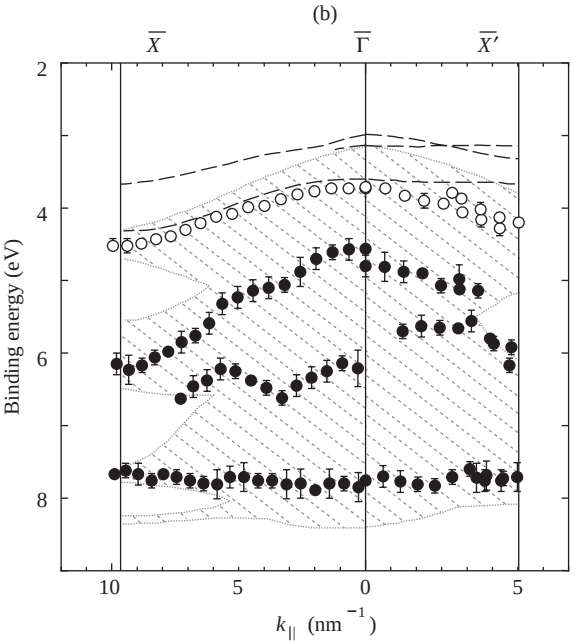

Figure 1.11 (*Continued*)

upper edge of the projected bulk bands along the major high-symmetry axes of the surface BZ. Therefore, it has been concluded that the experimental study is consistent qualitatively with the band structure given by two empirical tight-binding approaches.

The theoretical calculation of the band structure of ZnO mostly involves the local density approximation [45, 56–58], which is very demanding because of the cationic d electrons. If the d electrons are treated as core electrons, the calculated lattice constant underestimates the experimental values by as much as 18% for wurtzite ZnO, while inclusion of the d electrons in the valence band yields very accurate lattice constants. However, even if the d electrons are properly taken into account, the results of standard LDA calculations show distinct shortcomings, such as strongly underestimated bandgap and overestimated occupied cationic d bands, which are roughly 3 eV high in energy compared to those of the experiment. In addition, their interactions with the anion p valence bands are artificially enlarged, resulting in overestimated dispersion and bandwidth of the latter and shifting them unphysically close to the conduction bands. For example, the LDA underestimates the ZnO bandgap to be as low as $E_g^{LDA} = 0.23$ eV as opposed to $E_g^{Exp} = 3.37$ eV. However, by carrying out the plane-wave GW calculations deliberately with the experimental lattice constants and simply treating the d electrons as core electrons very close results have been obtained for the anion p valence bands and for the bandgap energies even though no assertion concerning the d band positions could be made [59]. As an

alternative approach for treating the II–VI semiconductors, approximate incorporation of the dominant self-interaction corrections has been suggested [48]. It has been shown that self-interaction corrections to LDA can be very important for a quantitative description of a system with strongly localized states such as 3d electrons. The results along with the LDA calculations without the corrections and the O 2p valence bands in more detail with ARPES data are shown in Figure 1.12 for comparison. The left panel in Figure 1.12a shows the standard LDA result, which reveals the above-mentioned shortcomings. The right panel shows the band structure as calculated with self-interaction corrected pseudopotential (SIC-PP) approach included in the LDA. It has been observed that the d bands are shifted down in energy considerably and concomitantly the bandgap is opened drastically. The dispersion and bandwidth of the O 2p are also changed. Compared to experimental data, the standard LDA result is obscured by the artificially high-lying bands leading to strong p–d interactions with the O 2p bands. The SIC-PP results are in better agreement with experiments. The calculated and measured energy gaps, the position of the cation d band, and anion valence bandwidths of ZnO are given in Table 1.3. Based on this table, the LDA-SIC-PP approximation gives close agreement with the

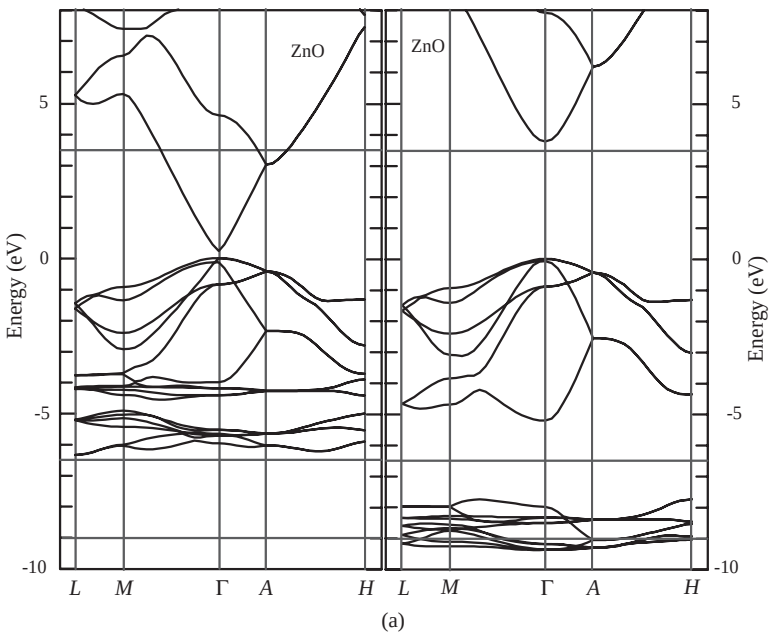

Figure 1.12 (a) LDA bulk band structure of ZnO as calculated by using a standard pseudopotential (PP) (left panel) and by using SIC-PP (right panel). The horizontal dashed lines indicate the measured gap energy and d-band width. (b) Comparison of calculated and measured valence bands of ZnO. The left panel shows the standard LDA, while the right panel shows SIC-PP results. (Courtesy of J. Pollmann [48].)

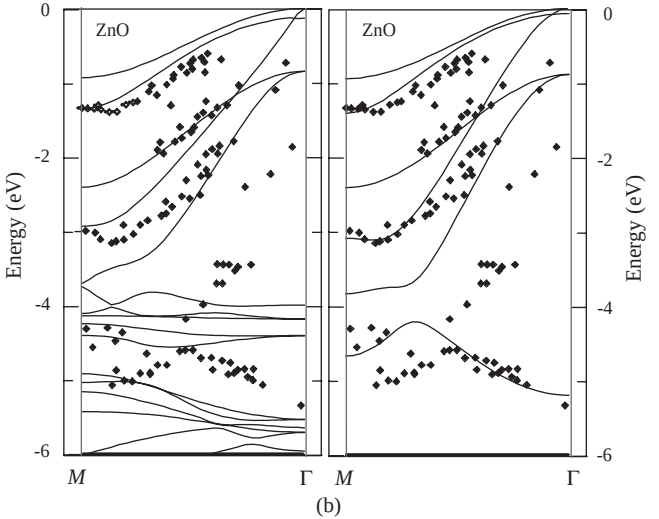

Figure 1.12 (*Continued*)

experimental results for bandgap and bandwidth compared to the standard LDA method. However, the d bands result in energy roughly 1 eV too low compared to the experimental value. This deviation was attributed to the measured exciton energies influenced by electronic relaxations, which is expected to be mostly pronounced for the highly localized cationic semicore d states.

The band structure of ZnO reveals three very closely spaced valence bands (usually referred to as the A, B, and C bands, or the heavy-hole, light-hole, and crystal field split-off bands, respectively, resulting from the spin–orbit coupling and crystal field splitting) near the zone center (Γ point), the details of which will be discussed in Chapter 3. Figure 1.13 shows the valence band structure of ZnO near the Γ point calculated using the atomic sphere approximation (ASA) and linearized muffin-tin orbital (LMTO) methods within the LDA [60]. The splitting energies between the A, B, and C bands have been calculated to be small, with $E_{AB} = 10$ meV and $E_{BC} = 34$

Table 1.3 Calculated and measured energy gaps E_g, cation d-band positions E_d, and anion p valence bandwidths W_p (all in eV) of ZnO.

	LDA-PP	LDA-SIC-PP	Experiment
E_g	0.23	3.77	3.4
E_d	−5.1	−8.9	−7.8
W_p	−3.99	−5.2	−5.3

After Ref. [48]. LDA-PP: local density approximation – pseudopotential. LDA-SIC-PP: local density approximation – self-interaction corrected pseudopotential.

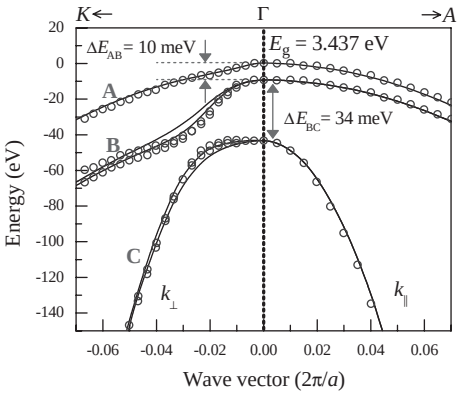

Figure 1.13 Valence band structure of ZnO near the Γ point. The open circles represent the calculation results using the ASA–LMTO method including spin–orbit coupling. The solid lines are fits to the Rashba–Sheka–Pikus effective Hamiltonian. (After Ref. [60].)

meV [60], where the experimental bandgap is 3.437 eV [61]. The calculated splitting energies are in good agreement with the experimental values of $E_{AB} = 9.5$ meV and $E_{BC} = 39.7$ meV [61]. The valence band splitting energies measured for several bulk crystals are given in Table 3.1.

The lattice constants change with temperature, as will be discussed in Section 1.6.1, and with pressure as already mentioned in Section 1.2. Consequently, the electronic band structure changes with temperature and pressure. The bandgap (at Γ point) shrinks with increasing temperature and the dependence is given by the empirical relationship [62]

$$E_g(T) = E_g(T=0) - \frac{\alpha T^2}{T+\beta}, \tag{1.6}$$

where the temperature coefficients are $\alpha = -5.5 \times 10^{-4}$ eV K^{-1} and $\beta = -900$ K for temperatures up to 300 K [63]. The excitonic transition energies associated with the A, B, and C valence bands have also been shown to follow the same dependence with $\alpha = -7.2 \times 10^{-4}$ eV K^{-1} and $\beta = -1077$ K [64]. Temperature dependence of the excitonic transitions in ZnO is further discussed in Section 3.2.5. With increasing hydrostatic pressure, the bandgap of wurtzite ZnO shows a sublinear increase [65]. The pressure dependence is well explained by a second-order polynomial, and the pressure coefficients measured at 6 K for the three bandgaps involving A, B, and C valence bands are given in Table 1.4.

To understand the transport phenomena and, for example, calculate the optical gain in semiconductors, the effective mass, which is one of the fundamental quantities in semiconductor physics, should be known for each of the electronic bands participating in the processes under investigation. The effective mass can be obtained from the electronic band structure calculations using the first-principles methods already

Table 1.4 Pressure coefficients for energy gaps associated with the A, B, and C valence bands in single-crystal ZnO measured at 6 K.

	E_g ($P = 0$)	dE/dP (meV GPa^{-1})	d^2E/dP^2 (meV GPa^{-2})
A	3.4410 ± 0.0001	24.7 ± 0.1	-0.28 ± 0.01
B	4.4434 ± 0.0001	25.3 ± 0.1	-0.28 ± 0.01
C	3.4817 ± 0.0002	25.6 ± 0.2	-0.28 ± 0.01

After Ref. [65].

mentioned above. The density functional theory within LDA, which is commonly used for this purpose, underestimates the effective masses in semiconductors as well as the bandgaps. The self-energy corrections using the GW approximation (GWA), however, have been shown to remove the LDA defects and result in quasiparticle effective masses in agreement with the experimental data [66]. Electron and hole effective masses derived from the calculated and measured energy band structures are listed in Table 1.5 [58, 60, 66–80].

The electronic band structure of the other phases of ZnO has also been calculated using various methods [18, 20, 82, 83]. For example, by utilizing both the LDA and the PBE96 forms of the GGA methods together with optimized Gaussian basis sets and by expanding the crystal orbitals and periodic electron density, the electronic structure for the B4 (wurtzite), B3 (zinc blende), B1 (rocksalt), and B2 (CsCl) phases has been calculated over a range of unit cell volumes [18]. Figures 1.14 and 1.15 show the calculated band structure and the total DOS (density of states) of ZnO for different phases. When wurtzite ZnO is compressed, it has been observed that the peak at the top of the upper valence band is slightly reduced in height and shifted down in energy, the O 2s- and Zn 3d-derived peaks are slightly broadened and shifted up in energy, and a splitting appears in the Zn 3d states. While transforming to the B1 structure at the transition pressure p_{T1}, significant changes have been observed; in particular, the peak near the valence band maximum is greatly reduced in height. The Zn 3d peak also becomes narrower, and the O 2s-derived states drop slightly in energy. Upon compression of the B1 phase ZnO through the wide pressure range from p_{T1} to p_{T2}, it has been observed that the upper valence band broadens greatly, the splitting of the Zn 3d peak in the DOS shows a large increase, and the O 2s-derived band moves down in energy and broadens. The fundamental bandgap also increases with increasing pressure in this range. With the B1 $\rightarrow$ B2 transition, the upper valence bandwidth remains almost unchanged but the peak near the valence band maximum reappears. The structure of the Zn 3d states changes radically with the O 2p-derived states because of heavy hybridization, and the O 2s-derived states broaden further and shift up in energy. From these observations of ZnO band structure with compression and changed atomic coordination, it has been argued that the key features are (a) changes in nearest-neighbor bond lengths as they affect overlaps and bandwidths and (b) changes in symmetry as they affect p–d hybridization and band repulsion. As the neighboring atoms approach each other with compression of the solid, basis

Table 1.5 Calculated and measured conduction band (electron) and valence band (hole) effective masses for wurtzite ZnO and rocksalt MgO.

	ZnO (wurtzite)		MgO (rocksalt)
	Calculated	**Experimental**	**Calculated**
$m^*_{e\parallel}$	0.28[b], 0.21[d], 0.30[f], 0.181[g], 0.14[h], 0.14[i], 0.19[j]	0.265[k], 0.24[n], 0.24[o], 0.3[p], 0.210[s]	0.35[t]
$m^*_{e\perp}$	0.24[c], 0.25[d], 0.177[g], 0.13[h], 0.14[i], 0.21[j]	0.24(0.29)[l], 0.28[n], 0.23(0.29)[r], 0.242[s]	
$m^*_{hh\parallel}$	0.67[a], 1.98[b], 2.74[e], 2.45[h], 2.27[i], 0.21[j]	0.45[m], 0.59[o]	1.60 [0 0 1][t], 2.77 [1 1 1][t]
$m^*_{hh\perp}$	0.63[a], 0.54[e], 0.35[i]	0.59[o]	
$m^*_{lh\parallel}$	0.67[a], 3.03[e], 2.98[h], 3.23[i], 4.33[j]	0.45[m], 0.59[o]	0.35 [0 0 1][t], 0.31 [1 1 1][t]
$m^*_{lh\perp}$	0.63[a], 0.55[e], 0.23[h], 0.30[i]	0.59[o]	
$m^*_{ch\parallel}$	0.25[a], 0.27[e], 0.17[h], 0.17[i], 0.33[j]	0.31[o]	
$m^*_{ch\perp}$	2[a], 1.12[e], 0.29[h], 0.54[i], 0.27[j]	0.55[o]	

$\perp$ and $\parallel$ refer to the directions perpendicular and parallel, respectively, to the *c*-axis.

[a] Calculated by using the $k\cdot p$ theory [67].

[b] Calculated by using the first-principles orthogonalized linear combination of atomic orbitals method in the local density approximation. The effective masses were found to be highly anisotropic and the values in the table are for Γ–*A*. Other values are 0.37 (Γ–*K*) and 0.32 (Γ–*M*) for the electron mass and 4.31 (Γ–*K*) and 4.94 (Γ–*M*) for the hole mass [58].

[c] Calculated from first principles: LMTO basis with the ASA and the self-energy correction within the Green function and the screened Coulomb potential approximation (GWA) [68].

[d] Calculated quasiparticle effective masses by using the density functional theory within the local density approximation including the correlation effects in the form of self-energy correction [66].

[e] Calculated by using the ASA and the LMTO density functional theory in the local density approximation [60].

[f] Calculated using the frozen-core projector augmented wave method based upon the DFT with the Perdew–Wang generalized gradient approximation for Γ–*A*. The electron effective masses were 0.31 and 0.32 for Γ–*K* and Γ–*M*, respectively [69].

[g] Calculated by using the $k\cdot p$ and empirical pseudopotential methods [70].

[h] Calculated by using the density functional theory within the LDA.

[i] Generalized gradient approximation.

[j] LDA with the multiorbital mean-field Hubbard potential (LDA + U) [71].

[k] From infrared reflectivity measurements on indium-doped ZnO crystals grown from the vapor phase [72].

[l] From free carrier Faraday rotation for the high-frequency conduction band mass in hydrothermally grown undoped and indium-doped ZnO single crystals. The value in parentheses (0.29) is for the low-frequency polaron mass [73].

[m] From two-photon magnetoabsorption in ZnO single crystals [74].

[n] From cyclotron resonance on bulk ZnO grown by vapor-phase reaction method. The same study also reports electron effective masses of $0.3m_0$ and $0.34m_0$ obtained from Zeemann splitting measurements for $m^*_{e\perp}$ and $m^*_{e\parallel}$, respectively [75].

[o] From Ref. [76].

[p] From far-infrared cyclotron resonance on hydrothermally grown *n*-ZnO (donors originate from O vacancies, excessive Zn and Li) [77].

[r] From infrared cyclotron resonance in n-type ZnO grown by seeded chemical vapor transport method (Eagle–Picher). The value in parentheses (0.29) is the effective polaron mass [78].

[s] Derived by comparing the experimental (ellipsometry on samples grown by chemical vapor transport and hydrothermal (Airtron Industries) methods) [81] and calculated imaginary parts of the dielectric function [79].

[t] From Ref. [80].

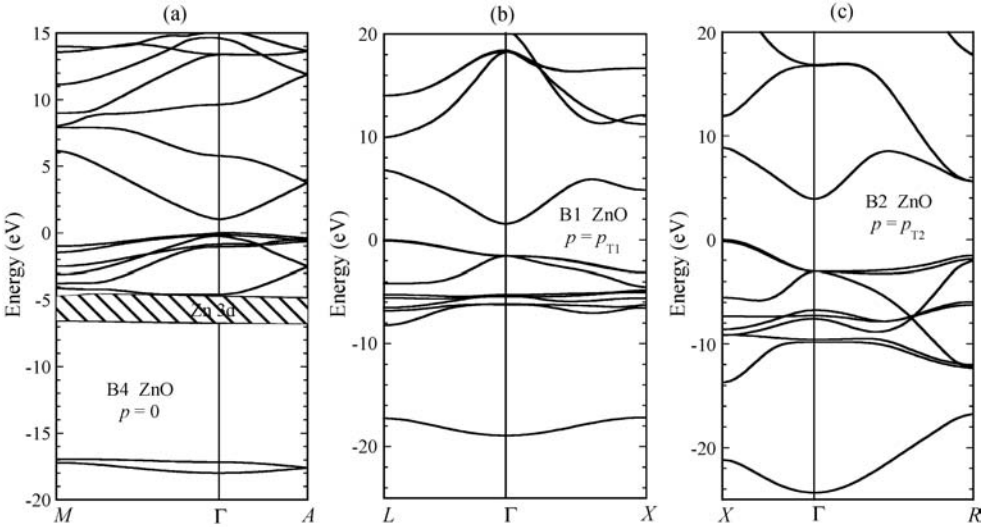

Figure 1.14 Band structure for ZnO: (a) B4 structure at $p = 0$, (b) B1 structure at $p = p_{T1}$, (c) B2 structure at $p = p_{T2}$. (Courtesy of J.E. Jaffe [18].)

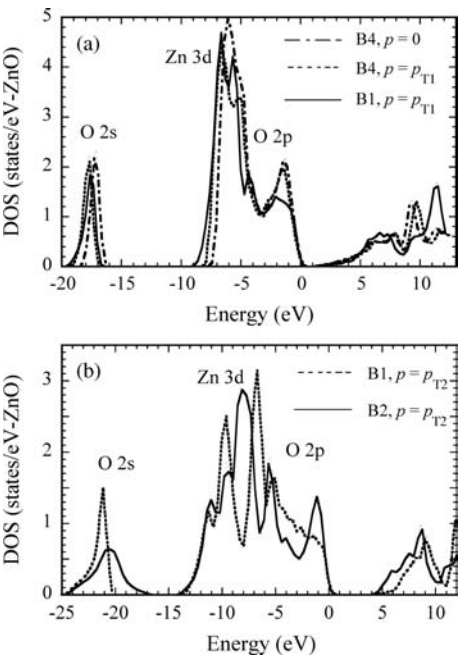

Figure 1.15 Total density of states for ZnO in the (a) B4 structure at $p = 0$ and $p = p_{T1}$ and B1 structure at $p = p_{T1}$, and (b) B1 and B2 structures at $p = p_{T2}$. (Courtesy of J.E. Jaffe [18].)

functions (and orbitals in a Hückel-like picture [84]) overlap more strongly, producing increased dispersion of the electron bands in *k*-space and consequently increased bandwidths along the energy axis.

However, it has also been considered that when there is a phase transition to a structure of increased coordination, the nearest-neighbor bonds lengthen even though the density is increased. The behavior of the bandwidths up to p_{T2} reflects these considerations. The band structures reveal further qualitative changes that occur with the change of symmetry at the structural transitions. Where the symmetry permits hybridization of O 2p- and Zn 3d-derived bands, there is an effective repulsion between them, which pushes the anion 2p states upward. In the tetrahedrally coordinated B4 phase, this repulsion is present throughout the Brillouin zone, but in the cubic B1 and B2 structures it is suppressed near the Γ point as a result of the inversion symmetry through the atomic center. Consequently, the high-energy valence bands are repelled upward near the zone boundaries but not at the zone center, so that the valence band maximum now occurs at the zone boundary. This accounts for the change in shape of the band edge seen in the total DOS plots. There is also a change in the form of the Zn 3d-derived bands, which are now narrowest near the gamma point as a result of the suppressed hybridization there. In the B2 structure, the Zn 3d and O 2p states are completely hybridized and cannot be disentangled.

1.4 Mechanical Properties

The mechanical properties of materials involve various concepts such as hardness, stiffness, and piezoelectric constants, Young's and bulk modulus, and yield strength. The solids are deformed under the effect of external forces and the deformation is described by the physical quantity *strain*. The internal mechanical force system that resists the deformation and tends to return the solid to its undeformed initial state is described by the physical quantity *stress*. Within the elastic limit, where a complete recoverability from strain is achieved with removal of stress, stress σ is proportional to strain ε. The generalized Hooke's law gives each of the stress tensor components as linear functions of the strain tensor components as

$$\sigma_{ij} = C_{ijkl}\varepsilon_{kl}, \tag{1.7}$$

where C_{ijkl} are the elastic *stiffness* coefficients. The inverse relationship may also be written in terms of the elastic *compliance* coefficients S_{ijkl} as

$$\varepsilon_{kl} = S_{ijkl}\sigma_{ij}. \tag{1.8}$$

Since both stress and strain are symmetric with respect to an interchange of the suffixes and the elastic coefficients form symmetric fourth-rank tensors, there are

21 independent elastic coefficients that can be formed into a symmetric 6×6 matrix. In hexagonal crystals, due to additional symmetry, there remains only five independent stiffness constants: C_{11}, C_{33}, C_{12}, C_{13}, and C_{44}. The stress–strain relations for the wurtzite crystal are therefore expressed as (c-axis is chosen to be the z-axis)

$$\begin{pmatrix} \sigma_{xx} \\ \sigma_{yy} \\ \sigma_{zz} \\ \sigma_{yz} \\ \sigma_{zx} \\ \sigma_{xy} \end{pmatrix} = \begin{pmatrix} C_{11} & C_{12} & C_{13} & 0 & 0 & 0 \\ C_{12} & C_{11} & C_{13} & 0 & 0 & 0 \\ C_{13} & C_{13} & C_{33} & 0 & 0 & 0 \\ 0 & 0 & 0 & C_{44} & 0 & 0 \\ 0 & 0 & 0 & 0 & C_{44} & 0 \\ 0 & 0 & 0 & 0 & 0 & (C_{11}-C_{12})/2 \end{pmatrix} \begin{pmatrix} \varepsilon_{xx} \\ \varepsilon_{yy} \\ \varepsilon_{zz} \\ \varepsilon_{yz} \\ \varepsilon_{zx} \\ \varepsilon_{xy} \end{pmatrix} \quad \text{(wurtzite)}. \tag{1.9}$$

Similarly, the relations using the compliance matrix can be written as

$$\begin{pmatrix} \varepsilon_{xx} \\ \varepsilon_{yy} \\ \varepsilon_{zz} \\ \varepsilon_{yz} \\ \varepsilon_{zx} \\ \varepsilon_{xy} \end{pmatrix} = \begin{pmatrix} S_{11} & S_{12} & S_{13} & 0 & 0 & 0 \\ S_{12} & S_{11} & S_{13} & 0 & 0 & 0 \\ S_{13} & S_{13} & S_{33} & 0 & 0 & 0 \\ 0 & 0 & 0 & S_{44} & 0 & 0 \\ 0 & 0 & 0 & 0 & S_{44} & 0 \\ 0 & 0 & 0 & 0 & 0 & 2(S_{11}-S_{12}) \end{pmatrix} \begin{pmatrix} \sigma_{xx} \\ \sigma_{yy} \\ \sigma_{zz} \\ \sigma_{yz} \\ \sigma_{zx} \\ \sigma_{xy} \end{pmatrix} \quad \text{(wurtzite)}. \tag{1.10}$$

In zinc blende (cubic) crystals, there are only three independent stiffness constants: C_{11}, C_{12}, and C_{44}. The above relations then take the form

$$\begin{pmatrix} \sigma_{xx} \\ \sigma_{yy} \\ \sigma_{zz} \\ \sigma_{yz} \\ \sigma_{zx} \\ \sigma_{xy} \end{pmatrix} = \begin{pmatrix} C_{11} & C_{12} & C_{12} & 0 & 0 & 0 \\ C_{12} & C_{11} & C_{12} & 0 & 0 & 0 \\ C_{12} & C_{12} & C_{11} & 0 & 0 & 0 \\ 0 & 0 & 0 & C_{44} & 0 & 0 \\ 0 & 0 & 0 & 0 & C_{44} & 0 \\ 0 & 0 & 0 & 0 & 0 & C_{44} \end{pmatrix} \begin{pmatrix} \varepsilon_{xx} \\ \varepsilon_{yy} \\ \varepsilon_{zz} \\ \varepsilon_{yz} \\ \varepsilon_{zx} \\ \varepsilon_{xy} \end{pmatrix} \quad \text{(zinc blende)}, \tag{1.11}$$

$$\begin{pmatrix} \varepsilon_{xx} \\ \varepsilon_{yy} \\ \varepsilon_{zz} \\ \varepsilon_{yz} \\ \varepsilon_{zx} \\ \varepsilon_{xy} \end{pmatrix} = \begin{pmatrix} S_{11} & S_{12} & S_{12} & 0 & 0 & 0 \\ S_{12} & S_{11} & S_{12} & 0 & 0 & 0 \\ S_{12} & S_{12} & S_{11} & 0 & 0 & 0 \\ 0 & 0 & 0 & S_{44} & 0 & 0 \\ 0 & 0 & 0 & 0 & S_{44} & 0 \\ 0 & 0 & 0 & 0 & 0 & S_{44} \end{pmatrix} \begin{pmatrix} \sigma_{xx} \\ \sigma_{yy} \\ \sigma_{zz} \\ \sigma_{yz} \\ \sigma_{zx} \\ \sigma_{xy} \end{pmatrix} \quad \text{(zinc blende)}. \tag{1.12}$$

In the wurtzite phase, elastic constants C_{11} and C_{33} correspond to longitudinal modes along the [1 0 0 0] and [0 0 0 1] directions, respectively. Elastic constants C_{44} and $C_{66} = (C_{11} - C_{12})/2$ (owing to symmetry) can be determined from the sound velocity of transverse modes propagating along the [0 0 0 1] and [1 0 0 0] directions, respectively. The remaining constant C_{13} is present in combination with four other moduli in the velocity of modes propagating in less symmetrical directions, such as [0 0 1 1]. The *bulk modulus* is related to elastic constants by [85]

$$B = \frac{(C_{11} + C_{12})C_{33} - 2C_{13}^2}{C_{11} + C_{12} + 2C_{33} - 4C_{13}}. \tag{1.13}$$

Although the wurtzite ZnO crystal is acoustically anisotropic, there is only a very small difference between the shear sound velocities v_{TA1} and v_{TA2} propagating along the [0 0 1] and [1 0 0] directions, respectively ($v_{TA2}/v_{TA1} \cong 0.98$). In the isotropic approximation, the Young's modulus E (in some texts Y is also used to denote the Young's modulus) and shear modulus G can also be evaluated using the relations $E = 3B(1 - 2\nu)$ and $G = E/2(1 + \nu)$, respectively. The term ν is the Poisson's ratio and is given by $\nu = C_{13}/(C_{11} + C_{12})$.

It has been argued that the most precise technique used to determine the elastic moduli of compound materials is ultrasonic measurement, which requires thick single crystalline samples, about 1 cm thick, to enable precise measurement of the time required for the plane-wave acoustic pulses to propagate through the crystal [86]. The measured quasilongitudinal and quasishear wave velocities can be used in the following equation to determine C_{13} [86]:

$$C_{13} = \frac{1}{\cos\alpha \sin\alpha}\left[(\lambda_{22} - \rho v_q^2)(\lambda_{33} - \rho v_q^2)\right]^{1/2} - C_{44}, \tag{1.14}$$

where for the hexagonal symmetry

$$\begin{aligned} \lambda_{22} &= C_{11}\cos^2\alpha + C_{44}\sin^2\alpha, \\ \lambda_{33} &= C_{44}\cos^2\alpha + C_{33}\sin^2\alpha. \end{aligned} \tag{1.15}$$

Here, α is the angle between the propagation direction and the c-axis, ρ is the mass per unit volume, and v_q is either the quasilongitudinal or the quasishear velocity.

As an optical technique, Brillouin scattering allows the determination of the elastic constants and hence of the bulk moduli through the interaction of light with thermal excitation in a material, in particular acoustic phonons in a crystal. In this technique, the elastic constants C_{11} and C_{66} can be directly obtained from measurement of the phase velocity of the longitudinal mode and of the shear horizontal mode traveling parallel to the crystal surface. The remaining constants,

C_{13}, C_{33}, and C_{44}, can be evaluated from measurement of the phase velocity of the Rayleigh surface wave and of the longitudinal bulk acoustic wave propagating at different angles from the surface normal. Various forms of X-ray diffraction, such as energy dispersive X-ray diffraction, angular dispersive X-ray diffraction (ADX), and X-ray absorption spectroscopy (XAS) can also be employed to determine the pressure dependence of the lattice parameters. From that, experimental equation of state (EOS), a widely used approach being the Murnaghan's equation of state and hence directly the bulk modulus, which is based on the assumption that the bulk modulus has a linear dependence on pressure P, can be deduced as [87]

$$V = V_0\left(1 + \frac{B'P}{B}\right)^{-1/B'}, \tag{1.16}$$

where B and V_0 represent the bulk modulus and unit volume at ambient pressure, respectively, and B' is the derivative of B with respect to pressure. X-ray diffraction leads to the determination of the isothermal bulk modulus, whereas Brillouin scattering leads to the adiabatic one. Nevertheless, in solids other than molecular solids there is no measurable difference between the two thermodynamic quantities. Besides the experimental investigations, many theoretical calculations have also been employed to determine the structural and mechanical properties of ZnO. Most of the calculations are based on density functional theory within the local density approximation using various types of exchange correlation functions and either plane-wave expansion for the pseudopotentials or the LMTO method.

Among the tetrahedrally bonded semiconductors, ZnO has the highest piezoelectric constants with electromechanical coupling larger than that in GaN and AlN [88]. This property makes it a technologically important material for many applications such as piezotransducers that require a large electromechanical coupling, which will be discussed in the context of piezoelectric devices in Section 8.6. In piezoelectric crystals, electrical polarization is produced in the presence of stress, which is described by using the piezoelectric strain coefficients e_{ijk} and piezoelectric stress coefficients d_{ijk} as

$$P_i = e_{ijk}\varepsilon_{jk} = d_{ijk}\sigma_{jk}. \tag{1.17}$$

d_{ijk} are also referred to as electromechanical constants as it is also possible to produce strain when the crystal is subjected to an electric field with components E_k:

$$\varepsilon_{ij} = d_{ijk}E_k. \tag{1.18}$$

Since the stress is a symmetric second-rank tensor, piezoelectric tensor has 18 independent elements forming a 3×6 matrix. Due to crystal symmetry, there remain

only three independent components (e_{31}, e_{33}, and e_{15}) in hexagonal wurtzite phase and one (e_{14}) in the cubic zinc blende phase, which characterize the full piezoelectric tensors of such crystals [89]. The polarization is then written as

$$\begin{pmatrix} P_{xx} \\ P_{yy} \\ P_{zz} \end{pmatrix} = \begin{pmatrix} 0 & 0 & 0 & 0 & e_{15} & 0 \\ 0 & 0 & 0 & e_{15} & 0 & 0 \\ e_{31} & e_{31} & e_{33} & 0 & 0 & 0 \end{pmatrix} \begin{pmatrix} \varepsilon_{xx} \\ \varepsilon_{yy} \\ \varepsilon_{zz} \\ \varepsilon_{xy} \\ \varepsilon_{yz} \\ \varepsilon_{zx} \end{pmatrix} = \begin{pmatrix} 0 & 0 & 0 & 0 & d_{15} & 0 \\ 0 & 0 & 0 & d_{15} & 0 & 0 \\ d_{31} & d_{31} & d_{33} & 0 & 0 & 0 \end{pmatrix} \begin{pmatrix} \sigma_{xx} \\ \sigma_{yy} \\ \sigma_{zz} \\ \sigma_{xy} \\ \sigma_{yz} \\ \sigma_{zx} \end{pmatrix} \quad \text{(wurtzite)}, \tag{1.19}$$

$$\begin{pmatrix} P_{xx} \\ P_{yy} \\ P_{zz} \end{pmatrix} = \begin{pmatrix} 0 & 0 & 0 & e_{14} & 0 & 0 \\ 0 & 0 & 0 & 0 & e_{14} & 0 \\ 0 & 0 & 0 & 0 & 0 & e_{14} \end{pmatrix} \begin{pmatrix} \varepsilon_{xx} \\ \varepsilon_{yy} \\ \varepsilon_{zz} \\ \varepsilon_{xy} \\ \varepsilon_{yz} \\ \varepsilon_{zx} \end{pmatrix} = \begin{pmatrix} 0 & 0 & 0 & d_{14} & 0 & 0 \\ 0 & 0 & 0 & 0 & d_{14} & 0 \\ 0 & 0 & 0 & 0 & 0 & d_{14} \end{pmatrix} \begin{pmatrix} \sigma_{xx} \\ \sigma_{yy} \\ \sigma_{zz} \\ \sigma_{xy} \\ \sigma_{yz} \\ \sigma_{zx} \end{pmatrix} \quad \text{(zinc blende)}. \tag{1.20}$$

As seen from Equation 1.19, two of the piezoelectric components in wurtzite phase measure the polarization induced along the *c*-axis, at zero electric field, by a uniform strain either along the *c*-axis or in the basal plane. The relevant relationship is [90]

$$P_z^{\text{piezo}} = e_{33}\varepsilon_z + e_{31}\varepsilon_\perp, \tag{1.21}$$

where ε_z and $\varepsilon_\perp$ are the strains along the *c*-axis and in the basal plane, respectively. The third independent component of piezoelectric tensor, e_{15}, describes the polarization induced by a shear strain, which is usually neglected for simplicity. The sign of the piezoelectric tensor is generally fixed assuming that the positive direction along *c*-axis goes from the cation to the anion.

The natural structure of ZnO is wurtzite, which has low symmetry resulting in the existence of spontaneous polarization along the *c*-direction. However, the absolute value of the spontaneous polarization in a nonferroelectric material has never been directly measured, while one invariably measures the polarization derivatives. In semiconductors, the spontaneous polarization may be deduced by investigating the two-dimensional electron gas and the redshift of the transitions in quantum wells albeit indirectly. From the theoretical point of view, there have been some efforts in

determining the value of the spontaneous polarization in ZnO. One conventional approach is to define the spontaneous polarization of a low-symmetry crystal (wurtzite) as the polarization difference with respect to a high-symmetry structure (zinc blende) of the same material.

The micro- and nanoindentation methods have been widely used to determine the hardness of ZnO over a wide range of size scales and temperatures. Hardness measurements are usually carried out on the (0 0 0 1) surface of the crystal using the conventional pyramidal or spherical diamond tip, or alternatively, with a sharp triangular indenter. The depth-sensing indentation measurements provide the complete information on the hardness and pressure-induced phase transformation of semiconductor materials. Table 1.6 shows the measured and calculated mechanical parameters for ZnO crystallized in the form of wurtzite, zinc blende, and rocksalt phases.

For ZnO, theoretical predictions appear to be in good agreement with experimental findings for certain bulk material properties. The quality of the crystals and theoretical approximations are of primary importance for the precise determination of the physical properties. In regard to the elastic constants, theory and experiments seem capable of producing data that are quite consistent for wurtzite-phase ZnO. Bulk modulus and its rate of change with pressure for all phases are in good agreement within the various experimental findings as well as the theoretical predictions with a few exceptions. Any deviation can be attributed to the sample quality, the accuracy of each experimental method, and phonon dispersion. Each calculation method also has its own limitations related to the basic material parameters, basis sets, and the precisions used in addition to the approximations of the method itself, leading to variations in the calculated parameters. Compared to group III nitrides (e.g., for GaN $C_{11} = 296$ GPa, C_{12} 130 GPa, $C_{13} = 120$ GPa, $C_{33} = 395$ GPa, $C_{44} = 241$ GPa, $B = 190$–245 GPa, see Chapter 2 in Ref. [91]), the elastic and bulk moduli of ZnO are small. Ultrasonic experiments on single-crystal specimens of the wurtzite (B4) phase of ZnO have shown that, under pressure, this material becomes softer against shear-type acoustic distortions.

Decremps *et al.* [92] have studied the pressure behavior of both longitudinal (C_{11} and C_{33}) and transverse (C_{44} and C_{66}) elastic moduli for the wurtzite phase of single-crystal ZnO using ultrasonic wave velocity measurements up to 10 GPa at three different temperatures. As shown in Figure 1.16, it has been observed that all the moduli exhibit a linear dependence on pressure up to the phase transition pressures, with positive values for the room-temperature longitudinal moduli ($dC_{11}/dP = 5.32$ and $dC_{33}/dP = 3.78$) but negative values for the shear moduli ($dC_{44}/dP = -0.35$ and $dC_{66}/dP = -0.30$). At high temperatures, the pressure derivatives of the elastic shear modes become more negative. Thus, the elastic shear softening observed at room temperature is enhanced at elevated temperatures. The effect of phonons and the role of bond-bending forces as a function of pressure in causing the elastic softening have also been investigated [92]. It has been observed that the pressure at which the phase transition (B4 $\rightarrow$ B1) commences decreases to about 6 GPa at 600 °C compared to 7.5 GPa at room temperature.

Table 1.6 Some mechanical properties of ZnO obtained by several experimental techniques and theoretical calculations.

Parameters	Wurtzite	Zinc blende	Rocksalt
C_{11} (GPa)	209.7[a], 206[b], 157[c], 190[d], 207[e], 209[f], 230[g], 231[h], 246[i]	193[i]	
C_{12} (GPa)	121.1[a], 117[b], 89[c], 110[d], 117.7[e], 85[f], 82[g], 111[h], 127[i]	139[i]	
C_{13} (GPa)	105.1[a], 118[b], 83[c], 90[d], 106.1[e], 95[f], 64[g], 104[h], 105[i]		
C_{33} (GPa)	210.9[a], 211[b], 208[c], 196[d], 209.5[e], 270[f], 247[g], 183[h], 246[i]		
C_{44} (GPa)	42.47[a], 44.3[b], 38[c], 39[d], 44.8[e], 46[f], 75[g], 72[h], 56[i]	96[i]	
C_{66} (GPa)	44.29[a], 44.6[b], 34[c], 40[d], 44.6[e], 62[f], 60[h], 115[i]		
Bulk modulus, B (GPa)	142.4[j], 183[k], 170[l], 160[m], 162.3[n], 133.7[o], 156.8[k]	161.7[n], 135.3[o], 154.4[k]	202.5[j], 228[p], 205[m], 205.7[n], 172.7[o], 203.3[k]
dB/dP	3.6[j], 4.0[p], 4.4[m], 4.05[n], 3.83[o], 3.6[k]	3.95[n], 3.72[o], 3.6[k]	3.54[j], 4.0[p], 4.88[m], 3.90[n], 3.77[o], 3.6[k]
Young's modulus, E (GPa)	111.2 ± 4.7[q]		
Hardness (GPa)	5.0 ± 0.1[q]		
e_{31} ($C\,m^{-2}$)	−0.62[r], −0.51[c], −0.39[s], −0.53[t], −0.51[u], −0.55[i], −0.66[v]		
e_{33} ($C\,m^{-2}$)	0.96[r], 1.22[c], 0.92[s], 1.19[t], 1.21[u], 1.19[i], 1.30[v]		
e_{15} ($C\,m^{-2}$)	−0.37[r], −0.45[c], −0.46[i]		
e_{14} ($C\,m^{-2}$)		0.69[i], 0.64[w]	
Spontaneous polarization ($C\,m^{-2}$)	−0.057[t], −0.047[x], −0.057[u]		
Born effective charge, Z^*	2.06[t], 2.11[u], 2.10[w], 2.1[x]		

[a]Ultrasonic measurement on single-crystal ZnO grown by chemical reaction in vapor state [86].
[b]Surface Brillouin scattering on polycrystalline ZnO film deposited by RF sputtering on (1 0 0) Si substrate [96].
[c]Acoustic investigation technique on ZnO film deposited by RF magnetron sputtering on sapphire substrate [97].
[d]Polarized Brillouin scattering on bulk ZnO single crystal [98].
[e]Ultrasonic resonance method on ZnO single crystal [99].
[f]Calculated by using LDA [14].
[g]Calculated by using GGA [14].
[h]Atomistic calculations based on an interatomic pair potential within the shell model approach [19].
[i]Calculated by using *ab initio* periodic LCAO method, based mainly on the Hartree–Fock Hamiltonian, with an all-electron Gaussian-type basis set [32].
[j]X-ray diffraction by using synchrotron radiation on polycrystalline ZnO (99.99% purity) [12].

[k]Calculation based on *ab initio* all-electron periodic Hartree–Fock linear combination of atomic orbitals [20].
[l]Calculation using molecular dynamics simulation based on Tersoff's potential [100].
[m]Calculation based on modern theoretical HF cluster and full potential scalar relativistic linearized augmented plane wave [13].
[n]Calculated by using LDA [18].
[o]Calculated by using GGA [18].
[p]X-ray diffraction and ^{67}Zn Mössbauer spectroscopy on bulk ZnO [13].
[q]Spherical nanoindentation on bulk ZnO [101].
[r]Resonance–antiresonance method on ZnO single crystal [99].
[s]Calculated using modern *ab initio* [88].
[t]Calculated using *ab initio* quantum mechanical level by using through the Berry-phase scheme applied to delocalized crystalline orbitals and through the definition of well-localized Wannier functions [33].
[u]Calculation based on *ab initio* using the Berry-phase approach to polarization in solids [90].
[v]Calculated by using a plane-wave pseudopotential implementation of density functional theory and density functional linear response within the local density approximation [82].
[w]Ref. [102].
[x]Calculated by using the LDA, HF, and a model GW scheme [46].

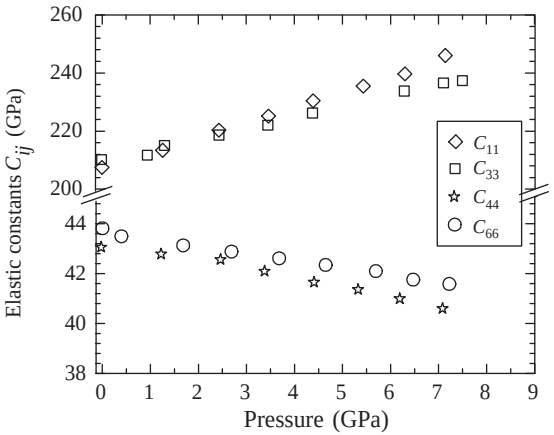

Figure 1.16 Elastic moduli of ZnO versus pressure at ambient temperature. The slope of the C_{11} and C_{33} pressure dependence is positive ($dC_{11}/dP = 5.32$ and $dC_{33}/dP = 3.78$), whereas that for C_{44} and C_{66} is negative ($dC_{44}/dP = -20.35$ and $dC_{66}/dP = -20.30$). (Courtesy of F. Decremps [92].)

Similar pressure dependence was also reported by Soga and Anderson [93], who measured the pressure derivatives of the room-temperature longitudinal (L) and transverse (T) sound velocities of polycrystalline ZnO. They obtained $(\partial v_L/\partial P)_T = 3.64\ 331\ 023\ \mathrm{km\,s^{-1}\,kbar^{-1}}$ and $(\partial v_T/\partial P)_T = 23.193\ 310\ 23\ \mathrm{km\,s^{-1}\,kbar^{-1}}$, corresponding to $(\partial B/\partial P)_T = 4.8$ and $(\partial G/\partial P)_T = -0.71$ (B is the bulk modulus and G is the shear modulus). On the theoretical side, a linear evolution under pressure was calculated for the two longitudinal modes C_{11} and C_{33} with pressure derivatives of 3.18 and 1.72, respectively, using atomistic calculations based on an interatomic pair potential within the shell model approach [19]. The shear moduli C_{44} and C_{66} exhibited negative pressure dependence with pressure derivatives of -0.30 and -0.84, respectively. The experimental and calculated values deviated some. The unusual negative values for both shear modes were attributed to two simultaneous effects [92]: (i) a major contribution of the second-nearest-neighbor interactions to the transverse acoustic phonon modes and (ii) an enhancement of the Coulomb forces screening between an atom and its second-nearest neighbor. Another explanation for the observed shear softening of ZnO was attributed to the decrease of bond-bending forces.

The deformation behavior of bulk ZnO single crystals was studied by a combination of spherical nanoindentation and atomic force microscopy [101]. ZnO exhibited plastic deformation for relatively low loads (>4–13 mN with $a \sim 4.2$ mm radius spherical indenter). The average contact pressure hardness H and Young's modulus E as a function of indenter penetration were determined by analyzing partial load–unload data. The hardness value of ZnO is measured to be 5.0 ± 0.1 GPa at a plastic penetration depth of 300 nm. The Young's modulus remained essentially constant over the indenter penetration depth, with $E = 111.2 \pm 4.7$ GPa. Previous indentation studies performed mostly on polycrystalline ZnO have reported a wide range of H (∼1.5–12 GPa) and E (∼40–120 GPa) values. However, it should be noted

from these results that ZnO is significantly softer than GaN, where $H(\text{GaN}) = 15.5 \pm 0.9$ GPa and $E(\text{GaN}) = 210 \pm 23$ GPa [94]. The lower value of H for ZnO is, in fact, expected due to a lower melting point (1975 °C) and larger ionicity (0.616) compared to that of GaN (2500 °C and 0.500, respectively) [95].

The spontaneous and piezoelectric polarization in ZnO have been studied theoretically by a number of groups and compared with a few available indirect experimental results. Dal Corso *et al.* [88] demonstrated applicability of *ab initio* studies of piezoelectricity within an all-electron scheme. A comparative analysis was performed to understand the microscopic origin of the peculiar behavior of ZnO. They have concluded that the piezoelectric effect results from two different contributions of opposite sign, which were referred to as the "clamped ion" and "internal strain." It has been shown that large piezoelectric tensor of ZnO is due to the low value of its clamped ion contribution (reducing the cancellation effect); besides, the piezoelectric tensor is dominated by the internal relaxation of anion and cation sublattices induced by the macroscopic strain. The piezoelectric tensor in ZnO has been calculated by using various techniques such as plane-wave analysis and ultrasoft pseudopotentials, and a GGA Hamiltonian, an all-electron basis set, and a HF Hamiltonian. The values of e_{31} and e_{33} were reported in the range of 0.39–0.66 (mostly, $\sim$0.52 C m^{-2}) and 0.92–1.30 C m^{-2} (mostly $\sim$1.20 C m^{-2}), respectively, which were in satisfactory agreement with the experimental data as tabulated in Table 1.6.

Furthermore, the spontaneous polarization of ZnO has also been computed and compared with a very indirect experimental estimate of the same quantity. Massidda *et al.* [46] calculated *ab initio* the electronic states, spontaneous polarization, and Born dynamical charge of ZnO by using the LDA, HF, and a model GW scheme. Among these schemes, the GW scheme gives a spontaneous polarization value of -0.047 C m^{-2}, which is about 0.010 smaller than the other two reports (-0.057 C m^{-2} [88, 90]). Although there are no direct experimental data available, these theoretical predictions are in good agreement with an indirect experimental value of -0.07 ± 0.02 C m^{-2} obtained from a model based on nonlinear optics. For Born dynamical charge, theoretical calculations and experimental data match quite well. From the value of the calculated Born dynamical charge, $\sim$2.1, it has been suggested that rigid-ion-like behavior of ZnO is dominant and its band-by-band decomposition has anomalous contributions from O 2s, Zn 3d, and O 2p bands, indicating a substantial interaction between the corresponding occupied atomic orbitals.

Hill and Waghmare [82] have also performed a first-principles study of the piezoelectric ZnO, named after the application, as a function of stress and temperature using a plane-wave pseudopotential implementation of density functional theory and density functional linear response within the local density approximation. The results are shown in Figure 1.17. The piezoelectric constant is strongly sensitive to both temperature and stress changing by about 20 and 15–30%, respectively, over the range of parameters considered. By analyzing various physical contributions, these dependences were primarily attributed to the changes in structural parameters as manifested through the phonon and strain coupling. The strong bond length dependent hybridization between the O 2p and Zn 3d electrons was believed to be the cause of the large magnitude and sensitivity of this coupling.

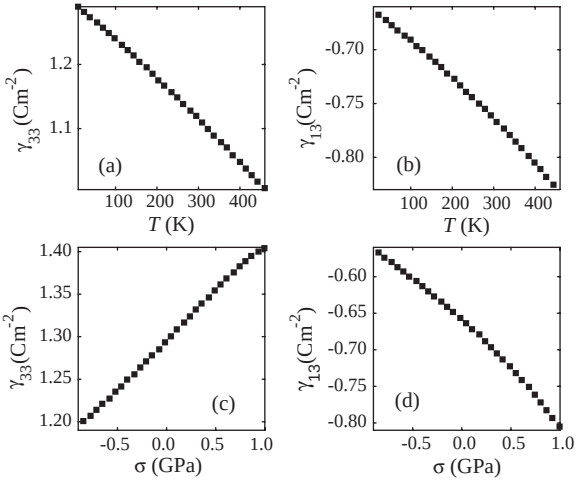

Figure 1.17 Dependence of piezoelectric constants γ_{33} and γ_{13} of ZnO on temperature (a and b) and stress (c and d), respectively. γ_{ij} used by Hill and Waghmare correspond to e_{ij} used here. (After Ref. [82].)

As alluded to earlier, ZnO is widely used in electroacoustic devices due to its large piezoelectricity (see Section 8.6 for a discussion of the piezoelectric devices). Therefore, a brief discussion of the acoustic wave propagation in wurtzite ZnO is warranted. The velocity of the acoustic wave propagation in semiconductors depends on the stiffness parameters. The three-dimensional equation of motion governing the macroscopic lattice displacement **u** as a function of time is [103]

$$\rho \frac{\partial^2 \mathbf{u}}{\partial t^2} = \nabla \cdot \sigma, \tag{1.22}$$

where ρ is the mass density and $\boldsymbol{\sigma}$ is the stress tensor. If we choose the *c*-direction as the *z*-direction, using the stress–strain relation in Equation 1.9 and the definition of the strain tensor $\boldsymbol{\varepsilon} = \bigtriangledown \mathbf{u}$, the acoustic phonon wave equations in wurtzite crystals are obtained as [103]

$$\begin{aligned}
&\rho \frac{\partial^2 u_x}{\partial t^2} = C_{11}\frac{\partial^2 u_x}{\partial x^2} + \frac{(C_{11}-C_{12})}{2}\frac{\partial^2 u_x}{\partial y^2} + C_{44}\frac{\partial^2 u_x}{\partial z^2} + \frac{(C_{11}+C_{12})}{2}\frac{\partial^2 u_y}{\partial x \partial y} \\
&+ (C_{13}+C_{44})\frac{\partial^2 u_z}{\partial x \partial z}, \rho \frac{\partial^2 u_y}{\partial t^2} = C_{11}\frac{\partial^2 u_y}{\partial y^2} + \frac{(C_{11}-C_{12})}{2}\frac{\partial^2 u_y}{\partial x^2} + C_{44}\frac{\partial^2 u_y}{\partial z^2} \\
&+ \frac{(C_{11}+C_{12})}{2}\frac{\partial^2 u_x}{\partial x \partial y} + (C_{13}+C_{44})\frac{\partial^2 u_z}{\partial y \partial z}, \ \rho \frac{\partial^2 u_z}{\partial t^2} = C_{33}\frac{\partial^2 u_z}{\partial z^2} + C_{44}\left(\frac{\partial^2 u_z}{\partial x^2} + \frac{\partial^2 u_z}{\partial y^2}\right) \\
&+ (C_{13}+C_{44})\left(\frac{\partial^2 u_x}{\partial x \partial z} + \frac{\partial^2 u_y}{\partial z \partial y}\right).
\end{aligned} \tag{1.23}$$

Assuming a solution in the form $\mathbf{u}(t) = (u_x\hat{x} + u_y\hat{y} + u_z\hat{z})e^{i(\mathbf{q}\cdot\mathbf{r}-\omega t)}$, with ω being the angular frequency and $\mathbf{r}$ the position vector, and choosing the y-axis such that the wave vector $\mathbf{q}$ lies in the yz plane, we may write the wave equations as

$$\begin{aligned}
\rho\omega^2 u_x &= \frac{1}{2}(C_{11}-C_{12})(q\sin\theta)^2 u_x + C_{44}(q\cos\theta)^2 u_x,\\
\rho\omega^2 u_y &= C_{11}(q\sin\theta)^2 u_y + C_{44}(q\cos\theta)^2 u_y + (C_{13}+C_{44})q^2\sin\theta\cos\theta u_z,\\
\rho\omega^2 u_z &= C_{33}(q\cos\theta)^2 u_z + C_{44}(q\sin\theta)^2 u_z + (C_{13}+C_{44})q^2\sin\theta\cos\theta u_y,
\end{aligned} \tag{1.24}$$

where θ is the angle between $\mathbf{q}$ and the z-axis (c-axis). For $\theta = 0$, these equations reduce to

$$\begin{aligned}
\rho\omega^2 u_x &= C_{44}q^2 u_x,\\
\rho\omega^2 u_y &= C_{44}q^2 u_y,\\
\rho\omega^2 u_z &= C_{33}q^2 u_z.
\end{aligned} \tag{1.25}$$

It is clear that there are two acoustic waves: transverse (x–y) and longitudinal (z), with velocities $v_z = \sqrt{C_{33}/\rho}$ and $v_{xy} = \sqrt{C_{44}/\rho}$, respectively. As will be discussed in Section 8.6, the electromechanical coupling results in an increase in the stiffness and therefore the sound velocity. For longitudinal acoustic wave propagation (i.e., along the c-axis), the effective stiffness constant including the electromechanical coupling becomes $C_{33,s} = C_{33}(1 + K^2)$, where K^2 is called the electromechanical constant. The resulting acoustic velocity is then

$$v_{z,s} = \sqrt{\frac{C_{33}(1+K^2)}{\rho}}. \tag{1.26}$$

An electromechanical coupling constant of 6% has been measured for ZnO [104], which would increase the sound velocity significantly, by ~3%.

1.5 Vibrational Properties

A fundamental understanding of the thermal and electrical properties in terms of low- and high-field carrier transport requires precise knowledge of the vibrational modes of the single crystal, which are related to mechanical properties and can be construed as such. Vibrational properties of ZnO probed by techniques such as Raman scattering were determined early on [105–111]. Here, phonons have been arbitrarily chosen to be discussed under the mechanical properties of the crystal rather than under its optical properties. A succinct discussion of vibrational modes,

Table 1.7 Acoustic and optical phonon modes in a crystal with wurtzite symmetry where s represents the number of atoms in the basis.

Mode type	Number of modes
Longitudinal acoustic	1
Transverse acoustic	2
Total acoustic modes	3
Longitudinal optical	$s-1$
Transverse optical	$2s-2$
All optical modes	$3s-3$
All modes	$3s$

The s parameter for wurtzite symmetry is 4. This table is also applicable to the zinc blende case but with $s=2$.

some of which are active Raman modes, some are active in IR measurements, and some are optically inactive (silent) modes, is provided [112]. Vibrational modes, which go to the heart of the mechanical properties, are very sensitive to crystalline defects, strain, and dopant in that the phonon mode frequencies and their frequency broadening can be used to glean very crucial information about the semiconductor. The method can also be applied to heterostructures and strained systems. Electronic Raman measurements can be performed to study processes such as electron–phonon interaction in the CW or time-resolved schemes. Time-resolved Raman measurements as applied to hot electron and phonon processes under high electric fields have important implications for carrier velocities.

In the case of wurtzite ZnO (similar to the case of wurtzitic nitrides) [113], the number of atoms per unit cell $s=4$, and there is a total of 12 phonon modes, namely, 1 longitudinal acoustic (LA), 2 transverse acoustic (TA), 3 longitudinal optical (LO), and 6 transverse optical (TO) branches, the details of which are listed in Table 1.7. In the zinc blende polytypes with $s=2$, only six modes are present, three of which are acoustical (one LA and two TA) and the other three are optical (one LO and two TO) branches. Infrared (IR) reflection and Raman spectroscopies have been commonly employed to derive zone center and some zone boundary phonon modes in ZnO. In the hexagonal structures with C_{6v}^4 symmetry, group theory predicts eight sets of phonon normal modes at the Γ point, namely, $2A_1 + 2E_1 + 2B_1 + 2E_2$. Among them, one set of A_1 and E_1 modes are acoustic, while the remaining six modes, namely, $A_1 + E_1 + 2B_1 + 2E_2$, are optical modes. In a more simplified manner, one can consider that the stacking order of the Wz polytype is AaBb while that for the zinc blende variety is AaBbCc. In addition, the unit cell length of the cubic structure along [1 1 1] is equal to the width of one unit bilayer, while that of the hexagonal structure along [0 0 0 1] is twice that amount. Consequently, the phonon dispersion of the hexagonal structure along [0 0 0 1] ($\Gamma \rightarrow$ A in the Brillouin zone) is approximated by folding the phonon dispersion for the zinc blende structure along the [1 1 1] ($\Gamma \rightarrow$ L) direction [114], as shown in Figure 1.18. Doing so reduces the TO phonon mode at the L point of the Brillouin zone in the zinc blende structure to the E_2 mode at the Γ point

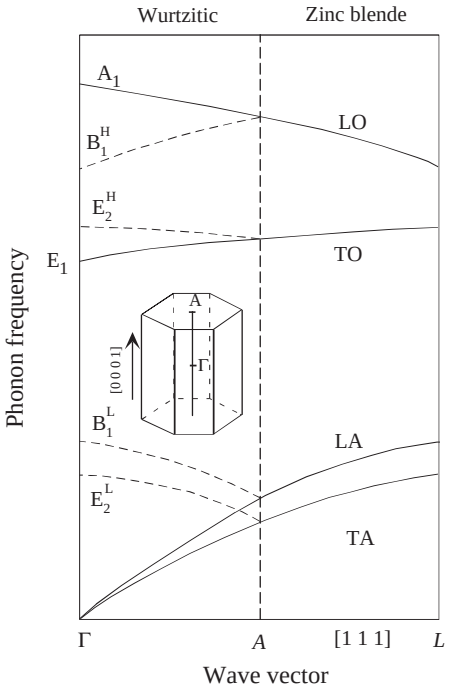

Figure 1.18 Schematic depiction of the phonon dispersion curves for zinc blende and Wz structures. Also shown are the Γ and *A* points of the zone in relation to the real-space hexagonal structure. Phonon branches along the [1 1 1] direction in the zinc blende structure are folded to approximate those of the wurtzite structure along the [0 0 0 1] direction because the unit cell length of the cubic structure along the [1 1 1] direction is equal to the width of one unit bilayer, while that for the hexagonal structure along the [0 0 0 1] direction is twice that amount. (Patterned after Ref. [114].)

of the Brillouin zone in the hexagonal structure. This vibrational mode is denoted as E_2^H with superscript H depicting the higher frequency branch of the E_2 phonon mode. In addition, one A_1 and one B_1 mode (B_1^H) derive from a singly degenerate LO phonon branch of the zinc blende system by zone folding, while one E_1 mode together with E_2^H derive from a doubly degenerate TO mode in the cubic system. As indicated in the figure, there is another E_2 mode at lower frequency labeled as E_2^L. This has its genesis in zone folding of the TA mode in the zinc blende structure. It should be noted that in the hexagonal structure, there is anisotropy in the macroscopic electric field induced by polar phonons. As a result, both TO and LO modes split into the axial (or A_1) and planar (or E_1) type modes where atomic displacement occurs along the *c*-axis or perpendicular to the *c*-axis, respectively. This splitting is not shown in Figure 1.18 as it is very small, just a few meV. Because the space group C_{6v} describes the crystalline structure of the wurtzite ZnO compound with two formula units in the primitive cell, the optical phonons at the Γ point of the Brillouin zone belong to the following irreducible representation. The A_1 and E_1 branches are both Raman and infrared active, the two nonpolar E_2 branches are Raman active only, and the B_1 branches are

inactive (silent modes). The A_1 and E_1 modes are each split into LO and TO components with different frequencies due to the macroscopic electric fields associated with the LO phonons. Because the electrostatic forces dominate the anisotropy in the short-range forces, the TO–LO splitting is larger than the A_1–E_1 splitting. For the lattice vibrations with A_1 and E_1 symmetry, the atoms move parallel and perpendicular to the *c*-axis, respectively. The low-frequency E_2 mode is associated with the vibration of the heavy Zn sublattice, while the high-frequency E_2 mode involves only the oxygen atoms. In the case of highly oriented ZnO films, if the incident light is exactly normal to the surface, only A_1(LO) and E_2 modes are observed and the other modes are forbidden according to the Raman selection rules.

The first-order phonon Raman scattering is due to phonons near the Γ point zone center, that is, with wave vector $k \approx 0$, because of the momentum conservation rule in the light scattering process. Raman measurements are typically employed to probe the vibrational properties of semiconductors. When done along the direction perpendicular to the (0 0 0 1) plane, the nomenclature used to describe this configuration is depicted as $Z(XY, XY)\,\bar{Z}$. Here, following Porto's notation [105], A(B,C)D is used to describe the Raman geometry and polarization where A and D represent the wave vector direction of the incoming and scattered light, respectively, whereas B and C represent the polarization of the incoming and scattered light. In Raman scattering, all the above-mentioned modes, with the exception of B_1 modes, are optically active. Because of their polar nature, the A_1 and E_1 modes split into longitudinal optical (A_1-LO and E_1-LO), meaning beating along the *c*-axis, and transverse optical (A_1-TO and E_1-TO), meaning beating in the basal plane. To reiterate, the A_1 and B_1 modes give atomic displacements along the *c*-axis, while the others, E_1 and E_2, give atomic displacements perpendicular to the *c*-axis, Here, the A_1 and E_1 modes are both Raman and IR active, while the two E_2 modes are only Raman active, and the two B_1 modes are neither Raman nor IR active, meaning silent modes. In the $Z(XY, XY)\,\bar{Z}$ configuration, only the E_2^1 (or E_2^L or E_2-low), E_2^2 (or E_2^H or E_2-high), and A_1(LO) modes should be observable. In particular, in the $Z(X, X)\,\bar{Z}$ and $Z(Y, Y)\,\bar{Z}$ geometries all three modes are observable, while in the $Z(X, Y)\,\bar{Z}$ or $Z(Y, X)\,\bar{Z}$ geometries only the E_2 modes are detected [106]. The details of the mode–Raman configuration relationship are provided in Table 1.8. Shown in Figure 1.19 are the modes and the Raman backscattered geometries in relation to hexagonal crystalline orientation that can be used to sense the various phonon modes indicated.

The acoustic modes are simple translational modes, and optical modes for wurtzite symmetry are shown in Figure 1.20. Table 1.9 gives a list of observed zone center optical phonon wave numbers along with those calculated for wurtzite ZnO.

The optical phonon energies are linked to the low- and high-frequency dielectric constants and therefore can be calculated from one another. Electromagnetic theory indicates that for any longitudinal electromagnetic wave to propagate, the dielectric function ε(ω) must vanish. Doing so leads to [113]

$$\frac{\varepsilon(\omega)}{\varepsilon(\infty)} = \frac{\omega_{LO}^2 - \omega^2}{\omega_{TO}^2 - \omega^2}, \tag{1.27}$$

Table 1.8 Raman measurement configuration needed to observe the phonon modes in hexagonal ZnO.

Mode	Configuration
$A_1(TO)$, E_2	$X(Y,Y)\bar{X}$
$A_1(TO)$	$X(Z,Z)\bar{X}$
$E_1(TO)$	$X(Z,Y)\bar{X}$
$E_1(TO)$, $E_1(LO)$	$X(Y,Z)Y$
E_2	$X(Y,Y)Z$
E_2	$Z(Y,X)\bar{Z}$
$A_1(LO)$, E_2	$Z(Y,Y)\bar{Z}$

where ω_{LO} and ω_{TO} represent the LO and TO phonon frequencies, and $\varepsilon(\omega)$ and $\varepsilon(\infty)$ represent the low and high (optical) frequency dielectric constants, respectively. When $\omega = \omega_{LO}$, the dielectric function vanishes, $\varepsilon(\omega_{LO}) = 0$. Equation 1.27 can be expanded to the directional dependence of the dielectric function in wurtzite ZnO. In the direction parallel to the *c*-axis or the *z*-direction, from the Γ point to the A point, in the *k*-space (with *x*, *y* representing the in-plane coordinates), the low- and high-frequency dielectric functions are related to each other with the help of $A_1(LO)$ and $E_1(TO)$ phonon frequencies through [119]

$$\varepsilon_{//}(\omega) = \varepsilon_{//}^{\infty} \frac{\omega^2 - \omega_{//}^2(LO)}{\omega^2 - \omega_{//}^2(TO)}. \tag{1.28}$$

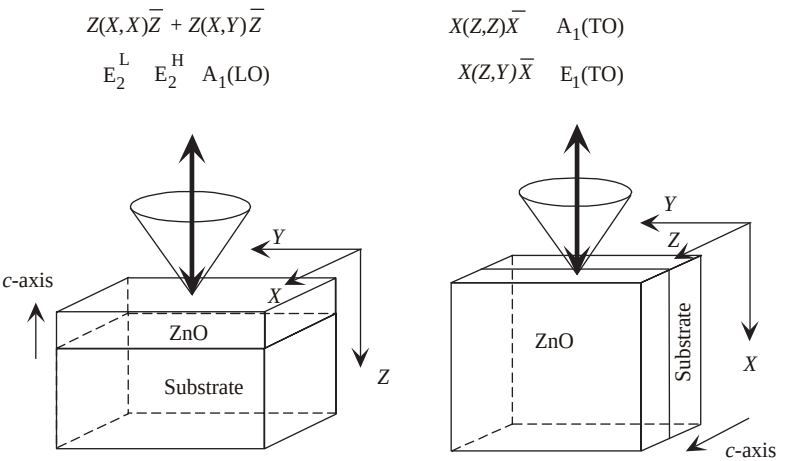

Figure 1.19 Schematic representation of two Raman configurations with incident and scattered light directions in the backscattering geometry for $Z(X,X)\bar{Z} + Z(X,Y)\bar{Z}$ configuration to sense E_2^L, E_2^H, and $A_1(LO)$ modes, $X(Z,Z)\bar{X}$ configuration to sense $A_1(TO)$ mode, and $X(Z,Y)\bar{X}$ configuration to sense $E_1(TO)$ mode.

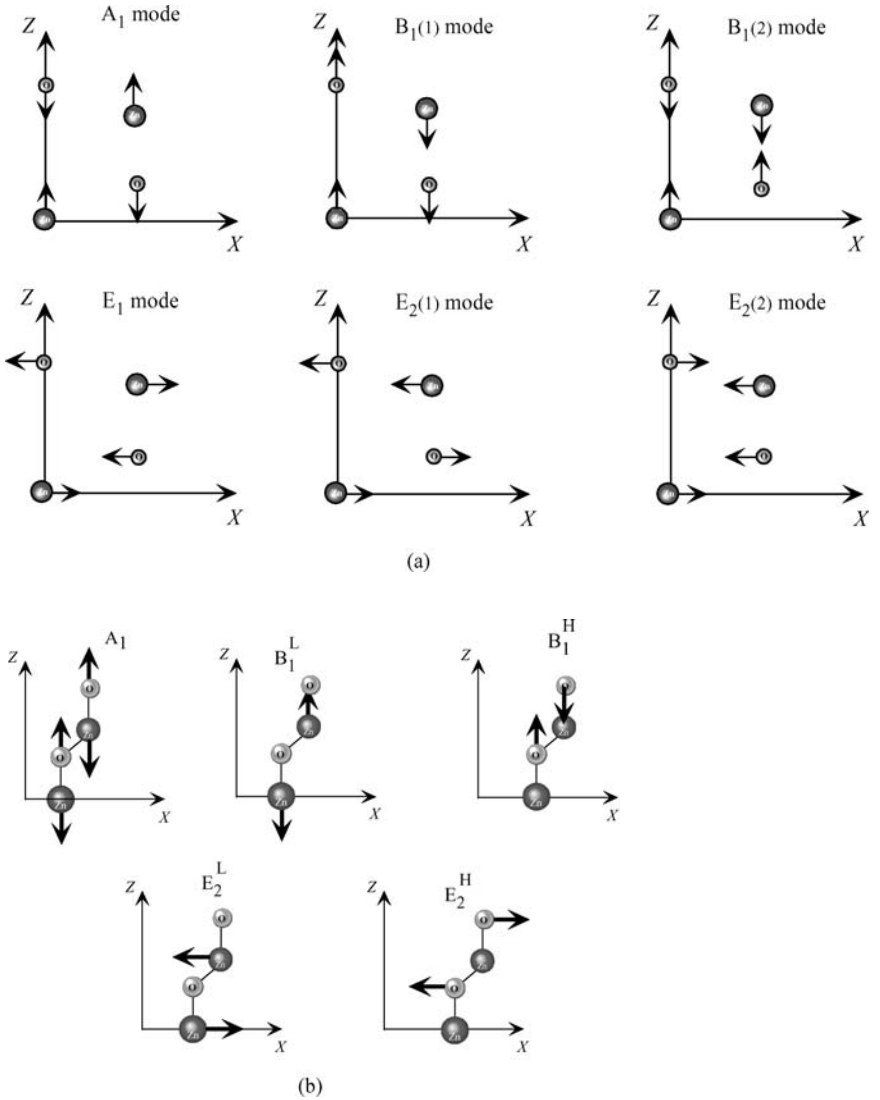

Figure 1.20 Atomic vibrations in Wz ZnO. The larger atom represents Zn while the smaller one represents O. $X = (1\,0\,0)$, $Y = (0\,1\,0)$, $Z = (0\,0\,1)$ represent the optical polarization directions: (a) for general wave vector and (b) for zone center phonons.

Table 1.9 Phonon mode frequencies (in units of cm^{-1}) of wurtzite ZnO at the center of the Brillouin zone obtained from infrared spectroscopic ellipsometry (IRSE) and Raman scattering measurements in comparison with theoretical predictions.

Symmetry	Raman spectroscopy	Infrared spectroscopy	Theoretical calculations
A_1-TO	380 (2)[a], 379 (2)[b], 380[c], 380[d], 378[e], 380[f]	380[g], 376.5[j]	382[h], 386[i]
E_1-TO	409 (2)[a], 410 (2)[b], 407[c], 413[d], 409.5[e]	409.1 (0.9)[a], 408.2 (0.3)[b], 412[g], 410.7[j]	316[h], 407[i]
A_1-LO	574[c], 576[e], 579[d], 579[f]	574.5 (0.3)[a], 577.1 (0.4)[b], 570[g], 574.1[j]	548[h]
E_1-LO	587 (2)[a], 591 (2)[b], 583[c], 588[e], 591[d]	588.3 (0.7)[a], 592.1 (0.2)[b], 591[g], 590.4[j]	628[h]
E_2-low	102 (1)[a], 102 (1)[b], 101[c], 101[d], 98[e], 99[f]		126[h], 98[i]
E_2-high	438 (1)[a], 437 (1)[b], 437[c], 444[d], 437.5[e], 438[f]		335[h], 433[i]
B_1-low			261[k]
B_1-high			552[k]

[a] ZnO epilayer grown on sapphire. Error bars in parentheses of the infrared spectroscopy data represent the 90% confidence limits. Error bars of the Raman data are determined by the experimental setup [123].
[b] Bulk ZnO. Error bars in parentheses represent the 90% confidence limits [123].
[c] Raman scattering on ZnO single crystal [105].
[d] Raman spectra on ZnO [106].
[e] Raman spectra [121].
[f] Raman spectra on ZnO film [115].
[g] IR reflection [116].
[h] Atomistic calculations based on an interatomic pair potential within the shell model approach [19].
[i] Calculation [109].
[j] Generalized IRSE on *a*-plane ZnO on *r*-plane sapphire [117].
[k] *Ab initio* calculations [118].

Likewise, Equation 1.27 can be expanded in the direction perpendicular to the *c*-axis or the *z*-direction, or in the basal plane or the (*x*, *y*) plane (in *k*-space between the Γ point and *M* (1/2, 0, 0) or *K* (1/3, 1/3, 0) points). In this case, the low- and high-frequency dielectric functions are related to each other with the help of A_1(TO) and E_1(LO) phonons through [119]

$$\varepsilon_{\perp}(\omega) = \varepsilon_{\perp}^{\infty} \frac{\omega^2 - \omega_{\perp}^2(\mathrm{LO})}{\omega^2 - \omega_{\perp}^2(\mathrm{TO})}, \tag{1.29}$$

where ⊥ and // indicate in the basal plane and along the *c*-direction, respectively.

For wurtzite materials, the various directional components of phonon modes correspond to $\omega_{\perp}(\mathrm{LO}) \rightarrow E_1(\mathrm{LO})$, $\omega_z(\mathrm{LO}) = \omega_{//}(\mathrm{LO}) \rightarrow A_1(\mathrm{LO})$, $\omega_{\perp}(\mathrm{TO}) \rightarrow E_1(\mathrm{TO})$, and $\omega_z(\mathrm{TO}) = \omega_{//}(\mathrm{TO}) \rightarrow A_1(\mathrm{TO})$. In the *z*-direction (along the *c*-direction) and the directions perpendicular to the *z*-direction (in basal plane), LO and TO phonons are not mixed. For any direction other than these in-plane and out-of-plane

configurations, the LO and TO phonons mix and hybridize. For a given propagation direction with an angle θ relative to the *c*-axis (*z*-axis), one finds three phonon branches. One is an ordinary TO phonon mode with atomic displacement in the *xy* plane. The other two branches have a mixed TO and LO character and their dielectric functions are given by the solutions of [120]

$$\varepsilon_{//} \cos^2 \theta + \varepsilon_{\perp} \sin^2 \theta = 0. \tag{1.30}$$

Using the above relationship, the phonon energy as a function of the angle can easily be calculated. Doing so leads to the conclusion that the upper branch (LO-like) remains between the A_1(LO) and E_1(LO) energies while the lower branch (TO-like) remains between the A_1(TO) and E_1(TO) energies. Therefore, the dispersion remains small compared to the LO–TO separation, owing to the relatively small cell asymmetry and the large ionicity of atomic bonds. A more important consequence of LO–TO mixing is that the TO-like mode couples to carriers whereas in the *c*-direction A_1(LO) mode and in the basal plane E_1(LO) phonons couple to the carriers.

For the special case $\omega = 0$ (or very small frequencies compared to the LO and TO phonon frequencies), the relationship between the optical and static dielectric constants reduces to the well-known Lyddane–Sach–Teller relationship

$$\frac{\varepsilon(\omega)}{\varepsilon(\infty)} = \frac{\omega_{LO}^2}{\omega_{TO}^2}, \tag{1.31}$$

which is often used to determine the optical frequency dielectric constant from knowledge of the A_1(LO) and A_1(TO) phonon frequencies along the *c*-direction and E_1(LO) and E_1(TO) in the basal plane. The static and high-frequency dielectric constants of ZnO are listed in Table 3.8.

A reasonably complete set of phonon mode frequencies has been measured by using either IR or Raman spectroscopy (RS) for both bulk and thin-film ZnO. In early measurements, phonon modes of bulk ZnO were explored and discussed extensively by several groups using RS measurements [105–108, 121]. Observation of the phonon modes in PLD-grown ZnO thin films was reported by Lu *et al.* [122] and Ashkenov *et al.* [117, 123]. No significant differences for the E_1(TO), A_1(TO), and E_2 mode frequencies were observed between the thin film and the bulk sample. The thin-film ZnO phonon mode frequencies are highly consistent with those of the bulk material. A small redshift of the longitudinal optical phonon mode frequencies of the ZnO films with respect to the bulk material was tentatively assigned to the existence of vacancy point defects within the films. The data obtained from IR and RS measurements are consistent with each other within the experimental accuracy. The predicted phonon frequencies reported by Tsuboi and Wada [109] are also in very good agreement with the experimental observations. The modes E_1(TO) and A_1(TO) reflect the strength of the polar lattice bonds. Accordingly, as discussed above no significant differences between the lattice constants of the film and bulk samples were observed.

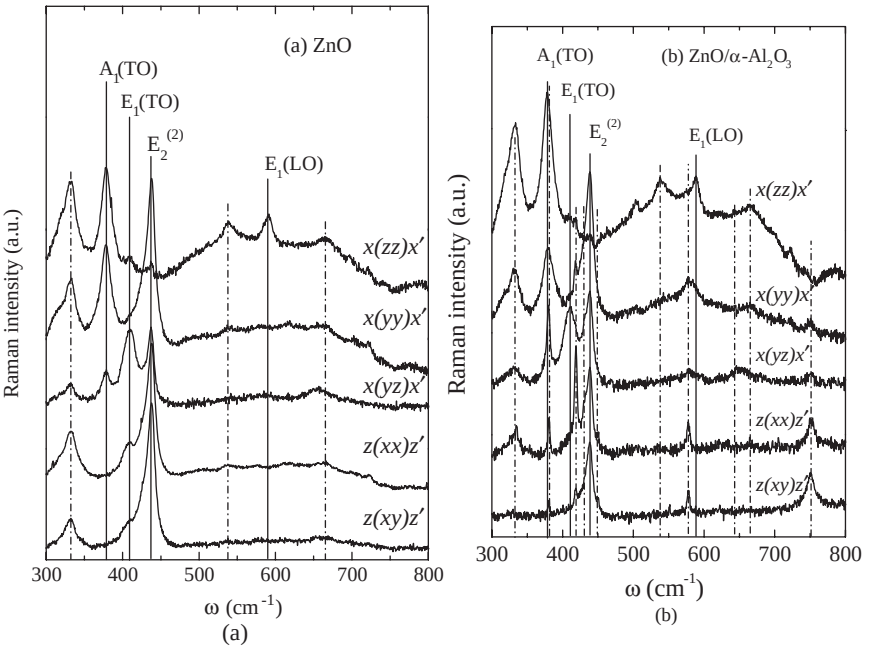

Figure 1.21 (a) Raman spectra of the bulk ZnO sample. First-order phonon modes of ZnO are indicated by the vertical solid lines. The vertical dashed–dotted lines mark the features due to multiple-phonon scattering processes. (b) Raman spectra for the thin-film ZnO sample. The vertical dotted lines indicate the Raman-active sapphire substrate phonon mode frequencies. (Courtesy of M. Schubert [123].)

Figure 1.21 shows typical Raman spectra of the bulk and thin-film ZnO samples [123]. In this particular study, solid lines in both figures indicate E_1, A_1, and E_2 phonon modes of ZnO. Dashed–dotted lines mark features observed at 332, 541, and 665 cm^{-1}, which were assigned to possible multiple-phonon scattering processes [105, 108]. Dotted lines are related to the sapphire phonon mode frequencies (A_{1g} mode: 417 and 645 cm^{-1}; E_g mode: 379, 430, 450, 578, and 751 cm^{-1}) [110]. For both samples A_1(LO) has not been observed and it was claimed that the scattering cross section for this mode is markedly smaller than that of the A_1(TO) mode due to the destructive interference between the Fröhlich interaction and the deformation potential contributions to the LO phonon scattering in ZnO [107]. Additionally, the occurence of the E_1(LO) mode in both samples was attributed to the breakdown of the selection rule due to the use of the Raman microscope.

Rajalakshmi *et al.* [124] have reported additional Raman peaks at 205, 331, and 539 cm^{-1} in their ZnO nanoparticle samples synthesized at ambient temperature using an electrochemical cell. Similar peaks (208, 332, and 541 cm^{-1}) that occur under resonance conditions were also reported for bulk ZnO [108]. In both studies, these peaks have been assigned to the second-order Raman spectrum arising from

zone boundary (*M* point) phonons 2-TA(*M*), 2-E_2(*M*), and 2-LA(*M*), respectively. However, the coupling to plasmons in highly doped material and stress-induced effects due to lattice mismatch with the substrate might play a role in the interpretation of the observed phonon frequencies.

The hydrostatic pressure dependence of the zone center phonon modes has also been studied. In conjunction with the previously reported results [111, 125], Decremps *et al.* [92] investigated in detail the pressure-induced Raman shifts in a single-crystal ZnO sample at room temperature using Raman spectroscopy and *ab initio* calculations based on a plane-wave pseudopotential method within the density functional theory. The pressure dependence of the zone center phonons (E_2, A_1, and E_1) was measured for the wurtzite structure up to the hexagonal/cubic phase transition pressure (~8.7 GPa), above which all Raman peaks disappeared. The pressure dependences of the phonon frequencies for the two high-pressure experiments are shown in Figure 1.22. Only the E_2-low mode exhibited a negative pressure dependence. The frequency shifts in the E_2-high, A_1(TO), E_1(TO), and E_1(LO) modes were observed to increase with pressure. The pressure dependence of the optical mode energies was also compared with the prediction of a model. No evidence of an anomaly in the E_2 and A_1 mode behaviors before the phase transition

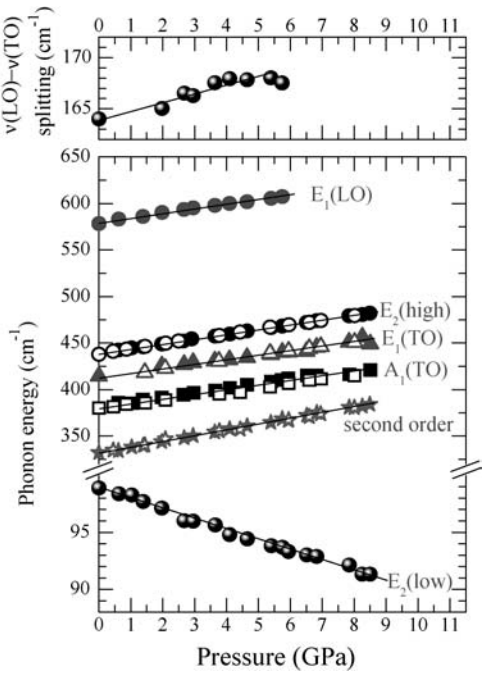

Figure 1.22 *Top*: ($\nu_{LO} - \nu_{TO}$) E_1 phonon mode splitting versus pressure. Solid lines are linear least-square fits to the experimental points. *Bottom*: Pressure dependence of the observed optical phonons. Open (full) symbols: propagation of light perpendicular (parallel) to *c*-axis. (Courtesy of F. Decremps [92].)

was detected. The corresponding perpendicular tensor component of the Born's transverse dynamic charge e_T^* (Z^* in table 1.6) is experimentally found to increase under compression as $e_T^*(P) = 2.02 - 6.4 \times 10^{-3}\,P$, whereas calculations give $e_T^*(P) = 2.09 - 2.5 \times 10^{-3}\,P$ (in units of the elementary charge e, P in GPa). It has also been noted that the observation of optical phonons under pressure does not show any softening of the optic A_1 and E_2-high modes as theoretically expected [126, 127]. Moreover, from both the experimental observation and the theoretical calculations, the LO–TO splitting of the E_1 phonon mode, which depends on the long-range electrostatic forces, has unusually shown weak pressure dependence. This behavior has been attributed to a small variation of the chemical bond ionicity of wurtzite ZnO with pressure. Experimentally, the second-order process observation (e.g., via optical phonon instabilities) could not be performed because the wurtzite-to-rocksalt first-order transition limits the pressure range within which the *wurtzite* structure exists.

The strong bond in ZnO and light O atoms result in high phonon frequencies and limit the range of possibly observable impurity-related local vibrational modes (LVMs) to even lighter elements at higher frequencies. So far, a number of reports have appeared for the infrared and Raman modes, which have been associated with local vibrational modes of impurities, dopants, and defect complexes. Kaschner *et al.* [128] have studied the influence of nitrogen, which is considered as a potential acceptor in ZnO, on the lattice dynamics of ZnO. They investigated a series of samples grown by chemical vapor deposition (CVD) containing different nitrogen concentrations. The Raman spectra revealed vibrational modes at 275, 510, 582, 643, and 856 cm^{-1} in addition to the host phonons of ZnO as discussed above. It has been observed that the intensity of these additional modes correlates linearly with the nitrogen concentration. Therefore, these modes were interpreted as local vibrational modes due to the vibrating nitrogen-related complexes. Bundesmann *et al.* [129] later measured the phonon modes of Fe-, Sb-, Al-, Ga-, and Li-doped ZnO thin films, grown by pulsed laser deposition (PLD) on *c*-plane sapphire substrates using polarized micro-Raman spectroscopy. Additional modes at about 277, 511, 583, and 644 cm^{-1}, which had been assigned to N incorporation, were observed for intentionally doped Fe, Sb, and Al films [129]. The mode at 277 cm^{-1} was also observed for Ga-doped films. Based on these observations, it has been stated that these modes cannot be related directly to N incorporation. Instead, the host lattice defects were suggested to be the origin of the additional modes [129]. This suggestion was supported by theoretical considerations, which stated that defects related to the incorporation of dopants might result in breakdown of the selection rules, and silent modes become Raman active [130]. Therefore, the above-addressed additional modes can be related to silent modes of ZnO.

First-principles calculations based on density functional theory within the local density approximation and the pseudopotential plane-wave method by Van de Walle [131] suggest that hydrogen atoms might act as shallow donors in ZnO. It has been argued that the incorporation of hydrogen accompanied by remarkably large relaxations of the surrounding atoms leads to an O–H bond, which in fact can be regarded as a new type of dopant atom in ZnO. To determine the microscopic

structure of hydrogen donors, the LVMs arising from these complexes have been investigated using IR and Raman spectroscopy [132–134]. The hydrogen-related defects in ZnO samples, hydrogenated using an H or a D plasma, have been investigated by a combination of local vibrational mode spectroscopy and compared with the first-principles calculations. Three new IR absorption lines at 3611.3, 3349.6, and 3312.2 cm^{-1} have been observed at 10 K. Based on polarization studies and first-principles calculations, the line at 3611.3 cm^{-1} was assigned to a single interstitial hydrogen atom at the bond center site oriented along the *c*-axis of the crystal although the possibility that this H atom is associated with an impurity cannot be ruled out. The lines at 3349.6 and 3312.2 cm^{-1} were attributed to a zinc vacancy that contains two inequivalent hydrogen atoms, one in an O–H bond roughly aligned with the *c*-axis and the other in an O−H bond that forms an angle of 100° with the *c*-axis [133].

McCluskey *et al.* [132] have also used IR spectroscopy to measure local vibrational modes in ZnO annealed in hydrogen gas. An IR absorption peak at 3326.3 cm^{-1} was observed at a temperature of 8 K and attributed to the O–H stretch mode based on comparison with the first-principles calculations of Van de Walle [131], in which the calculated mode frequencies were 3726 and 3384 cm^{-1} for the bond-centered and antibonding configurations, respectively, after subtracting 166 cm^{-1} due to the anharmonic terms in the potential causing the stretch-mode frequency to shift downward. However, because of the uncertainty in actual anharmonicity the bond-centered configuration was not ruled out. The IR spectrum of ZnO annealed in deuterium has revealed an additional stretch mode at 2470.3 cm^{-1} for the same temperature, which was tentatively assigned to the oxygen–deuterium (O–D) complexes. Using polarization measurements at room temperature, they also showed that the dipole of the O–H complex does not lie parallel to the *c*-axis of wurtzite ZnO [132, 135].

Using Raman backscattering spectroscopy, Nickel and Fleischer [136] have detected six local vibrational modes at 2854, 2890, 2918, 2948, 2988, and 3096 cm^{-1}. A Raman backscattering spectrum measured on an *as-grown* ZnO single crystal is shown in Figure 1.23. The peak positions were obtained by deconvolving the spectrum into six Gaussian lines. To elucidate the origin of the local vibrational modes, Nickel and Fleischer performed hydrogen effusion experiments on ZnO single crystals. Upon annealing some samples up to 950 °C to remove hydrogen, the subsequent measurement revealed that the local vibrational modes disappeared, from which the observed vibrational modes were attributed to the presence of hydrogen in the ZnO crystals. It was found that the stretching vibration of the corresponding hydrogen complex is *not* parallel to the *c*-axis. The vibrational modes located at 2854, 2890, 2918, 2948, and 2988 cm^{-1} were assumed to be due to the stretching modes of C–H, symmetric stretching modes of $C–H_3$, symmetric stretching modes of $C–H_2$, antisymmetric stretching modes of $C–H_3$, and antisymmetric stretching modes of $C–H_2$, respectively, based on the effusion data, where a significant concentration of hydrocarbons was detected. The local vibrational mode located at 3096 cm^{-1} was attributed to the N–H, assuming a considerable amount of hydrogen is bonded to nitrogen atoms based on the effusion experimental data. This

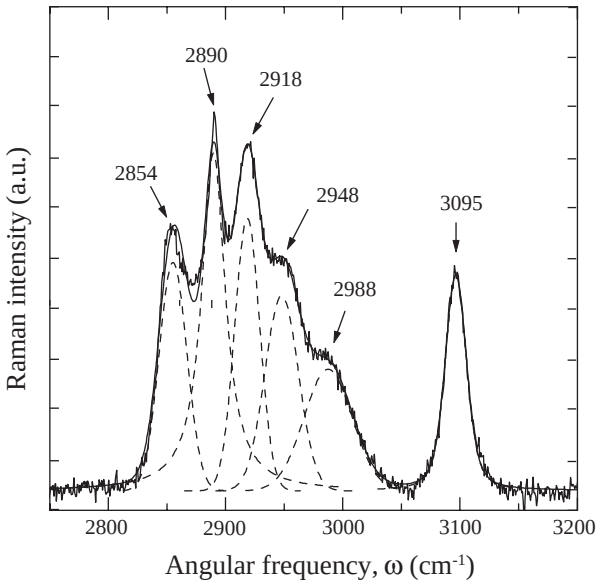

Figure 1.23 Raman backscattering spectrum of *as-grown* single-crystal ZnO after background subtraction. The sample was irradiated with the 488 nm line of an Ar laser and a power of 190 mW. The solid line represents a least-square fit of six Gaussian lines to the data. The dashed lines indicate the individual local vibrational modes. The peak positions are indicated in the plot. (Courtesy of N.H. Nickel [136].)

observed mode frequency was also found to be consistent with that reported for ZnSe compound semiconductors [137].

1.6 Thermal Properties

As in all solids, the atoms in a semiconductor at nonzero temperature are in ceaseless motion, oscillating about their equilibrium states. These oscillation modes are defined by phonons as discussed in Section 1.5. The amplitude of the vibrations increases with temperature, and the thermal properties of the semiconductor determine the response of the material to temperature changes. Thermal expansion, specific heat, and pyroelectricity are among the standard material properties that define the linear relationships between mechanical, electrical, and thermal variables. These thermal properties and thermal conductivity depend on the ambient temperature, and the ultimate temperature limit to study these effects is the melting temperature, which is ~1975 K for ZnO. It should also be noted that because ZnO is widely used in thin-film form deposited on foreign substrates, meaning templates other than ZnO, the properties of the ZnO films also intricately depend on the inherent properties of the substrates, such as lattice constants and thermal expansion coefficients.

1.6.1
Thermal Expansion Coefficients

The lattice parameters of semiconductors depend on temperature and are quantified by thermal expansion coefficients, which are denoted as $\Delta a/a$ or α_a and $\Delta c/c$ or α_c, for in-plane and out-of-plane cases, respectively. They depend on the stoichiometry, presence of extended defects, and free carrier concentration. The typical room-temperature values for ZnO are $\Delta a/a = 4.75 \times 10^{-6}\,\mathrm{K}^{-1}$ and $\Delta c/c = 2.9 \times 10^{-6}\,\mathrm{K}^{-1}$ [138]. Figure 1.24 depicts the percent thermal expansion of ZnO in the *c*-plane and along the *c*-axis as a function of temperature [139]. Also shown is the thermal expansion of polycrystalline ZnO.

The temperature dependence of the lattice constants *a* and *c* and the thermal expansion coefficients of hexagonal ZnO have been determined by the capacitive method [138]. The thermal expansion coefficients measured between 4 and 800 K are shown in Figure 1.25. Reeber [30] has employed X-ray powder diffraction methods instead to measure the temperature dependence of the lattice parameters of ZnO in the range of 4.2–296 K. The results are shown in Figure 1.26. When analyzing the dependence of the lattice parameters on temperature, fourth-order polynomials

$$a(T) = 3.248\,53 - 1.0811 \times 10^{-5} T + 6.820 \times 10^{-8} T^2 - 6.109 \times 10^{-11} T^3 + 2.143 \times 10^{-14} T^4 \quad (1.32)$$

were fitted by using the least-square method, which gives a minimum for the a_0 parameter at 93 K. The c_0 parameter did not give any minimum, most probably due to its low precision and uncertainty in the measurement. Using the same X-ray diffraction technique from 300 to 1373 K for powdered ZnO crystals, Iwanaga *et al.* [140] obtained second-order polynomials for the temperature dependence of

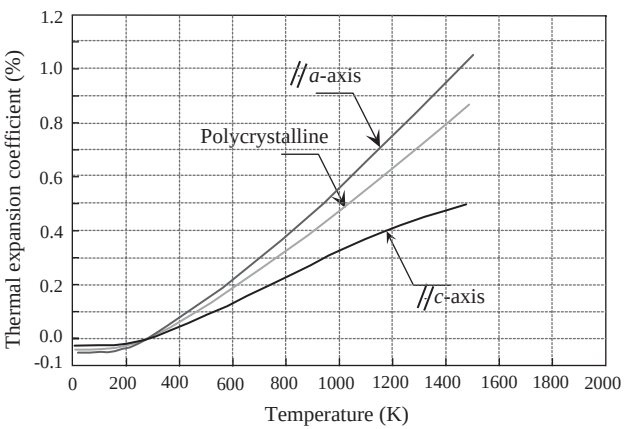

Figure 1.24 Thermal expansion of ZnO in the *c*-plane (along the *a*-axis) and along the *c*-axis as a function of temperature. Also shown is the thermal expansion coefficient of polycrystalline ZnO. (After Ref. [139].)

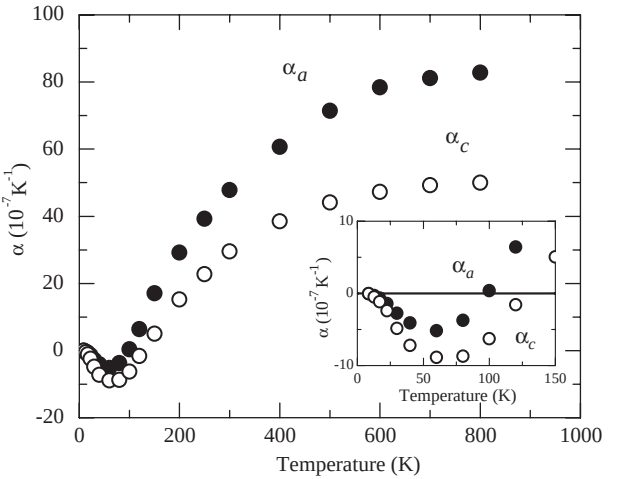

Figure 1.25 Thermal expansion coefficients α_a ($\perp c$) and α_c ($\|c$) of ZnO as a function of temperature. (After Ref. [138].)

the lattice parameters measured within an error of 5×10^{-4} Å:

$$\begin{aligned} a(T) &= 3.2468 + 0.623 \times 10^{-5} T + 12.94 \times 10^{-9} T^2, \\ c(T) &= 5.2042 + 0.522 \times 10^{-5} T + 12.13 \times 10^{-9} T^2, \end{aligned} \tag{1.33}$$

with corresponding thermal expansion coefficients of $\alpha_a = 4.31 \times 10^{-6}\,\mathrm{K}^{-1}$ and $\alpha_c = 2.49 \times 10^{-6}\,\mathrm{K}^{-1}$ at 300 K.

Hang and Jou [141] studied thermal properties of ZnO films prepared by RF magnetron sputtering on Si and GaAs substrates. Thermal stresses were determined by using bending beam technique where the specimens were thermally cycled from 25 to 400 °C. They investigated the thermal expansion coefficient as a function of growth parameters, such as substrate temperature and sputtering power. With a

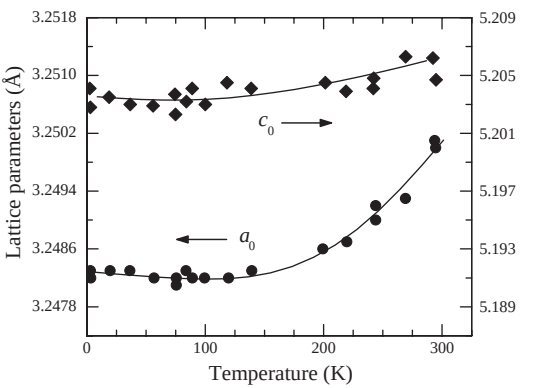

Figure 1.26 Wurtzite ZnO lattice parameters as a function of temperature. (After Ref. [30].)

few exceptions, they found no significant changes with the variation of total gas pressure from 0.53 to 2.1 Pa, substrate temperature from 250 to 450 °C, Ar-to-O pressure ratio from 0.3 to 3, and power from 100 to 300 W. It has been observed that the thermal expansion coefficient increases about 37% from 5×10^{-6} to $8 \times 10^{-6}\,^{\circ}\mathrm{C}^{-1}$ within the temperature range of 25–400 °C. Aoumeur *et al.* [100] calculated the thermal expansion coefficient for both zinc blende and rocksalt phases of ZnO using a molecular dynamics simulation based on Tersoff's potential. They found that $\alpha = 1.24 \times 10^{-5}\,\mathrm{K}^{-1}$ for the zinc blende and $\alpha = 0.16 \times 10^{-5}\,\mathrm{K}^{-1}$ for rocksalt structures.

As alluded to earlier, ZnO is widely used in thin-film form deposited on nonnative substrates. Therefore, the material quality, actually properties in general, of the ZnO films depends on the properties of the substrates used. Especially, the lattice parameters and thermal expansion coefficients of these substrates are extremely important since reduction of strain and dislocation density in ZnO thin films is the main objective, and substrates with parameters similar to those of ZnO are favorable in this context. Thermal expansion coefficients of various substrates used for thin-film ZnO growth are given in Table 2.3.

1.6.2 Thermal Conductivity

Thermal conductivity (κ), a kinetic property determined by the contributions from the vibrational, rotational, and electronic degrees of freedom, is an extremely important material property when high-power/high-temperature electronic and optoelectronic devices are considered. For pure crystals, phonon–phonon scattering, which is ideally proportional to T^{-1} above the Debye temperature, is the limiting process for thermal conductivity. Specifically, the heat transport is predominantly determined by the phonon–phonon Umklapp scattering and phonon scattering by point and extended defects, such as vacancies (inclusive of lattice distortions caused by them), impurities, and isotope fluctuations (mass fluctuation). As for other semiconductors point defects play a significant role in thermal conductivity of ZnO. The lattice contribution (phonon scattering) to the thermal conductivity κ is obtained from the kinetic theory as [142]

$$\kappa_{\mathrm{lattice}}(T) = \frac{1}{3} v_{\mathrm{s}} C_{\mathrm{lattice}}(T) L(T), \tag{1.34}$$

where T is the temperature, v_{s} is the velocity of sound (almost independent of temperature), $C_{\mathrm{lattice}}(T)$ is the lattice specific heat, and $L(T)$ is the phonon mean free path. In almost all materials, $\kappa(T)$ first increases with temperature, reaches a maximum (κ_{max}) at some characteristic temperature T_{ch}, and then decreases. At low temperatures, L is relatively long and is dominated by extrinsic effects such as "defects" and/or finite crystal size and $C_{\mathrm{lattice}}(T) \sim (T/\theta_{\mathrm{D}})^3$, where θ_{D} is the Debye temperature. As the temperature increases, $C_{\mathrm{lattice}}(T)$ begins to saturate and intrinsic temperature-dependent Umklapp processes become dominant, thus causing a decrease in L.

The electronic contribution to the thermal conductivity, which is negligible for carrier concentrations $\leq 10^{19}\,\mathrm{cm}^{-3}$, is [143]

$$\kappa_{\mathrm{electr}}(T) = \frac{\pi^2 n k_B^2 T \tau_{\mathrm{electr}}}{3 m_c^*}, \tag{1.35}$$

where n is the carrier density, k_B is the Boltzmann constant, τ_{electr} is the scattering time of the electrons, and m_c^* is the conduction band effective mass. The overall thermal conductivity generally decreases with increasing carrier concentration, because the decrease in the lattice component of κ due to increased phonon scattering from both impurities and free electrons outweighs the increase in the electronic contribution to κ [144].

Scanning thermal microscopy (SThM) [145] is a powerful technique used to measure thermal conductivity and is purported to provide nondestructive, absolute measurements with a high spatial/depth resolution of about 2–3 μm. Thermal imaging is achieved by using a resistive thermal element incorporated at the end of a cantilever/AFM tip, which forms one element of a Wheatstone bridge (for more information and a schematic see Ref. [91]). Upon contact with the sample, the tip tends to cool down due to heat conduction into the sample, which is related to its thermal conductivity, κ. The bridge circuit applies a compensating voltage (V_{out}) to maintain its target operating temperature. The feedback signal for constant resistance is a measure of the thermal conductivity of the material with which the tip is in contact, specifically V_{out}^2 is proportional to κ, because power dissipation is the mechanism here. Measurements of the absolute values of κ are based on a calibration procedure. This simply comprises calibrating the feedback signal, V_{out}^2, for a constant thermal element resistance against that for samples with known conductivities such as GaSb, GaAs, InP, Si, and Al metal. The influence of the surface roughness on the effective thermal conductivity is of concern. For a perfectly flat surface, the contact between the probe tip (radius of curvature ~1 μm) and the sample surface is very small. However, for rough surfaces the tip could impinge on a valley- or hillock-like feature with the result that a valley/hillock will lead to increased/decreased thermal signal with a corresponding change in the measured effective thermal conductivity.

SThM was applied to measure the room-temperature thermal conductivity on Zn and O faces of high-quality ZnO (0 0 0 1) single crystals, grown by a vapor-phase transport method [146]. The thermal investigation was performed in two ways: point-by-point (~2 μm resolution) and area scans. The point-by-point measurements on Zn-face samples produced $\kappa = 1.16 \pm 0.08$ and $1.02 \pm 0.07\,\mathrm{W\,cm^{-1}\,K^{-1}}$, while O-face samples showed $\kappa = 1.10 \pm 0.09$ and $0.98 \pm 0.08\,\mathrm{W\,cm^{-1}\,K^{-1}}$. The variations represent the standard deviation in the data, which was obtained by investigating approximately 15–20 points randomly distributed over a $6 \times 6\,\mathrm{mm}^2$ surface area. In this study, a correlation between the surface topography and thermal conductivity variations was also studied by acquiring the AFM and SThM scans simultaneously during the area scan. The effects of surface roughness on effective κ values were treated in terms of tip–surface geometry. It has been argued that when the

experimental voltage variations (proportional to κ) correspond to only 6–7% changes in the thermal conductivity, variations probably originate from the topography. Larger variations (>12%) in the SThM voltage reading for AFM topographical features with heights <100 nm would be an indication of intrinsic thermal conductivity variations across the area under investigation.

Pollak and coworkers [147] measured the thermal conductivity κ of several bulk ZnO (0 0 0 1) samples grown by CERMET, Inc. and prepared by the authors' group under different surface treatments. The measurements were made using SThM with a spatial/depth resolution of about 2–3 μm. The surface treatments of various samples are summarized in Table 1.10. The measurements were made at different points on each sample and the results are also shown in Table 1.10. For sample (a) in both positions, κ is considerably less than the previously reported values of about $1.0\,W\,cm^{-1}\,K^{-1}$ [146]. To be consistent with the earlier models, one would argue that forming gas annealing has resulted in surface roughness, which has considerably reduced κ. The same is mostly true for sample (e), which exhibits considerable inhomogeneity in the measured κ. At present, there is no explanation for this result, although Florescu *et al.* [144] did find that in GaN κ was a function of carrier concentration; that is, it decreased with increasing carrier concentration due to scattering of phonons from the ionized impurities. No information is available neither about the carrier concentrations/doping levels nor about their distribution for this or any other of the samples. For sample (b) the measured results for κ are similar to those reported in Ref. [146], while for samples (c) and (d) they are actually somewhat higher and are the highest κ values reported for ZnO. Thus, both air annealing and nitrogen plasma treatment result in a good surface.

Table 1.10 Thermal conductivity, κ ($W\,cm^{-1}\,K^{-1}$), at multiple positions of bulk ZnO samples with various surface treatments [147].

Sample	Surface treatment	Thermal conductivity ($W\,cm^{-1}\,K^{-1}$)
(a)	Forming gas annealed	(1) $\kappa = 0.67 \pm 0.08$
		(2) $\kappa = 0.46 \pm 0.05$
(b)	As received (O face)	(1) $\kappa = 1.00 \pm 0.08$
		(2) $\kappa = 0.95 \pm 0.06$
(c)	Air annealed	(1) $\kappa = 1.35 \pm 0.08$
		(2) $\kappa = 1.25 \pm 0.05$
(d)	Nitrogen plasma treated at 750 °C	(1) $\kappa = 1.44 \pm 0.08$
		(2) $\kappa = 1.47 \pm 0.08$
(e)	Oxygen plasma treated at 700 °C	(1) $\kappa = 0.87 \pm 0.06$
		(2) $\kappa = 0.75 \pm 0.06$
		(3) $\kappa = 0.80 \pm 0.06$
		(4) $\kappa = 1.24 \pm 0.05$
		(5) $\kappa = 0.54 \pm 0.07$

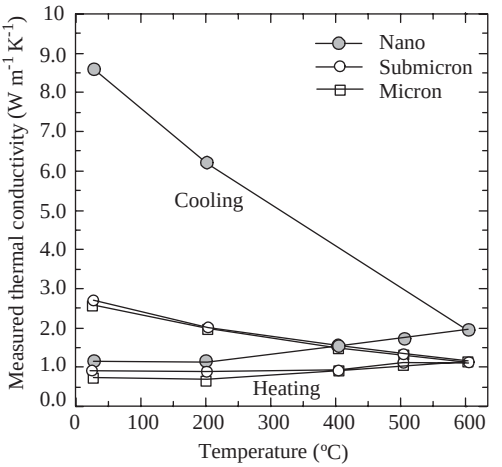

Figure 1.27 Thermal conductivity of nanometer-, submicrometer-, and micrometer-sized ZnO heated from room temperature to 600 °C at 3 °C min^{-1}. (After Ref. [148].)

Olorunyolemi *et al*. [148] measured the thermal conductivity of ZnO powders with different particle sizes (micrometer, submicrometer, and nanometer) from the as-received powder state to fully sintered state by using a laser flash technique. Curves of thermal conductivity versus temperature for the three sets of ZnO samples (micrometer, submicrometer, and nanometer) measured as they were heated to 600 °C and cooled back to 25 °C are shown in Figure 1.27. The first surprising observation is that the thermal conductivity at room temperature and up to 200 °C is the reverse of what is expected for the different particle sizes, with the nanopowder having the highest thermal conductivity. The room-temperature thermal conductivities were measured to be 0.745, 0.914, and 1.160 $W m^{-1} K^{-1}$ for micro-, submicron-, and nanosized samples with an average particle diameter of 1.0 μm, 0.2 μm, and 20 nm, respectively. The initial higher thermal conductivity of the nanopowder ZnO samples was attributed to the adsorbed water including chemisorbed water (more than that adsorbed by the submicrometer, which in turn is more than that adsorbed by the micrometer powder). Above 400 °C, the thermal conductivity of the nanosized particle increases faster with increasing temperature than that of the submicrometer- and the micrometer-sized samples. In this work, a model for interparticle neck growth was also developed based on the mass transfer of a powder to the neck region as a result of known temperature. The observed data were compared with the theoretical results obtained by the three-dimensional numerical code combined with this model.

Figure 1.28 shows the measured thermal conductivity of a fully sintered sample heated from room temperature to 1000 °C. The thermal conductivity decreases from 37 to 4 $W m^{-1} K^{-1}$ as the temperature is increased from room temperature to 1000 °C. This is the thermal conductivity curve for a fully dense ZnO crystal, where

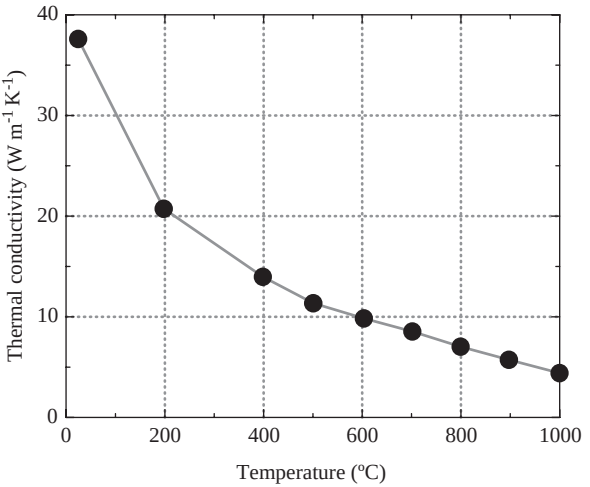

Figure 1.28 Thermal conductivity of fully sintered ZnO heated from room temperature to 1000 °C. (After Ref. [148].)

the resistive phonon–phonon interactions (Umklapp processes) are the dominant scattering mechanisms.

The thermal properties of ZnO doped with Al and Mg were also studied by a number of groups [149–153] for the evaluation of the thermoelectric performance. Tsubota *et al.* [152] investigated the thermal conductivity of sintered $(Zn_{1-y}Mg_y)_{1-x}Al_xO$ ($x = 0$–0.1, $y = 0$–0.1) samples determined from thermal diffusivity and specific heat capacity measured by the laser flash technique and differential scanning calorimetry (DSC), respectively. The temperature dependences of the thermal conductivities of $(Zn_{1-y}Mg_y)_{0.98}Al_{0.02}O$ ($y = 0$, 0.02, 0.1) are shown in Figure 1.29 in comparison with that of ZnO. The reduction of κ from

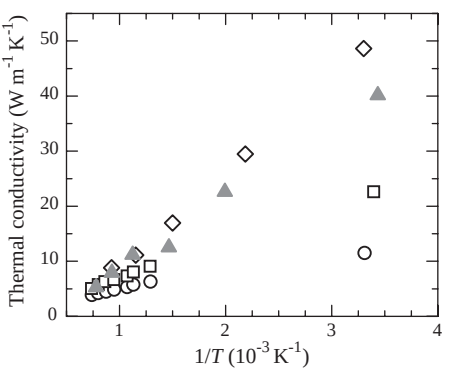

Figure 1.29 Thermal conductivities of ZnO (diamonds), $Zn_{0.98}Al_{0.02}O$ (triangles), and $(Zn_{1-y}Mg_y)_{0.98}Al_{0.02}O$ for $y = 0.02$ (squares) and 0.1 (circles) as a function of inverse temperature. (After Ref. [152].)

ZnO to $Zn_{0.98}Al_{0.02}O$ was almost negligible. Although addition of Al (using Al_2O_3) is considered to be ineffective in suppressing κ of ZnO-based materials, the difference in κ values between the MgO added samples and the $Zn_{0.98}Al_{0.02}O$ sample is significantly larger at low temperatures, indicating that the addition of MgO is very effective in reducing the thermal conductivity at low temperatures. From the temperature dependence behavior ($1/T$ dependence above the Debye temperature), the authors have concluded that the decrease in phonon–phonon scattering contribution is mainly responsible for the reduction of thermal conductivity upon the addition of MgO as well as Al_2O_3. The formation of a solid solution of MgO and ZnO is thereby considered to be effective in introducing phonon scattering centers to reduce vibrational component and thus the overall value of κ.

Similarly, thermal properties of $(Zn_{1-y}Mg_y)_{1-x}Al_xO$ ($0 < x < 0.05$ and $0 < y$ 0.16) ceramics synthesized from a powder precursor prepared by a polymerized complex method have also been investigated by Katsuyama *et al.* [151]. They observed similar dependence of thermal conductivity on temperature and doping constituents as Tsubota *et al.* [152]. The thermal conductivity decreased with increasing x, but it was further suppressed by the additional substitution of the Zn sites by Mg atoms with the resultant lattice contribution, that is, the point defects introduced by the addition of Mg enhanced the phonon scattering. However, in both studies, although the temperature dependence reveals $1/T$ behavior indicative of Umklapp scattering, room-temperature thermal conductivity of sintered ZnO, which is about $40\,W\,m^{-1}\,K^{-1}$ and reduces to $\sim 7\,W\,m^{-1}\,K^{-1}$ with increasing MgO concentration, is much smaller than the values reported for the high-quality single crystal discussed above. This indicates the large contribution due to enhanced phonon-point defect or -extended defect and -grain boundary scattering.

Because ZnO thin films deposited on foreign substrates are used in different applications, thermal conductivities of the substrates would be of concern when designing device structures. A comparison of thermal conductivities for various templates used for ZnO growth is provided in Table 2.3.

1.6.3
Specific Heat

The specific heat of a semiconductor has contributions from lattice vibrations, free carriers (very effective at low temperatures), and point and extended defects. For good quality semi-insulating crystal, the specific heat is determined mostly by the lattice vibrations. The available specific heat data for ZnO is very limited. Lawless and Gupta [154] investigated the specific heat for both pure and varistor type of ZnO samples between the temperature ranges of 1.7–25 K, where the latter has an average grain size of 10 μm. Specific heat measurements were performed using the pulse method. As seen in Figure 1.30, the specific heat of varistor ZnO diverges from that of pure ZnO below 20 K. This difference was attributed to the

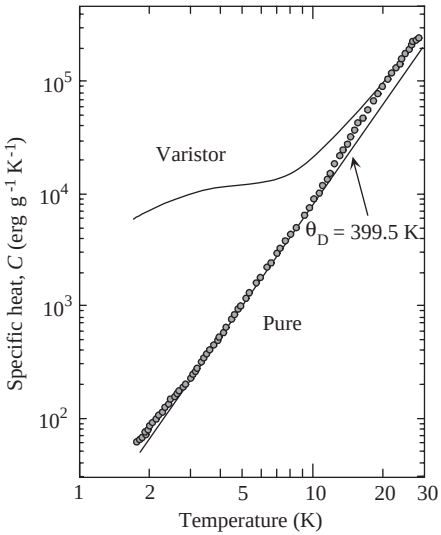

Figure 1.30 Specific heat data measured for pure ZnO compared to data for varistor ZnO. (After Ref. [154].)

contribution by the large amount of impurities, present in the region of the grain boundaries of varistor-type ZnO, giving rise to a very large excess specific heat below 20 K.

The specific heat data for pure ZnO were further analyzed by considering two non-Debye features at different temperature regions according to

$$C = C_{\text{Debye}} + C_{\text{Schottky}} + C_{\text{Einstein}}, \tag{1.36}$$

where C_{Debye}, C_{Schottky}, and C_{Einstein} represent the Debye, Schottky, and Einstein terms of the total specific heat of ZnO, respectively. In general, the Debye expression for the temperature dependence of specific heat in a solid at a constant pressure can be expressed as

$$C_{\text{Debye}} = 18R\left(\frac{T}{\theta_{\text{D}}}\right)^3 \cdot \int_0^{x_{\text{D}}} \frac{x^4 e^x}{(e^x - 1)^2} dx, \tag{1.37}$$

where $x_{\text{D}} \equiv \theta_{\text{D}}/T$ and $R = 8.3144\,\text{J mol}^{-1}\,\text{K}^{-1}$ is the molar gas constant. The coefficient in front of the term R has been multiplied by 2 to take into account the two constituents making up the binary compound. By fitting the measured temperature-dependent heat capacity to the Debye expression, one can obtain the Debye temperature θ_{D} specific to the heat capacity. It is often easier to extract a Debye temperature by using data either near very low temperatures or well below

the Debye temperature where the specific heat has a simple cubic dependence on temperature:

$$C_{\text{Debye}} = 234R\left(\frac{T}{\theta_D}\right)^3. \tag{1.38}$$

Unfortunately for ZnO, the samples contain large densities of free carriers and defects, which make the Debye specific heat expression unreliable. The Debye contribution to the specific heat of pure ZnO is also shown in Figure 1.30 as the curve labeled with a calorimetric Debye temperature of $\theta_D = 399.5$ K, and the deviation of the data below ~5 K is due to the Schottky term and that above ~10 K is due to the Einstein term. The latter has an exponential dependence and is given by

$$C_{\text{Einstein}} = 3Rr_E\left(\frac{\theta_E}{T}\right)^2 \exp\left(-\frac{\theta_E}{T}\right) \quad \text{for} \quad T \ll \theta_E, \tag{1.39}$$

where r_E is the number of Einstein oscillators per formula weight and θ_E is the Einstein temperature. Schottky term has a T^{-2} dependence and is expressed by

$$C_{\text{Schottky}} = bT^{-2}, \tag{1.40}$$

where $b = nR(\delta/2)^2$ ($n = r_E$ is assumed) is the Schottky coefficient.

The least-square fits of these two expressions to the experimental data for the corresponding temperature ranges are shown in Figure 1.31. Very good agreement with 2–3% uncertainty was achieved for the values of $\theta_E = 120.5$ K and $r_E = 8.72 \times 10^{-2}$ for the case of Einstein model and $b = 350.7\ \text{erg g}^{-1}\ \text{K}^{-1}$ for the Schottky term. The Zn interstitials ($3.6 \times 10^{21}\ \text{cm}^{-3}$) might be responsible for the dispersionless Einstein-type contribution to the specific heat above 10 K, whereas the Schottky contribution appearing below 4 K is due to ordering of, possibly, Zn interstitials with a characteristic energy of $\delta = 1.1 \times 10^5$ eV for such an ordering mechanism.

1.6.4 Pyroelectricity

Pyroelectricity is a first-rank tensor property that relates the change in temperature to a change in electrical displacement **D** (or polarization **P** since no field is applied):

$$\delta D_i = \delta P_i = p_i \delta T \quad \text{or} \quad p_i = (\delta P_i/\delta T)_E. \tag{1.41}$$

The constraint for obtaining the pyroelectric coefficient p_i (units $\text{C m}^{-2}\ \text{K}^{-1}$) is constant electric field E. Under constant strain, that is, when the sample is rigidly

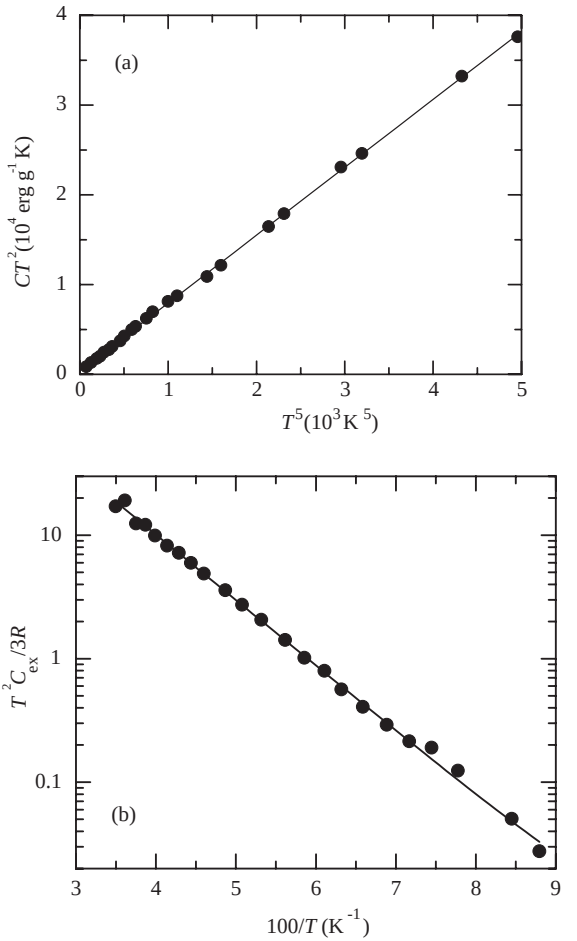

Figure 1.31 Fit to the pure ZnO data (a) using the Schottky model (with just Schottky and Debye contributions yielding a Debye temperature of 395.5 K) and (b) using the Einstein model. C_{ex} is the excess specific heat (ideally the Einstein contribution) obtained by removing the Debye and Schottky contributions from the total specific heat. The Einstein oscillators are identified as the Zn interstitials. (After Ref. [154].)

clamped to prevent thermal expansion or contraction, measurements reveal the "primary" pyroelectric coefficient, which originates from the change in the electric displacement due to internal rearrangements in the structure. However, most of the measurements are carried out under constant stress, meaning that the crystal deformation through thermal expansion is allowed. In this so-called "secondary" effect, the strain induced by thermal expansion alters the electric displacement through the piezoelectric process because all pyroelectric materials are also piezoelectric, such as ZnO. To exhibit pyroelectricity, the material should have no central

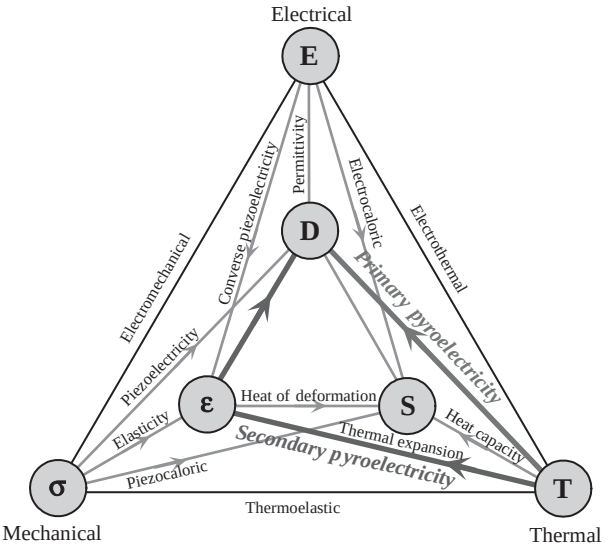

Figure 1.32 The well-known triangle used to describe the pathways between mechanical, electrical, and thermal energies in a class of noncentrosymmetric materials exhibiting piezoelectric effect, pyroelectric effect (converse of electrocaloric effect), piezocaloric effect (converse of thermal expansion), and so on. For simplicity, the magnetic property node is not shown. The variables denoted as the nodes are stress (σ), strain (ε), electric field (*E*), displacement (*D*), temperature (*T*), and entropy (*S*). The primary (*T* to *D*) and secondary (*T* to ε to *D*) pyroelectric effects are indicated.

symmetry, should have either no axis of rotational symmetry or a single axis of rotational symmetry that is not in an inversion axis, and its molecular structure should have a nonzero dipole moment.

The primary and the secondary pyroelectric effects are indicated in the well-known triangular diagram of Figure 1.32, which describes the pathways between the mechanical, electrical, and thermal energies. Measurement of the primary effect is extremely difficult as it is difficult to prevent the thermal expansion completely. The secondary effect, however, can easily be calculated by using the elastic stiffness and piezoelectric constants and the thermal expansion coefficient. The total (unclamped) pyroelectric coefficient (defined for constant stress as well as constant electric field) is given by the sum of the primary and secondary components and is what is usually measured in experiments. Pyroelectric coefficients measured for various materials are listed in Table 1.11 [155–157]. The pyroelectric effect is stronger in ferroelectric materials, which below a critical temperature, called the Curie temperature, exhibit strong hysteretic electrical polarization, the direction of which can be reversed by an applied electric field. Especially in ferroelectrics, the primary contribution to the pyroelectricity is generally larger than the secondary effect. In nonferroelectric or weakly ferroelectric materials such as ZnO, the pyroelectric coefficients are usually small and correlate well with the specific heat, which is also caused by thermal motions, as illustrated in Figure 1.33. In single-crystal hexagonal ZnO, the electric

Table 1.11 Primary, secondary, and total (experimentally measured) pyroelectric coefficients (in units of $\mu C\,m^{-2}\,K^{-1}$) for various materials.

	Primary coefficient	Secondary coefficient	Total (experimental value)
Ferroelectrics			
Poled ceramics			
$BaTiO_3$	−260	+60	−200
$PbZr_{0.95}Ti_{0.05}O_3$	−305.7	+37.7	−268
Crystals			
$LiNbO_3$	−95.8	+12.8	−83
$LiTaO_3$	−175	−1	−176
$Pb_5Ge_3O_{11}$	−110.5	+15.5	−95
$Ba_2NaNb_5O_{15}$	−141.7	+41.7	−100
$Sr_{0.5}Ba_{0.5}Nb_2O_6$	−502	−48	−550
$(CH_2CF_2)_n$	−14	−13	−27
Triglycine sulfate (TGS)	+60	−330	−270
$Pb(Zr_{0.54}Ti_{0.46})O_3$			−700
$PbTiO_3$			−1250
Nonferroelectrics and weak ferroelectrics			
ZnO	−6.9	−2.5	−9.4
ZnO [157]			−10.5
CdSe	−2.94	−0.56	−3.5
CdS	−3.0	−1.0	−4.0
Tourmaline	−0.48	−3.52	−4.0
$Li_2SO_4{\cdot}2H_2O$	+60.2	+26.1	+86.3

From Refs [155–157].

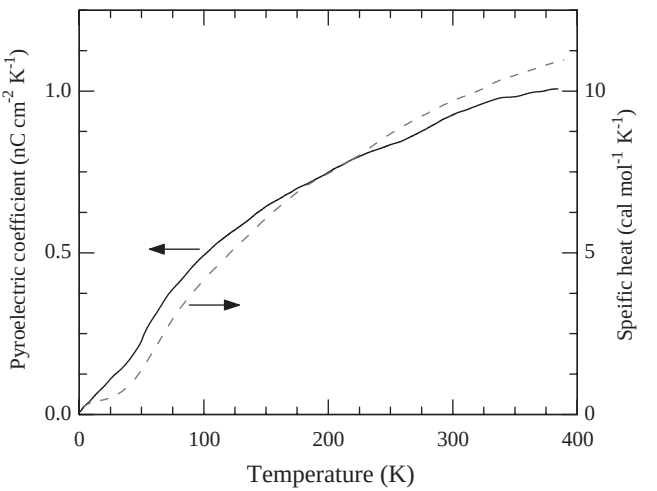

Figure 1.33 Pyroelectric coefficient and specific heat of ZnO as a function of temperature. (After Ref. [156].)

dipoles formed by the cations and anions add up as all the tetrahedral units point along the *c*-axis.

1.7
Electrical Properties of Undoped ZnO

As a direct and large bandgap material, ZnO is attracting much attention for a variety of electronic and optoelectronic applications. Advantages associated with a large bandgap include high-temperature and high-power operation, lower noise generation, higher breakdown voltages, and ability to sustain large electric fields. The electron transport in semiconductors can be considered for low and high electric fields. (i) At sufficiently low electric fields, the energy gained by the electrons from the applied electric field is small compared to the thermal energy of electrons and therefore the energy distribution of electrons is unaffected by such a low electric field. Because the scattering rates determining the electron mobility depend on the electron distribution function, electron mobility remains independent of the applied electric field, and Ohm's law is obeyed. (ii) When the electric field is increased to a point where the energy gained by electrons from the external field is no longer negligible compared to the thermal energy of the electron, the electron distribution function changes significantly from its equilibrium value. These electrons become hot electrons characterized by an electron temperature larger than the lattice temperature. Furthermore, as the dimensions of the device are decreased to submicron range, transient transport occurs when there is minimal or no energy loss to the lattice during a short and critical period of time, such as during transport under the gate of a field effect transitor or through the base of bipolar transistor. The transient transport is characterized by the onset of ballistic or velocity overshoot phenomenon. Because the electron drift velocity is higher than its steady-state value, one can design a device operating at frequencies exceeding those expected from linear scaling of dimensions.

1.7.1
Low-Field Transport

Hall effect is the most widely used technique to measure the transport properties and assess the quality of epitaxial layers. For semiconductor materials, it yields the carrier concentration, its type, and carrier mobility. More specifically, experimental data on Hall measurements over a wide temperature range (4.2–300 K) provide quantitative information on impurities, imperfections, uniformity, scattering mechanisms, and so on. The Hall coefficient and resistivity (ρ) are experimentally determined and then related to the electrical parameters through (for n-type conduction) $R_H = r_H/ne$ and $\mu_H = R_H/\rho$, where n is the free electron concentration, e is the unit electronic charge, μ_H is the Hall mobility, and r_H is the Hall scattering factor that depends on the particular scattering mechanism. The drift mobility is the average velocity per unit electric field in the limit of zero electric field and is related to the Hall mobility

through the Hall scattering factor by $\mu_H = r_H\mu$. As noted above, the Hall scattering factor depends on the details of the scattering mechanism, which limits the drift velocity. In degenerate semiconductors, the Hall factor is unity making the Hall mobility and drift mobility identical such as the case in FETs relying on 2D electron gas. As the carriers travel through a semiconductor, they encounter various scattering mechanisms that govern the carrier mobility in the electronic system. The parameter for characterizing the various scattering mechanisms is the relaxation time τ, which determines the rate of change in electron momentum as it moves in the semiconductor crystal. Mobility is related to the scattering time by

$$\mu = \frac{q\langle\tau\rangle}{m^*}, \tag{1.42}$$

where m^* is the electron effective mass, q is the electronic charge, and $\langle\tau\rangle$ is the relaxation time averaged over the energy distribution of electrons. The total relaxation time, τ_T, when various scattering mechanisms are operative, is given by Matthiessen's rule:

$$\frac{1}{\tau_T} = \sum_i \frac{1}{\tau_i}, \tag{1.43}$$

where i represents each scattering process, provided that electron while undergoing one scattering event is not simultaneously affected by another.

The major scattering mechanisms that generally govern the electron transport in III–V semiconductors are also valid for ZnO. They are briefly listed as follows:

(i) Ionized impurity scattering is due to deflection of free carriers by the long-range Coulomb potentials of the charged centers caused by defects or intentionally doped impurities. This can be thought as a local perturbation of the band edge, which affects the electron motion.

(ii) Polar longitudinal optical phonon scattering is caused by the interaction of a moving charge with an electric field induced by electric polarization associated with lattice vibration due to ionic nature of the bonds in a polar semiconductor.

(iii) Acoustic phonon scattering through deformation potential arises from the energy change of the band edges induced by strain associated with acoustic phonons, where the scattering rate increases with the wave vectors of the phonons.

(iv) Piezoelectric scattering arises from the electric fields that are produced by the strain associated with phonons in a crystal without inversion symmetry.

(v) If the density of dislocations and native defects are high in a semiconductor, dislocation scattering and scattering through defects are also considered as possible scattering mechanisms. Dislocation scattering is due to the fact that acceptor centers are introduced along the dislocation line, which capture electrons from the conduction band in an n-type semiconductor. The dislocation lines become negatively charged and a space charge region is

formed around it, which scatters electrons traveling across the dislocations, thus reducing the mobility.

Experimental investigation of the temperature-dependent carrier mobility and concentration can be used to determine the fundamental material parameters and understand the carrier scattering mechanisms along with an accurate comparison with theory. Table 1.12 gives the selected best values of electron mobility and corresponding carrier concentration in bulk and thin-film ZnO grown by various techniques. Even today, the electrical properties of ZnO are hard to quantify experimentally due to varying quality of the samples available.

The transport properties reported in the literature are mostly based on Hall effect measurements, assuming the Hall scattering factor to be unity. Using Monte Carlo simulations, Albrecht *et al.* [158] predicted the room-temperature electron mobility of ZnO to be $\sim 300\,\mathrm{cm^2\,V^{-1}\,s^{-1}}$. Nominally undoped ZnO with a wurtzite structure naturally becomes an n-type semiconductor due to the presence of intrinsic or extrinsic defects, which were generally attributed to native defects, such as the Zn-on-O antisite (Zn_O), the Zn interstitial (Zn_I) [169], and the O vacancy (V_O). However, first-principles investigations based on density functional theory suggest that hydrogen in ZnO occurs exclusively in the positive charge state and is responsible for the n-type conductivity of ZnO [131] (discussed in Section 3.3.1). The highest room-temperature electron mobility for a bulk ZnO single crystal grown by vapor-phase transport method is reported to be about $205\,\mathrm{cm^2\,V^{-1}\,s^{-1}}$ with a carrier concentration of $6.0 \times 10^{16}\,\mathrm{cm^{-3}}$ [159]. This value is very close to the predicted mobility value. The Hall data obtained as a function of temperature are shown in Figure 1.34. The mobility data were fitted by using Rode's method of solving the Boltzmann transport equation by taking into consideration the major scattering mechanisms, such as polar optical phonon scattering, acoustic phonon scattering through deformation and piezoelectric potentials, and Coulomb scattering from ionized impurities or defects. It was argued that the conduction is dominated by hopping at 8 K due to the carrier freeze-out effect, where the resistivity was measured to be $2.8 \times 10^4\,\Omega\,\mathrm{cm}$. For $15\,\mathrm{K} < T$ 40 K, the transport was determined by a combination of mixed band and hopping conduction, whereas above 40 K, the data were well fitted by using the usual statistical model (charge-balance equation) involving only the transport in the conduction band. The mobility showed a peak value of about $2000\,\mathrm{cm^2\,V^{-1}\,s^{-1}}$ at 50 K.

For the carrier concentration data shown in Figure 1.35, a two-donor charge-balance equation was applied to fit the experimental data:

$$n + N_A = \sum_i \frac{N_{Di}}{1 + n/\phi_i}, \tag{1.44}$$

where $\phi_i = (g_{0i}/g_{1i}) N'_c \exp(\alpha_i/k) T^{3/2} \exp(-E_{D0i}/kT)$, and g_{0i} (g_{1i}) is the unoccupied (occupied) state degeneracy of donor i. The term N'_c is the effective conduction band density of states at $T = 1$ K and α_i is the temperature coefficient defined by $E_{Di} = E_{D0i} - \alpha_i T$, where E_{Di} is the activation energy of donor i. Although their origin was left unclear in this work [159], it has been determined that the dominant

Table 1.12 A compilation of XRD results, electron mobilities, and corresponding carrier concentrations obtained in nominally undoped bulk and thin-film ZnO deposited on different substrates by various growth techniques.

Sample	FWHM of XRD rocking curves (arcsec)	Carrier concentration (cm^{-3})	Electron mobility ($cm^2 V^{-1} s^{-1}$)	References
Monte Carlo calculation	—	—	300	[158]
Bulk ZnO grown by vapor-phase transport method	n/a	6.0×10^{16}	205	[159]
Bulk ZnO grown by pressurized melt method	49 (0 0 0 2)	5.05×10^{17} (296 K), 3.64×10^{16} (77 K)	131 (296 K), 298 (77 K)	[160]
Bulk ZnO grown by hydrothermal method	18 (0 0 0 2)	8×10^{13} (Li compensated)	200	[161]
ZnO thin films grown on *c*-plane sapphire substrates by PLD	151 (0 0 0 2)	2.0×10^{16}	155	[162]
ZnO thin films grown on *c*-plane sapphire grown by MBE	42 (0 0 0 2)	1.2×10^{17}	130	[163]
ZnO thin films grown on *a*-plane sapphire by MBE	n/a	7.0×10^{16}	120	[164]
$Zn_{0.9}Mn_{0.1}O$/ZnO heterostructure grown on *c*-plane sapphire by PLD	n/a	8.8×10^{12} (areal concentration cm^{-2})	130	[165]
ZnO thin films grown on *c*-plane sapphire with ZnO/MgO double-buffer layers grown by MBE	18 (0 0 0 2), 1076 (1 0 $\bar{1}$ 1)	1.2×10^{17}	145	[166, 167]
ZnO thin films grown on MgZnO-buffered $ScAlMgO_4$ substrates by PLD	<12 (0 0 0 2), <12 (1 0 $\bar{1}$ 1)	1×10^{16}	440	[168]

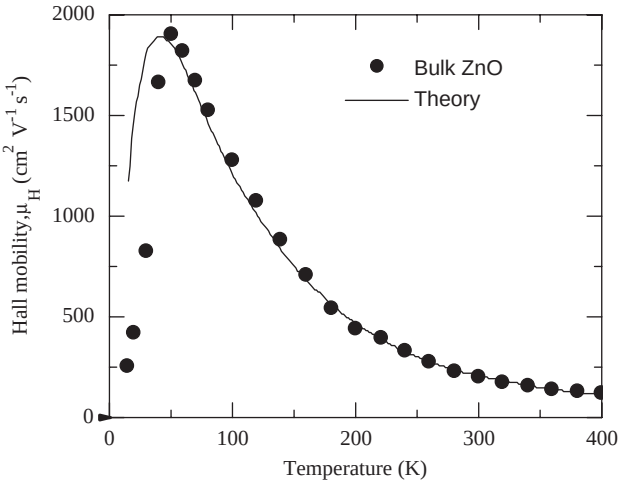

Figure 1.34 Experimental (circles) and theoretical (solid line) Hall mobility as a function of temperature in bulk ZnO. (After Ref. [159].)

hydrogenic shallow donor had a concentration of about $1 \times 10^{17}\,cm^{-3}$ and an energy of about 60 meV, whereas the total acceptor concentration was much lower, about $2 \times 10^{15}\,cm^{-3}$, resulting in a lower compensation ratio of 0.02. However, the shallower donor that was ruled out due to its smaller concentration (about one order of magnitude less than the deeper donor) at an energy of ~31 meV was further investigated later by the same group [169]. They reported that high-energy electron irradiation in ZnO produces shallow donors at about 30 meV. Because the process was found to depend on polarity, where the production rate is much higher for

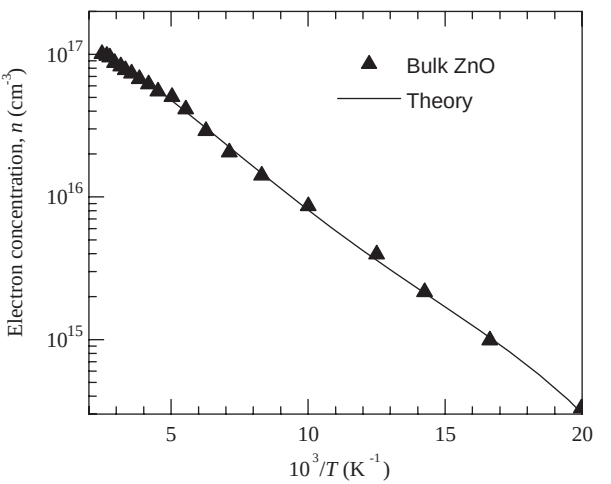

Figure 1.35 Experimental carrier concentration (triangles) corrected for Hall *r*-factor and theoretical fit (solid line) as a function of inverse temperature for bulk ZnO. (After Ref. [159].)

Zn-face [0 0 0 1] than O-face [0 0 0 $\bar{1}$] irradiation, it has been concluded that this native shallower donor is related to a Zn sublattice defect, most likely the interstitial Zn_I or a Zn_I-related complex.

Regarding the ZnO epilayers grown by various growth techniques on different substrates, room-temperature mobilities are relatively poor [170] (typically below 100 $cm^2 V^{-1} s^{-1}$) compared to bulk ZnO, particularly the variety grown by the vapor-phase transport method. However, as listed in Table 1.12, some room-temperature mobility values are comparable to the best reported value for bulk ZnO. Kaidashev *et al.* [162] reported the best reproducible electron mobilities from 115 up to 155 $cm^2 V^{-1} s^{-1}$ at 300 K in a narrow carrier concentration range from 2 to 5×10^{16} cm^{-3} for nominally undoped ZnO thin films of total thickness of 1–2 μm grown on *c*-plane sapphire substrates by a multistep PLD technique. They attributed this success to the multistep PLD process, which includes the insertion of 30 nm thin ZnO relaxation layers deposited at a reduced substrate temperature. The topographical properties of the films were correlated with the corresponding electrical properties. The high-mobility samples showed atomically flat surface structure with grain size of about 0.5–1 μm, whereas the surfaces of low-mobility films consisted of clearly resolved hexagonally faceted columnar grains of only 200 nm size. The observation of the excitonic features in low-temperature photoluminescence spectra also reflects the quality of the samples, which is of primary importance to improve the electrical properties of ZnO.

Kato *et al.* [163] and Iwata *et al.* [164] have performed similar studies on ZnO heteroepitaxial layers grown using plasma-assisted MBE and radical-source MBE techniques. Kato *et al.* [163] used (1 1 $\bar{2}$ 0)*a*-plane sapphire substrates and high-temperature growth with low-temperature buffer layers for high-quality undoped ZnO epitaxial films. They obtained electron mobilities as high as 120 $cm^2 V^{-1} s^{-1}$ and residual carrier concentrations as low as 7×10^{16} cm^{-3}. With further optimization of the growth condition such as O/Zn flux ratio, a maximum mobility of 130 $cm^2 V^{-1} s^{-1}$ with a residual carrier concentration of 1.2×10^{17} cm^{-3} was reported [171]. It has been suggested that stoichiometric ZnO films have the lowest dislocation density and the highest electron mobility compared to ZnO films grown under nonstoichiometric flux conditions [163]. Iwata *et al.* [164] used ZnO/MgO double-buffer layers for high electron mobility ZnO epilayers grown on *c*-plane sapphire. It has been argued that the precisely controlled low growth rate of the double-buffer layers was crucial for the improvement of electrical properties. The highest electron mobility of 145 $cm^2 V^{-1} s^{-1}$ in MBE-grown ZnO film was reported at room temperature [166]. This improvement was attributed to a decrease in dislocation density, based on both X-ray diffraction omega rocking curve measurements and calculated electron mobilities.

ZnO-based heterostructures, which contain magnetic impurities in the barrier layer, were grown on *c*-cut sapphire substrates by pulsed laser deposition by Edahiro *et al.* [165]. The temperature dependence of the mobility of the $Zn_{0.9}Mn_{0.1}O$/ZnO heterostructure exhibits the suppression of ionized impurity scattering below 100 K as shown in Figure 1.36. The carrier concentration and the mobility measured at 1.85 K are 4.0×10^{12} cm^{-2} and 360 $cm^2 V^{-1} s^{-1}$, respectively. These transport

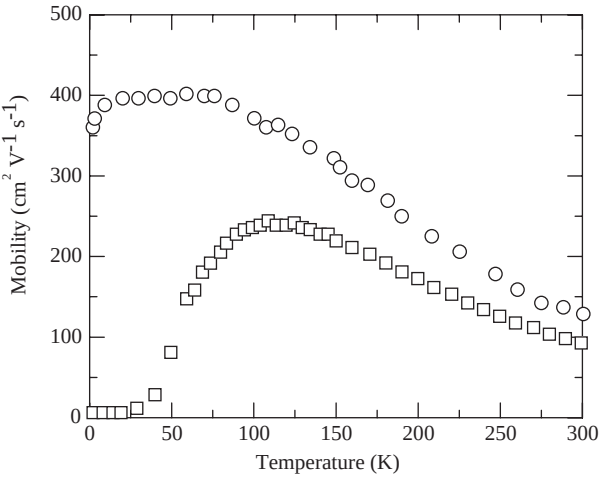

Figure 1.36 Temperature dependence of the mobility of the ZnMnO/ZnO heterostructure (circles) and the 1 μm thick ZnO single layer (squares) control sample. (After Ref. [165].)

properties revealed that two-dimensional electron gas is successfully formed at the $Zn_{0.9}Mn_{0.1}O$/ZnO interface.

1.7.2 High-Field Transport

Ensemble Monte Carlo (MC) simulations have been the popular tools to investigate the steady-state and transient electron transport in semiconductors theoretically. In particular, the steady-state velocity field characteristics have been determined using the Monte Carlo method for electric field strengths up to 350 kV cm^{-1} in bulk wurtzite structure ZnO at lattice temperatures of 300, 450, and 600 K [158]. The conduction bands of wurtzite-phase ZnO structure were calculated using FP-LMTO-LDA method. For the MC transport simulations, the lowest Γ valley (Γ_1 symmetry) and the satellite valleys located at Γ (Γ_3 symmetry) and at U point, U_{min} (U_1 symmetry), which is located two-thirds of the way between the M and L symmetry points on the edge of the Brillouin zone, have been considered.

The calculated electron drift velocity versus electric field characteristics are plotted in Figure 1.37 for wurtzite-phase ZnO along with GaN for comparison. The first change in the differential mobility curve near 50 kV cm^{-1} has been attributed to the onset of significant spontaneous polar optical phonon emission as the electrons are accelerated to energies greater than the longitudinal optical phonon energy of 72 meV. At higher temperatures, this effect reduces and becomes almost negligible at 600 K because the emission and absorption rates are of comparable magnitude at elevated lattice temperatures. With increasing electric field, the drift velocity increases and reaches a peak value of 3×10^7 cm s^{-1} at 250 K. Further increase of electric field results in negative differential effect. However, from examination of the

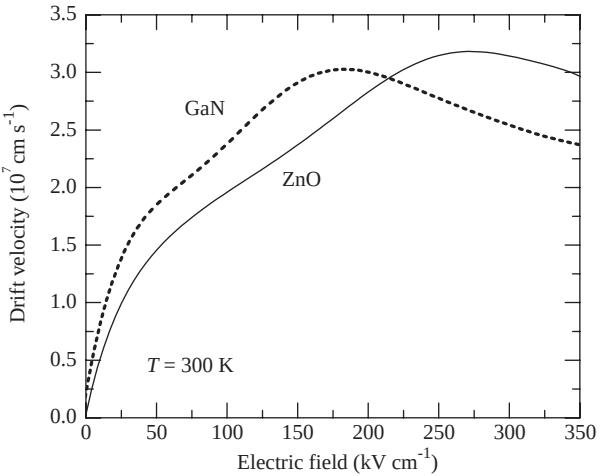

Figure 1.37 Comparison of calculated electron drift velocity versus electric field for wurtzite structure ZnO (solid) and GaN (dashed) at 300 K. (After Ref. [158].)

electron energy distributions that showed only insignificant transfer of electrons to the higher valleys, the strong decrease of the differential mobility with increasing electric field was attributed to the pronounced nonparabolicity of the central valley. A comparison of the drift velocity of ZnO to the calculated drift velocity of wurtzite GaN although shows comparable peak velocities (see Ref. [91] for details regarding GaN), the peak fields differ considerably, with the peak field for GaN being about 100 kV cm^{-1} lower than that of ZnO. It has been argued that this difference arises mainly from the lower satellite valleys in GaN, which have been demonstrated to exhibit a transferred electron effect, and from the stronger Fröhlich coupling in ZnO. Experimental investigations or any other theoretical work related to the high-field transport and energy and momentum relaxation in ZnO are not available in the literature. If the hot phonon effects prevalent in GaN were also to take place in ZnO, which is more than likely, much more refined work is needed on the theoretical side as well to get a representative velocity figure in ZnO at high fields (see Ref. [91] for a detailed discussion of hot phonon effects on heat dissipation and carrier transport).

References

1 Leszczynski, M. (1999) Common crystal structure of the group III-nitrides, in *Properties, Processing and Applications of Gallium Nitride and Related Semiconductors* (eds J.H. Edgar, S. Strite, I. Akasaki, H. Amano and C. Wetzel), *EMIS Datareviews Series No. 23*, INSPEC, The Institution of Electrical Engineers, Stevenage, UK, pp. 3–5.

2 Ambacher, O., Majewski, J., Miskys, C., Link, A., Hermann, M., Eickhoff, M., Stutzmann, M., Bernardini, F.,

Fiorentini, V., Tilak, V., Schaff, B. and Eastman, L.F. (2002) Pyroelectric properties of Al(In)GaN/GaN hetero- and quantum well structures. *Journal of Physics: Condensed Matter*, **14**, 3399.

3 Leszczynski, M., Suski, T., Perlin, P., Teisseyre, H., Grzegory, I., Bockowski, M., Jun, J., Porowski, S., Pakula, K., Baranowski, J.M., Foxon, C.T. and Cheng, T.S. (1996) *Applied Physics Letters*, **69**, 73.

4 Kisi, E. and Elcombe, M.M. (1989) *Acta Crystallographica Section C. Crystal Structure Communications*, **45**, 1867.

5 Kogure, T. and Bando, Y. (1993) *Journal of Electron Microscopy*, **47**, 7903.

6 Ashrafi, A.B.M.A., Ueta, A., Avramescu, A., Kumano, H., Suemune, I., Ok, Y.-W. and Seong, T.-Y. (2000) *Applied Physics Letters*, **76**, 550.

7 Kim, S.-K., Jeong, S.-Y. and Cho, C.-R. (2003) *Applied Physics Letters*, **82**, 562.

8 Bates, C.H., White, W.B. and Roy, R. (1962) *Science*, **137**, 993.

9 Gerward, L. and Olsen, J.S. (1995) *Journal of Synchrotron Radiation*, **2**, 233.

10 Recio, J.M., Blanco, M.A., Luaña, V., Pandey, R., Gerward, L. and Staun Olsen, J. (1998) Compressibility of high-pressure rock salt phase of ZnO. *Physical Review B: Condensed Matter*, **58**, 8949.

11 Jamieson, J.C. (1970) *Physics of the Earth and Planetary Interiors*, **3**, 201.

12 Desgreniers, S. (1998) High-density phases of ZnO: structural and compressive parameters. *Physical Review B: Condensed Matter*, **58**, 14102.

13 Karzel, H., Potzel, W., Köfferlein, M., Schiessl, W., Steiner, M., Hiller, U., Kalvius, G.M., Mitchell, D.W., Das, T.P., Blaha, P., Schwarz, K. and Pasternak, M.P. (1996) *Physical Review B: Condensed Matter*, **53**, 11425.

14 Ahuja, R., Fast, L., Eriksson, O., Wills, J.M. and Johansson, B. (1998) *Journal of Applied Physics*, **83**, 8065.

15 Recio, J.M., Pandey, R. and Luana, V. (1993) *Physical Review B: Condensed Matter*, **47**, 3401.

16 Wilson, M. and Madden, P.A. (1997) *Molecular Physics*, **90**, 75.

17 Liu, L.-G. and Bassett, W.A. (1986) *Elements, Oxides and Silicates: High-Pressure Phases with Implications for the Earth's Interior*, Oxford University Press, New York.

18 Jaffe, J.E., Snyder, J.A., Lin, Z. and Hess, A.C. (2000) *Physical Review B: Condensed Matter*, **62**, 1660.

19 Zaoui, A. and Sekkal, W. (2002) *Physical Review B: Condensed Matter*, **66**, 174106.

20 Jaffe, J.E. and Hess, A.C. (1993) *Physical Review B: Condensed Matter*, **248**, 7903.

21 Weast, R.C. (1997) *CRC Handbook of Chemistry and Physics*, 58th edn, CRC Press, Boca Raton, FL.

22 Bunn, C.W. (1935) *Proceedings of the Physical Society*, **47**, 836.

23 Braekken, H. and Jore, C. (1935) *Det Norske Videnskabers Skifter (The Norwegian Science Scripts)*, **NR8**, 1 (in Norwegian).

24 Heller, R.B., McGannon, J. and Weber, A.H. (1950) *Journal of Applied Physics*, **21**, 1283.

25 Rymer, T.B. and Archard, G.D. (1952) *Research (London)*, **5**, 292.

26 Cimino, A., Marezio, M. and Santoro, A. (1957) *Naturwissenschaften*, **12**, 348.

27 Gray, T.J. (1954) *Journal of the American Ceramic Society*, **37**, 534.

28 Mohatny, G.P. and Azaroff, L.V. (1961) *Journal of Chemical Physics*, **35**, 1268.

29 Khan, A.A., (1968) *Acta Crystallographica Section A*, **24**, 403.

30 Reeber, R.R. (1970) *Journal of Applied Physics*, **41**, 5063.

31 Bond, W.L. (1960) *Acta Crystallographica*, **13**, 814.

32 Catti, M., Noel, Y. and Dovesi, R. (2003) *Journal of Physics and Chemistry of Solids*, **64**, 2183.

33 Noel, Y., Zicovich-Wilson, C.M., Civalleri, B., D'Arco, Ph. and Dovesi, R. (2001) *Physical Review B: Condensed Matter*, **65**, 014111.

34 Himpsel, F.J. (1983) *Advances in Physics*, **32**, 1.

35 Rössler, U. (1969) Energy band of hexagonal II–VI semiconductors. *Physical Review*, **184**, 733.

36 Langer, D.W. and Vesely, C.J. (1970) *Physical Review B: Condensed Matter*, **2**, 4885.

37 Powell, R.A., Spicer, W.E. and McMenamin, J.C. (1971) *Physical Review Letters*, **27**, 97.

38 Powell, R.A., Spicer, W.E. and McMenamin, J.C. (1972) *Physical Review B: Condensed Matter*, **6**, 3056.

39 Ley, L., Pollak, R.A., McFeely, F.R., Kowalezyk, S.P. and Shirley, D.A. (1974) *Physical Review B: Condensed Matter*, **9**, 600.

40 Vesely, C.J., Hengehold, R.L. and Langer, D.W. (1972) *Physical Review B: Condensed Matter*, **5**, 2296.

41 Bloom, S. and Ortenburger, I. (1973) *Physica Status Solidi b: Basic Research*, **58**, 561.

42 Chelikowsky, J.R. (1977) *Solid State Communications*, **22**, 351.

43 Ivanov, I. and Pollmann, J. (1981) *Physical Review B: Condensed Matter*, **24**, 7275.

44 Lee, D.H. and Joannopoulos, J.D. (1981) *Physical Review B: Condensed Matter*, **24**, 6899.

45 Schröer, P., Krüger, P. and Pollmann, J. (1993) *Physical Review B: Condensed Matter*, **47**, 6971.

46 Massidda, S., Resta, R., Posternak, M. and Baldereschi, A. (1995) *Physical Review B: Condensed Matter*, **52**, R16977.

47 Schröer, P., Krüger, P. and Pollmann, J. (1994) *Physical Review B: Condensed Matter*, **49**, 17092.

48 Vogel, D., Krüger, P. and Pollmann, J. (1995) *Ab initio* electronic-structure calculations for II–VI semiconductors using self-interaction-corrected pseudopotentials. *Physical Review B: Condensed Matter*, **52**, R14316.

49 Girard, R.T., Tjernberg, O., Chiaia, G., Söderholm, S., Karlsson, U.O., Wigren, C., Nylèn, H. and Lindau, I. (1997) *Surface Science*, **373**, 409.

50 Duke, C.B., Lubinsky, A.R., Chang, S.C., Lee, B.W. and Mark, P. (1977) *Physical Review B: Condensed Matter*, **15**, 4865.

51 Duke, C.B., Meyer, R.J., Paton, A. and Mark, P. (1978) *Physical Review B: Condensed Matter*, **18**, 4225.

52 Wang, Y.R. and Duke, C.B. (1987) *Surface Science*, **192**, 309.

53 Göpel, W., Pollmann, J., Ivanov, I. and Reihl, B. (1982) *Physical Review B: Condensed Matter*, **26**, 3144.

54 Zwicker, G. and Jacobi, K. (1985) *Solid State Communications*, **54**, 701.

55 Ozawa, K., Sawada, K., Shirotori, Y., Edamoto, K. and Nakatake, M. (2003) Angle-resolved photoelectron spectroscopy study of the anion-derived dangling-bond band on ZnO $(1\,0\,\bar{1}\,0)$. Physical Review B: Condensed Matter, **68**, 125417.

56 Wei, S.H. and Zounger, A. (1988) *Physical Review B: Condensed Matter*, **37**, 8958.

57 Martins, J.L., Troullier, N. and Wei, S.H. (1991) *Physical Review B: Condensed Matter*, **43**, 2213.

58 Xu, Y.-N. and Ching, W.Y. (1993) *Physical Review B: Condensed Matter*, **48**, 4335.

59 Zakharov, O., Rubio, A., Blasé, X., Cohen, M.L. and Louie, S.G. (1994) *Physical Review B: Condensed Matter*, **50**, 10780.

60 Lambrecht, W.R.L., Rodina, A.V., Limpijumnong, S., Segall, B. and Meyer, B.K. (2002) *Physical Review B: Condensed Matter*, **65**, 075207.

61 Reynolds, D.C., Look, D.C., Jogai, B., Litton, C.W., Cantwell, G. and Harsch, W.C. (1999) Valence band ordering in ZnO. *Physical Review B: Condensed Matter*, **60**, 2340.

62 Varshni, Y.P. (1967) *Physica*, **34**, 149.

63 Landolt-Börnstein, *Numerical Data and Functional Relationships in Science and Technology*, Vols III/17b and III/41, Springer-Verlag, Berlin.

64 Ko, H.J., Chen, Y.F., Zhu, Z., Yao, T., Kobayashi, I. and Uchiki, H. (2000) Photoluminescence properties of ZnO epilayers grown on $CaF_2(1\,1\,1)$

by plasma assisted molecular beam epitaxy. *Applied Physics Letters*, **76**, 1905.

65 Mang, A., Reimann, K. and Rübenacke, St. (1995) *Solid State Communications*, **94**, 251.

66 Oshikiri, M., Aryasetiawan, F., Imanaka, Y. and Kido, G. (2002) *Physical Review B: Condensed Matter*, **66**, 125204.

67 Cardona, M. (1963) *Journal of Physics and Chemistry of Solids*, **24**, 1543.

68 Oshikiri, M., Imanaka, Y., Aryasetiawan, F. and Kido, G. (2001) *Physica B*, **298**, 472.

69 Ren, C.-Y., Chiou, S.-H. and Hsue, C.-S. (2004) *Physica B*, **349**, 136.

70 Fan, W.J., Abiyasa, A.P., Tan, S.T., Yu, S.F., Sun, X.W., Xia, J.B., Yeo, Y.C., Li, M.F. and Chong, T.C. (2006) *Journal of Crystal Growth*, **287**, 28.

71 Karazhanov, S.Zh., Ravindran, P., Grossner, U., Kjekshus, A., Fjellvåg, H. and Svensson, B.G. (2006) *Solid State Communications*, **139**, 391.

72 Weiher, R.L. (1966) *Physical Review*, **152**, 736.

73 Baer, W.S. (1967) *Physical Review*, **154**, 785.

74 Dinges, R., Fröhlich, D., Staginnus, B. and Staude, W. (1970) *Physical Review Letters*, **25**, 922.

75 Button, K.J., Cohn, D.R., von Ortenbert, M., Lax, B., Mollwo, E. and Helbig, R. (1972) *Physical Review Letters*, **28**, 1637.

76 Landolt-Börnstein (1982) *Numerical Data and Functional Relationships in Science and Technology*, Vol. 22a, Group III (ed. K.-H. Hellwege), Springer-Verlag, Berlin. Hümmer, K. (1973) *Physica Status Solidi b: Basic Research*, **56**, 249.

77 Oshikiri, M., Tanehaka, K., Asano, T. and Kido, G. (1996) *Physica B*, **216**, 351.

78 Imanaka, Y., Oshikiri, M., Takehana, K., Takamasu, T. and Kido, G. (2001) *Physica B*, **298**, 211.

79 Shokhovets, S., Gobsch, G. and Ambacher, O. (2006) *Superlattices and Microstructures*, **39**, 299.

80 Adachi, S. (2005) *Properties of Group-IV, III–V and II–VI Semiconductors*', John Wiley & Sons, Ltd, West Sussex, UK.

81 Jellison, G.E. and Boatner, L.A. (1998) *Physical Review B: Condensed Matter*, **58**, 3586.

82 Hill, N.A. and Waghmare, U. (2000) *Physical Review B: Condensed Matter*, **62**, 8802.

83 Jaffe, J.E., Pandey, R. and Kunz, A.B. (1991) *Physical Review B: Condensed Matter*, **43**, 14030.

84 Hückel, E. (1931) *Zeitschrift fur Physik*, **70**, 204.

85 Polian, A., Grimsditch, M. and Grzegory, I. (1996) *Journal of Applied Physics*, **79**, 3343.

86 Bateman, T.B. (1962) *Journal of Applied Physics*, **33**, 3309.

87 Murnaghan, F.D. (1944) *Proceedings of the National Academy of Sciences of the United States of America*, **30**, 244.

88 Dal Corso, A., Posternak, M., Resta, R. and Baldereschi, A. (1994) *Physical Review B: Condensed Matter*, **50**, 10715.

89 Nye, J.F. (1975) *Physical Properties of Crystals*, Clarendon, Oxford.

90 Bernardini, F., Fiorentini, V. and Vanderbilt, D. (1997) *Physical Review B: Condensed Matter*, **56**, R10024.

91 Morkoç, H. (2008) *Handbook of Nitride Semiconductors and Devices*, Vol. 1, Wiley-VCH Verlag GmbH, Weinheim.

92 Decremps, F., Zhang, J., Li, B. and Liebermann, R.C. (2001) *Physical Review B: Condensed Matter*, **63**, 224105.Decremps, F., Pellicer-Porres, J., Marco Saitta, A., Chervin, J.-C. and Polian, A. (2002) High pressure Raman spectroscopy study of wurtzite ZnO. *Physical Review B: Condensed Matter*, **65**, 092101.

93 Soga, N. and Anderson, O.L. (1967) *Journal of Applied Physics*, **38**, 2985.

94 Kucheyev, S.O., Bradby, J.E., Williams, J.S., Jagadish, C., Toth, M., Phillips, M.R. and Swain, M.V. (2000) *Applied Physics Letters*, **77**, 3373.

95 Phillips, J.C. (1973) *Bonds and Bands in Semiconductors*, Academic Press, New York.

96 Carlotti, G., Fioretto, D., Socino, G. and Verona, E. (1995) *Journal of Physics: Condensed Matter*, **7**, 9147.

97 Carlotti, G., Socino, G., Petri, A. and Verona, E. (1987) *Applied Physics Letters*, **51**, 1889.

98 Azuhata, T., Takesada, M., Yagi, T., Shikanai, A., Torii, K., Nakamura, A., Sota, T., Cantwell, G., Eason, D.B. and Litton, C.W. (2003) *Journal of Applied Physics*, **94**, 968.

99 Kobiakov, I.B. (1980) *Solid State Communications*, **35**, 305.

100 Aoumeur, F.Z., Benkabou, Kh. and Belgoumène, B. (2003) *Physica B*, **337**, 292.

101 Kucheyev, S.O., Bradby, J.E., Williams, J.S., Jagadish, C. and Swain, M.V. (2002) *Applied Physics Letters*, **80**, 956.

102 Martin, R.M. (1972) *Physical Review B: Condensed Matter*, **5**, 1607.

103 Yu, P. and Cardona, M. (1996) *Fundamentals of Semiconductors*, Springer-Verlag, Berlin.

104 Gorla, C.R., Emanetoglu, N.W., Liang, S., Mayo, W.E., Lu, Y., Wraback, M. and Shen, H. (1999) Structural, optical, and surface acoustic wave properties of epitaxial ZnO films grown on (0 1 $\bar{1}$2) sapphire by metalorganic chemical vapor deposition. *Journal of Applied Physics*, **85**, 2595.

105 Damen, T.C., Porto, S.P.S. and Tell, B. (1966) *Physical Review*, **142**, 570.

106 Arguello, C.A., Rousseau, D.L. and Porto, S.P.S. (1969) *Physical Review*, **181**, 1351.

107 Callender, R.H., Sussman, S.S., Selders, M. and Chang, R.K. (1973) *Physical Review B: Condensed Matter*, **7**, 3788.

108 Calleja, J.M. and Cardona, M. (1977) *Physical Review B: Condensed Matter*, **16**, 3753.

109 Tsuboi, M. and Wada, A. (1968) *Journal of Chemical Physics*, **48**, 2615.

110 Porto, S.P.S. and Krishnan, R.S. (1967) *Journal of Chemical Physics*, **47**, 1009.

111 Mitra, S.S., Brafman, O., Daniels, W.B. and Crawford, R.K. (1969) *Physical Review*, **186**, 942.

112 Cardona, M. (1982) *Light Scattering in Solids II, in Springer Topics in Applied Physics*, Vol. 50 (eds M. Cardona and G. Gűntherodt), Springer, Berlin, pp. 19–178.

113 Stroscio, M.A. and Dutta, M. (2001) *Phonons in Nanostructures*, Cambridge University Press.

114 Harima, H. (2002) Properties of GaN and related compounds studied by means of Raman scattering. *Journal of Physics: Condensed Matter*, **14**, R967.

115 Koyano, M., QuocBao, P., ThanhBinh, L.T., HongHa, L., NgocLong, N. and Katayama, S. (2002) *Physica Status Solidi a: Applied Research*, **193**, 125.

116 Venger, E.F., Melnichuk, A.V., Melnichuk, Lu. and Pasechnik, Yu.A. (1995) *Physica Status Solidi b: Basic Research*, **188**, 823.

117 Bundesmann, C., Ashkenov, N., Schubert, M., Rahm, A., Von Wenckstern, H., Kaidashev, E.M., Lorenz, M. and Grundmann, M. (2004) *Thin Solid Films*, **455–456**, 161.

118 Manjon, F.J., Mari, B., Serrano, J. and Romero, A.H. (2005) *Journal of Applied Physics*, **97**, 053516.

119 Duboz, J.Y. (2002) Hot photoluminescence in GaN: carrier energy relaxation and hot phonon effects. *Journal of Applied Physics*, **92**, 4312.

120 Lee, B.C., Kim, K.W., Dutta, M. and Stroscio, M.A. (1997) *Physical Review B: Condensed Matter*, **56**, 997.

121 Bairamov, B.H., Heinrich, A., Irmer, G., Toporov, V.V. and Ziegler, E. (1983) *Physica Status Solidi b: Basic Research*, **119**, 227.

122 Lu, Y.F., Ni, H.Q. and Ren, Z.M. (2000) *Journal of Applied Physics*, **88**, 498.

123 Ashkenov, N., Mbenkum, B.N., Bundesmann, C., Riede, V., Lorenz, M., Spemann, D., Kaidashev, E.M., Kasic, A., Schubert, M., Grundmann, M., Wagner, G., Neumann, H., Darakchieva, V., Arwin,

H. and Monemar, B. (2003) Infrared dielectric functions of phonon modes of high-quality ZnO films. *Journal of Applied Physics*, **93**, 126.

124 Rajalakshmi, M., Arora, A.K., Bendre, B.S. and Mahamuni, S. (2000) *Journal of Applied Physics*, **87**, 2445.

125 Minomura, S. (1984) Proceedings of the Ninth AIRAPT International High Pressure Conference on High Pressure in Science and Technology (eds C. Homan, R.K. MacCrane, and E. Whalley), North-Holland, New York, p. 277.

126 Limpijumnong, S. and Lambrecht, W.R.L. (2001) *Physical Review Letters*, **86**, 91.

127 Serrano, J., Rubio, A., Hernández, E., Muñoz, A. and Mujica, A. (2000) *Physical Review B: Condensed Matter*, **62**, 16612.

128 Kaschner, A., Haboeck, U., Strassburg, M., Strassburg, M., Kaczmarczyk, G., Hoffmann, A., Thomsen, C., Zeuner, A., Alves, H.R., Hofmann, D.M. and Meyer, B.K. (2002) *Applied Physics Letters*, **80**, 1909.

129 Bundesmann, C., Ashkenov, N., Schubert, M., Spemann, D., Butz, T., Kaidashev, E.M., Lorenz, M. and Grundmann, M. (2003) *Applied Physics Letters*, **83**, 1974.

130 Manjón, F.J., Mari, B., Serrano, J. and Romero, A.H. (2005) *Journal of Applied Physiology*, **97**, 053516.

131 Van de Walle, C.G. (2000) *Physical Review Letters*, **85**, 1012.

132 McCluskey, M.D., Jokela, S.J., Zhuravlev, K.K., Simpson, P.J. and Lynn, K.G. (2002) *Applied Physics Letters*, **81**, 3807.

133 Lavrov, E.V., Weber, J., Börrnert, F., Van de Walle, C.G. and Helbig, R. (2002) *Physical Review B: Condensed Matter*, **66**, 165205.

134 Lavrov, E.V. (2003) *Physica B*, **340–342**, 195.

135 Jokela, S.J., McCluskey, M.D. and Lynn, K.G. (2003) *Physica B*, **340–342**, 221.

136 Nickel, N.H. and Fleischer, K. (2003) Hydrogen local vibrational modes in zinc oxide. *Physical Review Letters*, **90**, 197402.

137 Wolk, J.A., Ager, J.W., III, Duxstad, K.J., Haller, E.E., Taskar, N.R., Dorman, D.R. and Olego, D.J. (1993) *Applied Physics Letters*, **63**, 2756.

138 Ibach, H. (1969) *Physica Status Solidi*, **33**, 257.

139 Touloukina, Y.S., Kirby, R.K., Taylor, R.E. and Lee, T.Y. (1977) *Thermal Expansion. Thermal Properties of Matter*, Vol. 13, Plenum, New York.

140 Iwanaga, H., Kunishige, A. and Takeuchi, S. (2000) Anisotropic thermal expansion in wurtzite-type crystals. *Journal of Materials Science*, **35**, 2451.

141 Han, M.-Y. and Jou, J.-H. (1995) *Thin Solid Films*, **260**, 58.

142 Bhandari, C.M. and Rowe, D.M. (1988) *Thermal Conduction in Semiconductors*, John Wiley & Sons, Inc., New York.

143 Kittel, C. (1986) *Introduction to Solid State Physics*, 6th edn., John Wiley & Sons, Inc., New York, p. 150.

144 Florescu, D.I., Asnin, V.M., Pollak, F.H., Molnar, R.J. and Wood, C.E.C. (2000) *Journal of Applied Physics*, **88**, 3295.

145 Florescu, D.I., Asnin, V.M., Pollak, F.H., Jones, A.M., Ramer, J.C., Schurman, M.J. and Ferguson, I. (2000) *Applied Physics Letters*, **77**, 1464.

146 Florescu, D.I., Mourokh, L.G., Pollak, F.H., Look, D.C., Cantwell, G. and Li, X. (2002) *Journal of Applied Physics*, **91**, 890.

147 Özgür, Ü., Gu, X., Spradlin, J., Cho, S.-J., Morkoç, H., Pollak, F.H., Nemeth, B. and Nause, J. (2006) *Journal of the Electrochemical Materials*, **85**, 550.

148 Olorunyolemi, T., Birnboim, A., Carmel, Y., Wilson, O.C., Jr, and Lloyd, I.K. (2002) *Journal of the American Ceramic Society*, **85**, 1249.

149 Tsubota, T., Ohtaki, M., Eguchi, K. and Arai, H. (1997) *Journal of Materials Chemistry*, **7**, 85.

150 Ohtaki, M., Tsubota, T., Eguchi, K. and Arai, H. (1996) *Journal of Applied Physics*, **79**, 1816.

151 Katsuyama, S., Takagi, Y., Ito, M., Majima, K., Nagai, H., Sakai, H., Yoshimura, K.

and Kosuge, K. (2002) *Journal of Applied Physics*, **92**, 1391.
152 Tsubota, T., Ohtaki, M. and Eguchi, K., Arai, H. (1998) *Journal of Materials Chemistry*, **8**, 409.
153 Cai, K.F., Müller, E., Drašar, C. and Mrotzek, A. (2003) *Materials Science and Engineering B*, **104**, 45.
154 Lawless, W.N. and Gupta, T.K. (1986) *Journal of Applied Physics*, **60**, 607.
155 Zook, J.D. and Liu, S.T. (1973) Pyroelectric effects in thin film. *Journal of Applied Physics*, **49**, 4604.
156 Newnham, R.E. (2005) *Properties of Materials: Anisotropy, Symmetry, Structure*, Oxford University Press, New York.
157 Ye, C.-P., Tamagawa, T. and Polla, D.L. (1991) Experimental studies on primary and secondary pyroelectric effects in Pb $(Zr_x,Ti_{1-x})O_3$, $PbTiO_3$, and ZnO thin films. *Journal of Applied Physics*, **70**, 5538.
158 Albrecht, J.D., Ruden, P.P., Limpijumnong, S., Lambrecht, W.R.L. and Brennan, K.F. (1999) *Journal of Applied Physics*, **86**, 6864.
159 Look, D.C., Reynolds, D.C., Sizelove, J.R., Jones, R.L., Litton, C.W., Cantwell, G. and Harsch, W.C. (1998) *Solid State Communications*, **105**, 399.
160 Nause, J. and Nemeth, B. (2005) *Semiconductor Science and Technology*, **20**, S45.
161 Maeda, K., Sato, M., Niikura, I. and Fukuda, T. (2005) *Semiconductor Science and Technology*, **20**, S49.
162 Kaidashev, E.M., Lorenz, M., Von Wenckstern, H., Rahm, A., Semmelhack, H.-C., Han, K.-H., Benndorf, G., Bundesmann, C., Hochmuth, H. and Grundmann, M. (2003) *Applied Physics Letters*, **82**, 3901.
163 Kato, H., Sano, M., Miyamoto, K. and Yao, T. (2003) *Japanese Journal of Applied Physics, Part 1: Regular Papers, Short Notes & Review Papers*, **42**, 2241.
164 Iwata, K., Fons, P., Niki, S., Yamada, A., Matsubara, K., Nakahara, K. and Takasu, H. (2000) *Physica Status Solidi a: Applied Research*, **180**, 287.
165 Edahiro, T., Fujimura, N. and Ito, T. (2003) *Journal of Applied Physics*, **93**, 7673.
166 Miyamoto, K., Sano, M., Kato, H. and Yao, T. (2004) *Journal of Crystal Growth*, **265**, 34.
167 Cho, M.V., Setiawan, A., Ko, K.J., Hong, S.K. and Yao, T. (2005) *Semiconductor Science and Technology*, **20**, S13.
168 Ohmoto, A. and Tsukazaki, A. (2005) *Semiconductor Science and Technology*, **20**, S1.
169 Look, D.C., Hemsky, J.W. and Sizelove, J.R. (1999) *Physical Review Letters*, **82**, 2552.
170 Ginley, D.S. and Bright, C. (2000) *Materials Research Bulletin*, **25**, 15.
171 Miyamoto, K., Sano, M., Kato, H. and Yao, T. (2002) *Japanese Journal of Applied Physics, Part 2: Letters*, **41**, L1203.

2
ZnO Growth

The growth of zinc oxide (ZnO) thin films has been studied by a variety of techniques, fuelled by applications such as acoustical and optical devices. The applications have been driven in part due to the excellent piezoelectric properties of ZnO and its tendency to grow with strong (0 0 0 1) preferential orientation on various kinds of substrates, including glass [1], sapphire [2], and diamond [3]. The early reports dealt with deposition of ZnO utilizing growth techniques such as magnetron sputtering [3, 4] and chemical vapor deposition [5–7]. However, the films were mainly polycrystalline. Later attempts paved the way to high-quality ZnO single-crystal films prepared by radio frequency (RF) magnetron sputtering [8, 9] and other growth techniques that allow fine control over the deposition procedure. Among the latter deposition techniques are molecular beam epitaxy (MBE) [10, 11], pulsed laser deposition (PLD) [12], organometallic vapor-phase epitaxy (OMVPE) [13], and hydride or halide vapor-phase epitaxy (HVPE), depending on the chemistry used [14, 15]. Table 1.12 compiles some of the structural and electrical properties obtained from ZnO samples grown by different techniques. As time went on, the improved quality of ZnO films allowed the observation of optically pumped lasing at room temperature [16]. Furthermore, the potential applications of ZnO to ultraviolet light emitters provide the impetus for considerable research effort on ZnO growth [16, 17]. Although high-quality ZnO substrates are available, which make homoepitaxy possible, most of the growth has been undertaken on sapphire (Al_2O_3) due to its low cost, availability in large quantities, and its wide energy bandgap despite its poor structural and thermal match to ZnO. It should be mentioned that the availability of high-quality ZnO substrates does not automatically pave the way for high-quality epitaxial layers, and much work remains to be done to attain epitaxial layer matching the bulk in quality. Clearly, the growth of ZnO will evolve to rely on ZnO substrates. As compared to GaN/Al_2O_3, ZnO/Al_2O_3 has approximately equivalent X-ray diffraction (XRD) and photoluminescence (PL) linewidths, and even lower dislocation densities [18]. Heteroepitaxial ZnO layers have been grown on several other substrates, such as CaF_2 [19], Si [20], GaAs [21, 22], and $ScAlMgO_4$ [23], as well as on GaN/Al_2O_3 templates [12].

2.1 Bulk Growth

Growth of large area and high-quality ZnO crystals is important not just for basic investigations but also for many device applications. Although sapphire has been conventionally used as the substrate for ZnO growth, high dislocation density caused by the large lattice mismatch (in-plane lattice mismatch: 18.4%) between the sapphire substrate and ZnO would deteriorate any device performance. High-quality large ZnO single crystals would be beneficial for the UV and blue-UV light-emitting devices, due to the potential advantages of homoepitaxy. With its perfect lattice matching (both in-plane and out-of-plane), homoepitaxy has the potential for eliminating strain induced by thermal expansion mismatch and highly defective substrate–layer interface, allowing lower overall defect density, easy control over the material polarity by using Zn face (0 0 0 1) or O face $(0\,0\,0\,\bar{1})$ substrate, and simple device design (ZnO substrates can be made very conductive). In addition to homoepitaxy, ZnO single-crystal substrates could also be useful for heteroepitaxy of GaN-based active layers. The stacking order of ZnO is the same as that of GaN, with a lattice mismatch of only 1.8%.

Growth of bulk ZnO crystals is mainly carried out by three methods: hydrothermal [24–27], seeded vapor transport (sublimation) [28–31], and melt growth [32, 33]. Because of its high vapor pressure, growth of ZnO from the melt is difficult, and growth by vapor-phase deposition is difficult to control. A small amount of supersaturation of the solution during hydrothermal reaction fuels crystal growth. The hydrothermal method is very well known for growth of quartz crystals and is well established. Therefore, its application to the large-area ZnO single crystals is quite suitable. The growth rate of ZnO through this method has been reported to be anisotropic. The growth rate in the [0 0 0 1] direction was ~0.25 mm/day, and the ratio of growth rates between the fast ([0 0 0 1]) direction and slow $([0\,0\,0\,\bar{1}])$ direction was 3 : 1 [34]. However, the hydrothermal crystals inevitably incorporate alkali metals (K and Li) and small amounts of metallic impurities from the solution.

Figure 2.1 shows a schematic diagram of a *hydrothermal growth* system [24]. Hydrothermal method uses ZnO single-crystal seeds (suspended by Pt wire), and sintered ZnO strings together with a KOH (3 mol l^{-1}) and LiOH (1 mol l^{-1}) aqueous solution are used as a nutrient. The seeds and the particular nutrient used are placed into a Pt crucible. This crucible is sealed by welding and placed in an autoclave. The autoclave is then placed into a two-zone vertical furnace. ZnO is transferred from the nutrient in the higher temperature zone to the seeds in the lower temperature zone. A Pt inner container is used to prevent impurity incorporation from the aqueous solution. The seeds grow to bulk ingots about 10 mm in size after 2 weeks. The growth temperature is 300–400 °C (typically 345 °C for the seeds and 355 °C for the nutrient) at a pressure between 70 and 100 MPa. Generally, about 70–85% of the volume can be filled. Depending on the particulars, the growth runs last some 20–50 days. Transparent ZnO crystals grown by this method to a size of $50 \times 50 \times 15\,mm^3$ showed a full-width at half-maximum (FWHM) of 8 arcsec for the (0 0 0 2) XRD rocking curve [27]. The ZnO crystals were surrounded by the (0 0 01), $(10\bar{1}1)$,

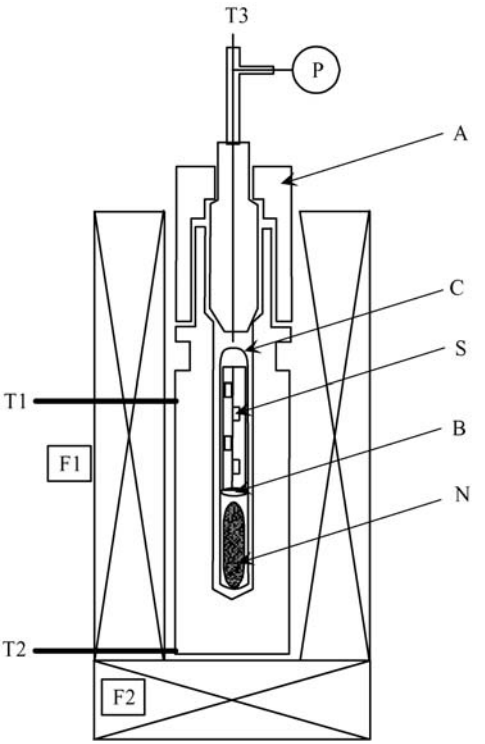

Figure 2.1 Schematic representation of a hydrothermal growth system. F: furnaces (1, 2), T_i: thermocouples for control of furnace temperatures ($i = 1, 2$) and monitor ($i = 3$), *P*: pressure gauge, A: autoclave, C: Pt crucible, S: seed crystals, N: nutrient, and B: baffle. (Courtesy of T. Sekiguchi [24].)

$(10\bar{1}0)$, $(10\bar{1}1)$, and $(000\bar{1})$ faces [26]. The crystal shapes were reported to depend on the precursor and the solution basicity, and on the shapes of seed crystals. The crystal color is nonuniform because of the anisotropic crystal growth in which the growth rate of each sector depends on orientation. When used as substrates for epitaxy, proper surface preparation is necessary to evaluate the quality of hydrothermally grown ZnO [34]. As confirmed by PL and XRD, improved polishing methods result in significantly improved surface quality. Properly polished hydrothermal ZnO exhibits optical properties similar to that of the vapor-phase-grown material.

The potential advantages of the hydrothermal growth are that it is truly a bulk growth method, and it can produce truly freestanding wafers up to 3 inch in diameter. Furthermore, high crystal quality is made available because the material experiences no thermal stress during growth. Continuing on with other attributes of the hydrothermally grown ZnO, low dislocation density is possible ($<10\ cm^{-2}$ in quartz), the growth takes place in chemical equilibrium growth (sometimes disadvantageous), spatially uniform alloys of ZnO are possible (e.g., ZnMgO grown at AFRL-Hanscom [35]), intentional doping of the bulk material with (e.g., Al, In, N,

Co as demonstrated at AFRL-Hanscom [35]) is possible, very high laser hardness can be obtained (as demonstrated in AFRL-Hanscom [35] crystals, even with $\sim 10^{18}$ electrons/cm^3), faceted growth for nonpolar material is possible and finally, hardware required for growth is essentially the same as that for quartz growth, which is very mature.

Going beyond the method itself and focusing on the accomplishments made possible by the hydrothermal method, excellent ~7.5 cm diameter *c*-axis single-crystal substrates have been grown (Tokyo Denpa) [36]. At AFRL-Hanscom, 2.5 cm diameter *c*-axis single-crystal substrates are routinely grown, albeit for research purposes only [35]. Structurally excellent large single crystals are grown by the Fukuda group in Sendai with XRD (0 0 0 2) reflection rocking curve FWHM values of about 20 arcsec [37]. It should also be added that unintentionally doped ZnO grown by the hydrothermal technique is highly resistive (n-type): $n \approx 1 \times 10^{14}\,\mathrm{cm}^{-3}$, $\mu_n \approx 200\ \mathrm{cm}^2\,\mathrm{V}^{-1}\,\mathrm{s}^{-1}$ [37]. The crystals with dislocation etch-pit densities <500 cm^{-2} can be obtained on a routine basis. Currently, the vacancy concentrations are about $\sim 10^{16}$ cm^{-3} as determined by positron annihilation that points to some needed improvement. Doping with N, which can be a p-type impurity (see Section 4.2.1), to levels of $\sim 10^{18}$ cm^{-3} has been demonstrated (AFRL-Hanscom [35]), and so have indium and aluminum doping (again n-type) [35].

The hydrothermal method also faces some challenges. Among them is the quality control of ZnO as "semiconductor crystal," which is more demanding than would be for other applications. Not specific to the hydrothermal method, a stable and well-characterized p-doping with high hole concentration is needed. The impurity levels need to be lowered further. As seen from Figure 2.2, the main impurities in hydrothermal ZnO are Si, Cd, and Li. The source of Si and Cd are the mineralizer and the raw material, respectively; and their concentrations can be reduced by using

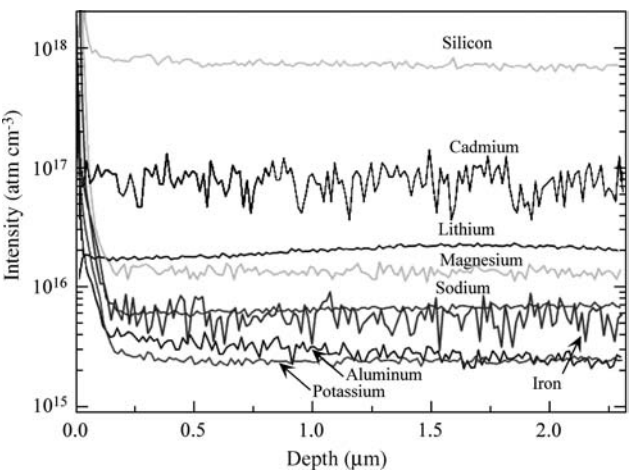

Figure 2.2 Results of secondary ion mass spectroscopy of hydrothermal ZnO (Courtesy of T. Fukuda, Tohoku University and Fukuda Crystal Lab.)

higher purity starting materials. The main challenge, however, is to reduce the Li concentration caused by the aqueous solution of LiOH, which is used as a mineralizer [24]. The segregation in the $c+$ and $c-$ directions, which manifests itself as the piling up of unintentional impurities near seed is another issue. Continuing on with challenges faced, the vacancy concentrations must also be reduced further.

A method that produces very high-quality bulk ZnO wafers is based on *seeded chemical vapor transport*. In this method, the reaction takes place in a nearly closed horizontal tube [28]. Pure ZnO powder used as the ZnO source is placed at the hot end (hot zone) of the tube that is kept at about 1150 °C. The material is transported to the cooler end of the tube, maintained at about 1100 °C, by using H_2 as a carrier gas. The carrier gas is necessary, because the vapor pressures of O and Zn are quite low over ZnO at these temperatures. The likely reaction in the hot zone is $ZnO(s) + H_2(g) \rightarrow Zn(g) + H_2O(g)$. At the cooler end, ZnO is formed by the reverse reaction, assisted by a single-crystal seed. To maintain the proper stoichiometry, a small amount of water vapor is added. Growth times of 150–175 h leads to 2 in. diameter crystals of about 1 cm in thickness, from which the wafers can be sliced and polished as shown in Figure 2.3. ZnO wafers with high spatial uniformity (<1% variation in cathodoluminescence measurements) have been demonstrated. Hall carrier concentration and mobility at 300 K have been measured to be about $6 \times 10^{16}\,cm^{-3}$ and $205\,cm^2\,V^{-1}\,s^{-1}$, respectively, and the peak mobility (at 50 K) was about $2000\,cm^2\,V^{-1}\,s^{-1}$. The chemical impurities for three of such wafers are listed in Table 2.1. Only boron and aluminum were detected among the suspected n-type dopants and nitrogen and sodium among the p-type dopants. Si was identified as the major impurity that was introduced from the quartz ampoule used. Vapor transport using chlorine and carbon as transporting agents has also been used to achieve ZnO crystal growth at moderate temperatures of 950 ~ 1000 °C [31]. FWHMs of (0 0 0 2) XRD rocking curves were around 30 arcsec, and room-temperature electron concentration in the crystals was as high as $3 \times 10^{19}\,cm^{-3}$. Like all other growth techniques, the seeded chemical vapor transport technique also comes with some disadvantages. To

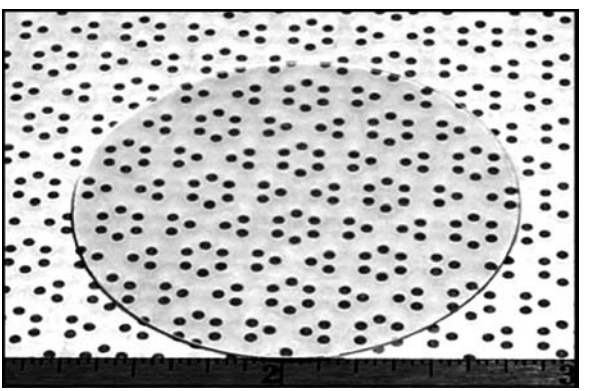

Figure 2.3 ZnO wafer grown by seeded chemical vapor transport with chemical mechanical polish finish on both faces (Courtesy of J.-J. Song, ZN Technology, Inc.)

Table 2.1 Chemical impurities (ppma) in ZnO wafers grown by seeded chemical vapor transport technique.

Impurity	Sample 1	Sample 2	Sample 3
B	0.012	0.012	0.028
C	0.040	0.004	0.091
N	0.028	0.180	1.200
Na	0.015	—	—
Al	0.009	0.007	0.020
Si	0.330	0.280	0.660
Ti	0.001	—	—
Sn	—	0.077	—
Pb	0.002	—	—
Total	0.437	0.560	1.999

After J.-J. Song, ZN Technology, Inc.

cite a few, the wafers have grain boundaries and the low growth rate is problematic which would undoubtedly result in high cost for wafers.

Another method for producing bulk ZnO is that of *melt growth*, which is employed, for example, at Cermet Inc. [32]. The Cermet Inc. melt growth method is based on a pressurized induction melting apparatus (Figure 2.4), where the melt is contained in a cooled crucible. Zinc oxide powder is used as the starting material. The RF energy produces joule heating until the ZnO is molten at about 1900 °C. Once the molten state is attained, the crucible is slowly lowered away from the heated zone to allow crystallization of the melt.

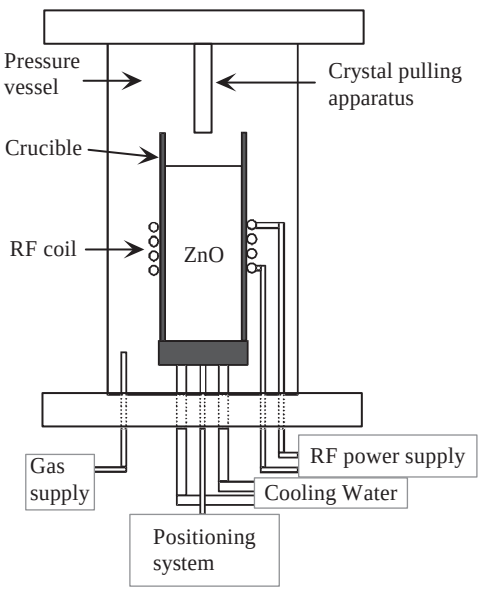

Figure 2.4 Schematic sketch of the ZnO crystal melt growth apparatus. (Courtesy of J. Nause [32].).

Compared to other growth techniques, pressurized melt growth offers advantages such as high-purity material, commercially viable growth rates (1–5 mm h^{-1}), multiple crystal orientations (*c*-, *a*-, or *m*-plane) made possible by three-dimensional nature of growth, and *in situ* doping control (semiinsulating or heavily n-type). The material characteristics of pressurized melt-grown ZnO can be summarized as relatively low defect density (etch-pit density of $\sim 10^4$ cm^{-2}), XRD FWHM of about 49 arcsec for the (0 0 0 2) XRD rocking curve [33], room-temperature electron concentration and mobility of 5×10^{17} cm^{-3} and 131 cm^2 V^{-1} s^{-1}, respectively [33], and an excitonic quantum efficiency of approximately 85%.

The pressurized melt growth method, however, has some undesirable characteristics as well, among which is the low-angle grain boundaries. Crystals without grain boundaries show XRD rocking curves narrower than 50 arcsec. Furthermore, the residual impurity concentration is high, and currently, only a limited amount of 50 mm wafers are available for growth due to small-angle boundaries. On the positive column, the growth vessel can be scaled so that substrates at a diameter of 75 mm or larger could be obtained. In terms of the impurities, the levels in the earlier material were about 19.7 ppm with primary impurities being Al, Si, Fe, Cd, and Pb, all of which come from metallic Zn used in the preparation of the ZnO source material. The impurity levels in improved powder sources have been significantly reduced: Cd (4 ppm), Fe (2 ppm), and Pb (5 ppm), with all others being below detection limit. In the resultant ZnO crystals, the impurity levels were Cd (2 ppm), Fe (2 ppm), and Pb (4 ppm). The analysis for Ca showed 1 ppm both in the powder source and the crystalline material that resulted [38].

In summary, ZnO wafers manufactured by employing different growth technologies are commercially available, and therefore, it is fair to say that bulk ZnO is a reality. Table 2.2 illustrates the current status of the three main growth techniques

Table 2.2 Nominal XRD rocking curve FWHM values and contaminants for ZnO material grown by different methods capable of producing 2 in. size wafers.

Supplier	Growth method	XRD rocking curve FWHM (arcsec)	Contaminants (ppm)
Cermet, Inc. [38]	Melt growth	42	Total = 10 Pb (4.0), Fe (2.0), Cd (2.0), Ca (1.0)
Tokyo Denpa [27]	Hydrothermal	18	Total < 13 Li (<12), Fe (<0.5), Al(<0.4), K(<0.2)
Eagle-Picher	Seeded chemical vapor transport (SCVT)	<100	Total = 3.2 Si(0.7), N(0.7), B(0.5), Ga(0.5)
ZN Technology, Inc.	SCVT	32	Total < 0.56 Si(0.3), N(0.2)

(Courtesy of T. Fukuda, summary of the data reported at "The 3rd International Workshop on ZnO and Related Materials," October 5–8, 2004, Sendai, Japan, Table 2.4P.)

used for bulk ZnO growth. At present, the hydrothermal growth of ZnO is the most mature technology. The hydrothermal material shows the best crystal quality, among the methods discussed, and low concentration of impurities, with an exception of Li (see Table 2.2). As has been shown by the large volume quartz crystal production, the hydrothermal technique is scalable for economical mass production by employing large autoclaves. ZnO growth rates of half the quartz growth rate (10 000 kg/year of quartz are produced) have been achieved. The main challenge, however, for the hydrothermal method is to produce Li-free ZnO. In addition, doping and alloying technologies need to be improved. The competing growth methods (pressurized melt growth and seeded chemical vapor transport) are still considered to be at the developmental stage. The near-term goal for the competing techniques is to resolve the problem of grain boundaries. Pressurized melt growth also suffers from high concentration of residual impurities. Although seeded chemical vapor transport provides the lowest concentration of residual impurities, cost reduction is challenging for this technique owing to low growth rate. As a common challenge to all techniques, growth of non-*c*-axis crystals might need to be explored as polarization charge in structures based on the polar *c*-plane of GaN, the technology for which is quite ahead than that of ZnO, is beginning to be viewed as a problem rather than an advantage. Learning from the GaN technology, the best way to obtain nonpolar surfaces is by growing the bulk material along the *c*-direction and slicing it along the, for example, *m*-plane. This approach eliminates problems induced by the low formation energy of basal stacking faults. It should be mentioned that the lack of midgap donor/acceptors would frustrate efforts to obtain high-resistivity wafers (may not be an intractable problem for high-purity crystals because the bandgap is large). To reiterate, Mg and Cd alloying and doping need to be improved considerably. Finally, the effects of impurities on the growth kinetics with respect to the morphology are not well understood and need further investigation.

2.2 Substrates

To reduce the strains and dislocation density in epitaxial ZnO and related films, closely lattice-matched substrates are favored for growth. Sapphire substrates are commonly used for ZnO heteroepitaxial growth, primarily on the (0 0 0 1) orientation (basal or *c*-plane), and also on the $(1\,1\,\bar{2}\,0)$ *a*-plane. In addition, ZnO and related oxides have been grown on Si [20], SiC [39], GaAs [21, 22], CaF_2 [19], and $ScAlMgO_4$ [23]. Lattice parameters of several substrate materials frequently used for ZnO growth and their mismatch to ZnO are listed in Table 2.3.

2.2.1 Sapphire Substrates for ZnO Epitaxy

Sapphire has the space group of $R\bar{3}c$, as described in the International Tables for Crystallography, and is primarily of ionic bond nature. It can be represented by both

Table 2.3 Lattice parameters of a number of the prospective substrate materials for ZnO.

Material	Crystal structure	Lattice parameters, a (Å), c (Å)	Lattice mismatch (%)	Thermal expansion coefficient, α (10^{-6} K^{-1})	Thermal conductivity, κ (W cm^{-1} K^{-1})	Space group
ZnO	Hexagonal	3.2498 5.2066	0	4.75 2.9	0.4–1.4	$P6_3mc$
MgO	Cubic/rocksalt	4.216	—	10.5		$Fm\bar{3}m$
GaN	Hexagonal	3.1893 5.1851	−1.9	5.59 3.17	2.3	$P6_3mc$
AlN	Hexagonal	3.1106 4.9795	−4.3	4.2 5.3	3.2	$P6_3mc$
α-Al_2O_3 (sapphire)	Rhombohedral	4.758 12.991	∼46 (26.8% after 30° in-plane rotation)	7.5 8.5	0.3–0.5	$R\bar{3}c$
4H-SiC	Hexagonal	3.073 10.053	−5.4			
6H-SiC	Hexagonal	3.0817 15.1123	−5.2	4.2 4.68	4.9	$P6_3mc$
Si	Cubic	5.4301	—	3.59	1.5	$Fd\bar{3}m$
$ScAlMgO_4$	Hexagonal	3.246 25.195	−0.12	6.2 12.2		$R3m$
GaAs	Cubic	5.6533	—	6.0	0.5	$F\bar{4}3m$

Lattice mismatch values are calculated with reference to ZnO.

rhombohedral unit cells, with a volume of 84.929 Å^3, and hexagonal unit cell, with a volume of 254.792 Å^3, which is displayed in Figures 2.5 and 2.6. In the rhombohedral unit cell, there are four Al^{3+} ions and six O^{2-} ions, that is, 10 ions in total. In the hexagonal unit cell, there are 12 Al^{3+} ions and 18 O^{2-} ions, that is, 30 ions in all. The oxygen is located at $(x,y,z) = (0.306,0,0.25)$. If this position is approximated to $(x,y,z) \approx (1/3,0,1/4)$, the anion framework forms an hcp lattice with $a = 0.476$ nm and $c = 1.299$ nm.

As shown in Figure 2.5, the unit cell described by Miller–Bravais indices consists of six close-packed (0 0 0 1) planes of O^{2-} ions sandwiching 12 planes of Al^{3+} ions that occupy two-thirds of the available octahedral voids created by the O^{2-} ions. An Al^{3+} ion is located at $(x, y, z) = (0,0,0.352)$ instead of $(0,0,1/3)$, and thus the cations are shifted by ± 0.025 nm along the c-axis from the ideal octahedral sites. The oxygen ion is larger than the aluminum ion by a factor of about three in terms of its radius; therefore, the steps on the substrate are limited to the steps in the oxygen sublattice, leading to step heights that are multiples of $c/6$ ($d_{(0006)} \approx 0.216$ nm). The (0 0 0 1) Al_2O_3 surfaces are oxygen terminated and present steps along $\{11\bar{2}0\}$ and $\{1\bar{1}00\}$ planes [40]. Two crystallographically equivalent surfaces are related by a symmetry operation of the space group. Along the [0 0 0 1] direction, A–A or B–B surfaces are separated by $c/3$, $2c/3$, and c steps. Steps separating two "A" surfaces are noted as

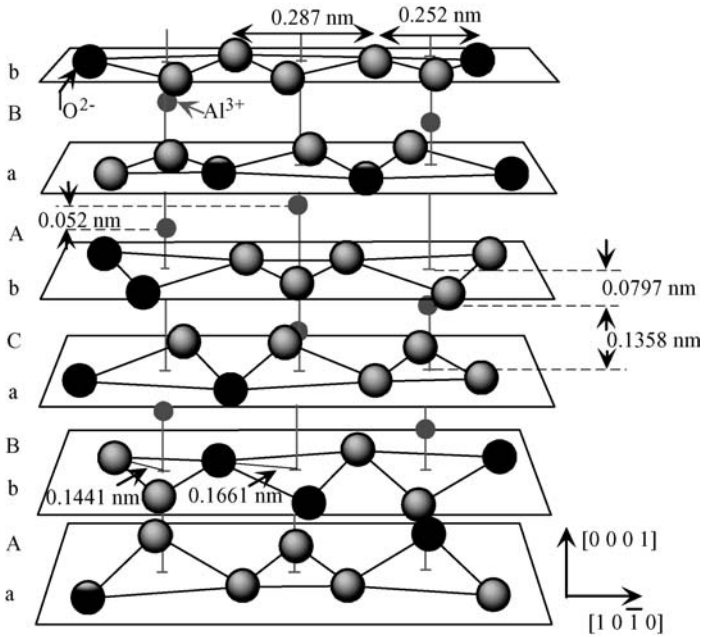

Figure 2.5 A schematic diagram of the Al_2O_3 sapphire unit cell, there are six oxygen layers in the unit cell, the distances between the various atomic layers change as shown in the figure. The oxygen ions form a pseudohexagonal lattice. The small Al ions occupy the octahedral sites. (Courtesy of P. Ruterana.)

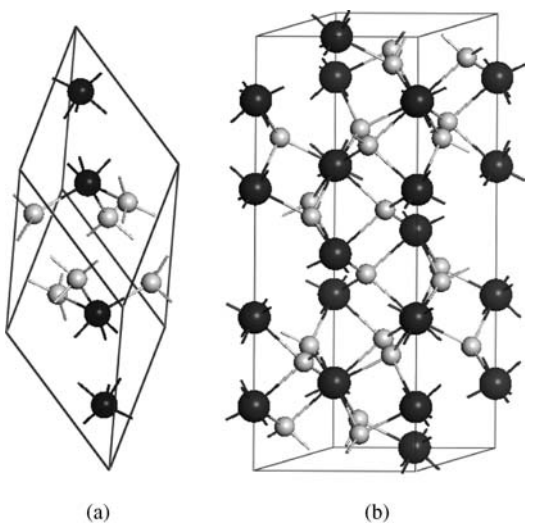

Figure 2.6 The unit cell of sapphire: (a) rhombohedral unit cell; (b) hexagonal unit cell. Smaller spheres are for O and large ones are for Al. (Courtesy of Q. Wang.)

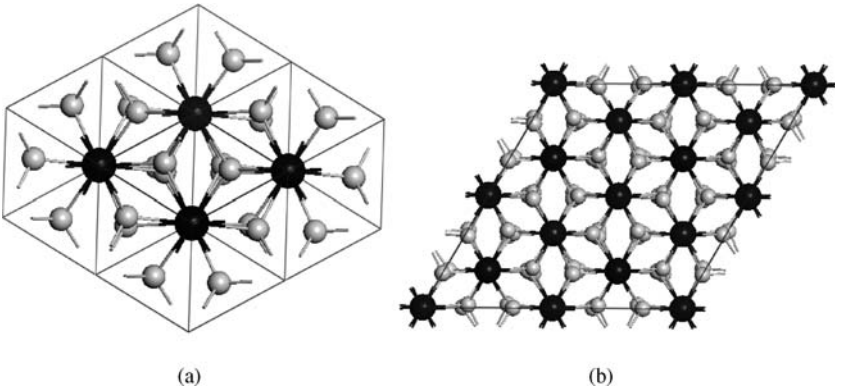

Figure 2.7 Perspective views in ($2 \times 2 \times 1$) unit cells: (a) along the [0 0 0 1] direction in a rhombohedral unit cell; (b) along the (0 0 0 1) direction in hexagonal unit cell. (Courtesy of Q. Wang.)

A–A, and $c/3$ steps of height $c/6$, $c/2$, or $5c/6$ separate the two surfaces related by a glide symmetry operator. Such steps are dubbed as the demisteps and are noted as A–B, $c/6$ [41, 42].

The unreconstructed basal *c*-plane perspective views for both unit cells are shown in Figure 2.7 [43], where the polyhedra are the cell boxes. A schematic representation of sapphire unit cell indicating the six O layers in the unit cell is shown in Figure 2.5. The oxygen ions form a pseudohexagonal lattice. The small Al ions occupy the octahedral sites. The labeling of planes and directions in the context of sapphire substrates are shown in Figure 1.3. Properties of sapphire are tabulated in Table 2.4. All common surfaces employed for ZnO epitaxy including the (0 0 0 1) and the $(1\bar{1}0\,0)$ are nonpolar. Thus, the polarity control on sapphire depends on the particulars of growth conditions employed, with the ominous inversion domain formation always a possibility. Because of heteroepitaxy of ZnO on sapphire, it is useful to display the thermal expansion coefficient of sapphire as is done in Figure 2.8.

As-received sapphire substrates contain scratches caused by mechanical polishing with root-mean-square (rms) roughness values between 0.8 and 2.1 nm over $1\,mm^2$ areas. Wet chemical etches such as phosphoric acid (H_3PO_4), sulfuric–phosphoric acid combination (H_2SO_4–H_3PO_4), fluorinated and chlorofluorinated hydrocarbons, tetrafluoro sulfur (SF_4), and sulfur hexafluoride (SF_6) have been employed. None of these techniques, however, produce a surface free of damage and scratches. For MBE growth, which does not allow *in situ* cleaning of the surface in H at high temperatures, a 3 : 1 solution of H_2SO_4:H_3PO_4 is used as the etchant. The substrate is dipped into this solution and kept at 300 °C for 20 min. This is followed by a rinse in DI water for 3 min. Though the hot etch removes some material, the resultant surface still bears the scratches caused by mechanical polish. However, the surface becomes flatter after etching with the rms roughness being reduced from 0.323 to 0.211 nm.

To eliminate surface damage altogether, a high-temperature annealing step has been employed, which gives rise to atomically smooth surfaces. A very high-temperature

Table 2.4 Properties of sapphire (in part after Ref. [43] and references therein).

Parameter	Value	Condition
Lattice constant (Å)	$a = 4.765$, $c = 10.2982$	20 °C
Melting point (°C)	2030	
Density ($g\,cm^{-3}$)	3.98	20 °C
Thermal expansion	6.66×10^{-6} || c-axis	20–50 °C
Coefficient (K^{-1})	9.03×10^{-6} || c-axis	20–1000 °C
	5.0×10^{-6} ⊥ c-axis	20–1000 °C
% Change in lattice constants with ΔT	$a/i_o = 0.83$, $c/c_o = 0.892$	293–1300 K
Thermal conductivity (W/cm K)	0.23 || c-axis	296 K
	0.25 || a-axis	299 K
Heat capacity ($J\,K^{-1}\,mol^{-1}$)	77.9	298 K
Young's modulus (GPa)	452–460 in [0 0 0 1] direction	
	352–484 in [1 1 $\bar{2}$ 0] direction	
Tensile strength (MPa)	190	300 K
Poisson's ratio	0.25–0.30	300 K
Hardness, Knoop nanoindentation (GPa)	23.9 ± 2.0	300 K
Energy bandgap (eV)	8.1–8.6	300 K Experimental value
Resistivity (Ω cm)	$>10^{11}$	300 K

annealing investigation of sapphire substrates was recently undertaken. Annealing experiments in air at 1000, 1100, 1200, 1300, and 1380 °C (the ceiling of the furnace employed) for 30 and 60 min were conducted to determine the best conditions with the aid of atomic force microscopy (AFM) images of the finished surface. This was followed

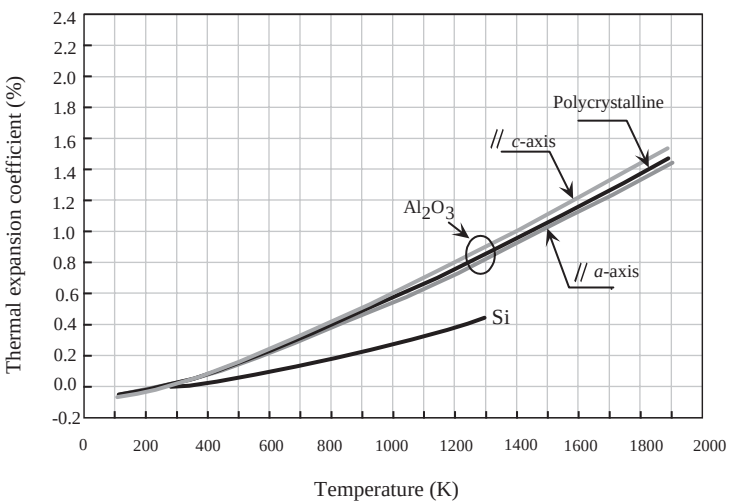

Figure 2.8 Thermal expansion coefficient of sapphire on the *c*-plane (along the *a*-axis) and along the *c*-axis, and that of Si as a function of temperature. (After Ref. [44].)

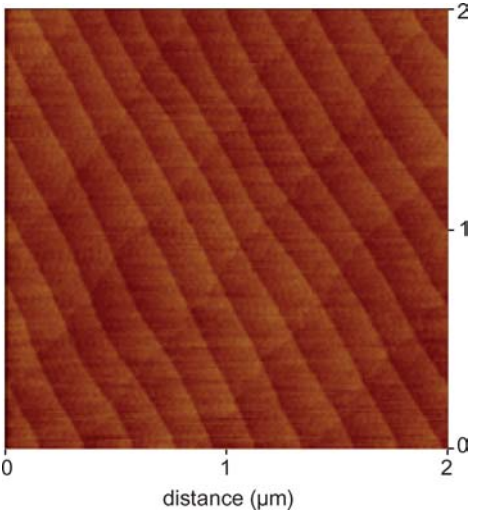

Figure 2.9 AFM image of sapphire following a 1380 °C 1 h anneal in atmosphere. Atomically flat surface is clearly visible. Atomic step heights are about 0.15 nm, which represent the only roughness in the image. The diagonal lines, from left to right, are the artifacts of AFM.

by the observation of reflection high-energy electron diffraction (RHEED) patterns once in an MBE system.

A small, but progressive, improvement was observed in reduction of scratches up to 1300 °C annealing. However, the anneals at 1380 °C for 1 h lead to scratch-free and smooth surfaces to the point where the only noticeable feature in AFM images are the atomic steps that are about 0.15 nm in height. AFM images indicated that the 1380 °C anneal for 1 h leads to atomically smooth surfaces as shown in Figure 2.9. RHEED images typically show extended and bright streaks associated with sapphire at temperatures as low as 600 °C during the temperature ramp-up as shown in Figure 2.10. Similar bright streaky RHEED patterns are observed for sapphire substrates after oxygen plasma treatment prior to ZnO growth by MBE, showing that such *in situ* treatment also produces atomically flat sapphire surface.

The calculated lattice mismatch between the basal ZnO before the in-plane rotation and the basal plane of sapphire is about 32%. However, the actual lattice mismatch of ZnO layers with sapphire is reduced by rotation of the ZnO lattice with respect to the substrate unit cell by 30°. Consequently, the lattice mismatch is reduced to ∼18.4%. This large mismatch would cause even the very thin layers to be fully relaxed at growth temperatures. When the samples are cooled down after the growth, a residual thermal strain is created.

Among the faces of sapphire that have been utilized for ZnO are the *c*-, *a*-, and *r*-planes. The stacking configurations perpendicular to the *c*- and *a*-planes of sapphire along with the atomic arrangements are displayed in Figure 2.11a and b, respectively. Figure 2.12 depicts the stacking arrangement perpendicular to the *r*-plane (a) and the atomic arrangement on the *r*-plane of sapphire (b).

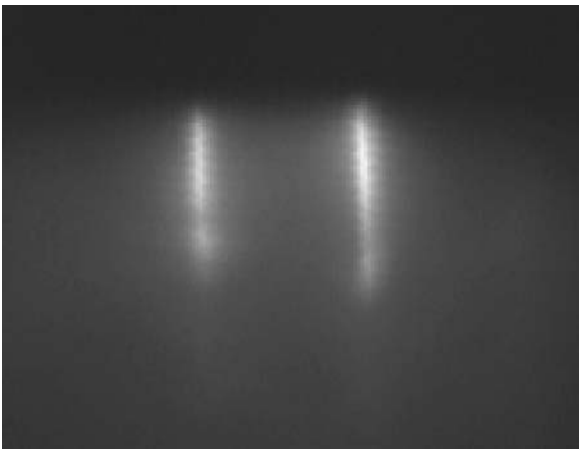

Figure 2.10 A RHEED image at about 800 °C of sapphire annealed at 1380 °C for 1 h ([11$\bar{2}$0] azimuth). Clear streaky RHEED pattern observed at temperatures as low as 600 °C indicates that the high-temperature annealing step produces clean epi-ready surfaces. Without the annealing procedure, the RHEED images are not as clear, elongated, and not reproducible.

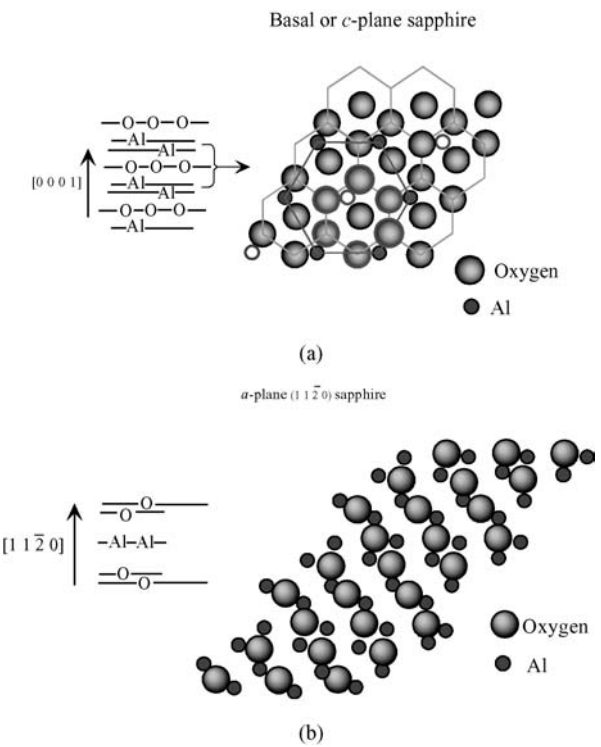

Figure 2.11 The stacking order (left) and the top view atomic arrangement (right) of (a) *c*-plane sapphire and (b) *a*-plane sapphire.

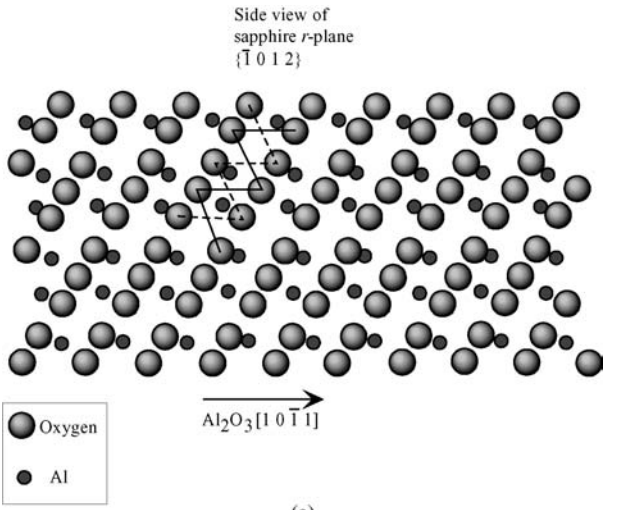

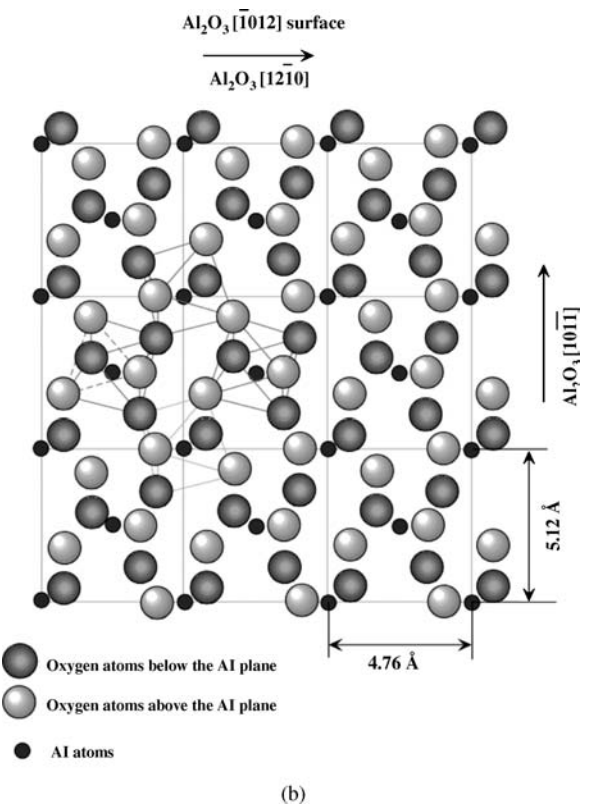

Figure 2.12 (a) Sapphire *r*-plane stacking sequence showing O atoms in larger clear circles and Al atoms in smaller filled circles. The salient feature is that each Al layer has an O layer above and below it. (b) The atomic arrangement of top three layers (uppermost one being O, immediately below is Al, and the third layer down is another O layer) on the *r*-plane of sapphire. The lines are just guides to eye and do not represent bonds.

Single-crystal ZnO films have been grown on sapphire with a high degree of surface flatness, which is essential for device fabrication. The ZnO layers have been grown on sapphire by using a variety of growth techniques, including PLD [12], OMVPE [45], and MBE [10, 46, 47]. Because of the large lattice mismatch between ZnO ($a = 0.3250$ nm, $c = 0.5213$ nm) and the underlying sapphire ($a = 0.4754$ nm, $c = 1.299$ nm), even after 30° in-plane rotation to reduce the mismatch, as-grown ZnO films usually display large mosaicity, high residual (most likely due to defect-induced native centers) carrier concentrations (in the $10^{17}\,cm^{-3}$ range), and low mobilities (less than $100\,cm^2\,V^{-1}\,s^{-1}$ at room temperature) compared to electron concentration of $\sim 10^{15}\,cm^{-3}$ and Hall mobility of $\sim 200\,cm^2\,V^{-1}\,s^{-1}$ typical for bulk single crystals [10, 23, 48], making their use for optoelectronic applications a challenge.

The growth of ZnO films on sapphire (0 0 0 1) (*c*-plane) substrates usually results in the epitaxial relationship of ZnO (0 0 0 1)//Al_2O_3 (0 0 0 1) and ZnO [$10\bar{1}0$]// Al_2O_3[$11\bar{2}0$] (basically, the *m*-plane normal direction of ZnO aligns with the *a*-plane normal of sapphire) [10, 11]. The lattice mismatch decreased to 18.4% with the 30° in-plane rotation. The epitaxial relationship of ZnO grown on *c*-axis sapphire is shown in Figure 2.13. ZnO layers were also successfully grown on sapphire $(11\bar{2}0)$ (*a*-plane) [49]. To eliminate the in-plane domain rotation, several lattice-matched substrates have been used for ZnO growth.

2.2.2
Other Substrates for ZnO Epitaxy ($ScAlMgO_4$, CaF_2, $LiTaO_3$, $LiNbO_3$)

Ohtomo *et al.* [23] selected hexagonal $ScAlMgO_4$ (0 0 0 1) substrates to grow ZnO by laser-assisted MBE. The lattice constants of hexagonal $ScAlMgO_4$ are $a = 3.246$ Å and $c = 25.195$ Å, giving rise to an in-plane lattice mismatch with ZnO as small as 0.09%. ZnO layers can be grown at temperatures ranging from 350 to 1000 °C, and the crystal

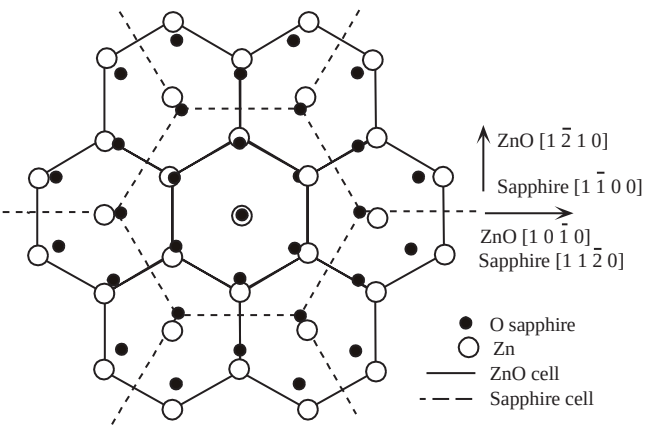

Figure 2.13 Schematic diagram showing the epitaxial relationships of ZnO (0 0 0 1) grown on Al_2O_3 (0 0 0 1).

perfection can be substantially improved by using $ScAlMgO_4$ (0 0 0 1) substrates. All the films showed an epitaxial relationship of ZnO (0 0 0 1)//$ScAlMgO_4$ (0 0 0 1) and ZnO $[1\,1\,\bar{2}\,0]$//$ScAlMgO_4[1\,1\,\bar{2}\,0]$ without any trace of the other in-plane orientation domains, which are characteristics of ZnO/sapphire(0 0 0 1). The residual carrier concentration and electron mobility were in the low $10^{16}\,cm^{-3}$ and $60 \sim 100\,cm^2\,V^{-1}\,s^{-1}$, respectively. The growth on CaF_2 (1 1 1) substrates (the lattice mismatch with ZnO is −15.8%) with the application of a low-temperature (LT) buffer layer has been performed to improve the ordering both in-plane and along the growth direction [19]. The epitaxial relationships between the ZnO films and CaF_2 (1 1 1) substrate are ZnO (0 0 0 1)//CaF_2 (1 1 1) and ZnO $[2\bar{1}\bar{1}0]$//$CaF_2[\bar{1}\,1\,0]$. For surface acoustic wave (SAW) device applications, single-crystal ZnO films have been grown on $(01\bar{1}2)$ $LiTaO_3$ [50] and (0 0 0 1) $LiNbO_3$ substrates [51] by electron cyclotron resonance (ECR) assisted MBE. The ZnO film orientation on $(01\bar{1}2)$ $LiTaO_3$ substrate was found to depend on the oxygen-to-zinc ratio. Under high oxygen to zinc ratios, $(1\,1\,\bar{2}\,0)$ ZnO with the *c*-axis parallel to the $LiTaO_3$ substrate resulted, while under low oxygen-to-zinc ratios, (0 0 0 1) ZnO with the *c*-axis perpendicular to the $LiTaO_3$ substrate was grown. The epitaxial relationships between ZnO and $LiNbO_3$ are (0 0 0 1)ZnO//(0 0 0 1) $LiNbO_3$ and $[\bar{1}2\,\bar{1}0]$ ZnO//$[\bar{1}100]$ $LiNbO_3$. ZnO growth on GaN templates is discussed in detail in Section 2.3.2.3.

2.2.3
ZnO Homoepitaxy

In addition to the heteroepitaxial growth on the above-mentioned substrates, ZnO homoepitaxy has been studied by several groups [52, 53]. Due to the nature of wurtzite structure along the [0 0 0 1] direction, that is, alternating O and Zn layers, the (0 0 0 1) ZnO wafer surfaces could be either Zn or O terminated, meaning [0 0 0 1] indicating Zn surface layer or $[0\,0\,0\,\bar{1}]$ indicating O surface layer. The chemical bonding of surface atoms for the aforementioned two polarities is different, which has an impact on surface preparation owing to the difference in surface hardness. Studies on the sublimation of ZnO basal plane showed that Zn atoms start to evaporate from the Zn face substrate at temperatures as low as 380 °C, while the sublimation of O surface takes place above ∼600 °C [54]. Homoepitaxial films have been grown on the two polar surfaces of ZnO substrates [52]. Under excess Zn supply, the surface was smooth on $-c$ oriented or $[0\,0\,0\,\bar{1}]$ (O polarity) but was completely covered with hillocks on $+c$ oriented or [0 0 0 1] (Zn polarity) ZnO substrates, as shown in Figure 2.14. It was concluded that excess Zn pressure at the initial growth stages is required for $-c$ direction growth, while excess O supply is needed for the $+c$ direction growth [52]. The O surface is more suitable than the Zn surface for film growth because mechanical damage can easily occur on the softer Zn surface. The Zn surface may also form different compositional domains in an oxygen environment. High-temperature annealing of single crystalline ZnO in air improves the structure, morphology, and optical properties of the O surface, but there is only a slight effect on the Zn polarity surface.

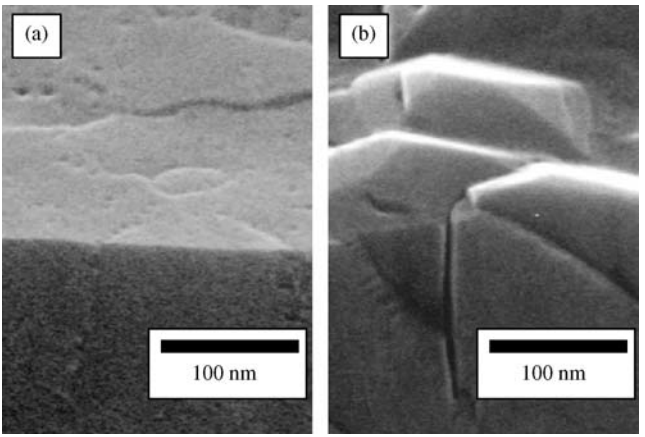

Figure 2.14 SEM images of faceting ZnO films grown on bulk ZnO substrates: (a) on $-c$ surface, (b) on $+c$ surface. (Courtesy of S. Fujita [52].)

2.3 Epitaxial Growth Techniques

Device applications in many cases require growth of thin films and multilayers. Common epitaxial deposition techniques used for semiconductors are applied to ZnO as well. Among these techniques, RF sputtering and pulsed laser deposition generally have limitations as they can provide material with up to certain quality, and mode-advanced techniques such as molecular beam epitaxy and chemical vapor deposition are necessary to improve the thin film crystallinity further. In terms of substrates, other than bulk ZnO for homoepitaxial growth, ZnO and related materials have been grown on foreign substrates, discussed in Section 2.2, most common ones being sapphire and GaN. In this section, deposition of ZnO and related materials using the above-mentioned techniques on different substrates are discussed briefly.

2.3.1 RF Magnetron Sputtering

One of the most popular growth techniques during the early ZnO investigations was sputtering (DC sputtering, RF magnetron sputtering, and reactive sputtering). As compared to sol–gel (spin-on method) and chemical vapor deposition [5–7], the magnetron sputtering was a preferred method because of its low cost, simplicity, and low operating temperature, as well as the reasonable quality of the resultant films [55]. The schematic diagram of a typical RF magnetron sputtering system is shown in Figure 2.15. In magnetron sputtering, the growth is usually carried out in an ambient of $O_2/Ar + O_2$ with ratios ranging from 0 to 1 at a pressure of 10^{-3}–10^{-2} Torr. O_2

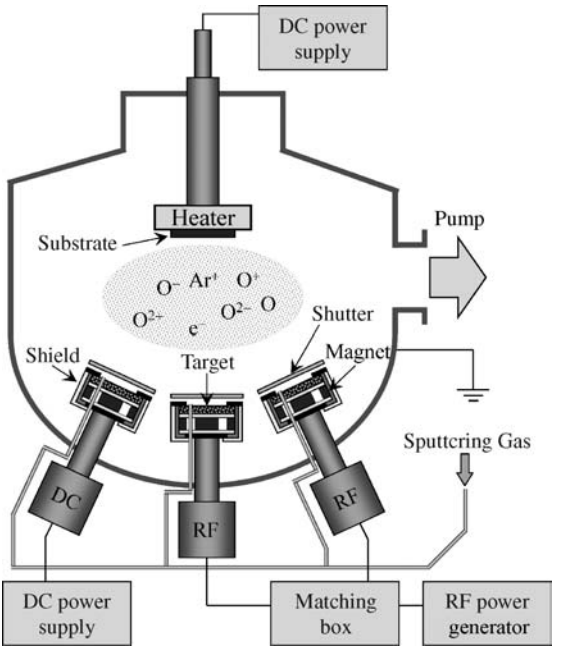

Figure 2.15 Schematic diagram illustrating an RF magnetron sputtering system combined with a DC power supply for applying a bias voltage to the substrate.

serves as the reactive gas and Ar acts as the sputtering enhancement gas. ZnO can also be grown by DC sputtering from a Zn target in an $Ar + O_2$ gas mixture. The RF power applied to the plasma is tuned to regulate the sputtering yield rate from the ZnO target. For these experiments, the target is presputtered for $5 \sim 15$ min before the actual deposition begins to remove any contamination on the target surface, make the system stable, and reach optimum conditions.

Although most of the earlier sputtered material was polycrystalline or even amorphous, some important accomplishments were reported. While sapphire substrates are the most popular choice due to the somewhat similar lattice structure and availability, other substrates have also been used for various device applications in conjunction with these early investigations. For SAW devices and piezoelectricity studies, ZnO films have been deposited on diamond (1 1 1) [3], glass [56–58], GaAs [21, 22], and Si substrates [20, 59–62]. The epitaxial relationship between ZnO thin film and the diamond was determined as $[1\,1\,\bar{2}\,0]$ ZnO//$[10\,1]$ diamond [3]. The growth temperature used in these studies ranged from room temperature to about 400 °C, and the ZnO thin films preferred the (0 0 0 1) orientation [61, 62]. Jeong *et al.* [59] reported the effects of growth ambient on PL properties of ZnO films grown on Si (100) by RF magnetron sputtering. Upon increasing the $O_2/Ar + O_2$ ratio in the growth ambient, the visible emission in the RT PL spectra was drastically suppressed without sacrificing the band-edge emission intensity in

the ultraviolet region. This tendency is attributed to the reduction of the oxygen vacancies and zinc interstitials in the film provided by improved stoichiometry, indicating that the visible emission in ZnO originates possibly from oxygen vacancy or zinc interstitial-related defects. An MgO buffer layer has been used for sputtered ZnO on Si (1 0 0) substrates to accommodate the large lattice mismatch [60]. The MgO films used as buffers were deposited by electron beam evaporation from MgO crystals, and ZnO films were formed by annealing the RF sputtered Zn metallic films in O_2. At an annealing temperature above 800 °C, the ZnO film underwent a phase transformation from ZnO to $Mg_xZn_{1-x}O$ alloy, although the composition was not reported. Intense UV band-edge PL from the MgZnO alloy was observed at room temperature.

The ZnO films with (0 0 0 1) orientation have been observed on both *c*- and *a*-plane sapphire substrates just as in the case of GaN on sapphire [63]. The effect of sputtering variables (substrate temperature, RF power, gas pressure, and composition) on the ZnO film structure and optical properties has been one of the major research topics. Kim *et al.* [8] reported high-quality single-crystal ZnO films prepared on sapphire (0 0 0 1) by RF magnetron sputtering. They found that high substrate temperature is essential to improve the crystal structure, but RF power had to be adjusted for the appropriate growth rate, as shown in Figure 2.16 [8]. The ZnO film deposited at 120 W and 600 °C exhibited the best FWHM of 0.13° for (0 0 0 2) XRD rocking curve, and the corresponding FWHM of RT PL was 76 meV. The cross-sectional transmission electron microscopy (TEM) revealed that the samples grown under the optimum temperature and RF power combination exhibited the largest grain size. A TEM study of crystallite structure and data from RT PL suggested that the origin of deep-level emission in the ZnO films could be due to the existence of oxygen vacancies, consistent with the result reported in Ref. [59]. In the sputtering

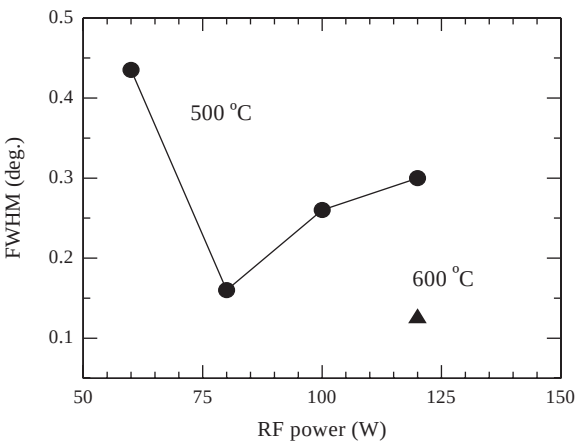

Figure 2.16 The FWHM variation of XRD θ rocking curve of ZnO film grown on (0 0 0 1) sapphire substrate at 550 and 600 °C. (After Ref. [8].)

growth of oxide films, O^- ions are mainly responsible for the resputtering phenomenon [64, 65]. The sputtering effect of O ions on the ZnO film surface was studied by applying a grid bias during the deposition on sapphire (0 0 0 1) [66]. The improved epitaxial quality at an optimum bias was attributed to a reduction of the flux of energetic oxygen anions bombarding the film surface and, thereby, to significant suppression of the resputtering phenomenon.

The stress in the sputtered ZnO was investigated as a function of the substrate temperature that ranges 250–450 °C, the sputtering pressure, and the type of substrate (Si or GaAs) [67–69]. Postdeposition annealing has also been used to relieve the stress and improve the structure and optical properties of the sputtered ZnO films [20, 56, 70]. Liu *et al.* [71] deposited ZnO thin films by RF magnetron sputtering in $Ar + O_2$ plasma. The samples annealed at 950 and 1000 °C showed the sharpest (0 0 0 2) XRD peak and the smallest rms surface roughness. During the annealing process, the atoms of ZnO gain energy to rearrange themselves in the lattice. The (0 0 0 2) XRD rocking curves were of the Gaussian shape and showed no tail caused by the deformed interfacial regions [72]. An atomic force microscopy study revealed an increase in the grain size with increasing annealing temperature, with a grain size distribution between 100 and 200 nm for the sample annealed at 1000 °C. Table 2.5 summarizes the results of XRD, AFM, and PL measurements on ZnO films annealed at different temperatures [71].

The attainment of p-type ZnO by RF magnetron sputtering method, albeit controversial, has also been reported. Phosphorus-doped p-type ZnO was obtained by sputtering a ZnO target with 1 wt% P_2O_5 and RTA annealing in N_2 [73]. It was also demonstrated that reactively sputtered ZnO thin films could be changed from n-type to moderate p-type by adjusting the O_2/Ar ratio in the sputtering plasma [74]. The ZnO films deposited on (1 0 0) Si substrates by reactive sputtering of a Zn target in O_2/Ar atmosphere produced n-type ZnO at low O_2/Ar ratios and moderately p-type ZnO at higher O_2/Ar ratios. In addition, when ZnO films were prepared on (0 0 1) GaAs substrates [22], p-type conductivity was observed after a postgrowth anneal in vacuum. The conductivity-type conversion was attributed to As diffusion from the substrate.

A more advanced sputtering technique utilizes ECR source to supply the power to the plasma. The advantage of the ECR sputtering system is that it enables the production of highly ionized plasma under low gas pressures. The ZnO films

Table 2.5 Structural and optical parameters for the ZnO samples obtained from AFM, XRD, and PL measurements.

Annealing temperature (°C)	rms Surface roughness (nm)	XRD (0 0 0 2) FWHM (arcmin)	10 K PL FWHM (meV)
As-grown	14.8	66.0	10
800	13.5	25.1	3.8
950	7.5	16.9	2.7
1000	6.8	16.2	3.0

deposited by ECR sputtering exhibited a high electrical resistivity ($\rho > 10^{10}\,\Omega\,\mathrm{cm}$) and good piezoelectric and optical properties [75, 76].

2.3.2 Molecular Beam Epitaxy

MBE is an extremely versatile vacuum deposition technique for preparing thin semiconductor heterostructures, wherein constituents are provided to the surface of the heated substrate as thermal beams in general [77]. For materials containing O, as in the case of ZnO, and N, as in the case of GaN, the gas species are provided in their reactive state, that is, through an RF plasma source. The main advantage of MBE is its precise control over the growth parameters and *in situ* diagnostic capabilities. With feedback from RHEED, the growth mode of ZnO epilayers can be monitored in real time dynamically. For more detailed information on RHEED, see Ref. [63].

The composition of the epilayer and its doping level depend on the arrival rates of the constituent elements and dopants, respectively [78]. Therefore, MBE growth is carried out under conditions that are governed primarily by the kinetics, rather than mass transfer [79]. A thorough understanding of the growth kinetics, especially the surface processes of growth, is therefore critical. As already mentioned, thin films are formed on a heated substrate through various reactions between thermal molecular beams (atomic beams in the case of RF activated oxygen) of the constituent elements participated by the surface species on the substrate originating from the substrate itself by surface or bulk contamination. The typical growth rate of $1\,\mu\mathrm{m\,h^{-1}}$, or slightly more than one monolayer per second ($\mathrm{ML\,s^{-1}}$), is sufficiently low to allow migration of the impinging species on the surface. In the case of growth along the (1 1 1) for cubic and *c* directions for wurtzitic systems, one monolayer constitutes a bilayer.

The sequence of processes taking place during growth by MBE are adsorption, desorption, surface diffusion, incorporation, and decomposition. All these processes, in effect, are in many ways in competition with each other during growth by MBE. Adsorption can be summed as the atoms or molecules impinge on the substrate surface and stick by overcoming an activation barrier. Desorption, on the contrary, is the process where the species not incorporated into the crystal lattice leave the substrate surface by thermal vibration. Surface diffusion, imperative for growth, describes the diffusion of the constituent atoms or molecules on the substrate surface to find the low-energy crystal sites for incorporation. During the incorporation phase, the constituent atoms or molecules enter the crystal lattice of the substrate or the epilayer already grown by attaching to a dangling bond, vacancy, step edge, and so on. Due to high temperatures involved, albeit much smaller than those employed in OMVPE, decomposition occurs; that is, the atoms in the crystal lattice leave the surface by breaking the bond.

An MBE deposition system for ZnO growth consists essentially of a conventional MBE chamber, but with added equipment, such as a compact RF source or H_2O_2 or O_3 for oxygen source. Because of O environment, the heating elements, particularly that for the substrate, are constructed out of Pt. Other measures must also be taken to

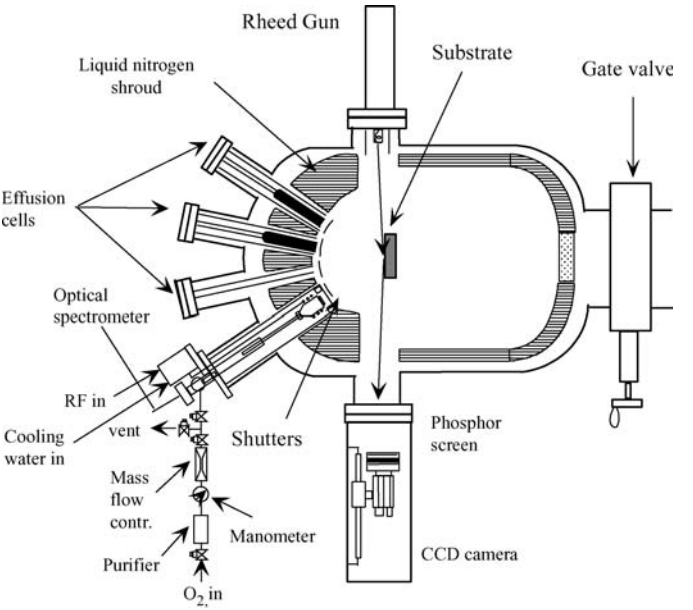

Figure 2.17 Schematic diagram of an RF MBE system used for ZnO growth at Virginia Commonwealth University. In the case of H_2O_2 oxygen source, the input to the chamber is through a nozzle with flow controlled basically by a mass flow controller.

make sure that the source material is not oxidized while in the effusion cell and condensation is prevented at the tips of the cells. Typically, two-zone cells with controlled apertures are used to mitigate the complications. The schematic diagram for a typical RF-MBE system is shown in Figure 2.17.

For ZnO thin film deposition by MBE, Zn metal and O_2 are usually used as the source materials. High-purity Zn metal is evaporated from an effusion cell, where the cell temperature can be varied to examine the effect of the Zn flux on the growth rate and the material properties. Because of the high molecular bonding energy of O_2 (5.16 eV [80]) hindering the thermal dissociation of oxygen at the substrate temperature, sources of reactive oxygen species must be used for ZnO MBE. Usually, the oxygen radical beam, which can be generated by an ECR [81, 82] or an RF plasma source [83], is directed on the film surface to obtain high oxidation efficiency. When the O plasma is used, the chamber pressure during growth is in the 10^{-5} Torr range. Because oxygen plasma attacks pyrolitic boron nitride, material usually used for manufacturing plasma-source cavities, high-purity quartz is employed in oxygen radical sources. Quartz is also used for electrical insulators instead of alumina ceramics to avoid unintentional doping of a growing material with aluminum acting as n-type dopant. However, disadvantages related to radical-source MBE (high price of the source and expensive maintenance, degradation of plasma sources due to high reactivity of oxygen radicals, contamination of growing films by source materials due to sputtering of source parts, etc.) provide impetus for seeking alternative sources of

active oxygen. Nitrogen dioxide (NO_2) was also utilized for MBE of ZnO on (0 0 0 1) sapphire substrates to keep the chamber pressure low in an effort to protect sensitive filaments and heaters [84], but the resultant crystal structures and the surface morphology were not satisfactory. Ozone source was used for the growth of ZnO layers on Si (1 1 1) substrates by Fujita *et al.* [85] Successful growth of ZnO films by using hydrogen peroxide (H_2O_2) vapor as a source of active oxygen has also been reported [86].

Oxygen radicals are extremely reactive; therefore, the lifetime of heating elements in the growth chamber, especially substrate heater, becomes a key issue for ZnO MBE. Materials resistant to oxidation and/or special design of the heaters that help to minimize the contact of hot parts with active oxygen are employed. Oxidation of effusion-cell charge, especially in the case of such highly reactive materials as Zn and Mg, is also a well-known problem in ZnO MBE.

RF radical sources are employed by most groups nowadays because of the high reactivity of oxygen radicals produced and reasonable oxygen pressures (typically $1 \sim 8 \times 10^{-5}$ Torr). For the correct RF plasma mode, the emission at 777 nm due to the atomic oxygen transition of $3p^5P–3s^5S^0$ should dominate the optical emission spectrum [11, 87], as shown in Figure 2.18. The II/VI ratio can be tuned through the Zn cell temperature as well as RF power and O_2 flow rate of the plasma source. For high-quality ZnO films, the reported growth temperature is in the range of 350–750 °C with a growth rate of 0.3–0.7 μm h^{-1} [10, 11, 88].

A discussion of MBE growth of ZnO on the most popular substrates, such as *c*- and *a*-plane sapphire, GaN templates, and ZnO, is warranted. Critical issues to be concerned with during crystal growth are the differences in polarity between two ZnO faces and how the growth mode, impurity incorporation, and dislocation formation are affected in the process. By employing various surface treatments, polarity control can be achieved either at the initiation stage of ZnO growth or shortly into the epitaxial growth. One of the main challenges for MBE growth of ZnO is that Zn has extremely high equilibrium vapor pressure at typical substrate temperatures (e.g., about 1 Torr even at a moderate temperature such as 500 °C). As a result, the

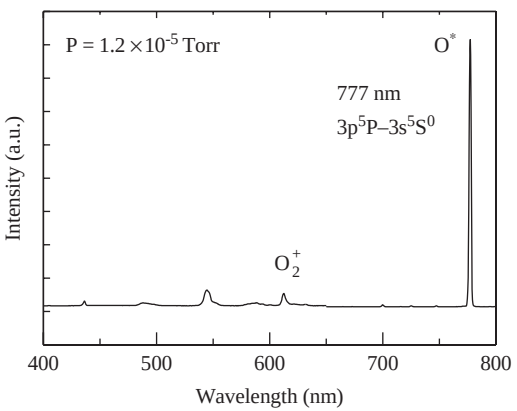

Figure 2.18 Optical emission spectrum of oxygen plasma.

ZnO surface is oxygen terminated (rich), regardless of its polarity, that is, O or Zn polarity. This makes the regimes that are optimal for high-quality ZnO growth dissimilar to those for GaN. Highly oxygen-rich growth conditions are needed to suppress 3D nucleation and provide 2D growth mode on the O-terminated (rich) Zn-polar surface, whereas 2D growth of ZnO films can be easily achieved in a wide range of O/Zn flux ratios on the O-polar surface. In addition, Kato *et al*. [89] have observed that for the same Zn fluxes and substrate temperatures and growth rates, the incorporation rate of Zn on the Zn-polar ZnO surface is larger by a factor of 3.7 than that on the O-polar ZnO surface. Authors attributed this effect to different dangling-bond configuration on the O-terminated Zn-polar and O-polar surfaces and its effect on the surface migration of Zn atoms.

Figure 2.19 shows a schematic of the side view of the atomic arrangements on O-terminated ZnO surfaces having Zn- and O-polarity, and their respective cross-sectional views along the *a*-axis. Each O atom on a Zn-polar ZnO surface has three

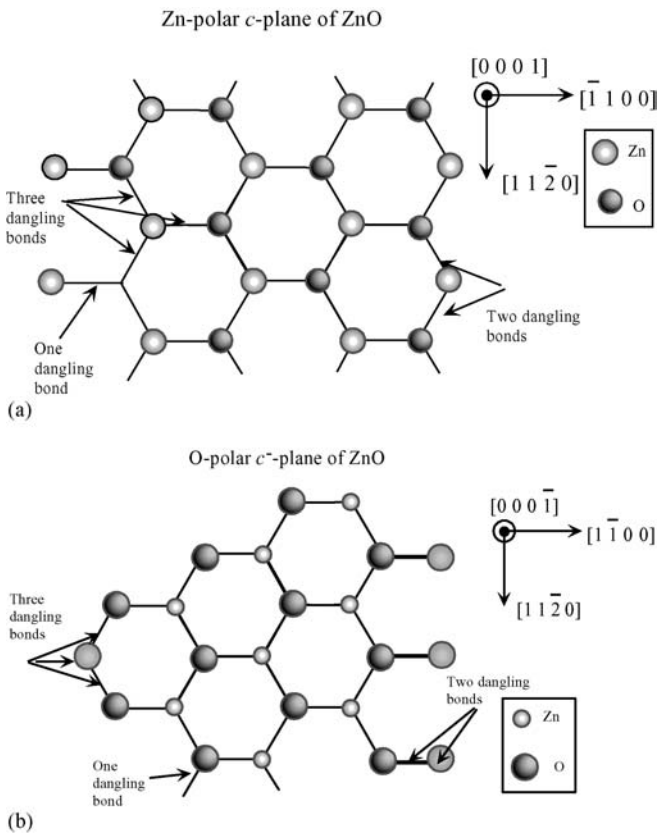

Figure 2.19 Schematics of atomic arrangements on O-terminated ZnO basal plane surfaces with (a) Zn polarity and (b) O polarity. The views of the same on the *a*-plane, (c) Zn polarity and (d) O polarity. (After Ref. [89].)

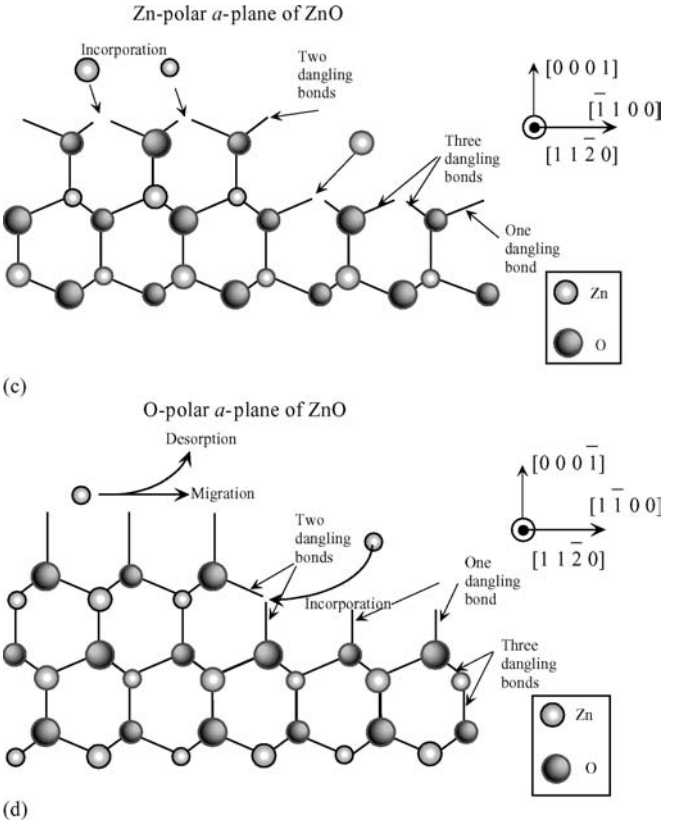

Figure 2.19 (*Continued*)

dangling bonds along the *c*-axis, whereas each O atom on the O-polar ZnO surface has a single dangling bond along the *c*-axis. The Zn migration length on the O-terminated surface of Zn-polar ZnO should therefore be smaller than that on the O face owing to differences in dangling-bond configuration. In addition, the step edge of Zn polarity is composed of one or two dangling bonds, whereas that of O polarity is composed of two or three dangling bonds. It would then be reasonable to conclude that in the case of O polarity migrating Zn species are incorporated at the step edges. Under O-rich flux conditions with a low Zn beam flux, the Zn-polar surface would be smooth because Zn adatoms bonded to O atoms on the O-terminated surface are stable due to the three-bond configuration. On the contrary, adatoms have lower probability of reevaporation than on the O-polar surface leading to a larger growth rate. At a high Zn beam flux, the growing surface on Zn-polar ZnO becomes rough due to 3D nucleation and growth, because bonding of Zn adatoms to O atoms on the O-terminated surface is unstable. Let us now discuss growth of ZnO on various orientations of sapphire.

2.3.2.1 Growth on c-Plane Sapphire

Despite a very large lattice mismatch (about 32%), several groups were successful in attaining MBE growth of ZnO ($a = 0.3250$ nm, $c = 0.5213$ nm) on *c*-plane (0 0 0 1) sapphire ($a = 0.4754$ nm, $c = 1.299$ nm) substrates [46, 47]. Chen *et al.* [11, 47] grew ZnO by using an oxygen microwave plasma source. The epitaxial layers exhibited 2D nucleation at the initial stages of growth, which gave way to a 3D growth mode as indicated by RHEED. An *in situ* oxygen plasma preexposure of the sapphire substrate was found to be critical for the initial two-dimensional nucleation. The sapphire substrates were exposed to oxygen generated by the plasma source for 30 min at 600 °C before the growth. The preexposure ensured an oxygen-terminated sapphire surface, which allowed the first monolayer of ZnO to conform to the oxygen sublattice of the Al_2O_3 substrate and thus minimize the lattice mismatch. (In the case of GaN growth on sapphire, the sapphire surface in the reactor is terminated with Al that reacts with N during nitridation to form AlN bonds.) The XRD rocking curve of ZnO showed a reasonably narrow (0 0 0 2) peak (FWHM ~0.005°) with a broad tail extending from the peak due to the in-plane mosaicity. The PL spectra exhibited the dominant donor-bound exciton emission with a FWHM of 3 meV at low temperatures and a free exciton emission combined with a very weak deep-level emission at RT.

As shown in Figures 2.5 and 2.11, the *c*-plane of sapphire is composed of alternating layers of oxygen (sixfold symmetry) and Al atoms (threefold symmetry), while in the wurtzite structure of ZnO, both O and Zn have sixfold symmetry about the ZnO *c*-axis. For films grown on *c*-plane sapphire, the orientational relationship along the direction normal to the surface was found to be $(0\,0\,0\,1)_{ZnO}//(0\,0\,0\,1)_{sapphire}$, but two types of in-plane alignment were observed: $[2\,\bar{1}\,\bar{1}\,0]_{ZnO}//[1\,\bar{1}\,0\,0]_{sapphire}$ and $[2\,\bar{1}\,\bar{1}\,0]_{ZnO}//[2\,\bar{1}\,\bar{1}\,0]_{sapphire}$ [10, 11]. The former, which dominates, represents a 30° rotation between the ZnO and sapphire *a*-axes, presumably owing to preferential bonding of Zn atoms with sapphire O atoms, while the latter replicates sapphire. Presence of both represents a dual domain structure. When only the former is present, representing the single domain case, the in-plane rotation reduces the lattice mismatch from 32 to 18.4%. But the presence of two types of in-plane rotational domains gives rise to, among other anomalies, increased carrier scattering as exemplified by low electron mobilities of 10–40 $cm^2\,V^{-1}\,s^{-1}$, which are typical. Two other types of rotational domains have been reported for ZnO on *c*-plane sapphire by Wang *et al.* [90] Those authors observed multiple domains with an in-plain epitaxial relationship $[1\,0\bar{1}\,0]_{ZnO}//[1\,1\bar{2}\,0]_{sapphire}$ and $[1\,1\bar{2}\,0]_{ZnO}//[5\,3\bar{8}\,0]_{sapphire}$, the latter being very unusual and needs more scrutiny.

As alluded to the above, the large lattice mismatch between ZnO and the underlying sapphire, even after the 30° in-plane rotation to reduce the lattice mismatch, causes the as-grown ZnO films to display large mosaicity, residual carrier concentrations above $10^{17}\,cm^{-3}$ (most likely due to defect-induced native centers), and low mobilities (less then 100 $cm^2\,V^{-1}\,s^{-1}$ at room temperature) [11]. On the other hand, an electron concentration of ~$10^{15}\,cm^{-3}$ and a Hall mobility of ~200 $cm^2\,V^{-1}\,s^{-1}$ are typical of bulk single crystals [28, 37, 48]. This large disparity makes the use of epitaxial layers for optoelectronic applications a challenge. To overcome the

very large lattice mismatch between *c*-plane sapphire and ZnO and eliminate the rotational domains, different approaches such as vicinal substrates and *a*-plane $(1\,1\,\bar{2}\,0)$ sapphire have been proposed and tested.

The effects of the substrate offset angle (vicinal substrates) on MBE growth of ZnO on *c*-plane sapphire were investigated by Sakurai *et al.* [91]. Twin-crystal RHEED patterns from both $(10\,\bar{1}0)$ and $(11\,\bar{2}0)$ planes and surface faceting observed on on-axis *c*-plane substrates were suppressed by extending the offset angle from near-zero to 2.87°, tilted from *c*-plane toward *a*-axis direction. As a result, the crystal structure and the surface morphology were improved.

Layer-by-layer growth of ZnO epilayers by plasma-assisted MBE on *c*-plane sapphire (0 0 0 1) substrates has been achieved by introducing a several-monolayer-thick interfacial MgO layer [48, 92–94]. The ionic radius of Mg^{2+} ion is close to that of Zn^{2+} [95]. Therefore, the replacement of Zn by Mg does not cause a significant change in the lattice constant of the MgZnO alloy. Insertion of an MgO interface layer is very effective in improving the surface morphology during the initial stages of growth and leads to an atomically flat surface. The 3×3 surface reconstruction of ZnO grown on MgO was observed from RHEED (see Figure 2.20). The twin defects with a 30° in-plane crystal orientation misalignment were completely eliminated, and the total dislocation density was reduced as evidenced by small linewidths of 13 and 84 arcsec for (0 0 0 2) and $(1\,0\,\bar{1}\,5)$ ω rocking curves, respectively [48]. The (1 1 1)-oriented rocksalt MgO grows on sapphire (0 0 0 1) with the following in-plane epitaxial relationship: $[\bar{1}\,\bar{1}\,2]_{MgO}$ //$[2\,\bar{1}\,\bar{1}\,0]_{sapphire}$and $[1\,\bar{1}\,0]_{MgO}$ //$[1\,\bar{1}\,0\,0]_{sapphire}$. As expected in the out-of-plane direction, the relationship is $[1\,1\,1]_{MgO}$//$[0\,0\,0\,1]_{sapphire}$. In a follow-up study, the same group reported on the effect of MgO thickness on the ZnO surface polarity [96, 97]. It should be mentioned that cubic thick AlN layers have also been used prior to ZnO deposition to invert the polarity [98].

Polarity control is an important issue for both GaN and ZnO as film properties depend strongly on the polarity. Considering the former, when GaN is grown by MBE on sapphire that does have a common stacking order, GaN and AlN initiation layers lead to predominantly N-polar and Ga-polar films, respectively. In the case of ZnO, both Zn- and O-polar ZnO films can be grown by using unipolar substrates such as ZnO and GaN [99]. As compared to this, controlling the polarity of ZnO epilayers on nonpolar sapphire substrates is difficult with O-polarity ZnO resulting predominantly. As the uncertainty in polarity has its roots in the lack of inversion symmetry, inversion of the polarity is possible by inserting a layer with inversion symmetry between ZnO and the substrate. MgO is one such material that could be synthesized in rocksalt symmetry and has been reported to provide an added advantage in efforts to improve the crystal quality of ZnO on sapphire [100]. The rocksalt symmetry of MgO initiation layer causes the polarity inversion of the overlaying ZnO.

Kato *et al.* [96] and Minegishi *et al.* [97] were able to obtain $-c$ (O) to $+c$ (Zn) polarities depending on the thickness of the MgO initiation layer between ZnO and sapphire. The polarity inversion was said to be caused by the difference in atomic structure between the wetting layer and islands of MgO. Figure 2.21 shows a schematic of the atomic arrangements of ZnO on *c*-plane sapphire with two types of MgO initiation layers. Due to the MgO growth taking place under O-rich

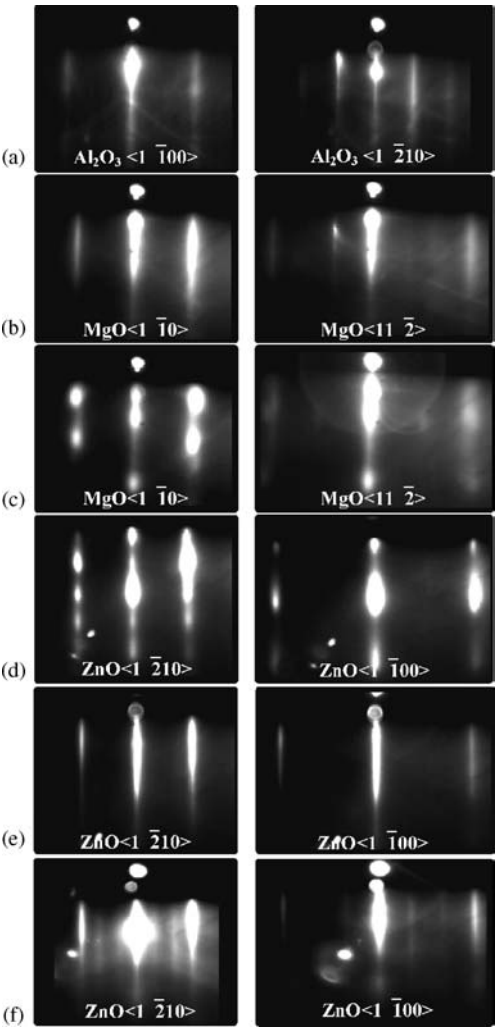

Figure 2.20 RHEED patterns show the surface morphology evolution during initial growth stages. (a) The Al_2O_3 (0 0 0 1) surface after oxygen plasma treatment. The MgO buffer layer (b) before and (c) after 2D–3D transition. The LT-grown ZnO layer on MgO buffer (d) before and (e) after annealing; (f) the ZnO epilayer after a few minutes growth on the buffer layer. (Courtesy of Y. Chen and T. Yao [48].)

conditions, growth proceeds mainly at the O-terminated surface. During the initial stages of growth up to 1 nm, wurtzite-phase MgO wetting layer (assuming the in-plane symmetry of the sapphire substrate) grows on O-terminated sapphire. Because the topmost O atoms in wurtzite MgO have single dangling bonds, each Zn atom of ZnO growing on it in contact with O atoms has three dangling bonds along the *c*-axis.

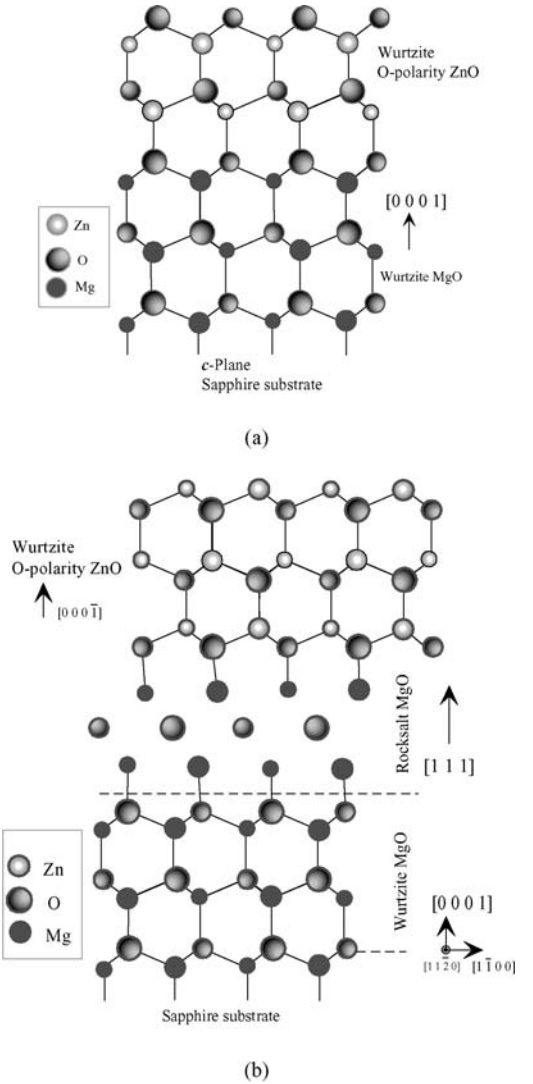

Figure 2.21 Schematic of atomic arrangement of ZnO on *c*-plane sapphire with (a) a 1 nm thick MgO initiation layer that is sufficiently thin to maintain sapphire symmetry leading to O polarity ZnO, and with (b) a MgO initiation layer that is thicker than 3 nm, relaxed, assumes its stable rocksalt symmetry leading to Zn polarity ZnO. (After Ref. [96].)

Consequently, the resultant ZnO film is O polarity. However, if the MgO layer, which would be under compressive strain in the wurtzitic from, is greater in thickness than a critical value, the wurtzite structure gives way to (1 1 1) rocksalt owing to relaxation. Eventually, for MgO layer thickness exceeding 3 nm, MgO islands with rocksalt

structure cover the entire surface. Owing to the topmost O atoms in rocksalt, MgO having three dangling bonds, each Zn atom in bonding with those O atoms would have a single dangling bond up along the *c*-axis, which is characteristic of Zn polarity. In short, MgO on sapphire is initially of wurtzitic nature for 1 nm or so, which gives way to the rocksalt symmetry as deposition continues. If ZnO is grown on wurtzitic MgO, O polarity ZnO layer is obtained. On the contrary, if the rocksalt phase of MgO is allowed to form, ZnO grown on it is of Zn polarity [97]. The in-plane epitaxial relationship between ZnO and sapphire in the latter case is $[2\,\bar{1}\,\bar{1}\,0]_{\text{ZnO}}$ // $[1\,\bar{1}\,0]_{\text{RS-MgO}}$ //$[2\,\bar{1}\,\bar{1}\,0]_{\text{Wz-MgO}}$ //$[1\,\bar{1}\,0\,0]_{\text{sapphire}}$and again represents a 30° rotation between the ZnO and sapphire lattices, but unlike on sapphire, the dispersion is relatively small.

2.3.2.2 Growth on a-Plane Sapphire

To eliminate the orientational domains often observed in ZnO thin films grown on (0 0 0 1) sapphire, $(1\,1\,\bar{2}\,0)$ sapphire substrates have been used for ZnO epitaxy. The lattice parameter $a = 0.3250$ nm of ZnO and parameter $c = 1.299$ nm of sapphire are related almost exactly by a factor of 4, with a mismatch less than 0.08% at room temperature. On the basis of this fact and coining the term "uniaxial locked epitaxy," Fons *et al.* [83, 101] initiated the investigation of ZnO epitaxy on *a*-plane $(1\,1\,\bar{2}\,0)$ sapphire, including a detailed analysis of the initial stages of growth [102]. The out-of-plane and in-plane orientational relationships are ZnO [0 0 0 1]//sapphire $[11\,\bar{2}0]$ and ZnO $[11\,\bar{2}0]$//sapphire [0 0 0 1], respectively. The epitaxial relationship is shown in Figure 2.22. As confirmed by the X-ray pole figure shown in Figure 2.23, no rotational domains or twins were present in the films. The use of *a*-plane sapphire substrates showed a significant improvement compared to the *c*-plane sapphire substrates. The residual carrier concentration was decreased to $6 \times 10^{16}\,\text{cm}^{-3}$ with electron mobility of about $120\,\text{cm}^2\,\text{V}^{-1}\,\text{s}^{-1}$. AFM revealed an rms roughness of less than 0.4 nm.

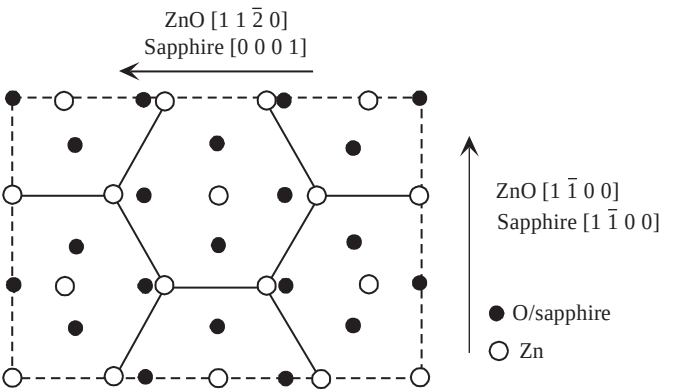

Figure 2.22 Schematic diagram of atom positions for basal ZnO grown on *a*-plane sapphire. The dots mark the O-atom positions and the dashed lines show the sapphire *a*-plane unit cells. The open circles mark Zn-atom positions and the solid lines show the ZnO basal-plane unit cell.

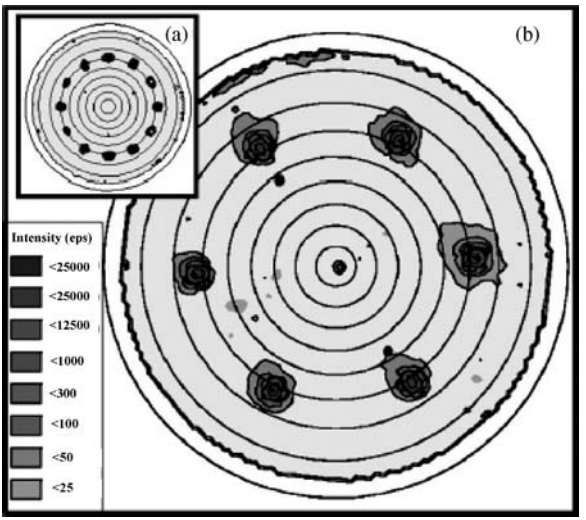

Figure 2.23 Stereographic projections of X-ray pole figure results for the ZnO $(1\,0\,\bar{1}\,1)$ reflection for a ZnO film grown on (a) (inset) *c*-plane sapphire substrate and (b) *a*-plane sapphire substrate. The orientation of the sapphire substrate was determined in a separate measurement using the sapphire $(1\,1\,\bar{2}\,6)$ poles [filled circles in (b)]. (Ref. [101].)

Different surface chemistry of sapphire substrates can lead to different growth modes. The surface chemistry of $(11\,\bar{2}\,0)$-oriented sapphire was alternated from O rich to Al rich by changing the pregrowth treatment from oxygen plasma to atomic hydrogen [103]. The two-dimensional growth was more favorable and continued longer on a hydrogen-treated surface, although the initial two-dimensional growth was eventually taken over by a three-dimensional growth for both types of pretreatments. Figure 2.24 shows different ZnO film surface morphologies grown on H- and O-pretreated sapphire substrates. The ZnO epilayers with electron mobility as high as

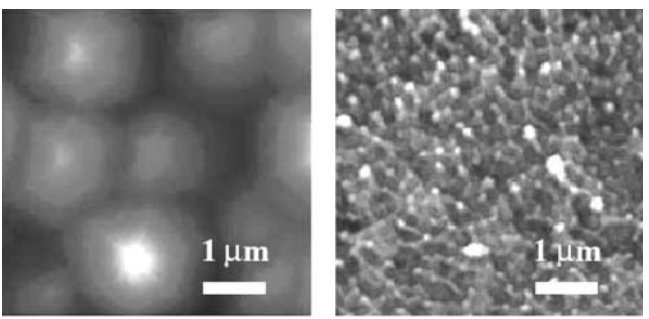

Figure 2.24 AFM surface observation with a contact mode. (a) H-pretreated sample (grain size 2.5 μm) (b) O-pretreated sample (grain size 0.2 μm). (Courtesy of T. Yao [103].)

130 $cm^2 V^{-1} s^{-1}$ and electron concentration of 1.4×10^{17} cm^{-3} were grown with good reproducibility by using the H pretreatment. A Ga preexposure after H and O pretreatment of the sapphire (0 0 0 1) surface was adopted by Du *et al.* just before the ZnO growth to eliminate the rotational domain structures [104]. The ZnO (0 0 0 2) XRD rocking curve had a FWHM of 67 arcsec, and the electron mobility was 109 $cm^2 V^{-1} s^{-1}$ with an electron concentration of 3.2×10^{17} cm^{-3}. Nitridation of (0 0 0 1) sapphire substrate was also used to improve the quality of ZnO films grown by plasma-assisted MBE [90]. A very thin nitrogen-polar AlN layer formed by nitridation acted as a template for the following ZnO growth, resulting in the elimination of the rotational domains that were often observed in the films grown without nitridation. For the nitridized substrates, the FWHM of (0 0 2) and (1 0 2) ω-scans decreased substantially from 912 to 95 arcsec and from 2870 to 445 arcsec, respectively.

The buffer layer is another critical factor affecting the growth of ZnO layers besides substrates. Although Fons *et al.* [10] reported sharp and streaky ZnO [11 $\bar{2}$ 0] RHEED patterns for both *c*-plane sapphire (Figure 2.25a) and *a*-plane sapphire [101] without using any buffer layer, ZnO growth on sapphire without a buffer layer usually changed from the 2D growth mode to 3D island growth as confirmed by the appearance of spotty RHEED pattern (Figure 2.25b) [11, 47, 103]. LT buffer layers are usually grown at 250 ∼ 400 °C, and the surface morphology of the buffer layer can be improved by thermal treatment at a temperature higher than 700 °C. This is followed by growth on the main ZnO layers at a temperature in the range of 600–700 °C [87, 105, 106]. By employing *a*-plane sapphire substrates and LT buffer layers, the electrical properties of undoped ZnO films have been improved; a carrier concentration of 7.6×10^{16} cm^{-3} and a mobility of 120 $cm^2 V^{-1} s^{-1}$ have been obtained [87].

The II/VI ratio has been studied for its effects on the surface morphology and electrical properties. Figure 2.26 shows the change of growth rate with Zn/O ratio [107]. ZnO thin films with MgO buffer layers have been grown on *c*-plane sapphire substrates. ZnO layers grown under stoichiometric and O-rich flux conditions showed larger hexagonal islands of 3 μm diameter, whereas those grown under Zn-rich flux conditions show smaller hexagonal islands of 0.2 μm diameter. The ZnO film was of O polarity. The observed surface morphology was explained as follows: for growth conducted on the O-polar surface, the surface diffusion length of

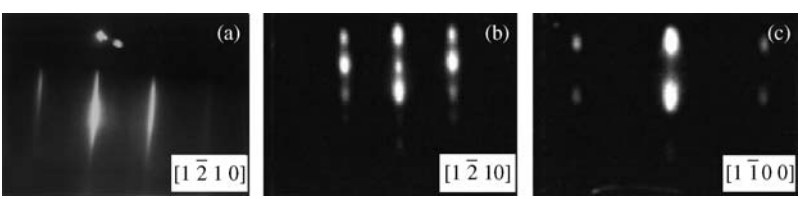

Figure 2.25 (a) RHEED pattern taken along the [1 $\bar{2}$ 1 0] direction of ZnO after 1 h of growth. (After Ref. [10]) RHEED patterns along the (b) [1 $\bar{2}$ 1 0] and (c) [1 $\bar{1}$ 0 0] azimuths of ZnO after deposition of about 300 nm. (Courtesy of Y. Chen and T. Yao [11].).

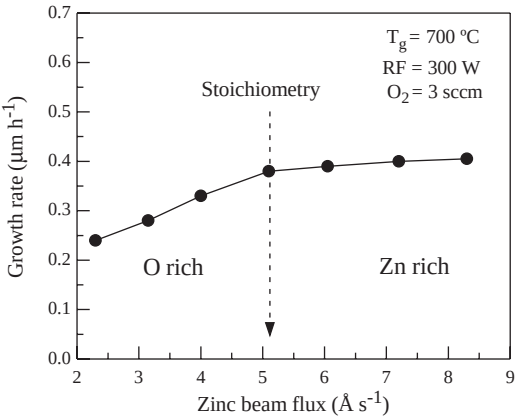

Figure 2.26 Growth rate of ZnO layers against Zn beam flux. (After Ref. [107].)

Zn adatoms was smaller under the Zn-rich conditions than under the stoichiometric or O-rich conditions. ZnO layers grown under stoichiometric flux conditions had high crystalline quality, the lowest dislocation density, and the highest electron mobility ($\sim 130\,cm^2\,V^{-1}\,s^{-1}$) when compared to ZnO films grown under nonstoichiometric flux conditions.

The control of the film polarity is an important issue in epitaxial growth of ZnO. When the film is grown in the [0 0 0 1] direction, Zn polarity ($+c$) is obtained and the top surface is Zn terminated. Likewise, when the growth is in the [0 0 0 $\bar{1}$] direction, O polarity ($-c$) is obtained and the top surface is O terminated. Much effort has been expended to determine the effects of polarity and to find a way of controlling the polarity during growth. The ZnO films grown by plasma-assisted MBE on as-polished (0 0 0 1) sapphire substrates with or without a MgO buffer layer have O polarity [11, 108, 109] mainly due to the growth conditions. The sapphire surface should be O terminated, since sapphire substrates are treated at elevated temperatures (600–700 °C) by O plasma prior to the growth. MgO buffer under the oxygen ambient most likely has O-stabilized MgO surface. As demonstrated for atomically flat sapphire (0 0 0 1) substrates, the polarity of ZnO grown by laser MBE is closely correlated with the in-plane orientation of ZnO, that is, ZnO [1 0 $\bar{1}$ 0]//Al_2O_3[11 $\bar{2}$ 0] in the case of O polarity and ZnO [11 $\bar{2}$ 0]//Al_2O_3[11 $\bar{2}$ 0] in the case of Zn polarity [110]. ZnO films with Zn polarity are preferentially obtained at low growth temperature and high growth rate. The control over the ZnO surface polarity has also been achieved on GaN substrates by plasma-assisted MBE [109, 111]. As confirmed by the coaxial impact collision ion scattering spectroscopy (CAICISS) (see Figure 2.27), Zn- and O-polar ZnO films were successfully grown with Zn and O plasma preexposure on Ga-polar GaN templates prior to ZnO growth, respectively.

2.3.2.3 Growth on GaN Templates

Although ZnO films grown on sapphire have shown promising electrical and optical properties as discussed above, the crystal quality still needs improvement, since high

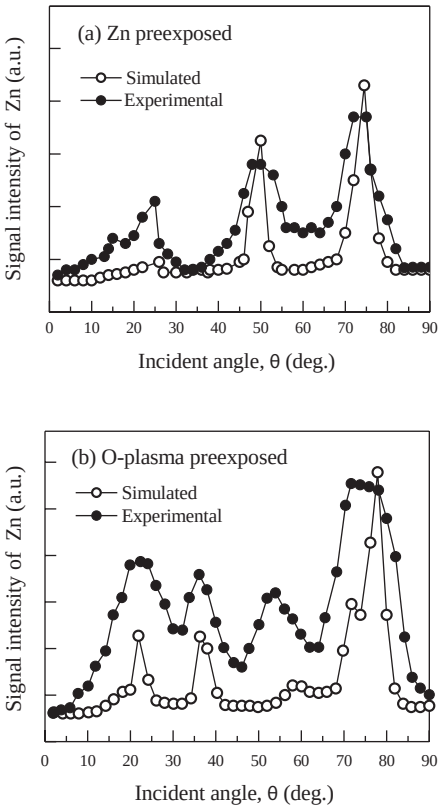

Figure 2.27 Polar-angle-dependent CAICISS spectra from ZnO films with (a) Zn preexposure and (b) O-plasma preexposure. Solid squares and open circles indicate experimental and simulated spectra [Zn polar for (a) and O polar for (b)], respectively. The spectra are plotted as a function of an incident angle, where 90° minus a polar angle is an incident angle. (After Ref. [111].)

density of defects are present at the interface and throughout the films as a consequence of a large lattice mismatch (18%) between ZnO and sapphire. On the contrary, GaN is a closely lattice-matched material to ZnO with a lattice mismatch of 1.8%. In this vein, Ko *et al.* [112, 113] studied the growth and characteristics of as-grown and annealed ZnO thin films with LT buffer layers on (0 0 0 1) GaN templates grown by metalorganic chemical vapor deposition (MOCVD) on sapphire. The LT ZnO buffer layers were grown at 250 ∼ 300 °C, and the surface was dramatically improved by a thermal treatment above 600 °C [71]. The growth temperature for the top ZnO layer ranged 500–700 °C. A 3×3 RHEED pattern was observed during cooling for the flat ZnO surface (see Figure 2.28) [71].

Ko *et al.* [112] also studied the possibility of controlling the ZnO/GaN interface by employing different surface treatment procedures prior to ZnO growth [114, 115]. A treatment of the GaN surface by using Zn or oxygen plasma preexposures affects the

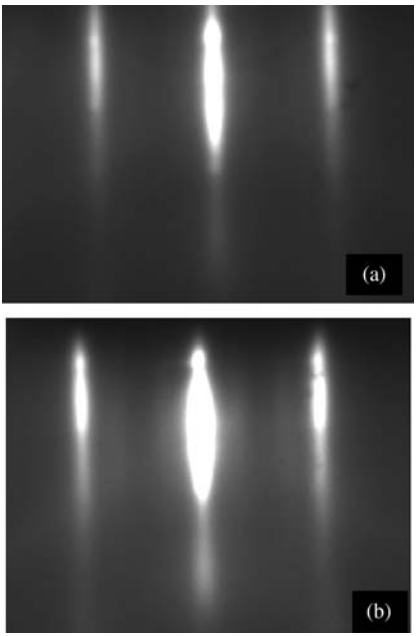

Figure 2.28 A 3×3 RHEED pattern of a ZnO layer grown on GaN/Al_2O_3 at 700 °C taken along $[1\,1\,\bar{2}\,0]$ direction during cooling down at a substrate temperature of (a) 550 °C and (b) 300 °C.

subsequent ZnO growth in different ways. The Zn pretreatment provides a well-ordered GaN surface without any interface layer, while the oxygen plasma pretreatment results in the formation of a disordered surface due to the formation of a Ga_2O_3 interface layer. Accordingly, the structural and optical properties of Zn-exposed samples are better than those of the O-exposed samples. TEM and XRD studies of the structural properties of epitaxial ZnO/epi-GaN/Al_2O_3 heterostructures revealed that the majority of the threading dislocations are of screw type, and high density of edge dislocations exists at the interfacial region [116]. As discussed above, a Zn and O plasma preexposure of Ga-polar GaN templates prior to ZnO growth produced Zn- and O-polar ZnO films, respectively [109, 111].

The pregrowth treatment and LT buffer layers have also been applied to the growth of ZnO on Si substrates. An initial deposition of a Zn layer followed by its oxidation produces a superior template for the subsequent ZnO growth [85]. The RHEED pattern suggests that the initial Zn layer and ZnO film are rotated by 30° with respect to the orientation of Si (1 1 1) substrate. Although the linewidth of the donor-bound exciton emission was as small as 6 meV at 10 K, the crystal quality of the ZnO films was not as good as those grown on sapphire [117].

2.3.2.4 Growth on ZnO Substrates

When the effects of the substrate orientation and buffer layers are considered, homoepitaxy of ZnO seems to be the most efficient way to improve the overall

epitaxial properties [53]. ZnO films have been grown on Zn-polar ZnO substrates, and two-dimensional growth with a smooth surface has been obtained under the O-rich flux condition. In addition to the improvement in the structural and optical properties, owing to the reduction in density of the edge-type threading dislocation, the residual carrier concentration in the homoepitaxial ZnO films was as low as $2.2 \times 10^{16}\,\mathrm{cm}^{-3}$, and the electron mobility of $158\,\mathrm{cm}^2\,\mathrm{V}^{-1}\,\mathrm{s}^{-1}$ was achieved.

Kato *et al.* [89] performed growth experiments of ZnO epilayers with MBE on Zn-face ZnO substrates by plasma-assisted molecular beam epitaxy. The salient result of this investigation is that with increasing O/Zn flux ratio from the stoichiometric to the O rich, the growth mode changed from three- to two-dimensional growth with accompanying linewidths of (0 0 0 2) and $(10\,\bar{1}0)$ ω rocking diffraction peaks recording a dramatic narrowing from 471 down to 42 arcsec and from 1635 to 46 arcsec, respectively. In terms of comparison to ZnO on sapphire substrates, these values are narrower. Moreover, A-, B-free excitons (FE_A, FE_B), and the $n = 2$ state of FE_A were clearly visible at 3.378, 3.393, and 3.424 eV, respectively, in the low-temperature (4.2 K) photoluminescence spectrum of layers grown under O-rich flux conditions. The authors suggested that growth under high O-rich flux conditions is imperative to produce high-quality Zn-polar ZnO films.

2.3.3
Pulsed Laser Deposition

In the PLD method, a stream of high-power laser pulses is used to evaporate material from targets so that the stoichiometry of the depositing material is preserved when the constituent species interact on the surface and for the semiconductor. Essentially, a supersonic jet of particles (plume) is directed normal to the target surface. The plume expands away from the target with a strong forward-directed velocity distribution of different particles. The ablated species condense on the substrate placed opposite to the target. A schematic diagram of a typical PLD system is shown in Figure 2.29. The main advantages of PLD are its ability to create high-energy source particles, permitting high-quality film growth at low substrate temperatures, typically ranging from 200 to 800 °C, its simple experimental setup, and operation in high ambient gas pressures ranging10^{-5} –10^{-1} Torr. For the growth of ZnO by PLD technique, usually UV excimer lasers (KrF: $\lambda = 248$ nm, ArF: $\lambda = 193$ nm) and Nd: YAG pulsed lasers ($\lambda = 355$ nm) are used for ablation of the ZnO target in an oxygen environment. In some cases, Cu-vapor laser emitting at $\lambda = 510$–578 nm [118] was also used for the same purpose. Cylindrical ZnO tablets made from pressed ZnO powder are usually used as targets. Single-crystal ZnO has been used to grow high-quality ZnO thin films [119]. Only in rare cases, a pure Zn metal is used [120, 121]. The properties of the grown ZnO films depend mainly on the substrate temperature, ambient oxygen pressure, and laser intensity. The earliest reports on high-quality ZnO growth by PLD were by, for example, Sankur and Cheung [122] and Nakayama [123]. However, the influence of the growth conditions on the ZnO properties was studied in detail much later [124–127].

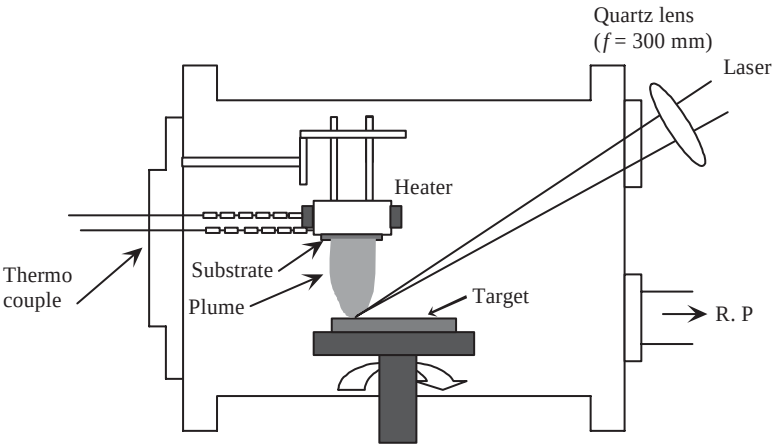

Figure 2.29 Schematic diagram of a pulsed laser deposition system. (After Ref. [125].)

Tsukazaki *et al.* [119] reported the high-quality ZnO thin film deposition on closely lattice-matched hexagonal $ScAlMgO_4$ substrates by laser MBE at high growth temperatures up to 1000 °C. The growth direction is identified as $[0\,0\,0\,\bar{1}]$ direction (oxygen face). The FWHM of (0 0 0 2) XRD rocking curve is less than 18 arcsec for 1 μm thick ZnO films. By using the high-quality undoped ZnO films, these authors also demonstrated ZnO p–i–n homojunctions for LED application [128]. Nitrogen was used as the p-type dopant by applying a "repeated temperature modulation epitaxy" method.

Choopun *et al.* [124] studied the influence of oxygen pressure on the surface morphology and optoelectronic properties of ZnO films grown on sapphire(0 0 0 1) by PLD. The films were grown at an optimized growth temperature of 750 °C. The growth was carried out under various oxygen background pressures ranging 10^{-5}–10^{-1} Torr. All the ZnO layers grown were found to be *c*-axis oriented. The films grown under lower oxygen pressure regimes (10^{-5}–10^{-4} Torr) had a *c*-axis lattice parameter 0.25% larger than that of the bulk material. This effect was attributed to both oxygen deficiency and compressive strain induced by the sapphire substrate. However, for the films deposited under higher oxygen pressures (10^{-2}–10^{-1} Torr), the *c*-lattice constant was found to approach the bulk value. The FWHM of XRD ω rocking curve was 0.069° for the film grown at an O_2 pressure of 10^{-4} Torr. The in-plane ordering, as determined from XRD ϕ scans of the ZnO $(1\,0\,\bar{1}\,1)$ planes, however, was strongly influenced by the oxygen pressure. The FWHMs of $(1\,0\,\bar{1}\,1)$ peaks were 0.43° and 0.78° for the ZnO films grown at 10^{-4} and 10^{-1} Torr, respectively.

Figure 2.30 shows the surface morphology of the ZnO films grown at various O_2 pressures [124]. The morphology of the films grown at 10^{-5}–10^{-4} Torr was dominated by a typical "honeycomb"-like structure with three-dimensional (3D) growth features as evidenced by the well-faceted hexagons (Figure 2.30a). The transition toward the growth of a smooth film was found at an O_2 pressure of 10^{-2} Torr. This change in the growth mode resulted in a substantial reduction of rms roughness to

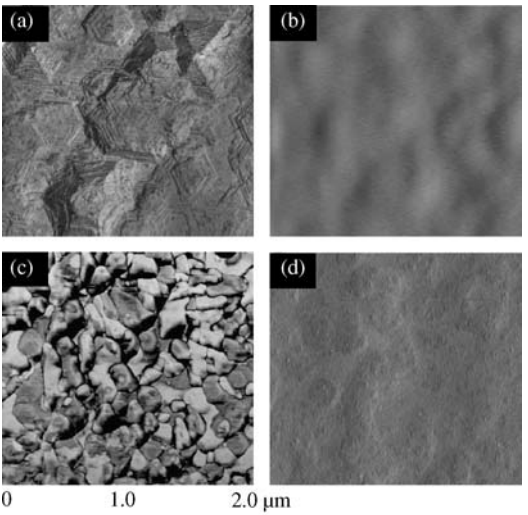

Figure 2.30 AFM images of the ZnO films grown at various oxygen pressures: (a) 10^{-4} Torr, (b) 10^{-2} Torr, (c) 10^{-1} Torr, and (d) 10^{-1} Torr, with a nucleation layer of 100 Å grown at 10^{-4} Torr. (Ref. [124].)

10–20 Å for a flat surface. A further increase of the O_2 pressure to 10^{-1} Torr showed an adverse effect on the surface morphology (Figure 2.30c) typically featured by high nucleation densities, irregular grains with different sizes, and the increase in surface roughness to about 400 Å.

The effect of oxygen pressure on the electrical properties (Hall mobility μ and carrier concentration *n*) of the ZnO films is shown in Figure 2.31 [124]. The highest electron mobility ($72\ cm^2\ V^{-1}\ s^{-1}$) was obtained for the film grown at 10^{-4}–10^{-3} Torr, but this film also showed a highest carrier concentration ($7 \times 10^{17}\ cm^{-3}$). Further increase in O_2 pressure reduced the Hall mobility, possibly as a result of electron scattering by defects/ionized impurities. The optical quality of the ZnO epilayer grown at 10^{-4} Torr was much higher than those grown at 10^{-1} Torr, as evidenced by a much higher excitonic luminescence intensity (by two orders of magnitude). This indicates that a high concentration of defects in ZnO film affects the radiative processes.

As seen from the above results, the PLD growth of high-quality epitaxial ZnO films with smooth surfaces and desirable electrical and optical properties has different optimum oxygen pressure regimes. To overcome this problem, a two-step growth procedure has been developed [124]. In this process, the nucleation layer is grown at low oxygen pressure (10^{-4} Torr), which produces a high-quality template for the subsequent growth of ZnO at a high oxygen pressure (10^{-1} Torr).

The preparation of highly conducting and transparent aluminum-doped zinc oxide films was reported by Singh *et al.* [125]. The films were deposited on quartz and Corning 7059 glass by focusing a XeCl ($\lambda = 308$ nm, 20 ns pulse width) excimer laser onto a target rotating at 15 rpm. The ZnO target was 2 in. in diameter and doped with 2 wt% Al_2O_3. For all the experiments, a repetition rate of 5 Hz and an energy density of

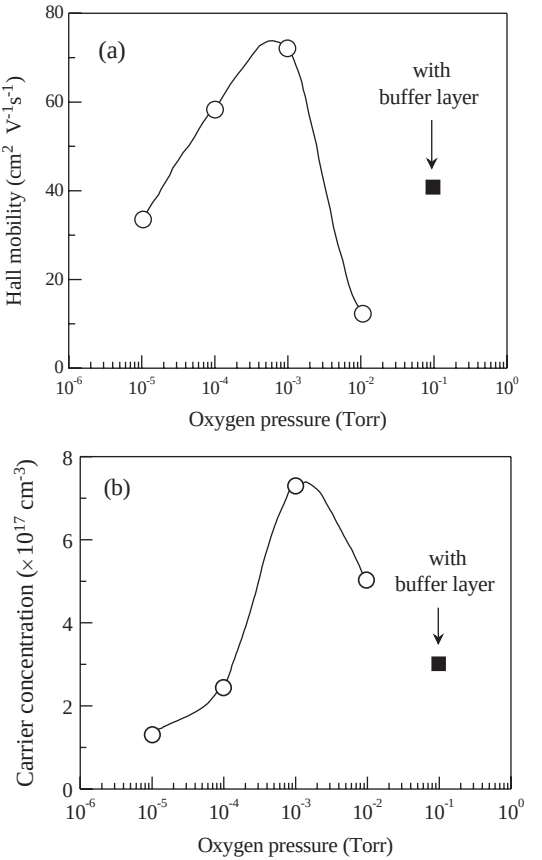

Figure 2.31 (a) Hall mobility and (b) carrier concentration versus oxygen pressure for ZnO growth. For comparison, the data for the ZnO film grown at 10^{-1} Torr with the nucleation layer grown at 10^{-4} Torr are also shown. (After Ref. [124].)

1.5 J cm^{-2} were used. The distance between the target and the substrate was 30 mm, and the deposition time was kept at 30 min. The effects of substrate temperature (from room temperature to 400 °C) and oxygen pressure (from 0.1 to 5 mTorr) were investigated by analyzing the optical and electrical properties of the films. The average transmittance was found to be in the range of 86–92%, and the resistivity varied from 3.56×10^{-3} to 7.0×10^{-3} Ω cm. The lowest resistivity measured was 1.4×10^{-4} Ω cm for the films grown at 300 °C and 1 mTorr oxygen pressure.

Matsubara *et al.* [126] used oxygen radical-assisted PLD to grow highly transparent and low-resistivity Al-doped ZnO films at room temperature. A KrF excimer laser ($\lambda = 248$ nm, 30 ns pulse width, 10 Hz repetition rate) was used for ablation. The oxygen partial pressure during deposition was 0.7–1.4×10^{-5} Torr, and the applied RF power was 150 W. The distance between the target and the substrate was approximately 6 cm. The minimum resistivity of the obtained transparent films was

$5 \times 10^{-4}\,\Omega$ cm. The average transmittance in the visible wavelength region was over 86% for ~0.7 μm thick films. The films grown in a low-pressure molecular oxygen atmosphere (1.4×10^{-5} Torr) were slightly black and had low transmittance in the visible and near-infrared regions of the optical spectrum, and had relatively lower resistivity. The radical source assisted the incorporation of oxygen into the films and made the films transparent.

Craciun *et al.* [127] deposited high-quality ZnO films on glass and silicon substrates by the PLD technique employing a KrF laser ($\lambda = 248$ nm) and studied the influence of the deposition parameters, such as substrate temperature, oxygen pressure and laser fluence on the properties of the grown films. All the films grown over a rather wide range of deposition conditions were found to be optically transparent, electrically conductive, and *c*-axis oriented, with the FWHM of the (0 0 2) XRD line being very often less than 0.25°. Investigations into the effect of different oxygen partial pressures showed that the best quality films could be obtained in the higher pressure range, that is, between 1 and 4×10^{-3} Torr. This result is quite different from that obtained previously and has been accounted for by the differences in the substrate-to-target distances employed. The electrical resistivity of the films was strongly affected by the oxygen pressure, increasing from 7–9 $\times 10^{-3}\,\Omega$ cm for the films deposited at 2×10^{-5} Torr to 5–8 $\times 10^{-2}\,\Omega$ cm for those deposited at 2×10^{-3} Torr. This behavior can be easily understood by taking into account that the electrical conductivity of ZnO is controlled by Zn interstitials or O vacancies. From these studies, it was concluded that the best conditions for PLD of ZnO films center around substrate temperatures between 300 and 350 °C, oxygen partial pressures from 1 to 2×10^{-3} Torr, and a laser fluence of around 2 J cm^{-2}. Within this range, the FWHM of the (0 0 2) XRD line is always below 0.18° and the transparency is above 85% in the visible region of the spectrum. Figure 2.32 shows the XRD pattern recorded for a ZnO film grown with a fluence of 2.1 J cm^{-2}, substrate temperature of 350 °C, and oxygen pressure of 2×10^{-3}

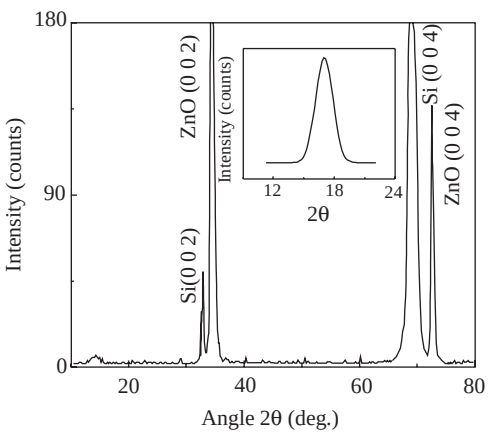

Figure 2.32 XRD pattern of a ZnO thin film deposited under optimized conditions. The rocking curve recorded for the (0 0 2) line is shown in the inset. (After Ref. [127].)

Torr [127]. Only the (0 0 2) and (0 0 4) XRD lines are present along with the Si (1 0 0) peak of the substrate. The FWHM of the (0 0 2) reflection was 0.13°, one of the lowest values yet reported in the literature for PLD-grown ZnO. The small peak at around 10° was attributed to the presence of a very thin amorphous transitional layer between the Si substrate and the grown ZnO film. The rocking curve measured for the (0 0 2) diffraction, as shown in the inset of Figure 2.32, is at 16.99° with a FWHM of 2.07°.

2.3.4 Chemical Vapor Deposition

Among other growth methods, chemical vapor deposition (CVD) technology is particularly interesting not only because it gives rise to high-quality films but also because it is applicable to large-scale production. This technique is widely used in the fabrication of epitaxial films toward various GaN-based optoelectronic devices, and similar trend might be expected for future applications of ZnO. There are several modifications of this method depending on precursors used. When metalorganic precursors are used, the technique is called MOCVD [13], metalorganic vapor-phase epitaxy (MOVPE) or OMVPE. In the case of hydride or halide precursors, the technique is named hydride or halide CVD or VPE (HVPE) [14, 15].

In the CVD method, ZnO deposition occurs as a result of chemical reactions of vapor-phase precursors on the substrate, which are delivered into growth zone by the carrier gas. The reactions take place in a reactor where a necessary temperature profile is created in the gas flow direction.

For hydride VPE growth of ZnO, hydrogen (H_2) was employed as a carrier gas [129–131]. In these particular cases, the typical pressure was $\leq$133 Pa and the flow rate was about 40 ml min^{-1}. Targets made from ZnO powder were placed in the evaporation zone in which the temperature was around 770 °C. The following chemical reaction between the ZnO target and H_2 carrier gas takes place in the evaporation zone:

$$ZnO + H_2 \rightarrow Zn + H_2O. \tag{2.1}$$

On the substrate (the deposition zone), where the temperature was kept in the range of 590–610 °C, the reverse reaction occurs:

$$Zn + H_2O \rightarrow ZnO + H_2. \tag{2.2}$$

The ZnO films grown by this method show quite high crystal, electrical, and luminescence properties [132, 133].

ZnO films were also grown by halide VPE employing oxygen gas and Zn chloride ($ZnCl_2$) [15] or Zn iodide (ZnI_2) [134] as sources of Zn and O, respectively. It was demonstrated that iodide system allows growing ZnO layers of higher optical and structural properties. The main advantage of this technique is its very high growth rate. The preparation of 100 μm ZnO films showing room-temperature ultraviolet emission with a PL FWHM as narrow as 10 meV was reported by Takashi *et al.* [135].

For ZnO growth, OMVPE/MOVPE technique typically involves the use of metal alkyls, usually dimethyl zinc $(CH_3)_2Zn$ (DMZn) or diethyl zinc $(C_2H_5)_2Zn$ (DEZn) in combination with a separate source of oxygen and argon or nitrogen as a carrier gas.

In earlier investigations, O_2 or H_2O were used as oxygen precursors [136–138]. However, DEZn and DMZn are highly reactive with oxygen and water vapor so that severe premature reaction in the gas phase occurs in the cold zone of the reactor, resulting in the formation of white powder that degrades the film quality. Nevertheless, great progress has been made in ZnO growth by OMVPE. The improvement of the material quality is related to improved reactor design [139] and/or the use of less reactive precursors, allowing one to minimize parasitic prereactions in the gas phase. Stable metalorganic source of zinc acetylacetonate in combination with oxygen was successfully used for the growth of high-quality ZnO films on *r*-plane [140] as well as on *c*- and *a*-plane [141] sapphire substrates by atmospheric pressure OMVPE. For the group VI precursor, a variety of oxygen compounds were employed: iso-propanol (*i*-PrOH) [142–145], tertiary butanol (*t*-BuOH) [146–149], aceton [136], N_2O [136, 150–153], and NO_2 [154].

High-quality ZnO layers have been prepared on GaN/sapphire [142, 144] and *c*-plane sapphire [134, 143] substrates by using DEZn and *i*-PrOH. FWHMs of the ω-2θ scans were 100 and 270 arcsec depending on the substrate, and the 5 K PL spectra showed strong near-band-edge emission with linewidths of 5–12 meV with phonon replicas [133, 142]. For the films grown on *c*-plane sapphire under optimized conditions, PL was dominated by strong near-band-edge lines with FWHM below 4 meV, and the excitonic signals were clearly visible in reflectivity measurements [143]. Hall effect measurements indicated an n-type background doping in the $10^{17}\,cm^{-3}$ range with carrier mobilities of more than $100\,cm^2\,V^{-1}\,s^{-1}$.

Kirchner *et al.* [149] have reported direct comparison of MOVPE growth of ZnO layers on *c*-plane sapphire using *i*-PrOH and *t*-BuOH as an oxygen precursor and DEZn as a zinc source. It has been demonstrated that two oxygen precursors show similar pressure dependence of the ZnO growth rate but large differences in the temperature-dependent growth rate (see Figure 2.33). The growth rate was found to

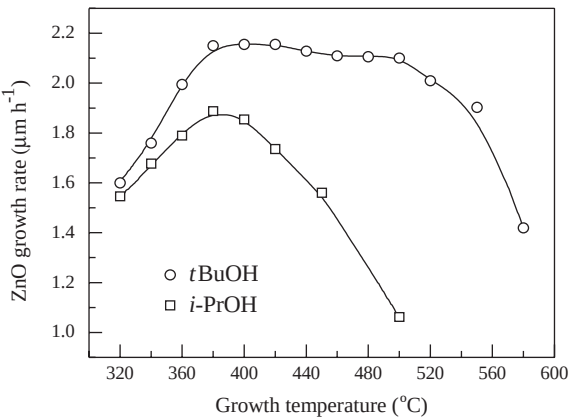

Figure 2.33 Temperature dependence of the ZnO growth rate using isopropanol (squares) or tertiary butanol (circles) as the oxygen precursor. DEZn flow rate is $100\,\mu mol\,min^{-1}$. Reactor pressure for both sets of samples is 400 mbar. (After Ref. [149].)

be almost constant over a wide temperature range from 380 to 510 °C in the case of *t*-BuOH, whereas for *i*-PrOH, the maximum growth rate was achieved at 380 °C. The optical quality of the ZnO layers grown with *t*-BuOH was superior to those grown with *i*-PrOH. For ZnO grown under optimized conditions using *t*-BuOH, strong near-band-edge emission lines with half-widths of 1.1 meV dominated the PL spectra.

The potential of nitrous oxide for MOVPE of ZnO was demonstrated by Ogata *et al.* [150]. Low reactivity allows one to grow ZnO films at high substrate temperature that results in high crystal perfection and good optical quality of the material. Oleynik *et al.* [145] reported superior characteristics of ZnO layers grown on GaN/Si substrates with the use of N_2O compared to those prepared with *i*-PrOH and acetone. The growth of a LT (500 °C) buffer layer of ZnO was demonstrated to be essential to enhance the initial nucleation process and to achieve high-quality ZnO overgrown layers at higher growth temperatures (600–700 °C) [150]. Dadgar *et al.* [153] used *t*-BuOH and DEZn as precursors for the growth of LT (450 °C) ZnO buffers on GaN/sapphire substrates. At the second stage, ZnO layers were grown at high temperature (900–950 °C) using N_2O. The layers showed smooth surface morphology and high crystalline quality as demonstrated by XRD [FWHM of (0 0 0 2) ω-scans for a 2.28 μm-thick layer was 160 arcsec]. The bright luminescence was dominated by narrow excitonic (FWHM <1.3 meV) emission lines. The effects of LT buffer thickness as well as substrate temperature on the optical quality of ZnO layers were studied systematically (see Figure 2.34).

High-quality homoepitaxial ZnO layers were grown on bulk ZnO substrates by using N_2O and DEZn [151]. Two conditions, proper thermal treatment of substrate prior to the growth for obtaining flat surface and high flow rate ratios of source materials, were found to be important to obtain high-quality layers. Surface

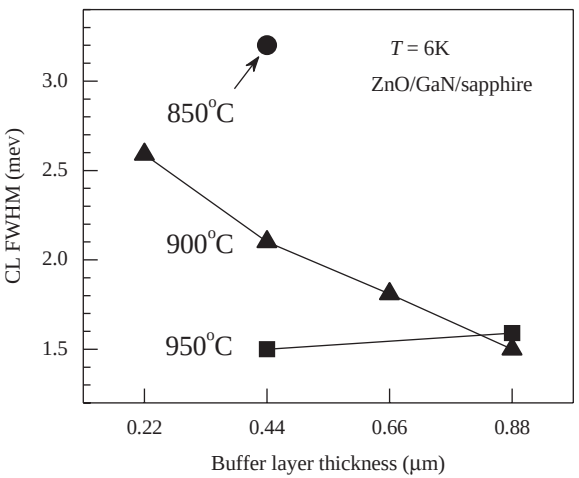

Figure 2.34 CL linewidth of the ZnO near-band-edge emission as a function of LT buffer layer thickness and growth temperature. The linewidth decreases with increasing growth temperature and layer thickness of LT ZnO buffer. (After Ref. [153].)

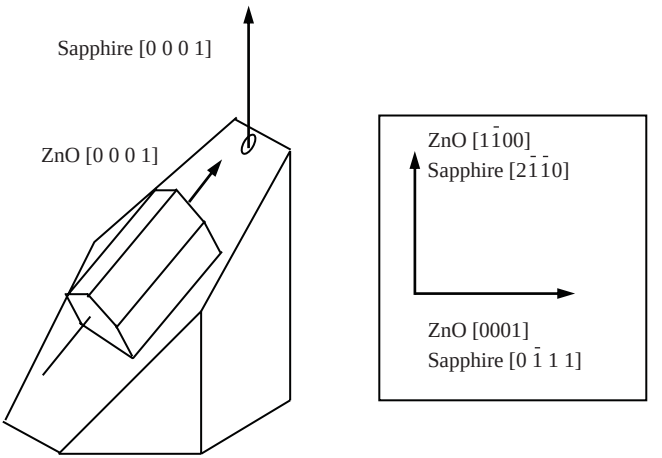

Figure 2.35 Epitaxial relationships for *a*-plane ZnO grown on *R*-plane sapphire. The relative orientation of ZnO on sapphire is shown in the boxed area as well.

roughness below 1 nm as well as strong free-exciton emission at 15 K was reported for the films grown under optimal conditions.

The improvement of OMVPE technology also gave rise to great progress in the quality of ZnO layers grown with the use of DEZn and O_2. The pressure used for the growth ranged5–250 Torr [139, 155, 156]. Lower pressure effect was investigated and the results showed that the crystal quality was better for films grown at 6 Torr than those grown at 0.05 Torr [157]. *R*-plane sapphire substrate has been used in OMVPE growth of ZnO [139]. The epitaxial relationship between ZnO and *R*-plane sapphire was found to be (1 1 $\bar{2}$ 0) ZnO//(0 1 $\bar{1}$ 2) sapphire and [0 0 0 1] ZnO//[0 $\bar{1}$ 1 1] sapphire. Figure 2.35 shows the epitaxial relationship. High-crystallinity ZnO epilayers were grown on sapphire (0 0 0 1) substrates with LT ZnO buffer layer [155]. The XRD rocking curve data of as-grown films exhibited FWHM values in the range of 0.04°–0.05°.

The in-plane orientation of ZnO epitaxial films grown on as-polished (0 0 0 1) sapphire substrates by OMVPE has been reported to depend on the initial conditions when starting the flow of DEZn over the substrate [158]. The epitaxial orientation can easily be controlled to be either ZnO [11 $\bar{2}$ 0]//sapphire [11 $\bar{2}$ 0] (no in-plane rotation) or ZnO [1 0 $\bar{1}$ 0]//sapphire [11 $\bar{2}$ 0] (30° in-plane rotation), but all the films had Zn polarity regardless of the in-plane orientation, in contrast to the result obtained by MBE [110].

The effect of oxygen partial pressure on the structural perfection as well as optical and electrical properties of ZnO films grown at 600 °C on Al_2O_3 (0 0 0 1) was studied by Ma *et al.* [159, 160]. It was found that the conduction type in undoped ZnO layers could be controlled by adjusting the oxygen partial pressure during growth. The films grown under an oxygen partial pressure lower than 45 Pa showed n-type conductivity. With increasing oxygen pressure, the crystallinity of the ZnO layers degraded to polycrystalline with additional (1 0 $\bar{1}$ 2) orientation, and intrinsic p-type ZnO (which

should be treated with some caution) was produced as the oxygen partial pressure became higher than 55 Pa. The hole concentration and the mobility reached $1.59 \times 10^{16}\,cm^{-3}$ and $9.23\,cm^2\,V^{-1}\,s^{-1}$, and the resistivity was $42.7\,\Omega\,cm$. The near-band-edge and deep-level emissions in RT PL spectra were influenced strongly by the oxygen partial pressure. Temperature-dependent PL spectra in n-type ZnO films showed a dominant neutral-donor bound exciton emission, while the p-ZnO was dominated by the neutral acceptor-bound exciton line. With decreasing temperature, both peaks increased in intensity and blueshifted. The band that originated from zinc vacancies emerged for temperatures below 155 K only in the p-type films. The origin of intrinsic p-type conductivity in ZnO thin films was attributed to zinc vacancies, the premise of which should be treated with a great deal of caution.

Evolution and growth of ZnO films grown on GaN/AlN/SiC(0 0 0 1) [161, 162] and ZnO [163] from DEZn and O_2 have been reported by Smith *et al*. From a microscopic study of initial growth stages, it was concluded that ZnO on GaN templates nucleated and grew via the Stranski–Krastanov mode [161]. At 500 °C, dense ZnO (0 0 0 1) films were formed via coalescence of islands either on GaN/AlN/SiC (0 0 0 1) substrates or on initial, coherent ZnO layers [162]. To check the possible effect of interface oxide layer on the growth mode and the film morphology, the GaN surface was preexposed to the reagents in different ways at the initiation of growth. Interfaces between ZnO and GaN exposed either simultaneously to diethylzinc and oxygen or only to diethylzinc were sharp and epitaxial. Interfaces formed after the exposure of the GaN to O_2 were less coherent, though an interfacial oxide was not observed by cross-sectional TEM [162]. A strong effect of the surface polarity was revealed for homoepitaxial growth of ZnO films on O- and Zn-terminated ZnO (0 0 0 1) substrates [163]. The films, grown on O-terminated ZnO surfaces, were initially dense. However, they changed to a textured polycrystalline microstructure after approximately 100 nm and exhibited a surface roughness of 7.3 nm. By contrast, the films grown on the Zn-terminated surface under the same conditions were fully dense and without texture and appeared to be monocrystalline with a significantly improved surface roughness of 3.4 nm.

An important advantage of OMVPE/MOVPE technique is the feasibility of catalyst-free growth of ZnO nanowires (nanorods) as discussed in Section 7.1.2. For DEZn and N_2O source materials, Ogata *et al*. [152] demonstrated a possibility to control the growth mode by tuning the growth parameters. At lower temperatures and/or lower VI/II ratio, the growth tended to be three-dimensional and nanorod structure could be grown on sapphire substrates. At higher temperatures, two-dimensional growth was performed, and the flat and uniform epilayers could be formed both on sapphire and on bulk ZnO substrates. The homoepitaxial ZnO layers exhibited an rms value of 3 nm and a FWHM of 0.5 meV in low-temperature (9 K) PL emission. With the use of different precursor systems, the OMVPE/MOVPE method was successfully applied to the catalyst-free growth of ZnO nanowires on various substrates, such as Si [164, 165], GaN/sapphire [164], *c*-plane sapphire [164, 166, 167], and GaAs (0 0 1) [168]. In the case of GaAs substrate, it was reported that postgrowth heat treatment resulted in p-type doping of nanowires owing to As diffusion from GaAs substrate [168]. Yang and Zhang [169] used OMVPE to grow ZnO single-crystal

whiskers on glass substrates. To investigate the possibility of a combination of bandgap engineering and nanopillar growth, Kling *et al*. [170] grew ZnMgO nanorods. The Mg incorporation was confirmed by PL measurements, and a blueshift of the bandgap of up to 170 meV could be achieved for the nanopillars with the highest Mg concentration. Park *et al*. [171] also demonstrated the growth of ZnO/$Zn_{0.8}Mg_{0.2}O$ nanorod single-quantum-well structures. Moreover, fabrication of high-mobility field-effect transistors (FETs) using ZnO nanorods grown by MOVPE has been reported [172]. A high transconductance of 1.9 μS and a high electron mobility above 1000 $cm^2 V^{-1} s^{-1}$ were achieved.

References

1 Yamamoto, T., Shiosaki, T. and Kawabata, A. (1980) *Journal of Applied Physics*, **51**, 3113.

2 Mitsuyu, T., Ono, S. and Wasa, K. (1980) *Journal of Applied Physics*, **51**, 2464.

3 Hachigo, A., Nakahata, H., Higaki, K., Fujii, S. and Shikata, S. (1994) *Applied Physics Letters*, **65**, 2556.

4 Gardeniers, J.G.E., Rittersma, Z.M. and Burger, G.J. (1998) *Journal of Applied Physics*, **83**, 7844.

5 Tiku, S.K., Lau, C.K. and Lakin, K.M. (1980) *Applied Physics Letters*, **36**, 318.

6 Kasuga, M. and Mochizuki, M. (1981) *Journal of Crystal Growth*, **54**, 185.

7 Srikant, V., Sergo, V. and Clarke, D.R. (1995) *Applied Physics Letters*, **16**, 439.

8 Kim, K.-K., Song, J.-H., Jung, H.-J., Choi, W.-K., Park, S.-J. and Song, J.-H. (2000) *Journal of Applied Physics*, **87**, 3573.

9 Kim, K.-K., Song, J.-H., Jung, H.-J., Choi, W.-K., Park, S.-J., Song, J.-H. and Lee, J.-Y. (2000) *Journal of Vacuum Science & Technology A: Vacuum Surfaces and Films*, **18**, 2864.

10 Fons, P., Iwata, K., Niki, S., Yamada, A. and Matsubara, K. (1999) Growth of high quality epitaxial ZnO films on α–Al_2O_3. *Journal of Crystal Growth*, **201–202**, 627.

11 Chen, Y., Bagnall, D.M., Koh, H.-J., Park, K.-T., Hiraga, K., Zhu, Z.-Q. and Yao, T. (1998) Plasma assisted molecular beam epitaxy of ZnO on *c*-plane sapphire: growth and characterization. *Journal of Applied Physics*, **84**, 3912.

12 Vispute, R.D., Talyansky, V., Choopun, S., Sharma, R.P., Venkatesan, T., He, M., Tang, X., Halpern, J.B., Spencer, M.G., Li, Y.X., Salamanca-Riba, L.G., Iliadis, A.A. and Jones, K.A. (1998) *Applied Physics Letters*, **73**, 348.

13 Liu, Y., Gorla, C.R., Liang, S., Emanetoglu, N., Lu, Y., Shen, H. and Wraback, M. (2000) *Journal of Electronic Materials*, **29**, 69.

14 Kasuga, M. and Ogawa, S. (1983) *Japanese Journal of Applied Physics*, **22**, 794.

15 Takahashi, N., Kaiya, K., Nakamura, T., Momose, Y. and Yamamoto, H. (1999) *Japanese Journal of Applied Physics*, **38**, L454.

16 Bagnall, D.M., Chen, Y.F., Zhu, Z., Yao, T., Koyama, S., Shen, M.Y. and Goto, T. (1997) *Applied Physics Letters*, **70**, 2230.

17 Tang, Z.K., Wong, G.K.L., Yu, P., Kawasaki, M., Ohtomo, A., Koinuma, H. and Segawa, Y. (1998) *Applied Physics Letters*, **72**, 3270.

18 Narayan, J., Dovidenko, K., Sharma, A.K. and Oktyabrsky, S. (1998) *Journal of Applied Physics*, **84**, 2597.

19 Ko, H.J., Chen, Y.F., Zhu, Z., Hanada, T. and Yao, T. (2000) *Journal of Crystal Growth*, **208**, 389.

20 Lad, R.J., Funkenbusch, P.D. and Aita, C.R. (1980) *Journal of Vacuum Science & Technology*, **17**, 808.

21 Shih, W. and Wu, M. (1994) *Journal of Crystal Growth*, **137**, 319.

22 Hwang, D., Bang, K., Jeong, M. and Myoung, J. (2003) *Journal of Crystal Growth*, **254**, 449.

23 Ohtomo, A., Tamura, K., Saikusa, K., Takahashi, K., Makino, T., Segawa, Y., Koinuma, H. and Kawasaki, M. (1999) *Applied Physics Letters*, **75**, 2635.

24 Sekiguchi, T., Miyashita, S., Obara, K., Shishido, T. and Sakagami, N. (2000) Hydrothermal growth of ZnO single crystals and their optical characterization. *Journal of Crystal Growth*, **214–215**, 72.

25 Sakagami, T., Yamashita, M., Sekiguchi, T., Miyashita, S., Obara, K. and Shishido, T. (2001) *Journal of Crystal Growth*, **229**, 98.

26 Li, W.-J., Shi, E.-W., Zhong, W.-Z. and Yin, Z.-W. (1999) *Journal of Crystal Growth*, **203**, 186.

27 Ohshima, E., Ogino, H., Niikura, I., Maeda, K., Sato, M., Ito, M. and Fukuda, T. (2004) Growth of the 2-in-size bulk ZnO single crystals by the hydrothermal method. *Journal of Crystal Growth*, **260**, 166.

28 Look, D.C., Reynolds, D.C., Sizelove, J.R., Jones, R.L., Litton, C.W., Cantwell, G. and Harsch, W.C. (1998) *Solid State Communications*, **105**, 399.

29 Shiloh, M. and Gutman, J. (1971) *Journal of Crystal Growth*, **11**, 105.

30 Matsumoto, K. and Noda, K. (1990) *Journal of Crystal Growth*, **102**, 137.

31 Ntep, J.-M., Hassani, S.S., Lusson, A., Tromson-Carli, A., Ballutaud, D., Didier, G. and Triboulet, R. (1999) *Journal of Crystal Growth*, **207**, 30.

32 Nause, J. (1999) ZnO broadens the spectrum. *III–Vs Review*, **12**, 28.

33 Nause, J. and Nemeth, B. (2005) Pressurized melt growth of ZnO boules. *Semiconductor Science and Technology*, **20**, S45.

34 Suscavage, M., Harris, M., Bliss, D., Yip, P., Wang, S.-Q., Schwall, D., Bouthillette, L., Bailey, J., Callahan, M., Look, D.C., Reynolds, D.C., Jones, R.L. and Litton, C.W. (1999) *MRS Internet Journal of Nitride Semiconductor Research*, **4S1**, G3.40.

35 Alexander, M.N. (2007) Air Force Research Laboratory Sensors Directorate, Electromagnetics Technology Division Hanscom AFB, MA, private communication.

36 http://www.compoundsemi.com/documents/articles/news/6303.html.

37 Maeda, K., Sato, M., Niikura, I. and Fukuda, T. (2005) Growth of 2 inch ZnO bulk single crystal by the hydrothermal method. *Semiconductor Science and Technology*, **20**, S49.

38 Nause, J. (2007) Cermet, Inc., private communication.

39 Johnson, M.A.L., Fujita, S., Rowland, W.H., Jr, Hughes, W.C., Cook, J.W., Jr, and Schetzina, J.F. (1992) *Journal of Electronic Materials*, **21**, 157.

40 Susnitzky, D.W. and Carter, C.B. (1986) *Journal of the American Ceramic Society*, **69**, 217.

41 Pond, R.C., Gowers, J.P. and Joyce, B.A. (1985) *Surface Science*, **152**, 1191.

42 Pierre Ruterana, Sánchez, Ana M. and Gérard Nouet (2003) Extended defects in wurtzite GaN layers: atomic structure, formation and interaction mechanisms, in *Nitride Semiconductiors: Handbook on Materials and Devices* (eds P. Ruterana, M. Albrecht, and J. Neugebauer), Wiley-VCH Verlag GmbH, Weinheim.

43 Liu, L. and Edgar, J.H. (2002) Substrates for gallium nitride epitaxy. *Materials Science & Engineering R-Reports*, **37**, 61.

44 Touloukina, Y.S., Kirby, R.K., Taylor, R.E. Lee, T.Y. (eds) (1977) *Thermal Expansion. Thermal Properties of Matter, Vol. 13*, Plenum, New York.

45 Kobayashi, K., Matsubara, T., Matsushima, S., Shirakata, S., Isomura, S. and Okada, G. (1995) *Thin Solid Films*, **266**, 106.

46 Johnson, M.A.L., Fujita, S., Rowland, W.H., Jr, Hughes, W.C., Cook, J.W., Jr, and Schetzina, J.F. (1996) *Journal of Electronic Materials*, **25**, 855.

47 Chen, Y., Bagnall, D.M., Zhu, Z., Sekiuchi, T., Park, K., Hiraga, K., Yao, T., Koyama, S., Shen, M.Y. and Goto, T. (1997) *Journal of Crystal Growth*, **181**, 165.

48 Chen, Y., Ko, H.-J., Hong, S.-K. and Yao, T. (2000) *Applied Physics Letters*, **76**, 559.

49 Fons, P., Iwata, K., Niki, S., Yamata, A., Matsubara, K. and Watanabe, M. (2000) *Journal of Crystal Growth*, **200**, 532.

50 Nakamura, K., Shoji, T. and Kang, H.-B. (2000) *Japanese Journal of Applied Physics, Part 2: Letters*, **39**, L534.

51 Kang, H.-B., Yoshida, K. and Nakamura, K. (1998) *Japanese Journal of Applied Physics, Part 1: Regular Papers, Short Notes & Review Papers*, **37**, 5220.

52 Sakurai, K., Kanehiro, M., Nakahara, K., Tanabe, T., Fujita, S. and Fujita, S. (2000) *Journal of Crystal Growth*, **209**, 522.

53 Kato, H., Sano, M., Miyamota, K. and Yao, T. (2003) *Japanese Journal of Applied Physics, Part 2: Letters*, **42**, L1002.

54 Kohl, D., Henzler, M. and Heiland, G. (1974) *Surface Science*, **41**, 403.

55 Vossen, J.L. (1977) *Physics of Thin Films*, Vol. 9 (eds G. Hass and M.H. Francombe), Academic Press, New York, pp. 1–71.

56 Ozaki, K. and Gomi, M. (2002) *Japanese Journal of Applied Physics, Part 1: Regular Papers, Short Notes & Review Papers*, **41**, 5614.

57 Xue, Z.Y., Zhang, D.H., Wang, Q.P. and Wang, J.H. (2002) *Applied Surface Science*, **195**, 126.

58 Lu, Y.M., Hwang, W.S., Liu, W.Y. and Yang, J.S. (2001) *Materials Chemistry and Physics*, **72**, 269.

59 Jeong, S., Kim, B. and Lee, B. (2003) *Applied Physics Letters*, **82**, 2625.

60 Chen, S.J., Liu, Y.C., Ma, J.G., Lu, Y.M., Zhang, J.Y., Shen, D.Z. and Fan, X.W. (2003) *Journal of Crystal Growth*, **254**, 86.

61 Water, W. and Chu, S.-Y. (2002) *Materials Letters*, **55**, 67.

62 Li, X.H., Huang, A.P., Zhu, M.K., Xu, Sh.L., Chen, J., Wang, H., Wang, B. and Yan, H. (2003) *Materials Letters*, **57**, 4655.

63 Morkoç, H. (2008) *Handbook of Nitride Semiconductors and Devices*, Vol. 1, Wiley-VCH Verlag GmbH, Weinheim.

64 Park, S.K. and Je, J.H. (1995) *Physica C*, **254**, 167.

65 Tominaga, K., Iwamura, S., Shintani, Y. and Tada, O. (1981) *Japanese Journal of Applied Physics, Part 1: Regular Papers, Short Notes & Review Papers*, **21**, 519.

66 Doh, S.J., Park, S.I., Cho, T.S. and Jung Ho J.E. (1999) *Journal of Vacuum Science & Technology A: Vacuum Surfaces and Films*, **17**, 3003.

67 Maniv, S., Westwood, W.D. and Colombini, E. (1982) *Journal of Vacuum Science & Technology*, **20**, 162.

68 Jou, J.-H., Han, M.-Y. and Cheng, D.-J. (1992) *Journal of Applied Physics*, **71**, 4333.

69 Hinze, J. and Ellmer, K. (2000) *Journal of Applied Physics*, **88**, 2443.

70 Ryu, M.K., Lee, S.H., Jang, M.S., Panin, G.N. and Kang, T.W. (2002) *Journal of Applied Physics*, **92**, 154.

71 Liu, C., Cho, S.-J. and Morkoç, H. unpublished.

72 Chen, Y., Bagnall, D. and Yao, T. (2000) *Materials Science and Engineering B: Solid State Materials for Advanced Technology*, **75**, 190.

73 Kim, K.-K., Kim, H.-S., Hwang, D.-K., Lim, J.-H. and Park, S.-J. (2003) *Applied Physics Letters*, **83**, 63.

74 Tüzemen, S., Xiong, G., Wilkinson, J., Mischuck, B., Ucer, K.B. and Williams, R.T. (2001) *Physica B*, **308–310**, 1197.

75 Kadota, M. and Minakata, M. (1998) *Japanese Journal of Applied Physics, Part 1: Regular Papers, Short Notes & Review Papers*, **37**, 2923.

76 Kadota, M., Miura, T. and Minakata, M. (2002) *Journal of Crystal Growth*, **237–239**, 523.

77 Shchukin, V.A., Ledentsov, N.N. and Bimberg, D. (2004) *Epitaxy of Nanostructures*, Springer-Verlag, Berlin.

78 Ledentsov, N.N. (1999) *Growth Processes and Surface Phase Equilibria in Molecular Beam Epitaxy*, Springer-Verlag, Berlin.

79 Herman, M.A. and Sitter, H. (1989) *Molecular Beam Epitaxy: Fundamental and Current Status*, Springer-Verlag, Berlin.

80 Lide, D.R. (ed.) (1998–1999) *CRC Handbook of Chemistry and Physics*, 79th edn., CRC Press, Boca Raton, FL.

81 Kang, H.-B., Nakamura, K., Lim, S.-H. and Shindo, D. (1998) *Japanese Journal of Applied Physics, Part 1: Regular Papers, Short Notes & Review Papers*, **37**, 781.

82 Kang, H.-B., Nakamura, K., Yoshida, K. and Ishikawa, K. (1997) *Japanese Journal of Applied Physics, Part 2: Letters*, **36**, L933.

83 Fons, P., Iwata, K., Niki, S., Yamada, A., Matsubara, K. and Watanabe, M. (2000) *Journal of Crystal Growth*, **209**, 532.

84 Sakurai, K., Iwata, D., Fujita, S. and Fujita, S. (1999) *Japanese Journal of Applied Physics, Part 1: Regular Papers, Short Notes & Review Papers*, **38**, 2606.

85 Fujita, M., Kawamoto, N., Tatsumi, T., Yamagishi, K. and Horikoshi, Y. (2003) *Japanese Journal of Applied Physics, Part 1: Regular Papers, Short Notes & Review Papers*, **42**, 67.

86 Izyumskaya, N., Avrutin, V., Schoch, W., El-Shaer, W.A., Reuss, F., Gruber, T. and Waag, A. (2004) *Journal of Crystal Growth*, **269**, 356.

87 Nakahara, K., Tanabe, T., Takasu, H., Fons, P., Iwata, K., Yamada, A., Matsubara, K., Hunger, R. and Niki, S. (2001) *Japanese Journal of Applied Physics, Part 1: Regular Papers, Short Notes & Review Papers*, **40**, 250.

88 Ohgaki, T., Ohashi, N., Kakemoto, H., Wada, S., Adachi, Y., Haneda, H. and Tsurumi, T. (2003) *Journal of Applied Physics*, **93**, 1961.

89 Kato, H., Sano, M., Miyamoto, K. and Yao, T. (2004) *Journal of Crystal Growth*, **265**, 375.

90 Wang, X., Iwaki, H., Murakami, M., Du, X., Ishitani, Y. and Yoshikawa, A. (2003) *Japanese Journal of Applied Physics*, **42**, L99.

91 Sakurai, K., Kanehiro, M., Nakahara, K., Tanabe, T., Fujita, S. and Fujita, S. (2000) *Journal of Crystal Growth*, **214–215**, 92.

92 Chen, Y., Ko, H.J., Hong, S., Yao, T. and Segawa, Y. (2000) *Journal of Crystal Growth*, **214–215**, 87.

93 Chen, Y.F., Ko, H.J., Hong, S.K., Inaba, K., Segawa, Y. and Yao, T. (2001) *Journal of Crystal Growth*, **227–228**, 917.

94 Miyamoto, K., Sano, M., Kato, H. and Yao, T. (2002) *Japanese Journal of Applied Physics, Part 2: Letters*, **41**, L1203.

95 Ohtomo, A., Kawasaki, M., Koida, T., Masubochi, K., Koinuma, H., Sakurai, Y., Yoshida, Y., Yasuda, T. and Segawa, Y. (1998) *Applied Physics Letters*, **72**, 2466.

96 Kato, H., Miyamoto, K., Sano, M. and Yao, T. (2004) Polarity control of ZnO on sapphire by the MgO buffer layer thickness *Applied Physics Letters*, **84**, 4562.

97 Minegishi, T., Yoo, J., Suzuki, H., Vashaei, Z., Inaba, K., Shim, K. and Yao, T Selective growth of Zn- and O-polar ZnO layers by plasma-assisted molecular beam epitaxy. *Journal of Vacuum Science & Technology B*, **23**, 1286.

98 Wang, Y., Du, X.L., Mei, Z.X., Zeng, Z.Q., Ying, M.J., Yuan, H.T., Jia, J.F., Xue, Q.K. and Zhang, Z. (2005) Cubic nitridation layers on sapphire substrate and their role in polarity selection of ZnO films. *Applied Physics Letters*, **87**, 051901.

99 Hong, S.K., Chen, Y., Ko, H.J., Wenisch, H., Hanada, T. and Yao, T. (2001) *Journal of Electronic Materials*, **30**, 647.

100 Chen, Y., Hong, S.-K., Ko, H.-J., Kirshner, V., Wenisch, H., Yao, T., Inaba, K. and Segawa, Y. (2001) *Applied Physics Letters*, **78**, 3352.

101 Fons, P., Iwata, K., Yamada, A., Matsubara, K., Niki, S., Nakahara, K., Tanabe, T. and Takasu, H. (2000) *Applied Physics Letters*, **77**, 1801.

102 Fons, P., Iwata, K., Yamada, A., Matsubara, K., Niki, S., Nakahara, K., Tanabe, T. and Takasu, H. (2001) *Journal of Crystal Growth*, **227–228**, 911.

103 Sano, M., Miyamoto, K., Kato, H. and Yao, T. (2003) *Japanese Journal of Applied Physics, Part 2: Letters*, **42**, L1050.

104 Du, X., Murakami, M., Iwaki, H., Ishitani, Y. and Yoshikawa, A. (2002) *Japanese*

Journal of Applied Physics, Part 2: Letters, **41**, L1043.

105 Nakahara, K., Takasu, H., Fons, P., Iwata, K., Yamada, A., Matsubara, K., Hunger, R. and Niki, S. (2001) *Journal of Crystal Growth*, **227–228**, 923.

106 Ogata, K., Koike, K., Tanite, T., Komuro, T., Yan, F., Sasa, S., Inoue, M. and Yano, M. (2003) *Journal of Crystal Growth*, **251**, 623.

107 Kato, H., Sano, M., Miyamoto, K. and Yao, T. (2003) *Japanese Journal of Applied Physics, Part 1: Regular Papers, Short Notes & Review Papers*, **42**, 2241.

108 Ohnishi, T., Ohtomo, A., Kawasaki, M., Takahashi, K., Yoshimoto, M. and Koinuma, H. (1998) *Applied Physics Letters*, **72**, 824.

109 Hong, S., Hanada, T., Chen, Y., Ko, H., Yao, T., Imai, D., Araki, K. and Shinohara, M. (2002) *Applied Surface Science*, **190**, 491.

110 Ohkubo, I., Ohtomo, A., Ohnishi, T., Mastumoto, Y., Koinuma, H. and Kawasaki, M. (1999) *Surface Science*, **443**, L1043.

111 Hong, S.K., Hanada, T., Ko, H.J., Chen, Y., Yao, T., Imai, D., Araki, K., Shinohara, M., Saitoh, K. and Terauchi, M. (2002) *Physical Review B: Condensed Matter*, **65**, 115331.

112 Ko, H.J., Chen, Y., Hong, S. and Yao, T. (2000) *Journal of Crystal Growth*, **209**, 816.

113 Hong, S., Ko, H.J., Chen, Y., Hanada, T. and Yao, T. (2000) *Journal of Crystal Growth*, **214–215**, 81.

114 Ko, H.J., Hong, S., Chen, Y. and Yao, T. (2002) *Thin Solid Films*, **409**, 153.

115 Hong, S., Ko, H.J., Chen, Y., Hanada, T. and Yao, T. (2000) *Applied Surface Science*, **159–160**, 441.

116 Hong, S., Ko, H., Chen, Y. and Yao, T. (2000) *Journal of Crystal Growth*, **209**, 537.

117 Kawamoto, N., Fujita, M., Tatsumi, T. and Horikoshi, Y. (2003) *Japanese Journal of Applied Physics, Part 1: Regular Papers, Short Notes & Review Papers*, **42**, 7209.

118 Dinh, L.N., Schildbach, M.A., Balooch, M. and McLean, W., II (1999) *Journal of Applied Physics*, **86**, 1149.

119 Tsukazaki, A., Ohtomo, A., Onuma, T., Ohtani, M., Makino, T., Sumiya, M., Ohtani, K., Chichibu, S.F., Fuke, S., Segawa, Y., Ohno, H., Koinuma, H. and Kawasaki, M. (2005) *Nature Materials*, **4**, 42.

120 Fouchet, A., Prellier, W., Mercey, B., Méchin, L., Kulkarni, V.N. and Venkatesan, T. (2004) *Journal of Applied Physics*, **96**, 3228.

121 Prellier, W., Fouchet, A., Mercey, B., Simon, C. and Raveau, B. (2003) *Applied Physics Letters*, **82**, 3490.

122 Sankur, H. and Cheung, J.T. (1983) *Journal of Vacuum Science & Technology A-Vacuum Surfaces and Films*, **1**, 1806.

123 Nakayama, T. (1983) *Surface Science*, **133**, 101.

124 Choopun, S., Vispute, R.D., Noch, W., Balsamo, A., Sharma, R.P., Venkatesan, T., Iliadis, A. and Look, D.C. (1999) *Applied Physics Letters*, **75**, 3947.

125 Singh, A.V., Mehra, R.M., Buthrath, N., Wakahara, A. and Yoshida, A. (2001) *Journal of Applied Physics*, **90**, 5661.

126 Matsubara, K., Fons, P., Iwata, K., Yamada, A. and Niki, S. (2002) *Thin Solid Films*, **422**, 176.

127 Craciun, V., Elders, J., Gardeniers, J.G.E. and Boyd, I.W. (1994) *Applied Physics Letters*, **65**, 2963.

128 Tsukazaki, A., Kubota, M., Ohtomo, A., Onuma, T., Ohtani, K., Ohno, H., Chichibu, S.F. and Kawasaki, M. (2005) Blue light-emitting diodes based on ZnO. *Japanese Journal of Applied Physics*, **44**, L643.

129 Abduev, A.Kh., Ataev, B.M. and Bagamadova, A.M. (1987) *Izvestia Akademii Nauk SSSR, Neorganicheskie Materialy*, **11**, 1928 (English translation: Bulletin of the Soviet Academy of Sciences, Inorganic Materials).

130 Rabadanov, R.A., Semiletov, S.A. and Magomedov, Z.A. (1979) *Solid State Physics*, **12**, 1431.

131 Ataev, B.M., Bagamadova, A.M., Mamedov, V.V., Omaev, A.K. and Rabadanov, R.A. (1999) *Journal of Crystal Growth*, **198–199**, 1222.

132 Chukichev, M.V., Ataev, B.M., Mamedov, V.V., Alivov, Ya. and Khodos, I.I. (2002) *Semiconductors*, **36**, 1052.

133 Ataev, B.M., Kamilov, I.K., Bagamadova, A.M., Mamedov, V.V., Omaev, A.K. and Rabadanov, M.Kh. (1999) *Journal of Technical Physics*, **69**, 138.

134 Kaiya, K., Omichi, K., Takahashi, N., Nakamura, T., Okamoto, S. and Yamamoto, H. (2002) *Thin Solid Films*, **409**, 116.

135 Takashi, N., Makino, M., Nakamura, T. and Yamamoto, H. (2002) *Chemistry of Materials*, **14**, 3622.

136 Kern, W. and Heim, R.C. (1970) *Journal of the Electrochemical Society*, **117**, 562.

137 Lau, C.K., Tiku, S.K. and Lakin, K.M. (1980) *Journal of the Electrochemical Society*, **127**, 1843.

138 Smith, F.T.J. (1983) *Applied Physics Letters*, **43**, 1108.

139 Gorla, C.R., Emanetoglu, N.W., Liang, S., Mayo, W.E. and Lu, Y.J. (1999) *Journal of Applied Physics*, **85**, 2595.

140 Kashiwaba, Y., Haga, K., Watanabe, H., Zhang, B.P., Segawa, Y. and Wakatsuki, K. (2002) *Physica Status Solidi b: Basic Research*, **229**, 921.

141 Yasuda, T. and Segawa, Y. (2004) *Physica Status Solidi b: Basic Research*, **241**, 676.

142 Gruber, T., Kirchner, C. and Waag, A. (2002) *Physica Status Solidi b: Basic Research*, **229**, 841.

143 Gruber, T., Kirchner, C., Thonke, K., Sauer, R. and Waag, A. (2002) *Physica Status Solidi a: Applied Research*, **192**, 166.

144 Oleynik, N., Dadgar, A., Christen, J., Blasing, J., Adam, M., Riemann, T., Diez, A., Greiling, A. and Seip, M. (2002) *Physica Status Solidi a: Applied Research*, **192**, 189.

145 Oleynik, N., Adam, M., Krtschil, A., Blasing, J., Dadgar, A., Bertram, F., Forster, D., Diez, A., Greiling, A., Seip, M., Christen, J. and Krost, A. (2003) *Journal of Crystal Growth*, **248**, 14.

146 Kaufmann, T., Fuchs, G. and Webert, W. (1988) *Crystal Research and Technology*, **23**, 635.

147 Hahn, B., Heindel, G., Pschorr-Schoberer, E. and Gebhardt, W. (1998) *Semiconductor Science and Technology*, **13**, 788.

148 Sallet, V., Rommeluere, J.F., Lusson, A., Riviere, A., Fusil, S., Gorochov, O. and Triboulet, R. (2002) *Physica Status Solidi b: Basic Research*, **229**, 903.

149 Kirchner, C., Gruber, T., Reuss, F., Thonke, K., Waag, A., Giessen, C. and Heuken, M. (2003) *Journal of Crystal Growth*, **248**, 20.

150 Ogata, K., Maejima, K., Fujita, S.Z. and Fujita, S.G. (2001) *Journal of Electronic Materials*, **30**, 659.

151 Ogata, K., Kawanishi, T., Maejima, K., Sakurai, K., Fujita, S.Z. and Fujita, S.G. (2002) *Journal of Crystal Growth*, **237**, 553.

152 Ogata, K., Maejima, K., Fujita, S.Z. and Fujita, S.G. (2003) *Journal of Crystal Growth*, **248**, 25.

153 Dadgar, A., Oleynik, N., Forster, D., Deiter, S., Witek, H., Blasing, J., Bertram, F., Krtschil, A., Diez, A., Christen, J. and Krost, A. (2004) *Journal of Crystal Growth*, **267**, 140.

154 Ogata, K., Maejima, K., Fujita, S.Z., Fujita, S.G., Extended abstracts of the 2000 US Workshop of Physics and Chemistry of II–VI materials, p. 119, October 30–November 1, Albuquerque, New Mexico, USA.

155 Park, W.I., An, S.-J., Yi, G.-C. and Jang, H.M. (2001) *Journal of Materials Research*, **16**, 1358.

156 Park, W.I., Yi, G.-C. and Jang, H.M. (2001) *Applied Physics Letters*, **79**, 2022.

157 Zhang, B., Manh, L., Wakatsuki, K., Ohnishi, T., Lippmaa, M., Usami, N., Kawasaki, M. and Segawa, Y. (2003) *Japanese Journal of Applied Physics, Part 1: Regular Papers, Short Notes & Review Papers*, **42**, 2291.

158 Zhang, B., Manh, L., Wakatsuki, K., Tamura, K., Ohnishi, T., Lippma, M., Usami, N., Kawasaki, M., Koinuma, H. and Segawa, Y. (2003) *Japanese Journal of Applied Physics, Part 2: Letters*, **42**, L264.

159 Ma, Y., Du, G.T., Yang, T.P., Qiu, D.L., Zhang, X., Yang, H.J., Zhang, Y.T., Zhao, B.J., Yang, X.T. and Liu, D.L. (2003) *Journal of Crystal Growth*, **255**, 303.

160 Ma, Y., Du, G.T., Yang, S.R., Li, Z.T., Zhao, B.J., Yang, X.T., Yang, T.P., Zhang, Y.T. and Liu, D.L. (2004) *Journal of Applied Physics*, **95**, 6268.

161 Smith, T.P., Mecouch, W.J., Miraglia, P.Q., Roskowski, A.M., Hartlieb, P.J. and Davis, R.F. (2003) *Journal of Crystal Growth*, **257**, 255.

162 Smith, T.P., McLean, H.A., Smith, D.J., Miraglia, P.Q., Roskowski, A.M. and Davis, R.F. (2004) *Journal of Electronic Materials*, **33**, 826.

163 Smith, T.P., McLean, H., Smith, D.J. and Davis, R.F. (2004) *Journal of Crystal Growth*, **265**, 390.

164 Muthukumar, S., Sheng, H.F., Zhong, J., Zhang, Z., Emanetoglu, N.W. and Lu, Y.C. (2003) *IEEE Transactions on Nanotechnology*, **2**, 50.

165 Zhong, J., Muthukumar, S., Saraf, G., Chen, H., Chen, Y. and Lu, Y. (2004) *Journal of Electronic Materials*, **33**, 654.

166 Park, W.I., Kim, D.H., Jung, S.-W. and Yi, G.-C. (2002) *Applied Physics Letters*, **80**, 4232.

167 Jeong, M.-C., Oh, B.-Y., Lee, W. and Myoung, J.-M. (2004) *Journal of Crystal Growth*, **268**, 149.

168 Lee, W., Jeong, M.-C. and Myoung, J.-M. (2004) *Acta Materialia*, **52**, 3949.

169 Yuan, H. and Zhang, Y. (2004) *Journal of Crystal Growth*, **263**, 119.

170 Kling, R., Kirchner, C., Gruber, T., Reuss, F. and Waag, A. (2004) *Nanotechnology*, **15**, 1043.

171 Park, W.I., An, S.J., Yang, J.L., Yi, G.C., Hong, S., Joo, T. and Kim, M. (2004) *The Journal of Physical Chemistry B*, **108**, 15457.

172 Park, W.I., Kim, J.S., Yi, G.C., Bae, M.H. and Lee, H.J. (2004) *Applied Physics Letters*, **85**, 5052.

3
Optical Properties

Optical properties and processes in ZnO as well as its refractive index were extensively studied many decades ago [1–19]. Compendiums dealing with optical properties of ZnO and to some extent its alloys from far infrared to vacuum ultraviolet including phonons, plasmons, dielectric constant, and refractive indices are available in the literature [20, 21]. The renewed interest in ZnO is fuelled and fanned by prospects of its applications in optoelectronics owing to its direct wide bandgap ($E_g \sim 3.3$ eV at 300 K), large exciton binding energy (~60 meV, Refs [22, 23]), and efficient radiative recombination. The large exciton binding energy paves the way for an intense near-band-edge excitonic emission at room and even higher temperatures, because this value is 2.4 times the room-temperature (RT) thermal energy ($k_B T = 25$ meV). Therefore, laser operation based on excitonic transitions, as opposed to electron–hole plasma, is expected. In this respect, there have also been a number of reports on laser emission from ZnO-based structures at room temperature and beyond.

The optical properties of a semiconductor have their genesis in both intrinsic and extrinsic effects. Intrinsic optical transitions take place between the electrons in the conduction band and the holes in the valence band, including excitonic effects caused by the Coulomb interaction. Excitons are classified into free and bound excitons. In high-quality samples with low impurity concentration, the excited states of free excitons can also be observed in addition to their ground-state transitions. Extrinsic properties are related to dopants/impurities or point defects and complexes, which usually create electronic states in the bandgap and therefore influence both optical absorption and emission processes. The electronic states of the bound excitons (BEs) strongly depend on the semiconductor material, in particular the band structure. In theory, excitons could be bound to neutral or charged donors and acceptors. A basic assumption in the description of the principal bound exciton states for neutral donors and acceptors is a dominant coupling of the like particles in the BE states. For a shallow neutral donor-bound exciton (DBE), for example, the two electrons in the bound exciton state are assumed to pair off into a two-electron state with zero spin. The additional hole is then weakly bound in the net hole-attractive Coulomb potential set up by this bound two-electron aggregate. Similarly, shallow neutral acceptor-bound excitons (ABEs) are expected to have a two-hole state derived from the topmost

valence band and one electron interaction. These two classes of bound excitons are by far the most important cases of extrinsic processes. Other extrinsic transitions could be seen in optical spectra such as free-to-bound (electron-acceptor), bound-to-bound (donor-acceptor), and the so-called yellow/green luminescence (GL). The well-known green band in ZnO luminescence spectra (manifesting itself as a broad peak around 500–530 nm), observed nearly in all samples regardless of growth conditions, is related to singly ionized oxygen vacancies by some and to residual copper impurities by others. Simply, a requisite consensus on this issue is still lacking.

3.1 Optical Processes in Semiconductors

One of the unique properties of direct bandgap semiconductors that revolutionized the optoelectronics field is their ability to produce light emission in response to excitation mainly by means of electrical or optical injection of minority carriers. Light emission through any process other than blackbody radiation is called luminescence and requires external excitation as it is a nonequilibrium process. When an external voltage is applied across a forward-biased *p–n* junction, as in the case of LEDs and lasers, electrons and holes that are injected into the medium from their respective ends recombine resulting in light emission called electroluminescence (EL). The emitted photon has energy equal to the difference in the energies of states occupied by electrons and holes prior to recombination. In indirect semiconductors, however, the energy relaxation dominantly takes place through phonons, which make this family of semiconductors inefficient light emitters unless highly spatially localized centers, such as N in GaP, are used. Another means of light emission, termed photoluminescence (PL), is a result of incident-photon *absorption* that generates electron–hole pairs and produces emission of a photon of a different wavelength. The incident photons, when absorbed, excite electrons usually from the valence band into the conduction band through momentum-conserving processes because the photon momentum is negligible. The electrons and holes thermalize to the lowest energy state of their respective bands via phonon emission before recombining across the fundamental bandgap or the defect levels within the bandgap and emitting photons of the corresponding energies. Although it is not applied to compact devices, PL is commonly employed in extracting important physical properties and performing materials characterization. Light emission can also be induced by raising the temperature of the semiconductor (*thermoluminescence*) and by subjecting the semiconductor to electron irradiation (*cathodoluminescence*) or other high-energy particle irradiation. All these excitation schemes are generally used to uncover the processes involved in light emission, mainly as a characterization tool. Typically, the emission spectrum is rich with emission associated with intrinsic processes, meaning those not involving defects and impurities of any kind, and extrinsic processes meaning those involving impurities and defects in the form of either simple phases or complexes. Both intrinsic and extrinsic processes can be effectively studied by analyzing the steady-state PL, time-resolved PL (TRPL), and PL excitation

(PLE) spectra. Optically detected magnetic resonance (ODMR), a variant of the PL technique, is also a very effective method, especially in identifying the nature of the defects involved. A typical PL apparatus is shown in Figure 3.1 and is composed of a light source for excitation (typically a He–Cd laser for ZnO), a sample holder, a dispersive element (grating monochromator), and an optical detector sensitive to the dispersed light.

In steady-state PL, the shape of the spectrum is determined by the level of excitation intensity as the defect-related PL often saturates at power densities on the order of 10^{-2} to $10^{-1}\,\mathrm{W\,cm^{-2}}$, and the overall PL spectrum may be skewed in favor of the excitonic emission at higher excitation densities. Similarly, focusing the laser beam and using small monochromator slit widths would also skew the PL in favor of excitonic transitions. In such a case, the chromatic dispersion of the lenses used to collect the PL, as well as the different effective sizes of the emission spots for the ultraviolet (UV) and visible emission attributed in particular to photon recycling process [24], may lead to a noticeable artificial enhancement of the UV (near band edge) over the visible part in the PL spectrum (mainly defect related). Qualitative terms such as "very intense PL" attesting to the high quality of the material are omnipresent in the literature on ZnO. In contrast to the wide use of PL measurements, relatively little effort has been made to estimate the absolute value of the PL intensity or its quantum efficiency (QE) for a quantitative analysis.

The time-resolved PL requires additional instrumentation for capturing the evolution of intensity, such as a fast CCD or a streak camera for detecting very fast transients. However, a simple digital oscilloscope in combination with a pulsed laser may be very useful for measuring the defect-related PL decays in ZnO, which by their very nature are slow and are typically in the range from a few nanoseconds to milliseconds.

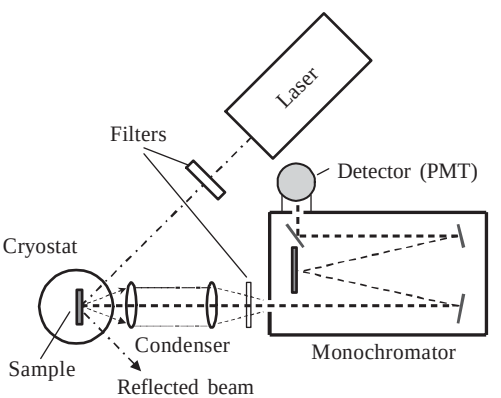

Figure 3.1 Schematic representation of a typical PL setup, including a laser as an excitation source, a grating monochromator as a dispersive element (grating monochromator), PMT as a detector, optical cryostat, filters, and collecting lenses.

The basic instrumentation required for acquiring photoluminescence excitation (PLE) spectrum of a given PL band is nearly the same as that for a PL setup. However, the excitation source must be a tunable source such as a tunable laser or a broadband lamp dispersed by a monochromator. The wavelength of the excitation source is varied, and the PL spectrum or simply the intensity of a particular transition (such as the peak PL intensity) is recorded at various excitation wavelengths to obtain the excitation spectrum. The PLE spectrum is similar to the absorption spectrum with the only difference that in the case of absorption spectrum several different transitions may contribute and complicate the spectral analysis. *Photoionization* of a defect is an inverse process to the luminescence, and in n-type ZnO such a process involves the transition of an electron from an acceptor-like level to the conduction band or to the excited state of the defect. Note that the photoionization spectra measured by PLE, absorption, photocapacitance, and photoconductivity methods should have more or less similar features because the mechanism of the photoexcitation is the same for all these approaches.

Cathodoluminescence (CL) results from absorption of high-energy electrons and subsequent spontaneous emission (SPE) of light associated with specific transitions in a semiconductor. These transitions are detected as a CL spectrum or as an image representing the distribution of CL intensity over a certain area of the sample surface. Imaging is conveniently attained in a scanning electron microscope coupled to a luminescence collection system. When an incident electron beam impinges on the sample under test, it first causes the emission of secondary electrons from a thin surface layer, which is on the order of 10 nm thickness, causing that region to be positively charged [25]. Those secondary electrons penetrate into the sample to some depth, which depends on the acceleration voltage (V_b). This negatively charged layer is much thicker than the positively charged surface layer. It should be noted that the penetration depth increases with increasing V_b, and the electron–hole pair generation rate is proportional to the beam power ($V_b I_b$). The resulting CL intensity is determined not only by the generation rate but also by the penetration depth through the process of self-absorption [26], surface recombination, competition of different recombination mechanisms, and evolution of charge migration [25, 27]. Depth-resolved CL experiments are usually conducted under a constant beam power or constant power density condition. The electron penetration depth, which is limited to about 5 μm, is varied by changing the accelerating voltage. CL imaging may help identify the luminescence bands and determine their spatial distribution and relation to structural defects.

Electron paramagnetic resonance (EPR) and its variant, ODMR, provide valuable information on the ground state and microscopic origin of defects by providing the values and angular dependencies of the Zeeman splitting (*g* tensor) and interpreting any hyperfine structure. Compared to EPR, ODMR relates the magnetic information to particular luminescence bands and assists in their identification. The *g*-value of the free electron is $g_e = 2.0023$. In the first-order perturbation theory, the deviation of the *g*-value for a particular center is given by $\lambda/\Delta E$, where λ is the spin-orbit interaction constant [28]. Usually, donors exhibit *g* values smaller than free electrons, and acceptors have a positive *g* shift.

3.1.1
Fundamentals of the Absorption and Emission Processes

When the electron–hole recombination results in photon emission, the process is termed *radiative recombination*. A recombination process that does not produce photons is termed *nonradiative recombination* in which the energy is exchanged with the lattice as heat through phonon emissions within defect states in a direct bandgap semiconductor. The radiative process that does not involve an electromagnetic field, such as in photoluminescence experiments and light emitting diodes, is called *spontaneous emission*. In other words, electron–hole (e–h) pairs are annihilated followed by photon emission. When an electromagnetic field of appropriate frequency, polarization, phase, and direction is involved in the process, this emission is termed stimulated emission (SE), such as the one in semiconductor lasers. Naturally, the intensity of stimulated emission is proportional to the field strength and photon population.

Photon absorption and emission are the most important optical processes taking place in semiconductors. Various absorption and emission spectroscopy techniques are therefore commonly taken advantage of to shed light on the materials' properties and gather data that could be used for devices. Simply stated, the semiconductor is transparent to below-bandgap radiation while absorbing above the bandgap radiation. Excitonic absorption is superimposed on top of the band-to-band absorption, which makes it convenient to investigate the role of excitons in device structures.

To understand the recombination processes clearly, one should start from the absorption, particularly the absorption coefficient. If $I(x)$ represents the optical intensity at point x in a semiconductor, the spatial rate of change of the intensity at the same point is proportional to the intensity and is given by

$$\frac{dI}{dx} = -\alpha I, \tag{3.1}$$

where α is the absorption coefficient with inverse length units. In an absorptive medium, the dielectric function is complex and can be expressed as

$$\varepsilon = \varepsilon' + j\varepsilon'' = \varepsilon_0(n + j\kappa)^2 = \varepsilon_0(n^2 - \kappa^2 + j2n\kappa), \tag{3.2}$$

where ε' and ε'' are the real and imaginary components of the dielectric constant, n and κ represent the refractive index and the extinction coefficient, respectively. The power of an electromagnetic field propagating along the x-direction depends on n and κ and is proportional to

$$\exp[-2(j(n + j\kappa)k_0 x)], \tag{3.3}$$

where $k_0 = 2\pi/\lambda_0$ is the free space wave vector. The real part of the exponent is associated with the *absorption coefficient* defined as

$$\alpha = 2\kappa k_0, \tag{3.4a}$$

where

$$\kappa = \frac{\varepsilon''}{2\varepsilon_0 n}. \tag{3.4b}$$

It is clear that the decay of the electromagnetic field propagating along the sample, that is, the absorption loss, is determined by the imaginary part of the dielectric constant. ZnO has a direct bandgap and a large absorption coefficient with near-bandgap values in excess of $10^5\ \mathrm{cm}^{-1}$ that bodes very well for optical devices such as LEDs, lasers, and detectors. In the case of population inversion in a cavity, such as in lasers, the absorption coefficient changes to become negative and is called the *gain coefficient*. In this case, the electromagnetic wave would be amplified as it traverses through the medium. When the gain exceeds the losses in the system, lasing oscillations would ensue. Immediately prior to the demonstration of semiconductor lasers, the large absorption coefficient, which beyond population inversion with its associated transparency gives way to gain, was seen as an insurmountable barrier to attaining semiconductor lasers.

It is imperative to discuss a first-order treatment for calculating the PL spectral distribution in semiconductors. We start with a brief discussion of emission and absorption rates in semiconductors. For a more detailed discussion, reader is referred [29]. Relying on the treatment of Planck, Einstein [30, 31] described absorption and stimulated emission constant per unit electromagnetic energy with energies between $h\nu$ and $h(\nu + \Delta\nu)$ (or frequencies between ν and $\nu + \Delta\nu$) using coefficients called the *Einstein's A and B coefficients* [32, 33]. In this nomenclature, for a two-level system, the transition probability of an electron from a higher lying level 2 to a lower lying level 1 is depicted by the coefficient B_{21} for stimulated emission. The spontaneous emission rate from level 2 to level 1 is depicted as A_{21}. The transition from level 1 to level 2 is called absorption and depicted by coefficient B_{12}. The rates of upward and downward transitions for this two-level system at thermal equilibrium at a given temperature T were expressed by Einstein as

$$\begin{aligned} r_{12} &= B_{12}\rho_e(\nu), \\ r_{12} &= B_{12}\rho_e(\nu), \end{aligned} \tag{3.5}$$

where the term $\rho_e(\nu)d\nu$ is the volume density of the electromagnetic energy in the frequency range ν and $\nu + d\nu$. In a semiconductor, occupation probabilities of level 1 and 2, f_1 and f_2, respectively, must also be considered in which case Equation 3.5 would be modified as

$$r_{21} = B_{21} f_2 (1 - f_1)\rho_e(\nu) \quad \text{and} \quad r_{12} = B_{12} f_1 (1 - f_2)\rho_e(\nu), \tag{3.6}$$

where $(1 - f_1)$ and $(1 - f_2)$represent the probabilities of levels 1 and 2 being empty, respectively. Essentially, if a transition is to occur between level 1 and level 2, there must be electrons available in level 1, indicated by f_1 and there must be empty states available in level 2, indicated by $(1 - f_2)$, to receive that electron making the transition from level 1 to level 2.

If N_2 and N_1 represent the populations (or photon occupation numbers) of levels 2 and 1, respectively, under thermodynamic equilibrium, we can write the rate of change in the population of level 2 through spontaneous emission (decay for population which is why the – sign) as [34]

$$\left.\frac{dN_2}{dt}\right|_{sp} = -A_{21} N_2. \tag{3.7}$$

Note that spontaneous emission is not coupled to the optical field and therefore does not depend on the photon density in the system having the same energy. The above rate equation simply indicates that the photon population in level 2 would decrease with a rate of $R_{21} = [A_{21} + B_{21}\rho(\nu)]N_2$ by which we can argue that the spontaneous emission lifetime is $\tau_{sp} = (A_{21})^{-1}$. Typically, this lifetime is on the order of 10^{-9} s. Similarly, the rate equation for the stimulated emission that involves transitions from level 2 to level 1 can be written as

$$\frac{dN_2}{dt}\Big|_{st} = -B_{21}N_2\rho_e(\nu). \tag{3.8}$$

Note that this process is coupled to the photons having the same energy in the system, which is the genesis for the $\rho_e(\nu)$ term. The product $\rho_e(\nu)N_2 d\nu$ represents the photon energy density in the frequency range of ν and $\nu + d\nu$. A decrease in the N_2 population due to transition from level 2 to level 1 would be accompanied by an equal increase in N_1, which means that Equation 3.8 can also be written as

$$\frac{dN_1}{dt}\Big|_{st} = B_{21}N_2\rho_e(\nu). \tag{3.9}$$

Stimulated absorption also takes place and has a proportionality constant of $R_{21} = [A_{21} + B_{21}\rho(\nu)]N_2$ (as absorption involves excitation of an electron from level 1 to level 2):

$$\frac{dN_2}{dt}\Big|_{absorp} = R_{12} = B_{12}N_1\rho_e(\nu) \quad \text{or} \quad \frac{dN_1}{dt}\Big|_{absorp} = -R_{12} = -B_{12}N_1\rho_e(\nu). \tag{3.10}$$

Note that the stimulated absorption depends on the photon density, having the same energy, in the system. Again the product $\rho_e(\nu)N_1 d\nu$ represents the photon energy density in the frequency range of ν and $\nu + d\nu$.

The sum of spontaneous emission and stimulated emission represents the total downward transitions from level 2 to level 1. The total rate of these two processes can then be expressed as

$$R_{21} = [A_{21} + B_{21}\rho_e(\nu)]N_2. \tag{3.11}$$

Under thermodynamic equilibrium, the upward transition must be balanced by a downward transition in which case we can write

$$R_{21} = R_{12} \Rightarrow A_{21}N_2 + B_{21}N_2\rho_e(\nu) = B_{12}N_1\rho_e(\nu). \tag{3.12}$$

Manipulation of Equation 3.12 leads to

$$\frac{N_2}{N_1} = \frac{B_{12}\rho_e(\nu)}{A_{21} + B_{21}\rho_e(\nu)}. \tag{3.13}$$

Determination of the photon density requires knowledge of the number of modes that can be accommodated in a cavity [34]. To find this one should begin with the wave equation

$$\frac{\partial^2 \boldsymbol{E}}{\partial x^2} + \frac{\partial^2 \boldsymbol{E}}{\partial y^2} + \frac{\partial^2 \boldsymbol{E}}{\partial z^2} = \frac{1}{(c/n_r)^2}\frac{\partial^2 \boldsymbol{E}}{\partial t^2}, \tag{3.14}$$

where c is the velocity of light in vacuum, and n_r is the refractive index. For an E field of the form $\boldsymbol{E}_x = \vec{E}_0 e^{-jkx}$, the dispersion relation reduces to

$$\left(\boldsymbol{k}_x^2 + \boldsymbol{k}_y^2 + \boldsymbol{k}_z^2\right) = \frac{(2\pi)^2}{\lambda^2} = \frac{(2\pi\nu)^2}{(c/n_r)^2} = \frac{(2\pi\nu n_r)^2}{c^2}. \tag{3.15}$$

Application of the boundary conditions (field strength is zero at the walls of the cavity) leads to discretization of the wavenumbers in x, y, and z direction as

$$\boldsymbol{k}_x = \frac{m_x\pi}{a}; \quad \boldsymbol{k}_y = \frac{m_y\pi}{b}; \quad k_z = \frac{m_z\pi}{c}, \quad \text{for} \quad m_x, m_y, m_z = 1, 2, 3\ldots \tag{3.16}$$

where, a, b, and c represent the cavity dimensions and m_x, m_y and m_z are integers describing available modes. Assuming a cubic cavity with a side dimension of a for simplicity, with the help of Equation 3.16, Equation 3.15 can be rewritten as

$$\left(\frac{m_x\pi^2}{a}\right) + \left(\frac{m_y\pi^2}{a}\right) + \left(\frac{m_z\pi^2}{a}\right) = \left(\frac{2\pi\nu n_r}{c}\right)^2. \tag{3.17}$$

Solving Equation 3.17 for frequency gives rise to

$$\nu = \left(\frac{c}{2n_r a}\right)\left(m_x^2 + m_y^2 + m_z^2\right)^{1/2} \quad \text{or} \quad \left(m_x^2 + m_y^2 + m_z^2\right) = \left(\frac{2n_r a\nu}{c}\right)^2 = R^2. \tag{3.18}$$

The number of modes between $\nu = 0$ and ν can be found by considering only the positive values of the integers, which limits us to the volume of one-eighth of a sphere, $1/8(4\pi R^3/3)$ with radius $R = 2na\nu/c$ (see Equation 3.18). Recognizing that each point represents two modes, TE and TM, we can find the total number of modes, that is, resonances between the frequencies 0 and ν as

$$N = 2x\frac{1}{8}\left(\frac{4\pi R^3}{3}\right) = \frac{8\pi n_r^3\nu^3}{3c^3}a^3. \tag{3.19}$$

Rather than the volume density of the electromagnetic energy, $\rho_e(\nu)d\nu$, it is more typical to express just the mode density $\rho(\nu)d\nu$ between ν and $\nu + d\nu$ (in a frequency interval $d\nu$) and for a unit volume, which can be obtained by taking the derivative of the total number of modes N versus ν and dividing by the total volume V:

$$\rho(\nu)d\nu = \frac{1}{V}\frac{dN}{d\nu}d\nu = \frac{8\pi n_r^3}{c^3}\nu^2 d\nu. \tag{3.20}$$

Note that $\rho(\nu)$ denotes the photon mode density in units of m^{-3} whereas $\rho_e(\nu)$ depicts the energy density in units of $J\,m^{-3}$.

The treatment is slightly different for a semiconductor, where the density of states would be considered to get the photon density. In that case, if the momentum vector is described as

$$k \approx \hat{x}k_x + \hat{y}k_y + \hat{z}k_z, \tag{3.21}$$

the density of allowed values of k in a volume V is the number of cubes of face $2\pi/a$ that can be fit in that volume in k-space. The density of states is then the number of

states between the momentum values of k and $k + \mathrm{d}k$. Recognize that the volume of a spherical shell of thickness $\mathrm{d}k$ is $4\pi k^2 \mathrm{d}k$, and the unit volume in k-space is $(2\pi/a)^3$. The density of modes is the number of states k-space divided by the volume in real space ($V = a^3$). Doing so leads to

$$\mathrm{d}N(k) = [2(4\pi k^2 \mathrm{d}k)/(2\pi/a)^3]/V. \tag{3.22}$$

The factor 2 is picked up due to two different polarizations, that is, TE and TM modes, for a photon with a given momentum. Rearranging Equation 3.22 with $k = (2\pi)/\lambda = (2\pi\nu n_\mathrm{r})/c$ leads to

$$\mathrm{d}N(k) = (k^2/\pi^2)\mathrm{d}k. \tag{3.23}$$

Noting that $\mathrm{d}k = (2\pi n_\mathrm{r}/c)\mathrm{d}\nu[1 + (\nu/n_\mathrm{r})(\mathrm{d}n_\mathrm{r}/\mathrm{d}\nu)]$ (the term in bracket is due to the dispersion of the refractive index as a result of its frequency dependence), and with $k = (2\pi)/\lambda = (2\pi\nu n_\mathrm{r})/c$, Equation 3.23 can be rewritten as

$$\mathrm{d}N(\nu) = \frac{8\pi n_\mathrm{r}^3 \nu^2}{c^3}[1 + (\nu/n_\mathrm{r})(\mathrm{d}n_\mathrm{r}/\mathrm{d}\nu)]\mathrm{d}\nu = \frac{8\pi n_\mathrm{r}^2 \nu^2}{c^3}[n_\mathrm{r} + \nu(\mathrm{d}n_\mathrm{r}/\mathrm{d}\nu)]\mathrm{d}\nu. \tag{3.24}$$

Often, a group refractive index, $\bar{n}_\mathrm{g} = n_\mathrm{r} + \nu(\mathrm{d}n_\mathrm{r}/\mathrm{d}\nu)$, is defined to account for the dispersion in the refractive index. If the refractive index dispersion is neglected, $\bar{n}_\mathrm{g} \approx n_\mathrm{r}$, the number of modes of Equation 3.24 takes the more familiar form of

$$\mathrm{d}N(\nu) = \frac{8\pi n_\mathrm{r}^3 \nu^2}{c^3}\mathrm{d}\nu. \tag{3.25}$$

The total number of modes in a volume V in a frequency interval around a central frequency ν is obtained by multiplying Equation 3.25 with volume V

$$\mathrm{d}N'(\nu) = \frac{8\pi n_\mathrm{r}^3 \nu^2 V}{c^3}\mathrm{d}\nu. \tag{3.26}$$

Instead of the number of photons in the frequency spectrum, the number of photon energy quanta around a certain photon energy is useful. To do so we replace $\nu \rightarrow E/h$ and $\mathrm{d}\nu \rightarrow \mathrm{d}E/h$ in Equation 3.26, which gives rise to

$$\mathrm{d}N'(E) = \frac{8\pi E^2 n_\mathrm{r}^3 V}{h^3 c^3}\mathrm{d}E. \tag{3.27}$$

The number of modes (photon density) per unit volume and per unit frequency (spectral density) is then the derivative of N' w.r.t. ν (or w.r.t. E for Equation 3.27) divided by the volume, which represents the spectral density:

$$\rho(\nu) = \frac{1}{V}\frac{\mathrm{d}N'}{\mathrm{d}\nu} = \frac{8\pi\nu^2 n_\mathrm{r}^3}{c^3}; \quad \rho(E) = \frac{1}{V}\frac{\mathrm{d}N'(E)}{\mathrm{d}E} = \frac{8\pi E^2 n_\mathrm{r}^3}{h^3 c^3}, \tag{3.28}$$

which is identical to Equation 3.20. Notice that by using Equation 3.23 we can write

$$\rho(\nu)\mathrm{d}\nu = \rho(E)\mathrm{d}E = \rho(k)\mathrm{d}k = \mathrm{d}N(k) = (k^2/\pi^2)\mathrm{d}k \quad \text{(three-dimensional)}. \tag{3.29}$$

Similarly, one can treat the density-of-states problem in a quantum well with one degree of confinement. As in the three-dimensional case, the density of states is the number of states between the momentum values of k and $k + \mathrm{d}k$ (or energy E and $E + \mathrm{d}E$). The unit area in k-space confined within the boundaries of the k-vector is $(2\pi/a)^2$, and the area of a circular shell of thickness $\mathrm{d}k$ is $2\pi k\mathrm{d}k$. The density of allowed values of k in an area A is the number of squares of face $2\pi/a$ that can be fit in that area in k-space. Therefore, and as done above, the density of states is the number of states in k-space divided by the area in real space ($A = a^2$). Doing so leads to [32, 33, 35]

$$\rho(k)\mathrm{d}k = \rho(E)\mathrm{d}E = [2(2\pi k\mathrm{d}k)/(2\pi/a)^2]/A = (k/\pi)\mathrm{d}k \quad \text{(two-dimensional)}. \tag{3.30}$$

The factor of 2 is picked up again due to the spin-up and spin-down polarization of electrons.

It would be informative to at least mention the density of states for one-dimensional systems (quantum wires). The unit length in k-space confined within the boundaries of the k-vector is $(2\pi/a)$ and the length of the wire is $2\mathrm{d}k$. The length in real space is $L = a$ and therefore we have for one-dimensional systems

$$\rho(k)\mathrm{d}k = \rho(E)\mathrm{d}E = [2(2\mathrm{d}k)/(2\pi/a)]/L = (2/\pi)\mathrm{d}k \quad \text{(one-dimensional)}. \tag{3.31}$$

Boltzmann statistics imply that the probability of a given cavity mode that lies between $h\nu$ and $h\nu + h\mathrm{d}\nu$ is proportional to $\exp(-h\nu/kT)h\mathrm{d}\nu$. Therefore, the average energy per mode and the average number of photons for each mode (obtained by dividing the former by $h\nu$) are given by

$$\langle E\rangle = \frac{h\nu}{\mathrm{e}^{h\nu/kT}-1} = \frac{E}{\mathrm{e}^{E/kT}-1} \quad \text{and} \quad \langle\rho\rangle = \frac{1}{\mathrm{e}^{h\nu/kT}-1} = \frac{1}{\mathrm{e}^{E/kT}-1}. \tag{3.32}$$

The photon energy mode density can be expressed as the product of Equations 3.28 and 3.32 giving the well-known *Planck's formula* (Planck's black body radiation distribution law):

$$\rho(\nu) = \frac{8\pi\nu^2 n_\mathrm{r}^3}{c^3}\frac{1}{\mathrm{e}^{h\nu/kT}-1}. \tag{3.33}$$

This relationship can also be written in terms of energy

$$\rho(E) = \frac{8\pi E^2 n_\mathrm{r}^3}{h^3c^3}\frac{1}{\mathrm{e}^{E/kT}-1}. \tag{3.34}$$

Moreover, by considering the dispersion of the refractive index, Equation 3.34 can be written in the form

$$\rho(E) = \frac{8\pi n_\mathrm{r}^3 E^2}{h^3c^3}\frac{1+(E/n_\mathrm{r})(\mathrm{d}n_\mathrm{r}/\mathrm{d}E)}{\exp(E/kT)-1}. \tag{3.35}$$

As stated in Equation 3.12 energy balance requires that the upward transition rate (R_{12}) must be equal to the total downward transition rate (R_{21}) at thermal equilibrium, which determines the *spectral distribution*. First, in thermal equilibrium the

Boltzmann statistics requires that

$$N_2 = N_1 \exp\left[-\left(\frac{E_2 - E_1}{kT}\right)\right] \quad \text{or} \quad N_2 = N_1 \exp\left[\frac{-h\nu}{kT}\right]. \tag{3.36}$$

Equation 3.12 can then be rewritten as

$$A_{21}\exp\left[\frac{-h\nu}{kT}\right] + B_{21}\rho_e(\nu)\exp\left[\frac{-h\nu}{kT}\right] = B_{12}\rho_e(\nu). \tag{3.37}$$

Solving Equation 3.37 for $\rho_e(\nu)$, we obtain

$$\rho_e(\nu) = \frac{A_{21}\exp[-h\nu/kT]}{B_{12} - B_{21}\exp[-h\nu/kT]} = \frac{A_{21}}{B_{21}} \frac{1}{(B_{12}/B_{21})\exp(h\nu/kT) - 1}. \tag{3.38}$$

Forcing $B_{21}/B_{12} = 1$ (which has some basis when the temperature-dependent terms are considered to cancel) [36] brings Equation 3.38 in line with Planck's formula given in Equation 3.33 (but multiplied with $(h\nu)$ since in Equation 3.33 $(p\nu)$ is defined as number of modes with energy $(h\nu)$. Equating Equations 3.33 and 3.38 leads to a relationship between the Einstein's A_{21} (associated with spontaneous emission) and B_{21} (associated with stimulated emission) coefficients as

$$A_{21} = \frac{8\pi h\nu^3 n_r^3}{c^3} B_{21}. \tag{3.39}$$

This condition may be obtained also by equating the temperature-independent components in the energy balance of Equation 3.12. Equating the temperature-dependent terms, as indicated above, leads to $B_{12} = B_{21}$. As given in Equation 3.20, the term relating the A_{21} and B_{21} coefficients in Equation 3.39 represents the density of the electromagnetic waves with the frequency between $h\nu$ and $h\Delta\nu$ inside the medium times $h\nu$; in other words, the density of the electromagnetic wave energy with the frequency between $h\nu$ and $h\Delta\nu$ inside the medium.

Using Equations 3.10 and 3.11, we can write the ratio of stimulated-to-spontaneous emission rate as

$$\frac{R_{21}(\text{st})}{R_{21}(\text{sp})} = \frac{B_{21}N_2\rho_e(\nu)}{A_{21}N_2}. \tag{3.40}$$

We should keep in mind that in the case of lasing, $\rho(h\nu)$ is not described by Equation 3.33 as $\rho(h\nu)$ is much larger than its equilibrium value. With the help of Equation 3.39, Equation 3.40 can be rewritten as

$$\frac{R_{21}(\text{st})}{R_{21}(\text{sp})} = \frac{c^3\rho_e(\nu)}{8\pi h\nu^3 n_r^3}. \tag{3.41}$$

Considering the absorption and assuming $B_{12} = B_{21}$, we can write

$$\frac{R_{21}(\text{st})}{R_{12}(\text{abs})} = \frac{N_2}{N_1}. \tag{3.42}$$

For stimulated emission to exceed photon absorption, *population inversion* must be achieved, which means from Equation 3.42 that $N_2 > N_1$. In addition, for stimulated

emission to far exceed spontaneous emission described in Equation 3.41, we must have large photon density that can be obtained only in an optical cavity. Population inversion is interesting in the sense that it is not consistent with usual semiconductor statistics at *equilibrium*, which calls for density reduction as the energy increases. In the case of population inversion, the density N_2 at a higher energy must be smaller than the density N_1 at a lower energy. This simply means lasers do not operate in thermal equilibrium; rather, they operate in nonthermal equilibrium.

3.1.2 Optical Absorption and Emission in Semiconductors

The above treatment can be extended to a semiconductor with the additional conditions that momentum conservation and Pauli's exclusion principle must hold [36]. As described in Equation 3.6, modifying the rate equations for semiconductors would for stimulated absorption lead to (rates are given in units $s^{-1}\,m^{-3}$)

$$R_{12}|_{\text{abs}} = B_{12} f_1 (1 - f_2) \rho(E_{21}). \tag{3.43}$$

The same for stimulated emission can be expressed as

$$R_{21}|_{\text{st}} = B_{21} f_2 (1 - f_1) \rho(E_{21}). \tag{3.44}$$

Electron can also make the transition from level 2 to level 1 via spontaneous emission, which can be formulated as

$$R_{21}|_{\text{sp}} = A_{21} f_2 (1 - f_1). \tag{3.45}$$

Again, note the involvement of the optical field in the absorption and stimulated emission by the term $\rho(E_{21})$ but not in the spontaneous emission process. Under thermal equilibrium, as in the case of Equation 3.12 but modified for a semiconductor, the downward transition rate must be equal to the upward transition rate

$$\begin{aligned} R_{21} = R_{21}|_{st} + R_{21}|_{sp} = R_{12}|_{\text{abs}} \Rightarrow A_{21} f_2 (1 - f_1) + B_{12} f_2 (1 - f_1) \\ \times \rho(E_{21}) = B_{12} f_1 (1 - f_2) \rho(E_{21}). \end{aligned} \tag{3.46}$$

By solving $\rho(E_{21})$ from Equation 3.46 and equating it to that of Equation 3.34 (by substituting E_{21} for E) while ignoring the dispersion in the refractive index, we obtain

$$\rho(E_{21}) = \frac{A_{21} f_2 (1 - f_1)}{B_{12} f_1 (1 - f_2) - B_{21} f_2 (1 - f_1)} = \frac{8\pi E_{21}^2 n_r^3}{h^3 c^3} \frac{1}{e^{E_{21}/kT} - 1}. \tag{3.47}$$

As we have done for the derivation of Equation 3.39, we will set $B_{21} = B_{12}$, which allows us to derive an expression for relating Einstein's A and B coefficients as

$$A_{21} = \frac{8\pi E_{21}^2 n_r^3}{h^3 c^3} B_{21}. \tag{3.48}$$

The necessary condition for population inversion (or gain) dictates that the downward transition rate represented by stimulated emission be larger than the upward transition rate represented by absorption (setting aside the spontaneous

emission, which automatically assumes that the medium is a cavity and the optical field involvement is considerable). This condition is expressed as

$$B_{21}f_2(1-f_1)\rho(E_{21}) > B_{12}f_1(1-f_2)\rho(E_{21}) \tag{3.49}$$

and because $B_{21} = B_{12}$, Equation 3.49 implies that

$$f_2(1-f_1) > f_1(1-f_2). \tag{3.50}$$

The lower level at an energy E_1 and the upper level at an energy E_2 in semiconductors are represented by valence and conduction bands, respectively, as shown in Figure 3.2. In considering the transitions depicted in Figure 3.2, we must recall that both momentum and energy, in addition to spin, must be conserved. Because transitions involving emission or absorption of photons do not change the momentum as photon momentum is nearly zero, transitions 1 and 3 are straight up and down in momentum. This means that a transition from level E_1 to level E_2 with process 1 must take place away from the zone center. However, transitions 2 and 4 involve phonons for conserving momentum that changes considerably between states before and after the transitions involved.

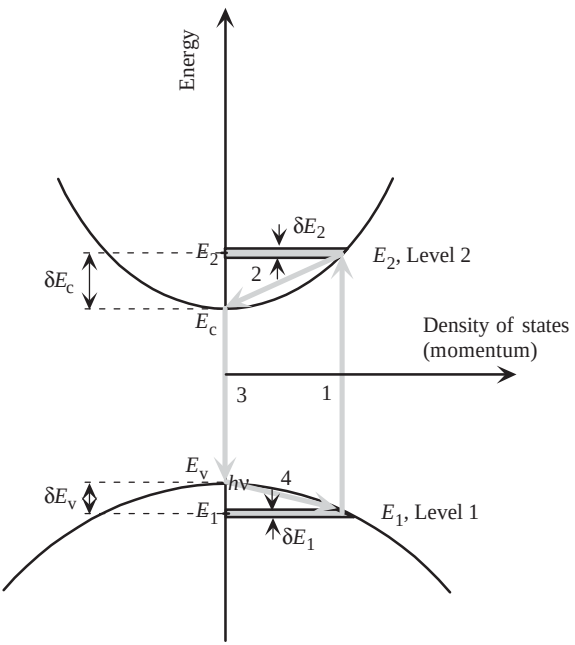

Figure 3.2 Optical transitions in a direct bandgap semiconductor on the energy versus momentum (which also represents energy versus density of states though the functional forms deviate) diagram, which is pumped beyond transparency. The transitions $i = 1, 2, 3,$ and 4 represent excitation, relaxation to the bottom of the conduction band, emission, and filling the hole state vacated by electron excitation to the conduction band (process 1), respectively.

Suppose, a single valence band participating in the optical processes, as shown in Figure 3.2, let us designate the wavenumbers in the conduction and valence bands associated with transition 1 as k_c and k_v. The momentum dispersion relationship in the parabolic band approximation, meaning energy-independent effective mass (not quite a very good approximation considering that the levels in question are well above the conduction band minimum and perhaps below the valence band maximum but still instructive), can be written for conduction and valence bands as

$$\begin{aligned} \delta E_c &= E_2 - E_c = \frac{\hbar^2 k_c^2}{2m_n^*} \quad \text{in the conduction band for transition 1,} \\ \delta E_v &= E_1 - E_v = \frac{\hbar^2 k_v^2}{2m_h^*} \quad \text{in the valence band for transition 1.} \end{aligned} \tag{3.51}$$

Because a photon momentum is negligible $k_c = k_v$, which allows us to relate the energy excursions into the conduction and valence bands to each other with the use of Equation 3.51 as

$$\delta E_c = \frac{m_p^*}{m_n^*} \delta E_v. \tag{3.52}$$

Using $h\nu = E_2 - E_1$, and Equations 3.51 and 3.52, we can write

$$\delta E_c = E_2 - E_c = \frac{m_p^*}{m_n^* + m_p^*}(h\nu - E_g) \quad \text{and} \quad \delta E_v = E_v - E_1 = \frac{m_n^*}{m_n^* + m_p^*}(h\nu - E_g), \tag{3.53}$$

where E_g is the bandgap of the semiconductor, and m_n^* and m_p^* represent the electron and hole effective masses respectively (m_e^* and m_h^* are also commonly used). We should mention that the extension of the quasi-Fermi levels into the conduction and valence bands is not the same ($\delta E_c \neq \delta E_v$ because of the inequality of the effective masses in the respective bands) and that the widths of such bands, depicted in Figure 3.2, relate to each other by

$$\delta E_2 = \frac{m_h^*}{m_n^*} \delta E_1. \tag{3.54}$$

Defining the reduced effective mass, $m_r^{*-1} = m_n^{*-1} + m_p^{*-1}$, the transition energy may be written as

$$E_2 - E_1 = h\nu = E_g + \frac{\hbar^2 k^2}{2m_r^*}. \tag{3.55}$$

As discussed in conjunction with Einstein's A and B parameters, in addition to the momentum, energy, and spin conservation, in upward transitions there must be electrons with characteristics matching the aforementioned conditions prevailing in the valence band and there must be empty states available in the conduction band, again together matching the aforementioned conditions. This means that the density of states and occupation or vacancy probabilities must be brought into the picture. Following the Fermi–Dirac statistics, applicable to semiconductors, let us define the occupation probabilities for energy levels E_1 and E_2:

$$f(E_i) = f_i = \frac{1}{1+\exp[(E_i - F_i)/k_B T]} \quad \text{with} \quad i = 1, 2, \tag{3.56}$$

where F_i represents the Fermi level for level i. These occupation probabilities subtracted from unity would lead to the probability of those states being unoccupied or empty. Expanding f_1 and f_2 represent the occupation probabilities of level 1 and level 2, respectively. Therefore, $(1 - f_1)$ and $(1 - f_2)$ represent the probability of levels 1 and 2 being empty. For a more accurate picture, Fermi levels for levels $i = 1$ and 2 should be replaced with quasi-Fermi levels (F_p and F_n for levels 1 and 2, respectively).

The population difference between levels 2 and 1 is

$$N_2 - N_1 = V\frac{8\pi k^2 \mathrm{d}k}{(2\pi)^3}[f_c(1-f_v) - f_v(1-f_c)], \tag{3.57}$$

where f_c and f_v denote the electron occupancy factors for the conduction and the valence bands in a semiconductor with excess carriers. The term $8\pi k^2 \mathrm{d}k/(2\pi)^3$ accounts for the density of the electromagnetic waves in k-space, and V is the volume. If $N_2 - N_1 > 0$, the semiconducting medium would amplify as opposed to the attenuate. Similarly, substituting Equation 3.56 into Equation 3.50 leads to the population inversion condition being expressed in terms of the Fermi levels associated with levels 2 and 1 as

$$F_2 - F_1 > E_2 - E_1 \quad \text{or in the semiconductor terms} \quad F_n - F_p > E_c - E_v = E_g. \tag{3.58}$$

In words, Equation 3.58 states that the quasi-Fermi-level separation must be larger than the bandgap for population inversion and therefore stimulated emission and gain to take place. This condition simply expresses the fact that the separation of the quasi-Fermi levels must exceed the bandgap energy and that the electron quasi-Fermi level would lie in the conduction band because the density of states in the conduction band is much smaller than the density of states in the valence band.

By solving k from Equation 3.55 and inserting it into Equation 3.57, we obtain

$$N(h\nu)\mathrm{d}(h\nu) = \frac{(2m_r^*)^{3/2}}{2\pi^2\hbar^3}(h\nu - E_g)^{1/2}\mathrm{d}(h\nu). \tag{3.59}$$

The absorption coefficient for a given $h\nu$ is proportional to the probability for a transition from the initial state to the final state and to the density of available electrons in the first state and the density of empty states in the excited state, as depicted by Equation 3.57. Equation 3.59 accounts for the dependence of the absorption coefficient on energy in a direct bandgap semiconductor. In other words, the absorption coefficient is proportional to the square root of the energy above the bandgap energy. For below-bandgap energies and in this ideal picture, the absorption coefficient tends to be zero.

Getting back to density of states, recalling that for a parabolic band we have

$$(\hbar k)^2 = 2m_n^*(E - E_c), \tag{3.60}$$

where m_n^* is the conduction band effective mass (density of states effective mass), density of states in 3D can be written using Equation 3.29 as

$$\rho_c(E-E_c)|_{3D} = \frac{1}{2\pi^2}\left(\frac{2m_n^*}{\hbar^2}\right)^{3/2}(E-E_c)^{1/2} \quad (\text{good} f or\ E \geq E_c). \tag{3.61}$$

For the 2D case, with the help of Equation 3.30 and noting from Equation 3.60 that $\hbar^2 k\mathrm{d}k = m_n^*\mathrm{d}E$, we can write the density of states as

$$\rho_c(E)\mathrm{d}E = \frac{k\mathrm{d}k}{\pi}\mathrm{d}E = \frac{m_n^*}{\pi\hbar^2}\mathrm{d}E \quad \text{and thus}$$
$$\rho_c(E-E_n)|_{2D} = \frac{m_n^*}{\pi\hbar^2} \quad (\text{good for } E \geq E_n). \tag{3.62}$$

The density of states of a given quantum state E_n is therefore independent of energy and well thickness for as long as there is confinement. Another equal quantity would be added to the density of states at the second excited state energy and so on, in which case we can write

$$\rho_c(E)|_{2D} = \frac{m_n^*}{\pi\hbar^2}\sum_i u(E-E_i), \tag{3.63}$$

where $u(E-E_i)$ is the step function, which is zero except when $E=E_i$, and i represents the ith confined level.

The density of states in a one-dimensional system per unit length of the wire at $T=0$ is given by (following a treatment similar to that for three-dimensional and two-dimensional systems provided above)

$$\rho_c(E-E_n)|_{1D} = \frac{2}{\pi\hbar}\sqrt{\frac{m_n^*}{2(E-E_n)}} \quad (\text{good for } E \geq E_n). \tag{3.64}$$

Clearly, Equation 3.64 represents a spiked dependence at energy $E=E_n$, which repeats itself at every quantum state.

As far as a zero-dimensional system (quantum dot) is concerned, the density of states can be represented by $N\delta(E-E_n)$ at each of the quantum states. The coefficient N contains the spin degeneracy factor, any accidental degeneracy of the bound state involved, and the number of quantum dots per unit volume [35]. See Figure 3.3 for a plot of the density of states in 3D, 2D, 1D, and 0D systems.

Assuming that only one of the bands in the valence band is participating in the optical processes, the density of states for a threedimensional system in the valence band is given by (similar to Equation 3.61)

$$\rho_v(E_v-E) = \frac{1}{2\pi^2}\left(\frac{2m_p^*}{\hbar^2}\right)^{3/2}(E_v-E)^{1/2} \quad (\text{good for } E \leq E_v), \tag{3.65}$$

where m_p^* is the hole effective mass (density of states effective mass) in the valence band. The density-of-states Equations 3.62 and 3.64 can similarly be modified for the valence band density of states for reduced dimensional systems.

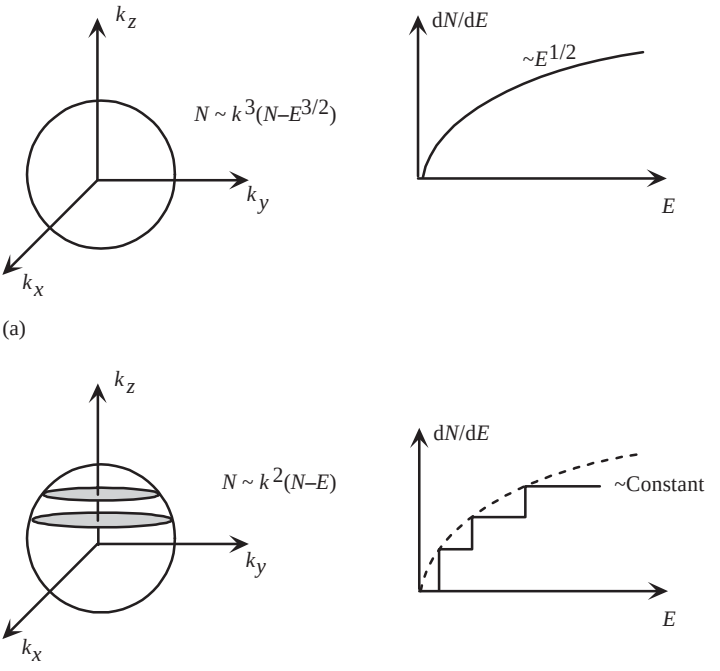

Figure 3.3 Constant energy surfaces and density of states for (a) 3D, (b) 2D, (c) 1D, and (d) 0D systems. The constant energy surfaces are represented by a sphere, a circle, a line, and a point in 3D, 2D, 1D, and 0D systems, respectively, in the conduction band of a semiconductor such as ZnO.

In optical devices relying on band-to-band transitions, both valence and conduction bands are involved. Therefore, it is often convenient to define *joint density of states*, which can be used to calculate the emission and/or absorption rates. Using Equation 3.29, we can define $\rho_{\text{joint}}(E)$ as

$$\rho_{\text{joint}}(h\nu) = (k^2/\pi^2)\frac{dk}{dE}, \quad \text{which is evaluated at } h\nu = E_2 - E_1. \tag{3.66}$$

Considering a parabolic band (Equation 3.60), we can write

$$dE = dE_2 - dE_1 = \hbar^2\left(\frac{1}{m_n^*} + \frac{1}{m_p^*}\right)k dk. \tag{3.67}$$

By solving dk/dE and substituting it into Equation 3.66, we obtain

$$\rho_{\text{joint}}(h\nu) \equiv \rho_{cv}(h\nu) = \frac{k}{\pi^2\hbar^2}\frac{m_n^* m_p^*}{m_n^* + m_p^*}. \tag{3.68}$$

Using the band parabolicity described by Equation 3.51 for both the conduction and the valence bands, which relate the momentum to energy, together with

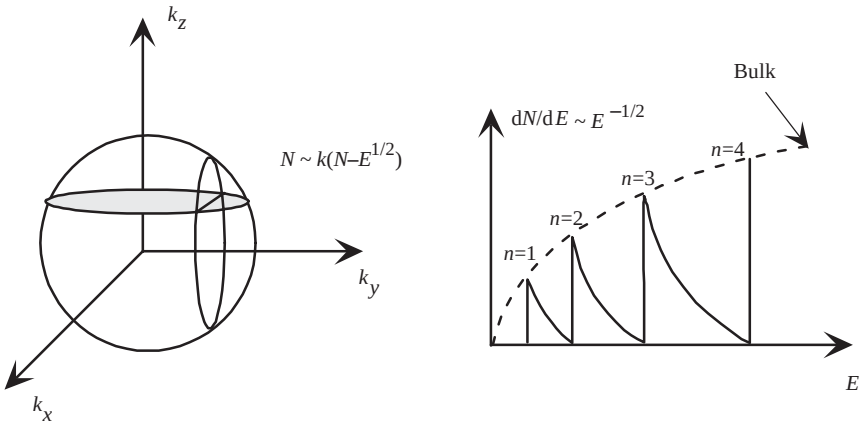

(c)

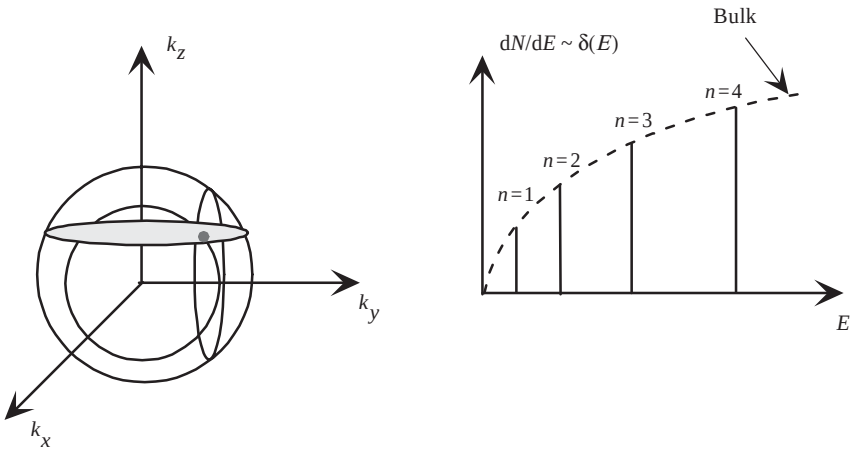

(d)

Figure 3.3 (*Continued*)

Equation 3.53, we can rewrite

$$\hbar k = \left[\frac{2m_n^* m_p^*}{m_n^* + m_p^*}(h\nu - E_g)\right]^{1/2} = [2m_r^*(h\nu - E_g)]^{1/2}, \tag{3.69}$$

where $m_r^* = (m_n^* m_p^*)/(m_n^* + m_p^*)$ is the reduced effective mass in Equation 3.55. Then

$$\rho_{cv}(h\nu) = \frac{1}{2\pi^2}\left(\frac{2m_r^*}{\hbar^2}\right)^{3/2}(h\nu - E_g)^{1/2} \quad \text{or} \quad \rho_{cv}(E) = \frac{1}{2\pi^2}\left(\frac{2m_r^*}{\hbar^2}\right)^{3/2}(E - E_g)^{1/2}. \tag{3.70}$$

Let us develop expressions for the emission and absorption rates in semiconductor emitters. Referring to Equation 3.46, we can write the net stimulated emission rate as

$$\begin{aligned} R_{21}|_{st} &= B_{21} f_2(1-f_1)\rho(E_{21}) - B_{12} f_1(1-f_2)\rho(E_{21}), \\ &= B_{12}(f_2-f_1)\rho(E_{21}). \end{aligned} \tag{3.71}$$

Using Equations 3.47 and 3.48, Equation 3.71 can be rewritten as

$$\begin{aligned} R_{21}|_{st} &= A_{21}(f_2-f_1)\frac{h^3c^3}{8\pi E_{21}^2 n_r^3}\,\frac{8\pi E_{21}^2 n_r^3}{h^3c^3}\,\frac{1}{e^{E_{21}/kT}-1} \\ &= A_{21}\frac{(f_2-f_1)}{e^{(E_{21}/kT)}-1} \end{aligned} \tag{3.72}$$

For its similarity to Equation 3.45 depicting the spontaneous emission rate ($R_{21}|_{sp}$), R_{21}(stim), which popularly has assumed the nomenclature of "stimulated emission rate," is defined as

$$R_{21}(\text{stim}) = R_{21}|_{st}(e^{E_{21}/kT}-1) = A_{21}(f_2-f_1). \tag{3.73}$$

Again the stimulated emission rate of Equation 3.73R_{21}(stim), describes the downward transition rate for stimulation of a similar photon. When this is multiplied by $(e^{E_{21}/kT}-1)^{-1}$, $R_{21}|_{sp}$ is arrived at, which represents the net stimulated emission rate. Notwithstanding customary use, to avoid confusion in this text, $R_{21}|_{st}$ is used for rate equations.

By solving the rate balance equation of Equation 3.46 for the absorption rate and recalling that $B_{21} = B_{12}$, we obtain

$$R_{12}|_{abs} = B_{12}(f_1-f_2)\rho(E_{21}). \tag{3.74}$$

The net absorption rate $R_{12}|_{abs}$ can be related to the absorption coefficient (when negative it is called the gain coefficient). Consider a plane-wave propagating along the z-direction (length of the waveguide) represented by $I_0\exp(-\alpha z)$. The loss (absorption) parameter α can then be expressed as

$$-\alpha(=g) = \frac{dI/dz}{I}. \tag{3.75}$$

The numerator in Equation 3.75 represents the net power emitted per unit volume, while the denominator represents the power per unit area. The term in the denominator is simply the photon density distribution per unit frequency (spectral photon density) multiplied by the group velocity, c/n_r. The term in the numerator can be represented by R_{12}/abs given in Equation 3.74. By rewriting Equation 3.75 in the light of the aforementioned discussion, we obtain for α (now recognizing its energy dependence)

$$\alpha(E_{21}) = \frac{B_{12}(f_1-f_2)\rho(E_{21})}{(c/n_r)\rho(E_{21})E_{21}} = \frac{B_{12}(f_1-f_2)}{(c/n_r)E_{21}} = -g(E_{21}). \tag{3.76}$$

Note that in Equation 3.76 the dispersion of the refractive index, $[1 + (\nu/n_r)(dn_r/d\nu)]$, is neglected and also note that $B_{12} = B_{21}$. It is clear that if $(f_1 - f_2) < 0$, which is the case in population inversion, $\alpha(E_{21}) < 0$ and $g(E_{21}) > 0$. The denominator in

Equation 3.76 can be expressed in terms of the stimulated emission rate by utilizing Equations 3.48 and 3.73 as

$$\alpha(E_{21}) = -g(E_{21}) = \frac{A_{21}(f_1 - f_2)}{(c/n_r)E_{21}} \frac{h^3c^3}{8\pi E_{21}^3 n_r^3} = -\frac{h^3c^2}{8\pi E_{21}^3 n_r^2} R_{21}(E_{21}, \text{stim}). \tag{3.77}$$

The absorption coefficient $\alpha(E_{21})$ can also be related to the spontaneous emission rate. From Equation 3.76, we obtain:

$$B_{12} = B_{21} = \alpha(E_{21}) \frac{E_{21}(c/n_r)}{(f_1 - f_2)} \quad \text{or} \quad \alpha(E_{21}) = B_{12}(f_1 - f_2)(n_r/c)(1/E_{21}). \tag{3.78}$$

By using Equation 3.45 ($R_{21}|_{sp} = A_{21}f_2(1 - f_1)$) and Equation 3.48 ($A_{21} = B_{21}(8\pi E_{21}^2 n_r^3)/(h^3c^3)$) the spontaneous emission rate can be rewritten as

$$R_{21}|_{sp} = B_{21}f_2(1 - f_1)(8\pi E_{21}^2 n_r^3)/(h^3c^3). \tag{3.79}$$

With the help of Equations 3.78, Equation 3.79 can be rewritten as

$$R_{21}(E_{21})|_{sp} = \alpha(E_{21}) \frac{f_2(1 - f_1)}{f_1 - f_2} \frac{8\pi E_{21}^3 n_r^2}{h^3c^2}. \tag{3.80}$$

Using the Fermi Dirac statistics given in Equation 3.56 for $f_i (i = 1,2)$ leads to

$$R_{21}(E_{21})|_{sp} = \alpha(E_{21}) \frac{8\pi E_{21}^3 n_r^2}{h^3c^2} \frac{1}{\exp[(E_{21} - F_2 + F_1)/kT] - 1}. \tag{3.81}$$

Equations 3.77 and 3.80 relate the stimulated emission rate and the spontaneous emission rate to the absorption coefficient, respectively. With the help of the same equations, the stimulated emission rate and the spontaneous emission rate can be related to each other. The implications of these equations are that both emission rates can be determined if the absorption coefficient along with its energy (or wavelength) dependence is known. Fortunately, the absorption coefficient is a measurable quantity. Therefore, once measured, the emission rates can be determined. The absorption rate can also be calculated with numerical techniques. Because the absorption coefficient, spontaneous emission rate, and stimulated emission rate can all be determined with the knowledge of Einstein's *B* coefficient (recall that the *A* coefficient can be calculated from the *B* coefficient), calculation of the *B* is sufficient to determine the absorption coefficient (the last part of Equation 3.78), spontaneous emission rate (Equation 3.79), and the stimulated emission rate (Equation 3.72 as *A* and *B* coefficients are related). A succinct description of the calculations leading to Einstein's *B* coefficient and/or the two emission rates is given below. The *B* coefficient represents the interaction of electron in the solid with the electromagnetic wave, which requires a quantum mechanical treatment. For further details, the reader is referred to [29].

Let us now develop expressions for the spontaneous emission in semiconductors. In an absorption measurement on a high-purity sample, the probabilities of having

an electron in the lower state (valence band) and in the higher state (conduction band) can be taken as 1 and 0, respectively. Hence, the absorption coefficient reduces to [37]

$$\alpha(h\nu) = A^*(h\nu - E_g)^{1/2}. \tag{3.82}$$

with

$$A^* \approx \frac{q^2(2m_r^*)^{3/2}}{nch^2m_n^*}, \tag{3.83}$$

where c is the velocity of light in vacuum. Once the absorption coefficient versus photon energy is calculated or measured, the spontaneous emission spectrum can be calculated from

$$I(h\nu) = (h\nu)r(h\nu) = (h\nu)g(h\nu), \tag{3.84}$$

where $r(h\nu)$ and $g(h\nu)$ are the recombination and generation rates that are equal at thermal equilibrium. In a photoluminescence experiment, this assumption can be used provided the exciting light intensity is very low. This leads to

$$I(h\nu) = \frac{8\pi\nu^2}{c^2} h\nu\alpha(h\nu)[f_c(1-f_v)]. \tag{3.85}$$

By simplifying the occupation probabilities for a nondegenerate semiconductor, which means replacing them with their Boltzmann factors, we get [38]

$$I(h\nu) = \frac{8\pi n^2 h\nu^3}{c^2}\alpha(h\nu)\exp\left(\frac{F_n - F_p}{kT}\right)\exp\left(\frac{-h\nu}{kT}\right). \tag{3.86}$$

The spectral emission response is proportional to the product of the absorption coefficient and $\exp(-h\nu/kT)$. On the lower energy side, the emission spectrum depends on the of the absorption coefficients and above the bandgap roughly declines exponentially.

3.1.3 Band-to-Band Transitions

The average lifetime of carriers before radiative recombination is called the *radiative lifetime* τ_r. The rate of emission of photons by recombining electrons, n, and holes, p, is a bimolecular process and is given by

$$R = Bnp, \tag{3.87}$$

where B is the radiative recombination probability. The terms R and B have the units of $\mathrm{cm}^{-3}\,\mathrm{s}^{-1}$ and $\mathrm{cm}^3\,\mathrm{s}^{-1}$, respectively. For a p-type (or n-type) semiconductor where the excess carrier concentration is much less than the equilibrium hole (or electron) concentration, radiative recombination lifetime reduces to $\tau_r = (pB)^{-1}$. For thermalized electrons and holes, the recombination time depends on the electron and hole energies, which means that it will depend on the photon energy. Consequently, it is customary to define an average lifetime as $\langle\tau_r\rangle$, which depends on the k-selection rules as is the case of perfect or nearly perfect semiconductors. In heavily excited

semiconductors, this does not hold. In electroluminescent devices with p-type active regions, such as LEDs and lasers, when an electron is injected in thermal equilibrium, in terms of electron and hole distributions, we define a lifetime called the *minority carrier radiative lifetime* τ_{rad}, also commonly termed as τ_r, to depict the radiative recombination process. This is the time it takes for an extra minority carrier to be annihilated radiatively by a majority (hole) carrier. In intrinsic and/or near-intrinsic semiconductors with very low electron/hole concentrations, the minority radiative recombination time is rather long as in the case of indirect semiconductors because the probability of these processes is very small. The radiative recombination time can be made smaller with increased doping up to a certain limit as the more the doping is increased the less the above expression is valid. The stimulated emission lifetime does not follow this rule as the stimulated emission rate depends also on the photon density.

In addition to the radiative processes, there are nonradiative processes in semiconductors because of imperfections that act as nonradiative centers. We should mention some defects as radiative recombination centers, which in a photoluminescence experiment can shed light on the energy levels of defect states. For a semiconductor containing nonradiative traps or recombination centers, in an experiment such as time-dependent PL, the decay in the integrated PL intensity versus temperature is related to the low-temperature integrated PL intensity as

$$I_{PL}(T) = \eta_{PL}(T) I_{PL}(0), \tag{3.88}$$

where $\eta_{PL}(T)$ is the temperature-dependent PL efficiency and $I_{PL}(T)$ and $I_{PL}(0)$ are the integrated PL intensities at temperatures T and zero, respectively.

The measured PL decay time can be expressed in terms of radiative and nonradiative lifetimes as

$$\tau_{PL}(T) = [1/\tau_r(T) + 1/\tau_{nr}(T)]^{-1}, \tag{3.89}$$

where $\tau_{PL}(T)$, also referred to as $\tau_{total}(T)$ or $\tau_{eff}(T)$, is total or effective recombination lifetime and is also the quantity that is experimentally measured. The magnitude of $\tau_{PL}(T)$ represents the average length of time a photoexcited carrier can remain in the conduction (or valence) band before recombination and is thus directly correlated to material quality, purity, and doping level approaching $\tau_r(T)$ or also referred to as $\tau_{rad}(T)$ in pure and defect-free material. The term $\tau_{nr}(T)$, also referred to as τ_{nonrad}, is the lifetime for all the nonradiative recombination channels combined. For an intrinsic material, the total recombination rate is

$$R_T = (1/\tau_{eff})(np/2n_i), \tag{3.90}$$

where n_i is the intrinsic carrier concentration, and n and p are the injected electron and hole concentrations, respectively. The radiative recombination rate is

$$R = (1/\tau_{rad})(np/2n_i). \tag{3.91}$$

The radiative efficiency is then

$$\eta = R/R_T = \tau_{nonrad}/(\tau_{rad} + \tau_{nonrad}) \quad \text{or} \quad \eta = \tau_{nr}/(\tau_r + \tau_{nr}). \tag{3.92}$$

The expression for radiative recombination efficiency can also be found by taking advantage of Equations 3.88 and 3.89, which results in expression Equation 3.93:

$$\eta_{PL}(T) = \tau_{PL}/\tau_r. \tag{3.93}$$

In the limit where there is no nonradiative recombination, which means that $1/\tau_{nonrad}$ is zero, the radiative efficiency becomes unity. The lifetime of excess minority carriers can be obtained by measuring the dynamic behaviors of optical emissions involved using time-resolved photoluminescence (TRPL).

In a PL experiment, the band-to-band emission lineshape is determined by the joint density of states and the probability of participating states being available for recombination. The former has the form $(h\nu - E_g)^{1/2}$ and the latter $\exp(-E/kT) = \exp(-h\upsilon/kT)$. When the semiconductor is excited by the above-bandgap photon radiation, the two lineshapes put together lead to a lineshape of the form

$$(h\nu - E_g)^{1/2}\left[\exp\left(\frac{-h\nu}{kT}\right)\right]. \tag{3.94}$$

Lower energy photons do not excite electrons into the conduction band, therefore the band-to-band emission will be zero in "linear" experiments.

3.1.4 Excitonic Transitions

When the charged center concentration in semiconductors is sufficiently low, in other words, the quality is high, a free electron and a free hole can be attracted to one another through Coulombic attraction. An electron can orbit the hole, called *exciton*, much the same way as in the case of a hydrogen atom. When the pair recombines, it emits in the form of a narrow spectral line whose peak energy is given by

$$\hbar\omega = E_g - E_x, \tag{3.95}$$

where E_x is the binding energy of the free exciton. At the cost of a lower transition probability, a direct transition can also occur with the emission of one or more optical phonons, with the energy of the emitted photon being (Ref. [37] and references therein)

$$\hbar\omega = E_g - E_x - mE_p \quad (m = 0, 1, 2, 3\ldots), \tag{3.96}$$

where E_p is the phonon energy and m is the number of phonons emitted per transition. In general, the larger m the lower the transition probability and the weaker the emission intensity. These transitions are referred to as phonon replicas with designations such as zero phonon replica for no phonon emission, one phonon replica for one phonon emission, and so on. Using the hydrogenic model, the binding energy or the ionization energy of such a system is given by

$$E_x = \frac{m_r^* q^4}{2h^2\varepsilon^2 n^2}, \tag{3.97}$$

where the quantities have their usual meanings and n is an integer with $n = 1$ corresponding to the ground state of the exciton. If the disparity of the electron and

hole effective masses is large, and the electron effective mass is the smaller of the two, the reduced mass can be approximated by the electron effective mass. As can be seen, in large-bandgap semiconductors that have large effective masses, the exciton binding energy is relatively large (60 meV for ZnO; 25 meV for GaN) and is comparable to kT at room temperature. Therefore, Coulombic effects may not be automatically neglected without further consideration [39]. In the intermediate excitation density regime in ZnO, emissions due to biexcitonic, exciton–exciton, and exciton–carrier interactions may be observed. The inelastic collision between the excitons results in an exciton excited into a higher state and photons whose energy is lowered by the same amount below the gap energy minus the exciton binding energy. At high excitation densities, electron–hole pair forms, which in the case of ZnO is in the low $10^{19}\,cm^{-3}$ range, comparable to that in GaN.

At low temperatures and in high-quality samples with low donor and acceptor concentrations, as well as at low density of defects, the photoexcited carriers with opposite charge are attracted not only to one another but also to neutral centers via the van der Waals interaction. Because this additional attraction reduces the exciton binding energy, the neutral impurities are efficient in trapping excitons to form bound excitons as denoted by D^0X and A^0X for neutral donor and acceptor bound excitons, respectively. Excitons can also be bound to ionized donors and acceptors and are termed D^+ X and A^-X. The donor-bound exciton can be considered analogous to a molecule ion with a binding energy of about 0. 1–0.2 that of the hydrogen atom. Not to be confused with an ionized donor-bound exciton is the hole bound to a neutral donor, which is depicted as D^0h and has the same charge state as the ionized donor-bound exciton. Actually, D^0h^+ should be reserved for describing a transition. To a first extent, the one with the larger binding energy should be more stable and is therefore more likely to occur. Whether this is so or not, however, depends on the electron and hole masses. The exact nature and behavior of excitons in semiconductors are rather complex. For example, excitons formed in the continuum state can interact with photons and phonons and relax through phonon emission. In the process, exciton dispersion curve splits into upper and lower branches, as will be discussed in Section 3.2.1.

3.2
Optical Transitions in ZnO

Optical transitions in ZnO have been studied by a variety of experimental techniques such as optical absorption, transmission, reflection, photoreflection, spectroscopic ellipsometry, photoluminescence, cathodoluminescence, calorimetric spectroscopy, and so on. The luminescence from bulk ZnO extends from the band edge to the green/orange spectral range with a common broadband centered around 2.45 eV. The sharp lines dominating the band-edge region of the spectra originate from various bound exciton recombinations (excitons bound to neutral donors, D^0X, and/or acceptors, A^0X) followed by longitudinal optical (LO) phonon replicas with an energy separation of 72 meV. On the high-energy side of the bound excitons,

free-exciton transitions appear with the A-valence band (FX_A) positioned at 3.377 eV. At lower energies from 3.34 to 3.31 eV, two-electron satellite (TES) recombination lines of the neutral donor bound excitons are observed. In some samples, a donor–acceptor pair (DAP) transition at ~3.22 eV that is again followed by phonon replicas is found, even though the chemical identity of the acceptor is unknown. In this chapter, a review of all these transitions is given. In addition, the refractive index of ZnO and MgZnO and stimulated emission and carrier dynamics in ZnO are discussed.

3.2.1
Free Excitons and Polaritons

The wurtzite ZnO conduction band is mainly constructed from the s-like state having Γ_7^c symmetry, whereas the valence band is a p-like state, which is split into three bands due to the influence of crystal field and spin-orbit interactions [40, 41]. The near-bandgap intrinsic absorption and emission spectrum is therefore dominated by transition involving these three valence bands and the conduction band. The related free-exciton transitions from the conduction band to these three valence bands or vice versa are usually denoted by A (also referred to as the heavy hole), B (also referred to as the light hole), and C (also referred to crystal-field split band). By treating the wurtzite energy levels as a perturbation of those in zinc blende, Hopfield [4] has derived the formulas for the valence band mixing, the extent of which is controlled by the relative magnitudes of the spin-orbit and crystal-field splittings. If the energy of the topmost valence band is taken as zero ($E_A = 0$), the energies of the two other exciton lines in this formalism are given by

$$E_{BC} = -\frac{\delta+\Delta}{2} \pm \sqrt{\left[\left(\frac{\delta+\Delta}{2}\right)^2 - \frac{2}{3}\delta\Delta\right]}, \tag{3.98}$$

where δ and Δ represent the spin-orbit and crystal-field parameters, respectively, which can be calculated by using the measured energy level splittings E_{AB} and E_{BC}. Figure 3.4 shows the band diagram of the zinc blende and the wurtzite ZnO structures derived by Birman [40], who suggests the A-Γ_9, B-Γ_7, and C-Γ_7 valence band ordering for wurtzitic ZnO. However, the ordering of the crystal-field and spin-orbit coupling split states of the valence band maximum in wurtzite ZnO has been a subject of controversy since the 1960s [3–7, 23, 40, 42, 43]. Thomas [3] was the first to propose, on the basis of the polarization dependence of the absorption and reflectivity spectra, that the valence band ordering of ZnO is anomalous compared to the usual one in other II–VI wurtzite materials and that the top of the valence band has A-Γ_7 symmetry, which can be understood in terms of an effective negative spin-orbit splitting. These results were later confirmed by Liang and Yoffe [12]; however, they were challenged by Park *et al.* [5]. The essential difference has its genesis in the interpretation of the spectral line, which was initially assigned to the intrinsic ground-state A-exciton transition by Thomas [3] and, in contrast to extrinsic, to the ionized donor-bound exciton complex transition by Park *et al.* [5]. The free-exciton nature of

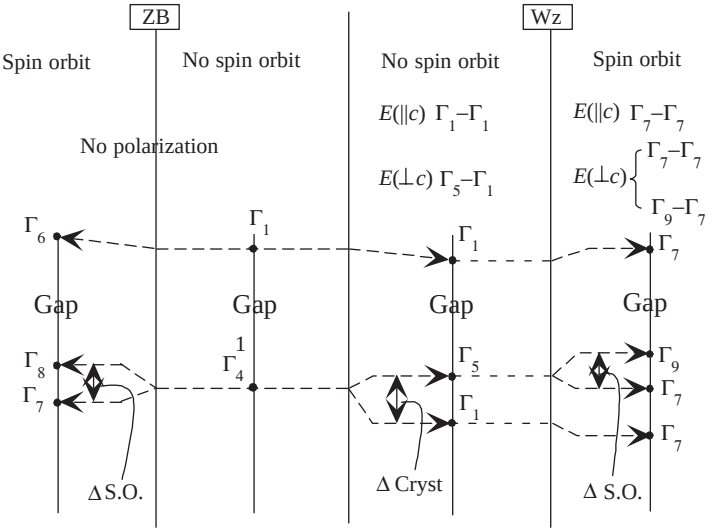

Figure 3.4 Band structure and selection rules for zinc blende and wurtzite structures. Crystal-field and spin-orbit splittings are indicated schematically. Transitions that are allowed for various polarizations of photon electric field vector with respect to the *c*-axis are indicated. (After Ref. [40].)

this absorption line was later confirmed by Segall [6], by studying the onset of phonon-assisted absorption. Usually, the polarization dependence of absorption, reflection, or PL individually does not provide sufficient information to determine the valence band symmetry. In contrast, angular dependent magneto-optical spectroscopy is considered a more reliable tool [23, 42, 44]. Availability of high-quality ZnO single crystals since these initial investigations has paved the way for the observation of intrinsic exciton transitions in low-temperature PL, magnetoluminescence, and reflectance measurements [23, 42, 44–46]. Reynolds *et al.* [23] readdressed this band ordering issue by using polarized magnetoluminescence and second-order PL spectra, which helped resolve the additional fine structure of the excitons. They concluded that the spectral line identified as an ionized DBE complex transition by Park *et al.* [5] was indeed a free-exciton line but that, nevertheless, the valence band symmetry ordering in ZnO is not reversed and is indeed consistent with most other wurtzitic II–VI structures and GaN (A-Γ_9, B-Γ_7, and C-Γ_7). Supporting these conclusions were calculations of energy positions and oscillator strengths of respective excitons by Gil [47], who showed that the reversal of this ordering would require ZnO films to be under high biaxial tension. However, Lambrecht *et al.* [42] argued that the analysis by Reynolds *et al.* [23] was not well taken owing to the assumptions made by Reynolds *et al.* about the sign of the Landé *g*-factor for holes and that the valence band ordering is in fact A-Γ_7, B-Γ_9, and C-Γ_7. The valence band ordering issue still remains somewhat controversial although most studies adopt the interpretation by Thomas [3].

Group theory arguments and the direct product of the group representations of the band symmetries (Γ_7 for the conduction band, Γ_9 for the A valence band, upper Γ_7 for

B valence band, and lower Γ_7 for C valence band) will result in the following intrinsic exciton ground-state symmetries:

$$\Gamma_7 \times \Gamma_9 \rightarrow \Gamma_5 + \Gamma_6,$$
$$\Gamma_7 \times \Gamma_7 \rightarrow \Gamma_5 + \Gamma_1 + \Gamma_2.$$

The Γ_5 and Γ_6 exciton ground states are both doubly degenerate, whereas Γ_1 and Γ_2 are both singly degenerate. In ideal, that is, strain free, wurtzite crystals, free excitons should obey the selection rules in optical one-photon processes; Γ_5 and Γ_1 are allowed transitions with $\mathbf{E} \perp \mathbf{c}$ and $\mathbf{E} \parallel \mathbf{c}$ polarizations, respectively, but the Γ_6 and Γ_2 are not allowed. Therefore, all three excitons are allowed in the σ polarization ($E \perp c$ and $k \perp c$), but the C-exciton is quite weak. The C-exciton is strongly allowed in the π polarization ($E \parallel c$ and $k \perp c$). However, the A-exciton is forbidden and the B-exciton is only weakly observable in this geometry. In the α polarization ($E \perp c$ and $k \parallel c$) all three transitions are clearly observable. Each of these fundamental excitonic states is expected to have a fine structure due to both the exciton-polariton longitudinal–transverse splitting and the splitting caused by electron–hole exchange interaction, which is on the order of a few millielectron volt [16, 48].

The transition energies of the intrinsic excitons were measured by employing the low-temperature absorption [12, 49], reflection [4, 23, 50], photoreflectance (PR) [51, 52], and PL [23, 45, 46, 50] spectroscopy techniques. These measurements are useful for the determination of exciton binding energies, exciton Bohr radii, the dielectric constant, and with the aid of the quasicubic model, spin-orbit and crystal-field parameters. Using the ground state and excited state energies and assuming that the exciton has a hydrogen-like set of energy levels, the exciton binding energy can be calculated from

$$E_n = E_{gap} - \frac{E_B}{n^2}, \tag{3.99}$$

where n is the main quantum number and $E_B = 4/3(E_2 - E_1)$ is the exciton binding energy. E_B can also be expressed in terms of the low-frequency dielectric constant ε_0 and the reduced exciton mass μ^*_{ex} as

$$E_B = \frac{e^4 \mu^*_{ex}}{2\hbar^2 \varepsilon_0^2} = 13.6 \frac{\mu^*_{ex}}{\varepsilon_0^2} (\text{eV}). \tag{3.100}$$

Using μ^*_{ex}, one can also estimate the effective exciton Bohr radius from

$$a_0 = \frac{\hbar^2 \varepsilon_0}{\mu^*_{ex} e^2} n^2. \tag{3.101}$$

The fundamental absorption edge and the exciton structure of ZnO were first studied by Thomas [3] in 1960, who measured the low-temperature absorption and reflectance spectra of polished and etched thin crystals grown from the vapor phase. Thomas analyzed the reflectance data by means of the Kramers–Kronig relation and three peaks arising from $n = 1$ exciton transitions involving holes from each one of the *three* valence bands. At 4.2 K, the $n = 2$ exciton states were apparent in reflection, allowing estimates to be made of the exciton binding energy and reduced mass. An

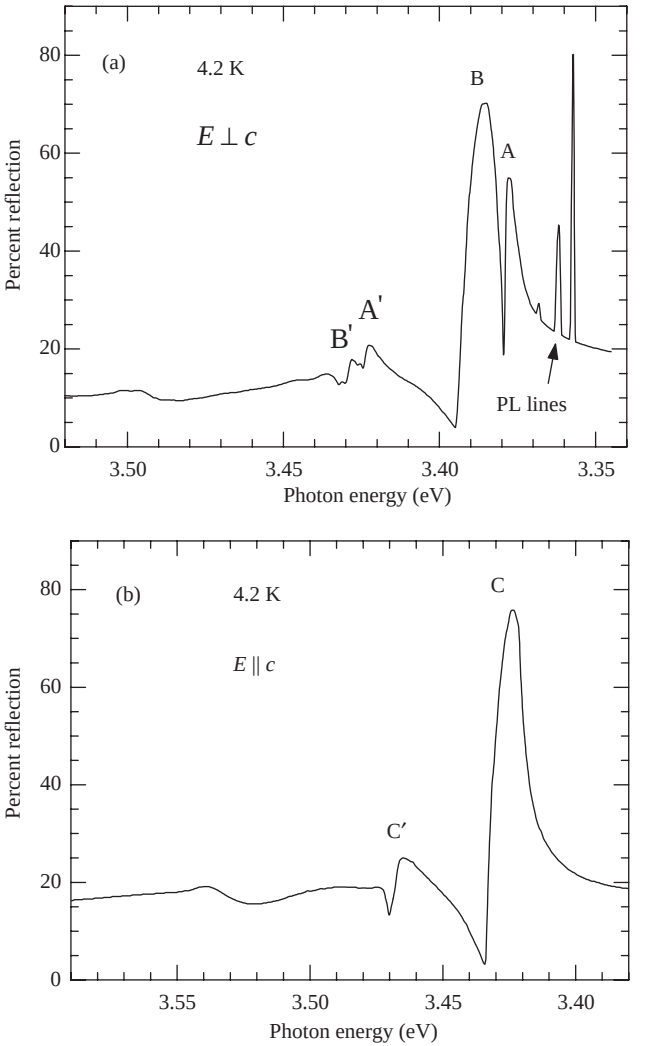

Figure 3.5 Reflection from ZnO at 4.2 K for (a) $E \perp c$ and (b) $E \parallel c$. Notice the PL lines for E ⊥ c data. (After Ref. [3].)

example of reflectance spectra obtained in the σ and π polarizations is given in Figure 3.5 for a single-crystal ZnO sample.

Park *et al.* [5] reported the fundamental spectra of ZnO and successfully explained the exciton spectrum on the basis of Birman's model [40] of the wurtzite structure analyzing the energy and polarization of the fine structure around the fundamental absorption region. Motivated by these results, Hopfield and Thomas [16] studied the polariton absorption lines in ZnO using a magnetic field in appropriate geometry to allow couplings at polariton crossings. A satisfactory agreement was attained when the crossing frequencies of the polariton dispersion and light with $E \parallel c$ and $E \perp c$

polarizations were compared with the measured absorption line energies. On the basis of these results, Hopfield and Thomas also argued that the B-exciton in fact belongs to the Γ_9 symmetry group.

Among these reports, there exists a discrepancy in the quoted values for the spin-orbit interaction energy and the exciton binding energies, which most likely may have its genesis in the difficulty of interpreting the complex spectra near the band edge. Table 3.1 lists some of the excitonic parameters for ZnO from various references. The features associated with A−, Bminus;, and C-exciton transitions, their excited states, exciton-polaritons, and exciton–LO phonon complexes are sometimes misinterpreted resulting in reports of different energy values. To shed more light, Liang and Yoffe [12] performed polarization-dependent transmission measurements on single-crystal ZnO thin platelets grown by the vapor transport method. In addition to the transitions associated with the ground, the first, and the second excited states of intrinsic excitons, the exciton–phonon complexes were also observed in the transmission spectrum. In the same vein, Reynolds *et al.* [53] later on reported the shift in intrinsic exciton transitions by analyzing the reflection data from strained ZnO single crystals grown by the vapor transport method. During growth, defect complexes (probably pairs) are preferentially incorporated in certain crystallographic

Table 3.1 Some excitonic parameters for ZnO.

Parameter	
E_{gap} (eV)	3.436[a], 3.435[b], 3.438[e], 3.437[h], 3.445[i]
A-exciton binding energy, E_B^A (eV)	0.0609[a], 0.042[b], 0.060[c], 0.064[e], 0.0604[f], 0.0595[g], 0.060[h], 0.067[i]
B-exciton binding energy, E_B^B (eV)	0.0593[a], 0.053[c], 0.053[e], 0.0575[f], 0.0566[g], 0.062[i]
C-exciton binding energy, E_B^C (eV)	0.058[a], 0.049[c], 0.0561[f], 0.0563[g], 0.061[i]
E_{AB} (eV)	0.0062[a], 0.040[b], 0.0095[d], 0.006[e], 0.0127[h], 0.0075[i], 0.0049[l]
E_{BC} (eV)	0.0385[a], 0.037[b], 0.0397[d], 0.0408[i], 0.0437[l]
Spin-orbit parameter, δ (eV)	−0.0087[a], 0.014[c], 0.016[d]
Crystal-field parameter, Δ (eV)	0.0410[a], 0.048[c], 0.043[d]
Exciton effective mass, $\mu_{ex}^*(m_0)$	0.31[a], 0.20[b]
Exciton Bohr radius, a_0 (Å)	14[a], 24[b]
Biexciton binding energy, E_B^{XX} (eV)	14.7[j], 15[k]

[a]Thomas [3] (needles grown from vapor phase).
[b]Park *et al.* [5] (platelets and bulk crystals grown from the vapor phase).
[c]Chichibu *et al.* [51] (bulk crystals grown by chemical vapor deposition).
[d]Reynolds *et al.* [23] (bulk crystals grown by a seeded physical vapor transport method).
[e]Thonke *et al.* [45] (bulk crystals grown by seeded chemical vapor transport).
[f]Reynolds *et al.* [43] (melt-grown bulk crystals).
[g]Reynolds *et al.* [43] (vapor-grown bulk crystals).
[h]Teke *et al.* [50] (melt-grown bulk crystals).
[i]Liang and Yoffe [12]. (platelets grown by vapor transport).
[j]Hvam [157].
[k]Yamamoto *et al.* [156] (epitaxial films grown by plasma-MBE).
[l]Meyer *et al.* [65].

orientations producing compressive strain in the vicinity of the defect pairs with the strain being oriented in the direction of the pair. By observing the changes in emission from the defect pairs as the annealing temperature is increased, Reynolds *et al.* [53] investigated the relaxation of strain following an increase in the number of nearer pairs. Intrinsic energy bands were observed to adjust to these changes by moving to lower energies. For an annealing temperature of 800 °C, shifts as much as 0.4 meV for the A-exciton transition and 3 meV for the B-exciton transition were quoted for σ polarization at 2 K.

Chichibu *et al.* [52] studied the photoreflectance spectra of high-quality ZnO epitaxial layers grown on $ScAlMgO_4$ substrates by laser MBE and observed clear excitonic resonances due to three excitons. A larger broadening was observed for the B- and C-excitons compared to the A-exciton, which was interpreted to be due to a contribution by the exciton-polaritons in terms of large longitudinal–transverse splitting of respective excitons. Chichibu *et al.* [51] also used polarized photoreflectance spectroscopy to study excitonic polaritons in a ZnO single crystal. Following those observations of longitudinal–transverse splitting of ground-state exciton polaritons and resonances due to the first excited states of respective excitons, the authors confirmed the valence band ordering to be A-Γ_{9v}, B-Γ^{u}_{7v}, and C-Γ^{l}_{7v}. The observed longitudinal–transverse splitting energies (1.5, 11.1, and 13.9 meV for A-, B-, and C-excitons, respectively) were in good agreement with earlier results by Hümmer and Gebhardt [54] (2, 11, and 16 meV for A-, B-, and C-excitons, respectively).

By measuring transmissions, Muth *et al.* [49] determined the absorption coefficient, bandgap, and exciton binding energies in epitaxial zinc oxide thin films grown by pulsed laser deposition (PLD) on *c*-plane sapphire substrates. It was found that the excitonic absorption features were sharper in films annealed in oxygen. The absorption coefficient was consistent with the earlier report on thin ZnO platelets by Liang and Yoffe [12]. However, assignments by Muth *et al.* shown in Figure 3.6 for the B- and C-exciton energies are very different from those in other reports most probably due to misinterpretation of the C-exciton as the B-exciton and the exciton–LO phonon complex transitions [12, 55] as the C-exciton. The absorption coefficient at the A-exciton transition energy is $\sim 2 \times 10^5\ cm^{-1}$ at room temperature and increases to $\sim 2.9 \times 10^5\ cm^{-1}$ at 77 K.

Another very powerful technique for studying exciton structure is PL. The low-temperature PL spectrum of ZnO single crystal has been investigated in many aspects by many researchers [23, 45, 46, 48, 50, 53, 56–59]. Figure 3.7 shows a typical PL spectrum in the energy range of fundamental excitonic region taken at 10 K by Teke *et al.* [50] in the $\mathbf{E} \perp \mathbf{c}$ polarization geometry for a high-quality ZnO crystal annealed under forming gas (FG) (5% H_2 and 95% N_2). The A-free excitons and their first excited state transitions are observed at $FX_A^{n=1} = 3.3771$ eV and $FX_A^{n=1} = 3.4220$ eV, respectively, for Γ_5 (3.3757 eV) and Γ_6(3.4202 eV) band symmetry. Although, Γ_6 exciton is forbidden at $k = 0$ in the measurement mode of polarization, it is still observed evidently due to the fact that the photon has a finite momentum. Geometrical effects such as not having the sample orientated exactly perpendicular to electric field might also be responsible for the observation of Γ_6

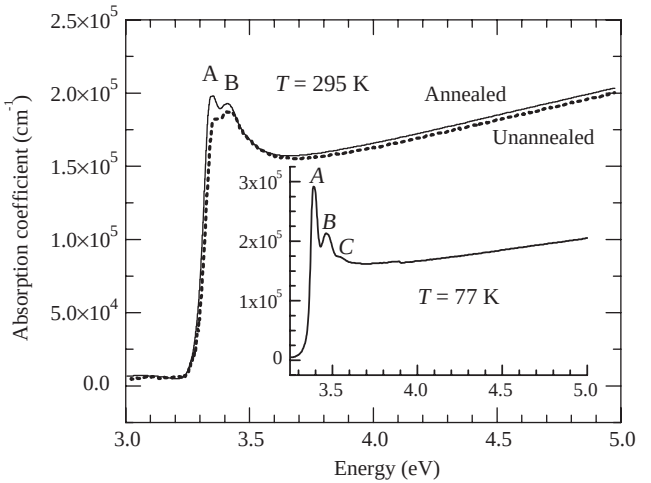

Figure 3.6 Absorption coefficient and excitonic structure for an annealed (solid lines) and an unannealed (dotted line) sample at room temperature. The inset shows the absorption coefficient for the annealed samples at 77 K. (After Ref. [49].) The C-exciton is misinterpreted as the B-exciton and the exciton–LO phonon complex transitions are misinterpreted as the C-exciton. (After Ref. [49].)

transition. By using the energy separations of ground-state and excited-state peak positions and assuming that exciton has a hydrogen-like set of energy levels, the exciton binding energy and bandgap energy can be predicted. The energy difference of about 45 meV between the ground and first excited states gives an A-free-exciton

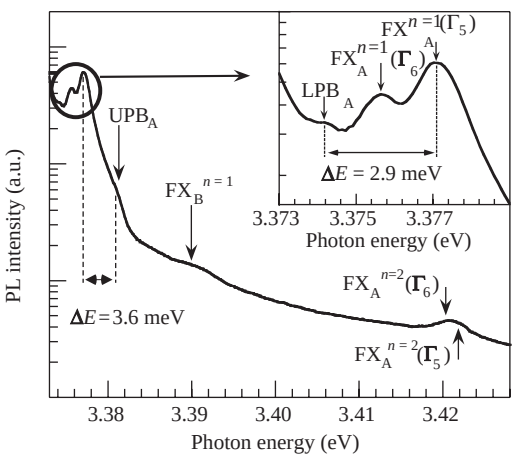

Figure 3.7 Free excitonic fine structure region of the 10 K PL spectrum for a forming gas-annealed ZnO substrate. (After Ref. [50]).

binding energy of 60 meV and a corresponding ZnO bandgap energy of 3.4371 eV at 10 K. Based on the reported energy separation of the A and B free excitons (in the range of $E_{AB} = 9$–15 meV) [3, 23, 46], the weak emission centered at 3.3898 eV, which is about 12.7 meV apart from the A-exciton, is assigned to the B-exciton transition.

In strongly polar materials such as ZnO, transverse Γ_5-excitons couple to photons to form polaritons. Γ_5-exciton couples to light polarized in the plane perpendicular to the *c*-axis. For wave vectors in the plane, these states are dipole coupled and split into a longitudinal state and a transverse state. In such a case, the usual transverse Γ_5-exciton dispersion $E_{ex} = E_{ex,0} + \hbar^2 k_{ex}^2 / 2m_{ex}$ will mix with the dispersion of the photon $E_{photon} = \hbar c k_{photon}$ to produce two new dispersion curves as seen in Figure 3.8, known as the upper polariton branch (UPB) and lower polariton branch (LPB). LPBs and UPBs can occur for excitons formed from all three valence bands, A, B, and C; however, in the PL spectra only LPB_A and UPB_A are observed.

In principle, although the polaritons can be formed anywhere along the dispersion curves, polariton lifetimes, which are higher at certain points, determine the observed peak positions. Therefore, as indicated in Figure 3.7, the $FX_A^{n=1}(\Gamma_5)$ exciton line has two components. The higher energy component at 3.3810 eV, which is 3.6 meV apart from the A-exciton, is assigned to the so-called longitudinal exciton, the energy of which is identical to that of the UPB_A at $k = 0$. The lower energy component at 3.3742 eV, which is about 2.9 meV apart from the A-exciton, most likely corresponds to the recombination from the "bottleneck" region of the lower polariton branch LPB_A, where the photon and free-exciton dispersion curves cross. The emission line at 3.3771 eV (which is assigned as the $FX_A^{n=1}(\Gamma_5)$ transition energy) is believed to result from a long-lifetime region of the LPB_A, which of course is not at $k = 0$ but has nearly the same energy as that of the free A-exciton, at $k = 0$. These assignments are also consistent with the theory used to calculate the energy separation between the main exciton and polariton branches. The longitudinal–transverse splitting is given by $\Delta E = E(\Gamma_5)4\pi\alpha/2\varepsilon$, where $E(\Gamma_5)$ is the energy of the (Γ_5) exciton with $4\pi\alpha$ denoting the polarizability and ε the optical dielectric constant.

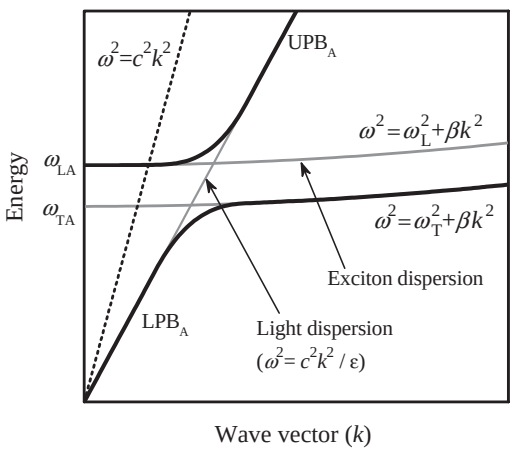

Figure 3.8 A simplified sketch of the exciton-polariton dispersion.

By using the reported values of 7.7×10^{-3} for polarizability [60] and 4.0–5.0 for optical dielectric constant [61, 62], the calculated value will be in the range of 2.6–3.3 meV for $E(\Gamma_5) = 3.3771$ eV. The measured energy splitting (2.9 meV for LPB_A and 3.6 meV for UPB_A) is comparable to the predicted values and also to the experimental values of Chichibu *et al.* [51] (1.5 meV), Lagois [63] (1.8 meV), and Hümmer and Gebhardt [54] (2 meV), supporting the assignment of these two peaks. Because the Γ_6 excitons do not have a transverse character, they do not interact with light to form polaritons and thus have only normal free-exciton dispersion curves as seen in the PL spectra. Therefore, the 3.3757 eV line in Figure 3.7 can be assigned to a low k-point of the Γ_6 dispersion curve (note that the transition cannot occur precisely at $k = 0$, because Γ_6-excitons are not allowed at $k = 0$).

Low-temperature reflectivity measurements performed by Teke *et al.* [50] validated the free-excitonic features and corresponding peak assignments depending on PL measurements. Figure 3.9 shows reflectivity measurements performed at 10 K for unpolarized and π-polarized light. For unpolarized light, ground and first excited states of A- and B-excitons along with a weak C-exciton feature are observed. The reflection minima at $FX_A^{n=1} = 3.3772$ eV and $FX_{AB}^{n=1} = 3.3901$ eV are in excellent agreement within the experimental resolution with the emission peaks for A- and B-free excitons in the PL spectra. The position of the first excited state ($FX_A^{n=2} =$ 3.421 eV) and thereby the binding energy of the A-free exciton (∼60 meV) were also confirmed by reflectivity measurements. In addition, the reflection minima at 3.427 eV and 3.433 eV were assumed to be related to the second and the first excited

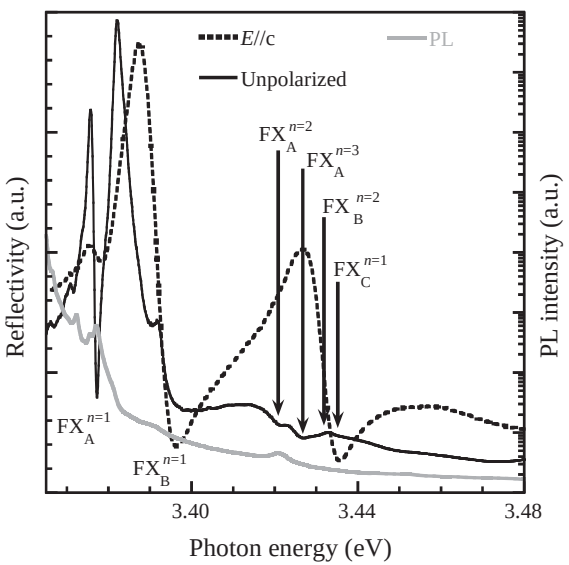

Figure 3.9 Reflection spectra of a forming gas-annealed ZnO substrate measured at 10 K with unpolarized light and with E//c. The PL spectrum is also superimposed for comparison. (After Ref. [50])

states of the A- and B-free excitons, respectively. As will be discussed below, the temperature evolutions of the A- and B-exciton PL peaks also reveal characteristic features related to these exciton transitions supporting this premise.

Table 3.2 tabulates the observed excitonic peak energies reported for high-quality ZnO single crystals from reflectance, photoreflectance, absorption, and PL measurements. The peak position of the A- and B-free excitons, and the first excited states of the A-exciton from Teke *et al.* [50], is in very good agreement, within the experimental accuracy, with the results reported by Reynolds *et al.* [23]. The observed polariton positions are also in reasonable agreement with the reported energies for bulk ZnO grown by Eagle-Picher using vapor-phase transport. It should be noted that the experimental resolution and the wavelength calibration of the particular setup used must be considered carefully to identify the exact peak positions of the very narrow excitonic lines.

3.2.2 Bound Excitons

Bound excitons are extrinsic transitions and are related to dopants, native defects, or complexes, which usually create discrete electronic states in the bandgap and therefore influence both optical absorption and emission processes. The electronic states of the bound excitons depend strongly on the semiconductor material, in particular the band structure. In theory, excitons could be bound to neutral or charged donors and acceptors. A basic assumption in the description of the bound exciton states for neutral donors and acceptors is a dominant coupling of the like particles in the bound exciton states. These two classes of bound excitons are by far the most important cases for direct bandgap materials. In high-quality bulk ZnO substrates, the neutral shallow DBE often dominates because of the presence of donors due to unintentional (or doped) impurities and/or shallow donor-like defects. In samples containing acceptors, the ABE is observed. The recombination of bound excitons typically gives rise to sharp lines with a photon energy characteristic of each defect. Many sharp donor- and acceptor-bound exciton lines were observed in the low-temperature PL spectra of ZnO in a narrow energy range between 3.348 and 3.374 eV. In different studies, the total number of the observed emission lines varies depending on the sample and the measurement technique; nevertheless, there are 12 transitions labeled from I_0 to I_{11}, following the general notation used in the earlier studies [64] that form the basic set of bound exciton transitions characteristic of ZnO. However, the chemical origin and the binding energy of the most underlying donor and acceptor atoms still remain unclear.

Figure 3.10 shows the bound exciton region of the 10 K PL spectrum for the melt-grown bulk sample (from Cermet, Inc.) characterized by Teke *et al.* [50]. The prominent lines are positioned at 3.3564 (I_9), 3.3598 (I_8), 3.3605 (I_6), 3.3618 (I_5), 3.3650 (I_4), 3.3664 (I_3), and 3.3724 (I_0) eV. The 3.3605 eV line is the most intense and has a full-width at half-maximum (FWHM) of about 0.7 meV, indicating the high quality of the sample. Several small peaks and shoulders can also be seen between these prominent lines. Different assignments for these emission peaks are present in

Table 3.2 Excitonic transition energies (eV) in ZnO single crystals.

	$FX_A(\Gamma_5)$			$FX_A(\Gamma_6)$			LPB_A UPB_A	FX_B			LPB_B UPB_B	FX_C			LPB_C UPB_C
	$n=1$	$n=2$	$n=3$	$n=1$	$n=2$	$n=3$		$n=1$	$n=2$	$n=3$		$n=1$	$n=2$	$n=3$	
Teke *et al.* [50] (melt grown)	3.3771	3.4220		3.3757	3.4206		3.3740 3.3810	3.3898							
Reynolds *et al.* [23] (vapor transport)	3.3773	3.4221	3.4303	3.3756	3.4209	3.4288		3.3895	3.4325						
Reynolds *et al.* [48] (vapor grown)	3.3793			3.3775			3.3743 3.3829								
Reynolds *et al.* [43] (melt grown)	3.3764	3.4217						3.3840	3.4271			3.4336	3.4657		
Reynolds *et al.* [43] (vapor grown)	3.3783	3.4229						3.3858	3.4283			3.4245	3.4667		
Hamby *et al.* [58] (vapor transport)	3.378						3.374 —	3.385							
Chichibu *et al.* [51] (chemical vapor deposition)		3.4231					3.3768 3.3783		3.4290		3.3830 3.3941		3.4679		3.4214 3.4353
Park *et al.* [5] (vapor grown)	3.3931	3.4243	3.4296					3.4331				3.4696			
Thomas [3] (needles)	3.3768	3.4225						3.3830	3.4275			3.4215	3.4650		
Liang and Yoffe [12] (vapor transport)	3.3781	3.4282	3.4375					3.3856	3.4324	3.4412		3.4264	3.4722	3.4808	
Lagois [63] (vapor grown)							3.3758 3.3776				3.3810 3.3912				3.4198 3.4317

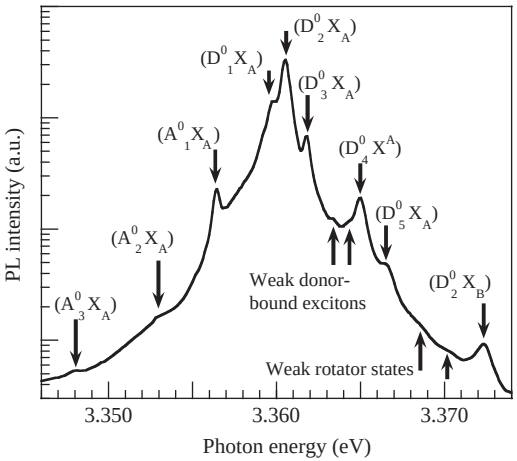

Figure 3.10 Bound excitonic region of the 10 K PL spectrum for a forming gas-annealed ZnO substrate. (After Ref. [50])

the literature. Some of the reported values for bound exciton peak energies observed in low-temperature PL are given in Table 3.3 for comparison. The emission peaks at 3.3598 (I_8), 3.3605 (I_6), 3.3618 (I_5), 3.3650 (I_4), and 3.3664 eV (I_3) have been assigned to the A-excitons bound to neutral donors (D^0X_A) [50]. The 3.3660–3.3665 eV (I_3) transition along with the 3.3674 eV (I_2) transition has also been attributed to the ionized donor-bound exciton complexes [44, 65], based on the splitting in magnetic field.

In the lower energy region, the main peak at 3.3564 eV (I_9) was commonly observed and was previously attributed to Na or Li acceptors [66]. However, the binding energy of the deep Li_{Zn} acceptor (~500 meV) measured by optically detected magnetic resonance [67, 68] rules out the possibility of observing such a near-bandgap acceptor-bound exciton. This 3.3564 eV (I_9) line that was initially assigned to an acceptor-bound exciton by Teke *et al.* [50] is in fact due to a neutral donor-bound exciton, as verified by others based on its thermalization behavior in annealing/PL studies [56] and in temperature-dependent magnetotransmission and magnetophotoluminescence measurements [44, 65]. Two other weak emissions at 3.3481 (I_{11}) and 3.3530 eV (I_{10}) are also visible in Figure 3.10, which may indicate the presence of deep acceptor states. However, their chemical origins have not yet been identified. Meyer *et al.* [65] could not observe any acceptor-bound excitons and assigned the 3.3510 eV (I_{10}) line attributed to the neutral acceptor-bound exciton (A^0X_A) by Teke *et al.* [50] to a neutral donor-bound exciton.

On the high-energy side of the neutral DBE region, transitions between 3.3664 and 3.3724 eV have been attributed to the excited states or excited rotator states of the ground state neutral donor-bound excitons. These excited states are analogous to the rotational states of the H_2 molecule. Several models have been proposed to explain the rotator states for different material systems. To identify these rotator states in bulk ZnO, Reynolds *et al.* [56] adopted the model, which is originally proposed by Rorison *et al.* [69] to explain their high magnetic field results in InP. In this model, DBEs are

Table 3.3 Bound exciton peak energies (eV) in ZnO single crystals.

Reference	A-exciton bound to neutral or ionized donors								Excited rotator states		B-exciton bound to neutral donor
	I_{11}	I_{10}	I_9	I_8	I_7, I_6	I_5	I_4	I_3	I_2	I_1	I_0
Teke *et al.* [50]	3.3481[a]	3.3530[a]	3.3564[a]	3.3598	3.3605	3.3618	3.3634 3.3643	3.3650 3.3664	3.3686	3.3702	3.3724
Reynolds *et al.* [56]			3.3562	3.3594	3.3602	3.3610	3.3624 3.3634	3.3652	3.3670 3.3662	3.3702 3.3714	
Alves *et al.* [59]			3.358[a]		3.361	3.362		3.364			
Thonke *et al.* [45]			3.3566[b]	3.3597	3.3606	3.3611	3.3628	3.364			
Boemare *et al.* [46]				3.3592			3.3622 3.3632	3.3653 3.3693	3.3693 3.3707	3.3741 3.3754	3.3707 3.3741 3.3754 3.3772
Meyer *et al.* [65]	3.3484	3.3531	3.3567	3.3598 3.3593	3.3608 3.3604 3.3600	3.3614	3.3628	3.3665 3.3660	3.3674[c]	3.3718[c] 3.3679[c]	3.3725[c]

[a]Assigned to neutral acceptor-bound excitons.
[b]Not reported if acceptor- or donor-bound exciton.
[c]Assigned to donor or ionized donor-bound excitons.

considered to be free excitons rotating around neutral donors, where one electron of the DBE state is strongly correlated with the hole and the other with the donor. The transitions observed at 3.3662 (Γ_6) and 3.3670 (Γ_5) eV were attributed to the rotator states associated with the ground-state neutral bound exciton line at 3.3564 eV (I_9) based on the annealing studies and magnetophotoluminescence measurements. After annealing at 800 °C, only these rotator states were observed with the only surviving donor bound exciton at 3.3564 eV. Using the energy difference of 10.6 meV, Reynolds *et al.* [56] calculated an excitonic molecule radius 1.5 times the excitonic radius of the free exciton (a_0), which agrees with the reported factors between 1.44 and 3.47 [70]. Based on the same energy difference, the peaks at 3.702 (Γ_6) and 3.3714 eV (Γ_5) were assigned to the rotator state of the neutral bound exciton at 3.3594 eV (I_8). In measurements by Teke *et al.* [50], very weak emissions at 3.3686 (Γ_6) and 3.3702 (Γ_5) eV with an energy separation of about 1.6 meV have been attributed to the rotator states associated with the main neutral bound exciton emission at 3.3605 eV. The splitting of these two peaks is consistent with the energy separation of the Γ_6 and Γ_5 band symmetries. The excited rotational states were also observed by Meyer *et al.* [65] for the I_4, I_6, and I_8 transitions with energy separations of 1.1, 1.2, and 1.5 eV, respectively. These separations are much smaller than those obtained by Reynolds *et al.* [56], whose calculations would suggest an exciton radius of more than $4a_0$ for such small separations. However, one would expect the Bohr radius to be reduced in ZnO due to the relatively large binding energy.

Another relatively strong emission line at 3.3724 eV (I_0) was attributed to the transition due to the B-free exciton bound to the same main neutral donor (D^0X_B) by Teke *et al.* [50]. The energy separation between this peak and the main peak at 3.3605 eV (I_6) is about 12 meV, which is consistent with their energy splitting of the A- and B-free exciton lines. Analysis of the temperature dependence of the PL spectrum also supports this assignment. Meyer *et al.* [65], on the contrary, observed peaks around 3.364 eV, which they assigned to neutral donor-bound B-excitons. As suggested by Boemare *et al.* [46], the emission peaks observed in this very narrow region on the high-energy side of the well-identified neutral donor-bound exciton lines may be attributed to ionized donor bound excitons, excited rotator states, and/or neutral donor-bound B-excitons. Identification of the fine structure in this energy range is not an easy task by just using the steady-state photoluminescence.

Reynolds *et al.* [56] have investigated the bound exciton region in detail by using low-temperature PL measurements performed for different polarizations and applied magnetic fields. They resolved seven bound exciton lines using the second-order grating configuration in the bound exciton spectral region. However, in this particular study there is almost a 2-meV shift between the first- and the second-order PL spectra that might be due to experimental issues associated with the setup used. Nevertheless, the peak energies of the neutral donor-bound excitons reported by Teke *et al.* [50] are almost at the same positions, within the experimental resolution, as those reported by Reynolds *et al.* [56]. Relative peak intensities of the particular donor-related exciton lines show some differences from sample to sample. For example, the most intense line was observed at 3.3628 eV by Thonke *et al.* [45], at 3.3624 eV by Reynolds *et al.* [56], at 3.3653 eV by Boemare *et al.* [46], and at 3.364 eV by Alves

et al. [59] and Hamby *et al.* [58], whereas Teke *et al.* [50] observed the most intense neutral donor-bound exciton line at 3.3605 eV. This is because the concentration of the particular donor as well as its capture cross section could vary from sample to sample depending on the growth technique and postgrowth treatment used.

Even though the chemical origin of most of the donor/acceptor bound exciton lines is unknown, there is some experimental evidence relating a number of these lines to certain impurities. For example, the 3.3628 eV (I_4) line, which is typical for ZnO grown by hydrothermal and seeded vapor transport methods, and is absent in samples grown from the vapor phase, is attributed to the hydrogen donor [65]. Reduction of the hydrogen-related electron nuclear double resonance signal along with the decrease in the neutral donor resonance amplitude measured by electron paramagnetic resonance and IR absorption measurements on the vibrational properties of hydrogen in ZnO [71, 72] strongly supports this assignment.

Based on the Al implantation studies of Schilling *et al.* [73], who observed an increase in the intensity of the 3.3605 eV (I_6) emission line with increased Al concentration in ZnO, the I_6 transition is attributed to the Al impurity. Secondary ion mass spectroscopy (SIMS) revealed that Al was the dominant impurity with a concentration of more than one order of magnitude higher than that for other group III and group VII elements for samples where only the 3.3605 eV neutral donor-bound exciton line was observed [65]. Al was suggested to be an omnipresent impurity in vapor-grown ZnO [67].

The 3.3598 eV (I_8) neutral donor-bound exciton line was observed to be prominent in Ga-doped epitaxial ZnO films and in ZnO epitaxial films that were grown on GaN templates, which resulted in Ga interdiffusion into ZnO, as verified by SIMS experiments [65]. The attribution of the I_8 line to the Ga impurity was also supported by the findings of Ko *et al.* [74], who also reported Ga-donor-bound exciton recombination at 3.359 eV.

The 3.3564 (I_9) and 3.3530 eV (I_{10}) emission lines were initially thought to be related to Na and Li impurities, because they were typically observed in films doped with these elements. However, PL studies of Meyer *et al.* [65] on Na (Li)-diffused samples using different Na(Li)-containing salts did not support this thesis. On the contrary, diffusion experiments using different concentrations of indium sulfate solutions led to the appearance of the I_9 line with In diffusion into bulk ZnO, which was confirmed by SIMS [65]. After the identification of In donor by optically detected magnetic resonance, it has also been stated that indium donor in Li-doped ZnO is an unintentional, residual impurity [67].

3.2.3
Two-Electron Satellites in PL

Another characteristic of the neutral donor-bound exciton transition is the TES transition in the spectral region of 3.32–3.34 eV. These transitions involve radiative recombination of an exciton bound to a neutral donor, leaving the donor in the excited state (2s, 2p states), thereby leading to a transition energy that is less than the DBE energy by an amount equal to the energy difference between the first excited (2s, 2p)

and ground states (1s) of the donor. The usual observation of the (D^0X_A) line of course occurs when the donor final state is the ground state. In the effective mass approximation, the energy difference between the ground-state neutral donor-bound excitons and their TES excited states can be used to determine the donor binding energies [45, 59] and catalog the different species present in the material. When the central cell corrections are also neglected, the donor excitation energy from the ground state to the first excited state equals to 3/4 of the donor binding energy, E_D.

The spectral region for the expected two-electron satellite transitions is shown in Figure 3.11 for a forming gas-annealed bulk ZnO sample. The main peak at 3.3224 eV is the TES $(D^0X_A)_{2e}$ associated with the most intense neutral donor-bound exciton at 3.3605 eV (D^0X_A). The shoulder seen at about 3.3268 eV on the high-energy side of the main TES peak is related to the excited state of the donor whose ground-state emission is at 3.3618 eV. A weak emission at 3.3364 eV is also attributed to the TES transition of the neutral donor whose ground state is at 3.3650 eV ($D_4^0X_A$). From the separation of the ground state and the corresponding excited states, the donor binding energies are calculated as 51 meV for the donor at 3.3605 eV, 47 meV for the donor at 3.3618, and 38 meV for the donor at 3.3650 eV. Teke *et al.* [50] could not identify two additional peaks, at 3.332 and 3.313 eV, in the TES region of the spectrum, which may be related to the excitons bound to structural defects that are rather pervasive in GaN.

Meyer *et al.* [75] studied the TES spectral range of different bulk ZnO samples in detail to obtain the binding energies of various donors. They have observed the splitting of TES lines into 2s and 2p states as a result of the effects of anisotropy and the polar interaction with optical phonons in polar hexagonal semiconductors. The effects of anisotropy and the polaron interactions were combined by employing the second-order perturbation theory and the results of numerical calculations of the

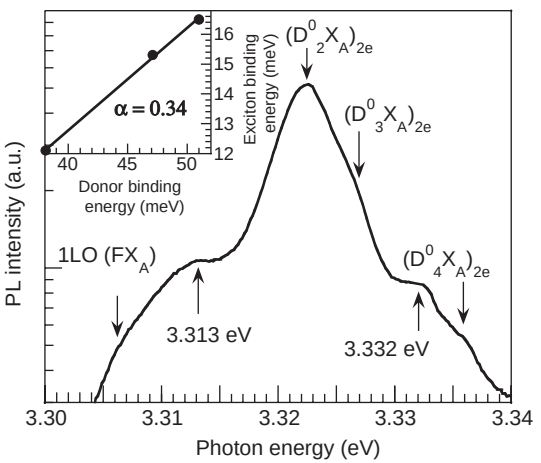

Figure 3.11 10 K PL spectrum for a forming gas-annealed ZnO substrate in the TES region of the main bound exciton lines. Inset shows the exciton binding energy versus donor binding energy. (After Ref. [50]).

Table 3.4 Binding energies and chemical identities of various donors.

		Energy (eV) (Donor binding energy, meV)			
PL line	**Chemical identity [75]**	**Meyer *et al.* [75]**	**Teke *et al.* [50]**	**Alves *et al.* [59]**	**Reynolds *et al.* [56]**
I_3			3.3650 (38)	3.364 (43)	
I_4	H	3.3628 (46)			3.3636 (55.5)
I_5		3.3614 (51.4)	3.3618 (47)	3.362 (52)	3.3614 (56.7)
I_6	Al	3.3604 (53)	3.3605 (51)	3.361 (55)	
I_8	Ga	3.3598 (54.5)			
I_9	In	3.3567 (63.2)			
I_{10}		3.3531 (72.6)			
Proportionality constant (b), Haynes' constant (α)		$b = 0.365$	$b = 0.34$ $\alpha = 0.32$	$\alpha = 0.3$	$\alpha = 2$

ground- and excited-state energies of bound polarons in the isotropic approximation. More precise donor binding energies extracted from the data using this approach are listed in Table 3.4 along with the data mentioned above.

From the separation between the A-free exciton and the ground-state neutral DBEs, Teke *et al.* [50] determined the localization energies as 16.6 meV (for 3.3605 eV), 15.3 meV (for 3.3618 eV), and 12.1 meV (for 3.3650 eV). According to the empirical Haynes' rule [76], the binding or localization energy of the DBEs is proportional to the binding energy of the corresponding donor, $E_{loc} = \alpha E_B$. However, a better fit was obtained using $E_{loc} = a + bE_B$, with $a = -1.1$ meV and $b = 0.34$. Indeed, the agreement with the linear fit is clearly seen in the inset of Figure 3.11. Meyer *et al.* [75] also observed a linear relationship between the donor binding energies and the exciton localization energies, with $a = -3.8$ meV and $b = 0.365$. For $a = 0$, data from Teke *et al.* [50] give a Haynes' proportionality constant, α=0.32, which is close to the 0.3 reported by Alves *et al.* [59], who calculated the binding energies of the donors as 43, 52, and 55 meV for the donors whose ground-state bound exciton lines were at 3.364, 3.362, and 3.361 eV, respectively.

Thonke *et al.* [45] also studied the TES transitions and found the binding energies of two shallow donors to be 39.9 and 55 meV. Reynolds *et al.* [56] reported binding energies of 55.5 and 56.7 meV for two donors at 3.3636 and 3.3614 eV, respectively. The Haynes' proportionality constant obtained from these binding energies is about 2, much higher than the values given above.

3.2.4
DAP and Shallow Acceptor-Bound Exciton Transitions and LO-Phonon Replicas in PL

The spectral region containing the donor–acceptor pair transition and LO-phonon replicas of the main transitions has not been studied widely for single crystal ZnO.

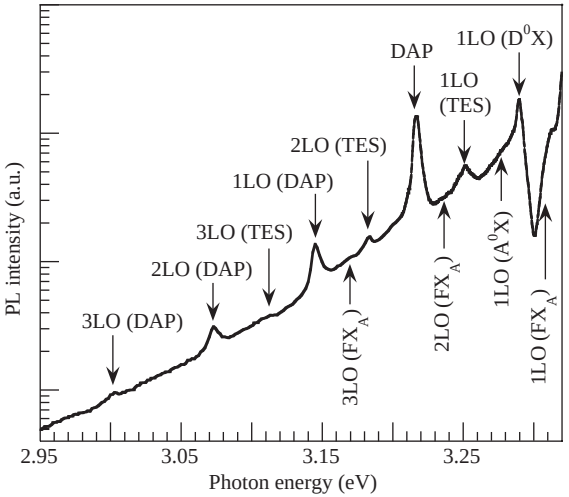

Figure 3.12 10 K PL spectrum for a forming gas-annealed ZnO substrate in the region where donor–acceptor-pair transition and LO-phonon replicas are expected to appear. (After Ref. [50].)

Figure 3.12 shows the corresponding spectrum taken by Teke *et al.* [50] at 10 K for a forming gas-treated sample. It should be noted that LO-phonon replicas occur with a separation of 71–73 meV, the LO-phonon energy in ZnO [77, 78]. Because some of the peaks are either very weak or mixed with other closely spaced peaks, temperature evolution of these peaks should be tracked carefully to make sure that the corresponding assignments are correct. As indicated in Figure 3.12, the bump at the higher energy side of the spectrum labeled as 1LO (FX_A) has a peak around 3.306 eV, which is at the expected position for the 1LO-phonon replica of the free-exciton peak (about 71 meV apart from the $FX_A^{n=1}$ free-exciton peak). Although they are weak, second- and third-order LO phonon replicas (labeled as 2LO (FX_A) and 3LO (FX_A)) are also observed in the PL spectrum.

The first-order LO-phonon replicas of the main neutral bound excitons should fall between 3.290 and 3.295 eV in Figure 3.12. However, due to the line broadening, the peaks corresponding to each individual bound exciton could not be resolved very well. Indeed, the peak labeled as 1LO (D^0X) has a linewidth of about 6 meV, which prevents a definitive resolution. The LO-phonon replicas of the peak at 3.3650 eV can be separated from the two other closely spaced peaks at 3.3618 and 3.3605 eV. The peak at 3.2898 eV is the first LO-phonon replica of both 3.3618 and 3.3605 eV lines, whereas the first LO-phonon replica of 3.3650 eV line is seen as a shoulder on the high-energy side of this intense peak. Resolving the second- and higher order LO replicas is even harder because the energy position (3.218–3.223 eV) falls in the spectral region where the DAP transition and its LO-phonon replicas are expected to appear in the PL spectra. In fact, Teke *et al.* [50] observed a radiative recombination peak at 3.217 eV that is attributed to the donor–acceptor pair (labeled as DAP in Figure 3.12) transition, along with its first, second, and third LO-phonon replicas at

3.145, 3.073, and 3.001 eV, respectively. Regarding the origin of the emission line at 3.2898 eV, Reynolds *et al.* [53] suggested on the basis of their study where internal strains were relieved by annealing that this line is associated with an acceptor-related transition, which disagrees with the interpretation by Teke *et al.* [50]. Although the latter investigation differs somewhat, it reports at least two closely spaced features at 3.2898 and 3.2920 eV, which are about 72 meV apart from the main neutral DBE lines at 3.3605 and 3.3650 eV. The temperature-dependent measurements also show that relative intensities of these LO-phonon replicas follow those of the main bound excitons. In addition, LO-phonon replicas are expected to be roughly two orders of magnitude less intense than the neutral donor-bound exciton lines [45]. This is also similar to the case of GaN and other II–VI semiconductors, where donor-related bound exciton lines couple only weakly to the optical phonons.

The relatively broad peak around 3.280 eV in Figure 3.12 is the first LO-phonon replica associated with the bound exciton line at 3.3564 eV. Finally, the first-, the second-, and the third-order LO-phonon replicas of the TES lines are also clearly observed in the PL spectra. These peaks are labeled as 1LO, 2LO, and 3LO (TES) and they are positioned at 3.252, 3.182, and 3.112 eV, respectively.

ZnO intentionally doped with nitrogen has also been investigated in detail, because nitrogen is believed to be the most promising acceptor in ZnO. In N-doped ZnO (with concentration up to $10^{19}\,cm^{-3}$), a relatively broad line at 3.315 eV dominates the PL spectrum [79]. Look *et al.* [79] attributed this line to an acceptor-bound exciton (A^0X), associated with the N_O acceptor. A weaker and broader line (or shoulder) appearing at 3.238 eV has been attributed to the DAP emission, involving the N_O acceptor, superimposed with the LO-phonon replica of the dominant (A^0X) emission. The activation energy of the N_O acceptor has been estimated at 0.17–0.20 eV from the above PL experiments. In another study [80], the PL spectrum of the p-type ZnO samples, doped with nitrogen by using NO gas, also contained a strong line at 3.309 eV followed by two LO-phonon replicas that could be attributed to the shallow N_O acceptor. A broad peak at 3.245 eV followed by LO-phonon replicas has been observed also by Matsui *et al.* [81] in N-doped ZnO grown by pulse laser deposition on ZnO and glass substrates. This line has been attributed to DAP transition involving the N_O acceptor. The characteristic DAP emission with the zero-phonon line at 3.235 eV was observed in PL spectrum of N-doped ZnO (Figure 3.13) and studied in more detail by Zeuner *et al.* [82]. Transient PL studies on this band confirmed its DAP nature. A nonexponential decay of PL intensity after pulse excitation was attributed to transitions between distant pairs. The acceptor binding energy has been estimated at (165 ± 40) meV from these experiments.

In ZnO doped with As, which is another potential acceptor in ZnO, a line at about 3.23–3.24 eV, followed by two LO-phonon replicas has been observed in the PL spectrum with an intensity exceeding the exciton emission intensity [83]. This emission has been attributed to the shallow As acceptor, the activation energy of which was estimated at 180 ± 10 meV from the temperature dependence of the PL spectrum. Concurrently with the DAP emission line, a sharp line at 3.325 eV appeared in these samples, tentatively attributed to the As acceptor-bound exciton [83]. In yet another study [84], the 3.322 and 3.273 eV lines greatly increased with

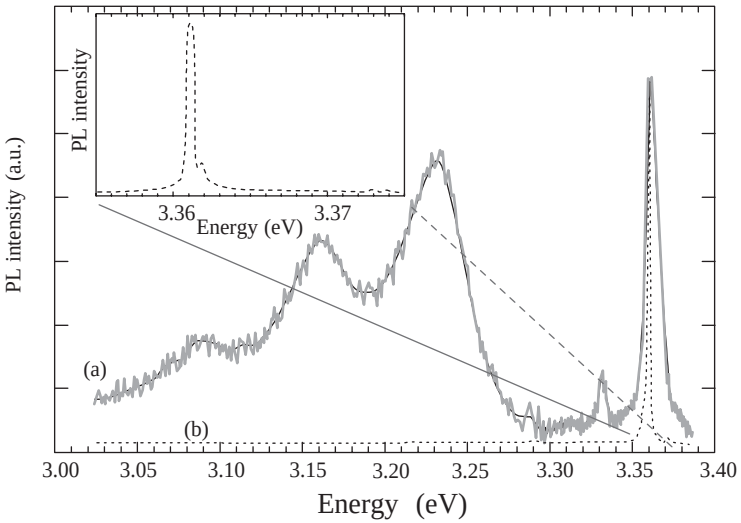

Figure 3.13 Low-temperature PL spectra (raw and fitted data) of (a) nitrogen-doped and (b) undoped ZnO films. The inset shows the expanded spectral region of the near-band-edge PL response from the undoped sample. (After Ref. [82].)

As doping, and the 3.219 and 3.172 eV lines dominated the PL spectrum at the highest chemical concentrations of As dopant in the low $10^{20}\,cm^{-3}$ range. Ryu *et al*. [84] attributed the 3.359 eV line to the (A^0X) exciton, 3.322 and 3.273 eV lines to the As-related e–A transitions, and the 3.219 and 3.172 eV lines to the DAP transitions. The activation energies of the two As-related acceptors were estimated at 115 and 164 meV.

3.2.5
Temperature-Dependent PL Measurements

To provide additional support for some of the peak assignments in the low-temperature PL spectrum of the high-quality ZnO substrate investigated, Teke *et al*. [50] studied the temperature evolution of these peaks. The temperature-dependent measurements were performed between 10 and 300 K. Figure 3.14 shows only the PL spectra for temperatures up to 160 K (at 10, 20, and up to 160 K with 20 K steps) because most of the important changes occur in this range. The spectrum for each temperature is displaced vertically for clarity.

The variation of both A- and B-exciton peak positions with temperature is shown in Figure 3.14. The A- and B-exciton peaks can be tracked up to ~160 K, above which line broadening prevents a satisfactory distinction between the two. This is clearly seen for the room-temperature PL spectrum (bottom curve in Figure 3.14 inset), where the peak position is at ~3.28 eV instead of the expected position of 3.31 eV (if the mostly accepted bandgap of 3.37 eV and the measured binding energy of 60 meV were used). As the temperature is increased, the convergence of the A- and B-excitons, and the

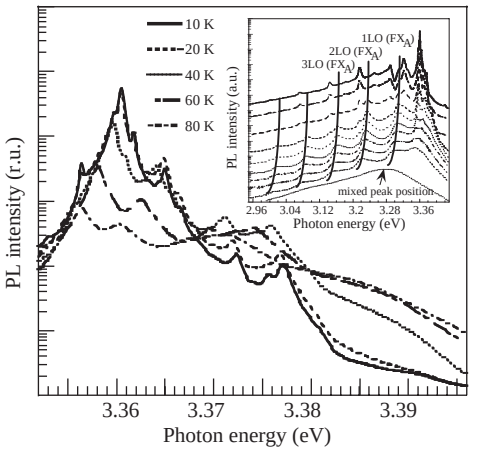

Figure 3.14 Temperature-dependent PL spectrum for a forming gas-annealed ZnO substrate. The inset shows the PL in the DAP and LO-phonon replicas region up to 160 K. The spectrum for each temperature is displaced vertically for clarity. The room-temperature PL data are also included at the bottom. The lines drawn on some peaks are for guidance. (After Ref. [50].)

1LO-phonon replica coupled with the line broadening of each of these peaks, hampers an accurate determination of the peak positions above 160 K. Therefore, the room-temperature peak should be considered a combination of these multiple peaks.

The intensity of A- and B-free excitons increases with temperature up to 40K and 80 K, respectively and then decrease as the temperature is increased further. Based on this observation, Teke *et al.* [50] attributed the 3.3771 and 3.3898 eV emission lines at 10 K to the free excitons corresponding to the A and B bands, respectively. The lower energy bound exciton peaks at 3.3564, 3.3530, and 3.3481 eV quench gradually with increasing temperature and disappear above 40 K. The temperature evolution of the main neutral donor-bound excitons was also tracked within the temperature range of 10–160 K (see also the Figure 3.14 inset). With increasing temperature, the main peak at about 3.3605 eV and its TES along with their LO-phonon replicas quenches. On the contrary, relative intensities of the bound exciton emissions lying between this main DBE peak and the A-free exciton peak increase initially, where the strength depends on the particular bound exciton, and then decrease at higher temperatures. The intensity of the bound exciton peak at 3.3724 eV, which was attributed to the B-exciton bound to the main donor rather than to a rotator state, follows the temperature behavior of the B-exciton up to 40 K supporting the assignment by Teke *et al.* [50]. Although the B-free exciton emission continues to increase up to 80 K, further increase of the donor-bound B-exciton intensity is prevented due to its partial dissociation above 40 K. The observed temperature characteristics of the free exciton and dominant bound exciton, where the relative intensity I_{FX}/I_{BX} is seen to increase with increasing temperature, can be interpreted by using the approach of Viswanath *et al.* [85] for the study of GaN. These authors also observed an increase consistent

with the aforementioned ratio and inferred that with increasing temperature the dominant donor-bound exciton dissociates into a free exciton and a neutral donor. Based on this argument and the works of Reynolds *et al.* [56] and Hamby *et al.* [58], Teke *et al.* [50] concluded that thermal dissociation of the 3.3605 eV bound exciton results in increase of the free excitons and the other shallow donor-bound excitons.

There is some controversy in the assignment of the ~3.23 eV peak, which is close to the main DAP transition at low temperatures. Hamby *et al.* [58] attributed this peak to the second LO-phonon replica of the A-free exciton. Hamby *et al.* attained a very good agreement in terms of the temperature-dependent energy positions of this peak with that of the predicted values by taking into account the temperature broadening effect. Teke *et al.* [50] also assigned this peak to the 2LO-phonon replica of the A-free exciton depending on its temperature evolution. As seen in Figure 3.14, the main DAP line and its LO-phonon replicas quench with increasing temperature, while the adjacent line at ~3.23 eV on the high-energy side increases and becomes more apparent at higher temperatures. The temperature dependence of this peak is similar to the A-free exciton; it increases with increasing temperature up to 60 K and then decreases at higher temperatures. Also, by following the approach of Hamby *et al.* [58], the variation of A-free exciton and its 1LO and 2LO peak energies with temperature are plotted in Figure 3.15. As seen in this figure, the expected and the measured energy peak positions of the 1LO and 2LO replicas of the A-free exciton agree well, supporting the assignments on these peaks. It is also noted that the temperature variation of the A-free exciton peak energy follows the Varshni's [77]

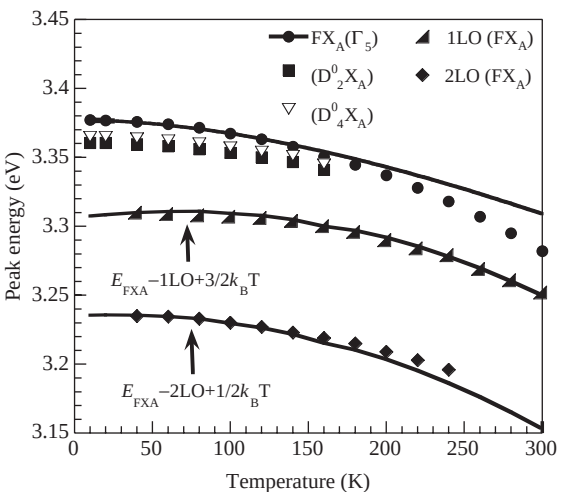

Figure 3.15 Temperature-dependent peak positions of the A-free exciton, $FX_A^{n=1}(\Gamma_5)$ and its 1LO- and 2LO-phonon replicas. Also shown are the temperature evolutions of the peak positions of two major neutral donor-bound exciton transitions at 3.3606 and 3.3650 eV. The $FX_A^{n=1}(\Gamma_5)$ data were fit using Varshni's equation and LO-phonon replicas were fit to the equation shown in the figure. (After Ref. [50].)

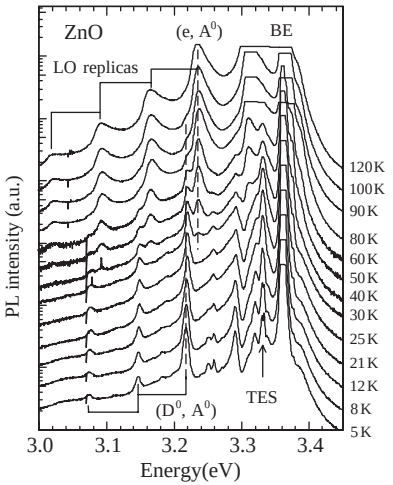

Figure 3.16 PL spectra of undoped ZnO at different temperatures. The plots are vertically shifted for clarity. Between 30 and 100 K, the DAP transition at 3.220 eV decreases and the adjacent e–A transition at 3.236 eV increases. (Courtesy of K. Thonke [45].)

$E_g(T) = E_g(0) - \alpha T^2/(T + \beta)$ formula (empirical), where $E_g(0)$ is the transition energy at 0 K, T is the temperature, and α and β are temperature coefficients. In Figure 3.15, a higher order LO-phonon replica of the A-free exciton also develops persistently with increasing temperature.

On the contrary, analyzing its temperature dependence, Thonke *et al.* [45] attributed the 3.236 eV peak to the free electron-acceptor (e, A^0) transition due to thermal ionization of the donor with increasing temperature. Figure 3.16 shows the appearance of the (e, A^0) peak with increasing temperature above 30 K as the DAP line at 3.220 eV quenches. By using the calculated donor binding energy of $E_D = 28$ meV (this is lower than the 39.9 meV deduced from the spacing of the TES lines) and the donor concentration $N_D = 1.7 \times 10^{17}\,\mathrm{cm}^{-3}$ extracted from Hall measurements, they determined the acceptor ionization energy as $E_A = 195 \pm 10$ meV from the absolute spacing of the (D^0, A^0) line from the bandgap:

$$E_A = [E_{gap} - E_D] - [E(D^0, A^0) - \alpha N_D^{1/3}], \tag{3.102}$$

where α is a material-dependent constant [45] and $E_{gap} = 3.438$ eV. The chemical species for the acceptor and the donor were proposed to be the substitutional nitrogen on O sites and hydrogen, respectively.

3.3 Defects in ZnO

Characteristically, defects represent one of the controversial areas of semiconductors, and ZnO is no exception, as the measurement techniques are not able to correlate

electrical or optical manifestation of defects to their origin precisely. It is highly appropriate to say that the point defects in ZnO are not so well understood. While numerous assignments of the defect-related luminescence bands can be found in literature, only a few of them are trustworthy. Over the years, oxygen vacancies were believed to be the dominant shallow donors in ZnO. Now it is becoming clear that these vacancies are formed in noticeable concentrations only after electron irradiation. As another vital misassignment till now, the green luminescence band in ZnO is commonly attributed to transitions from the oxygen vacancy (V_O) to the valence band. However, it is easy to show that such transition is highly unlikely in n-type ZnO. Problems in the identification of point defects are discussed from theoretical and experimental points of view in this section.

3.3.1 Predictions from First Principles

As in any semiconductors, point defects affect the electrical and optical properties of ZnO as well. Point defects include native defects (vacancies, interstitials, and antisites), impurities, and defect complexes. The concentration of point defects depends on their formation energies. Van de Walle *et al.* [86, 87] calculated formation energies and electronic structure of native point defects and hydrogen in ZnO by using the first-principles, plane-wave pseudopotential technique together with the supercell approach. In this theory, the concentration of a defect in a crystal under thermodynamic equilibrium depends upon its formation energy E^f in the following form:

$$c = N_{\text{sites}} \exp\left(-\frac{E^f}{k_B T}\right), \tag{3.103}$$

where N_{sites} is the concentration of sites in the crystal where the defect can occur. A low formation energy implies a high equilibrium concentration of the defect; a high formation energy means defects are unlikely to form.

The formation energy of a point defect in a charge state q is given by

$$E^f(q) = E^{\text{tot}}(q) - n_{\text{Zn}}\mu_{\text{Zn}} - n_O\mu_O - qE_F, \tag{3.104}$$

where $E^{\text{tot}}(q)$ is the total energy of a system containing n_{Zn} and n_O zinc and oxygen atoms, μ_{Zn} and μ_O are the chemical potentials for zinc and oxygen, respectively, and E_F is the Fermi energy. The total energy can be obtained from the state-of-art first-principles calculations that do not require any adjustable parameters or any input from experiments. The chemical potentials depend on the growth conditions. For the zinc-rich case, $\mu_{\text{Zn}} = \mu_{\text{Zn(bulk)}}$ and for the oxygen-rich case $\mu_O = \mu_{O2}$. For intermediate II–VI ratios, $\mu_O < \mu_{O2}$ and $\mu_{\text{Zn}} < \mu_{\text{Zn(bulk)}}$. However, the chemical potentials for Zn and O are not independent because both species are in equilibrium with ZnO: $\mu_{\text{Zn}} + \mu_O < \mu_{\text{ZnO}}$.

The formation energies of native defects in ZnO have been calculated by several groups of theorists and the results generally agree [86, 88–91]. The results for oxygen and zinc vacancies, interstitials, and antisites in ZnO are shown in Figure 3.17 for the

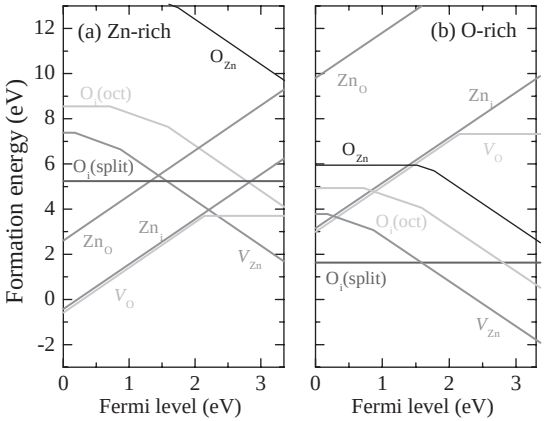

Figure 3.17 Calculated defect formation energies for main native point defects in ZnO as a function of the Fermi level under (a) zinc-rich conditions and (b) oxygen-rich conditions. Only the segments corresponding to the lowest formation energy values are shown. The zero of the Fermi level is set to the top of the valence band. Kinks for each defect indicate transitions between different charge states (0, −1, −2). (After Ref. [88].)

two limiting zinc chemical potential values [88]. Note that there are two possible interstitial sites in the wurtzite ZnO: one is tetrahedrally coordinated and another is octahedrally coordinated. It can be concluded that the two most common defects in ZnO are likely to be oxygen and zinc vacancies. Analysis of the formation energy for the native defects in ZnO shows that the dominant native defects in ZnO should be vacancies: cation vacancies in p-type material (when the Fermi level is close to the valence band) and anion vacancies in n-type material (when the Fermi level is close to the conduction band). Note that some of the native defects (with the formation energy of several electron volts), according to Equation 3.103, have extremely low probability to be formed during the growth. However, one should also note that these formation energies are calculated at thermodynamic equilibrium and may not represent conditions during real growth environment.

For example, V_O has a very high formation energy in n-type ZnO (the Fermi level close to the conduction band), even under extreme Zn-rich conditions. Therefore, V_O concentration should be very low under equilibrium conditions in as-grown undoped ZnO. Moreover, V_O is a deep rather than a shallow donor and it cannot be responsible for n-type conductivity of undoped ZnO, contrary to the conventional wisdom dominated in ZnO communities for decades. In contrast, the anion vacancies can be formed abundantly in p-type material and may be the main cause of the self-compensation. It should also be noted that V_O in n-type material can be formed after electron irradiation. Electron paramagnetic resonance studies indeed revealed the presence of V_O in electron irradiated ZnO as a signal with $g = 1.99$ [92–94].

First-principles calculations based on the density functional theory (DFT) within the local density approximation plus the Hubbard model (LDA + U) can predict not only the probability of the defect formation but also the energy levels of defects in

different charge states [88]. The defect transition levels $\varepsilon(q/q')$ in these calculations are defined as the Fermi-level positions for which the formation energies of the two consecutive charge states q and q' are equal. For Fermi-level positions below (above) $\varepsilon(q/q')$, charge state q·(q') is stable. The transition levels for the main native defects in ZnO are shown in Figure 3.18. A transition level corresponds to a position of the zero-phonon line in case of defect-related photoluminescence or PL excitation and is close to the thermal ionization energy in experiments such as PL and deep-level transient spectroscopy (DLTS). As far as the electronic structure of the main point defects in ZnO is concerned, oxygen vacancy in ZnO is a deep donor with two stable states (V_O^0 and V_O^{2+}), while its metastable state (V_O^+) can be observed in transitions involving optical excitation. It has also been identified as a negative U defect, because $\varepsilon(2+/+)$ lies above $\varepsilon(+/0)$, that is, with increasing Fermi level a transition occurs from the $+2$ to the neutral state, $+$ charge state is unstable at any Fermi level position. Transitions involving V_O^+ can be seen as a broad red band peaking at about 600 nm, as concluded from the optically detected EPR [94]. This result is in excellent agreement with the first-principles calculations for V_O [88]. Zinc vacancy is expected to have charge -2 in n-type ZnO where its formation is more favorable. The transition level between the -1 and -2 charge states of V_{Zn} occurs at 0.87 eV above the valence band [88]. Thus, we may expect transitions from the conduction band or a shallow donor to the V_{Zn} acceptor at around 2.5 eV in n-type ZnO. Thus, the broad green luminescence commonly observed in n-type ZnO can be attributed to V_{Zn}. This proposal is similar to the earlier prediction that negatively charged gallium vacancies are responsible for the yellow luminescence (YL) in GaN [95]. The $2+/0$ level of the oxygen vacancy is predicted at about 2.2 eV above the valence band [87, 88]. Because the positive charge state of V_O is unstable in ZnO, an EPR signal associated with this defect is not expected to be observable, at least in thermodynamically stable conditions [87].

The first-principles calculations also provide information on the mobility of point defects, that is, their ability to diffuse at certain temperature. The estimated annealing temperatures, above which point defects are mobile, and the energy migration barriers for the native defects in ZnO are listed in Table 3.5. It is evident

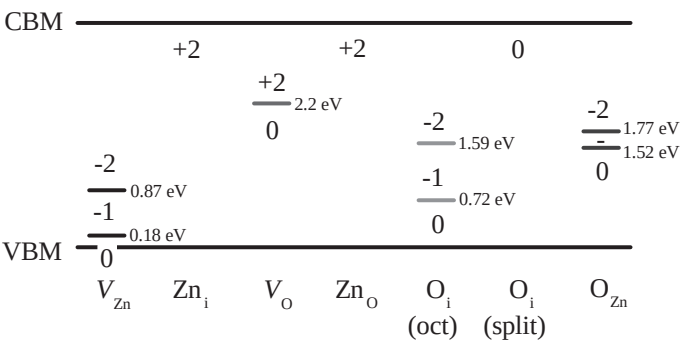

Figure 3.18 Thermodynamic transition levels for native defects in ZnO. (After Ref. [88].)

Table 3.5 Calculated migration barriers, E_b, and estimated annealing temperatures, T_{anneal}, for vacancies and interstitials in ZnO.

Defect	E_b (eV)	T_{anneal} (K)
Zn_i^{2+}	0.57	219
V_{Zn}^{2-}	1.40	539
V_O^{2+}	1.70	655
V_O^0	2.36	909
O_i(split)	0.87	335
O_i(oct)	1.14	439

(After Ref. [88].)

from Table 3.5 that zinc interstitials are mobile at temperatures well below the room temperature, resulting in the formation of complexes. Annealing temperatures provided in Table 3.5 are found consistent with the experimental results [88].

Since the native defects in ZnO cannot explain the n-type conductivity, there are some impurities introduced unintentionally during the growth that act as shallow donors. In ZnO, it is still not clear what the dominant shallow donor is. There are multiple experimental results indicating that hydrogen is involved in the formation of the shallow donor states. Unlike other semiconductors (where hydrogen is amphoteric, i.e., it occurs as H^+ in p-type material and as H^- in n-type material), hydrogen in ZnO is always positive; that is, it always acts as a donor [87]. Hydrogen is tightly bound to an oxygen atom in ZnO, forming an OH bond with a length of about 1.0 Å. In n-type ZnO, the formation energy for hydrogen is only 1.56 eV. In p-type ZnO, incorporation of hydrogen is even more favorable. In fact, this may be beneficial for obtaining p-type ZnO. Indeed, incorporation of hydrogen during growth may increase acceptor solubility and suppress the formation of compensating defects, similar to the behavior of hydrogen during doping of GaN with Mg acceptor. Then, the problem may reduce to the removal of hydrogen during a postgrowth annealing. However, it appears that a single type of the hydrogen-related defect cannot explain the variety of the experimental data. The first-principles calculations predict the formation of at least two types of the hydrogen-related shallow donors. Interstitial hydrogen has low formation energy, which is consistent with observed solubility and electron concentration in as-grown ZnO [96]. Above 500 °C, the interstitial H is unstable, which can explain the persistent conductivity. However, the observed dependence of the electron conductivity on oxygen pressure cannot be explained by the presence of the interstitial hydrogen. On the contrary, the substitutional hydrogen (H_O), also having low formation energy and acting as a shallow donor, is more stable and can explain the observed dependence of the conductivity on the oxygen partial pressure [97]. Hydrogen can be introduced as an unintentional donor in vapor-phase transport, hydrothermal growth, MOCVD (sources, carrier gas), MBE (residual gas), laser ablation, and sputtering in H_2 atmosphere, or during annealing in forming gas.

Among all the candidates for p-type doping, nitrogen was predicted to be the shallowest acceptor in ZnO [66]. Yan *et al.* [98] demonstrated that while N_O is a shallow acceptor, $(N_2)_O$ is a double shallow donor, and competition between N and N_2 during doping of ZnO with N controls the doping type. These authors suggest that the use of N_2 or N_2O gas is not effective in *p*-type doping because energy must be supplied to break the strong N−N bond. In contrast, NO or NO_2 molecules can readily form N_O acceptors, taking advantage of the fact that O atoms are host atoms. Below we give a succinct account of native defects in ZnO.

3.3.2
Defect-Related Optical Transitions in ZnO

Photoluminescence is a powerful tool to study point defects in wide-bandgap semiconductors. Most of the experimental results on point defects in ZnO have been obtained from the analysis of mainly the PL data. Typically, point defects with deep levels are responsible for the broad, often structureless bands in the PL spectrum. According to the first-principles calculations, we can expect that broad PL bands in ZnO are related to transitions involving vacancies. A common misconception is that the PL bands are broad because of many energy levels in the bandgap due to "imperfections" or interaction of defects. In fact, the main reason is the strong electron–phonon coupling, that is, in addition to a photon, a number of phonons are emitted during each recombination of electrons and holes bound to defects. Another common misconception is that PL provides only qualitative data (relative concentrations of defects) but not quantitative. In fact, quantitative methods have been developed, and one can find not only the concentrations of point defects but also the absolute internal quantum efficiency, carrier capture cross sections, charge states, excited states, and so on [99]. In undoped ZnO, the well-known GL band peaking at about 2.5 eV usually dominates the defect-related part of the PL spectrum [19]. There are studies also on other PL bands, in particular the orange/yellow luminescence in Li-doped ZnO [100].

In general, still very little is known about point defects in ZnO and a significant portion of the reported information seems to be false. A particular example is the attribution of oxygen vacancy in ZnO to the green luminescence band as will be discussed in the following section. Note that several (at least five) broadbands related to different point defects can be distinguished in undoped high-quality ZnO [101]. Although numerous attributions of the broad PL bands have appeared in the literature, very few of them can be considered as reliable. Among these are the green band with a fine structure and the zero-phonon line at 2.859 eV, which is clearly related to an internal transition in the Cu_{Zn} acceptor whose ground state is close to the conduction band [102], and the Gaussian-shaped orange band peaking at 1.96 eV at low temperatures, which is attributed to Li_{Zn} in ZnO [100]. The origin of other defects (presumably deep acceptors), and therefore the other PL lines, remains unknown, and even types of transitions are not always established. Reliable experimental results are needed on identification of defects and defect-related transitions that can be compared with the theory (PL, optically detected EPR, positron annihilation

spectroscopy, DLTS). Surfaces also need to be taken into consideration as they affect the electronic properties of ZnO, and significant surface conductivity has already been observed in ZnO [103, 104]. A very common myth is that room-temperature PL spectrum can provide direct information about the presence of point defects in ZnO. However, the strength of the broadband emission depends on the ambient at room temperature, as verified also for GaN. This fact again indicates that the surface plays a tremendous role in the electrical and optical properties of these wide-bandgap semiconductors. There is a significant band bending near the surface due to surface charge, which results mostly from the adsorption of ions and molecules from air.

3.3.2.1 Green Luminescence Band

The nature of the GL, appearing at about 2.5 eV in undoped ZnO, remained controversial for decades. Although in early studies it was unambiguously attributed to copper impurities, a wrong interpretation was later presented in favor of the oxygen vacancy as the defect responsible for the GL band. In numerous publications mentioning luminescence in ZnO, the green PL band is attributed to transitions from the deep donor level of V_O to the valence band after the works of Vanheusden *et al.* [105, 106]. This incorrect identification is based on erroneous assignment of the EPR signal with $g = 1.96$ to oxygen vacancy. It is well established that V_O is responsible for the EPR signal with $g = 1.995$, whereas the $g = 1.96$ signal belongs to the shallow donor [92–94]. Moreover, a transition from a donor state to the valence band is very unlikely in n-type semiconductors. As it will be discussed below, the GL band with a characteristic fine structure is most likely related to copper impurities, whereas the structureless GL band with nearly the same position and width is related to a native point defect such as V_{Zn}, namely, the transitions from the conduction band (or shallow donors) to the $2-/-$ level of V_{Zn}, in analogy with the transitions from the conduction band (or from shallow donors at cryogenic temperatures) to the $3-/2-$ level of V_{Ga} or $2-/-$ level of the $V_{Ga}O_N$ complex in GaN.

Dingle [102] studied wurtzite n-type ZnO crystals containing trace amounts of copper (4 ± 2 ppm), aluminum (<2 ppm), iron, magnesium, silicon, boron, and indium. The PL spectrum obtained was dominated by a broad GL band peaking at ~2.45 eV and revealed the characteristic fine structure (Figure 3.19). The zero-phonon line was composed of two sharp lines (A and B components) separated by ~0.1 meV (Figure 3.20). The ratio of the intensities of the two lines remained constant over the temperature range of 1.6–20.4 K and was independent of the crystal origin. Dingle [102] also studied the behavior of these lines and the band as a function of temperature, under uniaxial pressure, magnetic field, and polarized excitation source. The defining information for the identification of the defect responsible for the GL band has been obtained from the splitting of the A and B lines in applied magnetic field. Each component of the zero-phonon line split into four symmetrically disposed components when the magnetic field was applied parallel or perpendicular to the crystal *c*-axis. The *g*-factors obtained from the angle dependence of the splitting in magnetic field ($g_{||} = 0.73 \pm 0.05$, $g_{\perp} = 1.48 \pm 0.05$) are nearly identical to those obtained from EPR studies of a divalent copper ion Cu^{2+} in a zinc lattice site of ZnO ($g_{||} = 0.7383 \pm 0.0003$, $g_{\perp} = 1.5237 \pm 0.003$) [107]. In addition to these observations,

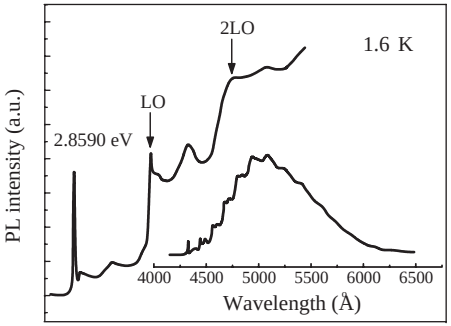

Figure 3.19 GL band in ZnO at 1.6 K. The enlarged portion shows fine structure at the high-energy side with the zero-phonon line at 2.859 eV. (After Ref. [102].)

the absence of thermalization between A and B lines in zero magnetic field, invariance of the A/B intensity ratio in different samples, and identical Zeeman patterns for A and B lines provided the basis for the unequivocal identification of the GL band with its characteristic fine structure as being due to the Cu_{Zn} defect [102].

The details of the ground state of the Cu_{Zn} acceptor in ZnO have been established from the EPR and infrared absorption studies [107]. The low-temperature absorption spectrum of the Cu-doped ZnO contained two sharp lines at 717 and 722 meV. The details of the absorption spectra, the Zeeman splitting in magnetic field, and the EPR data allowed Dietz *et al.* [107] to construct the following model of Cu_{Zn} in ZnO. The free ion term ^2D of the Cu^{2+} ion is split by the tetrahedral crystal field into the $^2E(D)$

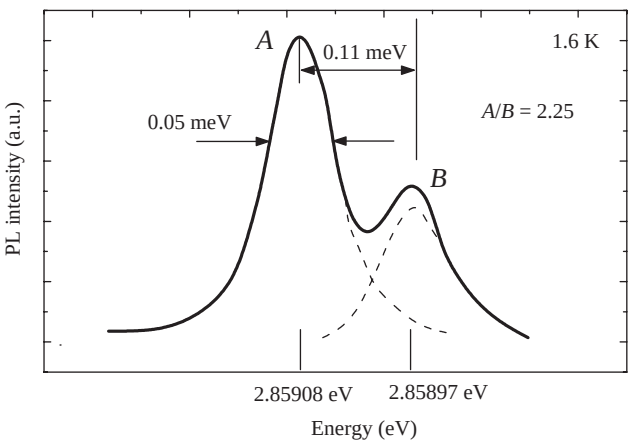

Figure 3.20 High-resolution spectra in the region of the zero-phonon line near 2.859 eV (composed of two sharp lines A and B). The intensity ratio $A/B = 2.25 \pm 0.05$ and is invariant in the temperature range of 1.6–20.4 K. The dashed lines are Gaussian fits to A and B peaks (After Ref. [102].)

and $^2T_2(D)$ states that in turn are split by a combination of weaker spin-orbit coupling and the trigonal crystal field. At low temperatures, intracenter transitions from the lowest sublevel of the $^2T_2$ state to two sublevels of the ^2E state are responsible for the absorption lines at 717 and 722 meV. Assignment of two components of the line at 717 meV (split by ~0.1 meV) as being due to two isotopes of Cu was confirmed by their transformation into a single line in the crystals doped with only ^{63}Cu isotope. Dietz *et al.* [107] concluded that the Cu^{2+} t_2 wave function is radially expanded (more than *e* wave function) relative to the *d* wave function of the free Cu ion, and the t_2 hole spends about 60% of its time on the Cu^{2+} ion, while it spends the rest of the time in the oxygen sp^3 orbitals. The inverse $^2E(D) \rightarrow {}^2T_2(D)$ transition of the Cu^{2+} ions in ZnO (a zero-phonon line at 717 meV) has been observed under electron-beam excitation at low temperatures [108].

The excited states of the Cu_{Zn} acceptor in ZnO have been revealed in the absorption and PLE spectra, namely, a characteristic triplet α, β, γ at 2.8594, 2.8680, and 2.8733 eV, respectively (Figure 3.21) [109–112]. The α line coincides with the zero-phonon line of the GL [102]. Remarkably, the isotope shift was also observed in the absorption and PLE spectra, at least for α and β lines [111]. These lines have been attributed to transitions $Cu^{2+}(d^9) + h\nu \rightarrow (Cu^{+}(d^{10}), h)$ in which the excited state is split into three levels corresponding to three valence bands *a*, *b*, and *c*.

A schematic diagram of various transitions in Cu-doped ZnO is shown in Figure 3.22. Dahan *et al.* [110] have introduced the concept of intermediately bound excitons to explain the experimental data associated with Cu in ZnO. They suggested that the 10th electron, bound to the Cu d-shell, has a larger orbit (or swollen wave function) than the other d-shell electrons due to hybridization with the Bloch states of the host atoms (the covalent swelling). This 10th electron creates the potential capturing a hole, so that the tenth d-shell electron and a loosely bound hole can be considered as an exciton bound to Cu. Intermediately bound excitons are typically formed in crystals with hexagonal wurtzite-type lattice [113] such as ZnO. There are

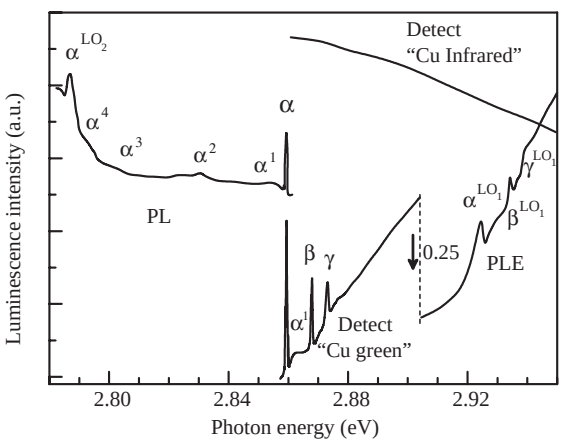

Figure 3.21 PL and PLE spectra near the zero-phonon transition of the GL associated with Cu in ZnO. (After Ref. [112].)

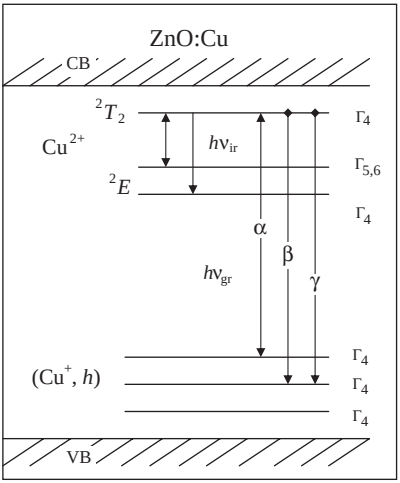

Figure 3.22 A schematic diagram of transitions in ZnO:Cu. (Courtesy of P. Dahan [110].)

three close levels in the forbidden energy gap for such an exciton in ZnO:Cu according to three split levels of the top of the valence band. During the excitation process, all three excited states of the exciton can be observed, whereas only the lowest one is observed in emission at low temperature. The theory of the intermediately bound excitons accounts very well for the isotope shift and *g*-factors of the α, β, γ lines in ZnO:Cu [110, 111].

Kuhnert and Helbig [114] studied the broad phonon sideband of the GL in ZnO (having maximum at 2.4 eV and FWHM 0.42 eV). The energy separation between the subsequent peaks is 72 meV, close to a LO-phonon mode of the ZnO crystal. The spectral distribution of the GL band can be described in terms of the one-dimensional configuration coordinate model. The Huang–Rhys factor $S = 6.5$ was obtained from the fitting. Later, Reynolds *et al.* [115] also analyzed the phonon-related fine structure of the GL in ZnO, but identified the peak at ∼2.26 eV as the zero-phonon line while attributing the high-energy peaks to hot luminescence. In another work, Reynolds *et al.* [116] suggested that transitions from the two shallow donor states to the same deep level are partially responsible for the fine structure of the GL band. However, this picture is in conflict with the fact that different authors observed the same shape of the GL fine structure in different ZnO samples [102, 109, 112, 114].

Garces *et al.* [117], studying PL of a bulk ZnO sample before and after annealing in air at 900 °C for 1 h, observed a remarkable transformation of a broad structureless green band peaking at 500 nm into a structured emission peaking near 510 nm with a structure identical to the Cu-related GL. These authors suggested that there might be two distinct mechanisms giving rise to GL band and that both involve Cu impurities but with different stable charge states (Cu^+ and Cu^{2+}) prior to optical excitation. Based on their EPR study of the samples, they concluded that the structureless GL band of the as-grown ZnO sample was due to DAP recombination between an electron bound to a shallow donor and a hole loosely bound to the Cu^+ ion before annealing, while the structured green emission after the 900 °C annealing was

assigned to localized excitation of the isolated Cu^{2+} ion as originally suggested by Dingle [102].

Structureless GL band in ZnO was attributed also to V_{Zn} acceptor [86, 118–120], a complex defect involving Zn_i [121], O_{Zn} [122], and V_O [105, 106, 123–126]. Different authors suggested different types of electron transitions to explain the GL band, for example, from the V_O donor level located near the conduction band to the valence band (D–h-type recombination) [105], from V_O or another donor level to deep V_{Zn} acceptor level (DAP type) [119, 120], from conduction band to the V_{Zn} acceptor (e–A type) [86], and between two states of V_O (intracenter transition) [125]. However, as indicated earlier, Van de Walle [87, 88] predicted that V_O in ZnO has only the level (2+ /0) at about 2.2 eV above the valence band. Note also that the D–h-type recombination is highly improbable in an n-type semiconductor [127]. Moreover, the DAP-type recombination observed in Ref. [120] may not be the same PL band as others detected because its maximum is at 2.3 eV (shifting to ~2.04 eV after time delay), which is, in the yellow range.

Remarkable correlations attained between the intensity of the GL band, the concentration of free electrons, and the concentration of the defect identified as V_O at different annealing conditions or oxidation seemingly provided strong arguments in support of the model considering V_O as the defect responsible for the GL band [105]. However, this assignment and interpretation of the experimental results are faulty because Vanheusden *et al.* [105] have assigned the EPR signal with $g = 1.956$ to V_O, and the concentration of V_O was determined from the intensity of this signal. Later it was shown that isotropic EPR signal with $g = 1.956$ is related to a shallow donor, whereas EPR signal from V_O is characterized with $g_{||} = 1.984$ and $g_{\perp} = 2.025$ [125]. ODMR studies [125] have revealed that the structureless GL band peaking at about 2.45 eV anticorrelates with the isotropic signal at $g = 1.956$ and correlates with two resonances (with $g_{||} = 1.984$ and $g_{\perp} = 2.025$) arising from a spin-triplet system ($S = 1$). Note that the *g*-values obtained on the structureless GL band [125] and on the GL with a distinct phonon structure [102, 117] are incompatible, and thus these two PL bands are related to different defects. The triplet resonances were detected only in the energy range of the structureless GL band, while the shallow donor signal (with $g = 1.956$) quenched the GL band and enhanced emission in the excitonic range. These findings strongly indicate that the shallow donor signal is transferred to the GL band by a shunt process or a spin-dependent energy transfer mechanism [125]. Leiter *et al.* [125, 126] have identified V_O as the defect responsible for the structureless GL band in ZnO and demonstrated striking similarities of this defect to the anion vacancy in other ionic host crystals: BaO, SrO, CaO, and MgO (F-centers). In the model of Leiter *et al.* [125, 126], the two-electron ground state of the neutral V_O is a diamagnetic singlet state. Absorption of a photon transfers the system into a singlet excited state. It relaxes nonradiatively into the emissive, paramagnetic state that can be detected by ODMR (Figure 3.23).

3.3.2.2 Yellow Luminescence Band

Doping ZnO with Li acceptor results in the YL band with a peak at about 2.2 eV and an FWHM of ~0.5 eV, Ref. [15]. In contrast to the GL band, the YL band decays very

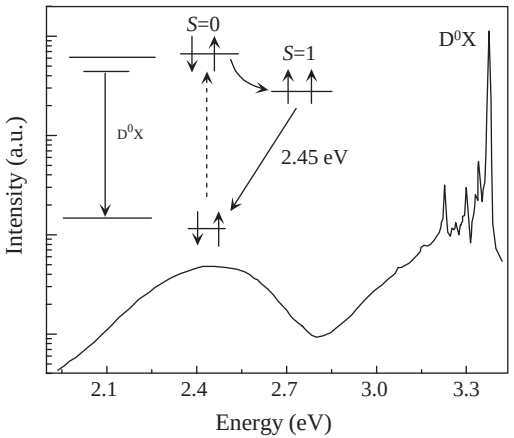

Figure 3.23 PL spectrum of undoped ZnO excited with the 325 nm line of an HeCd laser (5 K). The inset shows a recombination model for the GL band peaked at 2.45 eV. (After Ref. [125].)

slowly after switching off the excitation source and can be observed also in the thermoluminescence spectrum [15]. Li-doped ZnO is high resistive due to the deep location of the Li acceptor level (about 0.8 eV above the valence band) [15]. The YL band is polarized at low temperatures, which was explained by two metastable orientations of the Li_{Zn} center in the ZnO lattice [15]. ODMR studies of the YL band in ZnO:Li suggest that the DAP-type transitions including a shallow donor and the Li acceptor dominate at low temperatures [128].

YL with metastable behavior was observed also in undoped bulk ZnO [129]. Under irradiation with an He–Cd laser, the GL band gradually bleached, while the YL band emerged and eventually replaced the GL band (Figure 3.24). The YL band saturated with excitation intensity above $10^{-3}\,W\,cm^{-2}$, indicating low concentration of the related defects. The decay of the YL was nonexponential at low temperature, allowing the possibility of the DAP transitions for this band. The YL band quenched at temperatures above 200 K with an activation energy of about 0.5 eV.

3.3.2.3 **Red Luminescence Band**

A red luminescence (RL) band emerged at about 1.75 eV in the PL spectrum of undoped bulk ZnO after it was annealed in air at 700 °C (Figure 3.25) [129]. The RL band is broad with an FWHM of about 0.5 eV and its shape is Gaussian. With increasing temperature, in the range from 15 to 100 K, the RL band quenches with an activation energy of about 15 meV. The quenching of the RL band apparently causes the emergence of the GL band (Figure 3.25). This may be a result of competition for holes between the acceptors responsible for the GL and RL bands. At $T > 200$ K, the GL band quenches rapidly, so that the RL band is observed alone at room temperature (Figure 3.25). Preliminarily, results of transient PL demonstrate that the low-temperature PL decay of the RL band is nearly exponential with a characteristic time of about 1 μs.

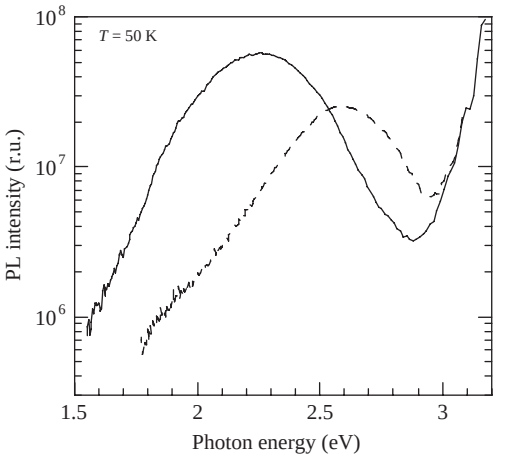

Figure 3.24 PL spectrum of undoped bulk ZnO annealed at 150 °C in air for 1 h. Solid (dashed) curve – after (before) HeCd irradiation for 2 h with an excitation density of 0.3 W cm^{-2}. Excitation density during the measurements was 10^{-3} W cm^{-2}.

3.4 Refractive Index of ZnO and MgZnO

Knowledge of the dispersion of the refractive indices of semiconductor materials is necessary for accurate modeling and design of optical devices. The wurtzite ZnO lacks cubic symmetry and therefore has anisotropic optical properties, as in the case of nitride semiconductor. The anisotropy results in uniaxial birefringence, two different refractive indices for polarization parallel (n_o-ordinary) and perpendicular

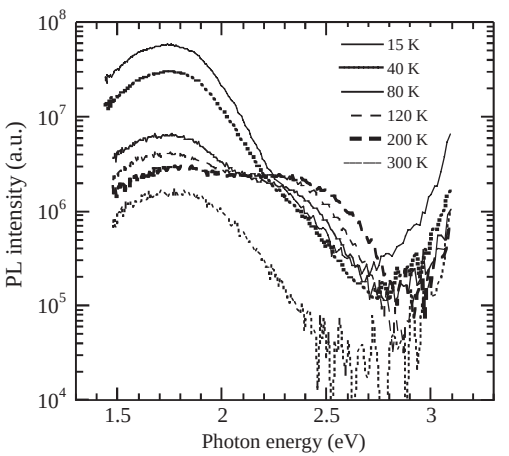

Figure 3.25 PL spectrum of undoped bulk ZnO at different temperatures. The sample was annealed at 700 °C in air for 1 h. Excitation density is 10^{-3} W cm^{-2}.

(n_e-extraordinary) to the *c*-axis. A summary of the methodologies used to measure and analyze refractive index in the form of reported results on ZnO dielectric constants and refractive index dispersion will be given in this section.

In the early 1950s and 1960s, several researchers reported the results of optical reflection measurements with light polarized parallel and perpendicular to the *c*-axis and used Kramers–Kronig analysis to determine the dielectric functions. Refractive index dispersion of single-crystal ZnO was initially reported by Mollwo [1] and Bond [11] using the method of minimum deviation at room temperature for the visible and near-infrared spectrum. Prisms fabricated from vapor transport-grown ZnO were used. For light below the direct band edge, traditional angle-of-minimum deviation methods produced very accurate values of the refractive index for both $\mathbf{E} \perp \mathbf{c}$ and $\mathbf{E} \parallel \mathbf{c}$. Park and Schneider [18] then extended the measurements to the spectral region near the onset of the exciton absorption at temperatures down to liquid helium temperature using transmission interferometry. A ZnO platelet sample (with the *c*-axis lying in the plane of the platelet) grown by vapor-phase transport was used for the measurements. By lowering the temperature, the dispersion curves were observed to get sharper and blueshifted. The refractive indices obtained at 4.2 K near the absorption edge are listed in Table 3.6.

Freeouf [14] obtained the dielectric functions above and below the bandgap by measuring the reflectivity from 0.6 to 30 eV before applying the Kramers–Kronig analysis to determine the dielectric functions. Matz and Lütz [130] determined the

Table 3.6 Some values of the refractive indices of ZnO at 4.2 K near the absorption edge.

$\mathbf{E} \perp \mathbf{c}$		$\mathbf{E} \parallel \mathbf{c}$	
λ (nm)	*n*	λ (nm)	*n*
366.43	9.843	363.71	3.525
366.72	6.734	365.67	2.917
367.01	9.414	367.54	2.722
369.04	3.089	369.79	2.598
371.19	2.747	371.52	2.539
373.51	2.595	373.85	2.478
375.65	2.513	375.68	2.441
377.84	2.454	377.90	2.407
379.69	2.417	380.49	2.374
381.87	2.382	381.90	2.358
385.86	2.332	383.44	2.343
387.43	2.316	385.08	2.328
390.92	2.286	388.70	2.300
392.85	2.272	392.83	2.273
394.89	2.258	395.02	2.260
397.04	2.245	399.92	2.237
399.39	2.232	405.31	2.215
401.89	2.220	408.19	2.204
		411.27	2.194

(After Ref. [18].)

optical functions of ZnO by using nulling ellipsometry at several wavelengths defined by interference filters.

Hu *et al.* [131] used optical transmission to measure the optical functions of thin-film ZnO prepared by pulsed laser deposition on α-SiO_2 substrates. The ordinary refractive indices deduced from transmittance oscillations were 0.02–0.03 lower than the bulk ZnO crystal data by Bond [11]. The existence of grain boundaries in the films was assumed to be the source for this difference. In addition, the measurement technique introduced a considerably large error resulting in large variations in the data. The best fits for the ordinary index using the three-term Cauchy equation,

$$n(\lambda) = A + \frac{B}{\lambda^2} + \frac{C}{\lambda^4}, \tag{3.105}$$

produced parameters of $A = 1.9281$, $B = -1.1157 \times 10^{-5}\,\mu m^2$, and $C = 5.9696 \times 10^{-3}\,\mu m^4$, whereas the bulk ZnO crystal [11] was best characterized by $A = 1.9436$, $B = -1.9714 \times 10^{-5}\,\mu m^2$, and $C = 7.0918 \times 10^{-3}\,\mu m^4$.

The Kramers–Kronig technique is far less accurate than the ellipsometric technique, because it relies on less accurate data (reflectance) and requires extrapolations to perform the Kramers–Kronig integrals. Measurements of complex dielectric functions later on were reported by Yoshikawa and Adachi [132] using spectroscopic ellipsometry in the photon energy range of 1.5–5.0 eV at room temperature. Samples grown by vapor-phase methods with surfaces oriented parallel to the *c*-axis were used and the data in the transparent region of ZnO were analyzed. The data for polarization parallel ($\mathbf{E} \,||\, \mathbf{c}$) and perpendicular ($\mathbf{E} \perp \mathbf{c}$) to the optical axis are shown in Figure 3.26 along with the data from Mollwo [1] and Bond [11]. Also shown in the figures are fits to a first-order Sellmeier equation:

$$n(\lambda)^2 = A + \frac{B\lambda^2}{\lambda^2 - C^2}, \tag{3.106}$$

where A, B, and C are the fitting parameters and λ is the wavelength. Best fits were obtained for $A = 2.84$, $B = 0.84$, and $C = 0.319\,\mu m$ for $\mathbf{E} \perp \mathbf{c}$ and $A = 2.85$, $B = 0.87$, and $C = 0.310\,\mu m$ for $\mathbf{E} \,||\, \mathbf{c}$.

Jellison and Boatner [133] employed a two-modulator generalized ellipsometry (2-MGE) technique to determine the anisotropic optical functions of ZnO, using samples grown by chemical-vapor transport and hydrothermal methods. Near and above the band edge, the resulting dielectric functions from both samples were identical within the experimental error, whereas the refractive indices of the hydrothermal-grown sample were $\sim 0.012 \pm 0.007$ smaller than the refractive index of the vapor transport-grown sample from 850 to 450 nm. 2-MGE is claimed to produce the most accurate results above the band edge, particularly more accurate than the results by Freeouf [14] in the measured spectral region of 3.3–5.0 eV, while the refractive indices determined below the direct band edge agree with the minimum deviation methods [11] within an accuracy of ± 0.003.

Refractive indices of $Mg_xZn_{1-x}O$ alloy, films grown on *c*-plane sapphire substrates by pulsed laser deposition, have been determined using the prism-coupled waveguide technique by Teng *et al.* [134]. Measurements were performed for samples with x up to 0.36 in the wavelength range of 457–968 nm. The results are shown in Figure 3.27a for

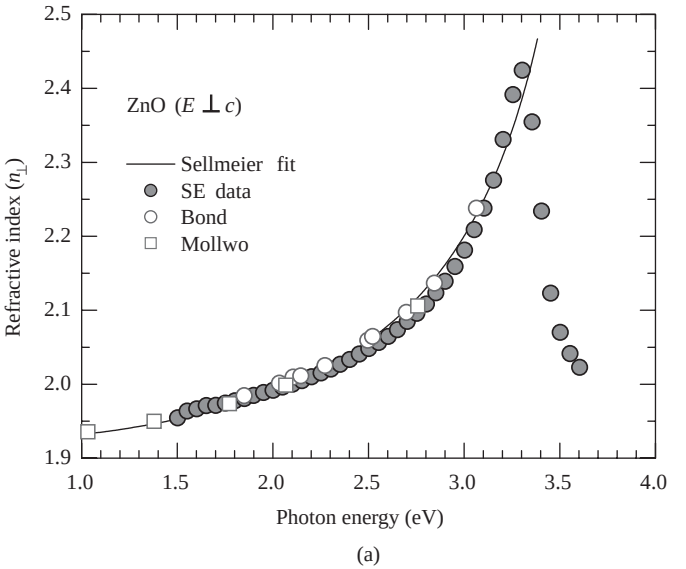

(a)

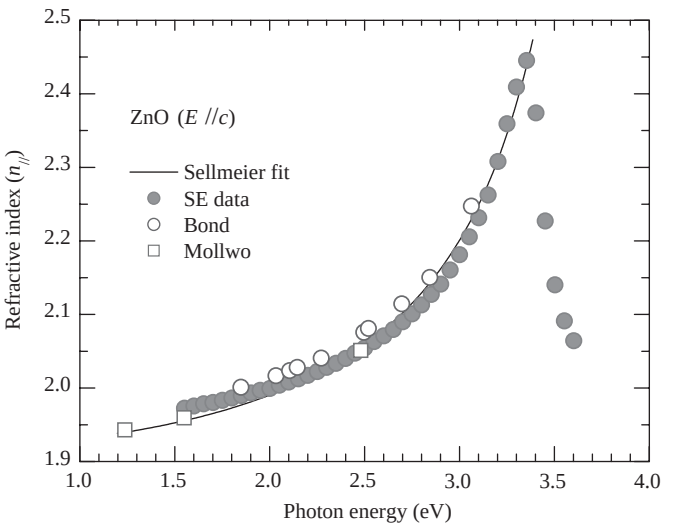

(b)

Figure 3.26 Refractive index dispersion of ZnO for (a) $E \perp c$ and (b) $E \parallel c$ below the fundamental absorption edge. The solid circles represent the spectroscopic ellipsometry data of Yoshikawa and Adachi [132]. The open circles and open squares represent the data obtained by Bond [11] and Mollwo [1] respectively. (After Ref. [132].).

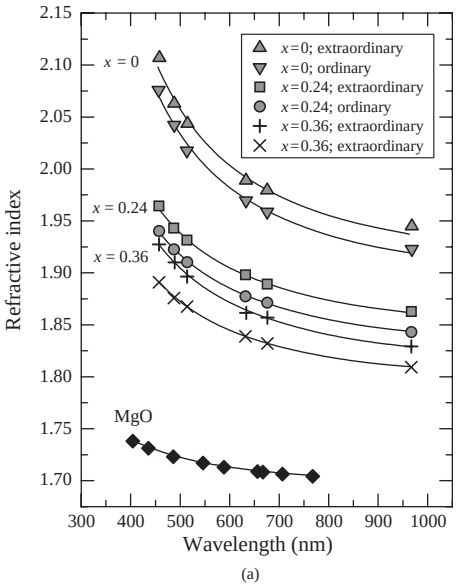

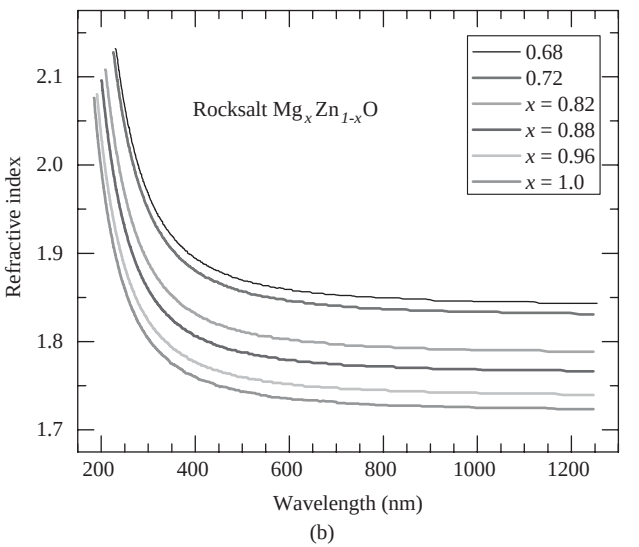

Figure 3.27 (a) The ordinary and extraordinary refractive indices of $Mg_xZ_{1-x}nO$ films ($x = 0$, 0.24, and 0.36). The solid curves are least-square fits to the first-order Sellmeier dispersion. The index of refraction of cubic MgO crystal measured by Stephens and Malitson [17] is also plotted for comparison. (Courtesy of Ü. Özgür [134].) (b) Refractive index for rocksalt $Mg_xZn_{1-x}O$ with x-values in the range of 0.68–1.0. (The data courtesy of M. Schubert.)

Table 3.7 Sellmeier coefficients for $Mg_xZn_{1-x}O$ films.

	Parameter	$x = 0$	$x = 0.24$	$x = 0.36$
Ordinary index	B	2.60 ± 0.02	2.37 ± 0.003	2.27 ± 0.004
E ⊥ c	C (μm)	0.2114 ± 0.0037	0.1793 ± 0.0012	0.1686 ± 0.0008
Extraordinary index	B	2.66 ± 0.02	2.43 ± 0.01	2.32 ± 0.01
E || c	C (μm)	0.2143 ± 0.0051	0.1815 ± 0.0016	0.1801 ± 0.0016

(After Ref. [134].)

the ordinary (**E ⊥ c)** and the extraordinary (E || c) refractive indices. The data were fit by the least-square method to the first-order Sellmeier dispersion relationship with $A = 1$ in Equation 3.106. The data for the ZnO sample were best characterized with fitting parameters $B = 2.60 \pm 0.02$ and $C = 0.2114 \pm 0.0037$ μm for the ordinary index and $B = 2.66 \pm 0.02$ and $C = 0.2143 \pm 0.0051$ μm for the extraordinary index. The Sellmeier parameters for $Mg_xZn_{1-x}O$ films are summarized in Table 3.7. Shown in Figure 3.27b are the refractive indices for a range of rocksalt $Mg_xZn_{1-x}O$ with Mg mole fractions of $x = 0.68$, 0.72, 0.82, 0.88, 0.92, and 1.0.

One of the reports of dielectric functions of ZnO is that by Ashkenov *et al.* [135] who characterized thin films grown by pulsed laser deposition on *c*-plane sapphire and a single-crystalline sample grown by seeded chemical vapor transport method. The static dielectric constant was obtained from infrared spectroscopic ellipsometry measurements. The high-frequency dielectric constant was calculated through the Lyddane–Sachs–Teller (LST) relation, $\frac{\varepsilon(\omega)}{\varepsilon(\infty)} = \frac{\omega_{LO}^2}{\omega_{TO}^2}$ (Equation 1.31), using the static constant and the TO- and LO-phonon mode frequencies. The results are compared with the data from some of the previous studies in Table 3.8.

Schmidt *et al.* [136] also reported room-temperature spectroscopic ellipsometry results on pulsed laser deposition-grown wurtzite $Mg_xZn_{1-x}O$ ($0 < x < 0.29$) thin films. The refractive index data were fit to a three-term Cauchy approximation type formula (Equation 3.105), and the anisotropic Cauchy model parameters A, B, and C for ZnO were obtained as 1.916, 1.76, and 3.9 for E ⊥ c and 1.844, 1.81, and 3.6 for

Table 3.8 Static and high-frequency dielectric constants of ZnO.

sample		Ashkenov *et al.* [135] Thin film	Ashkenov *et al.* [135] Bulk	Teng *et al.* [134] Thin film	Yoshikawa and Adachi [132] Bulk	Bond [11] Bulk
ε_0[a]	$E \perp c$	7.46	7.77	7.44	7.61	7.65
	$E \parallel c$	8.59	8.91	8.36	8.50	8.57
ε_∞	$E \perp c$	3.61	3.70	3.60	3.68	3.70
	$E \parallel c$	3.76	3.78	3.66	3.72	3.75

[a]Calculated via the LST relation with the phonon mode parameters obtained by Ashkenov *et al.* [135].

Table 3.9 Cauchy model parameters for the $Mg_xZn_{1-x}O$ alloy system.

	A	*B* (10^{-2} µm^2)	*C* (10^{-3} µm^4)	*a*	*b* (10^{-2} µm^2)	*c* (10^{-3} µm^4)
$E \perp c$	1.916	1.76	3.9	−0.574	−4.51	−4.90
$E \parallel c$	1.844	1.81	3.6	−0.782		

(Schmidt *et al.* [136].)

E || c, respectively. For the $Mg_xZn_{1-x}O$ alloy system, linear dependence of the Cauchy parameters on x was assumed:

$$n(\lambda) = A + ax + \frac{B + bx}{\lambda^2} + \frac{C + cx}{\lambda^4}. \tag{3.107}$$

The coefficients b and c were found isotropic, and the parameters obtained from fits to Equation 3.107 are listed in Table 3.9. Surprisingly, for all the $Mg_xZn_{1-x}O$ thin films investigated the birefringence was found negative unlike ZnO, which showed positive birefringence (0.05) in the transparency region. This change of the sign of the birefringence going from ZnO to the $Mg_xZn_{1-x}O$ alloy system is in contrast to the results reported by Teng *et al.* [134], where a positive birefringence of approximately 0.025 for ZnO and $Mg_xZn_{1-x}O$ for all Mg contents was found. When compared to the ZnO data by Teng *et al.* [134], Jellison and Boatner [133], Yoshikawa and Adachi [132], and Hu *et al.* [131], the ZnO ordinary and extraordinary refractive index values of Schmidt *et al.* [136] are about 0.02 lower and 0.03 higher, respectively, up to 700 nm, and the birefringence is larger.

3.5 Stimulated Emission in ZnO

Even though n- and later on p-type doping have been reported in ZnO thin films [137], there is no demonstration of electrically pumped lasing in ZnO-based structures. However, optically pumped stimulated emission (SE) has been observed by many researchers from ZnO epitaxial layers grown by a variety of methods [138–141]. There have also been earlier demonstrations, dating back to 1966, of SE and lasing in vapor-grown ZnO platelets, which were cleaved parallel to the *c*-axis and pumped by an electron beam [142–144].

Fabrication of low dimensional structures such as quantum wells and dots has been the focus of semiconductor laser research to decrease the threshold for lasing. Efficient stimulated emission may be obtained from these quantum structures because the transfer integral at the band edge is larger than that of the bulk semiconductor. Excitonic emission may also be used to obtain efficient lasing, which may be realized for ZnO due to its larger exciton binding energy compared to other wide bandgap semiconductors. Exciton–exciton scattering-induced stimulated emission is very important for the realization of low-threshold lasers because it occurs at a threshold lower than that for the electron hole plasma (EHP) recombination. The

demonstration of SE with excitonic origin paves the way for the realization of blue-violet laser diodes based on ZnO.

In the intermediate excitation density regime emissions due to biexcitonic, exciton–exciton, and exciton–carrier interactions may be observed. The inelastic collision between the excitons results in an exciton excited into a higher state and a photon with energy [145]:

$$E_n = E_{ex} - E_B^{ex}\left(1 - \frac{1}{n^2}\right) - \frac{3}{2}k_B T \quad (n = 2, 3, 4, \ldots, \infty), \tag{3.108}$$

where E_{ex} is the free exciton energy, E_B^{ex} is the binding energy of the exciton, n is the quantum number of the envelope function, and $k_B T$ is the thermal energy. Equation 3.108 gives 99 meV, which is in good agreement with the experimental results that will be discussed below. At very high excitation intensities, an EHP forms beyond the "Mott density," which is calculated as [138]

$$n_M = \frac{k_B T}{2a_B^3 E_B^{ex}} \sim 3.7 \times 10^{19}\ \mathrm{cm}^{-3}, \tag{3.109}$$

where $a_B = 18$ Å is the exciton Bohr radius and $E_B^{ex} = 60$ meV is the exciton binding energy of ZnO. Therefore, depending on the excitation intensity and the quality of the samples, SE originating from exciton interactions and/or EHP recombination can be observed.

Earliest experimental observations of SE and lasing in ZnO was reported under electron beam pumping for platelets prepared from vapor, with optical cavities formed by cleaving two surfaces parallel to the *c*-axis and perpendicular to the grown faces [142–144, 146]. Pulsed operation was demonstrated with emission in the UV at temperatures near [142, 143] and above [144] liquid nitrogen temperature. By investigating the spectral position of the SE peaks, Packard *et al.* [143] suggested that the laser emission is due to the annihilation of a bound exciton below 60 K and the annihilation of a free exciton with the simultaneous emission of one LO-phonon at 77 K. The required exciton density for SE in ZnO at 77 K was calculated as $10^{17}\ \mathrm{cm}^{-3}$. Iwai *et al.* [144] could observe SE at higher temperatures with the SE peak shifting to longer wavelength side more than the A-exciton LO line and argued that above 180 K the SE is due to the annihilation of a free exciton assisted by two LO-phonons.

These reports were followed by demonstrations of optically pumped lasing in ZnO [147, 148]. Using an Xe laser, Johnston [147] reported SE at 275 K from ZnO platelets but was unable to explain the data by exciton–LO-phonon theories. Later on, Reynolds *et al.* [149] showed optically pumped lasing in as-grown ZnO platelets using an HeCd laser with very low pump power ($4\ \mathrm{W\,cm}^{-2}$) at 2 K. Extremely well-formed lasing modes were observed from which a changeover from absorption to emission could be clearly detected.

As better quality ZnO layers and epitaxial cavities became available, more detailed investigations of optically pumped SE appeared in the literature. SE and lasing, which could survive even at temperatures as high as 550 K, have been observed by Bagnall *et al.* [139, 150] in ZnO thin films grown by plasma-enhanced

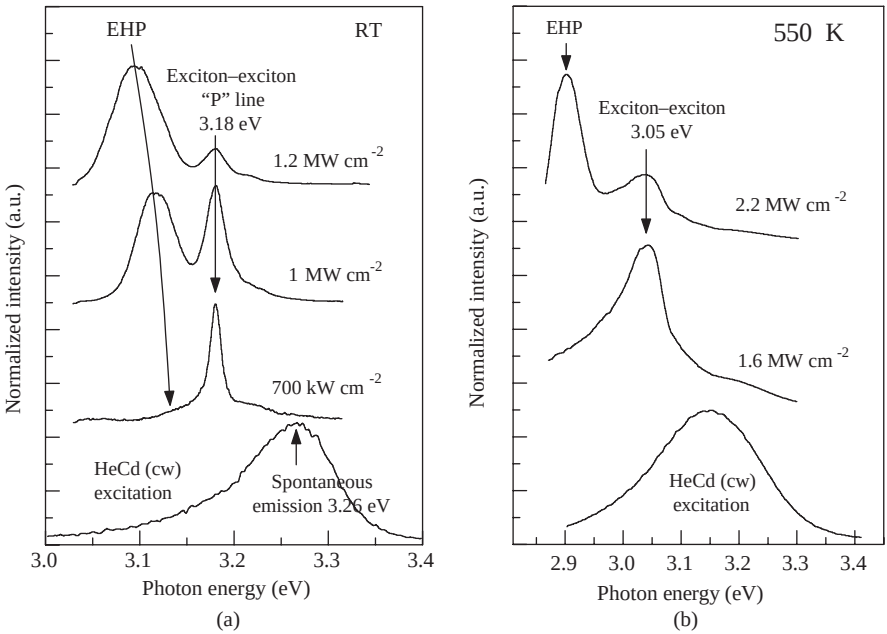

Figure 3.28 Normalized PL spectra for various excitation intensities (a) at room temperature and (b) at 550 K. (After Ref. [139].)

MBE on *c*-plane sapphire. At room temperature, for excitation intensities exceeding 400 kW cm^{-2}, the exciton–exciton scattering-related SE peak appeared at 3.18 eV and grew superlinearly. At higher excitation intensities (800 kW cm^{-2}), the electron–hole plasma peak appeared at 3.14 eV and broadened and redshifted due to bandgap renormalization with further increase in the excitation intensity. The thresholds for the SE lines were 1.2 and 1.9 MW cm^{-2} for the exciton–exciton scattering and EHP mechanisms, respectively. Figure 3.28 shows the SE observed at room temperature and at 550 K.

Bagnall *et al.* [151] reported optically pumped room-temperature lasing from cleaved ZnO cavities even though they were unable to observe the longitudinal cavity modes directly. In a later study [150], they could clearly see a very strong and stable mode structure on the room-temperature EHP emission peak of one of the ZnO epitaxial layers (see Figure 3.29). Although its origin was not explicitly identified, the lasing was claimed to be produced by a naturally formed or "accidental" ~70 μm cavity as calculated from the 0.5-nm mode spacing. In the same samples, pump-probe measurements revealed that the optical gain forms when photoexcited hot carriers cool down to an EHP state [140]. Yu and coworkers [141] also observed optically pumped lasing in 60-nm thick microcrystalline ZnO films grown on *c*-plane sapphire by laser MBE. However, the lasing mechanism was attributed to inelastic exciton–exciton scattering and a peak gain of 300 cm^{-1} was observed at a fluence of 3.8 μJ cm^{-2}. Although different optical pumping conditions could be a reason for the

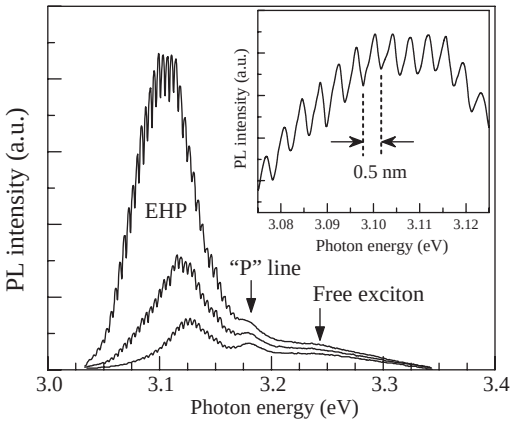

Figure 3.29 Room-temperature laser emission spectra. Inset shows clearly resolved modes. (After Ref. [150].).

observed discrepancy, the different crystal properties of the investigated epitaxial layers should also play a critical role in lasing mechanisms.

Özgür *et al.* [152] have shown that ZnO layers deposited directly on *c*-plane sapphire substrates by RF magnetron sputtering could have optical quality sufficient for excitonic laser action. Pulsed excitation, time-integrated PL (TIPL) was performed using ∼100 fs pulses at room temperature with average excitation energy densities varying between 5 and 700 μJ cm^{-2}. To obtain the SE thresholds (I_{th}), the spectrally integrated PL intensities were plotted as a function of the pump energy density. SE features were observed for the samples annealed above 800 °C. However, the as-grown samples didn't show any sign of SE for the maximum energy density used. The spectrally resolved TIPL for the sample annealed at 1000 °C is shown in the inset of Figure 3.30. For excitation densities above ∼50 μJ cm^{-2}, SE emerges at 3.167 eV as a sharp feature on the lower energy side of the SPE peak and grows superlinearly. This SE peak has been attributed to exciton–exciton scattering and lies below the free exciton energy by an exciton binding energy and the mean kinetic energy 3/2 k_BT [138, 139], where k_BT is the thermal energy. This peak then slightly redshifts to 3.160 eV because the inelastic exciton–exciton scattering leaves one exciton in an excited state which in turn reduces the emission energy of the recombining exciton [138]. As the excitation density is increased above 250 μJ cm^{-2}, a second peak emerges at 3.133 eV due to SE from the EHP. At these higher excitation densities, exciton wave functions start to overlap due to the increase in their density. Phase space filling and Coulomb interactions cause excitons to lose their individual character by ionization and eventually an EHP is formed. This EHP-induced SE peak shifts and broadens with increasing excitation as a result of bandgap renormalization. The coexistence of the exciton–exciton scattering and the EHP originates from the spatial nonuniformity of the sample as well as the laser beam profile, that is, the EHP and the exciton–exciton scattering-induced SE may come from different regions of the sample excited by the laser.

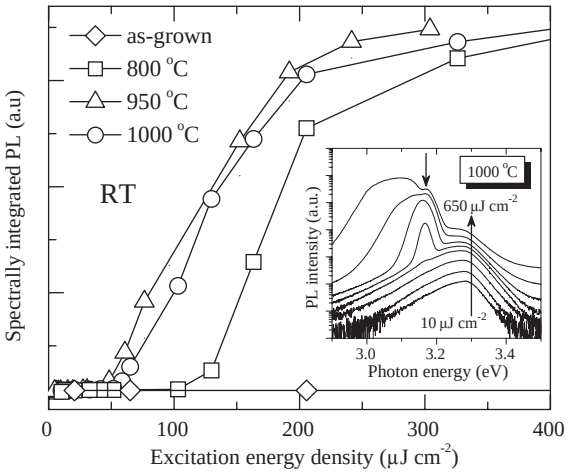

Figure 3.30 Room-temperature spectrally integrated PL for the ZnO samples normalized to the spontaneous emission. The inset shows the spectrally resolved PL for the 1000 °C sample for different excitation densities. The downward arrow in the inset indicates the exciton–exciton scattering-induced SE peak. (After Ref. [152].)

Özgür *et al.* [152] observed the SE peak attributed to exciton–exciton scattering also for another RF-sputtered sample annealed at 950 °C but not for the sample annealed at 800 °C. Due to the existence of exciton–exciton scattering, I_{th} for the 950 and 1000 °C samples (49 and 58 μJ cm^{-2}, respectively) were significantly lower than that for the 800 °C sample (130 μJ cm^{-2}). Figure 3.30 shows the PL data spectrally integrated between 3.1 and 3.4 eV for all the samples.

By using the variable stripe length method, Chen *et al.* [138] measured the optical gain spectrum of ZnO epilayers, which were grown on *c*-plane sapphire by P-MBE employing a thin MgO buffer layer. The sharp increase of the emission intensity with excitation stripe length indicates the presence of optical gain. Considering a one-dimensional amplifying medium, the spectra were analyzed by fitting to the equation

$$I(E) = \frac{I_0}{g}\left(e^{gL} - 1\right), \tag{3.110}$$

where g stands for the optical gain coefficient and L stands for the length of the excitation stripe. The evaluated optical gain as a function of photon energy is plotted in Figure 3.31. At an excitation density of 180 kW cm^{-2}, which is close to I_{th}, the peak gain is about 40 cm^{-1} and it increases to 177 cm^{-1} with a redshift of about 6 meV as the excitation density is increased to 220 kW cm^{-2}. The EHP peak appears at 3.135 eV with further increase of the excitation density to 300 kW cm^{-2}. Therefore, Chen *et al.* [138] argued that the observed optical gain resulted from the exciton–exciton scattering. For similar excitation densities, the peak gain seems smaller than that reported by Yu *et al.* [141], which may result from different pumping conditions as well as the lack of light confinement in some of the samples.

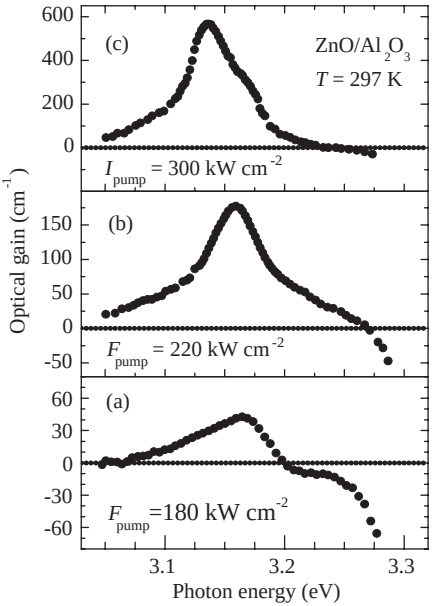

Figure 3.31 Optical gain spectrum of a ZnO epilayer at excitation density of (a) 180 kW cm^{-2}, (b) 220 kW cm^{-2}, and (c) 300 kW cm^{-2} at RT. (After Ref. [138].)

Yu *et al.* [141] have also investigated the effect of film thickness on the optical gain. The film also forms the propagation medium in the waveguide structure, and its thickness determines the mode of propagation. They attributed the large gain to the modification of the spontaneous emission rate by the dielectric planar waveguide structure of thin-film waveguides consisting of a thin ZnO layer ($n_2 = 2.45$) surrounded by air ($n_1 = 1$) on one side and sapphire ($n_3 = 1.8$) on the other. The film thickness values d, below which a guided mode of order m ceases to exist, can be calculated using the following expression:

$$\left(\frac{d}{\lambda}\right)_{\mathrm{TE}} = \frac{1}{2\pi\sqrt{n_2^2 - n_3^2}}\left[m\pi + \tan^{-1}\left(\frac{n_3^2 - n_1^2}{n_2^2 - n_3^2}\right)^{1/2}\right], \tag{3.111}$$

where λ is the wavelength in ZnO. For a thickness of 60 nm, only the TE_0 mode is supported; therefore, lasing emission should be TE polarized. For sufficiently thin films where the lowest order TE-guided mode exists, the spontaneous emission mostly goes into the TE_0 mode. This results in an increase in the SE and a reduction in the lasing threshold. There is an optimum thickness where the emission rate is maximum, and for thinner films this rate decreases rapidly and reaches zero at a cutoff value. Because all guided modes cease to exist below a finite layer thickness, no lasing occurs in very thin samples. According to Equation 3.111, the cutoff and the lowest threshold occur at thickness values of 29 nm and 55 nm, respectively, consistent with the observations of Yu *et al.* [141]. Figure 3.32 shows the lasing

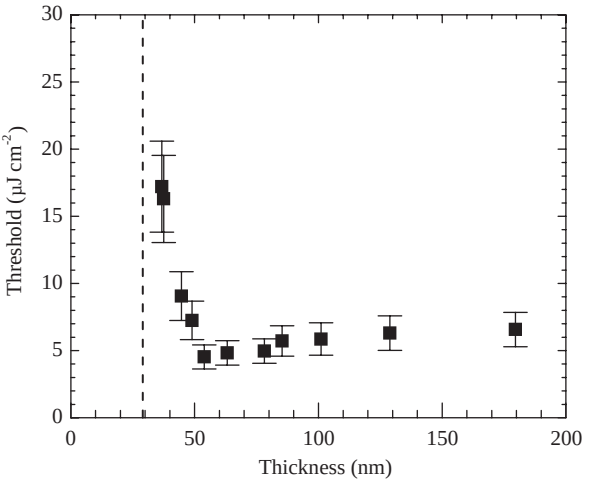

Figure 3.32 Lasing threshold as a function of film thickness. A 500 μm × 30 μm excitation stripe was used. Thickness values were determined from RHEED pattern intensity oscillations. (After Ref. [141].)

threshold as a function of the film thickness. As observed in this figure, the discrepancy in the threshold values from different measurements may also be due to varying thickness.

Kawasaki *et al.* [153] and Zu *et al.* [154] investigated the effects of nanocrystal size on stimulated emission in ZnO thin films fabricated on *c*-plane sapphire substrates by laser MBE. The films having small nanocrystal size of about 50 nm showed excitonic SE as well as the SE from the EHP. The spontaneous emission generated by exciton–exciton collisions, which showed a quadratic intensity dependence, was followed by SE from the same process at higher excitation intensities exhibiting an eighth power dependence. With further increase of the excitation intensity, the Coulomb interaction leads to ionization of excitons and the formation of a dense EHP. Therefore, the intensity of the excitonic SE peak is observed to reduce. This was not observed in previously mentioned reports due to the sample inhomogeneity. Another major observation was that, unlike the EHP-induced SE, the exciton–exciton scattering-induced SE was not present in the films having larger nanocrystal size. Kawasaki *et al.* [153] concluded that there is an optimum hexagonally shaped microcrystalline size of $(50\,\text{nm})^3$ for observing excitonic SE. Analyzing similar results, Ohtomo and coworkers [155] speculated that the excitonic-stimulated emission is due to the giant oscillator strength that can occur in high-quality nanocrystals with a dimension larger than the exciton Bohr radius (~2 nm) but smaller than the optical wavelength (390 nm). For large grain samples, the exciton supperradiance effect becomes weak such that exciton–exciton collision process should not occur. Thus, the grain boundaries between nanocrystals are considered to serve as barriers resulting in the confinement of excitons in nanocrystals.

In high-quality ZnO epitaxial films grown by MBE on GaN templates, biexciton formation was also reported and radiative recombination of the biexciton state was observed at ~3.35 eV for excitation densities lower than the threshold for exciton–exciton scattering-related SE [156]. The spectral shape of the biexciton PL, $I_{XX}(E)$, is generally expressed by an inverse Boltzmann distribution function,

$$I_{XX}(E) \propto \sqrt{E_X - E_B^{XX} - E}\exp\left(-\frac{E_X - E_B^{XX} - E}{kT}\right), \tag{3.112}$$

where E_X, E_B^{XX}, k, and T are the energy of the exciton state, biexciton binding energy, Boltzmann factor, and effective temperature, respectively. From fitting to the experimental data taken at 88 K, the biexciton binding energy, E_B^{XX}, was obtained as 15 meV. To confirm the biexcitonic origin of the luminescence peak at ~3.35 eV, Yamamoto *et al.* [156] measured the PLE spectrum. They observed a peak at ~3.370 eV due to one-photon excitonic absorption (X) and a shoulder at around 3.363 eV. This shoulder was thought to be due to two-photon absorption (TPA) of the biexciton state, because the giant oscillator strength of two-photon absorption is expected to occur at $E_X - E_B^{XX}/2 = 3.3625$ eV. Because the one-photon absorption band is broad, one- and two-photon absorptions presumably occur simultaneously in the energy region of the two-photon resonance. The broadening of the two-photon absorption band may result from local strain in the ZnO films. Thus, a shoulder rather than a clear PLE peak of two-photon absorption is seen. Therefore, the biexciton binding energy was verified to be 15 meV, which is close to the 14.7 meV value reported by Hvam *et al.* [157].

As shown in Figure 3.33, luminescence due to the radiative recombination of localized biexcitons has also been observed for the MQW (multiple quantum well) samples discussed in Section 3.5.2 at low temperatures (5 K) [158]. The excitation threshold for biexciton emission (denoted by XX) was significantly lower than that for exciton–exciton scattering (denoted by *P*) and decreased significantly (to less than 50%) when the well width was reduced from 3.7 to 1.75 nm. The average biexciton binding energies were determined from the energy separation of the localized exciton (denoted by X) and XX peaks to be 19 and 28 meV for MQWs with well widths of 3.7 and 1.75 nm, respectively. Both of these values are larger than the bulk biexciton binding energy of 15 meV. In view of the thermal activation energy at $T = 300$ K (25 meV), it is expected that the biexcitonic effect in ZnO-based quantum structures can play an important role at higher temperatures or even room temperature, which is desirable for the realization of ultralow-threshold lasers.

3.5.1 Polycrystalline ZnO Films and "Random Lasers"

As previously observed in Ti:Sapphire and TiO_2 disordered systems [159, 160], there have been reports of "random lasing" in polycrystalline ZnO films as a result of strong scattering in disordered dielectric media [161–163]. It was shown that in the case of such strong scattering and gain, recurring scattering events could provide coherent

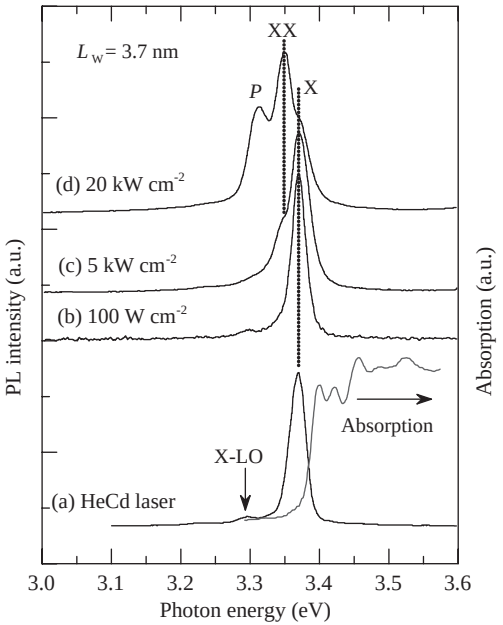

Figure 3.33 PL spectra at 5 K taken from a ZnO/$Zn_{0.74}Mg_{0.26}O$ MQW with barrier/well widths of 5/3.7 nm. The lowest traces represent the low-excitation PL and absorption spectra. (After Ref. [158].)

feedback and result in lasing [164]. When the scattering mean free path becomes equal to or less than the wavelength, photon may return to a scatterer from which it was scattered before, and thereby closed loop paths may be formed. If the amplification along such a loop path exceeds the loss, lasing could occur in the loop that serves as a resonator. Such a laser is called a "random laser," where the phase shift along the loop must be equal to a multiple of 2π. Unlike the traditional semiconductor lasers that have well-defined cavities, the random laser cavities are "self-formed" due to strong optical scattering in the polycrystalline films. The main requirement to observe this kind of laser emission is that the particle size should be less than the emission wavelength. The photon localization in this case is similar to Anderson localization of electrons in disordered systems [165].

The first observation of random laser emission in polycrystalline ZnO was made by Cao *et al.* [161, 162]. Figure 3.34 shows the evolution of the emission spectra as the pump intensity was increased [162]. At low excitation intensities, the spectrum consisted of a single broad spontaneous emission peak. As the pump power increased, the emission peak became narrower due to the preferential amplification at frequencies close to the maximum of the gain spectrum. When the excitation intensity exceeded a threshold, very narrow peaks emerged in the emission spectra. The linewidth of these peaks was less than 0.3 nm, which was more than 30 times smaller than the linewidth of the amplified spontaneous emission peak below the threshold. When the pump intensity increased further, more sharp peaks appeared.

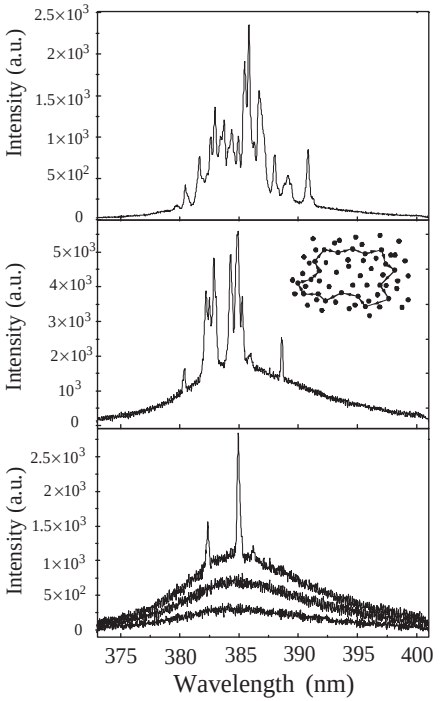

Figure 3.34 Spectra of emission from ZnO powder when the excitation intensity is (from bottom to top) 400, 562, 763, 875, and 1387 kW cm^{-2}. The thickness of the film of ZnO powder is 6 μm. The excitation area is about 1600 μm^2. The inset is a schematic diagram showing the formation of a closed loop path for light through recurring scattering in the powder. (After Ref. [162].)

The frequencies of the sharp peaks depended on the sample position, when the excitation spot was moved across the film, the frequencies of the sharp peaks changed. Above the threshold, the integrated emission intensity increased much more rapidly with the pump power, and the emission was measured to be strongly polarized indicating that laser action has occurred in the ZnO films.

The characteristics of lasing in semiconductor polycrystalline films exhibit remarkable differences from that of a conventional laser. First of all, the laser emission from the ZnO polycrystalline films can be observed in all directions, and the laser emission spectrum varies with the observation angle. Second, the pump intensity required to reach the lasing threshold depends on the excitation area. As the excitation area decreases, the lasing threshold density increases, and when the excitation area is reduced to below a critical size, lasing stops because the closed-loop paths are too short and the amplification along the loops is not high enough to achieve lasing. When the excitation area is increased, more lasing peaks emerge in the emission spectra that can be explained by forming more closed-loop paths for light and thus increasing the number of lasing modes. The shape and size of the laser

cavities change as the excitation spot is moved across the film. The size and shape of the laser resonators are determined by the optical gain coefficient, the grain size and distribution, the scattering cross section, and the boundary conditions, so the lasing frequencies vary across the film.

The microlasers have potential applications in integrated photonic circuits. The demonstration of random lasers opens up the possibility of using disordered semiconductor microstructures as alternative sources of coherent light emission. The fabrication of the conventional microlasers requires expensive state-of-the-art crystal growth and microfabrication facilities. The realization of lasing in semiconductor polycrystalline films, which are nonepitaxially grown on amorphous fused silica substrates, provides a possibility to fabricate semiconductor lasers on many different types of substrates. As a result, fabrication of such a polycrystalline film-based microlaser is much easier and less expensive than that of most microlasers. In this context, development of methods for growing high-quality polycrystalline ZnO films is important, because polycrystalline ZnO films also have many other applications as phosphors, coatings, and so on in various devices [166].

Several authors suggested very simple methods for growing polycrystalline ZnO films by oxidation of metallic Zn films deposited on different substrates [167–171]. Dimova-Alyakova *et al.* [167] obtained polycrystalline ZnO films by oxidation of metal Zn films deposited on sapphire substrates by thermal evaporation. However, the quality of the films was quite poor as judged by weak near-band-edge emission even at high excitation levels. Cho *et al.* [168] succeeded in preparing high-quality polycrystalline ZnO thin films having strong band-edge emission by oxidation of Zn films deposited on silica substrates by magnetron sputtering. Increasing the oxidation temperature from 300 to 1000 °C leads to an increase in the average grain size from 18 to 61 nm. Also as a result, the PL peak intensity increased, FWHM decreased, and the peak position redshifted (due to quantum confinement effects in grains) as shown in Figure 3.35. The PL FWHM was 107 and 23 meV for the samples annealed

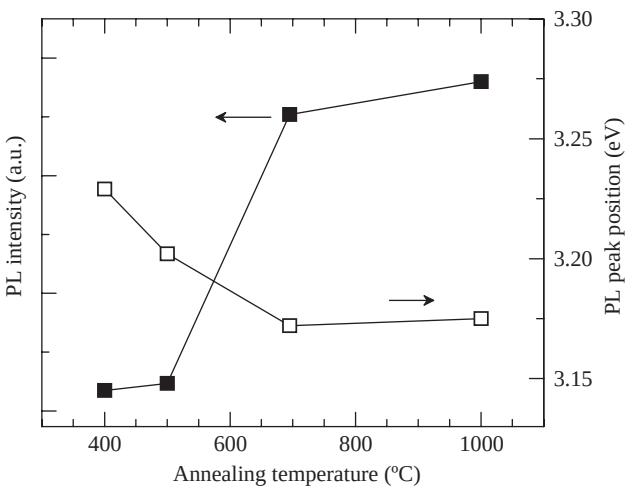

Figure 3.35 PL intensity and PL peak position versus annealing temperature. (After Ref. [168].)

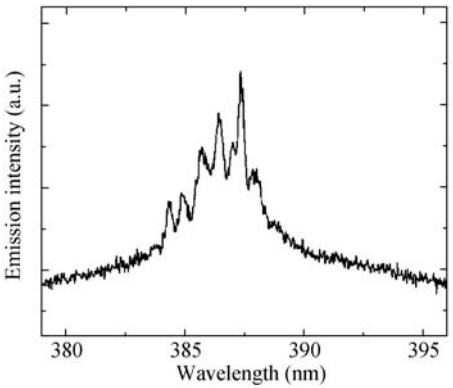

Figure 3.36 Lasing spectra of the polycrystalline ZnO thin film obtained by oxidation of metallic Zn films. The threshold intensity (I_{th}) for the lasing was ~9 MW cm^{-2}. Courtesy of J. Ketterson, and After Ref. [168].).

at 700 and 1000 °C, respectively. Optically pumped lasing action in these ZnO polycrystalline films was observed with a threshold intensity of 9 MW cm^{-2} (see Figure 3.36). These results indicate that polycrystalline ZnO thin films prepared by thermal oxidation from metallic Zn films are suitable for fabrication of random lasers (it should be mentioned that the concept of random lasers is somewhat controversial). The results reported by Chen *et al.* [169] were almost similar to those reported in Ref. [168]. However, Wang *et al.* [170] reported the optimum oxidizing temperature to be 410 °C at which the best crystallinity and the most intense PL emission were observed. The authors attributed this phenomenon to the low rate of formation of intrinsic defects at such low temperature.

Alivov *et al.* [171] studied the properties (crystal, optical, and electrical) of polycrystalline ZnO films obtained by oxidizing metallic Zn layers, which were electron beam-evaporated on various substrates. No predominating orientation was observed for the Zn and ZnO films deposited on glass, sapphire, and silica. Besides, the mean grain size, depending on the oxidation temperature, in Zn films (120 nm) as well as in the subsequent ZnO films was also independent of the substrate nature. A dramatic improvement of the PL with increasing oxidation temperature was observed as in Ref. [168]. The effect of oxygen partial pressure was studied recording the RT CL spectra of selected ZnO films oxidized at $T = 800$ °C and at different oxygen partial pressures. As seen from Figure 3.37, the UV CL intensity increased by almost a factor of 10 when the oxygen partial pressure was decreased from 760 to 5×10^{-5} Torr. FWHM of the UV CL band decreased from 125 to 81 meV in the same pressure range. When the annealing temperature was increased from 400 to 900 °C the mean grain size of the films increased from 138 to 245 nm, the resistivity ρ increased from 3.81×10^2 to 6.02×10^4 Ω cm, electron concentration decreased from 4.56×10^{15} to 7.32×10^{12} cm^{-3}, and mobility increased from 3.6 to 14.2 cm^2 V^{-1} s^{-1}. The variation of the electrical properties with the oxygen partial pressure was very small compared

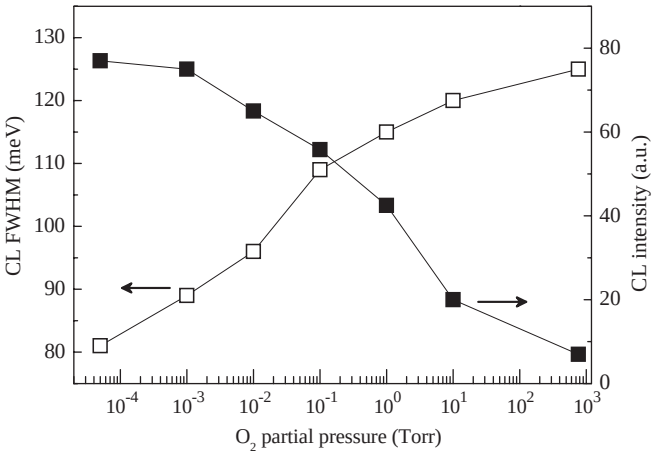

Figure 3.37 The dependences of the UV CL peak intensity and FWHM as a function of oxygen partial pressure. ($T = 300$ K, electron beam current of 1 μA was used for excitation) (After Ref. [171].)

to the oxidation temperature. The resistivity and mobility increased only by a factor of 2–4 when oxygen partial pressure was varied from 1.01×10^{-5} to 1.33×10^{-3} Pa.

3.5.2
Multiple Quantum Wells

In addition to the typical photoluminescence experiments, stimulated emission has been observed in quantum well structures utilizing the alloys of ZnO. It is expected that the observation of the excitonic SE phenomenon should be favored in quantum wells owing to the enhanced binding energy of excitons and hence by the larger stability of the exciton states. However, in other II–VI materials, SE has been mostly demonstrated only at low temperatures and rarely at room temperature. Ohtomo *et al.* [172] reported the observation of SE in ZnO/ZnMgO MQWs up to 373 K but did not elucidate the mechanism of SE. They investigated 10-period MQWs grown on $ScAlMgO_4$ (SCAM) substrates by laser MBE. The barriers were 5 nm thick, and the widths of the wells varied from 0.7 to 4.7 nm. The stimulated emission threshold was observed to increase with decreasing well width and also with increasing Mg composition in the barriers. Figure 3.38 shows the variation of the SE threshold with well width for two sets of samples having 12% and 26% Mg in the barriers.

Sun *et al.* [173] later investigated the mechanism of SE in the same MQW samples. They observed SE induced by both exciton–exciton scattering and EHP recombination. The exciton-based recombination mechanism of SE was studied further by measuring the temperature dependence of the SE peak position. It was observed that the exciton–exciton band has the same temperature dependence characteristics as that of a ZnO single layer, supporting the notion that this emission in ZnO/MgZnO MQWs is indeed due to exciton–exciton scattering. In addition, the measurements at

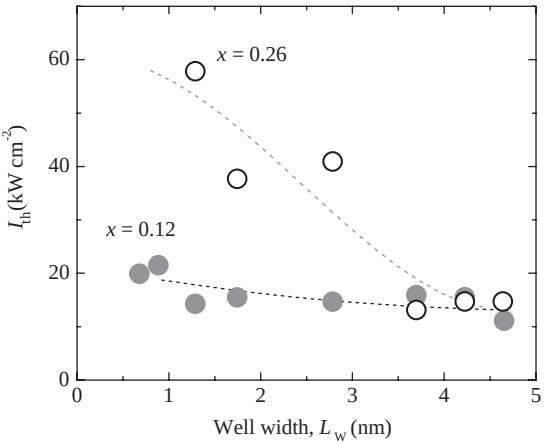

Figure 3.38 Well width (L_w) dependence of the stimulated emission threshold (I_{th}) in the superlattices with $x = 0.12$ (closed circles) and 0.26 (open circles). Stimulated emission did not take place for the $x = 0.26$ films with L_w below 1 nm because the excitation energy is lower than the absorption energy. (After Ref. [172].)

5 K revealed that the exciton binding energy increases with decreasing QW width, reaching over 100 meV for QW widths smaller than 1.75 nm in ZnO/$Mg_{0.27}Zn_{0.73}O$ MQWs with 5 nm barriers [174]. These binding energies were deduced from the energy difference between the exciton–exciton scattering-related and the free exciton emission lines.

3.6 Recombination Dynamics in ZnO

Time-resolved PL is a nondestructive, powerful technique commonly used for the optical characterization of semiconductors. The free carrier or exciton lifetime, an important parameter related to material quality and device performance, can be measured by TRPL spectroscopy. The exciton lifetimes will vary with crystal quality, becoming longer as the quality improves. The efficiency of the radiative recombination is strongly related to decay time of the particular transition.

Reynolds *et al.* [175] measured the recombination lifetime of the allowed (Γ_5) and forbidden (Γ_6, allowed by induced strain) free excitons at 2 K in a strained single-crystal ZnO grown by the hydrothermal method as 259 and 245 ps, respectively. The lifetime for the Γ_5 exciton was slightly higher, 322 ps, for an unstrained sample. They noted that free-exciton lifetimes are determined not only by the radiative decay but also by the nonradiative decay and capture processes leading to bound excitons [66]. Evidently, the measured single exponential decays reflect the effects from all three.

Teke *et al.* [50] measured the room-temperature TRPL from bulk ZnO samples; one as-received from Cermet, Inc. and the other annealed in forming gas. Figure 3.39

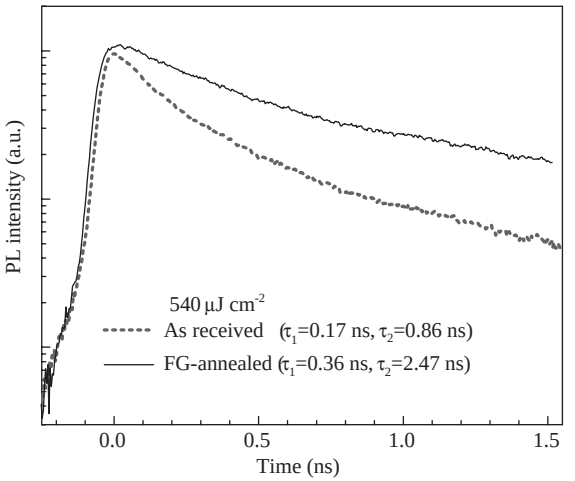

Figure 3.39 Room-temperature time-resolved PL data for the as-received and the forming gas-treated samples. (After Ref. [50].)

shows the TRPL data for both samples at an excitation energy density of 540 μJ cm^{-2}. The instrument-limited rise implies that the relaxation processes to cool the carriers from 3.81 eV excitation energy-defined states to the zero momentum excitonic band-edge states are very fast. For both samples, the decaying part of the TRPL data was well described by a biexponential decay function: $A_1 \exp(-t/\tau_1) + A_2 \exp(-t/\tau_2)$. Table 3.10 summarizes the decay constants and the amplitude ratios obtained from the fits.

The fast decay constant τ_1 is smaller for the as-received sample (170.4 ps) and most probably represents the effective nonradiative recombination at room temperature. The slow-decaying component is attributed to the radiative lifetime of the free exciton. The 0.86 ns value measured for the as-received sample is reasonably consistent with the 0.97 ns value measured by Koida *et al.* [176] for single-crystal ZnO. The relative magnitude of the slow-decaying component to the fast-decaying component ($A_2/A_1 = 0.094$ for 540 μJ cm^{-2}) for the as-received sample suggests that the nonradiative processes are dominant. It has been proposed that the nonradiative

Table 3.10 TRPL decay time constants and amplitude ratios for the ZnO samples at two different excitation energy densities.

		540 μJ cm^{-2}			54 μJ cm^{-2}		
	Samples	τ_1 **(ps)**	τ_2 **(ps)**	A_2/A_1	τ_1 **(ps)**	τ_2 **(ps)**	A_2/A_1
300 K (FX)	As-received	170.4 ± 1.8	863.9 ± 14.8	0.094	116.5 ± 1.5	585.0 ± 6.4	0.060
	FG-annealed	358.7 ± 8.8	2469 ± 256	2.536	428.3 ± 32.1	2969 ± 115	2.476
85 K (DBE)	As-received	310.2 ± 2.5	1130 ± 6.6	0.653	286.8 ± 2.9	1000 ± 5.9	0.820
	FG-annealed	474.0 ± 5.5	1285 ± 14.6	0.614	366.4 ± 4.1	1021 ± 7.3	0.869

FX and DBE denote the free and donor-bound excitons, respectively. (After Ref. [50].)

recombination processes are governed by the defects introduced by the Zn vacancy complexes [176]. After forming gas annealing the decay constants increased remarkably ($\tau_1 = 0.86$ ns, $\tau_2 = 2.47$ ns), and the slow-decaying component became dominant ($A_2/A_1 = 2.54$ for 540 μJ cm^{-2}), suggesting an increase in radiative recombination. This is also supported by the fact that the PL intensity increased by almost a factor of 4 in the forming gas-annealed ZnO sample compared to the as-received one. The increase in the decay times is clearly observed in Figure 3.39.

When the excitation density was decreased from 540 μJ cm^{-2} to 54 μJ cm^{-2}, Teke *et al.* [50] observed a blueshift in the PL peak by 15 meV, most probably due to reducing strength of the bandgap renormalization. For the as-received sample, the decay constants increase slightly with increasing excitation density, whereas the forming gas-treated sample follows an opposite trend. In addition, compared to the forming gas-treated sample, the as-received sample shows a more evident increase in the relative strength of the slow-decaying component when the excitation density is increased, as the nonradiative centers begin to saturate.

The decay time constants of both as-received and forming gas-annealed samples were also measured at 85 K [50]. At this temperature, the main DBE still dominates the overall continuous wave-PL spectrum even though A- and B-free excitons are clearly observed. However, a distinction between the bound and the free excitons could not be made in the TRPL measurements due to the resolution limitation of the experimental setup. Therefore, the TRPL data reflect mainly the decay due to the main DBE. To measure purely the free excitonic emission decay time, the measurements had to be performed at temperatures above 160 K where the bound exciton emission diminishes. The time constants measured at 85 K are also included in Table 3.10 for two different excitation densities. The main DBE emission lines in both samples are similar in terms of their intensities as observed from the time-integrated and the cw-PL. Compared to the as-received sample, the forming gas-annealed sample showed slightly larger decay constants. In addition, the decay times decreased with decreasing excitation energy density. In contrast to the significant improvement in free exciton lifetimes measured at room temperature, the postgrowth treatment is not observed to have a strong effect on the DBE decay times.

Epitaxial ZnO layers exhibit shorter carrier lifetimes, because they suffer from higher defect densities compared to the bulk samples. Koida *et al.* [176] studied the correlation between the excitonic PL lifetime at room temperature and point defect density in bulk and epitaxial ZnO layers. The defect density, Zn vacancy being the most probable defect, was analyzed by positron annihilation. The single-crystal sample showed biexponential behavior with decay constants of 0.97 and 14 ns, which were suggested to represent the free exciton lifetime, and the free carrier lifetime including trapping and emission processes. For ZnO epitaxial layers grown by laser MBE on $ScAlMgO_4$ (SCAM) substrates, the single-exponential TRPL decay time, which is mainly governed by nonradiative processes, increased from 46 to 110 ps with increasing growth temperature from 570 to 800 °C. However, because a homoepitaxial film exhibited the shortest decay time (36 ps) in spite of the smallest number of point defects among the epilayers, that is, no clear correlation was found between the PL decay time and the point defect density, the nonradiative process was considered

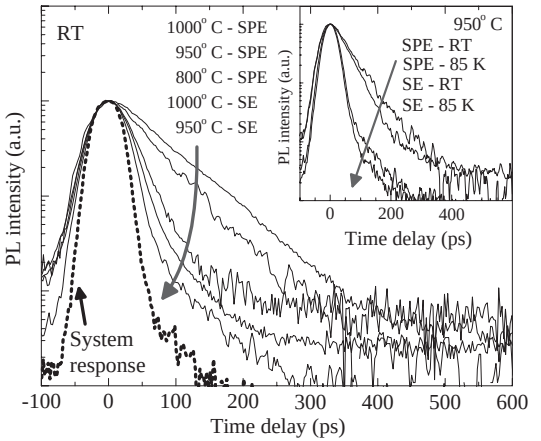

Figure 3.40 Room-temperature TRPL for the spontaneous emission and the stimulated emission from the annealed ZnO samples. The inset shows the 85 K and RT TRPL data for the sample annealed at 950 °C. (After Ref. [152].)

to be governed by certain defect species introduced by the presence of Zn vacancies such as vacancy complexes.

Jung *et al.* [177] reported biexponential decay for high-quality ZnO epitaxial layers grown on sapphire by low-pressure metalorganic vapor-phase epitaxy. Room-temperature TRPL measurements produced decay times of 180 ps and 1 ns, most probably representing the nonradiative and the radiative excitonic recombination times, respectively, consistent with the measurements of Teke *et al.* [50] and Koida *et al.* [176] on bulk ZnO samples. To investigate the effects of annealing and SE on carrier dynamics in RF-sputtered ZnO thin films, TRPL spectroscopy was employed at room temperature and at 85 K by Özgür *et al.* [152]. Figure 3.40 shows the TRPL data for three annealed samples at room temperature. The excitation densities were kept slightly below I_{th} ($\sim$30 μJ cm^{-2}) to measure the SPE decay times, while high excitation densities ($\sim$200 μJ cm^{-2}) were used to observe the recombination dynamics under the influence of SE. Single-exponential decay fits revealed the spontaneous recombination times as 74, 59, and 30 ps for the samples annealed at 1000, 950, and 800 °C, respectively. The decay time for the as-deposited sample was below the system resolution. The increase of the decay times with annealing temperature suggests a reduction in the density of nonradiative recombination centers. As expected, the SE-induced recombination occurs very fast (<30 ps). The TRPL data for above I_{th} excitations also show a much weaker and slower decaying component visible after the SE is over ($\sim$55 ps) with the characteristic decay time of the spontaneous recombination.

The spontaneous recombination times observed by Özgür *et al.* [152] for RF-sputtered ZnO thin films are comparable to other values reported in the literature. Guo *et al.* [119] reported 30 ps room-temperature excitonic recombination times for ZnO thin films grown on Si by OMVPE. Koida *et al.* [176] measured recombination

times of up to 110 ps for good quality ZnO thin films grown on $ScAlMgO_4$ substrates by MBE. These decay times, including the ones measured by Özgür *et al.* [152], are much shorter than those reported for bulk ZnO [50, 176] most probably due to effective nonradiative recombination in thin films at room temperature. Surprisingly, TRPL measurements performed on RF-sputtered ZnO thin films at 85 K didn't show any significant change in decay times. The inset in Figure 3.40 compares the room temperature and the 85 K TRPL data for the 950 °C annealed sample for both below and above I_{th}(950 °C). At 85 K, the SPE decay time is 49 ps indicating that an effective nonradiative recombination mechanism is still present. However, the characteristic single-exponential decay along with the strong photon emission suggests that the radiative decay component is also fast. The slight decrease in the decay time at 85 K may be explained by increased absorption at low temperatures and the weak carrier density dependence of the recombination times.

3.7 Nonlinear Optical Properties

We have heretofore had ample discussion of linear optical properties of ZnO and related materials. In this section, the nonlinear processes in ZnO are discussed, a topic that has been investigated in some detail. The research on nonlinear optical properties of semiconductors is motivated by electro-optic devices that can be used in telecommunications and optical computing as efficient harmonic generators, optical mixers, and tunable parametric oscillators, among others. The nonlinear optical properties such as *second harmonic generation* (SHG), that is, $(2\omega_1, 2\omega_2)$, and the *sum frequency generation* (SFG), that is, $(\omega_1 + \omega_2)$, can also be employed for materials' characterization, particularly surfaces, because the second-order susceptibility coefficient $\chi^{(2)}$ is very sensitive to the change in symmetry [178, 179]. The crystal should be of high quality to allow the measurement of nonlinear optical signals accurately. This is because the energy transfer between the incident beam and generated nonlinear optical field depends on their propagation distance in the material, and the availability of high-quality bulk ZnO allows high energy transfer efficiency.

It is instructive to first discuss the parameter defining optical nonlinearity. In an electrically polarizable material with negligible magnetic susceptibility, the electric and magnetic field vectors satisfy the following equations (in SI units)

$$\begin{aligned}
&\nabla \times \mathbf{E} = -\frac{\partial \mathbf{B}}{\partial t} \quad \text{and} \quad \nabla \times \boldsymbol{H} = \frac{\partial \boldsymbol{D}}{\partial t} \\
&\nabla \times \nabla \times \mathbf{E} = -\frac{\partial}{\partial t}\nabla \times \mathbf{B} = -\frac{\partial}{\partial t}\nabla \times \mu_0 \mathbf{H} = -\mu_0 \frac{\partial^2 \mathbf{D}}{\partial t^2} \\
&\frac{\partial}{\partial t}\nabla \times \mu_0 \mathbf{H} = -\mu_0 \frac{\partial^2 \mathbf{D}}{\partial t^2} \\
&\nabla^2 \mathbf{E} = \mu_0 \frac{\partial^2 \mathbf{D}}{\partial t^2} \quad \text{and}
\end{aligned} \tag{3.113a}$$

$$\mathbf{P} = \varepsilon_0 \mathbf{E} + \mathbf{P} = \varepsilon \mathbf{E} \quad \text{and} \quad \mathbf{P} = \varepsilon_0 \chi \mathbf{E} \quad \text{and} \quad \varepsilon = \varepsilon_0 (1 + \chi). \tag{3.113b}$$

The polarization component (**P**) can be related to the harmonics of the electric field (**E**) with help of optical susceptibly for each harmonic as [180]

$$\begin{aligned}\mathbf{P}(t) &= \varepsilon_0\chi^{(1)}\mathbf{E}(t) + \varepsilon_0\chi^{(2)}\mathbf{E}^2(t) + \varepsilon_0\chi^{(3)}\mathbf{E}^3(t) + \ldots \\ &= \mathbf{P}^{(1)}(t) + \mathbf{P}^{(2)}(t) + \mathbf{P}^{(3)}(t) + \ldots,\end{aligned} \tag{3.114}$$

where $\chi^{(1)}$ is the optical susceptibility, which describes a linear component of the relation between the incident optical field and induced electric polarization. The terms $\chi^{(2)}$ and $\chi^{(3)}$ represent the second-order and third-order optical susceptibilities, respectively. The above expressions are given in SI units, and ε_0 should be taken as 1 for cgs units. The susceptibility $\chi^{(n)}$ is also a tensor of rank $n+1$. It should be noted that often the second-order susceptibility is represented as the so-called *d* coefficient, where **d** is a tensor given by $d_{ikl} = d_{xyz} = (\chi^{(2)}_{ikl})/2$.

Now let's consider two optical fields, one along direction *k* with a frequency ω_1 and the other along direction *l* with a frequency ω_2, which are incident upon a nonlinear optical medium and can be expressed as [181]:

$$E_k^{\omega_1}(t) = \mathrm{Re}[E_k^{\omega_1} e^{-j\omega_1 t}] \quad \text{and} \quad E_l^{\omega_2}(t) = \mathrm{Re}[E_l^{\omega_2} \mathrm{e}^{-j\omega_2 t}]. \tag{3.115}$$

In a nonlinear medium, the presence of these two fields simultaneously would give rise to polarizations at frequencies of $m\omega_1 + n\omega_2$, where *m* and *n* are integers, and the polarization for the sum frequency $\omega_3 = \omega_1 + \omega_2$ along the *i*-direction can be expressed by

$$P_i^{\omega_3}(t) = \mathrm{Re}[P_i^{\omega_3} \mathrm{e}^{-j\omega_3 t}]. \tag{3.116}$$

The polarization for the sum frequency can be written by using the susceptibility tensor $\chi^{(2),\omega_3}_{ikl}$ as

$$P_i^{\omega_3} = \varepsilon_0 D^{(2)} \sum_{kl} \chi^{(2),\omega_3}_{ikl} E_k^{\omega_1} E_l^{\omega_2}. \tag{3.117}$$

Similarly, the polarization for the difference frequency $\omega_3 = \omega_1 + \omega_2$ is given by

$$P_i^{\omega_3} = \varepsilon_0 D^{(2)} \sum_{kl} \chi^{(2),\omega_3}_{ikl} E_k^{\omega_1} E_l^{-\omega_2}, \tag{3.118}$$

where from Equation 3.115 $E_l^{-\omega_2} = (E_l^{\omega_2})^*$, and $D^{(2)}$ is a degeneracy factor, which represents the number of distinct permutations of the three frequencies. $D^{(2)}$ is equal to 1 for indistinguishable fields and 2 for distinguishable fields. The negative frequency parts are considered to be distinguishable from the positive frequency parts.

In nonlinear crystals, the operation frequency band, inclusive of ω_1, ω_2, and ω_3, are chosen to fall in the transparency region; or conversely, the optical crystal is chosen so that it would have its lowest resonance frequency much larger than these frequencies. This would mean the absence of hysteresis in the dependence of electric polarization on electric field. Under these conditions, the nonlinear susceptibility is frequency independent and therefore the nonlinear polarization can be expressed by

$$P_i(t) = \varepsilon_0 D^{(2)} \sum_{kl} \chi^{(2)}_{ikl} E_k(t) E_l(t). \tag{3.119}$$

Because E_k and E_1 can be interchanged (intrinsic permutation symmetry), we can write $\chi^{(2)}_{ikl} = \chi^{(2)}_{ilk}$ or $d_{ikl} = d_{ilk}$. All the components of $\chi^{(2)}_{ikl}$ and d_{ikl} are real as the medium is lossless (transparent). Consequently, the subscripts k and l can be replaced with a single index according to piezoelectric contraction, that is, $xx = 1$, $yy = 2$, $zz = 3$, $yz = zy = 4$, $xz = zx = 5$, and $xy = yx = 6$. Therefore, the resulting 3×6 **d** tensor operates on the $\mathbf{E}^2$ column tensor to yield the polarization vector **P** as follows:

$$\begin{pmatrix} P_x \\ P_y \\ P_z \end{pmatrix} = \varepsilon_0 2 \begin{pmatrix} d_{11}\, d_{12}\, d_{13}\, d_{14}\, d_{15}\, d_{16} \\ d_{21}\, d_{22}\, d_{23}\, d_{24}\, d_{25}\, d_{26} \\ d_{31}\, d_{32}\, d_{33}\, d_{34}\, d_{35}\, d_{36} \end{pmatrix} \begin{pmatrix} E_x^2 \\ E_y^2 \\ E_z^2 \\ 2E_yE_z \\ 2E_zE_x \\ 2E_xE_y \end{pmatrix}, \tag{3.120}$$

where the susceptibility tensor elements, d_{ij}, are assumed frequency independent. The symmetry applicable to the susceptibility tensor is the same as in the piezoelectric tensor for a given crystal. In the case of a lossless medium, the full permutation symmetry also occurs, meaning that the susceptibilities are unchanged for the simultaneous permutation of subscripts from the Cartesian set $\{ikl\}$, such as $\chi^{(2)}_{ikl} = \chi^{(2)}_{kli}$. This is known as Kleinman symmetry, which is valid whenever the dispersion of the susceptibility can be neglected. Explicitly introducing the Kleinman symmetry results in only 10 independent **d** tensor elements:

$$\mathbf{d} = \begin{pmatrix} d_{11} & d_{12} & d_{13} & d_{14} & d_{15} & d_{16} \\ d_{16} & d_{22} & d_{23} & d_{24} & d_{14} & d_{12} \\ d_{15} & d_{24} & d_{33} & d_{23} & d_{13} & d_{14} \end{pmatrix}. \tag{3.121}$$

The symmetry group of ZnO is $P6_3mc$ (Hermann–Mauguin notation) and C^4_{6v} (Schoenflies notation). In optical nonlinearity nomenclature, hexagonal ZnO has class 6 mm symmetry. This being the case, many of the susceptibility tensor elements vanish. The only nonvanishing components are d_{15}, $d_{24} = d_{15}$, d_{31}, $d_{32} = d_{31}$, and d_{33}:

$$\mathbf{d} = \begin{pmatrix} 0 & 0 & 0 & 0 & d_{15} & 0 \\ 0 & 0 & 0 & d_{15} & 0 & 0 \\ d_{31} & d_{31} & d_{33} & 0 & 0 & 0 \end{pmatrix} \quad \text{for 6 mm symmetry.} \tag{3.122}$$

Under Kleinman symmetry conditions, $d_{31} = d_{15}$, and therefore the **d** tensor takes the form

$$\mathbf{d} = \begin{pmatrix} 0 & 0 & 0 & 0 & d_{15} & 0 \\ 0 & 0 & 0 & d_{15} & 0 & 0 \\ d_{15} & d_{15} & d_{33} & 0 & 0 & 0 \end{pmatrix} \quad \text{for 6 mm with Kleinman symmetry.} \tag{3.123}$$

Rewriting Equation 3.120 for ZnO with the above-mentioned vanishing elements and equalities, and replacing d_{ij} with the usual χ_{ijk} nomenclature, we obtain

$$\begin{pmatrix} P_x(2\omega) \\ P_y(2\omega) \\ P_z(2\omega) \end{pmatrix} = \varepsilon_0 \begin{pmatrix} 2\chi_{xxz}E_xE_z \\ 2\chi_{xxz}E_yE_z \\ \chi_{zxx}(E_x^2+E_y^2)+\chi_{zzz}E_z^2 \end{pmatrix}. \tag{3.124}$$

Let us represent the laser beam with an electric field of the form

$$E(t) = E_0 e^{-j\omega t} + E_0^* e^{j\omega t}. \tag{3.125}$$

The superscript (*) indicates the complex conjugate. Note that some workers in nonlinear optics use a factor of 1/2 in the definition of the fields, which is carried on to the equations to follow. The nonlinear polarization created in response to the electric field defined in Equation 3.125 is then given by (with the aid of Equation 3.114)

$$P^{(2)}(t) = \varepsilon_0\chi^{(2)}E^2(t) = (\varepsilon_0\chi^{(2)}E_0^2e^{-j2\omega t} + \text{c.c.}) + 2\varepsilon_0\chi^{(2)}E_0E_0^*. \tag{3.126}$$

where c.c. indicates the complex conjugate of the term ahead of it.

In the case of multiple laser beams incident on the nonlinear medium, sum and difference frequencies can be generated. Expressing the two electric fields of the relevant laser beams in a manner similar to that of Equation 3.125:

$$E(t) = E_1e^{-j\omega_1 t} + E_2e^{-j\omega_2 t} + \text{c.c.}, \tag{3.127}$$

where c.c. represent the complex conjugate of both fields. Applying Equation 3.126 to two electric fields yields

$$\begin{aligned} P^{(2)}(t) &= \varepsilon_0\chi^{(2)}\Big\{[E_1^2e^{-j2\omega_1 t} + E_2^2e^{-j2\omega_2 t} + 2E_1E_2e^{-j(\omega_1+\omega_2)t} \\ &\quad + 2E_1E_2^*e^{-j(\omega_1-\omega_2)t} + \text{c.c.}] + 2(E_1E_1^* + E_2E_2^*)\Big\} \\ &= \sum_n P(\omega_n)e^{-j\omega_n t}. \end{aligned} \tag{3.128}$$

The summation is carried over both positive and negative frequencies. The amplitudes of various frequency components that result can be expressed as (using the nomenclature for nonlinear susceptibility for each process)

$$\begin{aligned} P^{(2)}(2\omega_1) &= \varepsilon_0\chi^{(2)}(2\omega_1;\omega_1,\omega_1)E_1^2 \quad \text{(SHG)} \\ P^{(2)}(2\omega_2) &= \varepsilon_0\chi^{(2)}(2\omega_2;\omega_2,\omega_2)E_2^2 \quad \text{(SHG)} \\ P^{(2)}(\omega_1+\omega_2) &= 2\varepsilon_0\chi^{(2)}(\omega_1+\omega_2;\omega_1,\omega_2)E_1E_2 \quad \text{(SFG)} \\ P^{(2)}(\omega_1-\omega_2) &= 2\varepsilon_0\chi^{(2)}(\omega_1-\omega_2;\omega_1,-\omega_2)E_1E_2^* \quad \text{(DFG)} \\ P^{(2)}(0) &= 2\varepsilon_0\chi^{(2)}(0;\omega_1,-\omega_1)E_1E_1^* + 2\varepsilon_0\chi^{(2)}(0;\omega_2,-\omega_2)E_2E_2^* \quad \text{(OR)}, \end{aligned} \tag{3.129}$$

where the labels indicate the *second harmonic generation* (SHG) for ω_1 and ω_2, *sum frequency generation* (SFG), *difference frequency generation* (DFG), and *optical rectification* (OR). Similar expressions for negative frequencies can also be written. However, because they represent the complex conjugate of one of the above, it is not necessary to explicitly express them.

When the propagation and the polarization directions are fixed, it is customary to use an effective susceptibility, $d_{\text{eff}} = \chi^{(2)}/2$. The nonlinear polarization for the sum frequency ($\omega_3 = \omega_1 + \omega_2$) is then expressed as

$$P^{\omega_3} = \varepsilon_0 D^{(2)} 2 d_{eff} E^{\omega_1} E^{\omega_2}. \tag{3.130}$$

Expressions similar to the above for third harmonic generation (THG) can also be written following the same methodology. Similar to the second-order sum frequency polarization defined in Equation 3.117, the *i*th Cartesian coordinate of the third-order sum frequency polarization ($\omega_4 = \omega_1 + \omega_2 + \omega_3$) is given by

$$P_i^{\omega_4} = \varepsilon_0 D^{(3)} \sum_{klm} \chi_{iklm}^{(3),\omega_4} E_k^{\omega_1} E_l^{\omega_2} E_m^{\omega_3}. \tag{3.131}$$

The degeneracy factor $D^{(3)}$ in this case is the number of distinct permutations of the three frequencies and is equal to 1, 3, or 6 when three, two, or none of the fields are indistinguishable, respectively.

In second harmonic generation, if the incident beam(s) and the frequency-doubled beam are linearly polarized plane-waves propagating along the *z*- direction, they can be expressed in the phasor notation as

$$\begin{aligned} \mathbf{E}_1(\omega, z) &= \mathbf{A}_1(z) \mathrm{e}^{-jk_1 z}, \\ \mathbf{E}_2(2\omega, z) &= \mathbf{A}_2(z) \mathrm{e}^{-jk_2 z}. \end{aligned} \tag{3.132}$$

The corresponding polarization components of the above two waves are given by

$$\begin{aligned} \mathbf{P}^{(2)}(\omega, z) &= 2\varepsilon_0 \chi^{(2)}(2\omega, -\omega) \mathbf{E}_1^* \mathbf{E}_2 = 2\varepsilon_0 \chi^{(2)}(2\omega, -\omega) \mathbf{A}_1^*(z) \mathbf{A}_2(z) \mathrm{e}^{-j(k_2 - k_1)z}, \\ \mathbf{P}^{(2)}(2\omega, z) &= \varepsilon_0 \chi^{(2)}(\omega, \omega) \mathbf{E}_1 \mathbf{E}_1 = \varepsilon_0 \chi^{(2)}(\omega, \omega) \mathbf{A}_1^2(z) \mathrm{e}^{-2jk_1 z}. \end{aligned} \tag{3.133}$$

The phase difference between the above two polarizations represent the *phase mismatch*

$$\Delta k = 2k_1 - k_2 = \frac{4\pi}{\lambda_1} [n(\omega) - n(2\omega)],$$

where λ_1 is the wavelength of the fundamental beam and $n(\omega) - n(2\omega)$ represent the refractive index difference of the medium at frequencies ω and 2ω. If a phase mismatch is present, which implies that the phase velocity of the polarization at frequency ω is different from that of the polarization at frequency 2ω, the energy from the $\mathbf{E}_1(\omega, z)$ wave cannot be transferred to $\mathbf{E}_2(2\omega, z)$ wave effectively.

The origin of nonlinear optical properties is rooted in the asymmetric part of the charge distribution of chemical bonding. The magnitude and sign of nonlinear optical properties are strongly related to atomic interactions in solids such as chemical bonding [182]. In the case of wurtzite structures, nonlinearities are believed to be related to the excess charge in the bonding region of the covalent bond between the cation and anion atoms. The nonlinear polarizability of a bond arises when a large incident electric field causes perturbation on the linear susceptibility. A simple approach to calculate nonlinear susceptibility is through summing all individual

Table 3.11 Physical units of nonlinear optical parameters in both SI and cgs systems.

Parameter	SI	cgs	Conversion factor from cgs to SI
Polarization, $P^{(2)}$, $P^{(3)}$	$C\,m^{-2}$	$sV\,cm^{-1} = (erg\,cm^{-3})^{1/2}$	$1/3\times10^{-5}$
Electric field, E	$V\,m^{-1}$	$sV\,cm^{-1} = (erg\,cm^{-3})^{1/2}$	3×10^{4}
Second-order susceptibility, $\chi^{(2)}$	$m\,V^{-1}$	$cm\,s^{-1}\,V^{-1} = (cm^3\,erg^{-1})^{1/2} = esu$	$4\pi/3\times10^{-4}$
Third-order susceptibility, $\chi^{(3)}$	$m^2\,V^{-2}$	$cm^2\,s^{-1}\,V^{-2} = cm^3\,erg^{-1} = esu$	$4\pi/3^2\times10^{-8}$
Nonlinear refractive index (field coefficient), $\bar{n}_2$	$m^2\,V^{-2}$	$cm^2\,s^{-1}\,V^{-2} = cm^3\,erg^{-1}$	$1/3^2\times10^{-8}$
Nonlinear refractive index (intensity coefficient), n_2	$m^2\,W^{-1}$	$cm^2\,s\,erg^{-1}$	10^{3}
Intensity, I	$W\,m^{-2}$	$erg\,s^{-1}\,cm^{-2}$	10^{-3}
Two-photon absorption coefficient, β	$m\,W^{-1}$	$cm\,s\,erg^{-1}$	10^{5}

sV: statvolt; esu: electrostatic units; $1\,erg = 1\,g\,cm^2\,s^{-2}$.

polarizations in the crystal consisting of many identical bonds. The shortcoming of this method is its inability to relate the nonlinear susceptibility to the wavelength. If the complete electronic band structure of the crystal and the accurate wave function are known, for example, through the *full potential linearized augmented plane-wave* (FLAPW) theory [183, 184], nonlinear susceptibility can be directly calculated using the first-principles method [185–188] such as pseudopotentials with plane-waves in the Kohn–Sham *local density approximation* (LDA).

In the following sections, we will briefly discuss second-order and third-nonlinearities and some of the optical phenomena originating from them, namely, second harmonic generation, third harmonic generation, intensity-dependent refraction, and two-photon absorption. A general description of these optical processes will be given and some of the experimental results on ZnO will be discussed. Before we delve further into the discussion, the physical units of the parameters used in this section are given in both SI and cgs systems in Table 3.11.

3.7.1 Second-Order Nonlinear Optical Properties

Second-order nonlinear optical properties describe the coupling interaction between two electric fields (as described in Equation 3.129) and the crystal. For the ideal wurtzite ZnO, with the 6 mm symmetry, there are four nonvanishing second-order nonlinear susceptibility tensor elements, $\chi^{(2)}_{xzx} = \chi^{(2)}_{yzy}$, $\chi^{(2)}_{xxz} = \chi^{(2)}_{yyz}$, $\chi^{(2)}_{zxx} = \chi^{(2)}_{zyy}$, and $\chi^{(2)}_{zzz}$, with the coordinates corresponding to the crystal axes. As given in Equation 3.122, the **d** tensor corresponding to ZnO has only three nonzero components, namely, d_{31}, d_{33}, and d_{15}. These nonlinear susceptibilities have the units of picometer/volt ($pm\,V^{-1}$). For frequencies far from resonances, we can use Kleinman's symmetry conditions, which would reduce the independent number of $\chi^{(2)}_{ijk}$

components to two (see the text immediately prior to Equation 3.123):

$$\chi^{(2)}_{xzx} = \chi^{(2)}_{yzy} = \chi^{(2)}_{xxz} = \chi^{(2)}_{yyz} = \chi^{(2)}_{zxx} = \chi^{(2)}_{zyy} \quad \text{and} \quad \chi^{(2)}_{zzz}. \tag{3.134}$$

Similarly, the remaining **d** tensor elements are $d_{15} = d_{31}$ and d_{33}. The wurtzite crystalline structure under Kleinman's symmetry conditions further allows to a first approximation, the assumption $|\chi^{(2)}_{zzz}| = 2\chi^{(2)}_{xzx}$, that is, $|d_{33}| = 2d_{31}$. As a consequence, for a perfectly crystalline sample, the investigation may be limited to only the largest component, d_{33}. However, if the sample contains crystallites with different orientations, independent evaluation of at least two independent susceptibility components allows determination of the crystallites' main orientation. During measurements, ZnO thin films including all crystallites and grain boundaries are assumed to represent an isotropic uniaxial medium. Consequently, the second harmonic signal is always p-polarized independent of the polarization of the fundamental beam, as also verified by experimental observations.

3.7.1.1 Second-Harmonic Generation

Based on Equation 3.124, when the incident fields have the frequency $\omega_1 = \omega_2 = \omega$, the second-order optical process in ZnO can be reduced to the following forms

$$P^{(2)}_x(2\omega) = 2\varepsilon_0\chi^{(2)}_{xzx}E_z(\omega)E_x(\omega), \tag{3.135}$$

$$P^{(2)}_y(2\omega) = 2\varepsilon_0\chi^{(2)}_{xzx}E_z(\omega)E_y(\omega), \quad \text{and} \tag{3.136}$$

$$P^{(2)}_z(2\omega) = \varepsilon_0\chi^{(2)}_{zxx}[E^2_x(\omega) + E^2_y(\omega)] + \varepsilon_0\chi^{(2)}_{zzz}E^2_z(\omega), \tag{3.137}$$

where E_i represents the components of optical field along different directions.

Let us now discuss the second-order susceptibility, $d_{ikl} = (\chi^{(2)}_{ikl})/2$, for ZnO with a brief reference to the well-established nonlinear optical crystals. Table 3.12 collates the relevant parameters for commonly used optical crystals and semiconductors.

The macroscopic second-harmonic susceptibilities are treated as tensorial sums of the microscopic single-bond second-order susceptibilities. Assuming that the bonds in the wurtzite (w) and the zinc blende (z) crystals are identical, the bond additivity concept gives rise to the following simple expression [189]:

$$d^w_{zzz} = -2d^w_{xxz} = (2/\sqrt{3})d^z_{xyz}. \tag{3.138}$$

Further, symmetry arguments associated with wurtzitic crystals lead to

$$d^w_{xxz} = d^w_{zxx} = d^w_{xzx}. \tag{3.139}$$

The superscripts z and w distinguish the zinc blende and wurtzitic phases.

Generally, the optical nonlinearity is measured using two different techniques. The first method utilizes phase matching between the fundamental and harmonic waves (when the effective refractive indices at ω and 2ω are equal) and the second method is able to measure nonlinear optical properties of all crystals regardless of phase matching. Using the second method, the coherence length between the bound and

Table 3.12 Second-order nonlinear optical susceptibilities (d coefficients) of most commonly used nonlinear optical materials and some common semiconductors for comparison.

Material	Point group	d_{ik} (pm V^{-1})
Quartz	$32 = D_3$	$d_{11} = 0.4$
		$d_{14} = 0.01$
$LiNbO_3$	$3m = C_{3v}$	$d_{22} = 3.1$
		$d_{31} = 5.86$
		$d_{33} = -41.05$
LBO (LiB_3O_5)	$mm2$	$d_{24} = 0.74$
		$d_{31} = 0.8$–1.3
		$d_{33} \sim 0$
$BaTiO_3$	$4mm = C_{4v}$	$d_{15} = -17.2$
		$d_{31} = -18$
		$d_{33} = -6.7$
BBO (β-BaB_2O_4)	$3m = C_{3v}$	$d_{11} = 1.6$
		$d_{22} = 2.1$
		$d_{31} = 0.15$
KDP (KD_2PO_4)	$42m = D_{2d}$	$d_{14} = 0.5$
		$d_{36} = 0.46$
GaAs	$\bar{4}3m$	$d_{14} = 368.7$
GaSb	$\bar{4}3m$	$d_{14} = 628$
GaP	$\bar{4}3m$	$d_{14} = 147$–220
CdTe	$\bar{4}3m$	$d_{14} = 168$
ZnSe	$\bar{4}3m$	$d_{14} = 78$
ZnTe	$\bar{4}3$ m	$d_{14} = 90$
Wurtzite AlN	$6mm = C_{6v}$	$d_{31} = 0.2$
		$d_{33} = 7.4$
Wurtzite GaN	$6mm = C_{6v}$	$d_{31} = -3.45$
		$d_{33} = 5.76$
CdS	$6\,mm = C_{6v}$	$d_{15} = 44$
		$d_{31} = 40.2$
		$d_{33} = 77.9$
CdSe	$6mm = C_{6v}$	$d_{15} = 18$

[180, 218].

the free harmonic waves can be obtained from the spacing of the Maker fringes [190–192] associated with the oscillations of the second harmonic power versus transmitted pump-beam angle of incidence.

Using the Maker-fringes transmission technique, the second-order nonlinear susceptibilities of ZnO thin films have been measured [193–195] (Table 3.13). By using a four-layer system model (air–film–substrate–air), the transmitted second harmonic intensity can be written as a function of the incident angle θ of the fundamental beam as [190, 192]

$$I_{2\omega}(\theta) = \frac{512\pi^4 L^2}{cd^2\lambda_\omega^2} \frac{(t_{af}^{\omega})^4 (t_{fs}^{2\omega})^2 (t_{sa}^{2\omega})^2}{(n_{2\omega}\cos\theta_{2\omega})^2} \left[\chi_{eff}^{(2)}(\theta)\right]^2 \frac{\sin^2\Psi_{SHG}}{\Psi_{SHG}^2} I_\omega^2, \tag{3.140}$$

Table 3.13 A collection of reported second-order nonlinear optical susceptibilities (*d* coefficients) for bulk and thin-film ZnO.

Sample	Wavelength, λ_ω (nm)	d_{ij} (pm V^{-1})	Reference
ZnO bulk	1064	$d_{33} = -7.16 \pm 0.2$ $d_{31} = 0.68$	[197]
ZnO bulk	1064	$d_{33} = -5.86$ $d_{31} = 1.76$ $d_{15} = 1.93$	[199]
ZnO bulk	1064	$d_{33} = 7$ $d_{31} = 2$	[201]
ZnO thin films, laser ablation	1064	$d_{33} = 6.7$ $d_{31} = 1.8$	[193]
ZnO thin films, MOCVD	1064	$d_{33} = 4.6$ $d_{31} = 1.62$	[196]
ZnO thin films, laser MBE	1064	$d_{33} = -83.7$ $d_{31} = 14.7$ $d_{15} = 15.2$	[195]
ZnO nanorods, seeded growth in aqueous solution	1064	$d_{33} = -18$ $d_{31} = 2.88$	[201]
ZnO thin films, sputtering or PECVD	1064	$d_{33} = -8.95$ $d_{31} = 3.01$	[203]
ZnO thin films, spray pyrolysis	830	$d_{33} = -7.3$ $d_{31} = 2.1$ $d_{15} = 2.6$	[204]
ZnO thin films, dual-ion beam sputtering	1064	$d_{33} = 0.9 \pm 0.09$ $\lvert d_{15}\rvert = 0.53 \pm 0.05$ $\lvert d_{31}\rvert = 0.31 \pm 0.03$	[194]
	1543	$d_{33} = 0.25 \pm 0.02$ $\lvert d_{15}\rvert = 0.14 \pm 0.01$ $\lvert d_{31}\rvert = 0.10 \pm 0.01$	
	1907	$d_{33} = 0.16 \pm 0.02$ $\lvert d_{15}\rvert = 0.08 \pm 0.02$ $\lvert d_{31}\rvert = 0.08 \pm 0.02$	

where

$$\Psi_{\mathrm{SHG}} = \frac{2\pi L}{\lambda_\omega}\left(n_\omega \cos\theta_\omega - n_{2\omega}\cos\theta_{2\omega}\right) \tag{3.141}$$

is a phase factor, d is the incident beam spot diameter, I_ω is the fundamental beam intensity, λ_ω is the fundamental beam wavelength, L is the film thickness, c is the light velocity in air, and n_ω and $n_{2\omega}$ are the refractive indices at the fundamental and the second harmonic frequencies, respectively. θ_ω and $\theta_{2\omega}$ are the propagation angles in the material for the fundamental and the second harmonic waves, respectively, and

are given by the Snell's law as $\sin\theta = n_\omega \sin\theta_\omega$ and $\sin\theta = n_{2\omega} \sin\theta_{2\omega}$. t_{af}^{ω} is the field transmission coefficient at the air/film interface for the fundamental beam. $t_{fs}^{2\omega}$ and $t_{sa}^{2\omega}$ are the field transmission coefficients at the film/substrate and substrate/air interfaces, respectively, for the second harmonic beam, which is always p-polarized. For s-, 45°, and p-polarized fundamental beams, the effective susceptibilities for the wurtzite crystal are given by

$$\begin{aligned}
\chi_{\text{eff}}^{(2),\text{s}} &= \chi_{zxx}^{(2)} \sin\theta_{2\omega} \quad \text{s-polarized} \\
\chi_{\text{eff}}^{(2),45^\circ} &= \chi_{xxz}^{(2)} \sin\theta_{\omega} \quad 45^\circ\text{-polarized} \\
\chi_{\text{eff}}^{(2),\text{p}} &= \chi_{xxz}^{(2)} \cos\theta_{2\omega} \sin 2\theta_{\omega} + \chi_{zxx}^{(2)} \sin\theta_{2\omega} \cos^2\theta_{\omega} \\
&\quad + \chi_{zzz}^{(2)} \sin\theta_{2\omega} \sin^2\theta_{\omega} \quad \text{p-polarized.}
\end{aligned} \tag{3.142}$$

According to Equation 3.142, $\chi_{zzx}^{(2)}$ can be independently determined from the measurement for an s-polarized fundamental beam. Similarly, $\chi_{xxz}^{(2)}$ can be obtained from the measurements by using the 45°- linearly polarized fundamental beam. Finally, the measurements with p-polarized fundamental beam provides $\chi_{zzz}^{(2)}$. As discussed above in Equation 3.134, additional symmetry conditions simplify the analysis. Different polarization directions and the relevant axes of the ZnO crystal are shown in Figure 3.41.

Figure 3.42 shows the typical Maker-fringes data (SHG intensity versus incident angle) for ZnO thin films [193]. The solid lines are fits using Equation 3.140, where the value of I_ω^2 was determined from incident angle-dependent measurements on a Y-cut quartz plate, which is the common method as the second-order susceptibility $\chi^{(2)}$ for quartz is well known (see Table 3.11). $\chi_{zxx}^{(2)}$ and $\chi_{zzz}^{(2)}$ for ZnO (0 0 0 1) thin films were found to be as large as 3.6 and 13.4 pm V^{-1}, respectively, by substituting the $\chi_{\text{eff}}^{(2)}(\theta)$ values extracted from Equation 3.140 into Equation 3.142. The second harmonic beam was found to be always p-polarized, independent of the polarization of the fundamental beam. As seen from Figure 3.42, the second harmonic signal was significantly stronger when the fundamental beam was p-polarized. Samples with

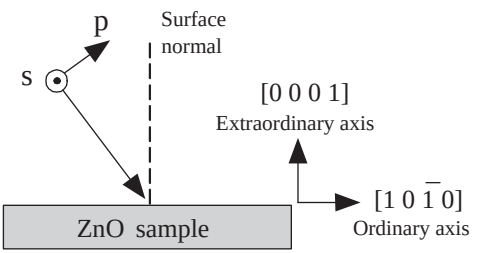

Figure 3.41 Different incident polarization directions and the relevant axes for (0 0 0 1) oriented ZnO.

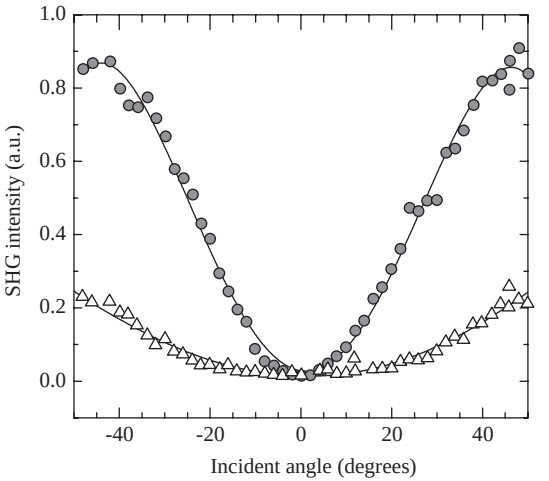

Figure 3.42 Transmitted second-harmonic intensity as a function of the incident angle of the fundamental beam having s-polarization (crosses) and p-polarization (closed circles) for an approximately 45-nm thick ZnO film deposited on *c*-plane sapphire by pulsed laser ablation. The solid curves are theoretical fits to data. (After Ref. [193].)

poor crystallinity (larger FWHM of (0 0 0 2) XRD ω-rocking curves) and smaller thickness were found to have larger second-order susceptibilities, suggesting that a significant part of the SHG signal is generated at grain boundaries and interfaces [193, 194]. Thin-film samples grown by MOCVD have shown pretty much the same trend, where the second-order susceptibility $\chi^{(2)}_{zzz}$ was observed to be larger for lower deposition temperatures, which also resulted in larger XRD linewidths, that is, lower crystalline quality [196]. For these MOCVD-grown samples, the susceptibility values deduced from Maker fringes measured at a fundamental beam wavelength of 1064 nm were $\chi^{(2)}_{zxx} = 2.24\,\mathrm{pm\,V^{-1}}$ and $\chi^{(2)}_{zzz} = 7.2\,\mathrm{pm\,V^{-1}}$ for the film deposited at 200 °C, $\chi^{(2)}_{zxx} = 3.24\,\mathrm{pm\,V^{-1}}$ and $\chi^{(2)}_{zzz} = 9.2\,\mathrm{pm\,V^{-1}}$ for the film deposited at 250 °C, while samples grown at higher temperatures (300–500 °C) produced much smaller values, for example, $\chi^{(2)}_{zxx} = 0.95\,\mathrm{pm\,V^{-1}}$ and $\chi^{(2)}_{zzz} = 3.2\,\mathrm{pm\,V^{-1}}$ for the film deposited at 300 °C [196].

There is some scatter in the second-order nonlinear susceptibility values reported for bulk ZnO. For single-crystal [0 0 0 1] ZnO platelets grown by the seeded vapor transport method (Eagle-Picher) $\chi^{(2)}_{zzz}$ and $\chi^{(2)}_{zxx}$ were determined by using the Maker fringes as $-14.31 \pm 0.4\,\mathrm{pm\,V^{-1}}$ and $1.36\,\mathrm{pm\,V^{-1}}$, respectively [197]. The minus sign for $\chi^{(2)}_{zzz}$ was not derived from the measurements but adopted from an earlier study [198]. By measuring the angular dependence of the p-polarized SHG intensity arising from an s-polarized fundamental beam incident on a [10 $\bar{1}$0] ZnO platelet, and therefore eliminating the influence from $\chi^{(2)}_{zzz}$ according to Equation 3.142, $\chi^{(2)}_{zxx}$ was determined as $1.41\,\mathrm{pm\,V^{-1}}$. For the [10 $\bar{1}$0] ZnO platelet, the measurements also

yielded $\chi^{(2)}_{zzz} = -14.77 \pm 0.4$ pm V^{-1}, which is almost the same as that measured for the *c*-plane platelet. Similar bulk values for $\chi^{(2)}_{zzz}$ have been measured by others: $\chi^{(2)}_{zzz} = -11.72$ pm V^{-1} [199, 200], $|\chi^{2}_{zzz}| = 14$ pm V^{-1} [201]. However, some other reported values for $\chi^{(2)}_{zxx}$ are higher: $\chi^{(2)}_{zxx} = 3.52$ pm V^{-1} [199], $\chi^{(2)}_{zxx} = 4$ pm V^{-1} [201].

The formulation of the SHG intensity measured using the Maker-fringes technique, which is described in detail by Jerphagnon and Kurtz [192] and results in the expression given in Equation 3.140 does not account for the absorption of the second harmonic beam and considers only isotropic materials. The assumptions that no absorption occurs at the second harmonic wavelength and that the birefringence is almost zero (extraordinary and ordinary refractive indices are almost identical) are generally valid, as usually infrared wavelengths significantly longer than the wavelength corresponding to the bandgap of ZnO are used in experiments for the fundamental beam. Herman and Hayden [202] have provided a more accurate derivation using complete boundary conditions for the second harmonic waves taking into account the birefringence of the medium and the absorption of the fundamental and second harmonic beams. They have also shown that when the experiments were performed far from the resonance of the nonlinear material to neglect the effects of absorption of the fundamental and the second harmonic beams, an accurate determination of the thickness and the absorption coefficient is absolutely necessary to obtain reliable results. Including the effects of absorption but neglecting reflections, the second harmonic intensity can be written as [202]

$$I_{2\omega}(\theta) = \frac{128\pi^3}{cA}\frac{(t^{\omega}_{af})^4(t^{2\omega}_{fs})^2(t^{2\omega}_{sa})^2}{(n_{2\omega}\cos\theta_{2\omega})^2} I^2_{\omega}\left(\frac{2\pi L}{\lambda_{\omega}}\right)^2 d^2_{eff}(\theta)\frac{\sin^2\Psi_{SHG} + \sin h^2\Delta}{\Psi^2_{SHG} + \Delta^2} e^{-2(\delta_1+\delta_2)}, \tag{3.143}$$

where

$$\Delta = \delta_{\omega} - \delta_{2\omega} = \left(\frac{2\pi L}{\lambda_{\omega}}\right)\left(\frac{n_{\omega}\kappa_{\omega}}{\cos\theta_{\omega}} - \frac{n_{2\omega}\kappa_{2\omega}}{\cos\theta_{2\omega}}\right) \quad \text{and} \quad \delta_{k\omega} = \frac{2\pi L}{\lambda}\frac{n_{k\omega}\kappa_{k\omega}}{\cos\theta_{k\omega}}. \tag{3.144}$$

A is the beam area, $\kappa_{k\omega}$ is the extinction coefficient at frequency $k\omega$ ($k = 1, 2$), and the other parameters are the same as those given in Equation 3.140. The transmission factors in Equation 3.143 are complex in general; however, they may be considered real for small extinction coefficients. Equation 3.143 transforms into Equation 3.140 when $\kappa_{k\omega}$ is set to zero, that is, when absorption is neglected.

Second-order nonlinear coefficients of ZnO have been deduced also by including the absorption at the second harmonic wavelengths for ZnO thin films, confirming the enhancement of the second-order nonlinearity due to the microcrystalline structure [195]. They were measured to be significantly larger than those in bulk ZnO. d_{33}, d_{31}, and d_{15} were reported to be -83.7, 14.7, and 15.2 pm V^{-1}, respectively, at $\lambda_{\omega} = 1064$ nm for ZnO thin films deposited on sapphire by laser MBE [195].

Studies on second harmonic generation in ZnO (0 0 0 1) nanorods have also shown that nonlinear susceptibilities higher than those in single-crystal ZnO films can be obtained by increasing the aspect ratio (height/diameter) of the nanorods [201]. When the aspect ratio was increased from 5.7 to 10.8 (667 nm average nanorod length and 62 nm average nanorod diameter) by simply increasing the growth time on a seeded quartz substrate in an aqueous solution, the nonlinear coefficients increased from $d_{33} = -7.8\,\mathrm{pm\,V^{-1}}$ and $d_{31} = 0.14\,\mathrm{pm\,V^{-1}}$ to $d_{33} = -18.0\,\mathrm{pm\,V^{-1}}$ and $d_{31} = 2.88\,\mathrm{pm\,V^{-1}}$, while they were measured as $d_{33} = 7\,\mathrm{pm\,V^{-1}}$ and $d_{31} = 2\,\mathrm{pm\,V^{-1}}$ for a 500-μm thick single-crystal ZnO sample.

As discussed above briefly, this general observation of enhancement of the second-order nonlinear effects in thin films compared to bulk has been attributed to interface and surface effects and grain boundaries resulting from micro/nanocrystalline structure. However, a clear understanding of this phenomenon still does not exist. Studies on thickness dependence do not seem to have produced consistent results. For example, $\chi^{(2)}_{zzz}$ and $\chi^{(2)}_{zxx}$ have been measured to be $-17.89\,\mathrm{pm\,V^{-1}}$ and $6.02\,\mathrm{pm\,V^{-1}}$, respectively, for ~44-nm thick ZnO films grown by reactive pulsed direct current sputtering or plasma-enhanced CVD (PECVD), larger than their values in bulk, and reduce with increasing film thickness [203]. However, no clear dependence on thickness or the grain size has been observed for thin films grown using spray pyrolysis [204].

Another point of importance is that for polar crystals such as wurtzite ZnO, the two nonlinear coefficients, d_{33} and d_{31}, should have opposite signs [198, 205], which has been confirmed by experiments some of which are mentioned above [195, 201]. However, some experimental results have produced same signs for these two coefficients [193, 196]. This discrepancy may originate from the interpretation of the data, as in some experimental configurations it is not possible to identify the sign.

3.7.2 Third-Order Nonlinear Optical Properties

Third-order nonlinear properties are also called *four-wave mixing* (FWM), because they are related to the interaction of four electromagnetic waves. Although the third-order susceptibility $\chi^{(3)}$ is usually smaller than $\chi^{(2)}$, a high-intensity pump laser can render the third-order signal sufficiently strong to be observable. In the third-order optical process, the polarization can be written as described in Equation 3.131:

$$P_i^{\omega_4} = \varepsilon_0 D^{(3)} \sum_{klm} \chi_{iklm}^{(3),\omega_4} E_k^{\omega_1} E_l^{\omega_2} E_m^{\omega_3}, \tag{3.145}$$

where $\chi^{(3)}$ is the third-order susceptibility for the nonlinear medium under consideration. In general, four different frequencies, including that of the mixed beam, would be involved. Any of the four waves can be resonantly enhanced in the third-order process, which makes the third-order process more complex than the second-order process.

For noncentrosymmetric crystals with a 6 mm point group symmetry, such as wurtzite ZnO, the third-order susceptibility tensor $\chi^{(3)}$ (χ_{ijkl}) has 21 nonzero

elements, 10 of which are independent:

$$\begin{aligned}
&\chi_{zzzz},\\
&\chi_{xxxx} = \chi_{yyyy} = \chi_{xxyy} + \chi_{xyyx} + \chi_{xyxy}\\
&\chi_{xxyy} = \chi_{yyxx}, \chi_{xyyx} = \chi_{yxxy}, \chi_{xyxy} = \chi_{yxyx}\\
&\chi_{yyzz} = \chi_{xxzz},\\
&\chi_{zzyy} = \chi_{zzxx}, \qquad \text{for 6 mm symmetry.}\\
&\chi_{zyyz} = \chi_{zxxz},\\
&\chi_{yzzy} = \chi_{xzzx},\\
&\chi_{yzyz} = \chi_{xzxz},\\
&\chi_{zyzy} = \chi_{zxzx}.
\end{aligned} \tag{3.146}$$

In the case of third harmonic generation, the frequencies of the input beams are the same ($\omega_1 = \omega_2 = \omega_3$) and the tripled beam has a frequency $\omega_4 = 3\omega_1$. Therefore, for the THG process, χ_{ijkl} should be invariant when the relative positions of *jkl* indices change. Consequently, the number of independent elements of the susceptibility tensor for the THG process I is reduced to just four: χ_{xxxx}, χ_{zzzz}, χ_{xxzz}, and χ_{zzxx}. Furthermore, when Kleinman symmetry conditions are adopted for experiments performed far from the resonances, one would have $\chi_{xxzz} = \chi_{zzxx}$, resulting in only three independent elements [206].

The third-order nonlinear process provides the means to study mechanisms involving ultrashort optical pulses including applications such as optical coherence control [207, 208]. Furthermore, four-wave mixing can measure the resonances on the polariton branches of all three excitons (A, B, and C) resulting from the s-like conduction band (symmetry Γ_7) and the p-like valence bands (with symmetries of $\Gamma_9, \Gamma_7, \Gamma_7$) generated by the crystal-field splitting and spin-orbit coupling. As discussed before in Section 3.2.1, polaritons are formed due to interaction between the photons and the exciton states. The resonances of third-order nonlinear optical response show a characteristic polarization dependence, consistent with the symmetry assignment of the valence bands [209]. When all four waves in the four-wave mixing interaction are at the same frequency, this mixing process is referred to as *degenerate four-wave mixing* (DFWM). In the wavelength degenerate two-pump FWM experiments to measure the third-order nonlinearities, the two-pump pulses with equal intensity but different wave vectors $\mathbf{k_1}$ and $\mathbf{k_2}$ form a time-dependent interference pattern on the sample, which translates to a density grating when the light is absorbed [210]. This density grating results in a refractive index grating due to intensity-dependent refractive index, the second pump pulse with wave vector $\mathbf{k_2}$ is *self-diffracted* by this grating, and the first diffracted order FWM signal appearing in the direction $2\mathbf{k_2} - \mathbf{k_1}$ is measured as indicated in Figure 3.43a [209, 211]. The spectrally resolved FWM signal can be measured at different time delays between the two pulses to obtain direct information about coherences involving excitons, biexcitons, and polaritons. Figure 3.43b shows wavelength degenerate two-pulse spectrally resolved FWM data obtained by using ↑↑ polarization (vertical linear polarization for both pump beams) and a photon energy of 3.379 eV from a c-plane bulk ZnO sample grown by the seeded vapor transport

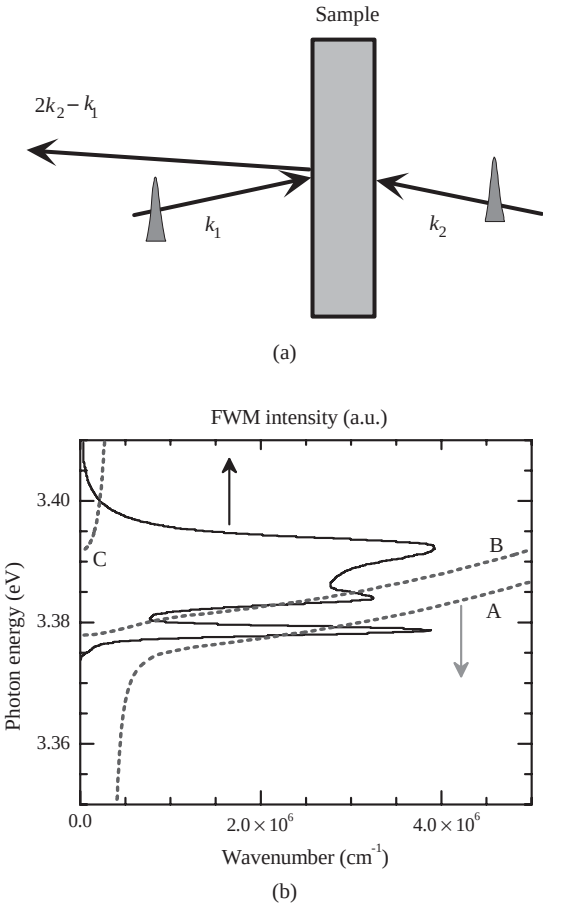

Figure 3.43 (a) Schematic representation of the *self-diffraction* two-pump FWM experimental setup. (b) Two-pulse spectrally resolved FWM spectrum from bulk ZnO obtained by using ↑↑ polarization at a delay time of 0.01 ps. The dotted lines show the polariton dispersion: A denotes the lower A polariton branch and B and C represent the mixed branches due to the upper A/lower B and upper B/lower C polaritons, respectively. (After Ref. [211].)

method [211]. The full-width at half-maximum values of the observed peaks, obtained by spectral decomposition using Gaussian line shapes were found to be smaller than the longitudinal–transverse splitting energies (1.5 meV for A exciton and 11.1 meV for B exciton) [51]; and therefore, the observed peaks were partially attributed to direct transitions from the polariton branches to the ground state.

3.7.2.1 Third Harmonic Generation

In the third-harmonic generation process, three photons with the same frequency ω mix and generate a new photon with a frequency 3ω. This nonlinear optical process,

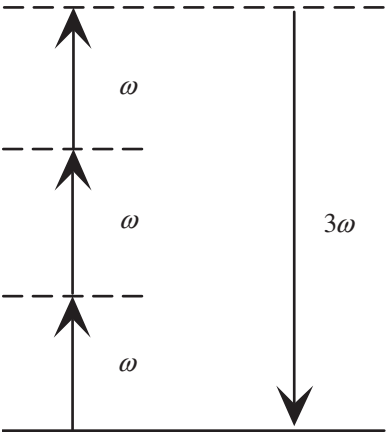

Figure 3.44 Schematic illustration of electron energy of third harmonic generation. Three incident photons with the same frequency ω couple through the third-order susceptibility to generate a new photon of frequency 3ω. The solid line is the electronic ground state while the dashed lines represent virtual transitions in the material.

as illustrated in Figure 3.44, depends on the crystal structure, the polarization, and the direction of the fundamental beam. As mentioned before, in wurtzite ZnO, the nonvanishing independent susceptibility tensor elements are $\chi^{(3)}_{zzzz}, \chi^{(3)}_{xxxx}, \chi^{(3)}_{xxzz}, \chi^{(3)}_{zzxx}$. For a c-axis-oriented film, when the incident beam is along the optical axis of the crystal, which is parallel to the surface normal, only the $\chi^{(3)}_{xxxx}$ component contributes to the third-order nonlinear polarization that is expressed as

$$P^{(3)}_{y}(3\omega) = \varepsilon_0 \chi^{(3)}_{xxxx}(3\omega = \omega + \omega + \omega) E^3_y(\omega), \tag{3.147}$$

where $E_y(\omega)$ is the fundamental field, which is parallel to the crystal surface.

Using different techniques such as Maker fringes and z-scan, the THG in thin-film [194, 212–215] and bulk ZnO [216, 219, 223] has been measured. For a *c*-axis-oriented ZnO sample, where the optical axis is along the surface normal, by using a p-polarized incident beam ($p_\omega p_{3\omega}$ configuration), it is possible to explore only the $\chi^{(3)}_{zzzz}$ component. As the THG may also occur in air, which has a large coherence length due to weak dispersion in the refractive index, it may in some cases be necessary to perform the experiments in vacuum.

The third harmonic power as a function of the incidence angle θ is given by [194]

$$P_{3\omega}(\theta) = \frac{2304\pi^6}{A} [t^{\omega}_{af}(\theta)]^6 [t^{3\omega}_{fa}(\theta)]^2 \frac{\sin^2 \Psi_{THG}}{[n^2_{\omega}(\theta) - n^2_{3\omega}(\theta)]^2} |\chi^{(3)}(\theta)|^2 P^3_{\omega}, \tag{3.148}$$

where P_ω is the fundamental beam power, n_ω and $n_{3\omega}$ are the refractive indices at the fundamental and third harmonic frequency, respectively, t^{ω}_{af} is the field transmission coefficient for the fundamental beam at the input face, $t^{3\omega}_{fa}$ is the

field transmission coefficient at the output face for the third harmonic beam, and the phase factor Ψ_{THG} is

$$\Psi_{THG} = \frac{3\pi L}{\lambda_\omega}[n_\omega(\theta)\cos\theta_\omega - n_{2\omega}(\theta)\cos\theta_{2\omega}]. \quad (3.149)$$

As defined before for SHG, λ_ω is the fundamental beam wavelength, L is the film thickness, and θ_ω and $\theta_{3\omega}$ are the propagation angles in the material for the fundamental and the third harmonic waves, respectively. It should also be mentioned that the oscillation in the Maker fringes disappear as the absorption depth becomes smaller than the THG coherence length ($\sim$4.6 μm for $\lambda_\omega = 1907$ nm [194]), resulting in a bell-shaped dependence on the incidence angle due to angle dependency of the reflection losses. As for the SHG experiments, the fundamental beam power can be obtained from calibration measurements by using quartz. By fitting the functional form in Equation 3.148 to the Maker fringes data for a fundamental beam wavelength of 1907 nm, the susceptibility tensor component $\chi^{(3)}_{zzzz}$ has been determined to be $185 \times 10^{-20}\,m^2\,V^{-2}$ (1.32×10^{-12} esu) for c-axis preferentially oriented polycrystalline ZnO thin films grown on glass substrates by using ion beam sputtering [194].

Both $\chi^{(3)}_{xxxx}$ and $\chi^{(3)}_{zzzz}$ susceptibility tensor components can be measured when samples with orientation perpendicular to the optical axis (c-axis) are used. For hydrothermally grown ZnO single crystals that are $\{10\bar{1}0\}$ oriented, both of the above-mentioned susceptibilities could be obtained by using the THG Maker fringes technique only by rotating the sample with respect to the fundamental beam polarization, as the $(10\bar{1}0)$ input face contains both the ordinary ($\perp$ *c*-axis) and the extraordinary (|| *c*-axis) optical axes, input polarization along which would help determine $\chi^{(3)}_{xxxx}$ and $\chi^{(3)}_{zzzz}$, respectively [216]. Using a fundamental beam wavelength of 1500 nm, $\chi^{(3)}_{xxxx}$ and $\chi^{(3)}_{zzzz}$ were both measured to be $(2.2 \pm 0.4) \times 10^{-12}$ esu in the transparency region. Dispersion of these nonlinear optical susceptibilities has also been measured taking into account the absorption using the imaginary part of the refractive index, and excitonic enhancement has been evidenced near the absorption edge with $\chi^{(3)}_{xxxx}$ and $\chi^{(3)}_{zzzz}$ values as large as 4×10^{-11} esu [216].

ZnO thin films have been doped with Ce, F, Er, Al, and Sn to modify their third-order susceptibilities [212]. THG measurements on samples grown by spray pyrolysis have shown that the strength of the optical nonlinearity increases with increasing film conductivity. Doping with Sn has been shown to result in the highest third-order conversion efficiency. $\chi^{(3)}$ determined from the Maker fringes using a fundamental beam wavelength of 1064 nm was 2.17×10^{-11} esu for ZnO:Sn. Figure 3.45 shows the dependence of the third-order susceptibility of ZnO on different dopants.

In noncentrosymmetric crystals such as ZnO, SHG may also take place simultaneously with THG. In addition to the THG signal via $\chi^{(3)}(3\omega = \omega + \omega + \omega)$, the optical signal at 3ω may include the sum-frequency signal via $\chi^{(2)}(3\omega = 2\omega + \omega)$ due to the fundamental beam at ω and the second harmonic signal at 2ω generated due to $\chi^{(2)}(2\omega = \omega + \omega)$. The coherence lengths for both processes have been shown to be very similar, suggesting similar modulation of the optical beam of frequency 3ω [194]. However, the cascaded THG through the SHG and the SFG in polycrystalline films has a very low efficiency, which is even lower for thin films and therefore be neglected.

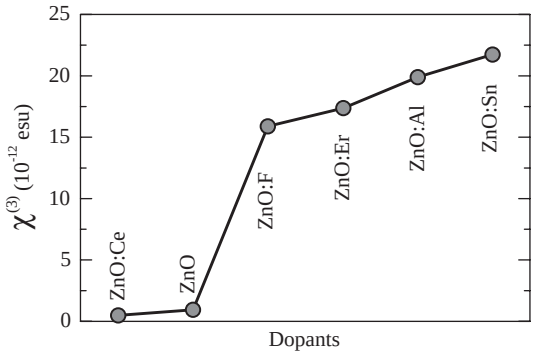

Figure 3.45 The third-order susceptibility of ZnO doped with various elements at 3.40 at. %. (After Ref. [212])

This has been experimentally confirmed by direct measurements of SHG power in nanocrystalline ZnO thin films, which has been shown to be several orders of magnitude weaker than the THG power [217].

In thin films of nanostructured ZnO (~200 nm thick) grown by PLD, a significant enhancement of $\chi^{(3)}$ compared to the epitaxially grown ZnO films has been observed with THG efficiencies as high as 1.3% at $\lambda_\omega = 1250$ nm, corresponding to $\chi^{(3)} = (1.4 \pm 0.7) \times 10^{-12}$ esu [217]. This enhancement has been attributed to the reduced dimensionality due to nanocrystalline structure, which has been shown to enhance also the second-order nonlinearities as discussed above. Such high efficiency of nonlinear optical conversion creates a potential for nanostructures ZnO thin films to be used in nonlinear optical devices.

Values for $\chi^{(3)}$ reported by different groups for thin-film and bulk ZnO are listed in Table 3.14. As can be judged from the dispersion in the experimental data for the third-order susceptibility, the strength of the third-order nonlinearity depends strongly on the film growth conditions and therefore the crystalline quality.

3.7.3
Intensity Dependent Refractive Index

Especially at high excitation densities, the refractive index of the material depends on the intensity of the light. Materials with large nonlinear refraction may potentially be used in applications such as optical switching, amplification, and limiting. As we have already described the interaction of an optical beam with the nonlinear optical medium in terms of the nonlinear polarization, we can express the polarization that influences the propagation of the optical beam of frequency ω as

$$\begin{aligned} P(\omega) &= \varepsilon_0 \chi^{(1)}(\omega) E(\omega) + 3\varepsilon_0 \chi^{(3)}(\omega = \omega + \omega - \omega) |E(\omega)|^2 E(\omega) \\ &= P^{\mathrm{L}}(\omega) + P^{\mathrm{NL}}(\omega). \end{aligned} \tag{3.150}$$

Notice that the second-order nonlinear term does not appear in Equation 3.150 as the second-order nonlinearity cannot result in an optical beam of frequency ω as

Table 3.14 Nonlinear refractive index and third-order nonlinear susceptibility values for a variety of semiconductors and optical materials.

Material	λ_ω (nm)	Bandgap (eV)	n_0	n_2 ($cm^2 W^{-1}$)	$\chi^{(3)}$ (esu)	References
Si		1.11	3.4	2.7×10^{-14}	2.0×10^{-10}	[180]
Ge		0.87	4.0	9.9×10^{-14}	4.0×10^{-11}	[180]
GaAs	1064	1.35	3.47	-3.3×10^{-13}	-1.0×10^{-10}	[221, 222]
ZnSe	1064	2.58	2.48	3.0×10^{-14}	4.4×10^{-12}	[180, 222]
	532	2.58	2.70	-6.8×10^{-14}	1.2×10^{-11}	[221, 222]
ZnTe	1064	2.26	2.79	1.2×10^{-13}	2.5×10^{-11}	[221, 222]
CdS	1064	2.42	2.34	5.1×10^{-14}	7.0×10^{-12}	[180]
	532	2.42	2.34	-6.1×10^{-13}	-8.4×10^{-11}	[222]
CdTe	1064	1.44	2.84	-3.0×10^{-13}	-6.0×10^{-11}	[221, 222]
MgO [100]	1064	7.77	1.72	3.9×10^{-16}	2.9×10^{-14}	[219]
Diamond		5.5	2.42	1.3×10^{-15}	1.8×10^{-13}	[180]
Al_2O_3	1064	7.30	1.75	2.9×10^{-16}	2.3×10^{-14}	[219]
TiO_2	1064	3.2	2.48	9.4×10^{-15}	1.5×10^{-12}	[219]
$SrTiO_3$	1064	3.2	2.31	4.8×10^{-15}	6.6×10^{-13}	[219]
Fused silica	1064	7.80	1.47	3.2×10^{-16}	1.8×10^{-14}	[180]
	1064	7.80	1.45	2.5×10^{-16}	1.3×10^{-14}	[219]
Air	1053		1.0003	5.0×10^{-19}	1.2×10^{-17}	[220]
Water	532,1064		1.33	4.1×10^{-16}	1.8×10^{-14}	[218]
Vacuum			1	1.0×10^{-34}	2.4×10^{-33}	[180]
ZnO single crystal	1064	3.37	1.93	5.4×10^{-15}	5.1×10^{-13}	[219]
ZnO single crystal	532	3.37	1.99	-0.9×10^{-14}	-0.9×10^{-12}	[223]
ZnO single crystal, hydrothermal	1500				2.2×10^{-12}	[216]
ZnO thin film, PLD	1250				1.4×10^{-12}	[217]
ZnO thin film, MOCVD	1064				3.8×10^{-12}	[213]
ZnO thin film, PLD	1064				9.6×10^{-12}	[214]
ZnO:F thin film, chemical spray	1064				7.2×10^{-13}	[215]
ZnO:Sn thin film, spray pyrolysis	1064				2.2×10^{-11}	[212]

described in Equation 3.129. The first and the second terms in Equation 3.150 describe the linear (L) and nonlinear (NL) polarizations, respectively. Using $P(\omega) = \varepsilon_0 \chi_{\text{eff}} E(\omega)$, one can write the effective susceptibility as

$$\begin{aligned} \chi_{\text{eff}} &= \chi^{(1)} + 3\chi^{(3)} |E(\omega)|^2 \\ &= \chi^{\text{L}} + \chi^{\text{NL}}, \end{aligned} \tag{3.151}$$

where the total (linear and nonlinear) refractive index is given by

$$\begin{aligned} n &= (1 + \chi_{\text{eff}})^{1/2} = (1 + \chi^{\text{L}} + \chi^{\text{NL}})^{1/2} \\ &= (1 + \chi^{(1)} + 3\chi^{(3)} |E(\omega)|^2)^{1/2}. \end{aligned} \tag{3.152}$$

Noting that the linear refractive index is $n_0 = (1 + \chi^{(1)})^{1/2}$ and $\chi^{\text{NL}} \ll n_0^2$, Equation 3.152 can be rewritten to obtain the nonlinear refractive index as

$$n = n_0 \left(1 + \frac{\chi^{\text{NL}}}{n_0^2}\right)^{1/2} \simeq n_0 \left(1 + \frac{1}{2n_0^2} \chi^{\text{NL}}\right) = n_0 \left(1 + \frac{1}{2n_0^2} 3\chi^{(3)} |E(\omega)|^2\right). \tag{3.153}$$

The nonlinear refractive index is expressed in terms of either the field ($\bar{n}_2$) or the intensity (n_2) coefficient forms of the second-order nonlinear refractive index as [180]

$$\begin{aligned} n &= n_0 + 2\bar{n}_2 |E(\omega)|^2 \\ &= n_0 + n_2 I, \end{aligned} \tag{3.154}$$

where the intensity is $I = 2\varepsilon_0 n_0 c |E(\omega)|^2$. The term n_2 is usually referred to as the intensity-dependent part of the refractive index or the second-order nonlinear refractive index as it is multiplied by the second power of the electric field and is given by (SI units)

$$n_2 = \frac{3}{4\varepsilon_0 n_0^2 c} \chi^{(3)}, \tag{3.155}$$

which is obtained by comparing Equations 3.153 and 3.154. $\bar{n}_2$ and n_2 are related by

$$n_2 = \frac{1}{\varepsilon_0 n_0 c} \bar{n}_2. \tag{3.156}$$

The change in the refractive index is also called the *Kerr effect*. For typical glasses, the values of n_2 are relatively small, on the order of $10^{-16}\,\text{cm}^2\,\text{W}^{-1}$. Optical beam intensities on the order of $1\,\text{GW}\,\text{cm}^{-2}$ (such as those produced by lasers) would be necessary to produce significant variations in refractive index. Even though n_2 is very small, intense laser beams, especially those from amplified pulsed lasers, can produce refractive index changes that can lead to dramatic nonlinear optical effects such as self-focusing, self-trapping, and laser beam filamentation [180, 218]. The nonlinear refractive index has been used in various applications such as nonlinear spectroscopy, optical switching/modulation, optical distortion correction, and optical communications. Second-order nonlinear refractive index (n_2) values along

with the linear refractive indices (n_0), third-order nonlinear susceptibilities ($\chi^{(3)}$), and bandgaps for some of the materials including ZnO are given in Table 3.14 [219–222].

II–VI semiconductors are among the materials with a very high nonlinear refractive index and therefore are promising materials for nonlinear optical device applications. The nonlinear refraction in single-crystal ZnO has been measured by using nearly degenerate three-wave mixing [219] and z-scan [223] techniques. n_2 has been measured to be as large as $5.4 \times 10^{-15}\,\mathrm{cm^2\,W^{-1}}$ for bulk ZnO [219], and $1.0 \times 10^{-13}\,\mathrm{cm^2\,W^{-1}}$ for ZnO thin films grown by pulsed laser deposition [214]. Further increase has been observed in Sn-doped ZnO thin films, producing $n_2 = 2.3 \times 10^{-13}\,\mathrm{cm^2\,W^{-1}}$ [212]. As mentioned right after Equation 3.125, some workers use a factor of 1/2 in the definition of the fields resulting in an alternative form of Equation 3.154, which has a factor of 1/2 in front of $\bar{n}_2$ instead of 2 making their values for n_2 four times smaller. All the values included in Table 3.14 are converted according to the definition described by the equations given in this section.

The origin of the nonlinear optical properties of a semiconductor depends on the photon energy. For photon energies larger than the bandgap, the nonlinear response results from the saturation of interband and excitonic absorption due to photoexcited free carriers and excitons, inducing a negative change in the refractive index. For photon energies smaller than the bandgap, on the contrary, the nonlinear response is due to the third-order nonlinearity arising from the bound electronic effects and the two-photon absorption, which will be discussed in Section 3.7.2.3. Sheik-Bahae *et al.* [224, 225] have measured the nonlinear refractive index of many semiconductors and observed a strong dispersion of the bound electronic nonlinearity near the two-photon absorption band edge, with n_2 becoming negative between the two-photon and single-photon absorption edges. This dependence was well explained by a two-parabolic band model using a simple Kramers–Kronig analysis [221, 222, 224, 225]. As also evident from the data on ZnO (see Table 3.14), n_2 is positive when two-photon absorption is absent ($\lambda_\omega = 1064\,\mathrm{nm}$) but negative when it is present. The bound electronic nonlinear refractive index, therefore, is a causal consequence of two-photon absorption. For a fundamental wavelength of 532 nm, which would result in two-photon absorption, z-scan measurements on bulk ZnO produced a negative value of $n_2 = -0.9 \times 10^{-14}\,\mathrm{cm^2\,W^{-1}}$ [223].

3.7.4
Two-Photon Absorption

Another intensity-dependent phenomenon in semiconductors is the TPA. Here, we will deal with the degenerate TPA where the two incident photons have the same energy. When the semiconductor is illuminated with a light source having an energy ($\hbar\omega$) less than the bandgap (E_g), there is a possibility of inducing a transition from the valence band to the conduction band if $2\hbar\omega \geq E_g$. However, the probability of such a process is very small compared to one-photon absorption, which is defined by the Beer–Lambert's law that gives the transmitted

intensity as

$$I(z) = I_0 e^{-\alpha_0 z}, \tag{3.157}$$

where I_0 is the intensity incident on the absorbing medium, α_0 is the one-photon absorption constant, and z is the thickness along which absorption occurs. The intensity variation of the light as it propagates through a nonlinear medium along the z-axis may be written as

$$\frac{d}{dz} I = -\alpha_0 I - \beta I^2, \tag{3.158}$$

where we have introduced an additional term that describes the TPA in terms of the TPA coefficient β. The total absorption constant is then given by

$$\alpha = \alpha_0 + \beta I. \tag{3.159}$$

The TPA rate for a two-parabolic band model may be obtained from the Fermi's golden rule as

$$\Gamma_{\text{TPA}} = \frac{2\pi}{\hbar} \sum_{c,v} \left| \sum_i \frac{\langle c|H_{\text{int}}|i\rangle\langle i|H_{\text{int}}|v\rangle}{E_i(\mathbf{k}) - E_v(\mathbf{k}) - \hbar\omega} \right|^2 \delta(E_c(\mathbf{k}) - E_v(\mathbf{k}) - 2\hbar\omega). \tag{3.160}$$

H_{int} is the optical interaction Hamiltonian given by $H_{\text{int}} = -e\mathbf{r}\cdot\mathbf{E}$, where $\mathbf{r}$ is the position vector and $\mathbf{E}$ is the optical field. $|c\rangle$ and $|v\rangle$ represent the states in the conduction and valence bands, respectively, and $|i\rangle$ is the virtual state within the transparency region. A simple model with a parabolic conduction band and a parabolic valence band gives for zinc blende semiconductors [226]

$$\begin{aligned} \beta(\omega) &= \frac{2\hbar\omega\Gamma_{\text{TPA}}}{I^2} = K_{\text{pb}} \frac{\sqrt{E_p}}{n_0^2(\omega) E_g^3} F_{\text{TPA}}(\hbar\omega/E_g), \\ F_{\text{TPA}}(2x) &= \begin{cases} \dfrac{(2x-1)^{3/2}}{(2x)^5}, & \text{for} \quad 2x > 1, \\ 0, & \text{for} \quad 2x \le 1. \end{cases} \end{aligned} \tag{3.161}$$

$E_p = 2|ed_{cv}|/m_0$ is approximately 21 meV for most of the III–V and II–VI semiconductors, n_0 is the linear refractive index, and K_{pb} is a material independent constant ($1940\ \text{cm GW}^{-1}\ (\text{eV})^{5/2}$ for a two-parabolic-band model). It should be mentioned that the above model does not correctly account for the degeneracy of the valence band (heavy hole, light hole, and spin-orbit/crystal-field split-off bands) and assumes single parabolic conduction and valence bands. Using the Kane band structure with three valence bands and including excitonic effects have been shown to produce larger TPA coefficients [227].

When photons of two different energies are present, that is, for the nondegenerate case, the absorption of the two light beams of intensities I_1 and I_2 is described by a

coupled set of equations with degenerate (β_{ii}) and nondegenerate (β_{ij}) terms

$$\begin{aligned}\frac{d}{dz}I_1 &= -\alpha_0 I_1 - \beta_{11} I_1^2 - 2\beta_{12} I_1 I_2 \\ \frac{d}{dz}I_2 &= -\alpha_0 I_2 - \beta_{22} I_2^2 - 2\beta_{21} I_1 I_2,\end{aligned} \tag{3.162}$$

where the nondegenerate TPA coefficient is given by [226]

$$\begin{aligned}\beta_{12}(\omega) &= K_{pb}\frac{\sqrt{E_p}}{n_0(\omega_1)n_0(\omega_2)E_g^3}F_{TPA}^{ND}(\hbar\omega_1/E_g, \hbar\omega_2/E_g) \\ F_{TPA}^{ND}(x_1, x_2) &= \begin{cases}\dfrac{(x_1+x_2-1)^{3/2}}{2^7 x_1 x_2^2}\left(\dfrac{1}{x_1}+\dfrac{1}{x_2}\right)^2 & \text{for} \quad x_1+x_2>1 \\ 0 & \text{for} \quad x_1+x_2 \le 1.\end{cases}\end{aligned} \tag{3.163}$$

Using the subpicosecond time-resolved nondegenerate pump-probe technique, the two-photon absorption spectrum of 1.5-mm thick polycrystalline ZnO samples has been measured [228]. A strong pump beam of 1.76 eV energy, slightly more than half the bandgap energy of ZnO, was focused on the sample, and the transmission of a much weaker continuum probe beam generated by focusing part of the beam onto a cuvette containing deionized water was recorded at different time delays between the pump and the probe beams. The TPA edge was observed at ~3.40 eV, slightly higher than the linear absorption band edge, and a degenerate TPA coefficient of $\beta = (1.3 \pm 0.4)$ cm GW^{-1} was reported. With the pump photon energy kept constant (1.76 eV), the nondegenerate TPA coefficient was observed to increase with increasing probe photon energy. The blueshift in the TPA band edge was attributed to the fact that the single photon absorption band edge is dominated by the impurity or excitonic transitions, which do not have the correct parity to contribute to TPA.

Z-scan is another technique to measure the third-order optical nonlinearity. In the single beam configuration, the sample is translated longitudinally through the beam-waist region of a focused Gaussian beam and the transmittance of the sample is measured as a function of the sample position (along the z-axis). The power transmitted through a small aperture placed on the system axis is measured to determine the on-axis intensity in the far field, the variation of which with sample position is proportional to the nonlinear phase shift experienced in passing through the sample. From this measured phase shift, the nonlinear refractive index and the TPA coefficient can be determined by using the known sample thickness and the laser intensity [224]. For a z-cut, 1-mm thick ZnO single crystal, a degenerate TPA coefficient of $\beta = 4.2 \pm 0.9$ cm GW^{-1} was obtained for the laser beam of 532 nm wavelength incident along the [0 0 0 1] axis [223]. This value is of the same order as that reported by Bolger *et al.* [228] for polycrystalline ZnO. The

Table 3.15 Two-photon absorption coefficients for a variety of materials.

Material	λ_ω (nm)	β (cm GW^{-1})
GaAs	1064	23 [231], 26 [221], 22 [226]
GaN (wurtzite)	390	17.5 [232]
	600	16.0 [233]
Diamond	282	2.3 [234]
Fused silica	267	0.045 [235]
ZnS	532	2.0–3.5 [231], 3.0 [226]
ZnSe	532	5.5 [231], 5.8 [221], 5.0 [226]
ZnTe	1064	4.5 [231], 4.2 [221], 1.2 [226]
CdTe	1064	15–22 [231], 26 [221], 18 [226]
ZnO	705	1.3 ± 0.4 [228]
ZnO	532	4.2 ± 0.9 [223]
ZnO	740	732 [230]

TPA coefficient is often overestimated when the free-carrier absorption effects are neglected [229].

In thin microcrystalline ZnO films, the TPA coefficients were measured to be more than two orders of magnitude larger than the above-mentioned numbers. In one particular study by Lin *et al.* [230], degenerate TPA coefficients as large as 732 cm GW^{-1} were measured for 1-μm thick microcrystalline ZnO thin films grown by high-vacuum laser deposition on quartz substrates. The TPA coefficient was shown to be smaller at higher excitation wavelengths (e.g., 91 cm GW^{-1} at 780 nm) but peak at the two-photon resonance of 760 nm (464 cm GW^{-1}) and then reduce to 297 cm GW^{-1} at 745 nm before increasing to 732 cm GW^{-1} at 740 nm, above which it decreased very slowly (to 681 cm GW^{-1} at 710 nm). This more than 100-fold increase in β compared to the value reported for bulk ZnO (4.2 ± 0.9 cm GW^{-1}) [223] is rather surprising, but it can be attributed to the enhancement due to the microcrystalline nature, which has been shown to enhance the second-order nonlinearities as discussed before. Table 3.15 compares the TPA coefficients measured for various semiconductors and optical materials with those reported for ZnO.

In summary, it is clear that ZnO has many attractive linear and nonlinear optical properties that would bode well for electro-optical device applications, as high optical quality ZnO thin films (judged from optical pumping experiments) and heterostructures can be produced with available technology. Reproducible p-type ZnO, however, remains to be the bottleneck in the realization of optical emitters based on electrical injection including lasers exploiting the remarkably high exciton binding energy of 60 meV and the efficient photon emission in ZnO. Pending its achievement, the unprecedented capabilities of ZnO can be harnessed for emitters that would be superior to those based on other semiconductors.

References

1 Mollwo, E. (1954) *Zeitschrift fur Angewandte Physik*, **6**, 257.
2 Reynolds, D.C. and Collins, T.C. (1969) *Physical Review*, **185**, 1099.
3 Thomas, D.G. (1960) *Journal of Physics and Chemistry of Solids*, **15**, 86.
4 Hopfield, J.J. (1960) *Journal of Physics and Chemistry of Solids*, **15**, 97.
5 Park, Y.S., Litton, C.W., Collins, T.C. and Reynolds, D.C. (1965) *Physical Review*, **143**, 512.
6 Segall, B. (1967) *Physical Review*, **163**, 769.
7 Dinges, R., Fröhlich, D., Staginnus, B. and Staude, W. (1970) *Physical Review Letters*, **25**, 922.
8 Collins, R.J. and Kleinman, D.A. (1959) *Journal of Physics and Chemistry of Solids*, **11**, 190.
9 Weiher, R.L. (1966) *Physical Review*, **152**, 736.
10 Bear, W.S. (1967) *Physical Review*, **154**, 785.
11 Bond, W.L. (1965) *Journal of Applied Physics*, **3**, 1674.
12 Liang, W.Y. and Yoffe, A.D. (1968) *Physical Review Letters*, **20**, 59.
13 Hutson, A.R. (1961) *Journal of Applied Physics*, **32**, 2287.
14 Freeouf, J.L. (1973) *Physical Review B: Condensed Matter*, **7**, 3810.
15 Schirmer, O.F. and Zwingel, D. (1970) *Solid State Communications*, **8**, 1559.
16 Hopfield, J.J. and Thomas, D.G. (1965) *Physical Review Letters*, **15**, 22.
17 Stephens, R.E. and Malitson, I.H. (1952) *Journal of Research National Bureau of Standards*, **49**, 249.
18 Park, Y.S. and Schneider, J.R. (1968) *Journal of Applied Physics*, **39**, 3049.
19 Heiland, G., Mollwo, E. and Stöckmann, F. (1959) *Solid State Physics*, **8**, 191.
20 Bundesmann, C., Schmidt-Grund, R. and Schubert, M. (2008) Far-infrared to vacuum-ultra-violet optical properties of ZnO: phonons, plasmons, dielectric constants, refractive indices, band-to-band transitions, and excitons, in *Transparent Conductive Zinc Oxide, Springer Series in Materials Science*, Vol. 104 (eds K. Ellmer, A. Klein and B. Rech). Springer, Berlin.
21 Bundesmann, C. (2005) Phonons and plasmons in ZnO-based alloy and doped ZnO thin films studied by infrared spectroscopic ellipsometry and Raman scattering spectroscopy, PhD Thesis, Universität Leipzig (Shaker, Aachen, 2006).
22 Look, D.C. (2001) *Materials Science and Engineering: B*, **80**, 381.
23 Reynolds, D.C., Look, D.C., Jogai, B., Litton, C.W., Cantwell, G. and Harsch, W.C. (1999) *Physical Review B: Condensed Matter*, **60**, 2340.
24 Tu, L.W., Lee, Y.C., Stocker, D. and Schubert, E.F. (1998) *Physical Review B: Condensed Matter*, **58**, 10696.
25 Cazaux, J. (1986) *Journal of Applied Physics*, **59**, 1418.
26 Knobloch, K., Perlin, P., Krueger, J., Weber, E.R. and Kisielowski, C. (1998) MRS Internet J. *Nitride Semiconductor Research*, **3**, 4.
27 Fleischer, K., Toth, M., Phillips, M.R., Zou, J., Li, G. and Chua, S.J. (1999) Depth profiling of GaN by cathodoluminescence microanalysis. *Applied Physics Letters*, **74**, 1114.
28 Pake, G.E. and Estle, T.L. (1973) *The Physical Properties of Electron Paramagnetic Resonance*, 2nd edn, Benjamin, Reading, MA.
29 Morkoç, H. (2008) *Handbook of Nitride Semiconductors and Devices*, Vol. III, Wiley-VCH Verlag GmbH.
30 Einstein, A. (1917) *Physik Zeitschrift*, **18**, 121.
31 Kittel, C. (1958) *Elementary Statistical Physics*, John Wiley & Sons, Inc., New York. p. 175.
32 Wang, S. (1989) *Fundamentals of Semiconductor Theory and Device Physics*, Prentice Hall, Englewood Cliffs, NJ.

33 Yu, P.Y. and Cardona, M. (1995) *Fundamentals of Semiconductors*, Springer, Berlin.

34 Svelto, O. and Hanna, D.C. (1976) *Principles of Lasers*, Plenum Press.

35 Weisbuch, C. and Vinter, B. (1991) *Quantum Semiconductor Structures*, Academic Press, New York.

36 Casey, H.C. and Panish, M.B. (1978) *Heterostructure Lasers*, Academic Press, New York.

37 Pankove, J.I. (1971) *Optical Processes in Semiconductors*, Prentice Hall, Englewood Cliffs, NJ.

38 van Roosbroeck, W. and Shockley, W. (1954) *Physical Review*, **94**, 1558.

39 Grindt, A., Koch, S.W. and Chow, W.W. (1998) *Applied Physics A*, **66**, 1.

40 Birman, J.L. (1959) *Physical Review Letters*, **2**, 157.

41 Mang, A., Reimann, K. and Rübenacke, St. (1995) *Solid State Communications*, **94**, 251.

42 Lambrecht, W.R.L., Rodina, A.V., Limpijumnong, S., Segall, B. and Meyer, B.K. (2002) *Physical Review B: Condensed Matter*, **65**, 075207.

43 Reynolds, D.C., Litton, C.W., Look, D.C., Hoelscher, J.E., Claflin, B., Collins, T.C., Nause, J. and Nemeth, B. (2004) *Journal of Applied Physics*, **95**, 4802.

44 Rodina, A.V., Strassburg, M., Dvorzak, M., Haboeck, U., Hoffman, A., Zeuner, A., Alves, H.R., Hofmann, D.M. and Meyer, B.K. (2004) *Physical Review B: Condensed Matter*, **69**, 125206.

45 Thonke, K., Gruber, T., Teofilov, N., Schönfelder, R., Waag, A. and Sauer, R. (2001) *Physica B*, **308–310**, 945.

46 Boemare, C., Monteiro, T., Soares, M.J., Guilherme, J.G. and Alves, E. (2001) *Physica B*, **308–310**, 985.

47 Gil, B. (2001) *Physical Review B: Condensed Matter*, **64**, 201310.

48 Reynolds, D.C., Look, D.C., Jogai, B. and Collins, T.C. (2001) *Applied Physics Letters*, **79**, 3794.

49 Muth, J.F., Kolbas, R.M., Sharma, A.K., Oktyabrsky, S. and Narayan, J. (1999) *Journal of Applied Physics*, **85**, 7884.

50 Teke, A., Özgür, Ü., Doğan, S., Gu, X., Morkoç, H., Nemeth, B., Nause, J. and Everitt, H.O. (2004) *Physical Review B: Condensed Matter*, **70**, 195207.

51 Chichibu, S.F., Sota, T., Cantwell, G., Eason, D.B. and Litton, C.W. (2003) *Journal of Applied Physics*, **93**, 756.

52 Chichibu, S.F., Tsukazaki, A., Kawasaki, M., Tamura, K., Segawa, Y., Sota, T. and Koinuma, H. (2002) *Applied Physics Letters*, **80**, 2860.

53 Reynolds, D.C., Look, D.C., Jogai, B., Jones, R.L., Litton, C.W., Harsch, H. and Cantwell, G. (1999) *Journal of Luminescence*, **82**, 173.

54 Hümmer, K. and Gebhardt, P. (1978) *Physica Status Solidi b: Basic Research*, **85**, 271.

55 Makino, T., Chia, C.H., Tuan, N.T., Sun, H.D., Segawa, Y., Kawasaki, M., Ohtomo, A., Tamura, K. and Koinuma, H. (2000) *Applied Physics Letters*, **77**, 975.

56 Reynolds, D.C., Look, D.C., Jogai, B., Litton, C.W., Collins, T.C., Harsch, W. and Cantwell, G. (1998) *Physical Review B: Condensed Matter*, **57**, 12151.

57 Zhang, X.T., Liu, Y.C., Zhi, Z.Z., Zhang, J.Y., Lu, Y.M., Shen, D.Z., Xu, W., Fan, X.W. and Kong, X.G. (2002) *Journal of Luminescence*, **99**, 149.

58 Hamby, D.W., Lucca, D.A., Klopfstein, M.J. and Cantwell, G. (2003) *Journal of Applied Physics*, **93**, 3214.

59 Alves, H., Pfisterer, D., Zeuner, A., Riemann, T., Christen, J., Hofmann, D.M. and Meyer, B.K. (2003) *Optical Materials*, **23**, 33.

60 Hopfield, J.J. and Thomas, D.G. (1960) *Journal of Physics and Chemistry of Solids*, **12**, 276.

61 Suga, S.K., Cho, P., Heisinger, P. and Koda, T. (1967) *Journal of Luminescence*, **12**, 109.

62 Weisbuch, C. and Ulbrich, R. (1977) *Physical Review Letters*, **39**, 654.

63 Lagois, J. (1981) *Physical Review B: Condensed Matter*, **23**, 5511.

64 Reynolds, D.C., Litton, C.W. and Collins, T.C. (1965) *Physical Review*, **140**, A1726.

65 Meyer, B.K., Alves, H., Hofmann, D.M., Kriegseis, W., Forster, D., Bertram, F., Christen, J., Hoffmann, A., Strassburg, M., Dworzak, M., Haboeck, U. and Rodina, A.V. (2004) *Physica Status Solidi b: Basic Research*, **241**, 231.

66 Kobayashi, A., Sankey, O.F. and Dow, J.D. (1983) *Physical Review B: Condensed Matter*, **28**, 946.

67 Gonzales, C., Block, D., Cox, R.T. and Hervé, A. (1982) *Journal of Crystal Growth*, **59**, 357.

68 Block, D., Hervé, A. and Cox, R.T. (1982) *Physical Review B: Condensed Matter*, **25**, 6049.

69 Rorison, J., Herbert, D.C., Dean, D.J. and Skolnick, M.S. (1984) *The Journal of Physical Chemistry*, **17**, 6435.

70 Akimoto, O. and Hanamura, E. (1972) *Journal of the Physical Society of Japan*, **33**, 1537.

71 Lavrov, E.V., Weber, J., Börrnert, F., van de Walle, C.G. and Helbig, R. (2002) *Physical Review B: Condensed Matter*, **66**, 165205.

72 McCluskey, M.D., Jokela, S.J., Zhuravlev, K.K., Simpson, P.J. and Lynn, K.G. (2002) *Applied Physics Letters*, **81**, 3807.

73 Schilling, M., Helbig, R. and Pensl, G. (1985) *Journal of Luminescence*, **33**, 201.

74 Ko, H.J., Chen, Y.F., Hong, S.K., Wenish, H. and Yao, T. (2000) *Applied Physics Letters*, **77**, 3761.

75 Meyer, B.K., Sann, J., Hofmann, D.M., Neumann, C. and Zeuner, A. (2005) *Semiconductor Science and Technology*, **20**, S62.

76 Haynes, J.R. (1960) *Physical Review Letters*, **4**, 361.

77 Varshni, Y.P. (1967) *Physica*, **34**, 149.

78 Wang, L. and Giles, N.C. (2003) *Journal of Applied Physics*, **94**, 973.

79 Look, D.C., Reynolds, D.C., Litton, C.W., Jones, R.L., Eason, D.B. and Cantwell, G. (2002) *Applied Physics Letters*, **81**, 1830.

80 Rommeluère, J.F., Svob, L., Jomard, F., Mimila-Arroyo, J., Lusson, A., Sallet, V. and Marfaing, Y. (2003) *Applied Physics Letters*, **83**, 287.

81 Matsui, H., Saeki, H., Tabata, H. and Kawai, T. (2003) *Journal of the Electrochemical Society*, **150**, G508.

82 Zeuner, A., Alves, H., Hofmann, D.M., Meyer, B.K., Hoffmann, A., Haboeck, U., Strassburg, M. and Dworzak, M. (2002) Optical properties of the nitrogen acceptor in epitaxial ZnO. *Physica Status Solidi b: Basic Research*, **234**, R7.

83 Morhain, C., Teisseire, M., Vézian, S., Vigué, F., Raymond, F., Lorenzini, P., Guion, J., Neu, G. and Faurie, J.-P. (2002) *Physica Status Solidi b: Basic Research*, **229**, 881.

84 Ryu, Y.R., Lee, T.S. and White, H.W. (2003) Properties of arsenic-doped p-type ZnO grown by hybrid beam deposition. *Applied Physics Letters*, **83**, 87.

85 Viswanath, A.K., Lee, J.I., Yu, S., Kim, D., Choi, Y. and Hong, C.H. (1998) *Journal of Applied Physics*, **84**, 3848.

86 Kohan, A.F., Ceder, G., Morgan, D. and van de Walle, C.G. (2000) First-principles study of native point defects in ZnO. *Physical Review B: Condensed Matter*, **61**, 15019.

87 van de Walle, C.G. (2001) *Physica B*, **308–310**, 899.

88 Janotti, A. and van de Walle, C. (2005) Oxygen vacancies in ZnO. *Applied Physics Letters*, **87**, 122102. Janotti, A. and van de Walle, C.(2007) Native point defects in ZnO. *Physical Review B: Condensed Matter*, **76**, 165202.

89 Zhang, S.B., Wei, S.-H. and Zunger, A. (2001) Intrinsic n-type versus p-type doping asymmetry and the defect physics of ZnO. *Physical Review B: Condensed Matter*, **63**, 75205.

90 Oba, F., Nishitani, S.R., Isotani, S., Adachi, H. and Tanaka, I. (2001) *Journal of Applied Physics*, **90**, 824.

91 Lee, E.-C., Kim, Y.-S., Jin, Y.-G. and Chang, K.J. (2001) Compensation mechanism for N acceptors in ZnO. *Physical Review B*, **64**, 85120.

92 Smith, J.M. and Vehse, W.E. (1970) ESR of electron irradiated ZnO, Confirmation of the F^+ centre. *Physics Letters A*, **31**, 147.

93 Soriano, V. and Galland, D. (1976) Photosensitivity of the EPR spectrum of the F^+ center in ZnO. *Physica Status Solidi b: Basic Research*, **77**, 739.

94 Vlasenko, L.S. and Watkins, G.D. (2005) Optical detection of electron paramagnetic resonance in room-temperature electron-irradiated ZnO. *Physical Review B: Condensed Matter*, **71**, 125210.

95 Neugebauer, J. and van de Walle, C.G. (1996) *Applied Physics Letters*, **69**, 503.

96 van de Walle, C.G. (2000) *Physical Review Letters*, **85**, 1012.

97 Janotti, A. and Van de Walle, C.G. (2007) *Nature Materials*, **6**, 44.

98 Yan, Y., Zhang, S.B. and Pantelides, S.T. (2001) *Physical Review Letters*, **86**, 5723.

99 Reshchikov, M.A. and Morkoç, H. (2005) *Journal of Applied Physics*, **97**, 061301.

100 Zwingel, D. (1972) *Journal of Luminescence*, **5**, 385.

101 Reshchikov, M.A., Morkoç, H., Nemeth, B., Nause, J., Xie, J., Hertog, B. and Osinsky, A. (2007) *Physica B*, **401–402**, 358.

102 Dingle, R. (1969) *Physical Review Letters*, **23**, 579.

103 Schmidt, O., Kiesel, P., van de Walle, C.G., Johnson, N.M., Nause, J. and Kohler, G.H. (2005) *Japanese Journal of Applied Physics*, **44**, 7271.

104 Look, D.C., Mosbacker, H.L., Strzhemechny, Y.M. and Brillson, L.J. (2005) *Superlattices and Microstructures*, **38**, 406.

105 Vanheusden, K., Seager, C.H., Warren, W.L., Tallant, D.R. and Voigt, J.A. (1996) *Applied Physics Letters*, **68**, 403.

106 Vanheusden, K., Warren, W.L., Seager, C.H., Tallant, D.R., Voigt, J.A. and Gnade, B.E. (1996) *Journal of Applied Physics*, **79**, 7983.

107 Dietz, R.E., Kamimura, H., Sturge, M.D. and Yariv, A. (1963) *Physical Review*, **132**, 1559.

108 Kimpel, B.M. and Schulz, H.J. (1991) *Physical Review B: Condensed Matter*, **43**, 9938.

109 Broser, I.J., Germer, R.K.F., Schulz, H.-J.E. and Wisznewski, K.P. (1978) *Solid State Electronics*, **21**, 1597.

110 Dahan, P., Fleurov, V., Thurian, P., Heitz, R., Hoffmann, A. and Broser, I. (1998) *Journal of Physics: Condensed Matter*, **10**, 2007.

111 Dahan, P., Fleurov, V., Thurian, P., Heitz, R., Hoffmann, A. and Broser, I. (1998) *Physical Review B: Condensed Matter*, **57**, 9690.

112 Dean, P.J., Robbins, D.J., Bishop, S.G., Savage, J.A. and Porteous, P. (1981) *Journal of Physics C: Solid State Physics*, **14**, 2847.

113 Dahan, P., Fleurov, V. and Kikoin, K. (1997) *Journal of Physics: Condensed Matter*, **9**, 5355.

114 Kuhnert, R. and Helbig, R. (1981) *Journal of Luminescence*, **26**, 203.

115 Reynolds, D.C., Look, D.C., Jogai, B., Van Nostrand, J.E., Jones, R. and Jenny, J. (1998) *Solid State Communications*, **106**, 701.

116 Reynolds, D.C., Look, D.C. and Jogai, B. (2001) *Journal of Applied Physics*, **89**, 6189.

117 Garces, N.Y., Wang, L., Bai, L., Giles, N.C., Halliburton, L.E. and Cantwell, G. (2002) *Applied Physics Letters*, **81**, 622.

118 Yang, X., Du, G., Wang, X., Wang, J., Liu, B., Zhang, Y., Liu, D., Liu, D., Ong, H.C. and Yang, S. (2003) *Journal of Crystal Growth*, **252**, 275.

119 Guo, B., Qiu, Z.R. and Wong, K.S. (2003) *Applied Physics Letters*, **82**, 2290.

120 Egelhaaf, H.-J. and Oelkrug, D. (1996) *Journal of Crystal Growth*, **161**, 190.

121 Korsunska, N.O., Borkovska, L.V., Bulakh, B.M., Khomenkova, L.Yu., Kushnirenko, V.I. and Markevich, I.V. (2003) *Journal of Luminescence*, **102–103**, 733.

122 Lin, B., Fu, Z. and Jia, Y. (2001) *Applied Physics Letters*, **79**, 943.

123 Vanheusden, K., Seager, C.H., Warren, W.L., Tallant, D.R., Caruso, J., Hampden-Smith, M.J. and Kodas, T.T. (1997) *Journal of Luminescence*, **75**, 11.

124 Studenikin, S.A., Golego, N. and Cocivera, M. (1998) *Journal of Applied Physics*, **84**, 2287.

125 Leiter, F.H., Alves, H.R., Hofstaetter, A., Hoffmann, D.M. and Meyer, B.K. (2001) *Physica Status Solidi b: Basic Research*, **226**, R4.

126 Leiter, F.H., Alves, H.R., Romanov, N.G., Hoffmann, D.M. and Meyer, B.K. (2003) *Physica B*, **340–342**, 201.

127 Reshchikov, M.A. and Korotkov, R.Y. (2001) *Physical Review B: Condensed Matter*, **64**, 115205.

128 Cox, R.T., Block, D., Hervé, A., Picard, R., Santier, C. and Helbig, R. (1978) *Solid State Communications*, **25**, 77.

129 Reshchikov, M.A. and Morkoç, H. (2000) unpublished.

130 Matz, R. and Lütz, H. (1979) *Applied Physics*, **18**, 123.

131 Hu, W.S., Liu, Z.G., Sun, J., Zhu, S.N., Xu, Q.Q., Feng, D. and Ji, Z.M. (1997) *Journal of Physics and Chemistry of Solids*, **58**, 853.

132 Yoshikawa, H. and Adachi, S. (1997) *Japanese Journal of Applied Physics*, **36**, 6237.

133 Jellison, G.E., Jr, and Boatner, L.A. (1998) *Physical Review B: Condensed Matter*, **58**, 3586.

134 Teng, C.W., Muth, J.F., Özgür, Ü., Bergmann, M.J., Everitt, H.O., Sharma, A.K., Jin, C. and Narayan, J. (2000) *Applied Physics Letters*, **76**, 979.

135 Ashkenov, N., Mbenkum, B.N., Bundesmann, C., Riede, V., Lorenz, M., Spemann, D., Kaidashev, E.M., Kasic, A., Schubert, M., Grundmann, M., Wagner, G., Neumann, H., Darakchieva, V., Arwin, H. and Monemar, B. (2003) Infrared dielectric functions of phonon modes of high-quality ZnO films. *Journal of Applied Physics*, **93**, 126.

136 Schmidt, R., Rheinlander, B., Schubert, M., Spemann, D., Butz, T., Lenzner, J., Kaidashev, E.M., Lorenz, M., Rahm, A., Semmelhack, H.C. and Grundmann, M. (2003) *Applied Physics Letters*, **82**, 2260.

137 Kim, K.-K., Kim, H.-S., Hwang, D.-K., Lim, J.-H. and Park, S.-J. (2003) *Applied Physics Letters*, **83**, 63.

138 Chen, Y., Tuan, N.T., Segawa, Y., Ko, H.-J., Hong, S.-K. and Yao, T. (2001) *Applied Physics Letters*, **78**, 1469.

139 Bagnall, D.M., Chen, Y.F., Zhu, Z., Yao, T., Shen, M.Y. and Goto, T. (1998) *Applied Physics Letters*, **73**, 1038.

140 Yamamoto, A., Kido, T., Goto, T., Chen, Y., Yao, T. and Kasuya, A. (1999) *Applied Physics Letters*, **75**, 469.

141 Yu, P., Tang, Z.K., Wong, G.K.L., Kawasaki, M., Ohtomo, A., Koinuma, H. and Segawa, Y. (1998) *Journal of Crystal Growth*, **184–185**, 601.

142 Nicoll, F.H. (1966) *Applied Physics Letters*, **9**, 13.

143 Packard, J.R., Campbell, D.A. and Tait, W.C. (1967) *Journal of Applied Physics*, **38**, 5255.

144 Iwai, S. and Namba, A. (1970) *Applied Physics Letters*, **16**, 354.

145 Klingshirn, C. (1975) *Physica Status Solidi b: Basic Research*, **71**, 547.

146 Shewchun, J., Garside, B.K., Kawasaki, B.S. and Efthymiopoulos, T. (1972) *Journal of Applied Physics*, **43**, 545.

147 Johnston, W.D., Jr, (1971) *Journal of Applied Physics*, **42**, 2731.

148 Goto, T. and Langer, D.W. (1971) *Journal of Applied Physics*, **42**, 5066.

149 Reynolds, D.C., Look, D.C. and Jogai, B. (1996) *Solid State Communications*, **99**, 873.

150 Bagnall, D.M., Chen, Y.F., Shen, M.Y., Zhu, Z., Goto, T. and Yao, T. (1998) Room temperature excitonic stimulated emission from zinc oxide epilayers grown by plasma assisted MBE. *Journal of Crystal Growth*, **184–185**, 605.

151 Bagnall, D.M., Chen, Y.F., Zhu, Z., Yao, T., Koyama, S., Shen, M.Y. and Goto, T. (1997) *Applied Physics Letters*, **70**, 2230.

152 Özgür, Ü., Teke, A., Liu, C., Cho, S.-J., Morkoç, H. and Everitt, H.O. (2004) *Applied Physics Letters*, **84**, 3223.

153 Kawasaki, M., Ohtomo, A., Ohkubo, I., Koinuma, H., Tang, Z.K., Yu, P., Wong, G.K.L., Zhang, B.P. and Segawa, Y. (1998) *Materials Science and Engineering B: Solid State Materials for Advanced Technology*, **56**, 239.

154 Zu, P., Tang, Z.K., Wong, G.K.L., Kawasaki, M., Ohtomo, A., Koinuma, H. and Segawa, Y. (1997) *Solid State Communications*, **103**, 459.

155 Ohtomo, A., Kawasaki, M., Sakurai, Y., Yoshida, Y., Koinuma, H., Yu, P., Tang, Z.K., Wong, G.K.L. and Segawa, Y. (1998) *Materials Science and Engineering B: Solid State Materials for Advanced Technology*, **54**, 24.

156 Yamamoto, A., Miyajima, K., Goto, T., Ko, H.J. and Yao, T. (2001) *Journal of Applied Physics*, **90**, 4973.

157 Hvam, J.M., Blattner, G., Reuscher, M. and Klingshirn, C. (1983) *Physica Status Solidi b: Basic Research*, **118**, 179.

158 Sun, H.D., Makino, T., Segawa, Y., Kawasaki, M., Ohtomo, A., Tamura, K. and Koinuma, H. (2001) *Applied Physics Letters*, **78**, 3385.

159 Lawandy, N.M., Balachandran, R.M., Gomes, A.S.L. and Sauvain, E. (1994) *Nature*, **368**, 436.

160 Wiersma, D.S., van Albada, M.P. and Lagendijk, A. (1995) *Physical Review Letters*, **75**, 1739.

161 Cao, H., Zhao, Y.G., Ong, H.C., Ho, S.T., Dai, J.Y., Wu, J.Y. and Chang, R.P.H. (1998) *Applied Physics Letters*, **73**, 3656.

162 Cao, H., Zhao, Y.G., Ho, S.T., Seelig, E.W., Wang, Q.H. and Chang, R.P.H. (1999) Random laser action in semiconductor powder. *Physical Review Letters*, **82**, 2278.

163 Mitra, A. and Thareja, R.K. (2001) *Journal of Applied Physics*, **89**, 2025.

164 Wiersma, D.S. and Lagendijk, A. (1996) *Physical Review E*, **54**, 4256.

165 Anderson, P.W. (1958) *Physical Review*, **109**, 1492.

166 Kuz'mina, I.P. and Nikitenko, V.A. (1984) *Zinc Oxides: Production and Optical Properties*, Nauka, Moscow.

167 Dimova-Alyakova, D.I., Malov, M.M., Dmitriev, V.V., Chernyi, V.D. and Mendakov, M.N. (1974) *Moscow Energetical Institute Transactions (Trudy MEI)*, **192**, 78 (in Russian).

168 Cho, S., Ma, J., Kim, Y., Sun, Y., Wong, G.K.L. and Ketterson, J.B. (1999) Photoluminescence and ultraviolet lasing of polycrystalline ZnO thin films prepared by the oxidation of the metallic Zn. *Applied Physics Letters*, **75**, 2761.

169 Chen, S.J., Liu, Y.C., Ma, J.G., Zhao, D.X., Zhi, Z.Z., Lu, Y.M., Zhang, J.Y., Shen, D.Z. and Fan, X.W. (2002) *Journal of Crystal Growth*, **240**, 467.

170 Wang, Y.G., Lau, S.P., Lee, H.W., Yu, S.F., Tay, B.K., Zhang, X.H. and Hng, H.H. (2003) *Journal of Applied Physics*, **94**, 354.

171 Alivov, Ya.I., Chernykh, A.V., Chukichev, M.V. and Korotkov, R.Y. (2005) *Thin Solid Films*, **473**, 241.

172 Ohtomo, A., Tamura, K., Kawasaki, M., Makino, T., Segawa, Y., Tang, Z.K., Wong, G.K., Matsumoto, Y. and Koinuma, H. (2000) *Applied Physics Letters*, **77**, 2204.

173 Sun, H.D., Makino, T., Tuan, N.T., Segawa, Y., Tang, Z.K., Wong, G.K.L., Kawasaki, M., Ohtomo, A., Tamura, K. and Koinuma, H. (2000) *Applied Physics Letters*, **77**, 4250.

174 Sun, H.D., Makino, T., Segawa, Y., Kawasaki, M., Ohtomo, A., Tamura, K. and Koinuma, H. (2002) *Journal of Applied Physics*, **91**, 1993.

175 Reynolds, D.C., Look, D.C., Jogai, B., Hoelscher, J.E., Sherriff, R.E., Harris, M.T. and Callahan, M.J. (2000) *Journal of Applied Physics*, **88**, 2152.

176 Koida, T., Chichibu, S.F., Uedono, A., Tsukazaki, A., Kawasaki, M., Sota, T., Segawa, Y. and Koinuma, H. (2003) *Applied Physics Letters*, **82**, 532.

177 Jung, S.W., Park, W.I., Cheong, H.D., Yi, G.-C., Jang, H. M., Hong, S. and Joo, T. (2002) *Applied Physics Letters*, **80**, 1924.

178 Shen, Y.R. (1994) *The Principle of Nonlinear Optics*, John Wiley & Sons, Inc., New York.

179 Gavrilenko, V.I., Wu, R. and Downer, M. (1999) *Bulletin of the American Physical Society*, **44**, 1910.

180 See for example. Boyd, R. W., (2003) *Nonlinear Optics*, 2nd edn, Academic Press, San Diego, CA.

181 See for example. Yariv, A., (1975) *Quantum Electronics*, 2nd edn, John Wiley & Sons, Inc.

182 Levine, B.F. (1973) Bond-charge calculation of nonlinear optical susceptibilities for various crystal structures. *Physical Review B: Condensed Matter*, **7**, 2600.

183 Wimmer, E., Krakauer, H., Weinert, M. and Freeman, A.J. (1981) Full-potential self-consistent linearized-augmented plane-wave method for calculating the electronic structure of molecules and surfaces: O_2 molecule. *Physical Review B: Condensed Matter*, **24**, 864.

184 Koelling, D.D. and Harmon, B.N. (1977) A technique for relativistic spin-polarised calculations. *The Journal of Physical Chemistry*, **10**, 3107.

185 Armstrong, J.A., Bloembergen, N., Ducuing, J. and Pershan, P.S. (1962) Interactions between light waves in a nonlinear dielectric. *Physical Review*, **127**, 1918.

186 Loudon, P. (1962) *Proceedings of the Royal Society of London Series A: Mathematical Physical and Engineering Sciences*, **80**, 952.

187 Bloembergen, N. and Shen, Y.R. (1964) Quantum-theoretical comparison of nonlinear susceptibilities in parametric media, lasers, and Raman lasers. *Physical Review*, **133**, A37.

188 Cheng, H. and Miller, P.B. (1964) Nonlinear optical theory in solids. *Physical Review*, **134**, A683.

189 Robinson, F.N.H. (1968) Relations between the components of the nonlinear polarisability tensor in cubic and hexagonal II–VI compounds. *Physics Letters A*, **26**, 435.

190 Maker, P.D., Terhune, R.W., Nisenhoff, M. and Savage, C.M. (1962) Effects of dispersion and focusing on the production of optical harmonics. *Physical Review Letters*, **8**, 21.

191 Pavlides, P. and Pugh, D. (1991) General theory of Maker fringes in crystals of low symmetry. *Journal of Physics: Condensed Matter*, **3**, 967.

192 Jerphagnon, J. and Kurtz, S.K. (1970) Maker fringes: a detailed comparison of theory and experiment for isotropic and uniaxial crystals. *Journal of Applied Physics*, **41**, 1667.

193 Cao, H., Wu, J.Y., Ong, H.C., Dai, J.Y. and Chang, R.P.H. (1998) Second harmonic generation in laser ablated zinc oxide thin films. *Applied Physics Letters*, **73**, 572.

194 Larciprete, M.C., Haertle, D., Belardini, A., Bertolotti, M., Sarto, F. and Günter, P. (2006) Characterization of second and third order nonlinearities of ZnO sputtered films. *Physics Letters B*, **82**, 431.

195 Zhang, X.Q., Tang, Z.K., Kawasaki, M., Ohtomo, A. and Koinuma, H. (2003) Resonant exciton second-harmonic generation in self-assembled ZnO microcrystallite thin films. *Journal of Physics: Condensed Matter*, **15**, 5191.

196 Liu, C.Y., Zhang, B.P., Binh, N.T. and Segawa, Y. (2004) Second harmonic generation in ZnO thin films fabricated by metalorganic chemical vapor deposition. *Optics Communications*, **237**, 65.

197 Wang, G., Wong, G.K.L. and Ketterson, J.B. (2001) Redetermination of second order susceptibility of zinc oxide single crystals. *Applied Optics*, **40**, 5436.

198 Miller, R.C. and Nordland, W.A. (1970) Relative signs of nonlinear optical coefficients of polar crystals. *Applied Physics Letters*, **16**, 174.

199 Miller, R.C. and Nordland, W.A. (1970) *Optics Communications*, **1**, 400.

200 Singh, S. (1986) Nonlinear optical properties, in *Handbook of Laser Science and Technology: Optical Materials*,Vol. 3, Part 1 (ed. M.J. Weber), CRC, Boca Raton, FL.

201 Chan, S.W., Barille, R., Nuzzi, J.M., Tam, K.H., Leung, Y.H., Chan, W.K. and Djurišić, A.B. (2006) Second harmonic generation in ZnO nanorods. *Applied Physics B: Lasers and Optics*, **84**, 351.

202 Herman, W.N. and Hayden, L.M. (1995) Maker fringes revisited: second harmonic generation from birefringent or absorbing materials. *Journal of the Optical Society of America B: Optical Physics*, **12**, 416.

203 Wang, G., Kiehne, G.T., Wong, G.K.L., Ketterson, J.B., Liu, X. and Chang, R.P.H. (2002) Large second harmonic response in ZnO thin films. *Applied Physics Letters*, **80**, 401.

204 Neumann, U., Grunwald, R., Greibner, U., Steinmeyer, G. and Seeber, W. (2004) Second-harmonic efficiency of ZnO nanolayers. *Applied Physics Letters*, **84**, 170.

205 Levine, B.F. (1969) Electrodynamical bond-charge calculation of nonlinear optical susceptibilities. *Physical Review Letters*, **22**, 787.

206 Yang, X. and Xie, S. (1995) Expression of third-order effective nonlinear susceptibility for third-harmonic generation in crystals. *Applied Optics*, **34**, 6130.

207 Weiner, A.M., Leaird, D.E., Wiederrecht, G.P. and Nelson, K.A. (1990) Femtosecond pulse sequences used for optical manipulation of molecular motion. *Science*, **247**, 1317.

208 Bonadeo, N.H., Erland, J., Gammon, D., Park, D., Katzer, D.S. and Steel, D.G. (1998) Coherent optical control of the quantum state of a single quantum dot. *Science*, **282**, 1473.

209 Hazu, K., Sota, T., Suzuki, K., Adachi, S., Chichibu, S.F., Cantwell, G., Eason, D.B., Reynolds, D.C. and Litton, C.W. (2003) Strong biexcitonic effects and exciton–exciton correlations in ZnO. *Physical Review B: Condensed Matter*, **68**, 033205.

210 Rossi, F. and Kuhn, T. (2002) Theory of ultrafast phenomena in photoexcited semiconductors. *Reviews of Modern Physics*, **74**, 895.

211 Hazu, K., Adachi, A., Sota, T. and Chichibu, S.F. (2005) Measurements of exiton-polariton dynamics in ZnO by using nonlinear spectroscopic techniques. *Journal of Luminescence*, **112**, 7.

212 Sofiani, Z., Sahraoui, B., Addou, M., Adhiri, R., Lamrani, M.A., Dghoughi, L., Fellahi, N., Derkowska, B. and Bala, W. (2007) Third harmonic generation in undoped and X doped ZnO thin films (X: Ce, F, Er, Al, Sn) deposited by spray pyrolysis. *Journal of Applied Physics*, **101**, 063104.

213 Liu, C.Y., Zhang, B.P., Binh, N.T. and Segawa, Y. (2004) Third-harmonic generation from ZnO films deposited by MOCVD. *Applied Physics B: Lasers and Optics*, **79**, 83.

214 Narayanan, V. and Thareja, R.K. (2006) Harmonic generation in ZnO nanocrystalline laser deposited thin films. *Optics Communications*, **260**, 170.

215 Castañeda, L., Morales-Saavedra, O.G., Acosta, D.R., Maldonado, A., de la, M. and Olvera, L. (2006) Structural, morphological, optical, and nonlinear optical properties of fluorine-doped zinc oxide thin films deposited on glass substrates by the chemical spray technique. *Physica Status Solidi a: Applied Research*, **203**, 1971.

216 Zappettini, A., Amore, F.D., Pietralunga, S.M., Terio, A., Martinelli, M., Bliss, D.F. and Callahan, M.J. (2004) Wavelength dependence of the third order non-linear coefficient in hydrothermally grown ZnO crystals. *Physica Status Solidi c*, **1**, 997.

217 Petrov, G.I., Scheslavskiy, V., Yakovlev, V.V., Ozerov, I., Chelnokov, E. and Marine, W. (2003) Efficient third-harmonic generation in a thin nanocrystalline film of ZnO. *Applied Physics Letters*, **83**, 3993.

218 Sutherland, R.L. (2003) *Nonlinear Optics*, 2nd edn, Marcel Dekker, New York.

219 Adair, R., Chase, L.L. and Payne, S.A. (1989) Nonlinear refractive index of optical crystals. *Physical Review B: Condensed Matter*, **39**, 3337.

220 Pennington, D.M., Henesian, M.A. and Hellwarth, R.W. (1989) Nonlinear index of air at 1.053 μm. *Physical Review A*, **39**, 3003.

221 Said, A.A., Sheik-Bahae, M., Hagan, D.J., Wei, T.H., Wang, J., Young, J. and van Stryland, E.W. (1992) Determination of bound and free-carrier nonlinearities in ZnSe, GaAs, CdTe and ZnTe. *Journal of the Optical Society of America B: Optical Physics*, **9**, 405.

222 Sheik-Bahae, M., Hutchings, D.C., Hagan, D.J. and van Stryland, E.W. (1991) Dispersion of bound electronic nonlinear refraction in solids. *IEEE Journal of Quantum Electronics*, **27**, 1296.

223 Zhang, X., Fang, H., Tang, S. and Ji, W. (1997) Determination of two-photon-generated free-carrier lifetime in semiconductors by a single-beam Z-scan technique. *Applied Physics B: Lasers and Optics*, **65**, 549.

224 Sheik-Bahae, M., Said, AA., Wei, T.-H., Hagan, D.J. and van Stryland, E.W. (1990) Sensitive measurements of optical nonlinearities using a single beam. *IEEE Journal of Quantum Electronics*, **26**, 760.

225 Sheik-Bahae, M., Hagan, D.J. and van Stryland, E.W. (1990) Dispersion and bandgap scaling of the electronic Kerr effects in solids associated with two-photon absorption. *Physical Review Letters*, **65**, 96.

226 Hutchings, D.C. and van Stryland, E.W. (1992) Nondegenerate two-photon absorption in zinc blende semiconductors. *Journal of the Optical Society of America B: Optical Physics*, **9**, 2065.

227 Lee, C.C. and Fan, H.Y. (1974) Two-photon absorption with exciton effect for degenerate valence bands. *Physical Review B: Condensed Matter*, **9**, 3502.

228 Bolger, J.A., Bar, A.K., Wherrett, B.S., DeSalvo, R., Hutchings, D.C. and Hagan, D.J. (1993) Nondegenerate two-photon absorption spectra of ZnSe, ZnS, and ZnO. *Optics Communications*, **97**, 203.

229 Dean, D.R. and Collins, R.J. (1973) Transient phase gratings in ZnO induced by two-photon absorption. *Journal of Applied Physics*, **44**, 5455.

230 Lin, J.-H., Chen, Y.-J., Lin, H.-Y. and Hsieh, W.-F. (2005) Two-photon assisted huge nonlinear refraction and absorption in ZnO thin films. *Journal of Applied Physics*, **97**, 033526.

231 van Stryland, E.W., Vanherzeele, H., Woodall, M.A., Soileau, M.J., Smirl, A.L., Guha, S. and Boggess, T.F. (1985) Two photon absorption, nonlinear refraction, and optical limiting in semiconductors. *Optical Engineering*, **24**, 613.

232 Petit, S., Guennani, D., Gilliot, P., Hirlimann, C., Hönerlage, B., Briot, O. and Aulombard, R.L. (1997) *Materials Science and Engineering B*, **43**, 196.

233 Sun, C.K., Liang, J.C., Wang, J.C., Kao, Fu.-Jen., Keller, S., Mack, M.P., Mishra, U. and DenBaars, S. P. 2000 Two-photon absorption study of GaN. *Applied Physics Letters*, **76**, 439.

234 Reuther, A., Laubereau, A. and Nikogosyan, D.N. (1997) *Optics Communications*, **141**, 180.

235 Streltsov, A.M., Ranka, J.K. and Gaeta, A.L. (1998) *Optics Letters*, **23**, 798.

4
Doping of ZnO

As amply mentioned in previous chapters, ZnO has a potential for various short-wavelength optoelectronic device applications. To realize them, however, the conductivity including its polarity in ZnO and related materials must be engineered controllably, which remains to be the foremost obstacle to device development, particularly the p-type conductivity. To attain the potential offered by ZnO, both high-quality n- and p-type ZnO are indispensable, with carrier concentrations well in excess of $10^{17}\,cm^{-3}$. However, difficulty in controlled bipolar carrier doping (both n- and p-type) in a wide range of concentrations in wide-bandgap semiconductors is a major obstacle, as seen in GaN and II–VI compound semiconductors including ZnS, ZnSe, and ZnTe [1–7]. In all cases, unintentionally doped ZnO has been observed to be n-type with the compensated electron concentrations reduced to less than $10^{14}\,cm^{-3}$ in bulk samples grown hydrothermally. The background concentration has been attributed to the presence of intrinsic defects and impurities. Intentional n-type doping is relatively well established through the substitution of group III elements (Al, Ga, In) on the Zn sites, producing highly conductive n-type ZnO. However, all efforts to obtain reliable p-type doping in ZnO have so far been mainly unsuccessful. The same intrinsic defects responsible for n-type conductivity tend to aggravate the efforts for p-type doping by compensating the potential acceptors. Predilection for unipolar doping is not all that surprising in wide-bandgap semiconductors: GaN, CdS, ZnS, and ZnSe are also easily doped to n-type whereas p-type doping is difficult. The situation is opposite for ZnTe and CdTe, where p-type doping is easily obtained whereas n-type doping is difficult. In general, the asymmetry arises from the fact that wide-gap semiconductors have either a low valence band maximum or a high conduction band minimum with respect to the vacuum level [6, 8]. As a result, some materials in which the valence band is relatively close to the vacuum level, for example, ZnTe, CdTe, and diamond, have preferable p-type conductivity. In contrast, materials with a valence band relatively far from the energetic position of the vacuum level, for example, ZnO, GaN, CdS, ZnS, and ZnSe, have preferable n-type conductivity.

Generally speaking, elements such as Al, Ga, and In on the Zn sites and Cl and I on the O sites can potentially form shallow donors in ZnO. Elements such as Li, Na, K, Cu, and Ag on the Zn sites and N, P, Sb, and As on the O sites have the potential of

forming acceptors, albeit deep, in ZnO. For p-type conductivity in ZnO, it appears as if the research completed a full cycle and the attention is now once again focused back on to N, which was originally thought to be the most promising p-type doping candidate due to its close ionic radius to O. This chapter focuses on issues related to only n-type and p-type doping of ZnO. Doping with transition metals for magnetic properties is discussed in Chapter 5.

4.1 n-Type Doping

ZnO with a wurtzite structure is naturally an n-type semiconductor because of deviation from stoichiometry due to the presence of intrinsic defects such as O vacancies (V_O) and Zn interstitials (Zn_i). Undoped ZnO shows n-type conductivity with electron densities as high as $10^{21}\,cm^{-3}$ [5], a value that fortunately has been reduced by molecular beam epitaxy (MBE) to about $10^{17}\,cm^{-3}$ [9, 10] and by hydrothermal growth to below $10^{14}\,cm^{-3}$ [11].

Although it is experimentally known that unintentionally doped ZnO is n-type, the responsible donors are not known exactly. For example, a first-principles study suggests that none of the native defects shows the characteristics of a shallow donor with high concentration [12]. Oxygen vacancies have been shown to be deep donors in ZnO using electron paramagnetic resonance (EPR) experiments; therefore, they cannot be responsible for n-type conductivity [13]. Unfortunately, however, because of their low formation energy in p-type ZnO, they can compensate acceptors (see Section 3.3.1 for a more detailed discussion). Look *et al.* [14] suggested that Zn_i rather than V_O is the dominant native shallow donor in ZnO with an ionization energy of about 30–50 meV, although it has high formation energy in n-ZnO. It has also been suggested that the n-type conductivity of unintentionally doped ZnO films is only due to hydrogen that, as was treated in Section 3.3.1, acts as a shallow donor with an ionization energy of about 30 meV [12, 15–17]. This conjecture is supported by the fact that hydrogen is always present in all growth methods and can easily diffuse into ZnO in large amounts even at temperatures as low as 600 °C due to its large mobility. Hydrogen also passivates acceptors such as N_O by forming complexes with them and can be identified by the donor-bound excitonic emission at 3.363 eV (I_4 line, see Section 3.2.2). First-principles calculations also suggest that unintentionally incorporated hydrogen acts as a source of conductivity and behaves as a shallow donor in ZnO [18]. ZnO samples exposed to remote H plasma showed increased electron concentration by as much as an order of magnitude, which tends to be consistent with the predicted donor nature of H [17].

To reiterate, attainment of intentional n-type doping of ZnO is relatively easy compared to p-type doping. As n-type dopants, group III elements B [19, 20], Al [21–33], Ga [34, 35], and In [36, 37], rare earth metals (group IIIB) Sc and Y [38], group IV elements Si [39], Ge [40], and Sn [41], and group VII elements F [42], Cl [43], and I can be used. Various deposition methods such as MBE, sputtering, PLD, and chemical vapor deposition (CVD) have been used to produce highly

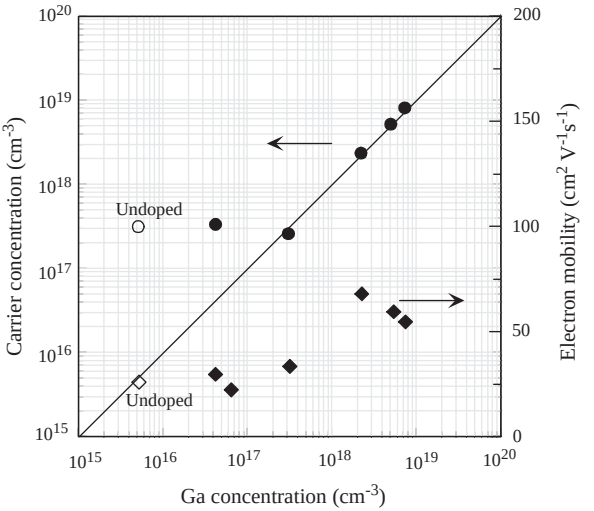

Figure 4.1 Room-temperature carrier concentration (circles) and mobility (diamonds) of Ga-doped ZnO films grown on GaN as a function of Ga concentration. Solid line represents a Ga activation ratio of unity. (After Ref. [50].)

conductive n-type ZnO films [44–49], where those produced particularly by MBE exhibited high crystalline quality [34, 50, 51]. Group III elements Al, Ga, and In as substitutional elements for Zn are probably more suitable for n-type doping of ZnO due to their lower vapor pressures compared to group VII elements such as Cl, Br, and I substituting for O. In addition, Cl and I may have memory effect in low-pressure deposition systems such that the residual electron concentration would not be low after Cl or I usage [34]. Oxidation of Al source during MBE growth may also become a problem because of its high reactivity with O. Ga and In are less reactive than Al. Furthermore, Ko *et al.* [34] estimated covalent bond lengths of Ga–O (1.92 Å) to be slightly smaller than those of Zn–O (1.97 Å), whereas the bond length of In–O was estimated higher (2.1 Å), not surprisingly considering the large ionic radius of In. The bond length of Ga–O is expected to cause only small deformation of the ZnO lattice even in the case of high Ga concentration, whereas the larger bond lengths of In–O would deform the ZnO lattice more seriously, which is also the case for Zn–Cl bonds (2.3 Å) for Cl doping. That is why Ga is likely an optimum choice for doping ZnO by techniques such as MBE. Successful Ga doping was demonstrated for ZnO films grown both on GaN templates and on *a*-plane sapphire [50]. Figure 4.1 shows the room-temperature carrier concentrations (circles) and mobility of Ga-doped ZnO films grown on GaN measured by the van der Pauw method as a function of Ga concentration obtained from secondary ion mass spectroscopy (SIMS). In spite of the possible problem of source oxidation, n-type conductivity by doping ZnO with Al by MBE has been reported by Ohgaki *et al.* [51]. Electrical properties of some of the MBE-grown n-type ZnO films doped with Al and Ga are compiled in Table 4.1.

Table 4.1 Carrier concentration, mobility, and XRD rocking curve FWHM values for n-type ZnO grown by MBE using Al and Ga dopants.

Dopant	Carrier concentration (cm^{-3})	Mobility ($cm^2 V^{-1} s^{-1}$)	(0002) XRD rocking curve FWHM (arcsec)	Substrate	Reference
Al	6.7×10^{20}			$ScAlMgO_4$	[30]
Al	$>10^{20}$			Sapphire	[51]
Ga	1.33×10^{18}	120.5	~350	GaN	[34]
	9.53×10^{19}	51.1	~900		
	1.13×10^{20}	—	~670		
Ga	6×10^{20}			$ScAlMgO_4$	[35]
Ga	7×10^{18}	55	~350	*a*-sapphire	[50]
	2×10^{18}	68	~330		

As discussed in Section 8.4.5, part of the motivation for n-type doping of ZnO comes from the need for transparent conducting oxides for transparent electrodes as ZnO is transparent to visible wavelengths [52]. Carrier concentrations above $10^{21}\,cm^{-3}$ and resistivities below $10^{-4}\,\Omega\,cm$ have been obtained for n-type ZnO films (see Table 8.4). Al-doped ZnO films prepared by photoassisted metalorganic vapor-phase epitaxy (MOVPE) were shown to exhibit a minimum resistivity of $6.2\times10^{-4}\,\Omega\,cm$ [44]. For ZnO:Al films deposited on glass substrates using PLD, Agura *et al.* [33] reported a minimum resistivity of $8.54\times10^{-5}\,\Omega\,cm$ and a mobility of $\sim50\,cm^2\,V^{-1}\,s^{-1}$ at a carrier concentration of $1.5\times10^{21}\,cm^{-3}$ that corresponds to an Al composition of 1.8 wt%. Resistivities as low as $1.2\times10^{-4}\,\Omega\,cm$ have also been reported for Ga-doped ZnO films grown by chemical vapor deposition [45]. It should be noted that the dopant concentrations in these ZnO films, which were meant to be used for transparent conductive electrodes, are relatively high. These heavily doped ZnO films have been shown to exhibit a systematic blueshift of the bandgap, which is attributed to the Burstein–Moss effect [53, 54]. The amount of blueshift was, for example, ~430 meV in ZnO:Ga films when Ga concentration was increased to $6\times10^{20}\,cm^{-3}$ [35], ~390 meV in ZnO:Al films having a carrier concentration of $10.5\times10^{20}\,cm^{-3}$ [27], and ~168 meV for ZnO:F films [42].

As touched upon to some extent in Section 3.2.3, donor binding energies can be extracted from low-temperature PL spectra. In the simple hydrogen-like effective mass approximation, the separation between the ground state of the neutral donor-bound exciton ($n=1$) and the corresponding excited state (two-electron satellite, $n=2$) is simply 3/4 of the donor binding energy in the effective mass theory, $E_{D,eff}$. Only the states having s symmetry would be affected by the short-range chemical potential of the impurity leading to a deviation of the real donor binding energy, E_D, from the effective mass value, $E_{D,eff}$. The donor binding energy in this case is given by

$$E_D = E_{2p\leftrightarrow1s} + \frac{1}{4}E_{D,eff}, \tag{4.1}$$

where $E_{2p\leftrightarrow 1s}$ is the separation between the TES line and the corresponding ground-state bound exciton emission line. However, in polar hexagonal semiconductors such as ZnO, the 2s and 2p states are further split (2s, $2p_z$, and $2p_{xy}$, where the *c*-axis is along the *z*-direction) due to anisotropy and the polar interaction with the optical phonons (polarons). The modified 1s, 2s, $2p_z$, and $2p_{xy}$ state energies have been obtained using the second-order perturbation theory [55]. For all donors having binding energies above 48 meV, the largest separation was found to be between 1s and $2p_{xy}$ states [55]. The extracted binding energies for various donors are listed in Table 3.4. The low-temperature donor-bound exciton PL lines generally designated as I_6 (3.3608 eV), I_8 (3.3598 eV), and I_9 (3.3567 eV) are assigned to Al, Ga, and In donors, having donor binding energies, E_D, of 53, 54.5, and 63.2 meV, respectively [55, 56]. Similar values are reported by others, for example, 51 and 55 meV for Al from Teke *et al.* [57] and Alves *et al.* [58], respectively, and 53 meV for Ga from Reuss *et al.* [59].

The binding or localization energies, E_{loc}, of the donor-bound excitons may also be correlated to the donor binding (ionization) energies, E_D, as formulated by Haynes, $E_{loc} = \alpha E_D$, where α is a proportionality constant [60]. The exciton localization energies are determined from the difference between the free exciton (E_{FX}) and the ground-state neutral donor-bound exciton (E_{D^0X}) emission energies. A more general form of the Haynes rule is

$$E_{loc} = E_{FX} - E_{D^0X} = a + bE_D, \tag{4.2}$$

where the coefficients *a* and *b* are determined from the experiments (see Section 3.2.3 for reported values). A plot of exciton localization energies versus the respective donor binding energies, namely, the Haynes plot, is shown in Figure 4.2 for bulk ZnO [55, 56]. I_4 is associated with the H donor, and the chemical origin of the I_{10} line is still not clear. For a discussion of donor-bound exciton PL line designations (I_i), see Section 3.2.2.

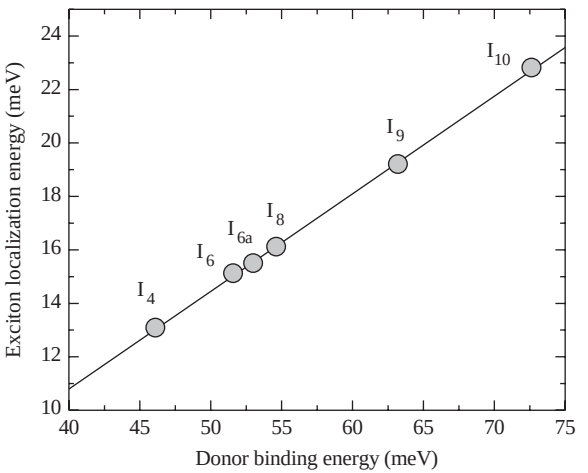

Figure 4.2 Exciton localization energies versus the respective donor binding energies (Haynes plot) for bulk ZnO. The solid line is a fit to Equation 4.2 with $a = -3.8$ eV and $b = 0.365$. (After Refs [55, 56].)

4.2 p-Type Doping

As mentioned repeatedly, it is very difficult, to varying degrees, to obtain p-type doping in wide-bandgap semiconductors such as ZnO, GaN, ZnS, CdS, and ZnSe. The difficulties can arise from a variety of causes. Attempted p-type dopants may be compensated by low-energy native defects, such as Zn_i [14] or V_O [61], or background impurities (H) with propensity to n-type doping. Some centers of compensation are pinned to the same level that hardly depends on the position of valences and conductive bands [62]. This compensation problem is the most challenging phenomenon in wide-gap semiconductors and ZnO in particular. The experimental data when scrutinized show instability of p-type conductivity in ZnO, reverting to n-type conductivity within a matter of days [63]. Low solubility of the dopant in the host material [64, 65] and precipitate formation [66] are also possible causes. The deep impurity level can also be a source of the doping problem causing significant resistance to the formation of shallow acceptor level [67].

There has been a plethora of reports of p-type behavior in ZnO, often with apparently very high hole concentrations but with low mobilities. In a few cases, the mobilities reported are unreasonably high. Even what is generally known as n-type dopants have been reported to produce p-type ZnO. Nitrogen, which is known to provide the shallowest acceptor impurity, is most likely a genuine p-type dopant. However, N has low solubility making it imperative to decrease the background donor concentration and increase solubility by codoping. As mentioned earlier, reports are also abound with the facts that the purported p-type doping is not stable in ZnO. There have also been p–n junctions reported, but efficiency of light emission is low, the emission width is arguably wide, and the source of emission is controversial and/or not well understood. The discrepancies in the reported data stem from the fact that the measurement methods applied to particular samples may no be appropriate.

Known acceptors in ZnO include group I elements, such as Li [68–70], Na, and K, Cu [71], Ag [72], and Zn vacancies, and group V elements such as N, P, Sb, and As. However, many of these form deep acceptors and do not contribute sufficiently to p-type conduction. Zn vacancies have low formation energy in n-ZnO and can be created by high-energy (2 MeV) electrons. They were shown to be dominant acceptors in as-grown n-type ZnO using positron annihilation spectroscopy [73]. It is believed that the most promising dopants for p-type ZnO are the group V elements, although theory suggests some difficulty in achieving shallow acceptor level [74]. Plasma sources are used for N doping, whereas conventional effusion cells can be employed for As, Sb, and P. The activation energy of P was reported to be 127 meV [75]. Among these candidates, N has the smallest ionic radius (1.68 Å), which is very close to O ionic radius of 1.38 Å, but as mentioned above, its solubility is low. The ionic radii for the other possible group V impurities that substitute for O in ZnO are 2.12, 2.22, and 2.45 Å for P^{3-}, As^{3-}, and Sb^{3-}, respectively.

A number of theoretical studies have addressed the fundamental microscopic aspects of doping in wide-bandgap semiconductors. The majority of these studies

have dealt with the manner in which dopant solubility [1, 64] or native defects [76, 77] such as vacancies, interstitials, and antisites interfere with doping. Various substitutional impurities for ZnO have been examined as p-type dopants by using the first-principles pseudopotential method [74, 78, 79]. It has been shown theoretically that codoping with acceptor (N) and donor (Al, Ga, In) impurities in a 2 : 1 ratio in ZnO can stabilize substitution of N at the appropriate lattice site through the formation of N–Ga–N bonds (ADA standing for acceptor–donor–acceptor). However, it should be realized that isolated Ga atoms can compensate the N–Ga–N acceptors [80]. Numerous experimental studies based on the above-mentioned codoping approach, which has been reported to be successful in GaN [81], have resulted in little or no success in terms of achieving stable p-type material [82].

While most of the initial efforts for p-type doping of ZnO have focused on N doping, other studies, albeit fewer, have considered other group V elements for substitutional doping on O sites, including P [75, 83–88], As [89–93], and even Sb [94–96]. Despite the fact that ionic radii of these dopants by far exceed that of oxygen as mentioned above, p-type conductivity was reported. To explain the experimental reports, Limpijumnong *et al.* [97] proposed a model for large-sized mismatched group V dopants in ZnO based on first-principles calculations. The model states that dopant atoms do not occupy the O sites as is widely perceived, but rather the Zn sites: each forms a complex with two spontaneously induced Zn vacancies in a process that involves fivefold As coordination. Calculations indicate that the $As_{zn}–2V_{zn}$ defect complex should have an acceptor level at about 150 meV, shallower than that of As_O, and lower formation energy than any of the parent defects. The same scenario is also true for Sb with the ionization energy of 160 meV. The calculated values of the ionization energies are in reasonable agreement with those found experimentally for Sb (0.14 eV [96]) and As (0.12 eV [98]) but much lower than those predicted for direct Sb and As substitution on O sites [74]. Therefore, these results suggest the formation of defect–impurity centers that are responsible for acceptor levels observed in ZnO doped with As or Sb. The implicit assumption here, of course, is that the experimental values are dependable. It should be pointed out that in systems with high localization, which is very likely to be the case here, Hall measurements might not really apply. Further, when applied, the prior state, temperature, and time would lead to changing results. In addition, the effects of any parallel conductivity in the entire sample structure must also be accounted for, which is seldom done. From the viewpoint of device applications, stability of these centers is a very important problem, because heat treatments during device fabrication or device operation in high-injection current regime and electric field can result in different data or complex decomposition, that is, conduction-type inversion.

To reiterate, the p-type doping in ZnO, which has been elusive, may be possible by substituting either group I elements (Li, Na, and K) for Zn sites or group V elements (N, P, Sb, and As) for O sites. It was shown using the density functional theory that group I elements could be better p-type dopants than group V elements in terms of shallowness of acceptor levels as shown in Table 4.2 [74]. However, group I elements tend to occupy the interstitial sites, in part mitigated by their small atomic radii, rather than the substitutional sites, and therefore act mainly as donors instead [74, 99].

Table 4.2 Calculated nearest-neighbor bond lengths, the defect energy levels (E_i) relative to the valence band maximum for negatively charged substitutional impurities, and the energy (ΔE) required to form the positively charged *AX* center from the substitutional acceptors.

	Element	Bond length (Å)	E_i (eV)	Δ(eV)
Group I	Li	2.03	0.09	0.21
	Na	2.10	0.17	1.04
	K	2.42	0.32	1.38
Group V	N	1.88	0.40	0.13
	P	2.18	0.93	−0.46
	As	2.23	1.15	−0.18

After Ref. [74].

Doping with Li has been shown to result in semi-insulating ZnO [100]. Moreover, significantly larger bond length for Na and K (see Table 4.2) than the ideal Zn–O bond length (1.93 Å) induces lattice strain, increasingly forming native defects such as vacancies that compensate the very dopants. These are among the many causes leading to difficulties in attaining p-type doping in ZnO. A similar behavior is observed for group V elements except for N. Both P and As also have significantly larger bond lengths compared to O and, therefore, are more likely to form antisites to avoid the lattice strain. The antisites, meaning group V elements on Zn sites, A_{Zn}, are donor-like and provide yet another unwelcome possible mechanism for compensating acceptors. It then appears that perhaps the best candidate for p-type doping in ZnO is N because among the group V impurities, N has the smallest ionization energy, it does not form the N_{Zn} antisite, and the *AX* center of N is only metastable [74].

Kobayashi *et al.* [101] also predicted that N is a good candidate for a shallow p-type dopant in ZnO although N is not very soluble in ZnO, suggesting that N doping can be achievable by ion implantation. Somewhat related to the current topic, Wu *et al.* [102] have demonstrated shallow N acceptors in N^+-implanted ZnSe using PL measurements. It is now well known that reactive N produced p-type ZnSe, which led to demonstration of laser diodes before being supplanted by GaN-based diode lasers [103]. However, p-type doping of ZnO has not been successful using pure nitrogen sources [104], while acceptor concentrations as high as 10^{18} cm^{-3} have been obtained for ZnSe using an N_2 plasma source [105]. This implies that N acceptors are more readily compensated in ZnO as compared to ZnSe.

4.2.1 Nitrogen Doping

Aided by success with ZnSe, nitrogen has been explored for p-type doping of II–VI semiconductors [105–107]. A number of groups have expended a good deal of effort to realize p-type ZnO using nitrogen as a possible shallow acceptor dopant.

However, N was found to create a rather deep acceptor level (∼0.2 eV), although shallower than that predicted by density functional theory (0.4 eV), and had limited incorporation on lattice sites [74]. Various types of nitrogen sources including N_2, NO, N_2O, NH_3, and Zn_3N_2 have been used depending on the growth technique, as elaborated below.

The wave function character of a shallow acceptor level is similar to that of the valence band maximum state, consisting of anion p, cation p, and cation d orbitals. Among the group V elements substituting the anion site in ZnO, N has the lowest p orbital energy as shown by first-principles calculations within the local density approximation, and therefore produces the lowest acceptor level [108]. However, the N_O acceptor level is deep (∼0.3 eV above the valence band) as the valence band maximum of ZnO is low, compared to, for example, GaN.

Iwata *et al.* [109] have attempted p-type doping of ZnO using MBE by simultaneously introducing O_2 and N_2 through a radio frequency(RF) plasma source. Although a nitrogen concentration as high as $10^{19}\,cm^{-3}$ was obtained, conduction-type conversion from n-type to p-type did not occur. However, some promising results have been reported. Look *et al.* [110] reported p-type ZnO by MBE with N doping (performed by Eagle Picher) using Li-diffused semi-insulating ZnO substrates and an N_2 RF plasma source. Nitrogen surface concentration ($10^{19}\,cm^{-3}$) in the N-doped ZnO film measured by secondary ion mass spectroscopy was two orders of magnitude higher than that in undoped ZnO, implying the presence of high doping. These N-doped ZnO showed p-type behavior with a hole concentration of $9 \times 10^{16}\,cm^{-3}$ and a hole mobility of $2\,cm^2\,V^{-1}\,s^{-1}$. The PL spectrum of Figure 4.3 shows a strong peak near 3.32 eV probably due to neutral acceptor-bound

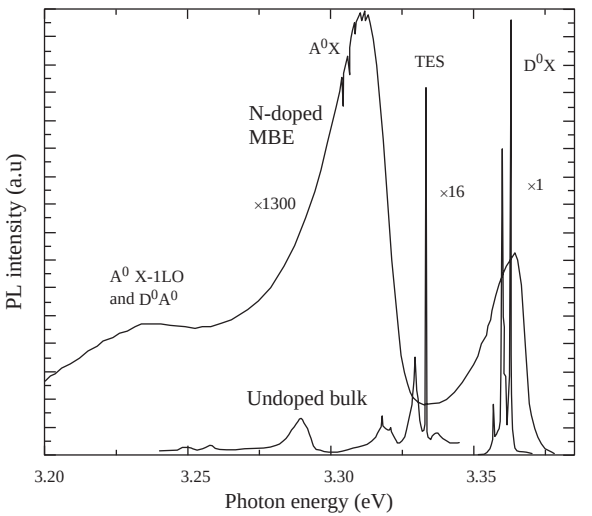

Figure 4.3 PL spectra at 2 K for two ZnO samples, an undoped bulk sample and an N-doped MBE-grown epitaxial layer. (After Ref. [110].)

excitons. The estimated acceptor level was between 170 and 200 meV based on the low-temperature PL measurements. It has become customary to assign the peaks appearing at or about this energy level to acceptors. Lacking an unequivocal link, it is possible that attempts to dope the samples cause defect states and complexes that might be responsible for the observed peak. It is incumbent on the research community to determine the genesis of this or other peaks.

As mentioned in Section 3.2.5, the acceptor binding energy can also be estimated from the donor–acceptor pair (DAP) transitions observed in low-temperature PL. For undoped ZnO, substitutional N on O sites was identified as the main acceptor, with an ionization energy of $E_A = 195 \pm 10$ meV [111]. Similarly, in N-implanted MOVPE-grown ZnO layers, the nitrogen acceptor was identified using the DAP transitions [59]. As shown in Figure 4.4a, the low-temperature PL spectra of N-implanted ZnO layers exhibit an additional DAP transition blueshifted by 20 meV–3.234 eV compared to the DAP observed in the reference ZnO layer. Temperature-dependent PL spectra shown in Figure 4.4b provide further evidence that the implanted N forms an acceptor level. With thermal ionization of the donors with increasing temperature, the DAP transition turns into a band-acceptor (e, A^0)

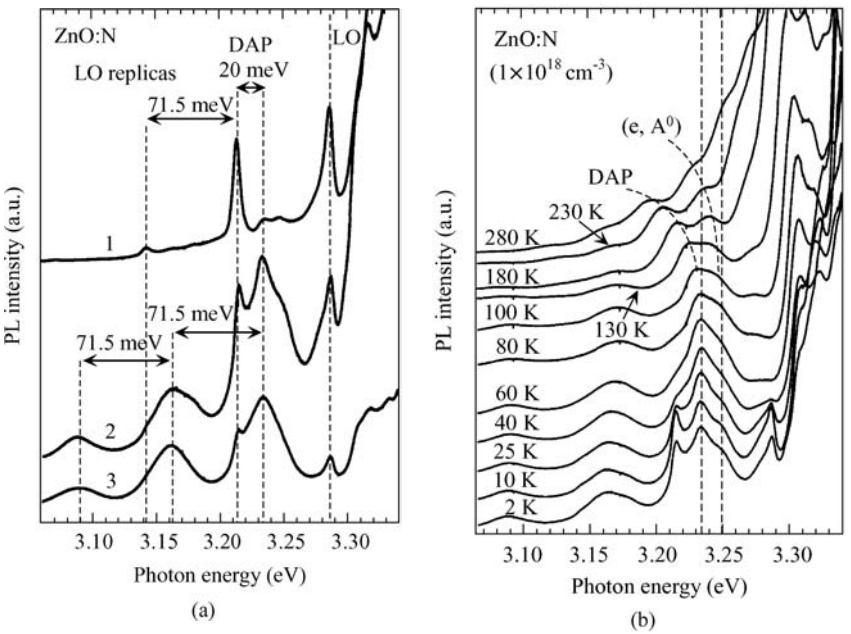

Figure 4.4 (a) Low-temperature PL spectra of (1) ZnO reference layer and N-implanted samples with (2) 1×10^{18} cm^{-3} and (3) 5×10^{18} cm^{-3} N concentrations after annealing at 800 °C. DAP transition and its phonon replicas are visible for all samples. The emission at 3.286 eV is the LO phonon replica of the donor-bound exciton. (b) PL spectra of a ZnO layer implanted with 1×10^{18} cm^{-3} N atoms taken at various temperatures. The DAP transition turns into a band–acceptor (e, A^0) transition with increasing temperature. The shifts in the energetic positions are indicated by dashed lines. (After Ref. [59].)

transition, which becomes more evident at higher temperatures. The DAP transition energy is given by (another form is given in Equation 3.102) [59]

$$E_{DAP} = E_{gap} - E_D - E_A + \alpha N_{A,D}^{1/3}, \tag{4.3}$$

where α is a material-dependent constant (2.7×10^{-8} eV cm for ZnO [59]), E_{gap} 3.438 eV at 2 K, $N_{A,D}^{1/3}$ is the majority impurity concentration, and E_D and E_A are the donor and acceptor binding energies, respectively. Even though the majority impurity concentration may not be known, it can be assumed to be between the residual donor (N_D) and implanted N acceptor (N_A) concentrations. Using $N_D = 1 \times 10^{17}\,cm^{-3}$, $N_A = 5 \times 10^{18}\,cm^{-3}$, and $E_D = 53$ meV (Ga as the major donor), the acceptor binding energy was estimated to be between 163 and 196 meV [59]. A value consistent with this range, $E_A = 165 \pm 40$ meV, has also been reported for N-doped ZnO [112].

Ashrafi *et al.* [113] also used nitrogen as a p-type dopant in conjunction with H_2O vapor as an oxygen source in metalorganic MBE. Thermal annealing increased the net acceptor concentration ($N_A - N_D$) by approximately two orders of magnitude ($\sim 5 \times 10^{16}\,cm^{-3}$). p-type conductivity was observed in spite of higher H concentration than that of N, suggesting that H may be more closely correlated to p-type conductivity rather than simply being a shallow donor or causing passivation, as the theory suggests.

Several groups reported attainment of p-type ZnO films by adding NH_3 in O_2 or H_2 gas as a nitrogen source. Minegishi *et al.* [114] reported the growth of p-type ZnO using CVD. The NH_3 gas was simultaneously added to the hydrogen carrier gas with excess Zn. The resistivity of the resulting films was high (100 Ω cm), suggesting that the acceptor level is relatively deep with a subsequent low free hole concentration. Ye *et al.* [115] also used NH_3 as the nitrogen source for DC reactive magnetron sputtering of p-type ZnO. Results showed a hole concentration of $3.2 \times 10^{17}\,cm^{-3}$ and a resistivity of 35 Ω cm. Ye *et al.* [115] proposed that the excess zinc and interstitial hydrogen play an important role in p-type doping as suggested by Ashrafi *et al.* [113]. However, the role of hydrogen in N-doped ZnO was explained somewhat differently by Wang *et al.* [116] They argued that when NH_3 increases in the organometallic vapor epitaxy (OMVPE) chamber, more hydrogen atoms are absorbed onto the substrate surface and introduced in the film due to the O−H bond that is stronger than Zn−N bond, resulting in a decrease in the nitrogen concentration.

Lu *et al.* [117] investigated p-type ZnO growth as a function of ammonia concentration in NH_3–O_2 ambient using DC reactive magnetron sputtering. While N-doped p-type ZnO films were achieved at ammonia concentrations of 25–75%, intrinsic ZnO film and zinc polycrystal film were obtained at 0 and 100% ammonia concentrations, respectively. The reference to p-type conductivity here merely reflects what has been reported. At 50% ammonia concentration, better electrical properties were obtained: hole concentration of $7.3 \times 10^{17}\,cm^{-3}$, hole mobility of $1.3\,cm^2\,V^{-1}\,s^{-1}$, and resistivity of 31 Ω cm. The results showed that the nitrogen incorporation in ZnO is increased in the presence of NH_3, enhancing the hole concentration. However, when ammonia concentration is high (100%), the densities of V_O and Zn_i are increased due to absence of O_2 in ambient, resulting in zinc

polycrystalline film. It cannot be understated that despite reports of p-type conductivity, the issue is still controversial. Much of the problem arises from very low mobilities in Hall experiments and a good deal of carrier localization in these ZnO films doped with impurities thought to be leading to p-type doping. As mentioned, other conducting channels must meticulously be accounted for as well.

One chain of thought is that to attain p-type ZnO through N doping, it may be necessary to provide oxygen also to suppress oxygen vacancies, V_O. One approach could be to use an O_2/N_2 mixture. However, at least in one instance such an effort did not turn out successful and p-type conductivity was not obtained even though various ratios of O_2/N_2 were employed [118].

Used as a nitrogen source by some researchers, N_2O gas is a mild oxidizing gas (stronger than O_2 and weaker than NO_2 as an oxidizing agent). Very pertinent to the topic of discussion is that the dissociation energy (N−N: 5.16 eV; N−O: 6.37 eV) and ionization potential (N_2O: 12.9 eV) of N_2O are lower than those of N_2 (N−N: 9.76 eV; N_2: 15.65 eV) [119]. In this vein, Guo *et al.* [119] used N_2O plasma for nitrogen doping of ZnO film by PLD. They found that nitrogen doping was enhanced using active N formed by N_2O gas flowing through an electron cyclotron resonance (ECR) source. The samples showed p-type conductivity with hole concentrations in the range of 3×10^{18} to $6 \times 10^{18}\,cm^{-3}$, resistivity in the range of 2–5 Ω cm, and hole mobility in the range of $0.1–0.4\,cm^2\,V^{-1}\,s^{-1}$.

Based on first principles, Yan *et al.* [120] proposed that the NO gas or NO_2 without an ECR plasma source is a more efficient N source than N_2O or N_2 as its use does not entail a supplemental energy to break the N–N bond, and therefore leads to much lower formation energies for substitutional N at an O site (N_O). NO is particularly preferable, as the formation of the N_O defect from NO source requires a lower energy than that from NO_2 for O-rich conditions. As shown in Figure 4.5a, the formation energy of N_O is negative under Zn-rich conditions, implying that no additional energy is required for N_O formation, while the formation energy of N_O from N_2 is positive, suggesting that additional energy is needed (e.g., plasma or high temperature to break N–N bonds). Even though the formation energy of N_O from N_2O is negative for the extremely Zn-rich conditions, the energy is much larger than that from NO. Therefore, it was suggested that NO molecules can be incorporated spontaneously to form N_O defects in ZnO. For comparison, Figure 4.5b shows the formation energies of the undesirable defect $(N_2)_O$ for different gas sources. When NO or NO_2 sources are used, the formation energies of $(N_2)_O$ are lower than N_O under Zn-rich conditions but higher under O-rich conditions. The negative formation energies under Zn-rich conditions indicate that the defect formation process is controlled by kinetics rather than thermodynamics, as two N atoms should arrive simultaneously at the same site on the growth surface to form $(N_2)_O$. The rate of this process is determined by squared ratio of N source molecule concentration to the O site concentration [120]. The formation of $(N_2)_O$ can therefore be suppressed by using dilute gases, that is, by ensuring that the concentration of NO or NO_2 molecules is much smaller than that of nominal O sites.

To add to the ranks of purported successful reports, growth of p-type ZnO doped with N by radical-source MBE has been reported [121, 122]. Murphy *et al.* [121] grew

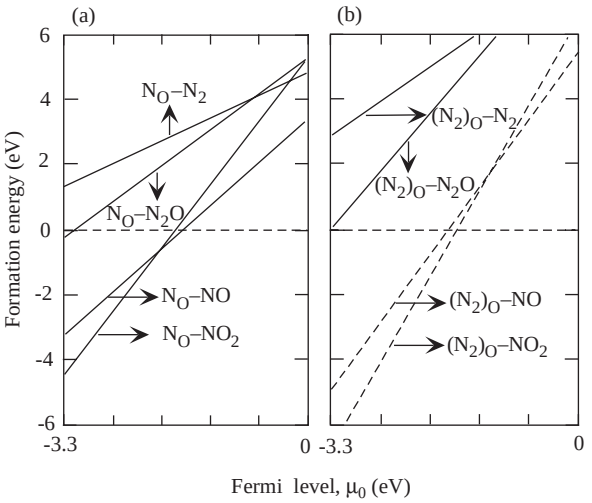

Figure 4.5 (a) Calculated formation energies of N_O as functions of the O chemical potential formed by atomic N (stripped off from an N_2 or an N_2O molecule), NO, or NO_2 molecule. The value $\mu_O = -3.3$ is for the Zn-rich limit condition and $\mu_O = 0$ is for the O-rich limit condition. (b) Calculated formation energies of an $(N_2)_O$ as functions of the O chemical potential for the defects formed by N_2, N_2O, NO, and NO_2 molecules. (After Ref. [120].)

ZnO layers with a hole concentration of $2.8 \times 10^{18}\,cm^{-3}$ and a mobility of $9\,cm^2\,V^{-1}\,s^{-1}$ using concurrent introduction of N_2 and O_2 into ECR plasma source. Liang *et al.* [122] reported the growth of the p-type material using NO gas as a source of both O and N radicals. The films showed a net acceptor concentration ($N_A - N_D$) of $1.2 \times 10^{18}\,cm^{-3}$ and a mobility of $0.53\,cm^2\,V^{-1}\,s^{-1}$. No conduction-type conversion from n-type to p-type was found for control samples grown with separate O_2 and N_2 plasma sources. However, the extremely low hole mobility in the last case points to some problems with the achievement of p-type conduction.

Wang *et al.* [123] attempted nitrogen doping in ZnO films by plasma-assisted OMVPE using diethyl zinc (DEZ) and N_2 gas, but p-type behavior was not obtained. However, Li *et al.* [124, 125] claimed to have succeeded in p-type doping by reacting DEZ with NO gas. In this case, NO gas was used to supply both O and N for p-type doping. Results indicated that N can be incorporated into ZnO films without plasma or high-temperature process and a high N concentration was obtained only under Zn-rich conditions as predicted by Yan *et al.* [120]. It should be stated that N does indeed incorporate as an acceptor. However, whether a sufficient amount of N acceptors would be generated to overcome the n-type background or any other donor-like defects introduced through parasitic processes is the real question.

As already mentioned, the solubility of nitrogen in ZnO is low and N from NO is more efficiently incorporated into ZnO than that from N_2. In search of better solubility perhaps, a different approach for growing N-doped p-type ZnO films was reported in Ref. [126]. p-type ZnO was obtained after thermal annealing of zinc

oxynitride (ZnON) alloy films deposited by RF reactive magnetron sputtering. The samples were grown at a relatively low substrate temperature of 200 °C compared to others [115, 117] and were subjected to postgrowth thermal annealing, which resulted in transformation from ZnON alloy to ZnO. In this case, annealing at 600 °C led to p-type behavior of the films. Further increase of the annealing temperature to 1000 °C in oxygen ambient was reported to eliminate all the N dopants and replace them by O, even though the crystalline quality was improved. Results indicated that there is a trade-off between the N doping efficiency and crystalline quality.

Lin *et al.* [127] obtained what was termed as p-type ZnO by nitrogen ion implantation of ZnO films grown on Si substrates with SiN buffer layers using RF magnetron sputtering. The p-type ZnO films implanted with 5×10^{12} to 1×10^{14} cm^{-2} N^+ dose showed good electrical properties (hole concentration of 5.0×10^{16} to 7.3×10^{17} cm^{-3}, hole mobility of 2.51–6.02 $cm^2 V^{-1} s^{-1}$, and resistivity of 10.1–15.3 Ω cm). Again, the results must be scrutinized to assure that the conductivity type is actually p-type, as ion implant induced donor-like defects would hinder efforts to obtain p-type conductivity and cause potential fluctuations that would hinder Hall measurements.

While most studies on N-doped p-type ZnO have relied on incorporation during deposition of ZnO, other approaches such as oxidation of Zn-containing compounds have been attempted as well. N-doped ZnO was obtained by oxidizing Zn_3N_2 films that were deposited by DC magnetron sputtering [128]. A sample oxidized at 500 °C showed p-type characteristics with a hole concentration of 5.8×10^{18} cm^{-3}. However, oxidization at 550 °C resulted in n-type conductivity purported to be due to insufficient N atoms to form N acceptors.

Enhancement of N doping in ZnO by thermal treatment has been undertaken. Garces *et al.* [129, 130] observed the formation of nitrogen acceptors in N-doped ZnO crystals using photoinduced EPR method after annealing in air or nitrogen atmosphere at a temperature range of 600–900 °C. The pathway for this was reported to be due to nitrogen substitution for the shallow impurity donors during thermal treatment.

Solid-source chemical vapor deposition (SS-CVD) [131] was also used for nitrogen doping of ZnO. Zinc acetate dihydrate [$Zn(CH_3COO)_2 \cdot 2H_2O$, solid] and ammonium acetate (CH_3COONH_4, solid) were used as the precursor and the nitrogen source, respectively. Samples showed p-type conductivity with a hole concentration of 9.8×10^{17} cm^{-3}, resistivity of 20 Ω cm, and hole mobility of 0.97 $cm^2 V^{-1} s^{-1}$. When such low mobilities are obtained, one must exercise considerable caution as severe carrier localization might be taking place making straightforward application of standard Hall measurements questionable.

Despite the above-mentioned reports on growth of p-type ZnO films by N doping, there have also been a number of cases where the authors were not able to reproduce these results even when the same growth methods, growth conditions, and N precursors were employed [109, 119, 132, 133]. Therefore, even if one assumes that the reported results represent truly p-type ZnO, the reproducibility still remains to be a major problem, and this must be solved before ZnO can be used in optoelectronics applications such as LEDs and LDs. Finally, until ZnO p–n junctions with at least

good injection efficiencies are attained, questions will continue to linger. The codoping method that addresses the solubility and deep acceptor nature, to be discussed next, is to some extent an attempt to address the aforementioned concerns.

4.2.2 Codoping Method

Although nitrogen has been considered as the best candidate for p-type doping for ZnO, the point should be remade that the solubility of N in ZnO is low and it introduces a relatively deep acceptor level. Therefore, it is necessary to find methods that can enhance the solubility of N in ZnO and lower the acceptor ionization energy. For this purpose, a donor–acceptor codoping method has been proposed to realize highly conducting p-type ZnO [65, 134, 135] and the experimental studies based on this approach have been performed [66, 136–140].

Yamamoto and Katayama-Yoshida [134] proposed a codoping method to solve the unipolarity in ZnO based on *ab initio* electronic band structure calculations. Codoping with acceptor (N) and donor (Al, Ga, In) impurities in the 2 : 1 ratio in ZnO was suggested to stabilize substitution of N at the appropriate lattice site through the formation of N–Ga–N bonds, very similar to the codoping experiments in GaN using Mg as acceptor and O as donor [81]. The enhancement in solubility to a level well above the standard single impurity solubility limit was explained in terms of the formation of ionic pairs between donor and acceptor ions as a consequent reduction in the Madelung energy. While the Madelung energy decreases with group III elements (Al, Ga, and In) for n-type doping, it increases with group V element N for p-type doping, indicating localization of the N states. Figure 4.6 shows the crystal

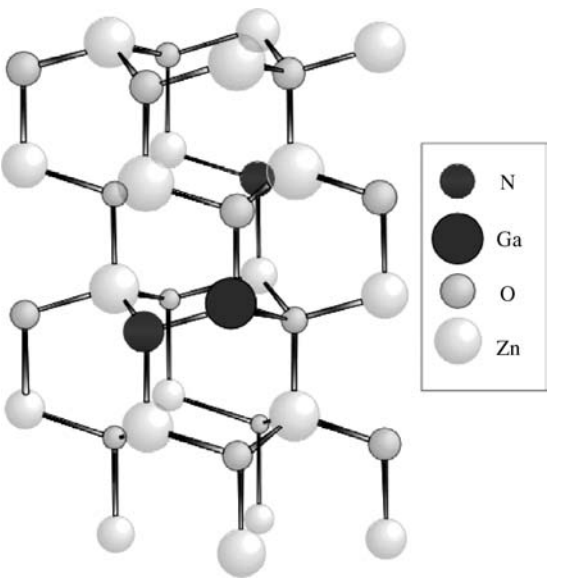

Figure 4.6 Crystal structure of a supercell for ZnO:(Ga, 2N). (After Ref. [135].)

structure of supercells for ZnO:(Ga, 2N) and the formation of complexes, III–N pairs, which occupy the nearest-neighbor sites and the next-nearest-neighbor sites based on *ab initio* total energy calculations. It is also indicated that there were no stable configurations for ZnO:2N with the same N concentration, holding out the possibility that N incorporation can be enhanced with the group III elements. Codoping of N with the reactant dopants has been reported to lower the acceptor level in the bandgap due to strong interaction between N acceptors and reactive donor codopants. As shown in Figure 4.7b–d, the shift of the DOS peak toward the top of the valence band implies that the acceptor levels are lowered. Yamamoto and Katayama-Yoshida [134]

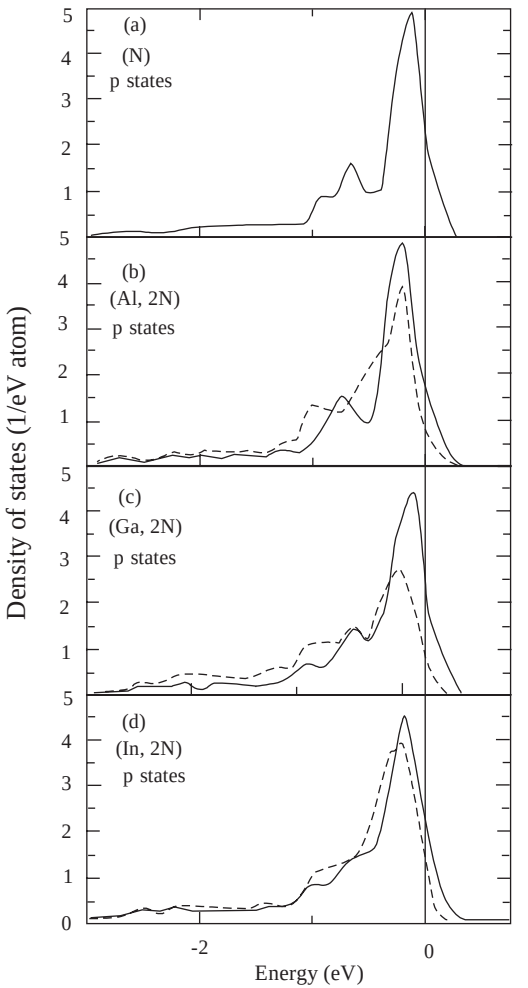

Figure 4.7 Site-decomposed DOS of p states at the N sites for (a) ZnO:N, (b) ZnO:(Al, 2N), (c) ZnO:(Ga, 2N), and (d) ZnO:(In, 2N). Dotted curve indicates the DOS at the N atom sites close to the reactive donor codopant; the solid curve indicates the DOS at the sites of next-nearest-neighbor N atoms. (After Ref. [65].)

also proposed codoping with Li as an acceptor with F as the reactive donor for the growth of low resistivity p-type ZnO. Wang and Zunger [141] later proposed the so-called cluster doping, that is, doping with even more partner atoms than in codoping, to optimize the acceptor formation further. However, it should be realized that isolated Ga atoms can compensate the N–Ga–N acceptors [80]. Numerous experimental studies based on this approach have revealed discrepancies between theory and experiment and resulted in little or no success in terms of achieving stable p-type material with reasonably high free carrier mobility.

A secondary ion mass spectrometry study [144] on the solubility limits of Ga and N in ZnO showed the enhancement of N solubility limit in coimplanted ZnO by a factor of 400 as compared to that in N-implanted ZnO. Using the codoping method, Joseph *et al*. [142] successfully grew what was termed as p-type ZnO films by a PLD system combined with a plasma gas source. For Ga and N codoping, N_2O gas was used as the nitrogen source instead of N_2 gas, because N_2O gas is effective in suppressing oxygen vacancies and introducing N as an acceptor simultaneously. p-type conductivity was confirmed using Hall and Seebeck measurements [143] (named after Thomas Johann Seebeck (1770–1831), it deals with open-circuit voltage produced when a temperature gradient is induced). The basis of hot probe used in determining the conductivity type is the Seebeck thermoelectric effect. The coefficient is defined as the open-circuit voltage produced between two points of a conductor for a uniform 1 K of difference (coefficient measurements with a resistivity of 0.5 Ω cm, a carrier concentration of $5 \times 10^{19}\,\mathrm{cm}^{-3}$, and a very low mobility of $0.07\,\mathrm{cm}^2\,\mathrm{V}^{-1}\,\mathrm{s}^{-1}$). The very low mobility brings the p-type conductivity into question. It was also indicated that low-temperature formation is essential for nonequilibrium growth in the codoping technique. Although p-type conductivity was observed in codoped ZnO films, the origin of p-type characteristics is not clear due to the lack of characterization, such as the donor and acceptor levels in the bandgap for the Ga and N dopants.

Ohshima *et al*. [138] have attempted to synthesize p-type ZnO by PLD using various codoping methods, including the ablation of ZnO:Ga target in NO gas and Al and N codoping using an ion gun and a microwave electron cyclotron resonance source. Although they could identify the presence of Ga–N bonds in ZnO, p-type ZnO film could not obtained.

The types of conductivity and carrier concentration in Ga and N codoped ZnO were reported to be dependent on the O_2 partial pressure in the sputtering gas mixture. Singh *et al*. [144] observed n-type conduction for deposited films for oxygen partial pressures between 0 and 40%. The conduction type of films deposited in the 40–50% oxygen partial pressure range was not clearly identifiable due to large resistivity. But the films deposited with partial pressures higher than 50% showed p-type conduction. Assuming that the p-type conductivity is real, this dependence of the conduction type on oxygen partial pressure showed the important role of oxygen vacancies in the type of conductivity achieved. Thus, as the O_2 partial pressure increases, V_O and Zn_i are suppressed or the background donor concentration is insufficient to compensate the acceptors from N substitution in ZnO, paving the way for p-type conduction (see Figure 4.8a). When the O_2 partial pressure ratio was increased from 50 to 60%, the mobility and resistivity decreased while the hole concentration increased as shown in

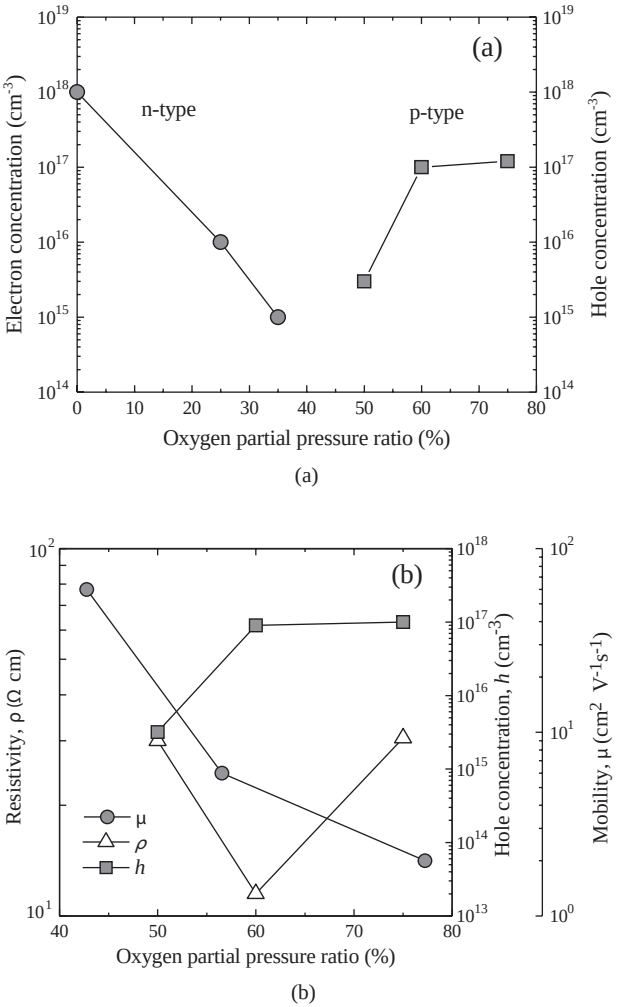

Figure 4.8 (a) Effect of oxygen partial pressure ratio on conduction type of codoped ZnO films. (b) Hole concentration, resistivity, and Hall mobility as a function of oxygen partial pressure. (After Ref. [144].)

Figure 4.8b. However, further increase in the O_2 partial pressure ratio caused a decrease in the mobility and an increase in the resistivity, probably because of the degradation of crystal quality, perhaps due to oxygen-mitigated defects.

Indium [145] and aluminum [146] have also been used as group III codoping metals. In codoping studies with In, the ultrasonic ultraspray pyrolysis method was used for growth. The aqueous solutions $Zn(CH_3OO)_2{\cdot}H_2O$ (AR, 0.5 mol l^{-1}), $(CH_3OONH_4)_2$ (AR, 2.5 mol l^{-1}), and $In(NO)_3$ (AR, 0.5 mol l^{-1}) were used as the sources of the Zn, N, and In, respectively. The grown p-type ZnO films had low film resistivity ($1.7 \times 10^{-2}\,\Omega\,cm$), high hole concentration ($2.44 \times 10^{18}\,cm^{-3}$), and incredibly high

hole mobility ($155\,cm^2\,V^{-1}\,s^{-1}$), which brings the validity of these results into question. The high mobility value suggests that the sample may have been n-type. Al + N codoping has been undertaken during the growth of ZnO films in an $N_2O + O_2$ atmosphere on glass substrates by DC reactive magnetron sputtering. At a substrate temperature of 500 °C, p-ZnO was realized with hole densities as high as $1.1 \times 10^{17}\,cm^{-3}$.

In other codoping experiments [66, 137, 140], however, no p-type conductivity was observed even though N concentrations as high as $2 \times 10^{20}\,cm^{-3}$ were noted in ZnO. However, such codoped ZnO layers in these experiments exhibited a dramatic increase (by eight to nine orders of magnitude) in resistivity. The formation of N–Ga–N acceptor centers in the samples was suggested to be the reason.

Again, despite reports of successful p-type ZnO and even reports of p–n junctions (see Refs [147, 148]), whether using codoping methods or otherwise, the choice of dopant and the method to be employed are controversial and the reliability and reproducibility of p-ZnO are open for debate.

Using first-principles band structure calculations, it has been shown that replacing the Zn atom by an isovalent impurity such as Mg or Be lowered the defect transition level of NO [108]. Since the isovalent atom has no occupied d orbital, the strong p–d coupling between N_O and the Zn cation, which is responsible for the deep N_O acceptor level, can be removed. The effect is more pronounced when all four Zn sites around N_O in the tetrahedral configuration are occupied with isovalent atoms. When four neighboring Zn cations of N_O were replaced with more electronegative Be, the ionization energy was calculated to be lowered from 0.31 to 0.12 eV. Similarly, the transition energy level of V_{Zn} was also shown to reduce by replacing its neighboring O atoms with more electronegative F atoms [108]. The calculated defect ionization energy levels after codoping acceptors, N and V_{Zn}, with donor (F_O) or isovalent (Mg or Be) atoms are given in Table 4.3.

To obtain p-type conductivity in ZnO, modification of the host band structure through codoping has also been proposed [149]. A fully passivated impurity band above the ZnO valence band edge can be created through heavily codoping with Ga

Table 4.3 Calculated defect complex binding energies, E_b, and acceptor transition energy levels (all in eV) in ZnO resulting from codoping acceptors (N or V_{Zn}) with donor (F_O) or isovalent (Mg, Be) atoms.

Defect	E_b	(0/−)	(−/2−)
N_O		0.31	
N_O–Mg_{Zn}	0.3	0.29	
N_O–4Mg_{Zn}	1.6	0.23	
N_O–Be_{Zn}	0.1	0.22	
N_O–4Be_{Zn}	1.9	0.12	
V_{Zn}		0.18	0.34
V_{Zn}–F_O	−2.3	0.16	

After Ref. [108].

and N. The impurity band then can be doped with excess N to create the shallow acceptor levels. Using this approach, ionization energies as small as 0.1–0.2 eV have been calculated for the N acceptor [149].

4.2.3 Other Dopants in Group V

While most efforts on p-type doping of ZnO have focused on nitrogen doping with/without codopants because of its relatively shallow level, considerably fewer studies have considered other group V elements for substitutionally replacing O [98, 147, 150–154]. Only in some of these studies, inversion of the film's conductivity from n-type to p-type was observed. Even though hole concentrations above $10^{18}\,cm^{-3}$ and hole mobilities of $20\,cm^2\,V^{-1}\,s^{-1}$ have been reported, the reliability of the measurements is again questionable.

Aoki *et al.* [147] used the PLD technique to produce phosphorus-doped p-type ZnO films using a zinc phosphide (Zn_3P_2) compound as the phosphorus source. In this process, a Zn_3P_2 film deposited on a ZnO substrate was exposed to excimer laser radiation in high-pressure nitrogen or oxygen ambient and was consequently decomposed into Zn and P atoms, which diffuse into ZnO, resulting in the formation of p-doped ZnO through the replacement of O atoms by P atoms. In this case, a p–n junction-like behavior was observed between an n-type ZnO substrate and a surface p-doped layer, although Hall measurements did not confirm p-type conductivity. It should be mentioned that a change in the Fermi level across the two regions of the layer would result in some barrier formation without one side necessarily being p-type, albeit with a lower offset voltage than that ascribed to p–n junctions. Similar results were obtained by Lee *et al.* [155], who also transformed a Zn_3P_2 layer on ZnO/sapphire to p-type ZnO by laser annealing.

Kim *et al.* [150] reported that a phosphorus-doped n-type ZnO film grown by RF sputtering using P_2O_5 as the phosphorus source led to p-type ZnO, following thermal annealing at a temperature above 800 °C in N_2 ambient (Figure 4.9). During thermal activation of dopants, P_2O_5 was reported to dissociate and consequently phosphorus atoms act as acceptors and oxygen atoms may compensate oxygen vacancies that otherwise would act as compensating donors. The ZnO films showed p-type behavior with hole concentrations in the range of 1.0×10^{17} to $1.7 \times 10^{19}\,cm^{-3}$, a mobility of $0.53–3.51\,cm^2\,V^{-1}\,s^{-1}$, and a low resistivity of 0.59–4.4 Ω cm. PL spectrum showed a strong peak at 3.35 eV, which is probably due to neutral acceptor-bound excitons, as observed by Look *et al.* [99]. Afterward, such p-type ZnO films were grown on n-type GaN to fabricate p-ZnO/n-GaN-type heterostructures [156]. Also, quite good p–n heterojunctions and electroluminescence properties were observed.

Another group was unsuccessful in achieving p-type ZnO using phosphorus [154]; however, that group reported p-type behavior in P-doped ZnMgO layers grown by pulsed laser deposition [157]. The different behavior of phosphorus in ZnO and ZnMgO layers is still not clear. Phosphorus-doped $Zn_{0.9}Mg_{0.1}O$ targets were fabricated using high-purity ZnO (99.9995%) and MgO (99.998%), with P_2O_5 (99.998%) serving as the doping agent. The majority carrier type was determined from

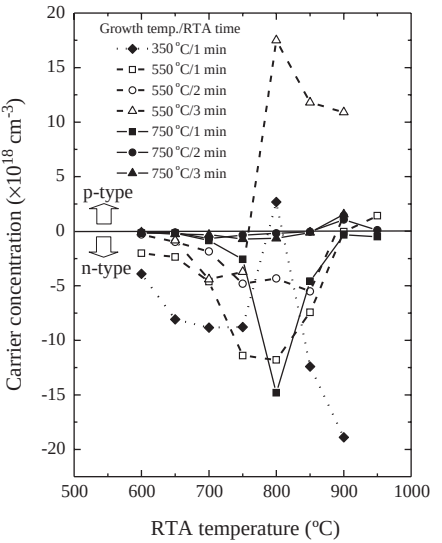

Figure 4.9 Carrier concentration of phosphorus-doped ZnO thin films treated by RTA. (Courtesy of S.-J. Park. [150].)

capacitance–voltage characteristics of metal–insulator–semiconductor devices fabricated, and the hole concentration and mobility were estimated to be $2 \times 10^{18}\,\mathrm{cm}^{-3}$ and $0.01–0.001\,\mathrm{cm}^2\,\mathrm{V}^{-1}\,\mathrm{s}^{-1}$, respectively. Minority carrier transport properties of p-$Zn_{0.9}Mg_{0.1}O$ were studied by employing electron beam induced current and cathodoluminescence methods [158], and the electron diffusion length and lifetime were found to be ~2.12 μm and ~34 ns, respectively. Both of these values increased after electron beam irradiation. Using these p-type layers, $Zn_{0.9}Mg_{0.1}O$/ZnO p–n junctions were fabricated with good rectifying diode-like current–voltage characteristics [157, 159].

Ryu *et al.* [151] employed GaAs substrates as an arsenic source for p-type doping of ZnO by PLD. In this case, a p-type ZnO layer was produced at the ZnO/GaAs interface after thermal annealing. The p-type ZnO films were grown on different substrates, ZnO, SiC, and sapphire, rather than on GaAs and As was supplied from an effusion cell in the PLD system. Thus, the postannealing process was not deemed necessary to diffuse As into ZnO film [152, 153].

Stemmed from the notion that addition of Mg in the lattice would reduce the binding energy of potential acceptors, a flurry of activity has emerged in N-doped MgZnO. It should be clear by now that the potential acceptors in ZnO, such as nitrogen, phosphorus, and arsenic, tend to be relatively deep and thus have small fractional ionizations at room temperature. Doping ZnO p-type is beset by solubility limit, large binding energy that hampers acceptor activation at room temperature, large background donor concentrations, and parasitic creation of donor-like defects when p-type doping is attempted The background n-type concentration can be lowered by incorporating Cu in ZnO or alloying it to Mg possibly perhaps mitigating attainment of p-type material. Mg also increases the bandgap. Doping ZnMgO with

group V acceptors at high concentrations, followed by annealing, has been employed to obtain type conversion to p-type [159]. Device quality nitrogen-doped p-type thin epitaxial ZnO films grown by chemical vapor deposition [160] and molecular beam epitaxy [122] have been claimed. One needs to integrate over a longer period of time to confirm the validity of truly p-type material, as the reported mobilities again are very low, so much so that it brings the application of Hall measurements into question.

Thus, the above-mentioned theoretical and experimental investigations indicate that P, As, and Sb appear to be the most promising candidates for p-type ZnO doping. Hole concentrations above $10^{18}\,cm^{-3}$ in P- [86], As- [90], and Sb-doped [95, 96] ZnO and hole mobility of $20\,cm^2\,V^{-1}\,s^{-1}$ in ZnO:Sb [95] and $11\,cm^2\,V^{-1}\,s^{-1}$ in ZnO:P [90] have been reported, although they are awaiting verification. While the focus in the literature and in the current study has been on ZnO, to attain high efficiency LEDs, preferably with QWs, p-type doping is imperative in the wider gap barrier, such as ZnMgO and ZnBeO. Weak p-type conductivity in p-doped ZnMgO grown by PLD has been reported [157, 161, 162]. Hall effect measurements at RT showed a hole concentration of $2.7 \times 10^{16}\,cm^{-3}$, a mobility of $8.2\,cm^2\,V^{-1}\,s^{-1}$, and a resistivity of $35\,\Omega\,cm$ [161]. Despite the rectifying behavior of *I–V* characteristics, attempts to observe band-edge emission from the junction biased in the forward direction were unsuccessful [162]. The lack of emission using these so-called p-type layers is indicative of the fact that the measurements and the interpretation of those measurements need to be scrutinized.

4.2.4 Concluding Remarks on Reliability of p-Type ZnO

Summarizing what we discussed in conjunction with p-type ZnO, one can state that despite large numbers of reports on p-type ZnO, to a lesser extent ZnMgO, and growth by various methods [163], no reproducible high-quality p-type layers became available as a result. The lack of efficient light emission using many of these p-type layers in the context of p–n homojunction diodes indicates that more stringent methods must be employed. Careful analysis of the experimental data, particularly the interpretation of the Hall data in cases of very low Hall mobilities and very high purported hole concentrations, better understanding of the physical properties of point defects, and development of some unconventional methods would be useful. In fact, studies of local conductivity in acceptor-doped ZnO using scanning capacitance microscopy (SCM) and scanning surface potential microscopy (SSPM) have shown that the p-type conduction depends strongly on the growth mode (two- or three-dimensional) for samples grown by MOCVD [164–166] and spray pyrolysis [167].

It has been demonstrated that impurities are preferentially incorporated at or near growth defects [164]. Depending on the growth parameters, largely extended p-type domains were observed, surrounded by n-type regions. The differences in local conductivity type were directly correlated to the topography revealing p-type behavior for smooth, two-dimensional surfaces and n-type conductivity in the case of three-dimensional island growth or structural defects, such as microcracks or surface pits. For MOCVD-grown ZnO codoped with As and N, the formation of stable p-type ZnO

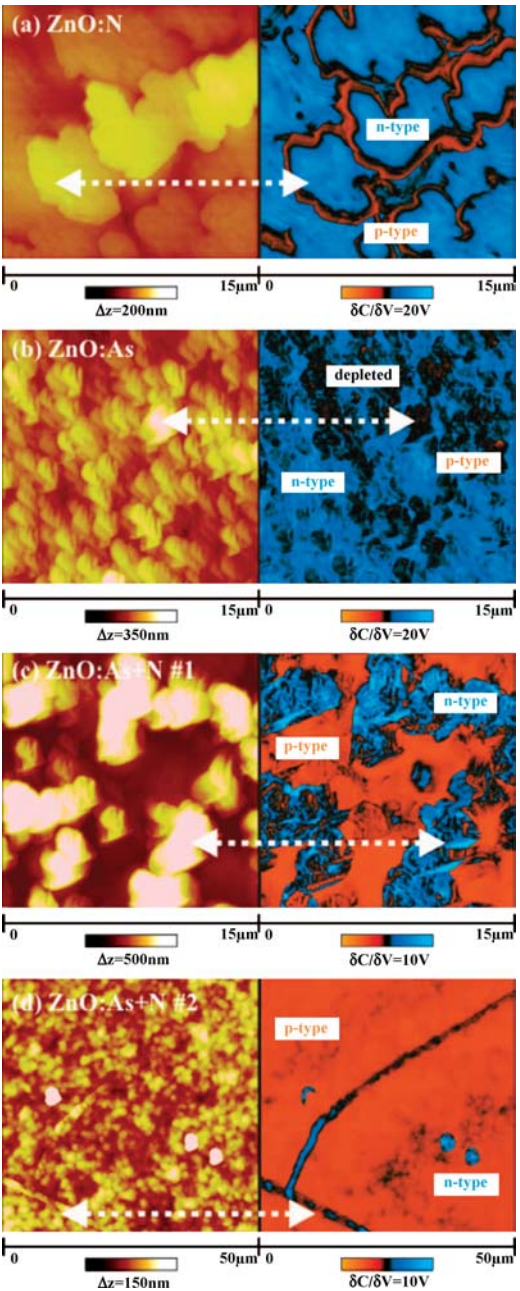

Figure 4.10 Typical AFM (left panel) and SCM images (right panel) of ZnO layers which were conventionally mono-doped with nitrogen (a) or arsenic (b), or dual-doped with both acceptor species (c) and (d), respectively. In SCM images *n*-type and p-type regions are indicated in blue and orange colors, respectively, and black regions indicate depleted areas. (Courtesy of A. Krost).

was achieved when the growth was two dimensional and yielded smooth surfaces. In contrast, the acceptor doping completely failed when the growth mode was three dimensional, as shown in Figure 4.10 for N- and As-doped ZnO [165]. The surfaces of ZnO:N and ZnO:As samples were composed of three-dimensional islands of typical diameters of about 5–8 and 1–2 μm, respectively. The corresponding SCM images showed dominant n-type regions (blue) despite the acceptor doping. Moreover, very small p-type domains (orange) were found only for ZnO:N and were exclusively limited to the island/grain boundaries, whereas ZnO:As revealed no significant p-type regions, but a majority of depleted areas (black) due to the smaller grains and the superimposed space charge regions. For the codoped layers, Figure 4.10c shows a typical sample with mixed conductivity, that is, with dominant three-dimensional islands that are n-type in SCM and with smoother p-type regions. In contrast, samples grown under optimized conditions (see Figure 4.10d) reveal dominant smooth p-type domains that are separated only by very few microcracks and small hillocks, which are all n-type. These results show that a deep understanding of impurity–defect interaction is of vital importance for control over the conductivity type in ZnO.

To obtain reproducible and high-quality p-ZnO, control over point and extended defects, which act as compensation centers for p-type impurities and regions of localization of such centers, respectively, is essential and can be achieved by employing homoepitaxy on high-quality bulk ZnO substrates. In addition, the impurities, many of which act as shallow or deep donors and therefore compensate acceptors, should be reduced in both thin films and bulk material by improving growth techniques and optimizing growth conditions. To understand the nature of acceptor centers and defect complexes in ZnO and predict their behavior and thermal stability, which will lead to improvement of incorporation and activation of p-type impurities, theoretical models can also be used.

References

1 Walukiewicz, W. (2001) Intrinsic limitations to the doping of wide-gap semiconductors. *Physica B*, **302–303**, 123.

2 Neumark, G.F. (1989) *Physical Review Letters*, **62**, 1800.

3 Chadi, D.J. (1994) *Physical Review Letters*, **72**, 534.

4 Zhang, S.B., Wei, S.-H. and Zunger, A. (2000) *Physical Review Letters*, **84**, 1232.

5 Minami, T., Sato, H., Nanto, H. and Takata, S. (1985) *Japanese Journal of Applied Physics*, **24**, L781.

6 Zhang, S.B., Wei, S.-H. and Zunger, A. (1998) *Journal of Applied Physics*, **83**, 3192.

7 Laks, D.B., Van de Walle, C.G., Neumark, G.F. and Pantelides, S.T. (1993) *Applied Physics Letters*, **63**, 1375.

8 Zhang, S.B., Wei, S.-H. and Zunger, A. (1999) Overcoming doping bottlenecks in semiconductors and wide-gap materials. *Physica B*, **273–274**, 976.

9 Kato, H., Sano, M., Miyamoto, K. and Yao, T. (2003) *Japanese Journal of Applied Physics, Part 1: Regular Papers, Short Notes & Review Papers*, **42**, 2241.

10 Iwata, K., Fons, P., Niki, S., Yamada, A., Matsubara, K., Nakahara, K. and Takasu, H. (2000) *Physica Status Solidi a: Applied Research*, **180**, 287.

11 Maeda, K., Sato, M., Niikura, I. and Fukuda, T. (2005) Growth of 2 inch ZnO bulk single crystal by the hydrothermal method. *Semiconductor Science and Technology*, **20**, S49.

12 Kohan, A.F., Ceder, G., Morgan, D. and Van de Walle, C.G. (2000) *Physical Review B: Condensed Matter*, **61**, 15019.

13 Vanheusden, K., Seager, C.H., Warren, W.L., Tallant, D.R. and Voight, J.A. (1996) *Applied Physics Letters*, **68**, 403.

14 Look, D.C., Hemsky, J.W. and Sizelove, J.R. (1999) *Physical Review Letters*, **82**, 2552.

15 Van de Walle, C.G. (2001) *Physica B*, **308–310**, 899.

16 Cox, S.F.J., Davis, E.A., Cottrell, S.P., King, P.J.C., Lord, J.S., Gil, J.M., Alberto, H.V., Vilão, R.C., Piroto Duarte, J., Ayres de Campos, N., Weidinger, A., Lichti, R.L. and Irvine, S.J.C. (2001) *Physical Review Letters*, **86**, 2601.

17 Strzhemechny, Y.M., Mosbacker, H.L., Look, D.C., Reynolds, D.C., Litton, C.W., Garces, N.Y., Giles, N.C., Halliburton, L.E., Niki, S. and Brillson, L.J. (2004) Remote hydrogen plasma doping of single crystal ZnO. *Applied Physics Letters*, **84**, 2545.

18 Van de Walle, C.G. (2000) *Physical Review Letters*, **85**, 1012.

19 Wenas, W.W., Yamada, A., Takahashi, K., Yoshino, M. and Konagai, M. (1991) *Journal of Applied Physics*, **70**, 7119.

20 Lokhande, B.J., Patil, P.S. and Uplane, M.D. (2001) *Physica B*, **302–303**, 59.

21 Ma, J., Ji, F., Zhang, D.H., Ma, H.L. and Li, S.Y. (1999) *Thin Solid Films*, **357**, 98.

22 Igasaki, Y. and Saito, H. (1991) *Journal of Applied Physics*, **70**, 3613.

23 Kim, K.H., Park, K.C. and Ma, D.Y. (1997) *Journal of Applied Physics*, **81**, 7764.

24 Cebulla, R., Wendt, R. and Ellmer, K. (1998) *Journal of Applied Physics*, **83**, 1087.

25 Cohen, D.J., Ruthe, K.C. and Barnett, S.A. (2004) *Journal of Applied Physics*, **96**, 459.

26 Pei, Z.L., Sun, C., Tan, M.H., Xiao, J.Q., Guan, D.H., Huang, R.F. and Wen, L.S. (2001) *Journal of Applied Physics*, **90**, 3432.

27 Agashe, C., Kluth, O., Hüpkes, J., Zastrow, U., Rech, B. and Wuttig, M. (2004) *Journal of Applied Physics*, **95**, 1911.

28 Fang, G., Li, D. and Yao, B. (2003) *Vacuum*, **68**, 363.

29 Kumar, M., Mehra, R.M., Wakahara, A., Ishida, M. and Yoshida, A. (2003) *Journal of Applied Physics*, **93**, 3837.

30 Makino, T., Tamura, K., Chia, C.H., Segawa, Y., Kawasaki, M., Ohtomo, A. and Koinuma, H. (2002) *Physica Status Solidi b: Basic Research*, **229**, 853.

31 Jiménez-González, A.E., Urueta, J.A.S. and Suárez-Parra, R. (1998) *Journal of Crystal Growth*, **192**, 430.

32 Islam, M.N., Ghosh, T.B., Chopra, K.L. and Acharya, H.N. (1996) *Thin Solid Films*, **280**, 20.

33 Agura, H., Suzuki, A., Matsushita, T., Aoki, T. and Okuda, M. (2003) Low resistivity transparent conducting Al-doped ZnO films prepared by pulsed laser deposition. *Thin Solid Films*, **445**, 263.

34 Ko, H.J., Chen, Y.F., Hong, S.K., Wenisch, H., Yao, T. and Look, D.C. (2000) *Applied Physics Letters*, **77**, 3761.

35 Makino, T., Segawa, Y., Yoshida, S., Tsukazaki, A., Ohtomo, A. and Kawasaki, M. (2004) *Applied Physics Letters*, **85**, 759.

36 Miki-Yoshida, M., Paraguay-Delgado, F., Estrada-López, W. and Andrade, E. (2000) *Thin Solid Films*, **376**, 99.

37 Agne, Th., Guan, Z., Li, X.M., Wolf, H., Wichert, Th., Natter, H. and Hempelmann, R. (2003) *Applied Physics Letters*, **83**, 1204.

38 Minami, T., Yamamoto, T. and Miyata, T. (2000) *Thin Solid Films*, **366**, 63.

39 Minami, T., Sato, H., Nanto, H. and Takata, S. (1986) *Japanese Journal of Applied Physics, Part 2: Letters*, **25**, L776.

40 Wang, R.P., King, L.L.H. and Sleight, A.W. (1996) *Journal of Materials Research*, **11**, 1659.

41 Ataev, B.M., Bagamadova, A.M., Mamedov, V.V., Omaev, A.K. and Rabadanov, M.R. (1999) *Journal of Crystal Growth*, **198–199**, 1222.

42 Xu, H.Y., Liu, Y.C., Mu, R., Shao, C.L., Lu, Y.M., Shen, D.Z. and Fan, X.W. (2005) *Applied Physics Letters*, **86**, 123107.

43 Ntep, J.-M., Said Hassani, S., Lusson, A., Tromson-Carli, A., Ballutaud, D., Didier, G. and Triboulet, R. (1999) *Journal of Crystal Growth*, **207**, 30.

44 Myong, S.Y., Baik, S.J., Lee, C.H., Cho, W.Y. and Lim, K.S. (1997) *Japanese Journal of Applied Physics*, **36**, L1078.

45 Ataev, B.M., Bagamadova, A.M., Djabrailov, A.M., Mamedo, V.V. and Rabadanov, R.A. (1995) *Thin Solid Films*, **260**, 19.

46 Assunção, V., Fortunato, E., Marques, A., Aguas, H., Ferreira, I., Costa, M.E.V. and Martins, R. (2003) *Thin Solid Films*, **427**, 401.

47 Liu, Z.F., Shan, F.K., Li, Y.X., Shin, B.C. and Yu, Y.S. (2003) *Journal of Crystal Growth*, **259**, 130.

48 Chen, M., Pei, Z., Xi, W., Sun, C. and Wen, L. (2001) *Materials Research Society Symposium Proceedings*, **666**, F1.2.

49 Minami, T., Nanto, H. and Takata, S. (1984) *Japanese Journal of Applied Physics*, **23**, L280.

50 Kato, H., Sano, M., Miyamoto, K. and Yao, T. (2002) Growth and characterization of Ga-doped ZnO layers on *a*-plane sapphire substrates grown by molecular beam epitaxy. *Journal of Crystal Growth*, **237–239**, 538.

51 Ohgaki, T., Kawamura, Y., Kuroda, T., Ohashi, N., Adachi, Y., Tsurumi, T., Minami, F. and Haneda, H. (2003) *Key Engineering Materials*, **248**, 91.

52 Minami, T. (2005) Transparent conducting oxide semiconductors for transparent electrodes. *Semiconductor Science and Technology*, **20**, S35.

53 Burstein, E. (1954) *Physical Review*, **93**, 632.

54 Moss, T.S. (1961) *Optical Properties of Semiconductors*, Academic Press, New York.

55 Meyer, B.K., Alves, H., Hofmann, D.M., Kriegseis, W., Forster, D., Bertram, F., Christen, J., Hoffmann, A., Straßburg, M., Dworzak, M., Haboeck, U. and Rodina, A.V. (2004) *Physica Status Solidi b: Basic Research*, **241**, 231.

56 Meyer, B.K., Sann, J., Hofmann, D.M., Neumann, C. and Zeuner, A. (2005) *Semiconductor Science and Technology*, **20**, S62.

57 Teke, A., Özgür, Ü., Doğan, S., Gu, X., Morkoç, H., Nemeth, B., Nause, J. and Everitt, H.O. (2004) *Physical Review B: Condensed Matter*, **70**, 195207.

58 Alves, H., Pfisterer, D., Zeuner, A., Riemann, T., Christen, J., Hofmann, D.M. and Meyer, B.K. (2003) *Optical Materials*, **23**, 33.

59 Reuss, F., Kirchner, C., Gruber, Th., Kling, R., Maschek, S., Limmer, W., Waag, A. and Ziemann, P. (2004) *Journal of Applied Physics*, **95**, 3385.

60 Haynes, J.R. (1960) *Physical Review Letters*, **4**, 361.

61 Walukiewicz, W. (1994) Defect formation and diffusion in heavily doped semiconductors. *Physical Review B: Condensed Matter*, **50**, 5221.

62 Kvit, A. and Oktyabrsky, S. (2001) Defects in CdTe and related compounds, in *Encyclopedia of Materials: Science and Technology* (ed. S. Mahajan), Elsevier.

63 Barnes, T.M., Olson, K. and Wolden, C.A. (2005) On the formation and stability of p-type conductivity in nitrogen-doped zinc oxide. *Applied Physics Letters*, **86**, 112112.

64 Van de Walle, C.G., Laks, D.B., Neumark, G.F. and Pantelides, S.T. (1993) *Physical Review B: Condensed Matter*, **47**, 9425.

65 Yamamoto, T. and Katayama-Yoshida, H. (1999) Solution using a codoping method to unipolarity for the fabrication of p-type ZnO. *Japanese Journal of Applied Physics, Part 2: Letters*, **38**, L166.

66 Nakahara, K., Takasu, H., Fons, P., Yamada, A., Iwata, K., Matsubara, K., Hunger, R. and Niki, S. (2001) Interactions between gallium and nitrogen dopants in ZnO films grown by radical-source molecular-beam epitaxy. *Applied Physics Letters*, **79**, 4139.

67 Pearton, S.J., Norton, D.P., Ip, K., Heo, Y.W. and Steiner, T. (2004) Recent advances in processing of ZnO. *Journal of Vacuum Science & Technology B: Microelectronics and Nanometer Structures*, **22**, 932.

68 Schirmer, O.F. and Zwingel, D. (1970) *Solid State Communications*, **8**, 1559.

69 Schirmer, O.F. (1968) *Journal of Physics and Chemistry of Solids*, **29**, 1407.

70 Valentini, A., Quaranta, F., Rossi, M. and Battaglin, G. (1991) *Journal of Vacuum Science & Technology A: Vacuum Surfaces and Films*, **9**, 286.

71 Kanai, Y. (1991) *Japanese Journal of Applied Physics, Part 1: Regular Papers, Short Notes & Review Papers*, **30**, 703.

72 Kanai, Y. (1991) *Japanese Journal of Applied Physics, Part 1: Regular Papers, Short Notes & Review Papers*, **30**, 2021.

73 Tuomisto, F., Ranki, V., Saarinen, K. and Look, D.C. (2003) *Physical Review B: Condensed Matter*, **91**, 205502.

74 Park, C.H., Zhang, S.B. and Wei, S.-H. (2002) *Physical Review B: Condensed Matter*, **66**, 073202.

75 Hwang, D.-K., Kim, H.-S., Lim, J.-H., Oh, J.-Y., Yang, J.-H., Park, S.-J., Kim, K.-K., Look, D.C. and Park, Y.S. (2005) Study of the photoluminescence of phosphorus-doped p-type ZnO thin films grown by radio-frequency magnetron sputtering. *Applied Physics Letters*, **86**, 151917.

76 Laks, D.B., Van de Walle, C.G., Neumark, G.F. and Pantelides, S.T. (1991) *Physical Review Letters*, **66**, 648.

77 Garcia, A. and Northrup, J.E. (1995) *Physical Review Letters*, **74**, 1131.

78 Cohen, M.L. (1982) *Physica Scripta*, **T1**, 5.

79 Ihm, J., Zunger, A. and Cohen, M.L. (1979) *The Journal of Physical Chemistry*, **12**, 4409.

80 Lee, E.-C., Kim, Y.-S., Jin, Y.-G. and Chang, K.-J. (2001) First-principles study of p-type doping and co-doping in ZnO. *Journal of the Korean Physical Society*, **39**, S23.

81 Morkoç, H. (2008) *Handbook of Nitride Semiconductors and Devices*, Vol. I, Wiley-VCH Verlag GmbH, Chapter 4.

82 Sanmyo, M., Tomita, Y. and Kobayashi, K. (2005) Preparation of zinc oxide films containing Be and N atoms by radio frequency magnetron sputtering. *Thin Solid Films*, **472**, 189.

83 Lim, S.H., Kim, J.W., Kang, H.S., Kim, G.H., Chang, H.W. and Lee, S.Y. (2005) Characterizations of phosphorus doped ZnO multi-layer thin films to control carrier concentration. *Superlattices and Microstructures*, **38**, 377.

84 Lin, C.-C., Chen, S.-Y. and Cheng, S.-Y. (2004) Physical characteristics and photoluminescence properties of phosphorous-implanted ZnO thin films. *Applied Surface Science*, **238**, 405.

85 Heo, Y.W., Kwon, Y.W., Li, Y., Pearton, S.J. and Norton, D.P. (2005) Properties of phosphorus-doped (Zn,Mg)O thin films and device structures. *Journal of Electronic Materials*, **34**, 409.

86 Chen, F., Ye, Z., Xu, W., Zhao, B., Zhu, L. and Lv, J. (2005) Fabrication of p-type ZnO thin films via MOCVD method by using phosphorus as dopant source. *Journal of Crystal Growth*, **281**, 458.

87 Vaithianathan, V., Lee, B.-T. and Kim, S.S. (2005) Pulsed-laser-deposited p-type ZnO films with phosphorus doping. *Journal of Applied Physics*, **98**, 043519.

88 Kang, S.-H., Hwang, D.-K. and Park, S.-J. (2005) Low-resistance and highly transparent Ni/indium-tin oxide ohmic contacts to phosphorous-doped p-type ZnO. *Applied Physics Letters*, **86**, 211902.

89 Look, D.C., Renlund, G.M., Burgener, R.H. and I.I. Sizelove, J.R. (2004) As-doped p-type ZnO produced by an evaporation/sputtering process. *Applied Physics Letters*, **85**, 5269.

90 Vaithianathan, V., Lee, B.-T. and Kim, S.S. (2005) Preparation of As-doped p-type ZnO films using a Zn_3As_2/ZnO target with pulsed laser deposition. *Applied Physics Letters*, **86**, 062101.

91 Wahl, U., Rita, E., Correia, J.G., Marques, A.C., Alves, E. and Soares, J.C. (2005) Direct evidence for As as a Zn-site

impurity in ZnO. *Physical Review Letters*, **95**, 215503.

92 Jeonga, T.S., Hana, M.S., Kima, J.H., Youna, C.J., Ryub, Y.R. and White, H.W. (2005) Crystallinity-damage recovery and optical property of As-implanted ZnO crystals by post-implantation annealing. *Journal of Crystal Growth*, **275**, 541.

93 So, S.-J. and Park, C.-B. (2005) Diffusion of phosphorus and arsenic using ampoule-tube method on undoped ZnO thin films and electrical and optical properties of p-type ZnO thin films. *Journal of Crystal Growth*, **285**, 606.

94 Aoki, T., Shimizu, Y., Miyake, A., Nakamura, A., Nakanishi, Y. and Hatanaka, Y. (2002) p-type ZnO layer formation by excimer laser doping. *Physica Status Solidi b: Basic Research*, **229**, 911.

95 Xiu, F.X., Yang, Z., Mandalapu, L.J., Zhao, D.T. and Liu, J.L. (2005) High-mobility Sb-doped p-type ZnO by molecular-beam epitaxy. *Applied Physics Letters*, **87**, 152101.

96 Xiu, F.X., Yang, Z., Mandalapu, L.J., Zhao, D.T. and Liu, J.L. (2005) Photoluminescence study of Sb-doped p-type ZnO films by molecular-beam epitaxy. *Applied Physics Letters*, **87**, 252102.

97 Limpijumnong, S., Zhang, S.B., Wei, S.-H. and Park, C.H. (2004) Doping by large-size-mismatched impurities: the microscopic origin of arsenic or antimony-doped p-type zinc oxide. *Physical Review Letters*, **92**, 155504.

98 Ryu, Y.R., Lee, T.S. and White, H.W. (2003) Properties of arsenic-doped p-type ZnO grown by hybrid beam deposition. *Applied Physics Letters*, **83**, 87.

99 Look, D.C., Jones, R.L., Sizelove, J.R., Garces, N.Y., Giles, N.C. and Halliburton, L.E. (2004) *Physica Status Solidi a: Applied Research*, **195**, 171.

100 Wardle, M.G., Goss, J.P. and Briddon, P.R. (2005) Theory of Li in ZnO: a limitation for Li-based p-type doping. *Physical Review B: Condensed Matter*, **71**, 155205.

101 Kobayashi, A., Sankey, O.F. and Dow, J.D. (1983) *Physical Review B: Condensed Matter*, **28**, 946.

102 Wu, Z.L., Merz, J.L., Werkhoven, C.J., Fitzpatrick, B.J. and Bhargava, R.N. (1982) *Applied Physics Letters*, **40**, 345.

103 Morkoç, H., Strite, S., Gao, G.B., Lin, M.E., Sverdlov, B. and Burns, M. (1994) *Journal of Applied Physics Reviews*, **76**, 1363.

104 Lee, E.-C., Kim, Y.-S., Jin, Y.-G. and Chang, K.J. (2001) *Physical Review B: Condensed Matter*, **64**, 85120.

105 Park, R.M., Troffer, M.B., Rouleau, C.M., DePuydt, J.M. and Hasse, M.A. (1990) *Applied Physics Letters*, **57**, 2127.

106 Svob, L., Thiandoume, C., Lusson, A., Bouanani, M., Marfaing, Y. and Gorochov, O. (2000) *Applied Physics Letters*, **76**, 1695.

107 Jung, H.D., Song, C.D., Wang, S.Q., Arai, K., Wu, Y.H., Zhu, Z., Yao, T. and Katayama-Yoshida, H. (1997) *Applied Physics Letters*, **70**, 1143.

108 Li, J., Wei, S.-H., Li, S.-S. and Xia, J.-B. (2006) Design of shallow acceptors in ZnO: first-principles band-structure calculations. *Physical Review B: Condensed Matter*, **74**, 081201(R).

109 Iwata, K., Fons, P., Yamada, A., Matsubara, K. and Niki, S. (2000) *Journal of Crystal Growth*, **209**, 526.

110 Look, D.C., Reynolds, D.C., Litton, C.W., Jones, R.L., Eason, D.B. and Cantwell, G. (2002) *Applied Physics Letters*, **81**, 1830.

111 Thonke, K., Gruber, T., Teofilov, N., Schönfelder, R., Waag, A. and Sauer, R. (2001) *Physica B*, **308–310**, 945.

112 Zeuner, A., Alves, H., Hofmann, D.M., Meyer, B.K., Hoffmann, A., Haboeck, U., Strassburg, M. and Dworzak, M. (2002) *Physica Status Solidi b: Basic Research*, **234**, R7.

113 Ashrafi, A.B.M.A., Suemune, I., Kumano, H. and Tanaka, S. (2002) *Japanese Journal of Applied Physics*, **41**, L1281.

114 Minegishi, K., Koiwai, Y., Kikuchi, Y., Yano, K., Kasuga, M. and Shimizu, A. (1997) *Japanese Journal of Applied Physics*, **36**, L1453.

115 Ye, Z.-Z., Lu, J.-G., Chen, H.-H., Zhang, Y.-Z., Wang, L., Zhao, B.-H. and Huang, J.-Y. (2003) *Journal of Crystal Growth*, **253**, 258.

116 Wang, J., Du, G., Zhao, B., Yang, X., Zhang, Y., Ma, Y., Liu, D., Chang, Y., Wang, H., Yang, H. and Yang, S. (2003) *Journal of Crystal Growth*, **255**, 293.

117 Lu, J., Zhang, Y., Ye, Z., Wang, L., Zhao, B. and Huang, J. (2003) *Materials Letters*, **57**, 3311.

118 Sato, Y. and Sato, S. (1996) *Thin Solid Films*, **281–282**, 445.

119 Guo, X.-L., Tabata, H. and Kawai, T. (2002) *Journal of Crystal Growth*, **237–239**, 544.

120 Yan, Y., Zhang, S.B. and Pantelides, S.T. (2001) *Physical Review Letters*, **86**, 5723.

121 Murphy, T.E., Chen, D.Y., Cagin, E. and Phillips, J.D. (2005) *Journal of Vacuum Science & Technology B: Microelectronics and Nanometer Structures*, **23**, 1277.

122 Liang, H.W., Lu, Y.M., Shen, D.Z., Liu, Y.C., Yan, J.F., Shan, C.X., Li, B.H., Zhang, Z.Z., Zhang, J.Y. and Fan, X.W. (2005) p-type ZnO thin films prepared by plasma molecular beam epitaxy using radical NO. *Physica Status Solidi a: Applied Research*, **202**, 1060.

123 Wang, X., Yang, S., Wang, J., Li, M., Jiang, X., Du, G., Liu, X. and Chang, R.P.H. (2001) *Journal of Crystal Growth*, **226**, 123.

124 Li, X., Yan, Y., Gessert, T.A., Perkins, C.L., Young, D., DeHart, C., Young, M. and Coutts, T.J. (2003) *Journal of Vacuum Science & Technology A: Vacuum Surfaces and Films*, **21**, 1342.

125 Li, X., Yan, Y., Gessert, T.A., DeHart, C., Perkins, C.L., Young, D. and Coutts, T.J. (2003) *Electrochemical and Solid-State Letters*, **6**, C56.

126 Ma, J.G., Liu, Y.C., Mu, R., Zhang, J.Y., Lu, Y.M., Shen, D.Z. and Fan, X.W. (2004) *Journal of Vacuum Science & Technology B: Microelectronics and Nanometer Structures*, **22**, 94.

127 Lin, C.-C., Chen, S.-Y., Cheng, S.-Y. and Lee, H.-Y. (2004) *Applied Physics Letters*, **84**, 5040.

128 Wang, C., Ji, Z., Liu, K., Xiang, Y. and Ye, Z. (2003) *Journal of Crystal Growth*, **259**, 279.

129 Garces, N.Y., Giles, N.C., Halliburton, L.E., Cantwell, G., Eason, D.B., Reynolds, D.C. and Look, D.C. (2002) *Applied Physics Letters*, **80**, 1334.

130 Garces, N.Y., Wang, L., Giles, N.C., Halliburton, L.E., Cantwell, G. and Eason, D.B. (2003) *Journal of Applied Physics*, **94**, 519.

131 Lu, J., Ye, Z., Wang, L., Huang, J. and Zhao, B. (2003) *Materials Science in Semiconductor Processing*, **5**, 491.

132 Zeuner, A., Alves, H., Sann, J., Kriegseis, W., Neumann, C., Hofmann, D.M., Meyer, B.K., Hoffmann, A., Haboeck, U., Straßburg, M. and Kaschner, A. (2004) *Physica Status Solidi b: Basic Research*, **1**, 731.

133 Yamauchi, S., Goto, Y. and Hariu, T. (2004) *Journal of Crystal Growth*, **260**, 1.

134 Yamamoto, T. and Katayama-Yoshida, H. (2000) *Journal of Crystal Growth*, **214–215**, 552.

135 Yamamoto, T. (2002) Co-doping for the fabrication of p-type ZnO. *Thin Solid Films*, **420–421**, 100.

136 Tsukazaki, A., Saito, H., Tamura, K., Ohtani, M., Koinuma, H., Sumiya, M., Fuke, S., Fukumura, T. and Kawasaki, M. (2002) *Applied Physics Letters*, **81**, 235.

137 Nakahara, K., Takasu, H., Fons, P., Yamada, A., Iwata, K., Matsubara, K., Hunger, R. and Niki, S. (2002) *Journal of Crystal Growth*, **237–239**, 503.

138 Ohshima, T., Ikegami, T., Ebihara, K., Asmussen, J. and Thareja, R. (2003) *Thin Solid Films*, **435**, 49.

139 Sumiya, M., Tsukazaki, A., Fuke, S., Ohtomo, A., Koinuma, H. and Kawasaki, M. (2004) *Applied Surface Science*, **223**, 206.

140 Alivov, Ya.I., Look, D.C., Ataev, B.M., Chukichev, M.V., Mamedov, V.V., Zinenko, V.I., Agafonov, Yu.A. and Pustovit, A.N. (2004) *Solid-State Electronics*, **48**, 2343.

141 Wang, L.G. and Zunger, A. (2003) Dilute nonisovalent (II–VI)–(III–V) semiconductor alloys: monodoping,

codoping, and cluster doping in ZnSe–GaAs. *Physical Review Letters*, **90**, 256401.

142 Joseph, M., Tabata, H. and Kawai, T. (1999) *Japanese Journal of Applied Physics, Part 2: Letters*, **38**, L1205.

143 Seebeck, T.J. (1823) Magnetische Polarisation der Metalle und Erze durch Temperaturdifferenz. *Abhandlungen der Deutschen Akademie der Wissenschaften zu Berlin*, 1, 265.

144 Singh, A.V., Mehra, R.M., Wakahara, A. and Yoshida, A. (2003) *Journal of Applied Physics*, **93**, 396.

145 Bian, J.M., Li, X.M., Gao, X.D., Yu, W.D. and Chen, L.D. (2004) *Applied Physics Letters*, **84**, 541.

146 Ye, Z.-Z., Zhu-Ge, Fei., Lu, J.-G., Zhang, Z.-H., Zhu, L.-P., Zhao, B.-H. and Huang, J.-Y. (2004) *Journal of Crystal Growth*, **265**, 127.

147 Aoki, T., Hatanaka, Y. and Look, D.C. (2000) ZnO diode fabricated by excimer-laser doping. *Applied Physics Letters*, **76**, 3257.

148 Ryu, Y.R., Lee, T.S., Leem, J.H. and White, H.W. (2003) Fabrication of homostructural ZnO p–n junctions and ohmic contacts to arsenic-doped p-type ZnO. *Applied Physics Letters*, **83**, 4032.

149 Yan, Y., Li, J., Wei, S.-H. and Al-Jassim, M.M. (2007) *Physical Review Letters*, **98**, 135506.

150 Kim, K.-K., Kim, H.-S., Hwang, D.-K., Lim, J.-H. and Park, S.-J. (2003) *Applied Physics Letters*, **83**, 63.

151 Ryu, Y.R., Zhu, S., Look, D.C., Wrobel, J.M., Jeong, H.M. and White, H.W. (2000) *Journal of Crystal Growth*, **216**, 330.

152 Ryu, M.K., Lee, S.H. and Jang, M.S. (2002) *Journal of Applied Physics*, **92**, 158.

153 Morhain, C., Teisseire, M., Vezian, S., Vigué, F., Raymond, F., Lorenzini, P., Guion, J., Neu, G. and Faurie, J.-P. (2002) *Physica Status Solidi b: Basic Research*, **229**, 881.

154 Heo, Y.W., Park, S.J., Ip, K., Pearton, S.J. and Norton, D.P. (2003) *Applied Physics Letters*, **83**, 1128.

155 Lee, S.Y., Shim, E.S., Kang, H.S., Pang, S.S. and Kang, J.S. (2005) *Thin Solid Films*, **473**, 31.

156 Park, S.-J. (2005) private communication.

157 Heo, Y.W., Kwon, Y.W., Li, Y., Pearton, S.J. and Norton, D.P. (2004) p-type behavior in phosphorus-doped (Zn,Mg)O device structures. *Applied Physics Letters*, **84**, 3474.

158 Lopatiuk, O., Burdett, W., Chernyak, L., Ip, K.P., Heo, Y.W., Norton, D.P., Pearton, S.J., Hertog, B., Chow, P.P. and Osinsky, A. (2005) *Applied Physics Letters*, **86**, 012105.

159 Ip, K., Heo, Y.W., Norton, D.P., Pearton, S.J., LaRoche, J.R. and Ren, F. (2004) *Applied Physics Letters*, **85**, 1169.

160 Egerton, E.J., Sood, A.K., Singh, R., Puri, Y.R., Davis, R.F., Pierce, J., Look, D.C. and Steiner, T. (2005) p-type doping utilizing nitrogen and Mg doping of ZnO using MOCVD for ultraviolet lasers and spintronics applications. *Journal of Electronic Materials*, **34**, 949.

161 Li, Y.J., Heo, Y.W., Kwon, Y., Ip, K., Pearton, S.J. and Norton, D.P. (2005) Transport properties of p-type phosphorus-doped (Zn,Mg)O grown by pulsed-laser deposition. *Applied Physics Letters*, **87**, 072101.

162 Norton, D.P., Ivill, M., Li, Y., Kwon, Y.W., Erie, J.M., Kim, H.S., Ip, K., Pearton, S.J., Heo, Y.W., Kim, S., Kang, B.S., Ren, F., Hebard, A.F. and Kelly, J. (2006) Charge carrier and spin doping in ZnO thin films. *Thin Solid Films*, **496**, 160.

163 Look, D.C. and Claflin, B. (2004) *Physica Status Solidi b: Basic Research*, **241**, 624.

164 Dadgar, A., Krtschil, A., Bertram, F., Giemsch, S., Hempel, T., Veit, P., Diez, A., Oleynik, N., Clos, R., Christen, J. and Krost, A. (2005) ZnO MOVPE growth: from local impurity incorporation towards p-type doping. *Superlattices and Microstructures*, **38**, 245.

165 Krtschil, A., Dadgar, A., Oleynik, N., Bläsing, J., Diez, A. and Krost, A. (2005) Local p-type conductivity in zinc oxide

dual-doped with nitrogen and arsenic. *Applied Physics Letters*, **87**, 262105.

166 Krtschil, A., Dadgar, A., Diez, A. and Krost, A. (2007) Electrical characterization of defect states in local conductivity domains in ZnO:NAs layers. *Journal of Materials Research*, **22**, 1775.

167 Zhao, J.-L., Li, X.M., Krtschil, A., Krost, A., Yu, W.D., Zhang, Y.-W., Gu, Y.-F. and Gao, X.-D. (2007) Study on anomalous high p-type conductivity in ZnO films on silicon substrate prepared by ultrasonic spray pyrolysis. *Applied Physics Letters*, **90**, 062118.

5
ZnO-Based Dilute Magnetic Semiconductors

The III–V and II–VI diluted magnetic semiconductors (DMSs) have attracted considerable attention because the spin-dependent magnetic phenomena can potentially be manipulated in these low-dimensional tailored magnetic thin films for various spin-based devices to unprecedented capabilities [1]. ZnO, in addition to GaN, has been predicted to retain its ferromagnetism at room temperature in contrast to other DMSs such as GaAs and ZnTe based varieties. Generally, 3d transition-metal ions (some species of magnetic ions, i.e., ions bearing a net magnetic moment such as Sc, Ti, V, Cr, Mn, Fe, Co, Ni, and Cu) and rare earth elements that have partially filled f states (e.g., Eu, Gd, Er) are substituted for the cations of the host semiconductors. As a consequence, the electronic structure of the substituted 3d transition metal (TM) impurities in semiconductors is influenced by two competing factors: strong 3d-host hybridization and strong Coulomb interactions between 3d–3d electrons. The latter is responsible for the multiplet structures observed in d–d optical absorption spectra. On the other hand, as specifically shown for the Mn-doped systems, the hybridization between the transition metal 3d and the host valence band gives rise to the magnetic interaction between the localized 3d spins and the carriers in the host valence band [2]. The above room temperature ferromagnetism in Mn-doped ZnO has been initially predicted to be in part due to this strong p–d hybridization owing to the small nearest-neighbor distance and small spin-orbit coupling. However, Sato and Katayama-Yoshida [3] predicted that the ferromagnetic (FM) state Co^{2+} (d^7) in Co-doped ZnO could be stabilized by s–d hybridization instead, pointing to the possibility that high-Curie-temperature ferromagnetic materials could be realized also in n-type ZnO.

Assuming that ZnO can be made ferromagnetic by doping with transition metals such as Mn, Fe, Cr, Co, V, and so on or spin injecting contacts to ZnO can be found, the material would be suitable for a number of devices such as spin FETs, and LEDs with circularly polarized light emission. In ZnO, the equilibrium solubility limit of 3d-transition metals such as Mn is larger than 10 mol%, and the electron-effective mass is as large as $\sim 0.3\, m_e$, where m_e is free-electron mass. Therefore, the amount of injected spins and carriers in the film can be large, thus making, for example, Mn-doped ZnO ideal for fabrication of spintronic devices. If made ferromagnetic, it can be used for drain and source in FETs provided that spin polarized injection of

carriers or spin coherence lengths comparable to the device dimensions, made possible by the available technology, can be obtained.

Injection of spin-polarized carriers is not straightforward. Among the approaches, spin injection through the metal–semiconductor interface suffers from the large conductivity mismatch between the adjacent regions [4], which is very severe for Ohmic contacts. A tunnel barrier between a metallic ferromagnet and a semiconducting paramagnet has been proposed to increase the spin injection efficiency [5], and room temperature spin injection has been achieved in GaAs from metal [6]. However, this approach can have only a limited number of applications because of the low injection currents caused by barrier resistance (high current levels are needed in semiconductor lasers for example). Therefore, the semiconductor–semiconductor interface is preferable for spin injection, which requires a ferromagnetic semiconductor with a Curie temperature T_C, higher than room temperature for practical devices. Therefore, T_C in diluted magnetic semiconductors, semiconductors in which a fraction of the host cations is substituted by transition metal or appropriate rare earth ions, is naturally the bottleneck issue.

Several groups have fabricated (Zn,TM)O (TM = Sc [7, 8], Ti [7, 8], V [7–9], Cr [7, 8, 10], Mn [7, 8, 10–16], Fe [8], Co [7, 8, 10, 17–20], Ni [7, 8, 10, 21], Cu [7, 8]) films by different techniques. Although there is a great deal of controversy and discrepancy about the actual ferromagnetic Curie temperature and source of ferromagnetism in transition metal-doped ZnO films found in various reports, T_C values above the room temperature are reported [22]. However, as in the case of GaN the results are conflicting [23, 24]. This is in part due to the use of highly sensitive superconducting quantum interference device (SQUID) magnetometer in combination with X-ray diffraction (XRD) that may be insufficient for revealing the origin of ferromagnetic ordering. The SQUID measurements are very sensitive to magnetic contamination and also are not by nature able to pinpoint the origin of magnetism all that well. Optical measurements such as magnetic circular dichroism (MCD) are more stringent. Particularly MCD is sensitive to the band structure of the host material and its response to the presence of magnetization through the Zeeman splitting. As in the case of GaN, the MCD measurements performed in magnetic ion doped ZnO have not led to positive results and in all cases led to antiferromagnetic (AFM) [7, 8] p–d exchange interaction and paramagnetic [25] DMS behavior, details of which are discussed later.

It should be pointed out that host ferromagnetism alone does not allow spin manipulations. In order to provide a degree of spin polarization at the Fermi level sufficient for device applications, the ferromagnetic coupling should be carrier mediated, which has not been unambiguously established in any of the reports. The interpretation of Hall effect measurements, a straightforward method that usually proves carrier mediated ferromagnetism via the detection of the anomalous Hall effect, is challenging for ZnO-based DMSs, because heavily doped ZnO (3.2×10^{18} to $1.3 \times 10^{20}\,cm^{-3}$) exhibits a negative magnetoresistance due to s–d exchange coupling without any doping with TMs [26]. In such a situation, the study of optical or electrical spin injection provides an avenue for insight into the nature of magnetic order in the material. In addition, ZnO doped with magnetic ions is

highly resistive preventing reliable magnetotransport measurements from being made.

In this chapter, an overview of the physics and some generic features of ZnO-based DMS heterostructures are provided. The discussion starts with a brief introduction to transition metal and rate earth doping of semiconductors, followed by a general review of DMS theoretical aspects, including the existing theories to explain magnetic interactions within the DMS. Because several interesting quantum structures derived from the ZnO-based DMSs (particularly, substituting Zn-site by Mn) provide a valuable framework for understanding of spin transport and dynamics in magnetically active quantum semiconductor structures, theoretical studies of magnetism in ZnO DMSs are described next. Then, a brief summary of the main experimental results on ZnO-based DMSs have been put forth for the explanation of the ferromagnetism in these compound semiconductors.

5.1 Doping with Transition Metals

Transition metal impurities are interesting from two points of view. One deals with acceptor-like doping in the context of electronic properties. The other deals with magnetic properties when the transition element concentration is relatively high but still within the dilute limit so as not to change the main structural nature of the ZnO matrix. On the magnetic side, extending the carrier-mediated magnetic interaction from diluted GaAs:Mn to zinc blende ZnO:Mn and GaN:Mn, Dietl *et al.* [27] predicted high-temperature ferromagnetism in diluted $Mn_xZn_{1-x}O$ and $Mn_xGa_{1-x}N$ with $x = 0.05$ and potential application of these materials to spin-transport electronics (spintronics). This started a flurry of activity in ZnO and GaN doped with Mn and also other transition metals with impetus being provided by the lure of electronics using charge and spin, primarily the latter.

When the host material is doped with Mn, the crystal field modifies emission energies associated with the internal transitions within the Mn atom. Moreover, transitions involving levels induced by Mn in the host material appear, the specifics of which depend on the interaction of the Mn atom with the host material. The nature of the internal transitions in Mn as an isolated atom as well as the one affected by the tetrahedral crystal field such as that in ZnO and GaN is shown in Figure 5.1 for the Mn^{2+} state. The Mn^{2+} (d^5) levels depicted in Figure 5.1 are expected to hybridize with s–p bands of the host and broaden into d bands, still narrow. An insight can thus be gained by discussing the nature of intratransitions in free Mn atom followed by the same in isolated Mn^{2+} occupying a cation site in the host material.

Transition metal elements have valence electrons corresponding to the 4s orbital, and have partially filled 3d shells, thus the name 3d transition metals (i.e., Mn with the shell structure of $1s^2\ 2s^2\ 2p^6\ 3s^2\ 3p^6\ 3d^5\ 4s^2$). The partially filled shells of transition metal ions warrant a discussion of protocol involved in labeling the ground and excited states. Consider a free or isolated ion, all the electronic shells of which are filled except one that is the 3d shell in transition metal elements and 4f shell in rare

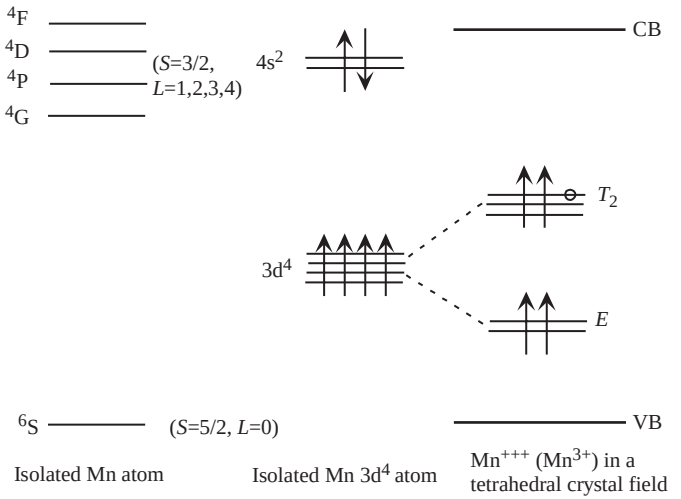

Figure 5.1 A schematic diagram showing the splitting of the lowest excited states of the $3d^5$ level (^4G) relative to the ground state (^6S) for a Mn^{++} [or Mn^{2+} (d^5)] ion in isolated case (left) and in the presence of a tetrahedral crystal field. The arrows indicate possible intra-Mn transitions. The picture is similar for the Mn^{3+} shell.

earth elements. Suppose the electron levels in the partially empty shell are characterized by an orbital angular momentum, l that assumes the value of 2 for 3d states (here, $n = 3$ and $l = n - 1 = 2$). In the particular shell, there are $2l + 1$ states $[-l, -(l-1), \ldots, 0, \ldots, (l-1), l]$ (assign a letter designation for each of l_z), each of which can have two electrons, one with spin-up and one with spin-down, which would result in 10 states for the 3d shell. If the electrons were not to interact with each other, the ionic ground state would degenerate. However, this degeneracy, albeit not completely, is lifted by electron–electron Coulomb interaction and electron spin orbit interaction.

The lowest levels, after the degeneracy is lifted, are governed by a simple set of rules, Russel–Saunders coupling (or LS coupling), and *Hund's rules* that come about as a result of complex calculations [28]. The former rule states that the Hamiltonian is commutative with the total electronic spin angular momentum (S), orbital angular momentum (L), and the total electronic angular momentum ($J = L + S$). Because the filled states have zero orbital spin ($L = 0$), the eigenvalues determine the quantum numbers that in turn describe the configuration of the partially filled shell and the ion. The latter rule has three components, one of which states that the electrons that lie lowest in energy have the largest total spin while adhering to the exclusion principle. This means, for example, that all the spin-up electrons must occupy the partially empty shell while adhering to the exclusion principle.

Hund's second rule prescribes that the total angular momentum L of the lowest lying states has the largest value without violating Hund's first rule and the exclusion principle. The value is equal to the largest magnitude that l_z can have, which means

that the first electron will go into the state with the largest $|l_z|$. Because Hund's first rule indicates that the second electron must have a spin to maximize the spin, it must go into the second state with the same spin as the first. Continuing on with this rule in mind, the value of L can be calculated using $L = |\sum l_z|$. With Hund's first and second rules, one can determine the values of S and L, leaving $(2L + 1)(2S + 1)$ states that can be further configured according to their total angular momentum J. The third rule then helps determine the J values as $J = |L - S|$ for $n \leq (2l + 1)$ and $J = ||L + S$ for $n \geq (2l + 1)$ or $J = (L - S_{\downarrow})$ and $(L + S_{\uparrow})$.

The 3d band of the Mn^{2+} ion is exactly half-filled with five electrons among the 10 available states, with a gap between the upspin (↑) occupied states and empty downspin (↓) states. For other transition metals, such as Fe, Co, and Ni, one of the bands is usually partially filled (up or down), as shown in Figure 5.2. Table 5.1 shows the oxidation and charge states for some of the transition metals in ZnO and GaN [29]. The TM-d bands of the transition metal hybridize with the host valence bands (N-p bands in GaN) to form the tetrahedral bonding. This hybridization gives rise to the exchange interaction between the localized 3d spins and the carriers in the host valence band. In the simplest of pictures, the s band of the conduction band does not mix with the TM-d bands, but it is still influenced by the magnetic ion.

For an element with 5 3d electrons (Mn) this means that all five would have spin-up. The total spin S, is calculated at $S = (1/2)(n_{\downarrow} - n_{\uparrow})$, which would be $(^1/_2)(5)$ or 5/2 for Mn (3d) because all d-shell electrons have the same spin. In Fe, however, there are six 3d electrons and one of them would have to have a spin-down configuration. In this case, the total spin would be $^1/_2(5 - 1) = 2$. The methodology regarding how the electrons are arranged in the d shell for transition metals including orbital angular momentum, spin angular momentum, and total momentum and the name designation for each of the available 10 d shell states is shown in Table 5.2.

As mentioned in the preceding paragraph, the element Mn is a unique case in that it has only five electrons in its 3d shell, half of all the available states, are all in their ground state. Following Hund's rule, which calls for all electrons to maximize the spin angular momentum (↑↑↑↑↑). As tabulated in Table 5.2 the electrons in their ground d shell (in Mn $3d^5$ state) have their orbital angular momentum $L = 0$ and spin angular momentum $S = (1/2)(5) = 5/2$ (the orbital angular momentum L is

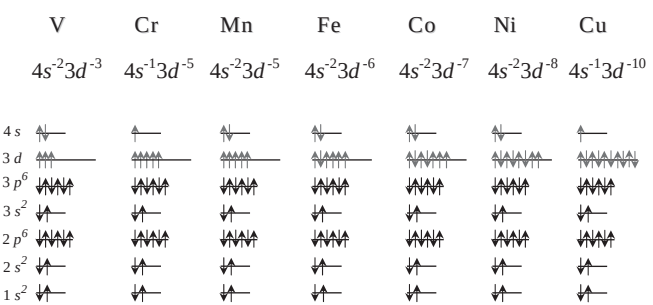

Figure 5.2 Electronic configuration of the 3d-states and 4s-states of transition metal elements (from V to Cu).

Table 5.1 Expected oxidation and charge state of some candidate transition metals in ZnO.

ZnO	$3d^3$	$3d^4$	$3d^5$	$3d^6$
Acceptor (negative charge)			Cr^{+}	Mn^{+}
Neutral		Cr^{2+}	Mn^{2+}	Fe^{2+}
Donor (positive charge)	Cr^{3+}	Mn^{3+}	Fe^{3+}	
Double donor (2^{+} charge)	Mn^{4+}	Fe^{4+}		

After Ref. [29].

quenched). The excited states of the d-shell electrons would have $L = 1,2,3$, and 4 values and are assigned the letter designation of, in the same order, P,D,F, and G. For electron to make the transition to one of these excited states, one electron must flip its spin ($\uparrow\uparrow\uparrow\uparrow\downarrow$), which changes the spin quantum number to $S = (1/2)(3) = 3/2$. In the notation of spectroscopy, the states are labeled with left superscript $^{2S+1}X_J$. Because the ground state has $S = 5/2$ and $L = 0$, the nomenclature used is $^6S_{5/2_{5/2}}$. Similarly, $L = 1,2,3$, and 4 states (with $S = 3/2$) are labeled as ^4G, ^4P, ^4D, and ^4F. Among these excited states, the ^4G ($S = 3/2$, $L = 4$) level has the lowest energy as shown in Figure 5.1. The transition from the $^6S \rightarrow {}^4G$ dominates the optical spectra involving a free Mn atom.

When a Mn atom is substitutionally placed into a tetrahedral crystal of the II–VI type or said to be in its oxidation state [to be more descriptive Mn^{2+} or $Mn^{2+}(3d^5)$, which also indicates that only two $4s^2$ electrons participate in the bonding], the four neighboring anion atoms exert a crystal field. This field causes the ninefold degenerate ^4G state to split into $^4A_1$ (nondegenerate), ^4E (twofold degenerate), $^4T_2$ (threefold degenerate), and $^4T_1$ (threefold degenerate) states. Of these, $^4A_1$ and ^4E states nearly coincide and are hardly affected by the crystal field as shown in Figure 5.1. In the notation used to describe the intra-Mn^{2+} transitions, the ground-state label ^6S gives way to $^6A_1$ that is spherically symmetric and nondegenerate. The calculations show that the crystal field lowers the energies of both $^4T_2$ and $^4T_1$ states.

Transitions between the ^6S ($S = 5/2$, $L = 0$) and any of the excited states ($S = 3/2$, $L = 1,2,3,4$) in free Mn atoms are forbidden as $\Delta S = 0$ spin parity requirement is not satisfied. For Mn^{+2}-isolated ions in the crystal, the selection rules are relaxed by the lack of inversion symmetry and crystal field. Therefore, transitions from $^6A_1$ ground state to the excited states, derivatives of the ^4G states become possible. This is one reason why a different nomenclature, from that used for intratransitions in free Mn, is used for isolated Mn^{+2} ion. Of the possible transitions, $^6A_1 \rightarrow {}^4T_1$ has the lowest energy and therefore constitutes the most important transition. As mentioned above, the Mn^{2+} ion is ideally suited in conjunction with discussions dealing with II–VI materials wherein Mn donates two of its electrons ($4s^2$) to bonding which in turn statistically spend more of their time in the orbitals of the O atom, making it O^{-2}.

For a full characterization of the state of magnetic impurities in ZnO and their participation in any magnetization combination of optical, magneto-optical, electron paramagnetic resonance (EPR), electron spin resonance (ESR), and electrical and magnetic measurements, not necessarily in that order, would be required.

Table 5.2 The electronic configuration for the d shell in transition metals, and the relevant spin, orbital, and total angular momentum along with the nomenclature used.

Element	d shell electrons ($l=2$) n	$l_z=-2$	$l_z=-1$	$l_z=0$	$l_z=+1$	$l_z=+2$	$S=(1/2)(n_\uparrow - n_\downarrow)$	$L=\lvert\sum l_z\rvert$	$J=(L-S_\uparrow)$ & $(L+S_\downarrow)$	Symbol X in the form $^{2S+1}X_J$
Sc	1	↑					1/2	2	3/2	$^2D_{3/2}$
Ti	2	↑	↑				1	3	2	$^3F_2$
V	3	↑	↑	↑			3/2	3	3/2	$^4F_{3/2}$
	4	↑	↑	↑	↑		2	2	0	$^5D_0$
Cr, Mn ($3d^5$)	5	↑	↑	↑	↑	↑	5/2	0	5/2	$^6S_{5/2}$
Mn ($3d^4$)	4	↑	↑	↑	↑		2	2	0	$^5D_0$
Fe	6	↑↓	↑	↑	↑	↑	2	2	4	$^5D_4$
Co	7	↑↓	↑↓	↑	↑	↑	3/2	3	9/2	$^4F_{9/2}$
Ni	8	↑↓	↑↓	↑↓	↑	↑	1	3	4	$^3F_4$
	9	↑↓	↑↓	↑↓	↑↓	↑	1/2	2	5/2	$^2D_{5/2}$
Cu, Zn	10	↑↓	↑↓	↑↓	↑↓	↑↓	0	0	0	$^1S_0$

The up and down arrows represent the spin-up and spin-down.

5.2
General Remarks About Dilute Magnetic Semiconductors

Transition metal-doped semiconductors, dating back to II–VIs such as (Zn–Mn)S, (Zn–Mn)Se, and (Cd–Mn)Te [2], and later to arsenide-based III–Vs such as $In_{1-x}Mn_xAs$ [30] and $Ga_{1-x}Mn_xAs$ [31] followed by GaN and ZnO, have been considered for magnetoelectronics. If the magnetic moment of transition metal elements can be made aligned, it could pave the way for many device concepts depending on the degree to which that alignment is controlled. The II–VI system suffers from a low critical temperature (<30 K) above which magnetic ordering is not maintained. That temperature in GaAs-based system is near 170 K and still improving as modulation-doping methods are employed to increase the hole concentration. Among wide bandgap semiconductors, heavy doping of GaN with magnetic ions goes beyond the realm of discussion of doped GaN in the hope of obtaining p-type material and extends over into the realm of magnetism. If the above room-temperature ferromagnetism were to be accomplished in ZnO and or other materials such as nitrides that might possibly form the base for charge, spin-based, or mixed spin and charge-based devices. The devices utilizing spin in one form or another fall into a newly coined nomenclature, *spintronics*.

As spun, spintronics is a new paradigm in which the spin degree of freedom of the electron that could also include nuclear spin, which is not discussed here, is harnessed either by exploiting the spin property in conventional charge-based devices or utilizing the spin alone. For successful incorporation of spin into existing semiconductor technology, several technical issues such as efficient injection, transport, control and manipulation, and detection of spin polarization as well as spin-polarized currents must be resolved. Faster and less power consuming transistors have been reported as being a possibility because flipping the spin takes 10–50 times less power and is 10 times faster than the transportation of an electron through the channel in traditional FETs. Challenges, however, are formidable in that in addition to coherent spin injection, the device dimensions must be comparable to, if not less than, the spin coherence lengths.

5.3
Classification of Magnetic Materials

Before delving further into the magnetic properties of diluted magnetic semiconductors, it is incumbent upon us to give a succinct review of magnetization in general. The genesis of magnetism has to do with the orbital and spin motions of electrons and how the electrons interact with one another as pertained to their spin. The classification of magnetic materials is based on how they respond to magnetic fields. Although as surprising as it may sound, all matter is magnetic to varying degrees. The main delineating factor is that in some materials there is no collective long range interaction between atomic magnetic moments, whereas in other materials there is a very strong interaction. The magnetic behavior of materials can be classified

into the following five major groups: diamagnetic, paramagnetic, ferromagnetic, antiferromagnetic, and ferrimagnetic. Alternatively, in terms of the phenomena, they are diamagnetism, paramagnetism, ferromagnetism, antiferromagnetism, and ferrimagnetism.

Although it is usually very weak, *diamagnetism* is a fundamental property of all matter. All nonmagnetic materials are diamagnetic including all nonmagnetic semiconductors such as Si, Ge, GaAs, GaN, ZnO, and so on except when these materials are doped with some transition metal elements such as Mn or rare earths such as Gd to render them magnetic. Diamagnetism arises from the tendency of electrical charge partially screening the interior of the body from the applied magnetic field. Diamagnetic substances are composed of atoms that have no net magnetic moments (i.e., all the orbital shells are filled and there are no spin unpaired electrons). In the absence of a magnetic field, the electron motion is spherically symmetrical, the angular momentum is zero, circulating current around the nucleus is zero, and the magnetic moment is zero. However, when exposed to a magnetic field, a Lorentz force is generated and the Lenz's law dictates that when the magnetic flux changes in a circuit, a current is induced to oppose that change. The centrifugal and centripetal forces are rebalanced by the magnetic force causing the orbital frequency of an electron with orbital magnetic moment parallel to the field to slow down and the one that is antiparallel to the field to speed up. Therefore, a negative magnetization is produced against the applied magnetic field and the susceptibility is negative, $\chi < 0$, and small. Magnetization M changes linearly with applied magnetic field H with a negative slope as shown in Figure 5.3. Negative susceptibility can be interpreted as material being poised to expel the applied field. The magnetic susceptibility ranges from -5.0×10^{-9} for Silicon to -1.6×10^{-4} for Bismuth. Another well-known characteristic of diamagnetic materials is that the susceptibility is temperature independent.

In materials exhibiting *paramagnetism*, some of the atoms or ions in the material have a net magnetic moment due to unpaired electrons in partially filled orbitals,

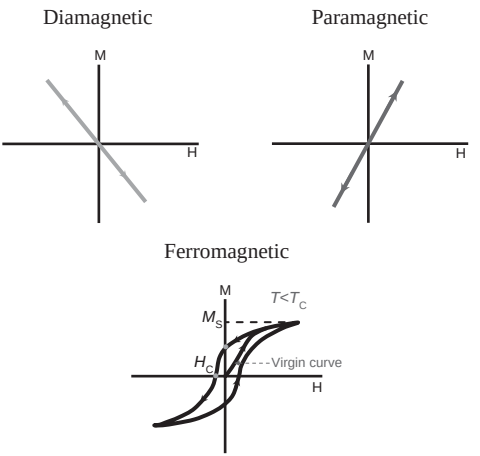

Figure 5.3 A cartoon showing diamagnetic, paramagnetic, and ferromagnetic cases.

such as that in transition metals and some rare earth elements. Electronic paramagnetism arises from, for example, atoms, molecules, and lattice defects, possessing an odd number of electrons (unpaired) causing a nonzero total spin. Free atoms and ions with a partially filled inner shell, such as transition elements, ions isoelectronic with transition elements, rare earth, and actinide elements have unpaired electrons in those shells, which lead to nonvanishing spin. Examples include V^{2+}, Cr^{2+}, Mn^{2+}, Fe^{2+}, Co^{2+}, and Ni^{2+} among the transition elements and Gd^{3+} among the rare earths. The magnetization M versus magnetic field H curve in these materials follows a linear relationship with a positive slope and positive susceptibility, $\chi > 0$, as shown in Figure 5.3, unlike the diamagnetic materials. The magnetization would eventually saturate, as all the magnetic ions would have their magnetic moments aligned, to the extent possible, by the magnetic field.

There are several theories concerning paramagnetism, which are valid for specific types of materials. The Langeven model, applicable to materials with noninteracting localized electrons, states that each atom has a magnetic moment that is randomly oriented as a result of thermal agitations. Application of a magnetic field creates a slight alignment of these moments and thus a low magnetization in the same direction as the applied field. As the temperature increases, however, the retention of alignment becomes harder due to the thermal agitations and thus the susceptibility decreases. This behavior is known as the Curie law ($\chi = C/T$, where C is a material constant called the Curie constant) as will be discussed later in this section (see Equation 5.8). Materials that obey this law are those in which the magnetic moments are localized at the atomic or ionic sites and in which there is no interaction between neighboring magnetic moments. It should in fact be recognized that the Curie law is a special case of the more general Curie–Weiss law [$\chi = C/(T - \theta)$], which incorporates a temperature constant (θ) and derives from the Weiss theory proposed for ferromagnetic materials that incorporates the interaction between magnetic moments.

In the Pauli model of paramagnetism, the conduction electrons are considered essentially to be free and under an applied field an imbalance between electrons with opposite spin is set up leading to a low magnetization in the same direction as the applied field. The susceptibility is independent of temperature, although the electronic band structure may be affected, which will then have an effect on the magnitude of the susceptibility.

When all the atomic magnetic moments in a lattice interact to align parallel to each other, the material exhibits *ferromagnetism* with nonzero magnetic moment (the susceptibility is positive, $\chi > 0$, and very large), even for zero applied field, called the spontaneous magnetic moment. As will be discussed later in this chapter in Section 5.5, if the alignment is caused by exchange interaction with carriers, as in the case of GaAs:Mn, the control over the hole concentration would lead to control of the degree to which the material is ferromagnetic. Initially, this effect was described by classical theory that assumed the presence of a molecular field within the ferromagnetic material, postulated first by Weiss in 1907. This field is sufficient to magnetize the material to saturation. In quantum mechanics, however, the Heisenberg model of ferromagnetism is used, describing the parallel alignment of magnetic moments in terms of an exchange interaction between neighboring

moments. Weiss postulated the existence of magnetic domains within which the atomic magnetic moments are aligned. The movement of these domains determines how the material responds to an applied magnetic field and as a result, the susceptibility is a function of the applied magnetic field. Therefore, ferromagnetic materials are usually compared in terms of saturation magnetization rather than susceptibility. Saturation magnetization occurs when all domains are aligned. Below the Curie temperature, the magnetization versus H curve for a ferromagnet shows hysteresis, as shown in Figure 5.3.

Among the elements, only Fe, Co, and Ni are ferromagnetic at and above room temperature. As ferromagnetic materials are heated, the thermal agitation of the atoms breaks the degree of alignment of the atomic magnetic moments and thus the saturation magnetization also decreases. As the temperature is further increased, the thermal agitation becomes so great that the material becomes paramagnetic. The temperature of this transition is the Curie temperature, T_C. The Curie temperatures for the above-mentioned naturally ferromagnetic elements are T_C (Fe) = 770 °C, T_C (Co) = 1131 °C, and T_C (Ni) = 358 °C. Above T_C, in the paramagnetic state, the susceptibility varies according to the Curie–Weiss law. In addition, above the Curie temperature an otherwise ferromagnetic material would behave as a paramagnetic material with linear dependence of magnetization on the H field. For completeness, if portions of the material are ferromagnetic and the rest paramagnetic, the material is called superparamagnetic.

In materials exhibiting *antiferromagnetism*, the neighboring spins are aligned in a regular fashion as in the ferromagnetic materials, but pointing in the opposite directions. In the simplest case, the material can be assumed to be composed of two sublattices, where the spins associated with sublattice A and sublattice B are completely antialigned so as to have zero net magnetization, despite the magnetic ordering. All of these antialignment effects only take place at temperatures below the Néel temperature, T_N. Above the Néel temperature, the material is typically paramagnetic. The only element exhibiting antiferromagnetism at room temperature is chromium with a Néel temperature of 37 °C. Cr has a body centered cubic lattice structure with the body center atomic spins are directed opposite to those at the cube corners, which are both equal in number. The clue to antiferromagnetism is the behavior of susceptibility above the Néel temperature, where the susceptibility obeys the Curie–Weiss law for paramagnets but with a negative intercept indicating negative exchange interaction energy. Antiferromagnetic materials, such as Cr and Mn, possess small but positive susceptibility, $\chi > 0$.

As alluded earlier, a material is ferromagnetic only if *all* of its magnetic ions are aligned and add a positive contribution to the net magnetization. If some of the magnetic ions *subtract* from the net magnetization (if they are partially antialigned), then the magnetic behavior is called *ferrimagnetism*. Ferrimagnetic materials such as ferrites that utilize transition element Fe as in Fe_2O_3 exhibit magnetism similar to ferromagnetic materials below the Curie temperature, T_C. Above this temperature, they become paramagnetic as in the case of ferromagnetic materials. Ferrimagnetism is observed only in compounds with complex crystal structures. In these materials, the exchange interactions lead to parallel alignment of atoms in some of

the crystal sites, sublattice A, and antiparallel alignment of others, those in sublattice B. The material breaks down into magnetic domains, as in antiferromagnetic materials. The main difference between ferrimagnetic and antiferromagnetic materials is that the magnetic moment associated with sublattice A atoms is larger than, as opposed to being equal to, that of sublattice B atoms so they do not null each other. The magnetic behavior in ferromagnetic and ferrimagnetic materials is also very similar. However, ferrimagnetic materials generally have lower saturation magnetizations. Ultimately, the magnitude of the spontaneous polarization M_s, depends on how well the sublattice moments are aligned, as thermal vibration of the atoms causes misalignment of the moments and a reduction in M_s. For ferrimagnetic materials, not all the moments align parallel, even at zero Kelvin and hence M_s will depend on the relative alignment of the moments as well as the temperature. As an example, in Barium ferrite ($BaO{\cdot}6Fe_2O_3$), the unit cell contains 64 ions of which the barium and oxygen ions have no magnetic moment, 16 Fe^{3+} ions have moments aligned parallel and 8 Fe^{3+} ions aligned antiparallel giving a net magnetization parallel to the applied field. The amplitude of the net magnetization, however, is relatively low as only one-eighth of the ions contribute to the magnetization of the material. Because ferrimagnetic materials are typically nonconducting and consequently do not suffer from eddy current and associated loss, they are useful in radio frequency applications.

To reiterate, the sign and the magnitude of susceptibility serve to classify materials: diamagnetic with negative and small magnetic susceptibility, paramagnetic with positive and small magnetic susceptibility, antiferromagnetic with positive but small magnetic susceptibility, and ferromagnetic or ferrimagnetic with positive and very large magnetic susceptibility.

5.4
A Brief Theory of Magnetization

In diamagnetic and paramagnetic materials, small applied magnetic fields lead to an internal magnetic induction that is directly proportional to the applied field through

$$\mathbf{B}_{\text{int}} = \mu\mathbf{H} = \mu_r\mu_0\mathbf{H}, \tag{5.1}$$

where μ_r and μ_0 represent the relative permeability of the medium and the permeability of free space, respectively. μ is called the permeability of the medium. If the sample is placed in an external magnetic induction $\mathbf{B}_0$ or an external magnetic field $\mathbf{H}$, the internal magnetic induction $\mathbf{B}_{\text{int}}$, can be expressed as (with the assumption that demagnetization effects are negligible and the internal magnetic field $\mathbf{H}_{\text{int}}$ can be approximated by the external magnetic field $\mathbf{H}$ that is justified for diamagnetic and paramagnetic materials)

$$\mathbf{B}_{\text{int}} = \mathbf{B}_0 + \mu_0\mathbf{M} = \mu_0(\mathbf{H} + \mathbf{M}). \tag{5.2}$$

We should note that many authors call $\mathbf{B}$, not $\mathbf{H}$, the magnetic field as "induction" already has other meanings in electrodynamics (such as induction of an electric field

by changing the magnetic field). To avoid confusion, these two fields will be referred to as the **H** field and the **B** field from here on.

With the aid of Equation 5.1 and Equation 5.2, we find

$$\mathbf{M} = (\mu_r - 1)\mathbf{H} = \chi\mathbf{H} \quad \text{or} \quad \mu_r = \chi + 1, \tag{5.3}$$

where χ (dimensionless) is the magnetic volume susceptibility.

For ferromagnetic materials, the internal field $\mathbf{H}_{int}$ cannot be approximated by the external **H** field and the **B** field can be expressed as

$$\mathbf{B} = \mathbf{H} + 4\pi\mathbf{M} \text{ in cgs} \quad \text{or} \quad \mathbf{B} = \mu_0(\mathbf{H} + \mathbf{M}) \text{ in SI units.} \tag{5.4}$$

Magnetization **M**, is defined as the magnetic moment per unit volume, and magnetic susceptibility χ, is the ratio of magnetization divided by the macroscopic **H** field:

$$\chi = \mathbf{M}/\mathbf{H}. \tag{5.5}$$

Similarly, the permeability of the medium is given by the ratio of the **B** and **H** fields: $\mu = \mathbf{B}/\mathbf{H} = \mu_0(1 + \chi)$. The magnetic polarization (J), also called the intensity of magnetization (I), is defined as $J = \mu_0 M$ and its saturation value is depicted by the nomenclature of J_s.

Because cgs and SI units are used in the literature, conversion factors between the two as well as definition of pertinent magnetism parameters along with their units are tabulated in Table 5.3.

It is instructive to briefly discuss the rudimentary basis for magnetism in an effort to get acquainted with the terminology, basis for various types of magnetism,

Table 5.3 The relationship between some magnetic parameters in cgs and SI units. (where G = Gauss, Oe = Oersted, T = Tesla, M = Mega = 10^6).

Quantity	Gaussian (cgs units)	SI units	Conversion factor (cgs to SI)
B-field (aliases magnetic induction, magnetic flux density)	G	T	10^{-4}
H-field (aliases magnetic field strength/intensity, applied field)	Oe	$A\,m^{-1}$	$10^3/4\pi$
Magnetization *(M)*	emu cm^{-3}	$A\,m^{-1}$	10^3
Magnetization ($4\pi M$)	G	—	—
Magnetic polarization (J)	—	T	—
Specific magnetization (s)	emu g^{-1}	$J\,T^{-1}\,kg^{-1}$	1
Permeability (μ)	Dimensionless	$H\,m^{-1}$	$4\pi \times 10^{-7}$
Relative permeability (μ_r)	—	Dimensionless	—
Susceptibility (χ)	emu $cm^{-3}\,Oe^{-1}$	Dimensionless	4π
Maximum energy product (BH_{max})	M G Oe	$k\,J\,m^{-3}$	$10^2/4\pi$

http://www.aacg.bham.ac.uk/magnetic_materials/type.htm.

temperature dependence of magnetism, and values of fundamental nature such as Bohr magneton. In this realm, let us consider N atoms per unit volume, each with a magnetic moment $\mathbf{m}$. Magnetic field, if any, will align those moments, but thermal disorder would resist the tendency to align. The energy of interaction of the moment $\mathbf{m}$ with the applied field $\mathbf{B}$ is given by [32]

$$U = -\mathbf{m} \cdot \mathbf{B}. \tag{5.6}$$

In thermal equilibrium, the magnetization is given by the *Langevin equation* as

$$M = NmL(x), \tag{5.7}$$

where $x \equiv (mB/kT)$ is the Langevin function $L(x) = \text{ctnh}\, x - 1/x$, and N, the number of atoms per unit volume. For $x \ll 1$ (or $mB \ll kT$), $L(x) \approx x/3$, which leads to the well-known *Curie law*

$$M \approx \frac{Nm^2B}{3kT} = \frac{C}{T}\frac{B}{\mu_0} = \chi H, \tag{5.8}$$

where k is the Boltzmann's constant and C, the *Curie constant* and is given by $C \equiv (Nm^2/3k)$. It should be noted that in some cases, the Curie law is expressed in cgs units, with H replaced by B, since the applied field B can be expressed as $\mu_0 H$, and $\mu_0 = 1$ in cgs units. The Langevin function for this regime is then expressed as

$$L(x) \cong \frac{x}{3} = \frac{mB}{3kT}. \tag{5.9}$$

Magnetic moment of an atom or ion in free space is given by

$$\mathbf{m} = \gamma\hbar\mathbf{J} = -g\mu_B\mathbf{J}. \tag{5.10}$$

The total angular momentum $\hbar\mathbf{J}$ ($\hbar$ is the Plank's constant) for the electronic system of an atom is the sum of the orbital angular momentum $\hbar\mathbf{L}$ and spin angular momentum $\hbar\mathbf{S}$, meaning $\hbar\mathbf{J} = \hbar\mathbf{L} + \hbar\mathbf{S}$. The factor γ is called the *gyromagnetic or magnetogyric ratio* and is represented by the ratio of magnetic moment to $\hbar$ units of the angular momentum. For electronic systems, a quantity g is defined to satisfy $g\mu_B \equiv -\gamma\hbar$ and is called the *g-factor, spectroscopic splitting factor, or Landé splitting factor*, as the magnitude of this factor determines how rapidly the energy levels split. Basically, this g-factor is represented by the number of Bohr magnetons divided by $\hbar$ units of angular momentum. For an electron spin, $g = 2.0023$, which is often truncated to 2. If the truncated value of 2 is used, the total magnetic moment of an atom can be expressed as

$$m = \mu_B(\mathbf{L} + 2\mathbf{S}). \tag{5.11}$$

This magnetic moment precesses around the direction $\mathbf{J}$ and is customarily expressed in Landé terminology as in Equation 5.10. For a free atom with an orbital angular momentum, the g-factor is given by the Landé equation as

$$g = 1 + \frac{J(J+1) + S(S+1) - L(L+1)}{2J(J+1)}. \tag{5.12}$$

The Bohr magneton is defined as

$$\mu_B = \frac{e\hbar}{2m_e c} \text{ in cgs units} \quad \text{and} \quad \mu_B = \frac{e\hbar}{2m_e} \text{ in the SI units.} \tag{5.13}$$

where m_e is the free-electron mass. The energy level of the system in magnetic field is

$$E = m_J g \mu_B B, \tag{5.14}$$

where m_J is the azimuthal quantum number and has the values of $J, J-1, \ldots, 0, \ldots -(J-1), -J$. For a simple spin without orbital moment $m_J \pm 1/2$ and $g=2$, the total energy (TE) splitting of an electron state in terms of the magnetic moment m is given by $2mB$ with $m = -g\mu_B S$, where S is the spin term.

In the realm of basics of magnetization, let us now consider atoms in a magnetic field. As mentioned above, an atom with angular momentum quantum number J has $J, J-1, \ldots 0, -(J-1), -J$ as many equally spaced energy levels, $2J+1$ in total. The magnetization in that case is given by

$$M = NgJ\mu_B B_J(x) \quad \text{where} \quad x \equiv \frac{gJ\mu_B B}{kT} \tag{5.15}$$

with the *Brillouin function* $B_J(x)$ given by

$$B_J(x) = \frac{2J+1}{2J}\text{ctnh}\left[\frac{(2J+1)}{2J}x\right] - \frac{1}{2J}\text{ctnh}\left(\frac{x}{2J}\right). \tag{5.16}$$

If one sets $J=1/2$, the magnetization would become $M = Nm\tanh x$. For $x \ll 1$, $ctnh\, x = \frac{1}{x} + \frac{x}{3} - \frac{x^3}{45} + \ldots$ and

$$\frac{M}{B/\mu_0} = \chi \approx \frac{NJ(J+1)g^2\mu_B^2}{3kT} = \frac{Np^2\mu_B^2}{3kT} = \frac{C}{T}, \tag{5.17}$$

where $p \equiv g\sqrt{J(J+1)}$ is the effective number of Bohr magnetons.

Electron has associated with it a magnetic moment that is equal to 1 Bohr magneton, μ_B. The electron magnetization given by the Curie relation is

$$M = \frac{N\mu_B^2}{kT} B, \tag{5.18}$$

which is temperature dependent. Instead nonferromagnetic materials have temperature-independent magnetization. Pauli argued that the Fermi Dirac statistics would apply to magnetization also and would bring the temperature dependence in the picture for completeness. Once the Fermi level is taken into account

$$M \approx \frac{N\mu_B^2}{kT} B \frac{T}{T_F} = \frac{N\mu_B^2}{kT_F} B, \tag{5.19}$$

which is temperature independent and comparable to observations. In the absence of an external magnetic field, Pauli magnetism at absolute zero also indicates that the

number of electrons in the spin "up" and spin "down" states adjusts to make the energies equal at the Fermi level, as shown in Figure 5.4. The chemical potential (Fermi level) of the spin-up electrons is equal to that of spin-down electrons, as shown in Figure 5.4a. However, when a magnetic field is applied, electrons with one spin, in this case spin-down, are moved in energy, albeit very small compared to that observed in the ferromagnetic state due to the large effective molecular field. Consequently, there would be an excess of spin-up electrons that are not spin paired, as shown in Figure 5.4b. It should be stated that the effect has been magnified arbitrarily in the figure to make the point. In ferromagnetic materials, be it magnetic semiconductor or ferromagnet below the critical temperature, the picture depicted in Figure 5.4b would hold figuratively without an external magnetic field.

In ferromagnetic samples and for temperatures above the Curie temperature, the electronic structure is similar to that shown in Figure 5.4a. However below the Curie temperature, the picture is similar to that shown in Figure 5.4b without any external magnetic field. As an example, an isolated nickel atom has the ($3d^8 4s^2$) configuration and the energy bands in metallic Ni are filled up to the Fermi energy with 9.46 electrons in the 3d states and 0.54 electrons in the overlapping 4s states. When Ni is in a paramagnetic state, for example, above the Curie temperature, the spin-up and spin-down bands are equally occupied. On the contrary, when Ni is in a ferromagnetic state, meaning below the Curie temperature, the very large effective field produces a very large shift of the spin-up states with respect to the spin-down states in which case the spin-down band is completely filled with five electrons while the spin-up band has

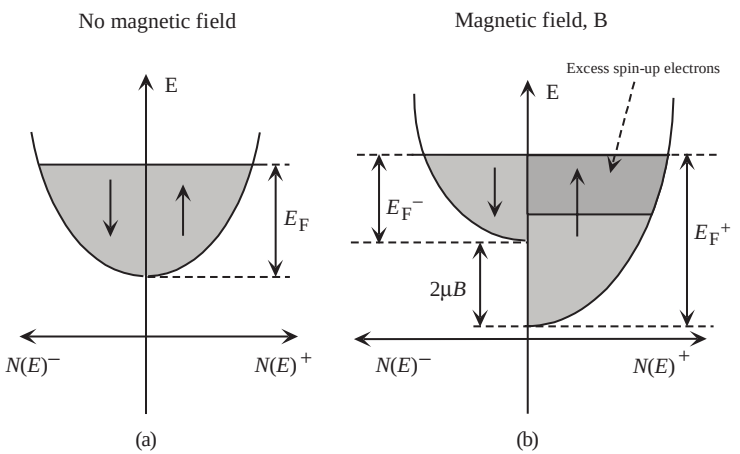

Figure 5.4 Density of states versus energy for the two spin components. In the nonmagnetic states (a), the occupancy by spin-up and spin-down electrons is the same. In Pauli magnetism at absolute zero when a magnetic field is applied, the spin-down and spin-up electrons are moved away from each other, which leads to unparity in that the number of electrons with one type of spin would dominate over the other (b). The effect of the applied magnetic field is amplified to show the point. In ferromagnetic material and below the Curie temperature, the effective field or the molecular field is so large, thus this splitting is sizeable and no external magnetic field is needed for the shift shown.

only 4.46 electrons giving rise to spin unparity of 0.54 electrons per atom. In semiconductor samples containing large concentrations of transition metal impurities, the density of states (DOSs) become distorted due to the band tail states, which clouds the picture somewhat, as shown in Figure 5.5.

Another topic to which frequent references are made is the splitting of intramagnetic ion levels due to the crystal environment, termed as the crystal field splitting. The same also is applied to elements that typically act as deep acceptors unlike rare earths, where the 4f shell lies deep inside the ions within the 5s and 5p shells in transition metals, or the iron group, the 3d shell is the outer most shell and experiences the intense and inhomogeneous electric field, which is called the *crystal field*. Of the immediate effect, this manifests itself as coupling of the orbital angular momentum (L) and spin angular momentum (J) gets, by and large, broken up and thus the states are no longer specified by their J values. Moreover, the $2L + 1$ sublevels associated with a given L that are degenerate in the free ion, may split up by the crystal field. Essentially, this splitting diminishes the contribution of the orbital motion to the magnetic moment. If the electric field does not have axial symmetry, the energy level will all be different.

Given that the alignment of the magnetic moments and the transition from paramagnetic to ferromagnetic state take place due to an internal interaction, that interaction can be construed as being caused by a magnetic field. This field is called the exchange field. The effect of exchange field is opposed by thermal agitations and above Curie temperature ferromagnetism is destroyed. The theory developed to explain the ferromagnetism in dilute magnetic semiconductors using this exchange field is called the *mean field theory* (MFT), and a rudimentary discussion of it is provided below.

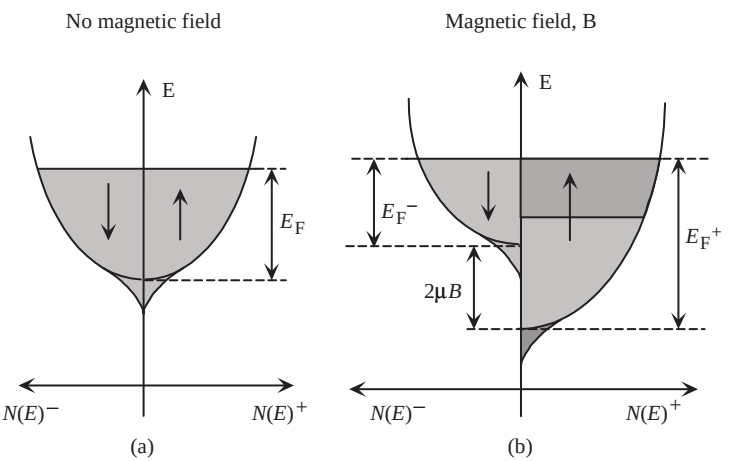

Figure 5.5 Density of states in samples, such as dilute magnetic semiconductors that are heavily doped with TM elements causing band tailing. As in the case of Figure 5.4 electrons adjust their numbers to make the energies of spin-up and spin-down electrons to be equal at the Fermi level in the nonmagnetic state (a). The excess spin of the spin-up electrons in the magnetic state or with large magnetic field applied (b).

In the MFT, the exchange interaction field B_E is given by

$$\mathbf{B}_E = \lambda \mathbf{M}, \tag{5.20}$$

where λ is a temperature-independent constant. However, for $T > T_C$, the system is a disordered paramagnet, and for $T < T_C$, the system is a ferromagnet.

We should mention that the main idea behind MFT is to replace all interactions to any one body with an average or effective interaction. This reduces any multibody problem, which is generally very difficult to solve exactly, into an effective one-body problem. The ease of solving MFT problems means that some insight into the behavior of the system can be obtained at a relatively low cost even at the expense of loosing some accuracy.

Let us find λ in terms of T_C. If $\chi_{paramag}$ is the susceptibility of the paramagnet, then the magnetization is given by

$$\begin{aligned} M &= \chi_{paramag}(H_a + H_E) \text{ in cgs units,} \\ \mu_0 M &= \chi_{paramag}(B_a + B_E) \text{ in SI units,} \end{aligned} \tag{5.21}$$

where H_a and B_a are the applied fields.

The susceptibility of a paramagnet is given by the Curie law,

$$\chi_{paramag} = \frac{C}{T}. \tag{5.22}$$

Using Equation 5.20 and Equation 5.21, we obtain

$$\begin{aligned} MT &= C(H_a + \lambda M) \text{ and} \\ \chi &= \frac{M}{H_a} = \frac{C}{T - C\lambda} \text{ in cgs units.} \end{aligned} \tag{5.23}$$

For $T_C = C\lambda$, a singularity occurs in that $\chi \to \infty$. For $T \leq \lambda C$, we have spontaneous magnetization and

$$\chi = \frac{C}{T - T_C} \quad \text{or} \quad \chi = \frac{C}{T - \theta} \text{ in cgs units,} \tag{5.24}$$

which represents the Curie–Weiss law. In fact the Curie law is a special case of the more general Curie–Weiss law. It should be mentioned that θ is often used for the *Curie temperature* as well.

In Equation 5.24, θ can either be positive, negative, or zero. The case of $\theta = 0$ corresponds to the situation when the Curie–Weiss law equates to the Curie law depicted in Equation 5.17 and Equation 5.22. A nonzero θ implies that there is an interaction between neighboring magnetic moments and the material is only paramagnetic above a certain transition temperature. If θ is positive, the material is ferromagnetic below the transition temperature and the value of θ corresponds to the transition temperature (Curie temperature, T_C). If θ is negative, the material is antiferromagnetic below the transition temperature (Néel temperature, T_N). However, the value of θ does not relate to T_N. We should note that this equation is only valid when the material is in a paramagnetic state. Similarly, it is not valid for many metals, as the electrons contributing to the magnetic moment are not localized. Having said

that the law does apply to some metals, such as the rare earths, where the 4f electrons that create the magnetic moment are closely bound.

Detailed calculations show that [32]

$$\chi = \frac{C}{(T - T_C)^{1.33}} \tag{5.25}$$

and

$$\lambda = \frac{T}{T_C} = \frac{3kT}{Ng^2 S(S+1)\mu_B^2}. \tag{5.26}$$

Let us apply what we learned so far to some known magnetic materials so as to gain an appreciation for the exchange interaction field B_E. For Fe, $T_C = 1000$ K, g is about 2, and S is about 1 and $\lambda \rightarrow 5000$, $M_s = 1700$, thus $B_E = \lambda M = 1700 \times 5000 = 8.5 \times 10^6$ Gauss. This exchange field in Fe is huge and much larger than the magnetic field due to ions in the crystal. A magnetic ion produces a field of $B_E = \mu_B / a^3 \approx 10^3$ Gauss at the neighboring lattice point.

5.5 Dilute Magnetic Semiconductor Theoretical Aspects

The important characteristic of a ferromagnetic material is the spontaneous magnetization below the Curie (T_C) temperature, also referred to as the critical temperature. As shown in Figure 5.4 in ferromagnetic materials [33], the d band is divided into spin-up and spin-down subbands, and the up and down states are displaced with respect to one another. The latter is displaced in energy so that the spin-up band is filled first, and the spin-down states contain the remaining, if any, electrons. The difference in the number of spin-up and spin-down electrons gives rise to the observed spontaneous magnetic moment.

In dilute magnetic semiconductors doped with Mn (when the concentration of Mn^{2+} is small, that is, $x < 0.01$), the Mn^{2+} spins can be regarded as isolated from one another in which case the magnetization can be described by using the standard Brillouin function as

$$M = xN_0 g_{Mn} \mu_B \langle S_z \rangle, \tag{5.27}$$

where $\langle S_z \rangle = -SB_S(g_{Mn}\mu_B SH/kT)$ is the thermal mean of the Mn spin along the magnetic field $H = H_z$, x is the Mn ion mole fraction, N_0 is the number of cations per unit volume (xN_0 therefore representing the number density of Mn ions), g_{Mn} is the g-factor for Mn^{2+} ions, $S = 5/2$ is the effective spin per Mn^{2+} ion, μ_B is the Bohr magneton, and k is the Boltzmann constant.

In the low field and high temperature limit (i.e., when $g_{Mn}\mu_B SH/(kT) \ll 1$), M is linear in H and static (DC) magnetic susceptibility χ, defined by $M = \chi H$ is of the Curie form [12]

$$\chi = xC_0/T \quad \text{with} \quad C_0 = \frac{N_0(g\mu_B)^2 S(S+1)}{3k}. \tag{5.28}$$

For DMS with sufficiently large magnetic ion concentration, where the magnetic ions can no longer be considered to be isolated, the magnetization cannot be expressed by the standard Brillouin function because of the $M^{2+} - Mn^{2+}$ interactions. At low magnetic fields, M has been found to be linear in H as in the dilute case. At high temperatures and low fields, χ follows a Curie–Weiss behavior described as

$$\chi = \chi_d + \frac{xC_0}{T - x\theta_0}, \tag{5.29}$$

where θ_0 is the Curie–Weiss temperature (the nomenclature T_C is also commonly used as mentioned before) and χ_d is the diamagnetic susceptibility of the host. The effective exchange integral between the nearest-neighbor transition ions, which determines the type of magnetism, can be estimated from

$$J_1 = \frac{3k_B\theta_0}{2S(S+1)z}, \tag{5.30}$$

where z is the number of nearest-neighbor cations ($z = 12$ for wurtzite structure). A negative value of J_1, which means that θ_0 in Equation 5.29 is negative, indicates that the interactions between the magnetic ions are antiferromagnetic.

For an external magnetic field B applied along the z-direction, the magnetization M_z of a DMS alloy containing Mn^{2+} ions is empirically written as

$$M_z = xN_0\langle S_z\rangle + xN_0 S_{sat} B_{5/2}(5\mu_B B/kT_{eff}), \tag{5.31}$$

where xN_0 is the number density of Mn^{2+} ions, $B_{5/2}(y)$ is the Brillouin function for $S = 5/2$, S_{sat} is the saturation value for the spin of an individual Mn^{2+} ion (i.e., smaller than 5/2), and $T_{eff} = T + T_0$ is the effective (rescaled) temperature that is higher than the actual temperature T by the correction term T_0 [34]. Along with the distribution of magnetic ions in a DMS lattice, isolated spins, pairs of spins, and triplets are also distributed. Therefore, the magnetization is dominated by the paramagnetic response of the isolated spins that are antiferromagnetically coupled. However, in a DMS, the ferromagnetic s,p–d exchange interaction between conduction band (s) and valence band (p) states and local moments (d) results in an enhanced electronic spin splitting given by

$$\Delta E = g\mu_B B - xN_0[f(\Psi)\alpha - g(\Psi)\beta]\langle S_z\rangle, \tag{5.32}$$

where α and β are the s–d and p–d exchange integrals, respectively, and $f(\Psi)$ and $g(\Psi)$ are the corresponding factors representing the wave–function overlaps of the conduction and valence band states with the local moments. The first term represents the simple Zeeman splitting due to the application of the magnetic field. The spin splitting is dominated by the second term in Equation 5.32, which represents the s, p–d spin exchange interaction, in part because the intrinsic g factor for electrons in ZnO is small and in part because of strong s,p–d exchange interaction. The exchange integral for the heavy-hole states is typically ~5 times larger than that for the conduction-band and light-hole states. Because of this reason, in most optical experiments, which probe heavy-hole excitations, the spin splitting is dominated

by that of the valence-band states. The effect of magnetic field on the confined electronic states in DMS heterostructures is generally probed using magneto-optical spectroscopy, such as magnetophotoluminescence, magnetic circular dichroism, magnetoabsorption, and Faraday/Kerr effect.

5.6 Measurements Techniques for Identification of Ferromagnetism

Magnetization is usually measured directly using a superconducting quantum interferometer device magnetometer, which provides the type of magnetism through *M–H* curves, as exemplified in Figure 5.3. SQUID measurements are extremely sensitive to any magnetization including magnetic impurities, precipitates, clusters, and mixed magnetic phases. Most of the reports on observation of ferromagnetism or ferromagnetic-like behavior with apparent Curie temperatures near or above room temperature in TM-doped ZnO are primarily based on magnetic hysteresis measurements performed by the SQUID magnetometer in combination with XRD that may be insufficient for revealing the origin of ferromagnetic ordering. Conventional XRD cannot reveal second phase inclusions in the nm scale. Impurity defect complexes may be another source of ferromagnetic order observed in DMSs by SQUID measurements. While some studies suggest a defect-mediated exchange involving oxygen vacancies [35], no direct observations of impurity-defect complexes in TM-doped have been reported in the literature. At the moment, very little is known about complex-related magnetic ordering. Spinodal decomposition has also been considered to be one of the problems in wide bandgap semiconductors ZnO and GaN [36–40]. Therefore, identification of the origin of ferromagnetism requires more detailed experimental microscopic techniques.

Magnetooptical and magnetoresistance measurements, particularly the combination of the two are the most reliable methods for unequivocally determining whether the material in question has ordered magnetization. One of the optical measurements relies on *Faraday rotation* (FR) that can be viewed simply as the rotation in polarization plane of linearly polarized light as it propagates through a magnetic medium, when a magnetic field should be applied along the propagation direction of the optical beam [41]. Faraday rotation is given by the well-known expression as [42]

$$\theta_F = \frac{El}{2\hbar c}(n^- - n^+), \tag{5.33}$$

where n^+, n^- are the refractive indices of the medium for right and left hand circularly polarized light, respectively. Different refractive indices for right and left hand circularly polarized light form the basis for circular birefringence. E is the photon energy, l is the length traversed by photons, $\hbar$ is the reduced Planck's constant and c is the speed of light in vacuum. The difference between n^+ and n^- can be related to the energy difference ΔE between transitions observed for $\hat{\sigma}^+$ and $\hat{\sigma}^-$ polarizations, due to Zeeman splitting. Another related phenomenon, called the *magneto optical Kerr effect* (MOKE) or *Kerr rotation* (KR), represents rotation of the

polarization plane of the reflected light from the surface of a magnetic material where the magnetization is perpendicular to the surface (polar Kerr rotation).

Another optical effect is the *magnetic circular dichroism*, which is caused by the difference in absorption or transmission of right (σ^+) and left (σ^-) hand circularly polarized light. MCD and Faraday effect are related through Kramers–Kronig relations. If the associated transmitted intensities and absorption coefficients for right (positive superscript) and left (negative superscript) hand polarized light are denoted as I^+ and I^-, and α^+ and α^-, respectively, the magnitude of the MCD signal in degrees is defined as [43]

$$\theta_{\mathrm{MCD}} \equiv \frac{90}{\pi}\left(\frac{I^+ - I^-}{I^+ + I^-}\right) \equiv \frac{180}{4\pi}(\alpha^- - \alpha^+). \tag{5.34}$$

To gain an understanding of this effect in the particular semiconductor of interest, polarization of each transition involving heavy, light, and spin orbit split-off bands must be known. In addition, the transition probabilities (oscillator strengths), at least the relative values, for each band are also needed. Continuing on, the knowledge of the selection rules as to the polarization for spin-up and spin-down electron in each of the bands are also required. These conditions reduce what needs to be known to a relationship between the degree of spin polarization

$$P_{\mathrm{spin}} = (n\uparrow - n\downarrow)/(n\uparrow + n\downarrow) \tag{5.35}$$

in terms of the spin populations $n\uparrow$ and $n\downarrow$ and the degree of circular polarization

$$P_{\mathrm{circ}} = [I(\sigma^+) - I(\sigma^-)]/[I(\sigma^+) + I(\sigma^-)], \tag{5.36}$$

where $I(\sigma^{\pm})$ is the intensity of the $\sigma^{\pm}$-polarized light, where $+$ and $-$ denote the right and left circular polarizations, respectively. The degree of circular polarization depends on oscillator strengths of transitions involving heavy hole (HH) and light hole (LH) valence band states and the spin coherence time. The spin coherence times naturally increase with increasing material quality. For example, availability of large area ZnO substrates produced by the hydrothermal and melt methods enables high-quality homoepitaxial growth that would lead to longer spin coherence times in ZnO [44] than in GaN [45]. Spin coherence in ZnO epitaxial layers was found to persist until RT, with a spin lifetime of 188 ps at 280 K (20 ns in bulk at $T = 30$ K and 2 ns in epilayers at $T = 10$ K), considerably longer than that observed in GaN films ($\sim$35 ps) [45]. In parallel with these observations, absence of spin polarization in electroluminescence and photoluminescence (PL) from InGaN/GaN spin LEDs was suggested to be resulting from fast spin relaxation [46, 47].

To measure the spin coherence time and to estimate the spin-polarized carrier injection efficiency from the electroluminescence data, the selection rules and the valence band structure in ZnO must be understood. The valence band in wurtzite materials is split into three bands (A, B, and C) due to crystal field and spin–orbit coupling as discussed before in Chapter 3. The spin degeneracy of these three bands and the conduction band is lifted in magnetic field resulting in small symmetric Zeeman splittings as shown in Figure 5.6 near the Γ point [48]. The allowed transitions following the selection rules $\Delta L_z = \pm 1$ (for $\sigma^{\pm}$ polarization) are indicated

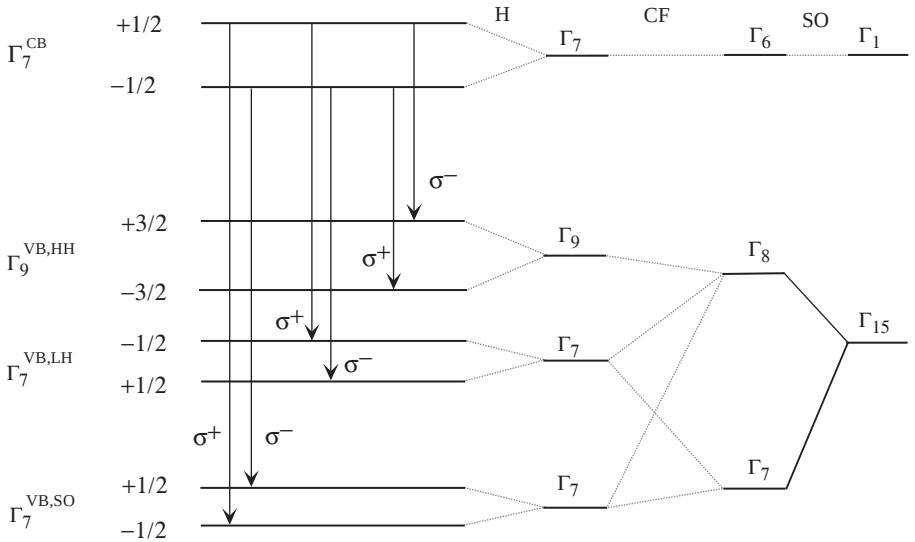

Figure 5.6 Breaking the symmetry scheme of the conduction and valence bands in wurtzite phase. The allowed transitions are marked by arrows.

by arrows. A net spin polarization of the photoexcited carriers can only be achieved when optical excitation ensures preferential spin orientation.

For strong spin–orbit interaction as in GaAs ($\Delta_{so} = 340$ meV), the relationship between P_{spin} and P_{circ} is easily obtained even for bulk samples with degenerate HH and LH states, as the optical transitions involving the HH states are three times stronger than those involving the LH states (therefore, $P_{spin} = 2\,P_{circ}$). For wurtzite materials, however, where the spin–orbit coupling is much weaker [Δ_{so}(ZnO) = 4 meV, Δ_{so}(GaN) = 4 meV], the transitions strengths for these valence bands (i.e., A and B bands) have been suggested to be comparable [47, 49–51]. Therefore, one complication here is possible cancellation of the PL polarization due to a spectral overlap of the radiative transitions involving A and B bands with opposite polarization, when both heavy and light hole valence band states are populated, governed by their densities of states, owing to small A–B splitting.

At the Γ point in wurtzite semiconductors, using band-to-band calculations, the transition strengths (or oscillator strengths) for the B (α_B) and C (α_C) bands relative to that for the A band (α_A) can be obtained for light propagation perpendicular to the *c*-axis as $\alpha_B/\alpha_A = a^2$ and $\alpha_C/\alpha_A = (1 - a^2)$ using [50]

$$a = \frac{1}{x\sqrt{1/x^2 + 1}}; \quad x = \frac{-(\Delta_1 - \Delta_2) + \sqrt{(\Delta_1 - \Delta_2)^2 + 8\Delta_3^2}}{2\sqrt{2}\Delta_3}, \tag{5.37}$$

where Δ_1 is the crystal field energy, and Δ_2 and Δ_3 are the spin–orbit coupling parameters parallel and perpendicular, respectively, to the *c*-axis. For ZnO, using $\Delta_1 = 43$ meV and $\Delta_2 = \Delta_3 = \Delta_{so}/3 \approx 5.3$ meV [52], a^2 is calculated as 0.97. Therefore, only $P_{circ} = 1.5\%$ polarization is possible when both HH and LH bands are excited.

However, in the band-to-band model, the excitonic effects have been neglected in that the short range electron–hole spin exchange interaction strongly mixes the excitons built from the Γ_7 and Γ_9 valence bands. This effect is small in GaN with a moderate exchange interaction (0.69 meV [53]) compared to the spin–orbit coupling and crystal field splitting parameters, and has almost no effect on the oscillator strengths of the optical transitions [54]. However, the exchange interaction in ZnO is much larger (4.7 meV) [55, 56]. Calculations by Gil [57] show that in such a case, the oscillator strength for the B exciton can be more than five times larger than that for the A exciton in unstrained materials, which would result in $P_{\text{circ}} = 70\%$. This is consistent with the reflectance measurements on bulk ZnO by Thomas [58], who reported that the oscillator strength of the B exciton is ~3.5 times that of the A exciton.

The oscillator strengths can also be modified by strain induced through growth on nonnative templates or heterojunctions. When integrated into the simple band-to-band model, the strain changes the relative oscillator strengths of the A, B, and C excitons drastically [59], as also verified by experiments in GaN [60]. Figure 5.7 shows the stress-induced variations of the oscillator strength calculated by Gil [57] (including the electron–hole spin exchange interaction) for Γ_5 excitons in ZnO at 2 K. When the excitonic effects are included, the oscillator strength of the A exciton is found to be always weaker than that of the B exciton, in contradiction with the predictions of the band-to-band calculations, but consistent with the experimental results [52]. In addition, the B exciton oscillator strength increases with decreasing biaxial tension (negative biaxial stress) in the material as compared to a decrease for the A exciton, which is consistent with reflectivity measurements [61].

Coming back to MCD measurements, in the Faraday geometry where the applied magnetic field and the light propagation are both along the crystal growth direction, both the right (σ^+) and left (σ^-) hand circular polarizations are allowed because of

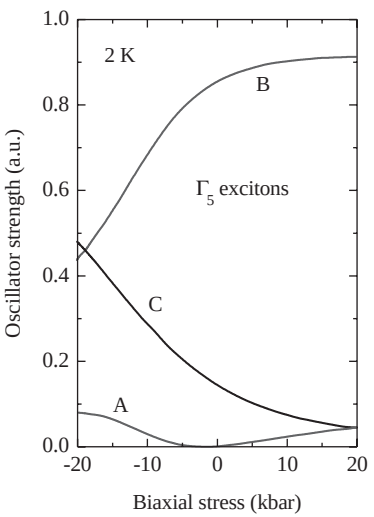

Figure 5.7 Stress-induced variations of the oscillator strength for Γ_5 excitons in ZnO at 2 K. (After Ref. [57].)

symmetry considerations. The optical transition energies for right and left circular polarization are different. For example, in zinc blende semiconductors, the energy for transition (σ^-) is larger than that for (σ^+) by $xN_0(\beta - \alpha)\langle S_z\rangle$, which represents the Zeeman splitting due to s,p–d spin exchange interaction. When the effect of the external magnetic field is also included, the energy difference between the above-mentioned transitions becomes (same as in Equation 5.32 assuming unity wave-function overlap factors)

$$\Delta E = g_{\text{eff}}\mu_B H = g\mu_B H - \langle S_z\rangle N_0 x(\alpha - \beta). \tag{5.38}$$

As shown in Figure 5.6, the Zeeman splits for the A and B valence bands in the wurtzite structure are suggested to have opposite polarities. When the spin–orbit coupling and the p–d exchange interaction anisotropies are neglected, simple expressions can be obtained for the Zeeman splitting energies of the A and B bands [7, 62]:

$$\begin{aligned}\Delta E_{A(2/3,\pm 2/3)} &= \Delta_1 + \Delta_2 \pm \frac{1}{2} N_0\beta x\langle S_z\rangle,\\ \Delta E_{B(2/3,\pm 1/3)} &= \frac{(\Delta_1 - \Delta_2)}{2} + \sqrt{\left(\frac{\Delta_1 - \Delta_2 \mp N_0\beta x\langle S_z\rangle}{2}\right)^2 + 2\Delta_2^2}.\end{aligned} \tag{5.39}$$

Using the values reported for ZnO and mentioned above after Equation 5.37 (Δ_1 43 meV and $\Delta_2 \approx 5.3$ meV), for $x = 0.01$ with $\langle S_z\rangle = 0.5$ and $|N_0\beta| = 1$ eV, the Zeeman splits in ZnO has been estimated to be 5 meV for the A valence band and 4.6 meV with opposite polarity for the B valence band. The overall magneto-optical response, therefore, may be reduced or even cancelled, as both splitting energies are similar in magnitude but opposite in polarity.

In the absence of an external magnetic field, the transmitted light intensity through a sample is given by

$$I = I_0 e^{-\alpha(E)L}, \tag{5.40}$$

where I_0 is the incident beam intensity, $\alpha(E)$ is the absorption coefficient at thermal equilibrium, E is the photon energy, and L is the thickness of the sample (light propagation distance in the absorbing material). Under the influence of a magnetic field, right (positive superscript) and left (negative superscript) hand circular polarized light beams experience different absorption constants:

$$\begin{aligned}\alpha^+(E) &= \alpha\left(E + \frac{\Delta E}{2}\right),\\ \alpha^-(E) &= \alpha\left(E - \frac{\Delta E}{2}\right),\end{aligned} \tag{5.41}$$

where ΔE represents the total Zeeman splitting for spin-up and spin-down electrons at energy E given by Equation 5.38.

Using Equation 5.41, θ_{MCD} defined in Equation 5.34 can be rewritten as

$$\theta_{MCD} = -\frac{45}{\pi}\Delta E\frac{d\alpha(E)}{dE}, \tag{5.42}$$

where $d\alpha(E)/dE$ describes the rate of change of the absorption coefficient with respect to energy or the energy derivative of the absorption coefficient. $d\alpha(E)/dE$ is mainly determined by the electronic band structure and has the largest values near the critical points (CPs, while ΔE represents the s,p–d exchange contribution to the MCD signal. θ_{MCD} in Equation 5.42 is defined per unit light propagation distance, and therefore, should be multiplied by the sample thickness when total MCD for a particular sample is considered. It should also be noted that $|N_0\beta| > N_0\alpha > 0$, because the p–d spin exchange interaction is stronger than the s–d spin exchange interaction.

In addition to the magnetooptical properties, progress toward understanding the mechanism limiting the Curie temperature T_C in ZnO doped with transition metals requires careful investigation of the transport behavior, namely, precise knowledge of the hole density, p. The Hall resistivity in magnetic semiconductors is given by

$$\rho_{xy} = \rho_{xy}^0 + \rho_{xy}^a = R_0 B + R_a(\rho_{xx}) M_\perp, \tag{5.43}$$

where the normal contribution ρ_{xy}^0 is proportional to the external magnetic field B, $R_0 = 1/pe$ is the normal Hall coefficient, and the anomalous contribution ρ_{xy}^a is proportional to the macroscopic magnetization $M_\perp$, which is normal to the sample surface. The anomalous Hall coefficient $R_a(\rho_{xx})$, which is a function of ρ_{xx}, arises from the spin–orbit interaction that induces anisotropy between scattering of spin-up and spin-down electrons. The Hall resistance is basically obtained by dividing the resistivity by the film thickness. For a given normal component of magnetization, the anomalous Hall effect is much stronger for holes than for electrons in the tetrahedrally coordinated semiconductors. Moreover, anomalous Hall effect depends on the extent to which the electrons are spin polarized, the effect ceases to be proportional to the magnetization when carrier spin splitting becomes comparable to the Fermi energy. Consequently, in ferromagnetic samples, the anomalous component dominates and the normal component can be neglected. If additionally, the skew scattering is the dominant process, the anomalous Hall coefficient would be proportional to the sheet resistance of the sample [30]. Thus, M can be calculated from the above expression as being proportional to the ratio of the Hall coefficient to the sheet resistance. The Hall measurements should be carried out in the applied magnetic-field limit where the magnetization is saturated (i.e., at low temperature and very high magnetic field).

The interpretation of Hall effect measurements is challenging for ZnO-based DMSs, because heavily doped ZnO (3.2×10^{18} to 1.3×10^{20} cm^{-3}) exhibits a negative magnetoresistance due to s–d exchange coupling without any doping with TMs [26]. Another source of misinterpretation of Hall measurements is an apparent anomalous Hall effect in a ferromagnetic metal/semiconductor structure due to the stray field [63]. Eventually, if and when ZnO-based DMS materials advance to the point where reliable Hall measurements can be made, the anomalous Hall effect would be a reliable means of determining whether the material is ferromagnetic and further what the Curie temperature is.

5.7
Magnetic Interactions in DMS

Above T_C, the ferromagnetic material loses its permanent magnetism due to thermal agitations. To have practical applications in functional devices, it would be desirable, to put it mildly, to have a Curie temperature well above room temperature. Further, for some device applications, it is also desirable to have the ferromagnetism of carrier-induced origin, so that the magnetic properties of the DMS can be manipulated by external means such as through the manipulation of the hole concentration. A better understanding of the underlying mechanisms will certainly provide the much-needed guidance for material design. To gain insight into the processes involved, a brief tutorial of the recently proposed mechanisms for ferromagnetism in DMS materials is presented in this section.

The mechanisms pertinent to magnetism are super direct exchange (antiferromagnetic), free carrier polarization, band polarization, indirect super-exchange (could be ferromagnetic), double exchange (ferromagnetic and stronger when mediated by holes), and magnetic polarons, to cite a few. The nature of the interaction of electrons of magnetic ions with those of conduction and valence bands of the host determine whether the resultant material is ferro or antiferromagnetic. Intuitively, everything else being equal, the closer the distance between the magnetic ions that occupy the cation sites and anions of the host, the better the coupling expected to be. The strength of magnetic ordering in relation to thermal agitation is characterized by the Curie temperature that is expected to be high for semiconductors with smaller lattice parameters.

What distinguishes DMS materials from more common semiconductors is that in DMS, there are two systems: one comprising the semiconductor host and the other comprising the magnetic ion (either transition metal with partially filled d shells or rare earths with partially filled f shells) with their own somewhat preserved properties and their limited interactions. The semiconductor system can be characterized by delocalized band electrons, which can be described by extended states. The magnetic ion, on the other hand, is characterized by localized 3d or 4f shell. Effective mass theory does well in describing the mobile carriers that are electrons in the conduction band and holes in the valence band. In this treatment, the crystal Hamiltonian and pertinent perturbations can be described by the Luttinger basis. In addition, tight binding calculations for wide bandgap semiconductors of interest here indicate that the Γ_6 conduction band Luttinger functions mainly consist of cation s-orbitals, whereas the Γ_8 and Γ_7 valence band associated functions, to a first extent, consist of anion p-orbitals. Primarily, the effective mass carriers determine electrical and optical properties of the semiconductor. However, the localized magnetic moments associated with the magnetic ions and their interaction with the host semiconductor determine the magnetic properties. The interaction that is responsible for the desired magnetic behavior is s,p–d in the case of transition metal magnetic ions and s,p–f in the case of rare earth magnetic ions.

5.7.1 Carrier–Single Magnetic Ion Interaction

The interaction between the ionic magnetic impurity and the host involving conduction and valence band electrons is described by direct Coulomb exchange, which is a first-order perturbation effect. For s-like conduction and p-like valence bands, which is the case for the semiconductors under consideration here, and transition metals with their open d-shell, the direct Coulomb exchange is represented by the ferromagnetic Kondo Hamiltonian. The magnetic impurities can be described by mole fraction of the magnetic impurity and in molecular field approximation, the spin operators are replaced with their averages. The carrier–ion direct exchange Hamiltonian for Γ_6 conduction band electrons (describing s–d interaction in the case of transition metal ions) is of the form

$$H_{\text{ex}} = -xN_0\alpha\langle S_{//}\rangle s_{//}, \tag{5.44}$$

where xN_0 is the concentration of the magnetic ions with x representing the mole fraction, α denotes the exchange constant for s-like electrons, $\langle S_{//}\rangle$ represents the component of the thermodynamical average of magnetic ion spin along the magnetic field, and $S_{//}$is the component of band electron spin along the magnetic field. Often the magnetic field is applied along the growth or the z-direction in which case the term $\langle S_z\rangle$ is used to describe the average of magnetic ion spin. The exchange Hamiltonian is a measure of the extent of the exchange interaction and thus the extent of Zeeman splitting of the energy levels in the host material. The extent of that splitting is generally taken proportional to $xN_0\alpha\langle S_{//}\rangle$, in which case, $N_0\alpha$ is treated as spin exchange integral for the conduction band. In II–VI DMS materials, the parameter α is of the order of about 0.2 eV.

As for the valence band, the picture is relatively complicated. Considering a single hole near the top of the Γ_8 valence band (for zinc blende crystal structure) and the magnetic ion with five d orbitals occupied by N electrons, the Hamiltonian that is applicable would have ionic, crystal, and hybridization components. The p–d hybridization mediated kinetic exchange depends on the filling of only the t_{2g} orbitals, not all the one-electron d-orbitals of the magnetic ion. The spin-dependent part of the exchange Hamiltonian for interaction between the Γ_8 valence band p-like electrons and all the three t_{2g} d-orbitals occupied by one electron can be described as

$$H_{\text{ex}} = -\frac{1}{3}xN_0\beta\langle S_{//}\rangle J_{//}, \tag{5.45}$$

where β is the exchange constant, $J_{//}$is the component of the total angular momentum of the Γ_8 valence band p-like electron parallel to the magnetic field. As in the case of conduction band, the exchange spin Hamiltonian for the valence band electron determines the Zeeman splitting associated with the valence band states of the host. The term β is proportional to what is called the hybridization constant and inversely proportional to the sum of the two terms that describe energies needed for transferring a d-shell electron from the magnetic ion into the band and transferring an electron from the band to the d-shell of the magnetic ion. Experiments performed

mainly in conjunction with II–VI DMSs indicated that β and α have opposite signs and that β is significantly larger than α by a factor of some 5–10 or even more depending on the host material. For Mn^{2+} and Fe^{2+}, that is, for singly occupied d orbitals, virtual transition of electrons from the ion to the valence band and vice versa are possible. In the case of Sc^{2+} or Ti^{2+}, only the virtual transitions from the valence band to the d-shell of the ion are possible. Band electrons with both spin-up and down can be transferred. According to the Hund's rule that applies to both types of ions mentioned, the transition increasing the total spin of the ion leads to lower energy. In the case of Fe^{2+} and Co^{2+}, the sixth electron of Fe and Co occupy the e_g orbitals lying at a lower energy than the t_{2g} orbitals. Consequently, $\beta_{Me} < \beta_{Fe} < \beta_{Co}$.

5.7.2
Interaction Between Magnetic Ions

Magnetic ion to magnetic ion interaction, or in the case of transition metal ions d–d interactions could also take place, which depends on the density of the magnetic impurity in the host. The exchange coupling tensor in effect can be described with three distinct interactions, such as Heisenberg, Dzyaloshinsky–Moriya (DM), and pseudodipolar. There are mainly four mechanisms leading to spin–spin interaction between magnetic ions. In the Ruderman–Kittel–Kasuya–Yoshida (RKKY) mechanism, the s,p–d exchange leads to the polarization of free electrons. In the Blombergen–Rowland (BR) interactions, the s,p–d exchange leads to band polarization. In both cases, the spin–spin interaction results from the induced polarization. In the other two remaining mechanisms, namely, the superexchange and double exchange mechanisms, the interaction, within the atomic picture, can be thought of in terms of virtual transitions between the ions (situated at the cation sites) and neighboring anions. The RKKY, BR, and superexchange interaction can be described by an effective Kondo-like Hamiltonian [64].

5.7.2.1 **Superexchange Mechanism**

The superexchange mechanism is a process wherein the spins of two ions are correlated owing to the spin-dependent kinetic exchange interaction between each of the two ions and the p-like valence band. For superexchange, it is more proper to employ the band picture to describe the spin–spin interaction in semiconductors as opposed to the atomic picture. In II–VI DMSs, the superexchange resulting from the s,p–d hybridization is by far the dominant spin–spin interaction mechanism for the observed isotropic (Heisenberg) and anisotropic (DM) exchange constants. To calculate the superexchange, the fourth order perturbation matrix for the hybridization Hamiltonian should be determined for the system of two magnetic ions in a semiconductor with a completely filled valence band.

Visualizing the virtual transition picture, one can construe the superexchange mechanism as being due to four virtual transitions, namely, from the p-like valence band state to the ions and back to the valence band characterized by arrows A, B, C, and D in Figure 5.8. This can take place in six sequences, namely ABCD, ABDC, BACD, BADC, ACBD, and CADB. The directions shown are for the transitions

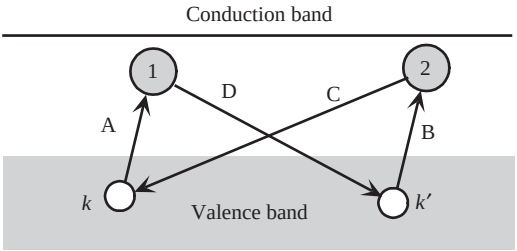

Figure 5.8 A cartoon of the four virtual transitions depicting the superexchange ion–ion interactions. The arrows show the direction of electron transfer for the path ABCD. For the path CADB, all the directions should be reversed. (After Ref. [64].)

ABCD. What is common to all the sequences is that they all start with the transfer of a band electron k to one of the ions, which produces a hole in the band but leads to different intermediate states in the perturbation Hamiltonian matrix depending on the sequence. The intermediate state after the first virtual transition should correspond to one magnetic ion with N and the second with $N + 1$ electrons. The virtual state after the second transition may be of two different types, either $N + 1$ electrons on both ions and two holes in the valence band (ABCD, ABDC, BACD, or BADC) or one ion with $N + 1$ and the other with $N - 1$ electrons and no holes in the valence band (ACBD or CADB). The unperturbed valence band states, which must be summed up over the entire Brillouin zone, are typically described within the empirical tight-binding model [64].

5.7.2.2 **Blombergen–Rowland Mechanism**

The *BR mechanism* is a process wherein the spins of two ions are correlated owing to the spin-dependent kinetic exchange interaction between each of the two ions and the p-like valence band and s-like conduction band. The BR process differs from the superexchange mechanism only by the specifics of the intermediate states and also allows for virtual transitions to the empty conduction band as illustrated in Figure 5.9. Naturally, this mechanism is less likely than the superexchange mechanism, particularly, in large bandgap semiconductors, as the path is more complex.

In this method, the intermediate states for the first virtual transition in the fourth-order perturbation matrix may correspond to one ion with N electrons and another with $N + 1$ electrons and one hole in the p-like valence band. The hole may be considered as being created by a valence band electron transferred to the ionic d-shell, as in the case of superexchange. In addition, one ion with N electrons and another with $N - 1$ electrons, and one electron in the conduction band may also describe the first intermediate state. The electron in question in the conduction band is the one that is transferred from the d-shell of the ion to the conduction band. The intermediate state after the second transition consists of two ions with N electrons, a hole in the valence band, and an electron in the conduction band. Or it may consist of one ion with $N + 1$ and the other with $N - 1$ electrons and no holes in the valence band and no electrons in the conduction band. This can pave the way for a ferromagnetic d–d

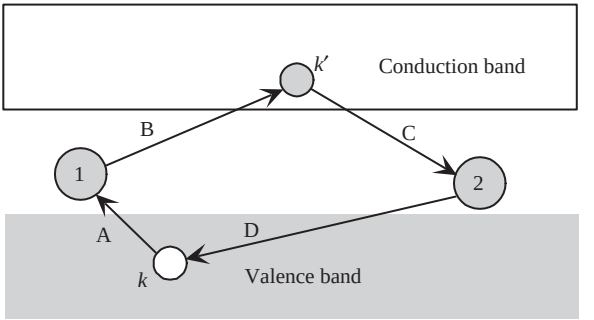

Figure 5.9 A cartoon of the virtual transitions involved in the Blombergen–Rowland interactions. Unlike the six sequences available in the superexchange mechanism, there are twelve different orders for the four A, B, C, and D transitions. These processes commence with the transfer of an electron either from the valence band to one of the ions (ABCD shown by the arrows, DCBA, ADBC, etc.), or from an ion to the conduction band (e.g., BACD, CBDA, etc.). (After Ref. [64].)

interaction even for the Mn^{2+} ions. However, this interaction was shown to be an order of magnitude less effective than the superexchange [64]. One might expect that Blombergen–Rowland interactions are much enhanced in narrow-gap alloys.

5.7.2.3 **Double Exchange Interaction**

The double exchange interaction, proposed by Zener [65] is based on coupling magnetic ions in different charge states by virtual hopping of the "extra" electron from one ion to the other [66]. Specifically, an Mn^{2+}–Mn^{3+} (or d^4–d^5) pair of ions with one d electron hopping virtually from one ion to the other via the p-orbitals of neighboring anions. Naturally, then the Zener double exchange interaction cannot be the mechanism leading to ferromagnetic correlation between the distant Mn spins, because the magnetic electrons remain localized at the magnetic ion and do not contribute to the charge transport. In this vein, Dietl in Matsukura *et al.* [67] suggested that the holes in the extended or weakly localized states mediate the long range interactions between the localized spins. The same processes apply to Cr^{1+}–Cr^{2+} magnetic ion pairs, and the superexchange interaction may also be in effect. The DMS fitting into this category is not all that uncommon and the best studied examples are the zero-gap II–VI compounds (HgSe and HgS) with Fe ions for which the 2+/3+ donor level is degenerate with the conduction band [64]. The coexistence of Mn^{2+} and Mn^{3+} ions leading to double exchange has been suggested for Mn-doped ZnO [68] and the chalcopyrite semiconductor $CdGeP_2$ [69]. The zero-gap II–VI compounds (HgSe and HgS) with Fe ions for which the 2+/3+ donor level is degenerate with the conduction band have also been investigated [70]. Although it is believed that the Mn ions in III–V compounds GaAs and InAs are in the high spin 2+ charge state [71], the precise nature of the centers associated with Mn ions has not yet been definitively determined.

The double exchange mechanism has been successfully used to explain the ferromagnetism observed in (In,Mn)As [65, 72, 73]. In a DMS material, if

neighboring TM magnetic moments are in the same direction, the TM-d band is widened by the hybridization between the upspin states. Therefore, in the ferromagnetic configuration the band energy can be lowered by introducing carriers in the d band. In these cases, the 3d electron in the *partially* occupied 3d-orbitals of the TM is allowed to hop to the 3d-orbitals of the neighboring TM, if the neighboring TM ions have parallel magnetic moments. As a result, the d-electron lowers its kinetic energy by hopping in the ferromagnetic state. Theoretical investigations for this so-called double exchange mechanism could not progress much because of the fact that both disorder and interactions are strong and must be taken into account nonperturbatively. This model is shown schematically in Figure 5.10. This kind of model can explain the physics of the dilute Mn limit, and can also easily be adopted to include the holes that are localized on ionized antisite defects, such as As in (Ga,Mn)As, rather than Mn acceptors. The relevance of this mechanism in mixed-valence DMSs has been discussed in the literature [64].

5.7.2.4 **Ruderman–Kittel–Kasuya–Yoshida Mechanism**

Early attempts to understand the magnetic behavior of DMS systems are based on models in which the local magnetic moments are assumed to interact with each other via RKKY interactions. The RKKY mechanism was originally introduced to explain the interactions between nuclear spins in metals via the conduction electrons and as such it is efficient only in cases where a high concentration of free carriers is present. Therefore, it is not really suitable to describe ion–ion interactions in DMSs. Nevertheless, it formed the basis for the carrier-mediated interionic spin interactions in metals and highly degenerate semiconductors. RKKY interaction is based on the exchange coupling between the magnetic ion and the band electrons described by the s–d Kondo Hamiltonian, which is a first order perturbation effect. It should be mentioned that s and d wavefunctions are orthogonal and would not lead to any interaction in perfect one electron system in cubic semiconductors. The conduction electron gas is magnetized in the vicinity of the magnetic ion, with the polarization decaying with the distance from the magnetic atom in an oscillatory fashion. This oscillation causes an indirect RKKY exchange interaction between two magnetic ions on the nearest or next nearest magnetic neighbors. This coupling may result in a parallel (ferromagnetic) or an antiparallel (antiferromagnetic) setting of the moments dependent on the separation of the interacting atoms. The ferromagnetism

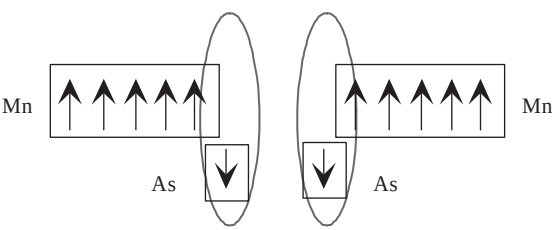

Figure 5.10 Local magnetic moments [Mn^{2+} (d^5)] with spin $S = 5/2$ are antiferromagnetically coupled to itinerant carriers with spin $s = 1/2$ in the model semiconductor GaAs:Mn.

observed in PbSnMnTe has been explained using the RKKY interaction between Mn spins via delocalized carriers [74]. However, if the carriers come from Mn-d states and are localized, which are far from being free-electron-like, the RKKY interaction may not be realistic.

5.7.2.5 Zener, Mean-Field, and Ab Initio Treatments

For carrier densities lower than in metals, Dietl *et al.* [27] have shown that the double exchange or RKKY can not be the mechanism leading to carrier-induced ferromagnetism in Mn-based III–V and II–VI DMSs, and proposed the Zener model based on ferromagnetic interactions mediated by free carriers in tetrahedrally coordinated semiconductors. In the Zener model, the direct interaction between d shells of the adjacent Mn atoms (*super-exchange*) leads to an antiferromagnetic configuration of the d shell spins because the Mn-d shell is half-filled. On the other hand, the indirect coupling of spins through the conduction electrons tends to align the spins of the incomplete d shells in a ferromagnetic manner. It is only when this dominates the direct super-exchange coupling between adjacent d shells that ferromagnetism is possible. Accordingly, the mean-field approach assumes that the ferromagnetism occurs through interactions between the local moments of the Mn atoms mediated by free holes in the material. The spin–spin coupling is also assumed to be a long range interaction, allowing the use of a mean-field approximation. The mean-field model calculates the effective spin density due to the Mn ion distribution. The direct Mn–Mn interactions are antiferromagnetic so that the Curie temperature T_C, for a given material with a specific Mn concentration and hole density (derived from Mn acceptors and/or intentional shallow level acceptor doping), is determined by a competition between the ferromagnetic and antiferromagnetic interactions. It should be mentioned that the Zener theory does not take into consideration the itinerant character of the magnetic electrons and the quantum (Friedel) oscillations of the electron spin polarization around the localized spins. Both of these were later established to be critical concepts for the theory of magnetic metals [27]. Because, the mean distance between the carriers is greater than that between the spins, the effect of the Friedel oscillations averages to be zero in semiconductors. The Zener model would become equivalent to RKKY if the presence of the quantum (Friedel) oscillations of the electron spin polarization around the localized spins are taken explicitly into account.

The mean field theory is based on double exchange hole interaction, meaning electronic in nature in p-type ZnO and also GaN. The theory dealing with ferromagnetism driven by the exchange interaction between carriers and localized magnetic ions (localized spin) was first proposed by Zener [64, 75, 76]. The mean-field Zener model proposed by Dietl *et al.* [27] is based on the original model of Zener [76] and the RKKY interaction and has been successful in explaining the transition temperatures observed for p-(Ga,Mn)As, which has roughly 2000× percentile fraction of Mn ions in the matrix, and (Zn,Mn)Te. The mean-field theory basically assumes that the ferromagnetism is a result of interactions between the local moments of the Mn atoms mediated by free holes in the material (double exchange interaction). The spin–spin coupling is also assumed to be a long range process that allows the use of a

mean-field approximation. On the experimental side, magnetism even in n-type ZnO and GaN has been reported. As compared to the RKKY interaction, the mean-field Zener model takes into account the anisotropy of the carrier-mediated exchange interaction associated with the spin–orbit coupling in the host material. In the process, it reveals the important effect of the spin–orbit coupling in the valence band in determining the magnitude of the T_C and the direction of the easy axis in p-type ferromagnetic semiconductors. Based on this model, it was predicted that TM-doped p-type ZnO and also GaN are the most promising candidates for ferromagnetic DMS with high Curie temperature. However, these predictions are predicated on the incorporation of some 5% transition metal element and hole concentrations of above $10^{20}\,\mathrm{cm}^{-3}$. Notwithstanding these seemingly yet to be demonstrated high hole concentration (which may in fact never be attainable), this prediction stimulated a plethora of activity to achieve high-Curie-temperature ferromagnetism by using ZnO and GaN-based DMSs.

Another simple model [77] has been put forth to explain the possible mechanism with specific attention to (Ga,Mn)As. In this model, holes are assumed to hop only between Mn acceptor sites, where they interact with the Mn moments via phenomenological exchange interactions. In some other models [27], the ferromagnetic correlation mediated by holes originating from shallow acceptors in the ensemble of localized spins and a concentration of free holes ($\approx 3.5 \times 10^{23}/\mathrm{cm}^3$) have been assumed for (Ga,Mn)As.

With due reverence and deference to the models mentioned above, it is increasingly becoming clear that a true picture can only be obtained by performing first principles calculations. For example, it is stated that the mean-field theory overestimates the critical temperature substantially when the magnetic ion density is small. It has also become clear that in Mn-doped GaN magnetic ion concentration has a profound effect on the way the levels split and whether the ferromagnetic or antiferromagnetic state is stable.

In the first principles approach, the total energy and electronic structures are calculated by using the density functional theory (DFT). At temperature $T = 0$, the ground-state structure of the system corresponds to a minimum of the total energy. DFT [78, 79] is a successful approach for the description of ground-state properties of metals, semiconductors, and insulators. Implementation of DFT is based on approximations for the exchange–correlation potential, which arises from the overlap of the electron wave functions due to chemical bond formation. One effective and common approximation is the local (spin) density approximation (LDA) that locally allows substitution of the exchange–correlation energy density of an inhomogeneous system by that of an electron gas evaluated at the local density, and generalized gradient approximation (GGA) that locally substitutes the exchange–correlation energy density by that of an electron gas evaluated at the local density and its gradient and higher terms. The magnetic state of the DMSs can be investigated by calculating the electronic structure of a ferromagnetic DMS (all the magnetic moments of TMs are parallel to each other) and that of a spin-glass-like (magnetic moments of TM point randomly with respect to each other) DMS. The total energy is calculated for both states as a function of transition-metal density. Then, $\Delta E = \mathrm{TE}$ (spin-glass

state)-TE (ferromagnetic state) is calculated to determine the stability of the ferromagnetic state, that is, when ΔE is positive, the ferromagnetic state is more stable than the spin-glass state.

In addition to the models mentioned above, an alternative model considers whether ferromagnetic ordering of the Mn moments could originate from carriers (holes) present in the material, but localized at the transition-metal impurity [77, 80]. Furthermore, ferromagnetism in DMS has been accounted for by the percolation of *bound magnetic polarons* [80–86]. This, in a sense, relies on localized carrier creating a spin polarization of the magnetic moments within the span of its wave function. The basic idea is schematically illustrated in Figure 5.11. The localized holes of the polarons act on the transition-metal impurities surrounding them, thus producing an effective magnetic field and aligning all spins. Transition to the insulating state takes place due to localization of the charge carriers (basically holes) at temperatures higher than the Curie temperature. As temperature decreases, the interaction distance (boundary) grows. Below the Curie temperature, the neighboring magnetic polarons overlap and interact via magnetic impurities forming correlated clusters of polarons. A ferromagnetic transition is seen, when the size of such clusters is equal to the size of the sample. This model is inherently attractive for low carrier density systems such as many of the electronic oxides. The polaron model is applicable to both p- and n-type host materials [81]. Even though the direct exchange interaction of the localized holes is antiferromagnetic, the interaction between bound magnetic polarons may be ferromagnetic for sufficiently large concentrations of magnetic impurities. This enables ferromagnetic ordering of the Mn ions in an otherwise insulating or semi-insulating material.

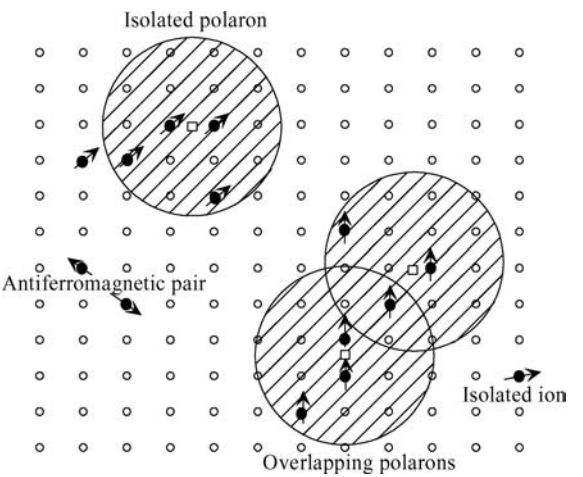

Figure 5.11 Representation of magnetic polarons. A donor electron in its hydrogenic orbit couples with its spin antiparallel to impurities with a 3d shell that is half-full or more than half-full. The figure is drawn for magnetic cation concentration $x = 0.1$ and when the orbital radius of the magnetic cation is sufficiently large. Cation sites are represented by small circles. Oxygen is not shown; the unoccupied oxygen sites are represented by squares. (After Ref. [84].)

5.8
Theoretical Studies on ZnO-Based Magnetic Semiconductors

The motivation for magnetic ion doped semiconductors and the basis for various theoretical treatments of magnetic ion doped semiconductors as it pertains to magnetic properties that ensue are given in the previous sections. Simply, as in the case of GaN, ZnO has been predicted to be a good candidate for ferromagnetism when doped with a magnetic ion. Although the experimental and theoretical results are dispersed in terms of their conclusions, a treatment pertinent to ZnO only is given here.

Sato and Katayama-Yoshida [68] performed first principles *ab initio* calculations of the electronic structures of TM-doped ZnO and proposed the double exchange mechanism for the carrier-induced ferromagnetism. The first principles calculations predict that transition metals V, Cr. Fe, Co, and Ni-doped ZnO [87] showed ferromagnetism with concentration from 5 to 25%, whereas the Mn-doped ZnO shows spin-glass state at ground state because of the exact half-filled d^5 state of Mn ions [68]. For comparison, V^{2+}, Cr^{2+}, Fe^{2+}, Co^{2+}, and Ni^{2+} have d^3, d^4, d^6, d^7, and d^8 electronic configurations, respectively. The ferromagnetic state in Mn-doped ZnO is stabilized by acceptor-doping shown schematically in Figure 5.12, due to the double exchange mechanism. The calculated total energy difference between the spin-glass state and the ferromagnetic state obtained for 25% V-doped ZnO is 1.36 mRy, which is very large compared to 0.12 mRy for 5% Mn-doped GaAs. Suppose the total energy difference is a good estimate for T_C, and taking the experimental T_C of 110 K in 5% Mn-doped GaAs into consideration, high-T_C is suggested for V-, Cr-, Fe-, Co-, and

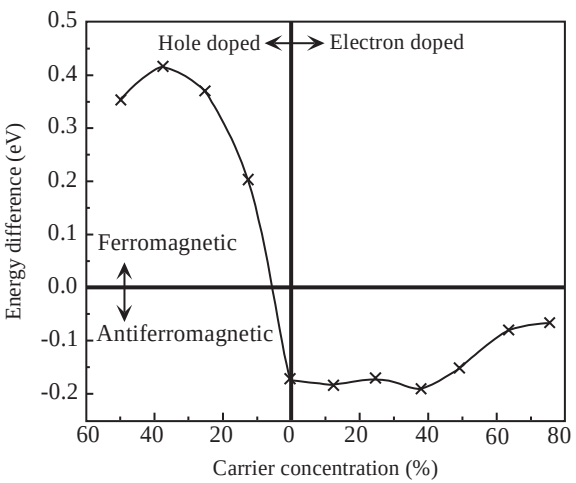

Figure 5.12 Stability of the ferromagnetic ordering of Mn magnetic moments in ZnO. The energy difference of $\Delta E = TE$ (spin-glass) $-$ TE(ferromagnetic) is plotted as a function of carrier concentration. The carrier concentration means N (acceptor doping) and Ga (donor doping) concentration in the supercell. (After Ref. [68].)

Ni-doped ZnO [87]. For the ZnO family, the solubility of TM elements especially Mn and Co, can reach up to 35% into ZnO. Despite the weight of the predictions supporting only p-type (Zn,Mn)O leading to ferromagnetism, experimental observations of ferromagnetism for insulating (Zn,Mn)O [13] and n-type (Zn,Mn)O [14, 88] have been reported by different research groups. Values of T_C above room temperature have been reported for insulating Co-doped ZnO films [89]. Ando *et al.* [7, 25, 90] reported a large magneto-optical effect in $Zn_{1-x}Co_xO$ thin films as measured by magnetic circular dichroism spectra, suggesting $Zn_{1-x}Co_xO$ to be suitable as a DMS material, although the p–d exchange interaction is antiferromagnetic in the samples being studied. Even though the common wisdom indicates the hole exchange to be dominant, Sato and Katayama-Yoshida [3] predicted that the ferromagnetic state $Co^{2+}(d^7)$ in Co-doped ZnO could be stabilized by s–d hybridization, pointing to the possibility that high-Curie-temperature ferromagnetic materials could be realized in n-type ZnO as well.

As discussed above in Section 5.7.2.5, the high Curie temperatures expected and measured for ZnO DMS have been explained using an alternative model based on bound magnetic polarons [84]. The shallow donors in ZnO, which may originate from the defects formed during growth, are suggested to mediate the ferromagnetic exchange by forming bound magnetic polarons that can overlap to create a spin-split impurity band for sufficiently large concentration of magnetic ions. The presence of empty minority spin or majority spin d states at the Fermi level in the impurity band results in high Curie temperatures. Ferromagnetism is observed only when the donor concentration is above the polaron percolation threshold and the magnetic cation concentration is below the cation percolation threshold.

Sato and Katayama-Yoshida [68, 87, 91–94] first applied *ab initio* calculations based on the local density approximation to study TM-doped ZnO. With the exception of Mn, transition metals V, Cr. Fe, Co, and Ni-doped ZnO show ferromagnetism with concentration ranging from 5 to 25%, as shown in Figure 5.13, [87]. The magnetism in the ZnO-based DMSs under both n- and p-type carrier doping treatment has been investigated [3, 95]. The results show that ferromagnetism was induced by hole doping in the Mn-doped ZnO, but found no effect of electron doping. In (Zn,Mn)O, the Mn impurity has a d^5 electron configuration due to the substitution of Zn^{2+} by Mn^{2+} ion, so that there is no itinerant carrier. In this case, it is suggested that the antiferromagnetic superexchange interaction between Mn ions stabilizes the spin-glass state. On the other hand, V^{2+}, Cr^{2+}, Fe^{2+}, Co^{2+}, and Ni^{2+} have d^3, d^4, d^6, d^7, and d^8 electronic configurations, respectively. In the case of Cr, one 4s electron and one 3d electron precipitate in bonding in the II–VI divalent environment and is therefore left in the $Cr^{2+}(d^4)$ state. Therefore, the 3d-band of upspin states or downspin states in these elements is not fully occupied. In mean-field theory and other theories, ferromagnetism arises from a competition between the double exchange interaction and the antiferromagnetic superexchange interaction in these materials. When ZnO:Mn is doped with nitrogen ($1s^2 2s^2 2p^3$), holes are itinerant in keeping with their d-character due to the large hybridization of the N 2p states with the Mn 3d states. Therefore, the kinetic energy is lowered so efficiently that the ferromagnetic state is stabilized by the double exchange mechanism. On the other

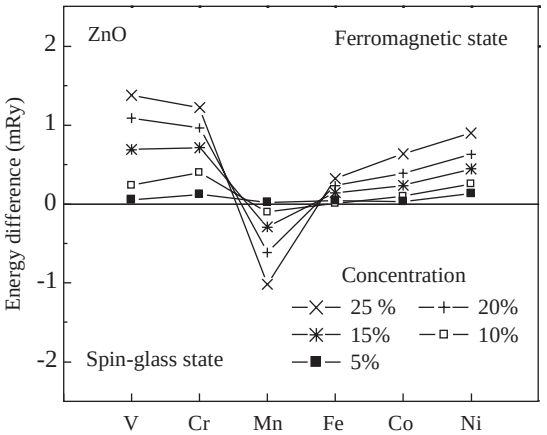

Figure 5.13 The stability of the ferromagnetic states in ZnO-based DMSs. V, Cr, Mn, Fe, Co, or Ni is doped as a magnetic impurity. The vertical axis is the energy difference per one formula unit between the ferromagnetic and the spin-glass state. A positive energy difference indicates that the ferromagnetic state is more stable than the spin-glass state. (After Ref. [87].)

hand, when the system is doped with donors, the doped electrons never go into the Mn 3d states but into the host conduction band, and therefore the double exchange mechanism does not act to stabilize the ferromagnetism in (Zn,Mn)O.

Other first-principle calculations suggested that the n-type doping in ZnO can increase the Curie temperature of Fe-, Co-, and Ni-doped samples when the effects of disorder are taken into account by the coherent potential approximation (CPA) [95]. This reference has a detailed review of the first principles calculations of II–VI compound-based and III–V compound-based DMSs. Considering that the n-type ZnO is readily available and the intrinsic defects such as O-vacancies and Zn-interstitials form donor states, it is concluded that (Zn,Fe)O, (Zn,Co)O, and (Zn,Ni)O are promising candidates for high-T_C ferromagnets. It was also suggested [95] that (Zn,Mn,Fe)O, (Zn,Mn,Co)O, or (Zn,Mn,Ni)O may show carrier-induced ferromagnetism with electron doping by tuning the ratio of Mn to Fe, Co, or Ni. This point might warrant experimental investigations and requires specific designs for ferromagnetism. Sharma *et al.* [16] reported on the *ab initio* total energy calculations within GGA, and predicted a ferromagnetic ground state for (Zn,Mn)O with Mn composition of 4.2%, and antiferromagnetic ground state for Mn composition above 5%, which is consistent with the results obtained by Sato and Katayama-Yoshida [95]. The ferromagnetism above room temperature was also observed experimentally in both bulk and thin film forms of $Zn_{1-x}Mn_xO$ with $x < 4\%$ [16].

The local spin density approximation and coherent potential approximation used in the first principles calculation may not be adequate to handle the strong correlation and lattice relaxations. This is particularly so for thin films prepared by different deposition techniques under nonequilibrium conditions. In (Zn,Mn)O, the 3d electron onsite Coulomb interaction U is estimated to be 5.2 eV, which is comparable

to the 6.0 eV value in MnO [96]. This means that the correlation effects should be taken into account in the theoretical treatments, which leads to the generalized gradient approximation + U (GGA + U) scheme, or the local spin density approximation + U (LSDA + U) scheme.

Ferromagnetism in 3d transition metal-atom-doped ZnO has been investigated by *ab initio* electronic structure calculations based on the generalized gradient approximation (GGA) and GGA + U approximations [97]. The results are quite different from those reported by Sato and Katayama-Yoshida [68] in that Mn, Co, or Cu-doped ZnO are ferromagnetic semiconductors with Mn-doped ZnO having the maximum magnetic moment, while other TM-doped ZnO are metallic. The electronic structures and magnetism of several 3d and 4d transition metal-doped ZnO ($TM_{0.25}Zn_{0.75}O$: TM = Ti, Cr, Mn, Fe, Co, Ni, Ru, Pd, and Ag) have been calculated using the full potential linearized augmented plane wave (LAPW) method based on GGA for exchange correlation potential [98]. The calculations show that Mn has the largest magnetic moment 4.93 μ_B. A Bohr magneton is defined as $\mu_B = (e\hbar)/2mc$ in cgs system and as $\mu_B = (e\hbar)/2m$ in the SI system. The 3d TM-doped ZnO samples are predicted to show half-metallic behavior except for the Co-doped case, whereas the 4d TM-doped ZnO showed normal metallic behavior with finite density of states at the Fermi level for both the minority and majority spin states. Based on the first-principles spin-density functional calculations, Lee and Chang [99] also found that electron doping stabilizes the ferromagnetic ordering in Co-doped ZnO, but the ground state is spin-glass without doping due to the short-range interactions between the transition metal atoms. High electron concentrations and high Co concentrations are necessary to induce ferromagnetism in (Zn,Co)O.

Wang *et al.* [100, 101] used first principles calculations based on the density functional theory and GGA for exchange and correlation to calculate the total energies of a (Zn,Mn)O $(10\bar{1}0)$ thin film with Mn substituted at the Zn site. The thin film was modeled by a slab consisting of eight layers. Different configuration of Mn substitution of Zn sites were chosen so that the Mn–Mn separation as well as the nearest neighbor environment vary. In the dilute limit when Mn atoms are far apart, the system will display paramagnetic behavior. As the Mn concentration increases, Mn atoms tend to come close to each other and cluster around the O atom. This leads to exhibition of antiferromagnetic behavior. The ground state of Mn-doped ZnO $(10\bar{1}0)$ thin film changes from antiferromagnetic to ferromagnetic when codoped with N [102]. Density of states calculations show the distinct overlap between Mn 3d and N 2p states in the spin-up bands which leads to significant DOS at the Fermi energy and hence to the half-metallic character of N codoped (Zn,Mn)O system. Doping with N atoms introduces carriers, and Mn and N atoms prefer to exist as nearest neighbors in ZnO. The magnetic moment of Mn polarizes the spins at the neighboring N sites antiferromagnetically, which results in a ferromagnetic coupling between the Mn atoms. The spin alignments of the Mn atoms and the interlocking N atoms can be shown as Mn(↑)−N(↓)−Mn(↑), indicating that ferromagnetism is mediated through the p–d exchange interaction between the carriers and Mn atoms. The energy difference between the antiferromagnetic and ferromagnetic states due to N doping is shown in Figure 5.14. The maximum energy difference for 25% N doping is

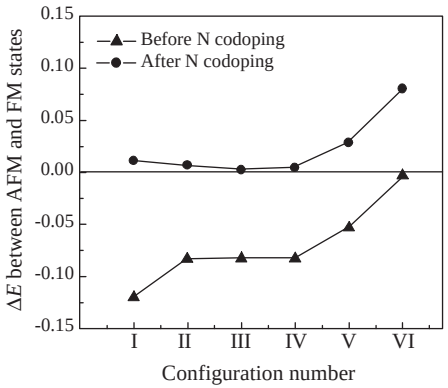

Figure 5.14 The energy difference $\Delta E = [E(\text{AFM}) - E(\text{FM})$ eV/Mn atom] between AFM and FM states for the six different configurations for Mn and N substitution. The solid triangle is for the $Zn_{28}Mn_4O_{32}$ supercell, and the solid circle is for the $Zn_{28}Mn_4O_{24}N_8$ supercell (Courtesy of Q. Wang [102].)

~0.10 eV/Mn atom. The high N concentration used in the model, that is, from 6.25 to 25%, however, may be a challenge from a synthesis standpoint.

Feng [103] employed the Becke three parameter Lee–Yang–Parr (B3LYP) hybrid density functional method in the GGA approximation to study the electronic structure and possible ferromagnetic ordering in Co- and Mn-doped ZnO. The results, which are displayed in Figure 5.15, show that in n-type ZnO electrons would occupy the empty Cu 3d states leading to Cu^{1+} states instead of Cu^{2+} ions because the unoccupied Cu 3d state is lower than the host conduction band states, which leads to a decrease in the number of n-type carriers. This means that the free-electron concentration in the conduction band is reduced. If the sample is even marginally p-type, then the addition of Cu would tilt the balance in favor of p-doping. This may be the mechanism for increased holes in ZnO codoped with Cu and other TM elements [19, 104]. On the other hand, the unoccupied Mn 3d state is well above the lowest host conduction band states due to the large exchange splitting, so that no hole-providing mechanism is found in Mn-doped ZnO. Similarly, the calculation on the effect of Cu + Co codoping in ZnO also shows the p-type doping from Cu-induced ferromagnetic interactions between Co ions [105]. The experimental results will be discussed in detail in the next section.

In the vein of codoping, the electronic structures and magnetic properties of ZnO-based potentially diluted magnetic semiconductor codoped with transition metals such as $Zn_{1-2x}(FeCo)_xO$ and $Zn_{1-2x}(FeCu)_xO$ have been investigated by Park and Min [106]. Their results show that the double exchange mechanism is not effective in $Zn_{1-2x}(FeCo)_xO$, but Fe and Cu ions in (Fe, Cu) doped ZnO have a tendency to form Fe–O–Cu clusters, and the much sought after double-exchange-like interaction is expected to induce ferromagnetism in (Fe,Cu) doped ZnO.

Venkatesan *et al.* [107] used a spin-split donor impurity-band model to explain the observed systematic variation of magnetic moments across the TM-doped ZnO

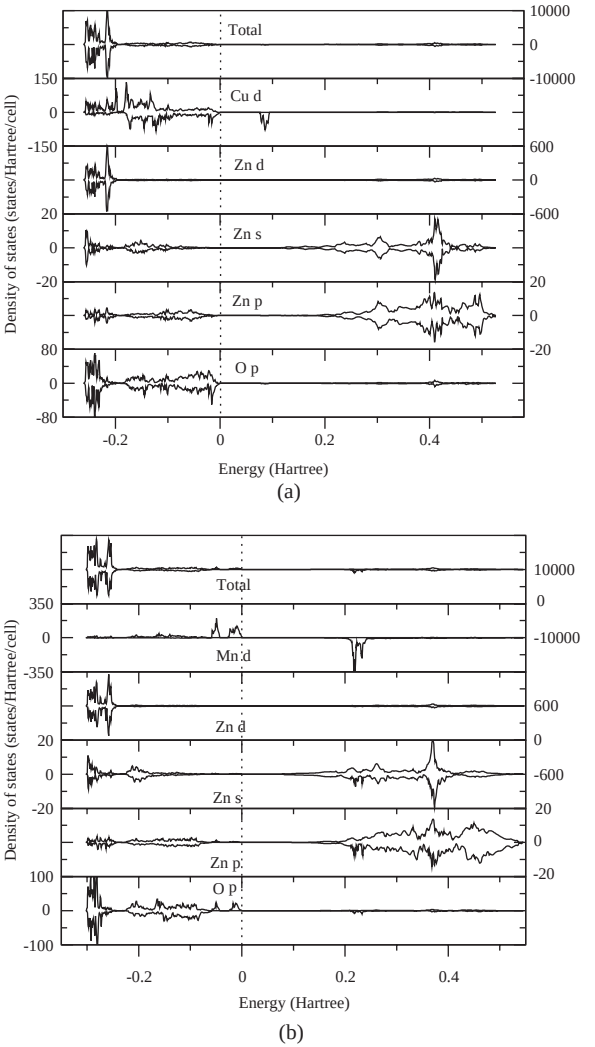

Figure 5.15 The B3LYP DOSs of (a) Cu-doped ZnO and (b) Mn-doped ZnO. Positive and negative DOSs are for spin-up and spin-down electrons, respectively. In (a), the supercell consists of eight primitive cells of ZnO, in which one Zn ion is substituted by Cu. Ferromagnetic ordering of Cu ions is assumed. The magnetic moment of Cu is 0.75 μ_B. In (b), the supercell consists of eight primitive cells of ZnO, where two Mn ions are substituted for Zn ions along the *c*-axis. Ferromagnetic ordering of Mn ions is assumed. The Mn–Mn distance is 5.205 Å. (Courtesy of X. Feng [103].)

series, where V and Co showed much larger magnetic moment than other TM metals. For the light 3d elements, the 3d↑ states lie high in the 2p(O) and 4s(Zn) gap, overlapping the donor impurity band that is spin split, as shown in Figure 5.16. In the middle of the series, there is no overlap with the 3d levels and the exchange is weak, but toward the end of the series, the 3d↓ states overlap the impurity band, which then

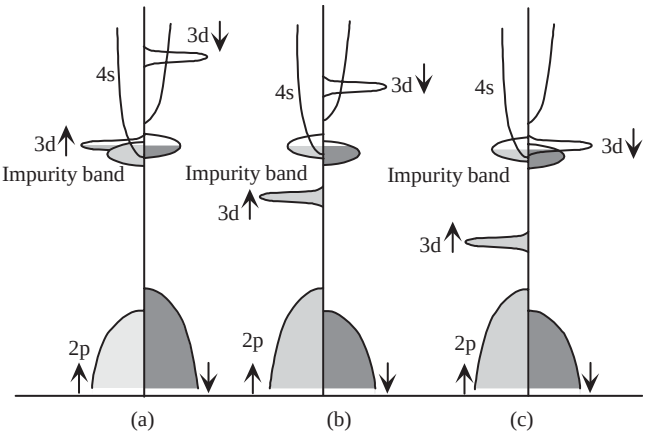

Figure 5.16 Schematic density of states for (a) TM = Ti, (b) TM = Mn, and (c) TM = Co. The Fermi level lies in a spin-split donor impurity band. (After Ref. [107].)

has the opposite spin splitting for the same occupancy. High Curie temperatures are found whenever unoccupied 3d states overlap the impurity band, but not otherwise. The likely origin of the donor impurity band in ZnO films is in lattice defects, such as oxygen vacancies. Detailed studies are needed for the role of different defects. The authors found no relationship between the conductivity and magnetic properties.

5.9
Experimental Results on ZnO-Based Dilute Magnetic Semiconductors

Experimentally, transition metal-doped ZnO has received a great deal of attention since the prediction of above room-temperature ferromagnetism in Mn-doped p-type ZnO [27] (hole concentration on the order of $10^{20}\,cm^{-3}$) and in Co-doped n-type ZnO [68]. For spin applications involving the ZnO family, the solubility of TM elements in ZnO, especially Mn and Co, can reach up to 35%, which is also very promising for spin applications. As-grown ZnO thin films are usually n-type. High electron carrier density can also be realized via group III substitutional doping. On the other hand, p-type doping remains a challenge. Tsukazaki *et al.* [108] reported p-type doping by N in ZnO layers grown on high-quality ZnO. If indeed these results could be confirmed and if the hole-mediated ferromagnetism is the dominant mechanism, attainment of p-type ZnO could pave the way for promising potential of TM-doped ZnO and devices. So far, magnetic properties of ZnO doped with a variety of 3d transition metals have resulted in conflicting experimental results (see the review by Liu *et al.* [1]). (Zn,Co)O [23], (Zn,Ni)O [109, 110], (Zn,Sn)O [20], and (Zn, Mn)O [12, 23, 111] were found to be paramagnetic, while some authors reported ferromagnetism in (Zn,Co)O [10, 89, 112], (Zn,V)O [9, 113], and (Zn,Mn)O [16]. Che Mofor *et al.* [114] have reported paramagnetic behavior of (Zn,Mn)O doped to moderate Mn concentrations, whereas the material containing about 19% Mn

showed weak ferromagnetism, which was attributed to Mn-rich clusters observable by transmission electron microscope (TEM). Several recent studies on (Zn,Mn)O and (Zn,Co)O showed that any magnetic ordering is strongly method-specific [10, 16, 115] and appears to be sensitive to chemical ordering of the TM ions and defects such as vacancies and interstitials.

Continuing with experimental investigations, Fukumura *et al*. [11] reported (Zn,Mn)O by pulsed laser deposition (PLD). In this particular work up to 35% Mn was incorporated into ZnO without affecting much the crystallographic quality of the DMS, whereas about 5% is tolerable for III–V-based hosts. A relatively higher solubility might be expected in II–VI hosts owing to Mn^{2+} nature, which can be achieved easily by having the $4s^2$ electrons participate in the bonding process. The 4s electrons are much closer to the O atom that lacks two electrons in its 2p shell and Mn has exactly half-filled 3d shell depicted by Mn^{2+} d^5 [2]. It will cost a considerable amount of energy to add an electron with the opposite spin to the $3d^5$ orbit. The gist of this discussion is that the Mn behaves in much the same way as Zn and thus high solubility should be expected, although the fact that Zn is a relatively larger atom must not be ignored.

Clearly and somewhat reiteratively, the report of high solubility of Mn in ZnO [11] triggered intensive research on the experimental side as well in TM-doped ZnO by many groups employing various thin film growth techniques. Growth of these ferromagnetic materials by thin film techniques, such as MBE [116], metalorganic chemical vapor deposition (organometallic vapor phase epitaxy (OMVPE)) [117], and PLD [118], provides excellent control of the dopant concentration and the ability to grow single-phase layers. However, the results concerning the existence of ferromagnetism have been rather controversial. While some groups have reported ferromagnetism in (Zn,TM)O systems with T_C ranging from 30 to 550 K [9, 10, 13, 14, 16, 21, 98, 104, 119], others reported observations of antiferromagnetic and spin-glass behavior [8, 12, 23, 120–122]. The distribution of TM elements in the host ZnO is also an important issue to be addressed. To refresh our memory, the term DMS refers to the case wherein some fraction of the atoms, in an otherwise nonmagnetic semiconductor host like ZnO, are replaced by magnetic ions. A key unanswered question is whether the resulting material indeed contains uniformly distributed transition metal elements or contains clusters, precipitates, or second phases that are responsible for the observed magnetic properties. Table 5.4 summarizes reports of magnetic properties of transition-metal-doped ZnO.

Most probable reason of the controversy in the magnetic properties of ZnO-based DMS as stated above might in part have its roots in the insufficient/inappropriate characterization of the samples [131]. As discussed in the theory tutorial section, the mechanism for the observed magnetic behavior is complex and appears to depend on a number of factors, including Mn–Mn spacing, and the carrier density and type. These parameters affect the band and electronic structure of the material, which in turn strongly affect its magnetic properties. Depending on the growth conditions employed for producing the DMS material, the properties of DMSs can be very different. Therefore, it might be necessary to decide on a case-by-case basis as to which mechanism is dominant. This can only be achieved by a careful correlation of

Table 5.4 List of reported magnetic properties of ZnO-based DMS.

Compound	TM content	Substrate (for thin film) or bulk	Fabrication method	Growth temperature (°C)	Oxygen pressure (Torr)	Postannealing	T_C (K)	Notes	Reference
(Zn,Mn)O	<0.35	*c*-Sapphire	PLD	600	5×10^{-5}				[11]
(Zn,Mn)O	0.36	*c*-Sapphire	PLD	600	5×10^{-5}			Spin-glass	[120]
(Zn,TM)O		*c*-Sapphire	PLD	500–600	1×10^{-9} to 10^{-6}				[8]
(Zn,Mn)O	0.01–0.36	*c*-Sapphire	PLD	610	5×10^{-5}			Paramagnetic	[121]
(Zn,Mn)O	0–0.3	*c*-Sapphire	PLD				>30–45	0.15–0.17 μ_B/Mn	[13]
(Zn,Mn)O	<0.04		Sintered pellets	500–700	Air, 1 atm		>425	0.16 μ_B/Mn	[16]
(Zn,Mn)O	0.0221	Fused quartz	PLD	400	0.2		>425	0.05 emu g^{-1} single phase	[16]
(Zn,Mn)O	0.04–0.09	*c*-Sapphire	Reactive sputtering	200–380			>400	3 μ_B/Co	[123]
(Zn,Mn)O	0.07	*a*-Sapphire	Sputtering	400	0.06			Paramagnetic	[124]
(Zm,Mn)O	0.03 & 0.2	GaAs (001)	Sputtering	500–600	8×10^{-4} in Ar				[125]
ZnO:(Mn,Sn)	0–0.3	Bulk ZnO	Implantation			700 °C, 5 min RTA in N_2	250	Ferromagnetic	[14]
ZnO:(Mn,Sn)	Mn 0.03 Sn < 0.1	*c*-Sapphire	PLD	400–600	0.02		>300	Ferromagnetic	[126]
ZnO:(Co, Mn, Cr, or Ni)	0.05–0.25	*c*-Sapphire	PLD	350–600	$2–4\times10^{-5}$		280–300	2 μ_B/Co	[119]
ZnO:(Mn, Co)	0.02–0.15		Crystalline precursor					Antiferromagneteic	[23]
ZnO:(Mn, Co)	<0.05		Melt-growth					Paramagnetic	[122]

(Zn,Co)O	0.03–0.05	Bulk ZnO	Ion implantation			700 °C, 5 min, in O_2	>300	Conanocrystals	[20]
(Zn,Co)O	0–0.25	*c*-Sapphire	Sol–gel	<350		RTA 700 °C, 1 min in O_2	>350	0.56 μ_B/Co	[89]
(Zn,Co)O	0.015		PLD	650	5×10^{-5}		>300	Ferromagnetic	[17]
ZnO:(Co, Al)	0.04–0.12	Glass	RF sputtering		1×10^{-2} in Ar		>350	0.21 μ_B/Co	[127]
(Zn,Co)O	0.02–0.5	*c*-Sapphire	PLD	300–700	1×10^{-6} to 10^{-1}			Spin-glass	[120]
ZnO:Co	0.1	O face ZnO	PLD					Antiferromagnetic	[128]
ZnO:Co	<0.35	*r*-Sapphire	OMVPE	300–650	40	500 °C, 20 min in vacuum	>350	Ferromagnetic	[129]
ZnO:(Co, Fe)	<0.15	SiO_2/Si	Magnetron sputtering	600	2×10^{-3}	600 °C, 10 min, 1×10^{-5} Torr	>300	12–15 emu cm^{-3}	[119]
ZnO:(Cu, Fe)	Fe < 0.07 Cu < 0.01	Bulk	Solid-state reaction	897			550	0.75 μ_B/Fe	[104]
(Zn,Ni)O	0.01–0.25	*c*-Sapphire	PLD	300–700	1×10^{-5}			Super para- or ferromagnetic	[21]
(Zn, V)O	0.05–0.15	*r*-Sapphire	PLD	300	10^{-5} to 10^{-3}		>350	0.5 μ_B/Co	[9]
ZnO:Mn	0.1	*r*-Sapphire	PLD	650	0.1			0.075 μ_B/Mn	[130]
ZnO:(Mn, Cu)	Mn 0.1, Cu 0.05	*r*-Sapphire	PLD	650	0.1		400	0.1 μ_B/Mn	[130]
ZnO:(Sc, Ti, V, Fe, Co, and Ni)	0.05	*r*-Sapphire	PLD	600	0.1–750		>300	2.6 μ_B/Co 0.5 μ_B/Ti 0.3 μ_B/Sc	[107]

The TM content listed corresponds to the magnetic property and T_C in the "Note" and "T_C" columns. Magnetic moment per TM atom is listed when it is available. *c*-Sapphire, *a*-sapphire, and *r*-sapphire means the substrate surface is perpendicular to [0 0 0 1], [1 1 $\bar{2}$ 0], and [1 $\bar{1}$ 0 2] direction, respectively.

the measured magnetic properties with materials analysis methods that are capable of detecting other phases and precipitates.

Table 5.5 lists some second phase precipitates reported in TM-doped ZnO. Although XRD measurements play an important role in attempts to detect any impurity phases present, the sensitivity may not be good enough to identify minute amounts of precipitates in the samples. SQUID is too sensitive and detects minute magnetization including that from contamination. Other characterization techniques [140], such as scanning electron microscope (SEM), reflection high energy electron diffraction (RHEED), transmission electron microscope, electron probe microanalysis (EPMA), and secondary ion mass spectrometry (SIMS), might have to be employed to identify the precipitates down to nanoscale level and investigate the uniformity of dopant distribution in the host material. Fukumura *et al*. [131] gave a detailed review of the characterization techniques for oxide-based DMS. It was also pointed out that in the case of magnetic measurement of a thin film on a substrate, the measured signal, which is in proportion to the sample volume, includes the magnetic moment not only from the film but also from the substrate (which is, in general, diamagnetic) owing to the much larger volume of substrate than that of the film. Therefore, a careful analysis of magnetization measurements must be carried out in

Table 5.5 Second phases observed in TM-doped ZnO and their magnetic properties. Curie temperature (for Ferro- or ferromagnetic material) or Néel temperature (for antiferromagnetic material) of each possible TM-related phase is given.

Phase	Nature of magnetism	Curie temperature or Néel temperature (K)	Reference
MnO	Antiferromagnetic	116	[13]
MnO_2	Antiferromagnetic	92	[132]
Mn_2O_3	Antiferromagnetic	76	[132]
Mn_3O_4	Ferromagnetic	43	[132]
Mn_3O_4 (distorted spinal)	Ferromagnetic	46	[133]
Mn_3O_4 (Humanity)	Ferromagnetic	40	[134]
$(Zn,Mn)Mn_2O_4$	Ferromagnetic	40	[135]
$ZnMnO_3$ (cubic)	Spin-glass		[136]
Zn_3MnO_6 (hexagonal)			[136]
Co	Ferromagnetic	1373	[20]
CoO	Antiferromagnetic	291	[119, 137]
CuO (monoclinic)	Antiferromagnetic	230	[138]
Cu cluster	Antiferromagnetic	154	[138]
FeO (cubic)	Antiferromagnetic	198	[104]
$(Zn, Fe)_3O_4$	Ferromagnetic	440	[137]
$ZnFe_2O_4$ (bulk, normal spinel)	Nonmagnetic		[139]
$ZnFe_2O_4$ (nanocrystalline, inverted spinel)	Ferrimagnetic		[139]

conjunction with reports of ferromagnetism based simply on magnetic hysteresis. The magnetism measurements would be much more useful if the magnetic moment per magnetic ion in the sample is also determined. The considerable controversy regarding the origin of ferromagnetism in ZnO-based DMSs reported in the literature notwithstanding, we discuss what has been reported on the experimental side in the following section.

5.9.1
Properties of Mn-Doped ZnO

Jin *et al.* [8] determined the solubility limits of transition metal dopants in ZnO thin films grown by laser MBE. Figure 5.17 shows these limits determined by the presence of impurity peaks in the X-ray diffraction patterns. The transition metal compositions were measured by EPMAas well.

The solubility of Mn into ZnO can exceed the equilibrium limit (~13%) and reaches up to 35% [11] as a result of the nonequilibrium PLD film growth process. With increasing Mn content, the lattice constants a and c of wurtzite $Zn_{1-x}Mn_xO$ increase due to the fact that the ionic radius of Mn^{2+} (0.66 Å) is larger than that of Zn^{2+} (0.60 Å) [23, 119, 121, 132, 135], and the bandgap expands with considerable mid-gap absorption. This mid-gap absorption peak centered around 3 eV in Mn-doped ZnO is usually broad and structureless at room temperature owing to the overlap of the intra-d shell transitions of Mn^{2+} from its ground state $^6A_1(S)$ to $^4T_1(G)$, $^4T_2(G)$, $^4A_1(G)$, and $^4E(G)$ [141]. Figure 5.18a shows the optical transmittance at room temperature for $Zn_{1-x}Mn_xO$ films with different Mn contents. As the Mn content is increased, the gap absorption around 3 eV develops and the absorption edge blue-shifts. It should be mentioned that any change in the bandgap of Mn-doped ZnO depends on whether the Mn atom orbitals hybridize in such a way as to lead to bonding state.

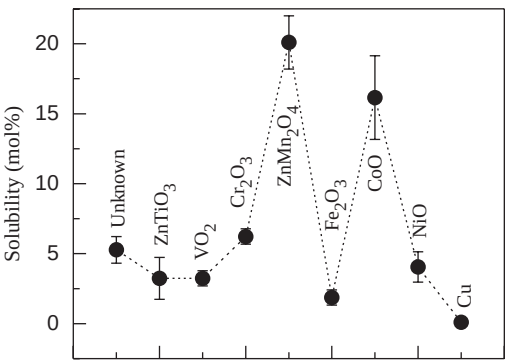

Figure 5.17 Solubility limit of TM ions in ZnO. The upper and lower limit of the error bars corresponding, respectively, to the lowest x of the compounds precipitated and the highest x of the compounds without precipitation. The precipitated phases are also shown. (After Ref. [8].)

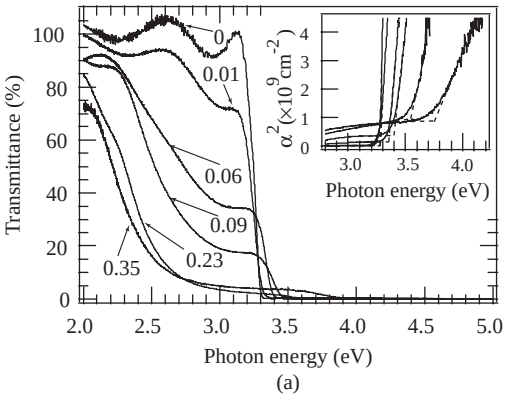

(a)

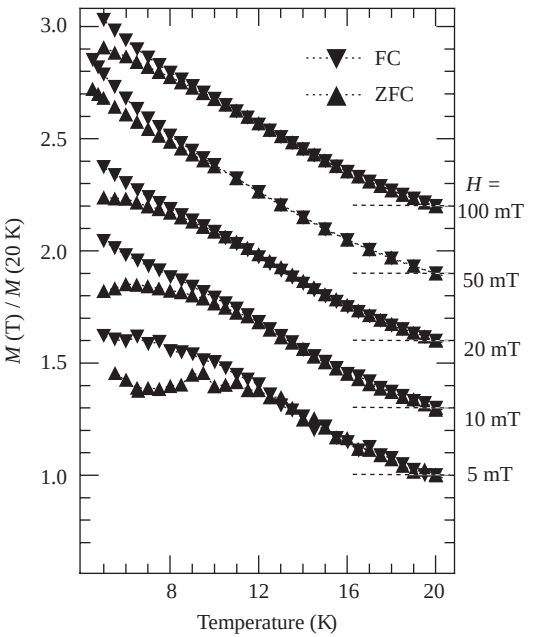

(b)

Figure 5.18 (a) Transmission spectra of $Zn_{1-x}Mn_xO$ films measured at room temperature for various x values. Numbers in the figures denote x. Inset shows the photon energy dependence of squared absorption constant (α^2) around the bandgap (E_g). (b) Magnetization normalized to the value at 20 K for a $Zn_{0.64}Mn_{0.36}O$ film measured during ZFC and FC runs in various magnetic fields shown on the right side. The curves are vertically shifted as represented by the dotted lines. (Courtesy of T. Fukumura [11, 12].)

The ZnO thin films with high Mn concentration, however, did not show ferromagnetic behavior. Field-cooled (FC) and zero-field-cooled (ZFC) temperature dependence of the magnetization (M vs. T) for a $Zn_{0.64}Mn_{0.36}O$ thin film grown by pulsed laser deposition [12] is shown in Figure 5.18b. The nomenclature FC

denotes the procedure of cooling the sample in the field, H, and measuring the magnetization, M, with the field on. The nomenclature ZFC denotes the procedure of cooling the sample in zero field and measuring the magnetization, M, upon warming with the field H on. The magnetization for the ZFC run deviates from that for the FC run at around ~10 K. The cusps in the ZFC and FC magnetization are typically interpreted as indications of spin-glass behavior [2]. The effective Mn content linked to the net magnetization compared to the fully saturated magnetization of the Mn^{2+} spin is very small ($0.021\,\mu_B$), also implying a strong antiferromagnetic exchange coupling. This result is consistent with the *ab initio* calculations by Sato and Katayama-Yoshida [3], who predicted a transition from the antiferromagnetic state to the ferromagnetic state only with the introduction of holes.

The blueshift of bandgap energy and the increase of mid-band absorption have also been observed from $Zn_{0.93}Mn_{0.07}O$ deposition by RF magnetron sputtering [124]. The Auger electron spectroscopy showed that Mn is uniformly distributed throughout the film. The magnetic property has been concluded as paramagnetic because the field-dependent magnetization of (Zn,Mn)O can be described well with Curie–Weiss law. Liu *et al.* [136] studied the structure of Mn-ZnO deposited by RF magnetron sputtering on sapphire substrates. The Mn-doped ZnO showed magnetic hysteresis at 5 K while the magnetization at 300 K is much weaker. Although the wurtzite crystal structure was maintained, the incorporation of Mn led to a large amount of structural disorder in the crystalline–columnar ZnO lattice. The substitutional fraction of Mn was about 25% in the Mn-doped ZnO film as derived from Rutherford backscattering (RBS) measurement, indicating that most of the Mn incorporated in the film was present in other forms. The TEM structure analysis revealed that the Mn-doped ZnO layer included a high density of round-shaped cubic and elongated hexagonal MnZn oxide precipitates. Detailed analyses of the precipitates by energy dispersive spectroscopy (EDS) and lattice spacing measurement identified the round shaped precipitates to be the perovskite phase of $ZnMnO_3$ and the elongated hexagonal precipitates to be Zn_3MnO_6. Figure 5.19a shows the columnar growth mode of the undoped ZnO buffer layer. When Mn doping is initiated, the crystalline columns are disrupted and the Mn-doped ZnO layer contains a high density of precipitates, some of which appear as dark areas in Figure 5.19a. Figure 5.19b shows magnified cross-sectional TEM images of one of the round-shaped cubic and elongated hexagonal precipitates.

Han *et al.* [135] demonstrated that in polycrystalline (Zn,Mn)O synthesized by solid state reaction, the $(Zn,Mn)Mn_2O_4$ precipitates are responsible for the observed ferromagnetic transition. In Figure 5.20, the X-ray absorption spectroscopy at Mn $L_{2,3}$ edges indicates the existence of Mn^{3+} charge states in the sample that has the (Mn, $Zn)Mn_2O_4$ precipitates. The bulk (Zn,Mn)O without the second phase precipitates showed paramagnetic behavior.

Lawes *et al.* [23] conducted a study on bulk $Zn_{1-x}Mn_xO$ and $Zn_{1-x}Co_xO$ with $x = 0.01$ and 0.15. No evidence for a ferromagnetic transition in these systems was observed above 2 K. The authors proposed a model that considers two subsets of spins to explain the observed magnetic properties. One subset of spins, which belongs to the TM ions with no TM nearest neighbors, is completely free (isolated spins). The

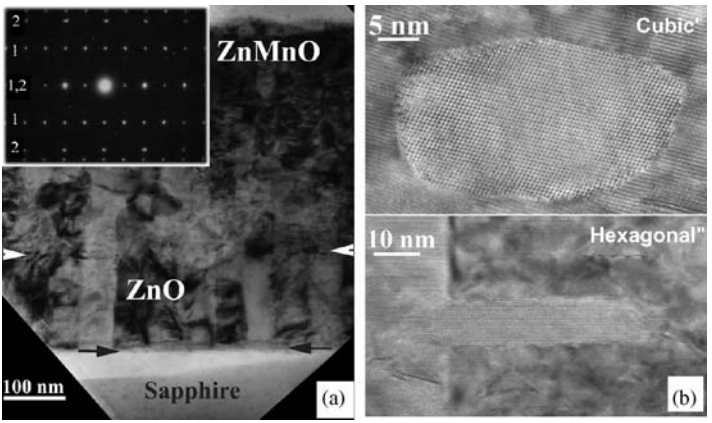

Figure 5.19 (a) Bright-field cross-sectional TEM image of the Mn-doped ZnO thin film. The interfaces of undoped ZnO buffer/sapphire and Mn-doped ZnO/undoped ZnO buffer are indicated by arrows. A trimetallic $(AlMn)ZnO_3$ phase was found in the ZnO/sapphire interface region. The inset is the selective-area electron diffraction pattern from the undoped ZnO buffer layer. (b) Magnified cross-sectional TEM images of the cubic and hexagonal precipitates in the Mn-doped ZnO layer. (After Ref. [136].)

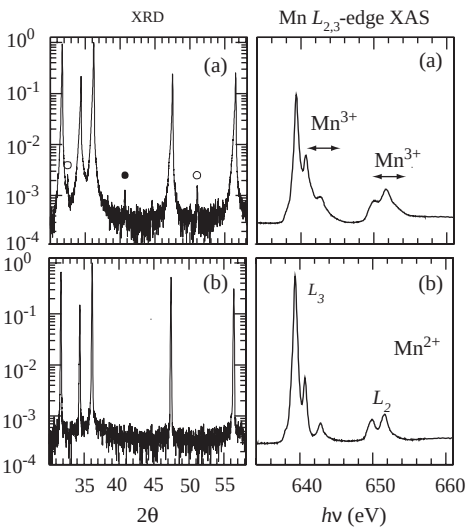

Figure 5.20 X-ray diffraction pattern is displayed as the left panels for samples (a) sintered at 1170 K (upper panel) and (b) sintered at 1370 K (lower panel). The large peaks in (a) and (b) belong to the ZnO structure, while the small peaks in (a) are from secondary phases, MnO (≏ solid circle) and $(Mn,Zn)Mn_2O_4$ (♦ open circle). The right panels (a) and (b) show Mn 2p–3d X-ray absorption spectrum for samples (a) (upper panel) and (b) (lower panel), respectively. Note that the $L_{2,3}$-edge shape of sample (a) deviates from the Mn^{2+} character of sample (a) at the high energy side as indicated by arrows. This deviation is caused by Mn^{3+}. (Courtesy of Y.-H. Jeong [135].)

second subset of spins, which belongs to those TM ions with at least one TM nearest neighbor, is affected by mean-field interactions (clustered spins). With the increase of Mn concentration, the fraction of Mn ions belonging to the second subset increases so that the antiferromagnetic interaction reduces the net magnetization. Separating the TM ions into two noninteracting subsets of spins also gives an excellent description of the susceptibility over the temperature range that has been measured, as can be seen in Figure 5.21. The feature of the susceptibility, namely, a high temperature regime that appears to be close to linear, followed by significant curvature at lower temperatures, is also observed by other researchers [122]. It is

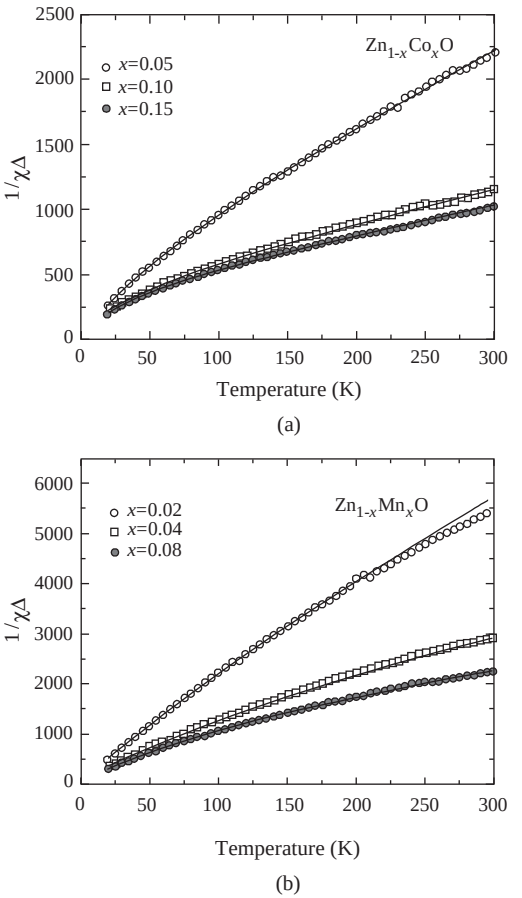

Figure 5.21 Inverse susceptibility for $Co_xZn_{1-x}O$ (a) and $Mn_xZn_{1-x}O$ (b) as a function of temperature. The susceptibility was determined by looking at the difference in magnetization between $B = 2T$ and $B = 1T$. The solid lines show fits the function defined by separating the TM ions into two subsets of spin, one following a simple Curie behavior, the other a Curie–Weiss function. (Courtesy of G. Lawes [23].)

desirable to verify the presence of two distinct spin populations in TM-doped ZnO by using techniques such as electron paramagnetic resonance or Mössbauer spectroscopy.

In harmony with theoretical predictions that ferromagnetism in (Zn,Mn)O appears mainly in p-type materials, a study of carrier effect on magnetic properties of (Zn,Mn)O [142] showed that N-capped Mn^{2+}:ZnO nanocrystals exhibit strong ferromagnetism with $T_C > 350$ K. Furthermore, the magnetization of Mn^{2+}:ZnO nanocrystal is enhanced with N-containing molecule absorption onto the surface, or reduced with exposure of Zn vapor. Lim *et al.* [125] observed room-temperature ferromagnetism from (Zn,Mn)O thin films deposited on GaAs substrates by RF sputtering. A p-type conduction is realized, when the films were deposited above 530 °C to encourage As diffusion into ZnO, hopefully as acceptor. The reported hole concentration is in the lower $10^{20}/cm^3$ range. These observations provide experimental evidence for theoretical studies, and encourage more detailed studies, especially about the chemical identity of N or As in (Zn,Mn)O, toward elucidating the underlying mechanism of ZnO-based ferromagnetic DMSs.

Ferromagnetic behavior has also been observed in n-type or insulating (Zn,Mn)O. For example, Jung *et al.* [13] observed ferromagnetic ordering in $Zn_{1-x}Mn_xO$ films grown by Laser MBE. The Curie temperatures in this case were $T_C = 30$ and 45 K for $Zn_{1-x}Mn_xO$ of $x = 0.1$ and 0.3, respectively. Kim *et al.* [15] also reported T_C 30–40 K for $Zn_{1-x}Mn_xO$ ($x = 0.1$–0.3) deposited on Si substrates by sol–gel. However, through TEM and EDS measurements, the ferromagnetism is considered most probably due to the Mn_3O_4 precipitate appearing at the interface between $Zn_{1-x}Mn_xO$ and Si.

Sharma *et al.* [16] reported ferromagnetism above room temperature in bulk pellets, thin films, and powder form of $Zn_{1-x}Mn_xO$ x with $x < 4\%$. The unique feature of their sample preparation was the low-temperature processing, that is, sintering temperature less than 700 °C to avoid the formation of the secondary phase. Ferromagnetic resonance (FMR) spectra (Figure 5.22) showed clear room-temperature ferromagnetism for pellets sintered at 500 °C, and T_C is determined to be well above 425 K. It should be noted that the spectra at 425 K is not shown in their report. Contrary to Sharma *et al.*'s [16] results, Kolesnik and Dabrowski [132] found that MnO_2 and Mn_2O_3 phase exists when the annealing temperature is below 900 °C. Single-phase (Zn,Mn)O fabricated with annealing temperatures higher than 900 °C showed only paramagnetic behavior.

By combining the near-edge X-ray absorption fine structure (NEXAFS) technique and first principles calculations, Kunisu *et al.* [143] first studied the local environment of Mn dopant in ZnO. In polycrystalline bulk ZnO NEXAFS at Mn *K*-edge was found to remain in the same shape as shown in Figure 5.23 up to 5%. The experimental spectra is reproduced well by first principles calculations of (Zn,Mn)O solid solution, which confirmed that Mn substituted at the Zn sites. For Mn concentration higher than 5%, Mn_3O_4 precipitates started to appear.

Based on the tenet that Mn provides the localized spins needed for carrier-mediated ferromagnetism, with the additional dopant added to control the carrier concentration in the material, Norton *et al.* [14] reported that ferromagnetic behavior

with $T_C \sim 250$ K can be obtained using Mn codoped with Sn in ZnO by PLD. In a more detailed study, Ivill *et al.* [126] investigated the carrier density dependence of saturation magnetization in (Zn,Mn)O with Mn concentration of 3%. Sn is believed to act as a doubly ionized donor introducing deep states in the energy gap. The resistivity of (Zn,Mn)O:Sn films drops from 195 to 0.185 Ω cm, as Sn concentration increased from 0 to 0.1%. The saturation magnetization increases initially with Sn, then decreases with the increase of Sn concentration, as shown in Figure 5.24. This result is interesting but the underlying mechanism between the carrier concentration and magnetic properties observed is not clear, although the authors used the bound magnetron polaron argument to explain the effect of Sn on the observed magnetization through moving up the Fermi energy and changing the hole density.

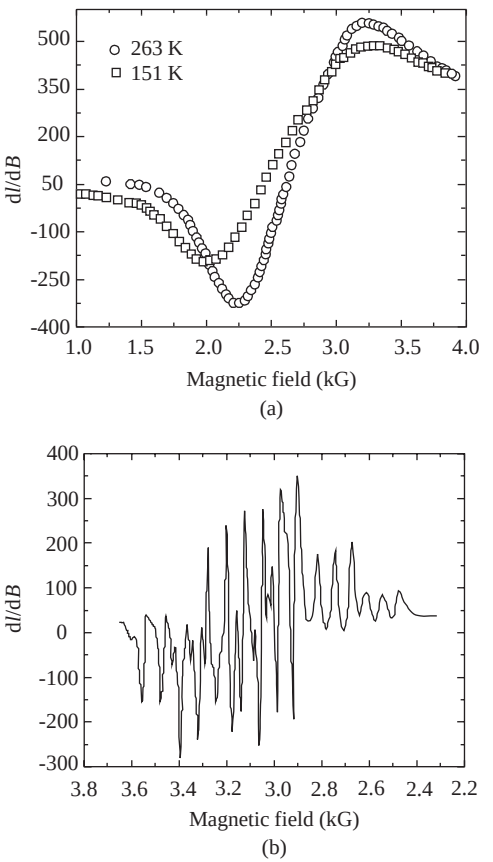

Figure 5.22 Ferro- and paramagnetic resonance spectra for a nominal 2 at.% Mn- doped ZnO pellet. (a) Ferromagnetic resonance spectra for a sample sintered at 500 °C. (b) Room-temperature paramagnetic resonance spectra for the same sample sintered at 900 °C. (After Ref. [16].)

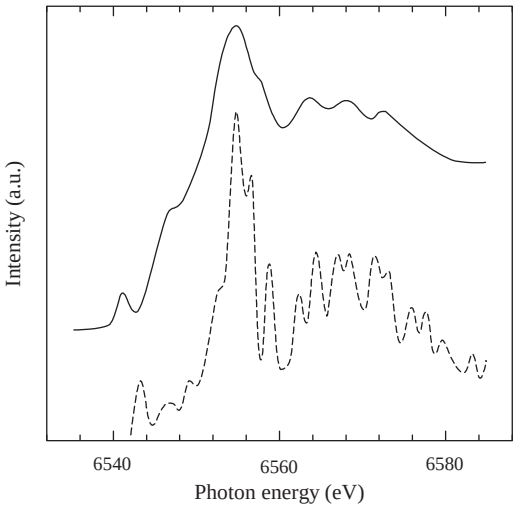

Figure 5.23 Comparison of NEXFAS spectra between calculations and experiments for polycrystal (Zn,Mn)O with 5% Mn. Solid and dashed curves are experiments and calculations, respectively. Absolute energies of all theoretical spectra were shifted by −20 eV ($\Delta E/E = 0.3\%$). (Courtesy of I. Tanaka [143].)

To confirm the theoretical prediction that Cu codoping could increase the hole concentration (by trapping electrons) and help induce ferromagnetism in TM-doped ZnO [103], $Zn_{0.9}Mn_{0.1}O$ and $Zn_{0.85}Cu_{0.05}Mn_{0.1}O$ thin films were grown by PLD on *r*-sapphire substrates [130], the magnetization of which is shown in Figure 5.25. It should be mentioned that even if Cu worked as intended, if and when the Fermi level is lowered in the bandgap, hallmark of p-type polarity, near and below the Cu level(s),

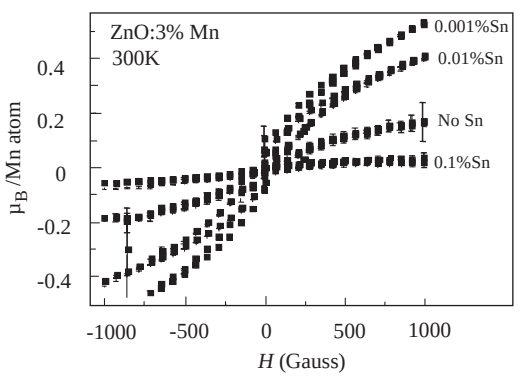

Figure 5.24 Magnetization measured at 300 K for epitaxial ZnO:3% Mn films that are codoped with 0.001% Sn, 0.01% Sn, 0.1% Sn, and no Sn. There appears to be an inverse correlation of the Sn content with the saturation magnetization. (Courtesy of D.P. Norton [126].)

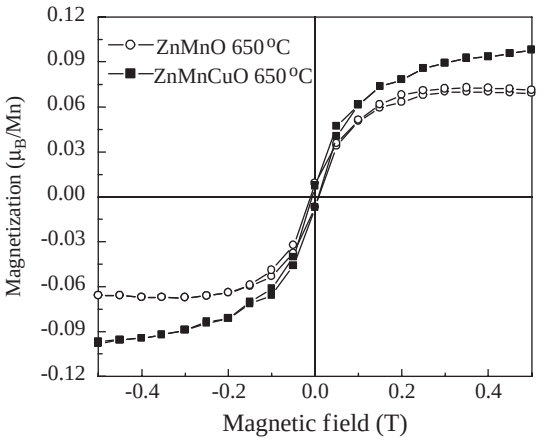

Figure 5.25 Magnetization versus magnetic field at 300 K for the $Zn_{0.9}Mn_{0.1}O$ and $Zn_{0.85}Mn_{0.1}Cu_{0.05}O$ thin films fabricated under the same condition. (Courtesy of N.H. Hong [130].)

the captured electrons would be released anyway creating a paradoxical situation. In any case, guided by their results, the authors [130] argued that growth conditions are very important factors (which are often cited but do not really help clarify any of the vexing issues without incisive comments) in affecting the magnetic properties of the thin films and Mn doping could indeed induce room-temperature ferromagnetism in ZnO. Codoping with Cu was not found to be very crucial, as theories have predicted, although it might enhance the magnetic moment in some specific cases. The observed magnetic property changes with growth conditions were attributed to the increase of oxygen vacancies, which act as shallow donors [144] and provide more n-type carriers. If this is true, it is clearly opposite to the role of Cu codoping predicted.

5.9.2
Properties of Co-Doped ZnO

The existence of ferromagnetic ordering in Co-doped ZnO has been first theoretically proposed to be due to double exchange interaction [3, 68] or the RKKY interaction between Co ions [145]. But a later calculation also showed that the ground state of Co-doped ZnO is spin-glass without doping due to the short-range interactions between transition metal atoms [99]. Experimental studies have been carried out to verify the predictions. Ueda *et al.* [10] investigated $Zn_{1-x}TM_xO$ films (n-type ($x = 0.05$–0.25) and TM = Co, Mn, Cr, Ni) grown on sapphire substrates by PLD. The Co-doped ZnO films showed the maximum solubility limit of nearly 50%. They first reported a room-temperature ferromagnetic feature in $Zn_{1-x}Co_xO$, but the reproducibility of the method was less than 10%. The follow-up magnetic circular dichroism measurements on these samples showed ferromagnetic metal behavior, which indicates that the observed ferromagnetism may be originated from Co-related ferromagnetic precipitates [131]. The ferromagnetism observed in (Zn,Co)O fabricated by ion

implantation of Co to (1 1 0)-oriented Sn-doped ZnO substrates is also shown to be originated from Co nanoclusters [20].

In a systematic study of magnetism in TM-doped (from Sc to Cu) ZnO, Venkatesan *et al.* [107] reported that the magnetic moment of Co, 1.9 μ_B per Co, is the largest among all other transition metal elements in (Zn,TM)O with 5% of TM (Figure 5.26). The films were grown by PLD on *r*-sapphire substrates. Lee *et al.* [89] reported that $Zn_{1-x}Co_xO$ with $x = 25\%$ fabricated by the sol–gel method exhibits ferromagnetic behavior with T_C higher than 350 K. The films are insulating with n-type carrier concentration in the $10^{17}\,cm^{-3}$ range. In samples with $x = 20$ and 25%, both magnetization and carrier concentration increase with temperature. It was argued that a higher Co concentration could enhance "trapping" of the electrons, which may induce the ferromagnetic spin–spin interaction between Co atoms. Increase of magnetization with temperature is similar to what has been reported for Mn-doped ZnO by Heo *et al.* [88], which has been explained by randomness and disorder on percolating ferromagnetic clusters. Tuan *et al.* [129] prepared epitaxial $Zn_{1-x}Co_xO$ ($x < 35\%$) films on *r*-sapphire by organometallic vapor phase epitaxy and found that a weak ferrromagnetic behavior persists even above 350 K. The conductivity was observed to increase with postgrowth annealing in vacuum instead of Al-doping. The increase of the saturation magnetization with conductivity or carrier concentration observed in these reports [89, 129] seems to agree with some theoretical predictions that electron doping is necessary to induce ferromagnetism in (Zn, Co)O [99]. Ferromagnetism has also been reported by several other groups [17, 18, 146] in (Zn,Co)O with 10–40% of Co.

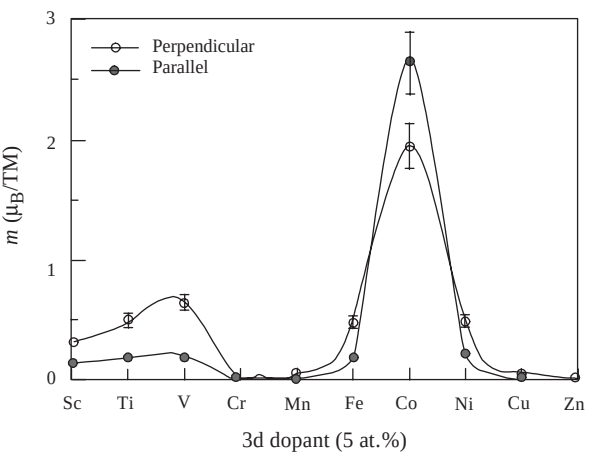

Figure 5.26 Magnetic moment of $Zn_{1-x}TM_xO$ films, TM = Sc; Ti; . . .; Cu; Zn, measured at room temperature. Solid circles are for the field-applied perpendicular to the film plane and open circles are for the field applied in the plane of the film. The moment is expressed as μ_B/TM. The trend measured at 5 K is similar. (Courtesy of J.M.D. Coey [107].)

Similar to the situation in Mn-doped ZnO, there are plenty of reports about the absence of ferromagnetism in Co-doped ZnO. Kim *et al.* [120] reported spin-glass behavior for homogeneous $Zn_{1-x}Co_xO$ films. Room-temperature ferromagnetism was found only in inhomogeneous films, which led the authors to attribute their observations to the presence of Co clusters. Kane *et al.* [122] investigated bulk $Zn_{1-x}Co_xO$ and $Zn_{1-x}Mn_xO$ fabricated by a melt-growth method, and found no evidence of ferromagnetic behavior in any of these nominally noncarrier-doped samples, which can be explained by diluted magnetic semiconductor mean-field. Instead, the magnetic properties showed paramagnetic behavior for $Zn_{1-x}Mn_xO$ dominated by antiferromagnetic Mn–Mn exchange interaction at low temperatures. Although $Zn_{1-x}Co_xO$ showed hysteresis, the ZFC and FC magnetization, shown in Figure 5.27, revealed that the hysteresis was due to nanoscale paramagnetic Co clusters embedded in a diamagnetic ZnO matrix. The authors concluded that in the bulk single-crystal form intrinsic and noncarrier-doped $Zn_{1-x}TM_xO$ is not ferromagnetic; thus creative processing and doping techniques are necessary to achieve practical ferromagnetism in these materials. Paramagnetic behavior has been observed to be dominant in polycrystalline $Zn_{1-x}Co_xO$ ($x < 0.15$) [111] and bulk $Zn_{1-x}Co_xO$ ($x < 0.1$) [23].

Consistent with some theoretical predications [103], Lin *et al.* [19] argued that additional Cu doping into bulk $Zn_{0.98}Co_{0.02}O$ grown by standard solid-state reaction method is essential to achieve room-temperature ferromagnetism. Cu can be doped up to 1% ($Zn_{0.97}Cu_{0.01}Co_{0.02}O$) without forming a secondary phase as confirmed by HRTEM. Saturation magnetization at 300 K increased with Cu concentration (Figure 5.28). PL showed increasing peak intensity at 518 nm, which was attributed to

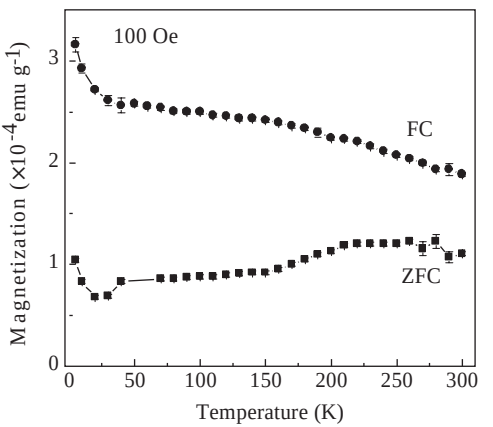

Figure 5.27 FC and ZFC magnetization versus the temperature plots taken at 100 Oe for the $Zn_{1-x}Co_xO$ ($x = 0.01$) sample. Note that the extrapolated slopes versus temperature are of opposite signs in the ZFC and FC curves and there is a significant deviation in these two values. This indicates a superparamagnetic cluster-type behavior. (Courtesy of M.H. Kane [122].)

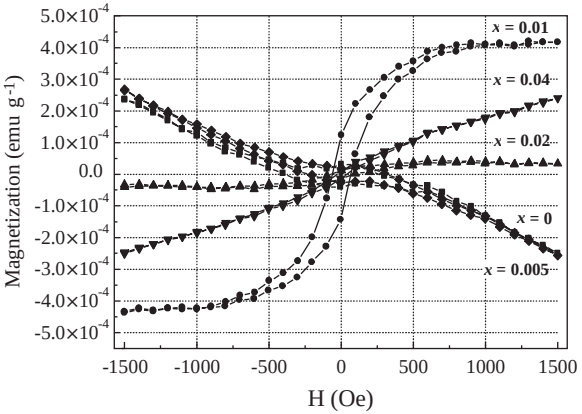

Figure 5.28 Hysteresis curves measured at room temperature of bulk $Zn_{0.98-x}Cu_xCo_{0.02}O$ samples. (Courtesy of T.-S. Chin [19].)

defects in ZnO due to the incorporation of Cu and Co, but the UV emission peak diminished with Co or Cu + Co doping.

Substitution of cobalt cations in the tetrahedral sites of the wurtzite structure was confirmed by optical spectroscopy. In its neutral charge state, the Co^{2+} ion has an [Ar] $3d^7$ electron configuration. The atomic ^4F ground state splits under the influence of the tetrahedral component of the crystal field into an $^4A_2$ ground state and $^4T_2 + {}^4T_1$ excited states. The smaller trigonal distortion and spin-orbit interaction split the ground $^4A_2$ state into $E_{1/2} + E_{3/2}$. The existence of the Co^{2+} oxidation state has been verified by a series of characteristic optical absorption bands in both the infrared and visible bands that have been correlated with d–d* transitions of the high-spin Co^{2+} $3d^7(^4F)$ ion in the tetrahedral oxygen coordination. The absorption in the visible band was thought to derive from the $^4A_2(^4F) \rightarrow {}^2E(^2G)$ and $^4A_2(^4F) \rightarrow {}^4T_1(^4P)$ transitions, and those in the infrared from the $^4A_2(^4F) \rightarrow {}^4A_1(^4G)$ transition [147]. These d–d* adsorption levels of Co^{2+} ions have been reported to be around 570, 620, and 660 nm, that is, 2.18, 2.00, and 1.88 eV, respectively [18, 119, 122, 146, 148, 149]. Figure 5.29 shows the optical transmission spectrum for $Zn_{1-x}Co_xO$ with x 0.05–0.19 [149]. The evidence of Co^{2+} state in ZnO lattice has also been obtained from EPR [128] and X-ray photoelectron spectroscopy (XPS) [129] measurements.

5.9.3
Other TM-Doped ZnO

Among other ZnO-based DMSs, ZnO:V appears to be one of the most promising systems for spin manipulation. Ferromagnetism in ZnO:V has been predicted for n-type material [68]. Vegard's-like behavior has been observed for V concentrations up to as high as 15% assuming its substitutional incorporation on the lattice sites [9, 150]. At the same time, a blueshift in the fundamental absorption edge of ZnO:V was observed with the increasing V content. Therefore, a ZnVO layer can serve as an injector of spin-polarized carriers as well as providing quantum confinement.

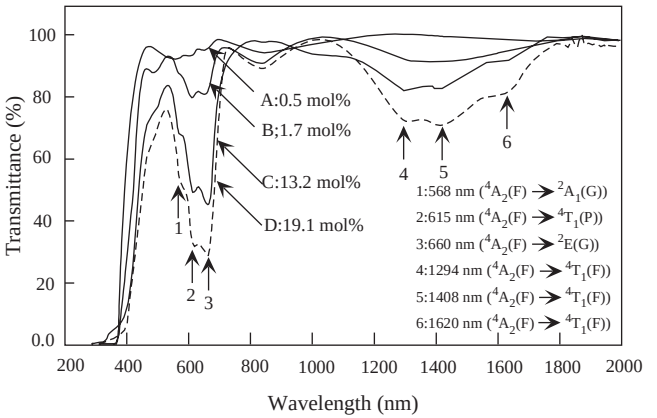

Figure 5.29 Optical transmission spectrum of $Zn_{1-x}Co_xO$. The assignment of the absorption peak is also shown. The dashed line corresponds to the sample showing the solubility limit. (After Ref. [149].)

Saeki *et al.* [9] reported Curie temperatures higher than 350 K for V-doped ZnO films [n-type $Zn_{1-x}V_xO(x = 0.05–0.15)$] with electron concentrations above $10^{18}\,cm^{-3}$ grown by PLD. They found out that only the samples with carrier concentrations as high as $10^{18}\,cm^{-3}$ showed ferromagnetism, while the insulating samples were not ferromagnetic. The transmittance spectrum for the $Zn_{0.95}V_{0.05}O$ film was also measured and showed absorption peaks around 480, 560 ($^4T_1(e^2t^1) \rightarrow {}^4T_1(e^1t^2)$), and 850 nm ($^4T_1(e^2t^1) \rightarrow {}^4A_2$), which correspond to the typical d–d* transitions of V^{2+} ions in a tetrahedral crystal field (Figure 5.30). Ishida *et al.* [151] investigated the photoemission spectra of ferromagnetic $Zn_{0.95}V_{0.05}O$. Figure 5.31a shows the valence band

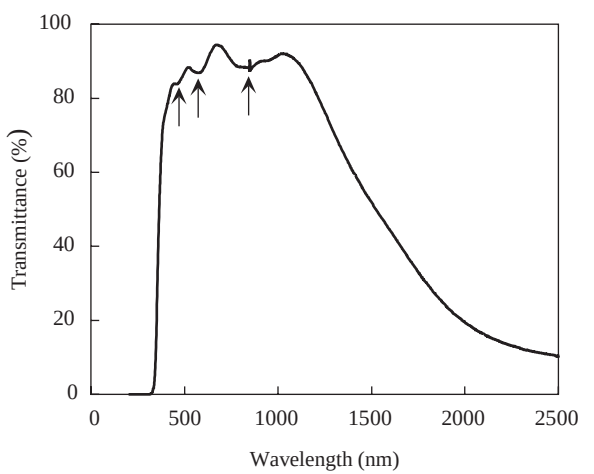

Figure 5.30 Optical transmission spectra for $Zn_{0.95}V_{0.05}O$ film. Typical absorption peaks of V^{2+} ions are indicated with arrows. (After Ref. [9].)

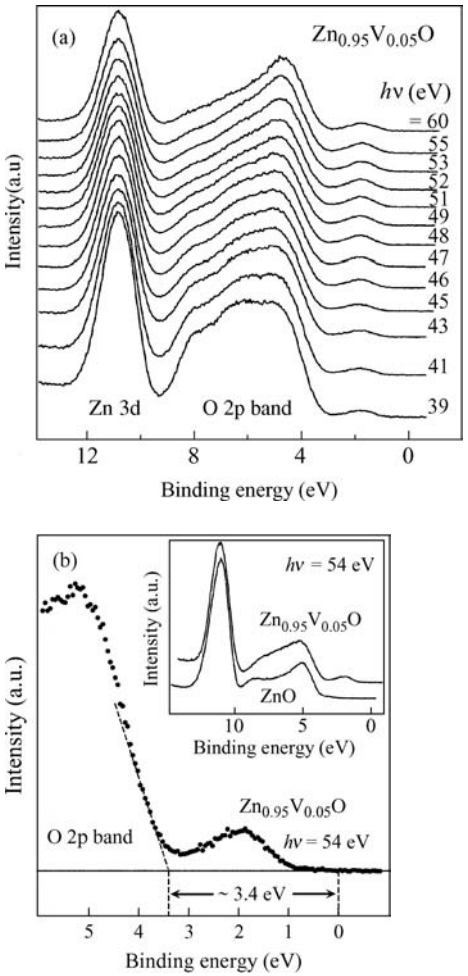

Figure 5.31 (a) Valence band (VB) spectra of $Zn_{0.95}V_{0.05}O$ in the V 3p–3d excitation region; (b) VB spectra near the Fermi level. In the inset, the VB spectra of $Zn_{0.95}V_{0.05}O$ and ZnO are compared. (Courtesy of Y. Ishida [151].)

spectra of $Zn_{0.95}V_{0.05}O$ recorded in the V 3p–3d excitation region ($h\nu = 46$ eV). The binding energy structure at 1.8 eV increased considerably on the high binding energy side of the O 2p band at the V 3p–3d absorption edge, which indicates hybridization of V 3d into the O 2p band. As shown in Figure 5.31b, a 1.8 eV structure appears within the bandgap of the host ZnO. The Fermi level is estimated to be near the Zn 4s conduction band minimum. It was therefore concluded that the electrons provided by intentional donors in this material, which were assumed to induce the ferromagnetism, are expected to have strong Zn 4s character.

The results obtained in the author's laboratory [152] on V^+ ion-implanted bulk ZnO samples grown by hydrothermal technique agree well with these findings.

Samples with $N_d - N_a \sim 3 \times 10^{18}\,cm^{-3}$ have exhibited RT ferromagnetism, and no magnetic ordering was found for samples with low electron density ($<10^{16}\,cm^{-3}$). Such a behavior for the material prepared by different techniques may be treated as only indirect evidence of carrier-mediated coupling. However, further investigations are needed to confirm or rule out this assumption.

Hong *et al*. [153] reported on magnetic properties of $Zn_{1-x}V_xO$ thin films deposited on *r*-plane sapphire substrates by PLD. The films grown below 650 °C (V concentration 8.3–11.1%) showed ferromagnetic behavior at room temperature and spin-glass at low temperature, as observed from the ZFC and FC magnetization scans in Figure 5.32. An increase of the substrate temperature above 650 °C seems to favor a secondary phase that is antiferromagnetic.

Wakano *et al* reported about the magnetic properties of Ni-doped ZnO thin films [21]. Ni was found to dissolve in ZnO up to 25% without precipitation. For films doped with 3–25% Ni, ferromagnetism was observed at 2 K. Above 30 K, superparamagnetic behavior was observed. Schwartz *et al*. [154] observed robust ferromagnetism with T_C above 350 K in Ni-doped ZnO nanocrystalline thin films prepared using high-quality colloidal DMS quantum dots as solution precursors. The resultant magnetization hysteresis loops are shown in Figure 5.33. In addition to ferromagnetism, substantial superparamagnetism was also evident from the ZFC and FC magnetization data shown in the inset of Figure 5.33. When Ni-doped ZnO nanocrystalline structures were fabricated by a modified process [155], the magnetic properties were influenced remarkably by the aggregation conditions. Distinct ferromagnetism was observed following slow (reaction-limited) aggregation, but was absent or only weakly observed following rapid aggregation.

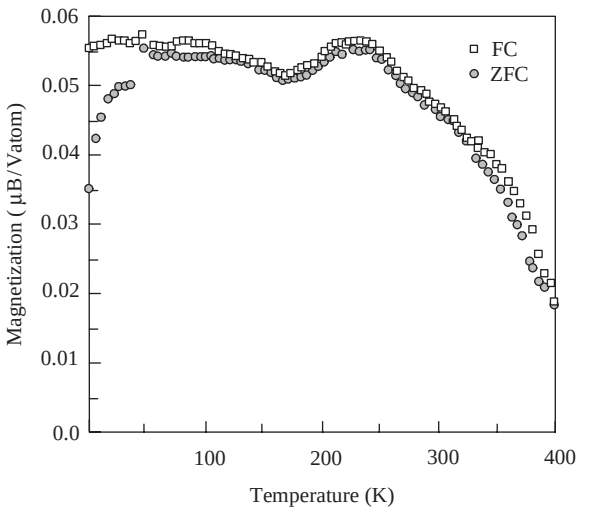

Figure 5.32 ZFC and FC magnetization curves of a V-doped film fabricated at 600 °C versus temperature measured at 0.2 T. (Courtesy of N.H. Hong [153].)

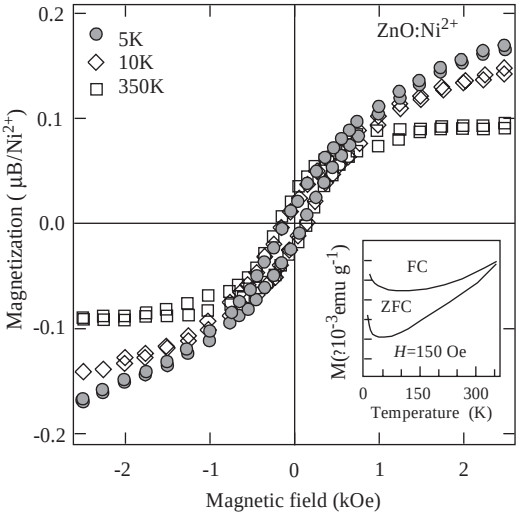

Figure 5.33 Magnetization hysteresis loops for the spin-coated 1.5% Ni^{2+}:ZnO nanocrystalline thin film at 5, 10, and 350 K. The data have been corrected only for the diamagnetic background of the substrate, measured at 350 K. The optical transparency of the thin film is demonstrated by the image in the upper left inset. The lower right inset shows ZFC and FC magnetization data collected with an applied field (H) of 150 Oe. (After Ref. [154].)

There were also efforts to produce ZnO-based DMS by doping double TM elements such as (Fe, Co) or (Fe, Cu). Cho *et al.* [119] observed room-temperature ferromagnetism for $Zn_{1-x}(Fe_{0.5}Co_{0.5})_xO$ films fabricated using reactive magnetron cosputtering. The samples seemed to have the single phase of the same wurtzite structure as pure ZnO up to $x = 0.15$. Rapid thermal annealing under vacuum led to increases in T_C, the magnetization, and the carrier concentration. Han *et al.* [104] also observed ferromagnetism in $Zn_{1-x}(Fe_{1-y}Cu_y)_xO$ bulk samples with $T_C \sim 550$ K. The saturation magnetic moment was determined to be 0.75 μ_B per Fe, and increases as the Cu-doping ratio increased up to 1%. In addition, a large magnetoresistance was observed below 100 K. The origin of ferromagnetism in $Zn_{0.95-x}Fe_{0.05}Cu_xO$ bulk samples mentioned above was investigated using zero-field [57] Fe nuclear magnetic resonance and neutron diffraction [139]. These measurements revealed that at low concentrations Cu doping into $Zn_{0.95-x}Fe_{0.05}Cu_xO$ causes the formation of $ZnFe_2O_4$ nanoclusters with inverted spinel structure, which is ferrimagnetic at room temperature. Ferromagnetism in Fe- and Cu-codoped ZnO stems from the secondary phase, while the majority of Fe ions substituted into the ZnO lattice appears to remain magnetically inert.

Because of a lack of detailed microstructural characterization in some of the reports mentioned above, there is still a good deal of controversy over the fate of these magnetic impurities (nanosize clusters/precipitates and/or individual atoms in substitutional sites) and whether the magnetic behavior is an intrinsic property of

the films or due to the presence of nanoclusters of a magnetic phase or a combination of both. In addition to macroscopic characterization, the detailed lattice structure, especially surrounding the transition metal ion in the lattice, information on the magnetic state of these ions, and the electronic state of the TM ions in a high concentration range are of fundamental importance to understand the interplay between carrier concentration and magnetic exchange coupling. It must be stated that there are still notable variations in the reported magnetic behavior, with some films exhibiting only paramagnetism and even those with ferromagnetism showing a wide range of apparent Curie temperatures. Although considerable research resulted in the observation of spontaneous magnetic moment at or above room temperature, the magnetic moment is much smaller than that expected from the concentration of the magnetic dopants, for example, 1.35 μ_B/Mn [142] as compared to the predicted value of $\sim$4 μ_B/Mn. In short, the origin of the observed ferromagnetism needs further clarification.

5.9.4
Magneto-Optical Properties of ZnO-Based DMSs

As mentioned earlier, SQUID magnetization measurements are so sensitive that the results are easily affected by the substrate and other magnetic contaminants. On the other hand, magneto-optical spectroscopy probes the magneto-optical signal as a function of photon energy, and can be used to probe the magnetic properties of the DMS materials only. The magneto-optical effect in dilute magnetic semiconductors is directly related to the interaction between the d-electrons of the transition metal ions and the s,p electrons of the host semiconductor. Particularly, MCD spectroscopy is useful for studying thin films because the effect of substrate on the spectrum is negligible unlike the magnetization measurements. The MCD signal is generally enhanced at the absorption edge (and other critical points) of the DMS host semiconductor [7, 90, 156], as a result of carrier-mediated exchange interaction between localized spins. When the MCD signal is proportional to the applied magnetic field, one can surmise the paramagnetic behavior. The theoretical background for MCD spectroscopy is provided briefly in Section 5.6.

Ando *et al.* [25, 157] discussed the advantages of magneto-optical spectroscopy for characterizing DMSs. As discussed briefly in Section 5.6, MCD can be used to detect the difference in optical absorption or reflection for left and right circularly polarized light in the presence of a magnetic field parallel to the light propagation direction. It is well known that an external magnetic field causes Zeeman splitting of the atomic energy levels. In DMS, the magnetic field effect on the s,p-band electrons is amplified by the magnetic moment of the transition metal ion through the s,p–d exchange interaction causing enhanced splitting of the band structure. A strong MCD signal indicates a strong s,p–d exchange interaction, and the polarity (positive or negative) of the MCD signal at critical point energies can be used to interpret the polarity of the exchange constant. To make the point clear and allow the reader to familiarize himself/herself with a well-behaved system, the schematic band splitting of $Cd_{1-x}Mn_xTe$ at the Γ point, which has been studied in detail, is shown in Figure 5.34 [157].

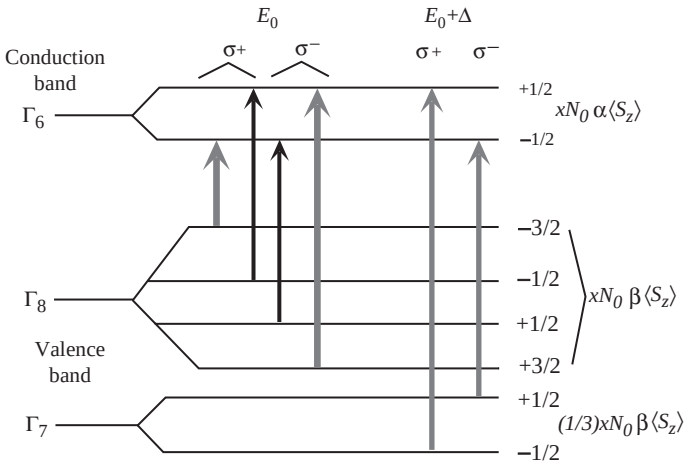

Figure 5.34 The schematic band splitting of $Cd_{1-x}Mn_xTe$ at the Γ point. Here, x is the concentration of magnetic ions, and $\langle Sz\rangle$ is the average component of the spin of the magnetic ion along the external field in the z-direction. $N_0\alpha$ is the s–d exchange constant, and $N_0\beta$ is the p–d exchange constant. $\sigma+$ presents the right circular polarization, and $\sigma-$ presents the left circular polarization. (After Ref. [157].)

Each material has its own set of critical point energies reflecting its electronic band structure. The CP of the band structure will clearly show up in the MCD spectrum that provides a fingerprint for each material. This allows the identification of the material responsible for the observed MCD signal.

Intrinsic ferromagnetism in $In_{1-x}Mn_xAs$, $Ga_{1-x}Mn_xAs$, and $Zn_{1-x}Cr_xTe$ (both are unquestionably well-behaved ferromagnetic materials) has been confirmed by using MCD spectroscopy [7, 25]. To investigate the magneto-optical properties of ZnO, Ando *et al.* [7, 25] measured the MCD spectra in films alloyed with Sc, Ti, V, Cr, Mn, Fe, Co, Ni, and Cu and grown with pulsed laser deposition on sapphire substrates. Figure 5.35 shows the MCD spectra of (0 0 0 1) oriented (Zn,TM)O films obtained at 5 K. ZnO shows a weak and positive diamagnetic MCD signal near the bandgap energy of 3.4 eV at the measurement temperature of 5 K. No enhancement of the MCD signal due to transition metal doping with Sc, Ti, V, and Cr is observed. The ZnO films doped with Mn, Fe, Co, Ni, and Cu show enhanced MCD structure at the bandgap 3.4 eV, with the signal from the Fe and Co doped samples being the most pronounced. The ZnO films doped with Mn, Fe, Co, Ni, and Cu, were therefore, argued to be DMS systems. The amplitude of the MCD signal shown in Figure 5.36 for Co-doped ZnO ($>2^\circ\ cm^{-1}\ Oe^{-1}$ for a Co mole fraction of 0.016 at 5 K) is more than two orders of magnitude larger than that for ZnO and comparable to typical II–VI DMS materials. Consequently, an increased effective g-factor was estimated from the MCD data for $Zn_{1-x}Co_xO$ ($x = 0.016$) using Equation 5.38, $g_{eff} = 9.3$, as compared to $g_{eff} = 0.14$ for ZnO. The real effective g-factor, however, may be even larger as the magneto-optical response may be weakened due to opposite polarities of the Zeeman

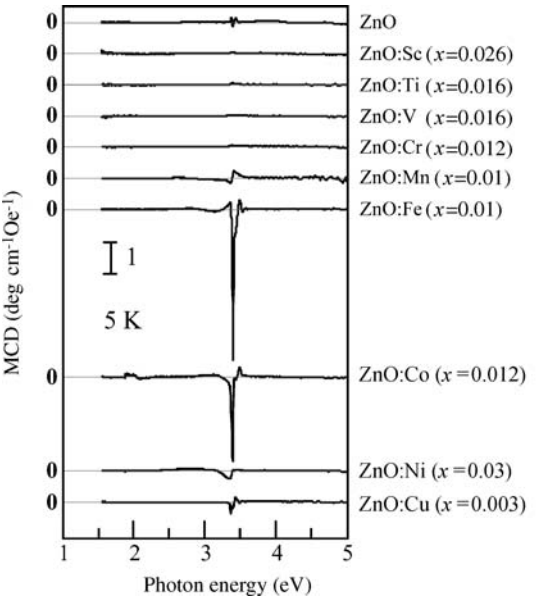

Figure 5.35 Transmission MCD spectra of ZnO and ZnO:TM at 5 K. The magnetic field dependence of the MCD amplitude was observed to be linear for all of the samples, indicating paramagnetic behavior. (Courtesy of K. Ando [7, 25].)

splits of the closely-spaced A and B valence bands as discussed in Section 5.6. The MCD feature seen near 2 eV is most likely associated with ${}^4A_2(F) \rightarrow {}^4T_1(P)$, ${}^2E(G)\mathrm{d}-d^*$ transitions of Co^{2+} ions situated at the T_d symmetry sites. However, even though ZnO thin films doped with Mn, Fe, Co, Ni, and Cu represent DMS systems, the temperature dependence of the MCD spectra indicates all these films to

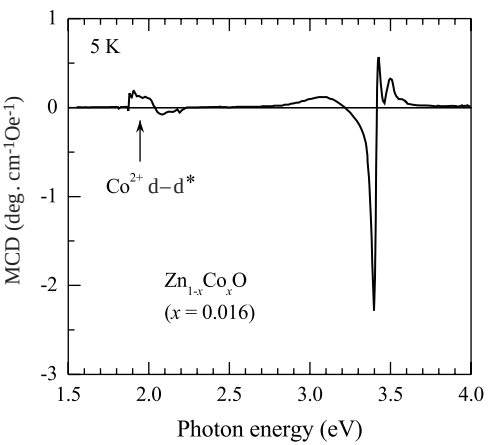

Figure 5.36 MCD spectrum of $Zn_{1-x}Co_xO$ ($x = 0.016$) at 5 K. (Courtesy of K. Ando [90].)

be paramagnetic. A ZnO sample doped with Co and reported to be ferromagnetic with a critical temperature above 300 K was also measured for MCD signal whose temperature and magnetic field dependence allowed decomposing the MCD signal into paramagnetic and ferromagnetic components, with the latter not showing peaks near 2 and 3.4 eV. Therefore, it has been concluded that the ferromagnetic component may not be related to ZnO and it may just simply be due to the Co metal. The MCD observed near the band edge for high quality $Zn_{1-x}Co_xO$ layers grown by plasma-assisted MBE on sapphire have also been shown to follow the paramagnetic behavior of isolated substitutional Co impurities even for Co contents up to 15% [158]. In the MCD data of Kittilstved *et al.* [159] for Co doped ZnO, the deeper band (2 eV) exhibited hysteresis, which might suggest Co^{2+}-residual donor–acceptor hybridization. MCD data have also been taken by another group [160] in Co, Mn, V, and Ti doped ZnO with a conclusion that above about 150 K, the magnitude of the MCD signal is dominated by ferromagnetism and is almost temperature independent although the data do not seem to be that clear.

Cathodoluminescence (CL) measurements of the TM-doped samples [8] showed two peaks at 2.97 and 3.71 eV for Cr-doped samples at the expense of the exciton emission peak of pure ZnO. The authors argue that these peaks are due to oxygen-rich local structures caused by Cr-doping, because similar but broader peaks were also observed in undoped ZnO thin films treated under oxygen-rich conditions [161]. We should mention that this correlation is not necessarily a solid one, as material development is in its infancy and there is a good deal of variation from wafer to wafer, the cause of which is not yet well understood. Moreover, CL measurements also revealed that Mn is a quencher of luminescence. In short, despite all these tantalizing results, no unequivocal indication of ferromagnetism was observed for $Zn_{1-x}TM_xO$ (TM = Sc, Ti, V, Cr, Mn, Fe, Co, Ni, and Cu) films down to 3 K. Magneto-optical response (measured by MCD) is consistent with the absorption spectra observed for Mn- and Co-doped samples [8].

We can only conclude that more work needs to be done to understand the phenomena observed in ZnO doped with TMs. As in the case of GaN, questions are raised whether TM or RE doped ZnO is really ferromagnetic and granting that it is, whether it can be manipulated as in carrier-mediated ferromagnetism. On the theoretical side, the results from different theoretical approaches do not agree well with experimental data. No single model is capable of explaining the properties of a wide class of dilute magnetic semiconductors including ZnO and GaN. Additionally, the current information about the microstructure of DMSs is insufficient, extended X-ray absorption fine structure and scanning electron microscopy studies are required to understand the detailed microscopic structure of the lattice, which is more complicated than assumed in at least some of the theoretical approaches discussed here.

On the experimental side, despite inordinate number of published papers, measurements other than those with SQUID magnetometers (which in and of itself is too sensitive and swayed by contamination/precipitates) are murky and thus do not confirm ferromagnetism. It is still not sufficiently clear if the uniformly doped host or some other phase or even defect–impurity complexes are responsible for the

observed magnetic hysteresis. Invoking other techniques, for example, MCD measurements, can shed some light on the intrinsic or extrinsic nature of magnetic ordering. Again, state-of-the-art techniques for structural investigations can give a deeper insight into phase composition as well as the nature of defect–impurity complexes. Conclusive demonstration of injection of spin-polarized carriers from ZnO-based DMS is needed as a mandatory step towards device applications. One more important issue that has to be resolved theoretically and confirmed experimentally is the existence of carrier-mediated ferromagnetic exchange in these materials, which is the most desirable exchange mechanism for manipulating spin-polarized carriers for device applications.

References

1 Liu, C., Yun, F. and Morkoç, H. (2005) Critical review of ferromagnetism in ZnO and GaN. *Journal of Material Science: Materials in Electronics (JMS, MEL)*, **16**, 555.

2 Furdyna, J.K. (1988) Diluted magnetic semiconductors. *Journal of Applied Physics*, **64**, R29.

3 Sato, K. and Katayama-Yoshida, H. (2001) *Japanese Journal of Applied Physics*, **40**, L334.

4 Schmidt, G., Ferrand, D., Molenkamp, L.W., Filip, A.T. and van Wees, B.J. (2000) Fundamental obstacle for electrical spin injection from a ferromagnetic metal into a diffusive semiconductor. *Physical Review B: Condensed Matter*, **62**, R4790.

5 Rashba, E.I. (2000) Theory of electrical spin injection: tunnel contacts as a solution of the conductivity mismatch problem. *Physical Review B: Condensed Matter*, **62**, R16267.

6 Zhu, H.J., Ramsteiner, M., Kostial, H., Wassermeier, M., Schonherr, H.P. and Ploog, K.H. (2001) Room-temperature spin injection from Fe into GaAs. *Physical Review Letters*, **87**, 016601.

7 Ando, K., Saito, H., Jin, Z., Fukumura, T., Kawasaki, M., Matsumoto, Y. and Koinuma, H. (2001) Magneto-optical properties of ZnO-based diluted magnetic semiconductors. *Journal of Applied Physics*, **89**, 7284.

8 Jin, Z., Fukumura, T., Kawasaki, M., Ando, K., Saito, H., Sekiguchi, T., Yoo, Y.Z., Murakami, M., Matsumoto, Y., Hasegawa, T. and Koinuma, H. (2001) High throughput fabrication of transition-metal-doped epitaxial ZnO thin films: a series of oxide-diluted magnetic semiconductors and their properties. *Applied Physics Letters*, **78**, 3824.

9 Saeki, H., Tabata, H. and Kawai, T. (2001) *Solid State Communications*, **120**, 439.

10 Ueda, K., Tabata, H. and Kawai, T. (2001) *Applied Physics Letters*, **79**, 988.

11 Fukumura, T., Jin, Z., Ohtomo, A., Koinuma, H. and Kawasaki, M. (1999) An oxide-diluted magnetic semiconductor: Mn-doped ZnO. *Applied Physics Letters*, **75**, 3366.

12 Fukumura, T., Jin, Z., Kawasaki, M., Shono, T., Hasegawa, T., Koshihara, S. and Koinuma, H. (2001) *Applied Physics Letters*, **78**, 958.

13 Jung, S.W., An, S.-J., Yi, G.-C., Jung, C.U., Lee, S.-I. and Cho, S. (2002) *Applied Physics Letters*, **80**, 4561.

14 Norton, D.P., Pearton, S.J., Hebard, A.F., Theodoropoulou, N., Boatner, L.A. and Wilson, R.G. (2003) *Applied Physics Letters*, **82**, 239.

15 Kim, Y.M., Yoon, M., Park, I.-W., Park, Y.J. and Lyou, Jong H. (2004) *Solid State Communications*, **129**, 175.

16 Sharma, P., Gupta, A., Rao, K.V., Owens, F.J., Sharma, R., Ahuja, R., Osorio Guillen, J.M., Johansson, B. and Gehring, G.A. (2003) *Nature Materials*, **2**, 673.

17 Rode, K., Anane, A., Mattana, R., Contour, J.-P., Durand, O. and LeBourgeois, R. (2003) *Journal of Applied Physics*, **93**, 7676.

18 Ramachandran, S., Tiwari, A. and Narayan, J. (2004) *Applied Physics Letters*, **84**, 5255.

19 Lin, H.-T., Chin, T.-S., Shih, J.-C., Lin, S.-H., Hong, T.-M., Huang, R.-T., Chen, F.-R. and Kai, J.-J. (2004) *Applied Physics Letters*, **85**, 621.

20 Norton, D.P., Overberg, M.E., Pearton, S.J., Pruessner, K., Budai, J.D., Boatner, L.A., Chisholm, M.F., Lee, J.S., Khim, Z.G., Park, Y.D. and Wilson, R.G. (2003) *Applied Physics Letters*, **83**, 5488.

21 Wakano, T., Fujimura, N., Morinaga, Y., Abe, N., Ashida, A. and Ito, T. (2001) *Physica C*, **10**, 260.

22 Pearton, S.J., Heo, W.H., Ivill, M., Norton, D.P. and Steiner, T. (2004) *Semiconductor Science and Technology*, **19**, R59.

23 Lawes, G., Risbud, A.S., Ramirez, A.P. and Seshadri, R. (2005) Absence of ferromagnetism in Co and Mn substituted polycrystalline ZnO. *Physical Review B: Condensed Matter*, **71**, 045201.

24 Rao, C.N.R. and Deepak, F.L. (2005) Absence of ferromagnetism in Mn- and Co-doped ZnO. *Journal of Materials Chemistry*, **15**, 573.

25 Ando, K., Saito, H., Zayets, V. and Debnath, M.C. (2004) Optical properties and functions of dilute magnetic semiconductors. *Journal of Physics: Condensed Matter*, **16**, S5541.

26 Reuss, F., Frank, S., Kirchner, C., Kling, R., Gruber, T. and Waag, A. (2005) Magnetoresistance in epitaxially grown degenerate ZnO thin films. *Applied Physics Letters*, **87**, 112104.

27 Dietl, T., Ohno, H., Matsukura, F., Cibert, J. and Ferrand, D. (2000) Zener model description of ferromagnetism in zinc-blende magnetic semiconductors. *Science*, **287**, 1019.

28 Ashcroft, N.W. and Mermin, N.D. (1976) *Solid State Physics*, Saunders College Publishing, Forth Worth, FL.

29 Graf, T., Goennenwein, S.T.B. and Brandt, M.S. (2003) *Physica Status Solidi b: Basic Research*, **239**, 277.

30 Ohno, H., Munekata, H., Penney, T., von Molnar, S. and Chang, L.L. (1992) *Physical Review Letters*, **68**, 2664.

31 Ohno, H. (1998) Making nonmagnetic semiconductors ferromagnetic. *Science*, **281**, 951.

32 See for example Kittel, C. (1996) *Introduction to Solid State Physics*, John Wiley & Sons, Inc. Blakemore, J.S. (1985) *Solid State Physics*, 2nd edn, Cambridge University Press. Beam, Walter (1965) *Electronics of Solids*, 7th edn, McGraw-Hill.

33 Prinz, G.A. (1998) Magnetoelectronics. *Science*, **282**, 1660.

34 Heiman, D., Shapira, Y., Foner, S., Khazai, B., Kershaw, R., Dwight, K. and Wold, A. (1984) Exchange energy, magnetization, and Raman scattering of (Cd, Mn)Se. *Physical Review B: Condensed Matter*, **29**, 5634.

35 Chakraborti, D., Narayan, J. and Prater, J. (2007) *Applied Physics Letters*, **90**, 062504.

36 Dietl, T. (2006) *Nature Materials*, **5**, 673.

37 Sato, K., Katayama-Yoshida, H. and Dederichs, P. (2005) *Japanese Journal of Applied Physics Part 2-Letters*, **44**, L948.

38 Kuroda, S., Nishizawa, N., Takita, K., Mitomo, M., Bando, Y., Osuch, K. and Dietl, T. (2007) *Nature Materials*, **6**, 440.

39 Martinez-Criado, G., Somogyi, A., Ramos, S., Campo, J., Tucoulou, R., Salome, M., Susini, J., Hermann, M., Eickhoff, M. and Stutzmann, M. (2005) *Applied Physics Letters*, **86**, 131927.

40 Bonanni, A., Kiecana, M., Simbrunner, C., Li, T., Sawicki, M., Wegscheider, M., Quast, M., Przybylińska, H., Navarro-Quezada, A., Jakiela, R., Wolos, A., Jantsch, W. and Dietl, T. (2007) Paramagnetic GaN:Fe and ferromagnetic (Ga,Fe)N: the relationship between structural, electronic, and magnetic

properties. *Physical Review B: Condensed Matter*, **75**, 125210.

41 Faraday, M. (1846) *Philosophical Transactions of the Royal Society*, **136**, 1.

42 Bartholomew, D.U., Furdyna, J.K. and Ramdas, A.K. (1986) Interband Faraday rotation in diluted magnetic semiconductor $Zn_{1-x}Mn_xTe$ and $Cd_{1-x}Mn_xTe$. *Physical Review B: Condensed Matter*, **34**, 6943.

43 Ando, K., Takahashi, K., Okuda, T. and Umehara, M. (1992) Magnetic circular dichroism of zinc-blende-phase MnTe. *Physical Review B: Condensed Matter*, **46**, 12289.

44 Ghosh, S., Sih, V., Lau, W.H., Awschalom, D.D., Bae, S.-Y., Wang, S., Vaidya, S. and Chapline, G. (2005) Room-temperature spin coherence in ZnO. *Applied Physics Letters*, **86**, 232507.

45 Beschoten, B., Johnston-Halperin, E., Young, D.K., Poggio, M., Grimaldi, J.E., Keller, S., DenBaars, S.P., Mishra, U.K., Hu, E.L. and Awschalom, D.D. (2001) Spin coherence and dephasing in GaN. *Physical Review B: Condensed Matter*, **63**, 121202.

46 Chen, W.M., Buyanova, I.A., Nishibayashi, K., Kayanuma, K., Seo, K., Murayama, A., Oka, Y., Thaler, G., Frazier, R., Abernathy, C.R., Ren, F., Pearton, S.J., Pan, C.-C., Chen, G.-T. and Chyi, J.-I. (2005) Efficient spin relaxation in InGaN/GaN and InGaN/GaMnN quantum wells: an obstacle to spin detection. *Applied Physics Letters*, **87**, 192107.

47 Buyanova, I.A., Izadifard, M., Chen, W.M., Kim, J., Ren, F., Thaler, G., Abernathy, C.R., Pearton, S.J., Pan, C.-C., Chen, G.-T., Chyi, J.-I. and Zavada, J.M. (2004) On the origin of spin loss in GaMnN/InGaN light-emitting diodes. *Applied Physics Letters*, **84**, 2599.

48 Stępniewski, R., Potemski, M., Wysmołek, A., Pakuła, K., Baranowski, J.M., Łusakowski, J., Grzegory, I., Porowski, S., Martinez, G. and Wyder, P. (1999) Symmetry of excitons in GaN. *Physical Review B: Condensed Matter*, **60**, 4438.

49 Tackeuchi, A., Kuroda, T., Shikanai, A., Sota, T., Kuramata, A. and Domen, K. (2000) No spin polarization of carriers in InGaN. *Physica E*, **7**, 1011.

50 Campo, J., Julier, M., Coquillat, D., Lascaray, J.P., Scalbert, D. and Briot, O. (1997) Zeeman splittings of excitonic transitions at the Γ point in wurtzite GaN: a magnetoreflectance investigation. *Physical Review B: Condensed Matter*, **56**, R7108.

51 Choi, C.K., Lam, J.B., Gainer, G.H., Shee, S.K., Krasinski, J.S., Song, J.J. and Chang, Yia-Chung (2002) Polarization dependence of the excitonic optical Stark effect in GaN. *Physical Review B: Condensed Matter*, **65**, 155206.

52 Reynolds, D.C., Look, D.C., Jogai, B., Litton, C.W., Cantwell, G. and Harsch, W.C. (1999) Valence-band ordering in ZnO. *Physical Review B: Condensed Matter*, **60**, 2340.

53 Julier, M., Campo, J., Gil, B. and Lascaray, J.P. (1998) Determination of the spin-exchange interaction constant in wurtzite GaN. *Physical Review B: Condensed Matter*, **57**, R6791.

54 Gil, B. and Briot, O. (1997) Internal structure and oscillator strengths of excitons in strained α-GaN. *Physical Review B: Condensed Matter*, **55**, 2530.

55 Langer, D.W., Euwena, R.N., Era, K. and Koda, T. (1970) Spin Exchange in Excitons, the Quasicubic Model and Deformation Potentials in II–VI Compounds. *Physical Review B: Condensed Matter*, **2**, 4005.

56 Gil, B., Lusson, A., Sallet, V., Said-Hassani, S.A., Triboulet, R. and Bigenwald, P. (2001) Strain-fields effects and reversal of the nature of the fundamental valence band of ZnO epilayers. *Japanese Journal of Applied Physics Part 2-Letters*, **40**, L1089.

57 Gil, B. (2001) Oscillator strengths of A, B, and C excitons in ZnO films. *Physical Review B: Condensed Matter*, **64**, 201310.

58 Thomas, D.G. (1960) The exciton spectrum of ZnO. *Journal of Physics and Chemistry of Solids*, **15**, 86.

59 Chuang, S.L. and Chang, C.S. (1996) k.p method for strained wurtzite semiconductors. *Physical Review B: Condensed Matter*, **54**, 2491.

60 Skromme, B.J. (1997) Optical and magneto-optical characterization of heteroepitaxial gallium nitride. *Materials Science and Engineering B: Solid State Materials for Advanced Technology*, **50**, 117.

61 Gruber, Th., Prinz, G.M., Kirchner, C., Kling, R., Reuss, F., Limmer, W. and Waag, A. (2004) Influences of biaxial strains on the vibrational and exciton energies in ZnO. *Journal of Applied Physics*, **96**, 289.

62 Arciszewska, M. and Nawrocki, M. (1986) *Journal of Physics and Chemistry of Solids*, **47**, 309.

63 Johnson, M., Bennett, B.R., Yang, M.J., Miller, M.M. and Shanabrook, B.V. (1997) *Applied Physics Letters*, **71**, 974.

64 Kacman, P. (2001) Spin interactions in diluted magnetic semiconductors and magnetic semiconductor structures. *Semiconductor Science and Technology*, **16**, R25.

65 Zener, C. (1951) Interaction between the d-shells in the Transitions Metals.II. Ferromagnetic Compounds of Mangenese with Perovskite Structure. *Physical Review*, **82**, 403.

66 Anderson, P.W. and Hasegawa, H. (1955) *Physical Review*, **100**, 675.

67 Matsukura, F., Ohno, H. and Dietl, T. (2002) III–V Ferromagnetic Semiconductors, in *Handbook of Magnetic Materials*, **Vol.14** (ed. K.H.J. Buschow), Elsevier, Amsterdam, pp. 1–42.

68 Sato, K. and Katayama-Yoshida, H. (2000) *Japanese Journal of Applied Physics*, **39**, L555.

69 Medvedkin, G.A., Ishibashi, T., Nishi, T., Hayata, K., Hasegawa, Y. and Sato, K. (2000) *Japanese Journal of Applied Physics*, **39**, L949.

70 Wilamowski, Z. (1990) *Acta Physica Polonica A*, **77**, 133.

71 Szczytko, J., Twardowski, A., Swiatek, K., Palczewska, M., Tanaka, M., Hayashi, T. and Ando, K. (1999) *Physical Review B: Condensed Matter*, **60**, 8304.

72 Akai, H. and Dederichs, P.H. (1993) *Physical Review B: Condensed Matter*, **47**, 8739.

73 Akai, H. (1998) *Physical Review Letters*, **81**, 3002.

74 Story, T., Galazka, R.R., Frankel, R.B. and Wolff, P.A. (1986) *Physical Review Letters*, **56**, 777.

75 Zener, C. (1951) Interaction between the d-shells in the Transitions Metals. III. Calculation of the Weiss Factors in Fe, Co, and Ni. *Physical Review*, **83**, 299.

76 Zener, C. (1951) Interaction between the d-shells in the transition metals. *Physical Review*, **81**, 440.

77 Berciu, M. and Bhat, R.N. (2001) Effects of disorder on ferromagnetism in diluted magnetic semiconductors. *Physical Review Letters*, **87**, 107203.

78 Hohenberg, P. and Kohn, W. (1964) *Physical Review*, **136**, 864.

79 Kohn, W. and Sham, L.J. (1965) *Physical Review*, **140**, 1133.

80 Kaminski, A. and Das Sarma, S. (2001) Polaron percolation in diluted magnetic semiconductors. *Physical Review Letters*, **88**, 247202.

81 Das Sarma, S., Hwang, E.H. and Kaminski, A. (2003) Temperature-dependent magnetization in diluted magnetic semiconductors. *Physical Review B: Condensed Matter*, **67**, 155201.

82 Warnock, J. and Wolff, P.A. (1985) Spherical model of acceptor-associated bound magnetic polarons. *Physical Review B: Condensed Matter*, **31**, 6579.

83 Sawicki, M., Dietl, T., Kossut, J., Igalson, J., Wojtowicz, T. and Plesiewicz, W. (1986) Influence of s–d exchange interaction on the conductivity of $Cd_{1-x}Mn_xSe$:In in the weakly localized regime. *Physical Review Letters*, **56**, 508.

84 Coey, J.M.D., Venkatesan, M. and Fitzgerald, C.B. (2005) Donor impurity band exchange in dilute ferromagnetic oxides. *Nature Materials*, **4**, 173.

85 Dietl, T. and Spalek, J. (1982) Effect of fluctuations of magnetization on the bound magnetic polaron: comparison with experiment. *Physical Review Letters*, **48**, 355.

86 Dietl, T., Matsukura, F. and Ohno, H. (2002) Ferromagnetism of magnetic semiconductors: Zhang–Rice limit. *Physical Review B: Condensed Matter*, **66**, 033203.

87 Sato, K. and Katayama-Yoshida, H. (2001) *Physica B*, **308–310**, 904.

88 Heo, Y.W., Ivill, M.P., Ip, K., Norton, D.P. and Pearton, S.J. (2004) *Applied Physics Letters*, **84**, 2292.

89 Lee, H.-J., Jeong, S.-Y., Cho, C.R. and Park, C.H. (2002) *Applied Physics Letters*, **81**, 4020.

90 Ando, K., Saito, H., Jin, Z., Fukumura, T., Kawasaki, M., Matsumoto, Y. and Koinuma, H. (2001) Large magneto-optical effect in an oxide diluted magnetic semiconductor $Zn_{1-x}Co_xO$. *Applied Physics Letters*, **78**, 2700.

91 Sato, K. and Katayama-Yoshida, H. (2001) *Japanese Journal of Applied Physics*, **40**, L651.

92 Sato, K. and Katayama-Yoshida, H. (2001) *Physica E*, **10**, 251.

93 Yamamoto, T. and Katayama-Yoshida, H. (1999) Solution using a codoping method to unipolarity for the fabrication of p-type ZnO. *Japanese Journal of Applied Physics*, **38**, L166.

94 Katayama-Yoshida, H. and Sato, K. (2003) *Physica B*, **327**, 337.

95 Sato, K. and Katayama-Yoshida, H. (2002) *Semiconductor Science and Technology*, **17**, 367.

96 Mizokawa, T., Nambu, T., Fujimori, A., Fukumura, T. and Kawasaki, M. (2002) *Physical Review B: Condensed Matter*, **65**, 085209.

97 Chien, C.-H., Chiou, S.H., Guo, G.Y. and Yao, Y.-D. (2004) *Journal of Magnetism and Magnetic Materials*, **282**, 275.

98 Yun, S.Y., Cha, G.-B., Kwon, Y., Cho, S., Soon, S.C. and Hong, C. (2004) *Journal of Magnetism and Magnetic Materials*, **272–276** (Supplement 1), E1563.

99 Lee, E.-C. and Chang, K.J. (2004) *Physical Review B: Condensed Matter*, **69**, 085205.

100 Wang, Q. and Jena, P. (2004) *Applied Physics Letters*, **84**, 4170.

101 Wang, Q., Sun, Q., Rao, B.K. and Jena, P. (2004) *Physical Review B: Condensed Matter*, **69**, 233310.

102 Wang, Q., Sun, Q., Jena, P. and Kawazoe, Y. (2004) *Physical Review B: Condensed Matter*, **70**, 052408.

103 Feng, X. (2004) Electronic structures and ferromagnetism of Cu- and Mn-doped ZnO. *Journal of Physics: Condensed Matter*, **16**, 4251.

104 Han, S.-J., Song, J.W., Yang, C.-H., Park, S.H., Park, J.-H., Jeong, Y.H. and Rhie, K.W. (2002) *Applied Physics Letters*, **81**, 4212.

105 Spaldin, N.A. (2004) *Physical Review B: Condensed Matter*, **69**, 125201.

106 Park, M.S. and Min, B.I. (2003) *Physical Review B: Condensed Matter*, **68**, 224436.

107 Venkatesan, M., Fitzgerald, C.B., Lunney, J.G. and Coey, J.M.D. (2004) Anistropic ferromagnetism in substituted ZnO. *Physical Review Letters*, **93**, 177206.

108 Tsukazaki, A., Ohtomo, A., Onuma, T., Ohtani, M., Makino, T., Sumiya, M., Ohtani, K., Chichibu, S.F., Fuke, S., Segawa, Y., Ohno, H., Koinuma, H. and Kawasaki, M. (2005) *Nature Materials*, **4**, 42.

109 Park, Y.D., Hanbicki, A.T., Erwin, S.C., Hellberg, C.S., Sullivan, J.M., Mattson, J.E., Ambrose, T.F., Wilson, A., Spanos, G. and Jonker, B.T. (2002) *Science*, **295**, 651.

110 Ando, K. (2003) Magneto-optical studies of s,p–d exchange interactions in GaN:Mn with room-temperature ferromagnetism. *Applied Physics Letters*, **82**, 100.

111 Risbud, A.S., Spaldin, N.A., Chen, Z.Q., Stemmer, S. and Seshadri, R. (2003)

Physical Review B: Condensed Matter, **68**, 205202.

112 Prellier, W., Fouchet, A., Mercey, B., Simon, Ch. and Raveau, B. (2003) *Applied Physics Letters*, **82**, 3490.

113 Avrutin, V., Özgür, Ü., Chevtchenko, S., Litton, C. and Morkoç, H. (2007) *Journal of Electronic Materials*, **36**, 483.

114 Che Mofor, A., El-Shaer, A., Bakin, A., Waag, A., Ahlers, H., Siegner, U., Sievers, S., Albrecht, M., Schoch, W., Izyumskaya, N., Avrutin, V., Sorokin, S., Ivanov, S. and Stoimenos, J. (2005) *Applied Physics Letters*, **87**, 062501.

115 Park, J.H., Kim, M.G., Jang, H.M. and Ryu, S. (2004) *Applied Physics Letters*, **84**, 1338.

116 For details of MBE growth, see Herman, M.A. and Sitter, H., (1996) *Molecular Beam Epitaxy: Fundamentals and Current Status*, 2nd edn, Springer, Berlin.

117 For details of OMVPE growth, see Stringfellow, G.B. (1999) *Organometallic Vapor-Phase Epitaxy: Theory and Practice*, 2nd edn, Academic Press, London.

118 For details of PLD growth, see Chrisey, Douglas B. and Hubler, Graham K. (1994) *Pulsed Laser Deposition of Thin Films*, John Wiley & Sons, Inc., New York.

119 Cho, Y.M., Choo, W.K., Kim, H., Kim, D. and Ihm, Y.E. (2002) Effects of rapid thermal annealing on the ferromagnetic properties of sputtered $Zn_{1-x}(Co_{0.5}Fe_{0.5})_xO$ thin films. *Applied Physics Letters*, **80**, 3358.

120 Kim, J.H., Kim, H., Ihm, Y.E. and Choo, W.K. (2002) Magnetic properties of epitaxially grown semiconducting $Zn_{1-x}Co_xO$ thing films by pulsed laser deposition. *Journal of Applied Physics*, **92**, 6066.

121 Tiwari, A., Jin, C., Kvit, A., Kumar, D., Muth, J.F. and Narayan, J. (2002) *Solid State Communications*, **121**, 371.

122 Kane, M.H., Shalini, K., Summers, C.J., Varatharajan, R., Nause, J., Vestal, C.R., Zhang, Z.J. and Ferguson, I.T. (2005) *Journal of Applied Physics*, **97**, 023906.

123 Pearton, S.J., Norton, D.P., Ip, K. and Heo, Y.W. (2004) Recent advances in processing of ZnO. *Journal of Vacuum Science & Technology B*, **22**, 932.

124 Cheng, X.M. and Chien, C.L. (2003) *Journal of Applied Physics*, **93**, 7876.

125 Lim, S., Jeong, M., Ham, M. and Myoung, J. (2004) Hole-mediated ferromagnetic properties in $Zn_{1-x}Mn_xO$ thin films. *Japanese Journal of Applied Physics*, **43**, L280.

126 Ivill, M., Pearton, S.J., Norton, D.P., Kelly, J. and Hebard, A.F. (2005) *Journal of Applied Physics*, **97**, 053904.

127 Yang, S.G., Pakhomov, A.B., Hung, S.T. and Wong, C.Y. (2002) *IEEE Transactions On Magnetics*, **38**, 2877.

128 Jedrecy, N., von Bardeleben, H.J., Zheng, Y. and Cantin, J.-L. (2004) *Physical Review B: Condensed Matter*, **69**, 041308.

129 Tuan, A.C., Bryan, J.D., Pakhomov, A.B., Shutthanandan, V., Thevuthasan, S., McCready, D.E., Gaspar, D., Engelhard, M.H., Rogers, J.W., Jr, Krishnan, K., Gamelin, D.R. and Chambers, S.A. (2004) *Physical Review B: Condensed Matter*, **70**, 054424.

130 Hong, N.H., Brize, V. and Sakai, J. (2005) *Applied Physics Letters*, **86**, 082505.

131 Fukumura, T., Yamada, Y., Toyosaki, H., Hasegawa, T., Koinuma, H. and Kawasaki, M. (2004) *Applied Surface Science*, **223**, 62.

132 Kolesnik, S. and Dabrowski, B. (2004) *Journal of Applied Physics*, **96**, 5379.

133 Guo, L.W., Peng, D.L., Makino, H., Inaba, K., Ko, H.J., Sumiyama, K. and Yao, Y. (2000) *Journal of Magnetism and Magnetic Materials*, **213**, 321.

134 Chartier, A., D'Arco, P., Dovesi, R. and Saunders, V.R. (1999) *Physical Review B: Condensed Matter*, **60**, 14042.

135 Han, S.-J., Jang, T.-H., Kim, Y.B., Park, B.-G., Park, J.-H. and Jeong, Y.H. (2003) Magnetism in Mn-doped ZnO bulk samples prepared by solid state reaction. *Applied Physics Letters*, **83**, 920.

136 Liu, C., Yun, F., Xiao, B., Cho, S-.J., Moon, Y.-T., Morkoç, H., Abouzaid, M.,

Ruterana, P., Yu, K.M. and Walukiewicz, W. (2005) *Journal of Applied Physics*, **97**, 126107.

137 Kolesnik, S., Dabrowski, B. and Mais, J. (2004) *Journal of Applied Physics*, **95**, 2582.

138 Brumage, W.H., Dorman, C.F. and Quade, C.R. (2001) *Physical Review B: Condensed Matter*, **63**, 104411.

139 Shim, J., Hwang, T., Lee, S., Park, J., Han, S. and Jeong, Y.H. (2005) *Applied Physics Letters*, **86**, 082503.

140 For more specific information of these characterization methods, the readers are referred to Brundle, C.R., Evans, C.A., Jr, and Wilson, S. (1992) *Encyclopedia of Materials Characterization: Surfaces, Interfaces, Thin Films*, Butterworth-Heinemann, London.

141 Jin, Z., Yoo, Y.-Z., Sekiguchi, T., Chikyow, T., Ofuchi, H., Fujioka, H., Oshima, M. and Koinuma, H. (2003) *Applied Physics Letters*, **83**, 39.

142 Kittilstved, K.R., Norberg, N.S. and Gamelin, D.R. (2005) *Physical Review Letters*, **94**, 147209.

143 Kunisu, M., Oba, F., Ikeno, H., Tanaka, I. and Yamamoto, T. (2005) *Applied Physics Letters*, **86**, 121902.

144 Özgür, Ü., Alivov, Ya.I., Liu, C., Teke, A., Reshchikov, M., Doğan, S., Avrutin, V., Cho, S.-J. and Morkoç, H. (2005) *Journal Applied Physics*, **98**, 04301.

145 Jalbout, A.F., Chen, H. and Whittenburg, S.L. (2002) *Applied Physics Letters*, **81**, 2217.

146 Lim, S.-W., Hwang, D.-K. and Myoung, J.-M. (2003) *Solid State Communications*, **125**, 231.

147 Koidl, P. (1977) *Physical Review B: Condensed Matter*, **15**, 2493.

148 Jin, Z., Murakami, M., Fukumura, T., Matsumoto, Y., Ohtomo, A., Kawasaki, M. and Koinuma, H. (2000) *Journal of Crystal Growth*, **214–215**, 55.

149 Jin, Z.-W., Fukumura, T., Hasegawa, K., Yoo, Y.-Z., Ando, K., Sekiguchi, T., Ahmet, P., Chikyow, T., Hasegawa, T., Koinuma, H. and Kawasaki, M. (2002) Optical and electrical properties of Co doped epitaxial ZnO films. *Journal of Crystal Growth*, **237**, 548.

150 Ramachandran, S., Tiwari, A., Narayan, J. and Prater, J.T. (2005) Epitaxial growth and properties of $Zn_{1-x}V_xO$ diluted magnetic semiconductor thin films. *Applied Physics Letters*, **87**, 172502.

151 Ishida, Y., Hwang, J.I., Kobayashi, M., Fujimori, A., Saeki, H., Tabata, H. and Kawai, T. (2004) High-energy spectroscopy study of ferromagnetic diluted magnetic semiconductor $Zn_{1-x}V_xO$. *Physica B*, **351**, 304.

152 Avrutin, V., Özgür, Ü., Lee, H., Bo Xiao, C., Liu, H., Morkoç, A., El-Shaer, A., Mofor, A. Che, Bakin, A., Waag, Izyumskaya, N., Schoch, W., Sorokin, S., Ivanovm, S. and Callahan, M. (2006) Optical and magneto-optical studies of ZnO doped with transition metals. Proceedings of SPIE – The International Society for Optical Engineering, Vol. 6122, Zinc Oxide Materials and Devices, 61220B.

153 Hong, N.H., Sakai, J. and Hassini, A. (2005) *Journal of Physics: Condensed Matter*, **17**, 199.

154 Schwartz, D.A., Kittilstved, K.R. and Gamelin, D.R. (2004) Above room temperature ferromagnetic Ni^{2+}-doped ZnO films prepared from colloidal diluted magnetic semiconductor quantum dots. *Applied Physics Letters*, **85**, 1395.

155 Radovanovic, P.V. and Gamelin, D.R. (2003) *Physical Review Letters*, **91**, 157202.

156 Ando, K., Hayashi, T., Tanaka, M. and Twardowski, A. (1998) *Journal of Applied Physics*, **83**, 6548.

157 Ando, K. (2000) *Magneto-Optics*, (eds S. Sugano and N. Kojima), Springer, Berlin, p. 211.

158 Pacuski, W., Ferrand, D., Cibert, J., Deparis, C., Gaj, J.A., Kossacki, P. and Morhain, C. (2006) Effect of the s,p–d exchange interaction on the excitons in $Zn_{1-x}Co_xO$ epilayers. *Physical Review B: Condensed Matter*, **73**, 035214.

159 Kittilstved, Kevin R., Liu, William K. and Gamelin, Daniel R. (2006) Electronic

structure origins of polarity dependent high-T_c ferromagnetism in oxide diluted magnetic semiconductors. *Nature Materials*, **5**, 291.

160 Neal, J.R., Behan, A.J., Ibrahim, R.M., Blythe, H.J., Ziese, M., Fox, A.M. and Gehring, G.A. (2006) Room-temperature magneto-optics of ferromagnetic transition-metal-doped ZnO thin films. *Physical Review Letters*, **96**, 197208.

161 Sekiguchi, T., Haga, K. and Inaba, K. (2000) *Journal of Crystal Growth*, **214**, 68.

6
Bandgap Engineering

A crucial threshold in designing modern optoelectronic and electronic devices is the realization of bandgap engineering to create barrier layers and quantum wells in device heterostructures. To realize such optoelectronic devices, modulation of the bandgap is required. This has been demonstrated by the development of $Mg_xZn_{1-x}O$ [1–13] and $Be_xZn_{1-x}O$ [14, 15] alloys for the larger bandgap material and $Cd_yZn_{1-y}O$ alloy for the smaller bandgap material [1, 13, 16–21], allowing bandgap tuning in a wide range. The energy gap $E_g(x)$ of the ternary semiconductor $A_xZn_{1-x}O$ (where A = Mg, Be, or Cd) is determined by the following equation [22]:

$$E_g(x) = (1-x)E_{ZnO} + xE_{AO} - bx(1-x), \tag{6.1}$$

where b is the bowing parameter and E_{AO} and E_{ZnO} are the bandgap energies of compounds AO (MgO, CdO, and BeO) and ZnO, respectively. The bowing parameter b depends on the difference in electronegativities of the end binaries ZnO and AO. The bandgap can be increased (or decreased) by incorporating Mg [3–5] and Be [14, 15] (Cd [16–18]) into ZnO. The bandgap versus the in-plane lattice constant for all the three ternaries mentioned above, namely, $Be_zZn_{1-z}O$, $Mg_xZn_{1-x}O$, and $Cd_yZn_{1-y}O$ is shown in Figure 6.1. One should exercise caution in using the above expression for large mole fractions of Mg, Cd, and Be as Mg containing ZnO changes to cubic beyond 40%, and the bowing parameters are not well known for the remaining ternaries.

Figure 6.2 shows the dependence of the optical bandgaps of $Cd_yZn_{1-y}O$ and $Mg_xZn_{1-x}O$ alloys on the composition of Cd and Mg in the ZnO lattice. Data for $Cd_yZn_{1-y}O$ are limited to small mole fractions and data for $Mg_xZn_{1-x}O$ are limited to compositions corresponding to the wurtzite phase. Figure 6.3 shows the a and c lattice parameters as a function of composition for $Cd_yZn_{1-y}O$ with small Cd composition and for wurtzite compositions of $Mg_xZn_{1-x}O$. The relatively small change in the lattice parameters with composition as compared to the case of GaN and its ternaries is useful for heterojunction formation without misfit dislocation generation. For example, a (Cd,Zn)O/(Mg,Zn)O heterojunction having nearly a perfect lattice match between the heterolayers with a maximum barrier height of 0.09 eV can be realized by choosing an appropriate combination of Cd and Mg concentrations, because a-parameters for both layers are monotonically increasing functions of the alloy composition. This is a substantial advantage over (In,Ga)N/(Al,

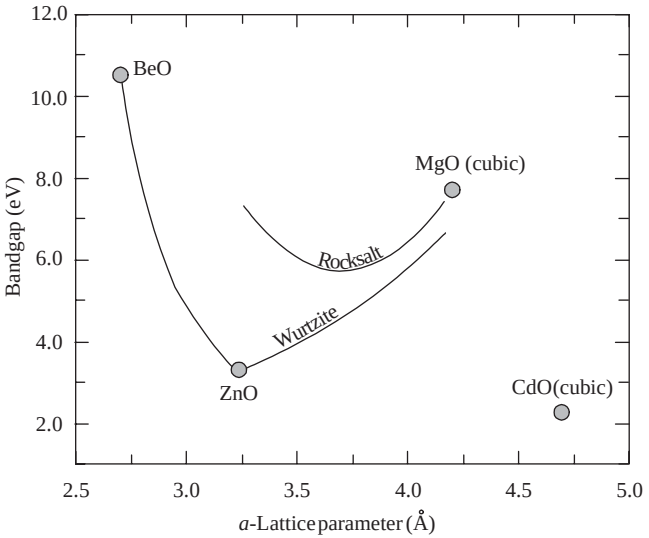

Figure 6.1 Bandgap versus in-plane lattice constant for the ternaries of ZnO, namely, $Be_zZn_{1-z}O$, $Mg_xZn_{1-x}O$, and $Cd_yZn_{1-y}O$. Note that the end binaries MgO and CdO are cubic in their equilibrium state. While the bandgap versus composition for $Mg_xZn_{1-x}O$ is reasonably established, those for $Be_zZn_{1-z}O$ and $Cd_yZn_{1-y}O$ are not. The bandgaps for cubic and wurtzitic varieties of $Mg_xZn_{1-x}O$ are given.

Ga)N MQWs because, in addition to misfit, if the lattice constant of the well layer differs from that of the barrier layer in a wurtzite structure, strain field exists inside the well layers, which causes polarization charge and the associated quantum-confined Stark effect.

6.1 $Mg_xZn_{1-x}O$ Alloy

$Mg_xZn_{1-x}O$ alloy has been considered as a suitable material for the barrier layers in ZnO/(Mg, Zn)O superlattice structures [1], because alloying ZnO with MgO ($E_g \sim 7.7$ eV) [23, 24] enables widening of the bandgap of ZnO. According to the phase diagram of the ZnO–MgO binary system, the thermodynamic solid solubility of MgO in ZnO is less than 4 mol% [25]. Furthermore, ZnO has a wurtzite structure ($a = 3.24$ Å and $c = 5.20$ Å, reiterating to contrast MgO), while MgO has a cubic structure ($a = 4.24$ Å). The exciton binding energy in cubic MgO ($E_B \sim 80$ meV) [24] is also larger than that in wurtzite ZnO (60 meV), which bodes well for high Mg content material in that it might be advantageous for deep UV excitonic light emitter applications.

One of the first reports on the synthesis of $Mg_xZn_{1-x}O$ with a Mg content of up to 33% was presented by Ohtomo *et al.* [2] by pulsed laser deposition (PLD). Figure 6.4

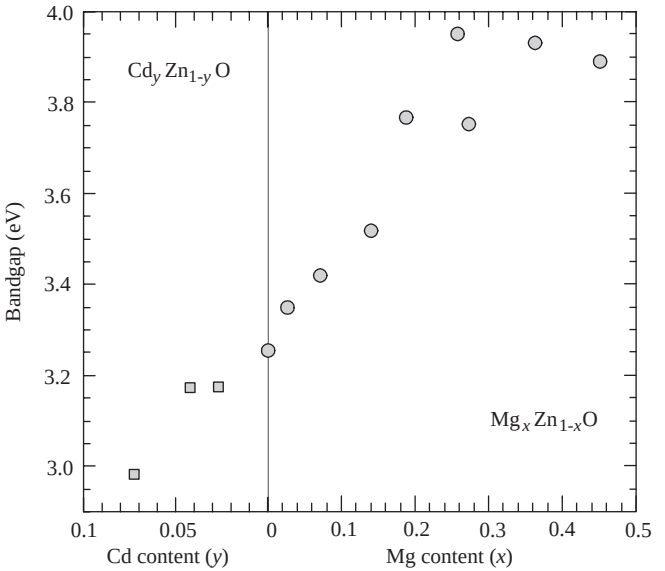

Figure 6.2 Optical bandgaps of $Cd_yZn_{1-y}O$ and $Mg_xZn_{1-x}O$ alloys as a function of Cd and Mg composition in the ZnO lattice. Data are limited for $Cd_yZn_{1-y}O$ to small compositional fractions. The data shown for $Mg_xZn_{1-x}O$ are for compositions corresponding to wurtzite structure. (Data provided by A. Ohtomo.)

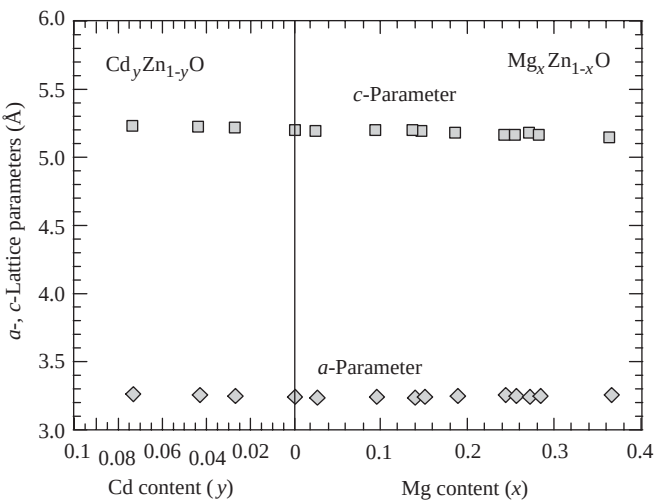

Figure 6.3 Lattice parameters *a* and *c* for $Cd_yZn_{1-y}O$ and $Mg_xZn_{1-x}O$ alloys as a function of Cd and Mg composition in the ZnO lattice. The data available for $Cd_yZn_{1-y}O$ are for small compositional fractions. The data shown for $Mg_xZn_{1-x}O$ are for compositions corresponding to wurtzite structure. Note the relatively small change in lattice parameters with composition, which would allow formation of heterostructure without any concern about misfit dislocation generation at the interfaces. (Data provided by A. Ohtomo.)

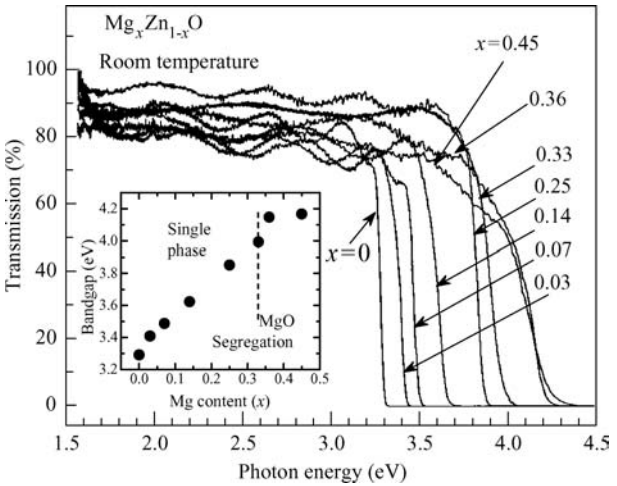

Figure 6.4 Transmittance spectra of $Mg_xZn_{1-x}O$ films measured at room temperature. The inset shows the bandgap (E_g) determined from the spectra assuming an $\alpha \propto (h\nu - E_g)$ [2] dependence, where α and $h\nu$ are the absorption coefficient and the photon energy, respectively. (Courtesy of A. Ohtomo [2].)

shows the transmittance spectra measured at room temperature of this alloy. The bandgap E_g linearly increases with x up to 4.15 eV for $0 \leq x \leq 0.36$ and saturates for higher Mg concentrations due to MgO segregation (Figure 6.4, inset). This indicates that $Mg_xZn_{1-x}O$ is a suitable material for barrier layers in ZnO/(Mg,Zn)O heterostructures with a bandgap offset up to 0.85 eV. A linear dependence of E_g on x up to 0.36 shows that the bowing parameter b is 0 eV, although a final declaration must wait for additional and more refined experiments. In other material systems, the accuracy of the bowing parameter determination was shown to depend on the quality of the measurement near the midpoint between the end binaries. This is, however, not quite feasible in $Mg_xZn_{1-x}O$ as it begins to transform from a wurtzitic symmetry to a cubic (rocksalt) one. Increasing the Mg composition further resulted in $Mg_xZn_{1-x}O$ films in metastable cubic phase with bandgaps above 5.0 eV [4]. The Mg content in the crystal was observed to be strongly dependent on the growth temperature that causes strong dependence of bandgap energy on the growth temperature ranging from room temperature to 750 °C.

The compositional dependence of the bandgap parameter as well as the a and c lattice parameters for the $Mg_xZn_{1-x}O$ alloy has been studied over the entire compositional range [2, 4, 7, 26–32]. As expected, the film quality is inferior in the wurtzite-cubic transition region where mixture of the two structures may be present. The bandgap data versus composition for both wurtzite and rocksalt portions are shown in Figure 6.5. Also shown is the fit to the Γ point E_0^A transitions for the wurtzitic ternary using

$$E_0^A(x) = E_0^A(x=0) + xp^A + x^2q^A, \tag{6.2}$$

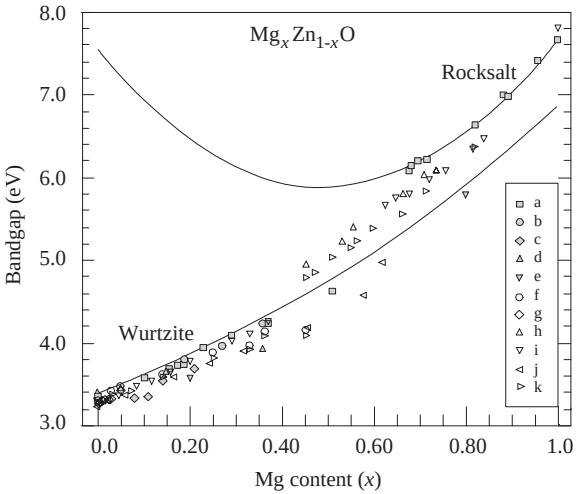

Figure 6.5 The bandgap dependence of $Mg_xZn_{1-x}O$ over the entire compositional range. Energies of the fundamental band-to-band transitions E_0^A of wurtzitic ZnO and those of rocksalt structure. It should be kept in mind that the layers in the region corresponding to wurtzite-cubic transitions might be of mixed structure. (a) Refs [37–39] (spectroscopic ellipsometry), (b) Ref. [40] (transmission), (c) Ref. [41] (spectroscopic ellipsometry), (d) Ref. [42] (transmission), (e) Ref. [43] (spectroscopic ellipsometry), (f) Ref. [2] (transmission), (g) Ref. [10] (transmission), (h) Ref. [4] (transmission), (i) Ref. [29] (transmission), (j) Ref. [7] (transmission), and (k) Ref. [30] (transmission). (Data provided by M. Schubert and A. Ohtomo and data from Refs [26, 28].)

with $E_0^A(x=0)=3.37\,\text{eV}$, $p^A=1.93\,\text{eV}$, and $q^A=1.57\,\text{eV}$. Similarly, the bandgap versus the composition can be empirically determined with parameters $E_0^D=7.6\,\text{eV}$, $p^D=-7\,\text{eV}$, and $q^D=7\,\text{eV}$, the results of which are also shown with a solid line in Figure 6.5. The bandgap of the relaxed wurtzite MgO structure seems to be $E_0^A(x=1)=6.9\,\text{eV}$, and the bandgap of the rocksalt ZnO $E_0^D(x=0)=7.6\,\text{eV}$. However, the theoretical estimate for rocksalt ZnO bandgap is about 5.4 eV and it is indirect with the associated Γ point gap energy $E_0^D(x=0)=6.54\,\text{eV}$, which is much larger than the $E_0^A(x=0)=3.34\,\text{eV}$ of the wurtzite ZnO [33–35].

The dependence of the a and c lattice parameters for the $Mg_xZn_{1-x}O$ alloy as a function of composition up to the wurtzite rocksalt transition is shown in Figure 6.6. The a lattice parameter for the rocksalt phase above the transition composition is also shown in Figure 6.6. The quality of the layers in the transition region as well as the mixed phase nature of the layers gives rise to a wide transition region within which reliable lattice parameter data are not available. The maximum Mg incorporation for the single-phase wurtzite MgZnO has been reported to be 43% for samples grown on (1 1 1)-oriented Si by molecular beam epitaxy (MBE) [36]. The bandgap dependence on Mg composition (x) was found to be linear: $E_g(x)=3.37+2.51x$.

Vibrational properties of $Mg_xZn_{1-x}O$ have been measured over the entire compositional range covering the wurtzite structure on the low end and cubic on the high end. The phonon mode frequencies of $Mg_xZn_{1-x}O$ versus x, as obtained by utilizing

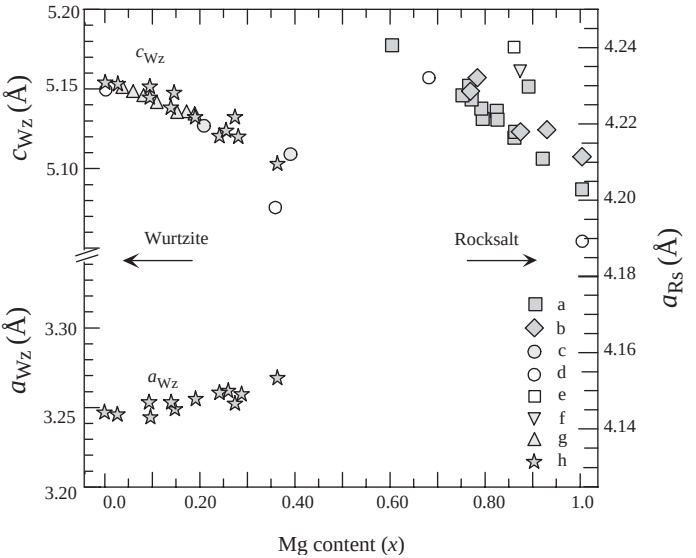

Figure 6.6 The dependence of *a* and *c* lattice parameters for the wurtzite $Mg_xZn_{1-x}O$ (in the composition range corresponding to the wurtzite phase) and the *a* lattice parameter for rocksalt phase of $Mg_xZn_{1-x}O$ (in the composition range corresponding to the rocksalt phase). (a) Refs [44, 45], (b) Ref. [46], (c) Ref. [47], (d) Ref. [31], (e) Ref. [4], (f) Ref. [48], (g) Ref. [49], and (h) Ref. [2]. (Data kindly provided by A. Ohtomo.)

Raman scattering and IR spectroscopic ellipsometry (IRSE), have been reported [26, 27, 50] and are reproduced in Figure 6.7 for $0 \leq x \leq 1$. The A_1 symmetry is indicated by triangles in Figure 6.7a and the E_1 symmetry (triangles) in Figure 6.7b, both for wurtzitic ternary, and with circles for the cubic $Mg_xZn_{1-x}O$ thin films. Empty and filled symbols represent TO and LO modes, respectively. The dashed lines are linear fits to the modes of the cubic $Mg_xZn_{1-x}O$ thin films [50], the solid lines represent the calculations using the modified random element isodisplacement (MREI) model [51] for wurtzite $Mg_xZn_{1-x}O$ thin films redrawn from Ref. [52]. The shaded area marks the compositional range where the phase transition occurs.

For the wurtzitic $Mg_xZn_{1-x}O$ thin films (corresponding to compositions somewhat below $x \leq 0.53$), a one-mode behavior with an additional weak mode between the TO and LO modes for the phonons with E_1 and A_1 symmetries has been observed. The A_1(TO), A_1(LO), and the upper branch of the E_1(LO) modes of the hexagonal $Mg_xZn_{1-x}O$ show a nearly linear behavior. On the other hand, the lower branch of the E_1(LO) modes and the two E_1(TO) branches exhibit a nonlinear behavior. The MREI model describes well the phonon mode behavior versus *x*, with a resulting good agreement for the E_1(TO), A_1(TO), and A_1(LO) branches [52]. The additional modes associated with the upper TO branch with E_1 symmetry have been assigned to the mixed mode of the $Mg_xZn_{1-x}O$ alloy that originates from the local mode $\omega_{loc,\ ZnO:Mg}$ of Mg in ZnO [26, 27]. An extrapolation to $x = 0$ leads to an experimental value of $\omega_{loc,\ ZnO:Mg} = 509\,cm^{-1}$ that agrees well with the calculated local mode

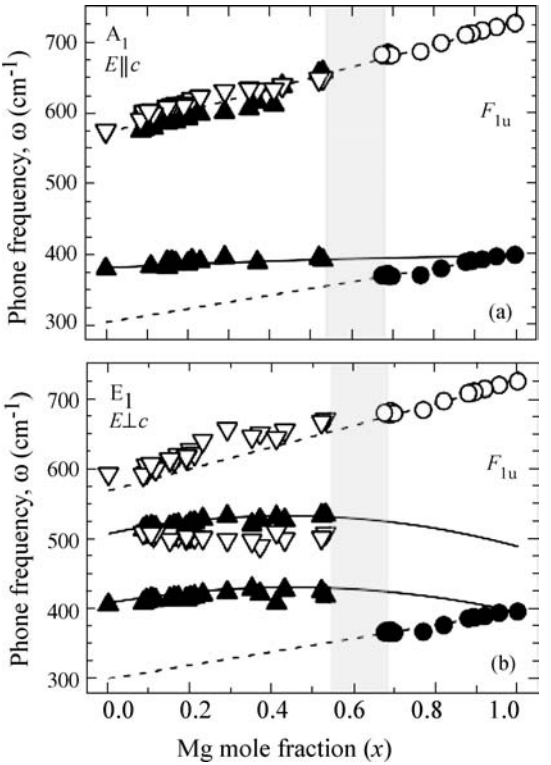

Figure 6.7 Phonon mode frequencies of wurtzite $Mg_xZn_{1-x}O$ thin films with A_1 symmetry [triangles in (a)] and E_1 symmetry [triangles in (b)], and of cubic $Mg_xZn_{1-x}O$ thin films (circles, F_{1u} mode) in dependence on the Mg mole fraction x (data from Refs [27, 46, 50]). Empty and filled symbols represent TO and LO modes, respectively. The dashed lines are linear fits to the modes of the cubic $Mg_xZn_{1-x}O$ thin films [50], the solid lines represent the modified random element isodisplacement (MREI) calculations for the wurtzite $Mg_xZn_{1-x}O$ thin films redrawn from Ref.[52]. The shaded area marks the composition range where the phase transition occurs. (Courtesy of C. Bundesmann and M. Schubert [54].)

$\omega_{loc,\ ZnO:Mg} = 518\,cm^{-1}$ obtained using the model described in Ref. [53]. A detailed collage of the infrared optical properties of the MgZnO alloy has been reported [54].

Focusing our attention now on cubic $Mg_xZn_{1-x}O$ thin films with $x \geq 0.69$, a one-mode behavior was found by IRSE, where both the TO and LO modes shift linearly with x [26, 27]. The vibrational mode frequencies of the cubic MgO thin film agree well with those of MgO single crystals ($\omega_{TO} = 401\,cm^{-1}$, $\omega_{LO} = 719\,cm^{-1}$) [53]. The shift in the TO and LO modes with mole fraction, x, has been successfully represented by a linear compositional dependence in the form of $\omega_{TO,LO}(x) = xm_{_{TO,LO}} + n_{TO,LO}$. The coefficients for the best fit are $m_{TO} = 97(4)\ cm^{-1}$, $n_{TO} = 300\,(3)\,cm^{-1}$, $m_{LO} = 157(10)\,cm^{-1}$, and $n_{LO} = 571(9)\,cm^{-1}$, where the values in parentheses represent error bars from 90% confidence limits [27]. An extrapolation to $x = 0$ yields a value of $\omega_{TO} \sim 300\,cm^{-1}$ and $\omega_{LO} \sim 570\,cm^{-1}$, which would represent the ω_{TO} and ω_{LO} modes, respectively, for cubic ZnO.

While there are no experimental data available for cubic ZnO at atmospheric pressure, *ab initio* calculations for phonon properties of cubic ZnO, which relied on experimental data of rocksalt ZnO studied under high pressures (~8 GPa) as input parameters, have been undertaken [55]. The predictions by such an exercise for ω_{TO} and ω_{LO} lead to 235 cm^{-1} and 528 cm^{-1}, respectively, for cubic ZnO. The values are smaller than those obtained by extrapolating the IRSE analysis. However, it should be pointed out that both extrapolations follow the same trend in predicting phonon mode frequencies and that they are smaller than those of hexagonal ZnO. The width of phonon modes depends on sample quality and processes that lead to broadening. A discussion of phonon mode broadening parameters can be found in Ref. [26, 27].

Changing the topic to spectral absorption, Teng *et al.* [40] measured the room-temperature absorption coefficients and exciton binding energies of $Mg_xZn_{1-x}O$ epitaxial films grown by PLD on sapphire substrates with x up to 0.36 by transmission spectroscopy. The excitonic absorption features were clearly visible at room temperature despite alloy broadening. As expected, the exciton broadening parameters for these ternary alloys were found to be much larger than those of ZnO. However, the broadening is compensated by the extremely high binding energy of the exciton. The binding energies, E_B, for A, B, and C excitons, extracted using broadened Lorentzian lineshape fits to the excitonic absorption data, were independent of the Mg composition, x (60.4 meV for A, 51.5 meV for B, and 50.5 meV for C exciton) for thin films having Mg compositions 0.19, 0.27, and 0.36 [40]. However, spectroscopic ellipsometry measurements on wurtzite-phase MgZnO grown also by PLD on *c*-sapphire, with Mg content up to 29%, showed a strong bowing in E_B, which decreased from 61 meV for ZnO to a minimum value of 50 meV for $x = 0.17$ and then increased to 58 meV for $x = 0.29$ [37]. For rocksalt MgZnO, reports show E_B decreasing linearly from ~85.3 meV to ~60 meV with decreasing Mg content from 1 to 0.68 [38], suggesting that there is a discontinuity near the phase-transition region.

The bandgap energy of the rocksalt $Mg_xZn_{1-x}O$ thin films has been shown to exhibit strong bowing using spectroscopic ellipsometry [38]. Consistent with the analysis of bulk crystals ($E_g = 7.77$ eV, $E_B \sim 80$ meV) [24], the bandgap for rocksalt MgO was 7.764 ± 0.005 eV with an exciton binding energy of 85.3 ± 1.5 meV [38]. The dependence of the bandgap on the Mg content between 0.68 and 1 was well explained by a second-order polynomial:

$$E_g(x) = 7.6 \pm 0.5 - (7 \pm 1)x + (7 \pm 1)x^2, \tag{6.3}$$

which suggests a rocksalt ZnO bandgap of 7.6 eV, consistent with the direct bandgap (Γ point) theoretical estimate of 6.64 eV [33], and a bowing parameter of $b = 7$ eV.

Ohtomo *et al.* [3] studied the thermal stability of the wurtzite-phase $Mg_xZn_{1-x}O$ alloy and $ZnO/Mg_xZn_{1-x}O$ bilayers grown by laser molecular beam epitaxy. When a $Mg_{0.23}Zn_{0.78}O$ film was annealed, the segregation of MgO started at 850 °C and the bandgap was reduced to the value for a film with $x = 0.15$ after annealing at 1000 °C. The $Mg_{0.15}Zn_{0.85}O$ films showed no change in the bandgap even after annealing at 1000 °C. From these results, authors concluded that the thermodynamic solubility limit of MgO in $Mg_xZn_{1-x}O$ epitaxial film is about 15%. In addition, the thermal diffusion of Mg across the $Mg_xZn_{1-x}O/ZnO$ interface was observed only after

annealing above 700 °C. The bowing parameter of the as-grown films calculated using the bandgap values obtained from the absorption spectra is very high ($b = 3.11$). As will be discussed subsequently, others reported zero bowing parameter, meaning a linear relationship between the composition and the bandgap. The discrepancy is a sign of the nascent nature of the field.

Gruber *et al.* [5] grew MgZnO epilayers and ZnO/MgZnO quantum well structures by MOVPE and studied their properties. All the samples were grown on GaN/sapphire templates in a horizontal flow reactor at a growth temperature of 600 °C. A 1 μm ZnO buffer was also included to improve the quality of the structures. Diethylzinc (DEZn), bis(methylcyclopentadienyl)magnesium ($MeCp_2Mg$), and nitrous oxide were used as the zinc, magnesium, and oxygen precursors, respectively. The Mg incorporation into the ZnO host material and its effect on the bandgap was determined by PL measurements. An increase of 200 meV in the bandgap at a Mg concentration of 10% has been achieved, and using MgZnO as the barrier material, ZnO/MgZnO quantum wells with different well widths were grown. The quantum well luminescence showed the quantization behavior and an enhancement in the exciton binding energy ($E_B > 96$ meV). The exciton binding energy is much higher than that in ZnO, but needs to be corroborated. The blueshift of the PL emission for the deposited $Zn_{1-x}Mg_xO$ epilayers as a function of the Mg supply (composition, i.e., the relative $MeCp_2Mg$/DEZn flux ratio) showed almost a linear dependence suggesting zero bandgap bowing. This is in some sense expected because for mole fractions well below the midpoint, the band is not bowed all that much and linear relationship between the bandgap and the composition ensues. Had the ternary not transformed into cubic (rocksalt), a more meaningful bowing parameter could have been defined.

6.2
$Be_xZn_{1-x}O$ Alloy

Substitution of Be for Zn increases the bandgap of ZnO. Unlike MgZnO that changes into the cubic form near 40% Mg concentration, $Be_zZn_{1-x}O$ is wurtzitic throughout the entire compositional range as the equilibrium state of BeO is wurtzitic. Ryu *et al.* [14] investigated this ternary up to a Be concentration of 60%. As indicated in Figure 6.1, the energy bandgap of $Be_zZn_{1-x}O$ can, in theory, range from the bandgap of ZnO (3.3 eV) to that of BeO (10.6 eV). It should be noted that the bandgap of BeO is not well established and reported values range from 7.8 to 10.7 eV [56, 57]. Compared to wurtzite ZnO ($a = 3.25$ Å and $c = 5.20$ Å), BeO has much smaller lattice constants: $a = 2.698$ Å and $c = 3.38$ Å [58, 59].

Ryu *et al.* [60] used a hybrid beam deposition (HBD) method to attain $Be_zZn_{1-x}O$ layers. This method collectively employs some features of PLD, MBE, and chemical vapor deposition (CVD). Plasma created by laser ablation from a metal oxide target and oxygen from an RF-plasma source are used concomitantly for increased reactive oxygen flux. For doping purposes, evaporation of solid sources as in the case of MBE or gas sources as in the case of MBE or CVD were used. Ryu *et al.* [15] applied the $Be_zZn_{1-x}O$/ZnO heterojunction system to produce electroluminescence from what

was termed as p–n junction LEDs comprised of a $Be_zZn_{1-x}O$/ZnO active layer containing seven quantum wells. Arsenic and gallium were used for p-type and n-type doping, respectively. The quantum well region was straddled with an n-type $Be_{0.3}Zn_{0.7}O$ and a p-type $Be_{0.3}Zn_{0.7}O$ followed by a p-type ZnO layer. The entire structure was grown on n-type ZnO substrate. Two dominant electroluminescence peaks, one between 360 and 390 nm and a broad peak at 550 nm, were observed.

6.3 $Cd_yZn_{1-y}O$ Alloy

$Mg_xZn_{1-x}O$ alloy has been considered as a suitable material for barrier layers due to its wider bandgap than that of ZnO. For narrower bandgaps, which are desirable for wavelength tunability and attaining bandgaps corresponding to the visible spectrum, $Cd_yZn_{1-y}O$ alloy would be a good candidate because of the small direct bandgap of CdO (2.3 eV) [61]. However, the equilibrium structure of CdO is cubic, with a lattice constant of $a = 4.69$ Å [14, 18, 59]. The maximum Cd incorporation, by remote plasma-enhanced MOCVD, achieved for the wurtzite phase so far is ~70%, which corresponds to a minimum bandgap of 1.85 eV [62].

Makino *et al.* [13] have demonstrated single-phase $Cd_yZn_{1-y}O$ alloy films grown by PLD on sapphire (0 0 0 1) and $ScAlMgO_4$ (0 0 0 1) substrates with Cd content of up to 7%. As shown in Figure 6.8, the bandgap energy, E_g, decreases as Cd content (y)

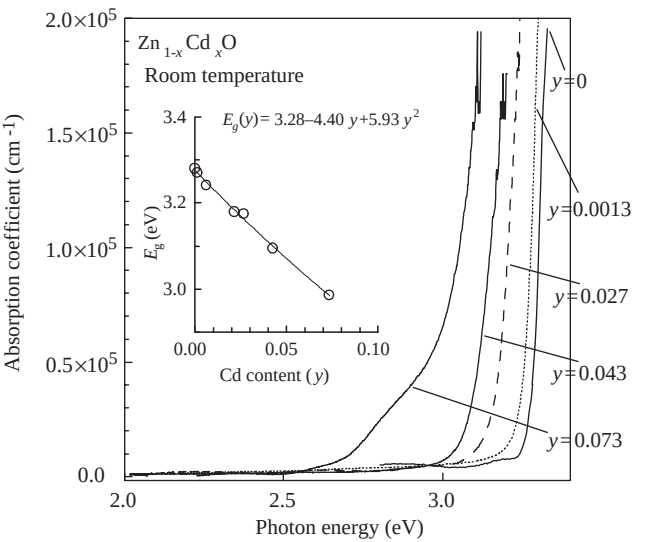

Figure 6.8 Concentration (y) dependence of absorption spectra of $Cd_yZn_{1-y}O$ epilayers obtained at room temperature. The curves, from right to left correspond to those of the samples with $y = 0$, 0.0013, 0.027, 0.043, and 0.073. (Courtesy of T. Makino [13].)

increases and can be estimated as $E_g(\gamma) = 3.29–4.40\,\gamma + 5.93\,\gamma^2$. The bandgap was observed to be decreasing from 3.28 eV down to 2.99 eV by introducing 7.3% of Cd. Figure 6.8 shows concentration (γ) dependence of the room temperature absorption spectra in as-grown films. The spectrum of $Cd_{0.07}Zn_{0.93}O$ encompassed a broad shoulder on the lower energy side, indicating the formation of a cadmium-rich phase, the density of which is relatively low. Bandgap energies (E_g) are plotted in the inset of Figure 6.8. The wurtzite lattice constants were also shown to have a second-order polynomial dependence on the Cd content, and can be estimated from $a_{CdZnO}(\gamma) = 3.252 + 0.143\,\gamma - 0.147\,\gamma^2$, $c_{CdZnO}(\gamma) = 5.204 + 0.956\,\gamma - 5.42\,\gamma^2$ [13].

In 150 nm thick $Cd_\gamma Zn_{1-\gamma}O$ layers grown by MOVPE on *c*-plane sapphire substrates, a decrease in the PL peak energy up to 300 meV was observed with increasing Cd composition, while introducing a lattice mismatch of only 0.5% with respect to binary ZnO. The redshift of the PL peaks of the samples correlated very well with the Cd concentrations in the $Cd_\gamma Zn_{1-\gamma}O$ layers determined by high resolution XRD. Furthermore, the resulting dependence strongly deviated from a linear behavior and was described by $E_{PL} = (3.35–9.19\,\gamma + 8.14\,\gamma^2)$ eV. However, the samples in this work were shown to consist of laterally distinguishable regions with different Cd incorporation. Therefore, the corresponding very large bowing parameter ($b = 8.14$ eV) is not very reliable and is inconsistent with the results of Makino *et al.* [13]

Ma *et al.* [17] succeeded in depositing good quality $Cd_xZn_{1-x}O$ thin films on glass and sapphire substrates using the DC reactive magnetron sputtering method. Samples exhibited good transmittance (over 85%) in the visible spectral range and a redshift was observed in the PL with increasing Cd composition. Films with $x \leq 0.53$ had the structure of pure $Cd_xZn_{1-x}O$ with *c*-axis perpendicular to the substrate surface, while the films with $x = 0.77$ were a mixture of hexagonal ZnO phase and cubic CdO phase. The bandgaps of the $Zn_{1-x}Cd_xO$ alloy films ($0 \leq x \leq 0.53$) could be nonlinearly tuned from 3.28 to 2.65 eV with the Cd contents from $x = 0$ to $x = 0.53$.

Clearly, the bandgap of ZnO can be increased by alloying with Mg and Be and can be reduced as well by alloying with Cd. In the case of Mg, the MgZnO alloy is wurtzitic up to Mg concentrations of approximately 40% and clearly cubic (rocksalt) for concentrations higher than 60%. In the intermediate region, phase mixture occurs with very poor material quality. However, when alloyed with Be, the alloy over the entire compositional range is wurtzitic. Incorporating Cd in ZnO reduces the bandgap of the alloy in relation to that of ZnO. Therefore, both smaller and larger bandgaps, as compared to ZnO, can be obtained paving the way for heterostructures that are necessary for many advanced devices to be formed.

References

1 Ohtomo, A., Tamura, K., Kawasaki, M., Makino, T., Segawa, Y., Tang, Z.K., Wong, G.K., Matsumoto, Y. and Koinuma, H. (2000) *Applied Physics Letters*, **77**, 2204.

2 Ohtomo, A., Kawasaki, M., Koida, T., Masubuchi, K. and Koinuma, H. (1998) $Mg_xZn_{1-x}O$ as II–VI widegap semiconductor alloy. *Applied Physics Letters*, **72**, 2466.

3 Ohtomo, A., Kawasaki, M., Ohkubo, I., Koinuma, H., Yasuda, T. and Segawa, Y. (1999) *Applied Physics Letters*, **75**, 980.

4 Choopun, S., Vispute, R.D., Yang, W., Sharma, R.P., Venkatesan, T. and Shen, H. (2002) *Applied Physics Letters*, **80**, 1529.

5 Gruber, T., Kirchner, C., Kling, R., Reuss, F. and Waag, A. (2004) *Applied Physics Letters*, **84**, 5359.

6 Ogata, K., Koike, K., Tanite, T., Komuro, T., Yan, F., Sasa, S., Inoue, M. and Yano, M. (2003) *Journal of Crystal Growth*, **251**, 623.

7 Minemoto, T., Negami, T., Nishiwaki, S., Takakura, H. and Hamakawa, Y. (2000) *Thin Solid Films*, **372**, 173.

8 Krishnamoorthy, S., Iliadis, A.A., Inumpudi, A., Choopun, S., Vispute, R.D. and Venkatesan, T. (2002) *Solid-State Electronics*, **46**, 1633.

9 Makino, T., Ohtomo, A., Chia, C.H., Segawa, Y., Koinuma, H. and Kawasaki, M. (2004) *Physica E*, **21**, 671.

10 Shan, F.K., Kim, B.I., Liu, G.X., Liu, Z.F., Sohn, J.Y., Lee, W.J., Shin, B.C. and Yu, Y.S. (2004) *Journal of Applied Physics*, **95**, 4772.

11 Cohen, D.J., Ruthe, K.C. and Barnett, S.A. (2004) *Journal of Applied Physics*, **96**, 459.

12 Sun, H.D., Makino, T., Segawa, Y., Kawasaki, M., Ohtomo, A., Tamura, K. and Koinuma, H. (2002) *Journal of Applied Physics*, **91**, 1993.

13 Makino, T., Segawa, Y., Kawasaki, M., Ohtomo, A., Shiroki, R., Tamura, K., Yasuda, T. and Koinuma, H. (2001) *Applied Physics Letters*, **78**, 1237.

14 Ryu, Y.R., Lee, T.S., Lubguban, J.A., Corman, A.B., White, H.W., Leem, J.H., Han, M.S., Park, Y.S., Youn, C.J. and Kim, W.J. (2006) Wide-band gap oxide alloy: BeZnO. *Applied Physics Letters*, **88**, 052103.

15 Ryu, Y., Lee, T.-S., Lubguban, J. A., White, H. W., Kim, B.-J., Park, Y.-S. and Youn, C.-J. (2006) Next generation of oxide photonic devices: ZnO-based ultraviolet light emitting diodes. *Applied Physics Letters*, **88**, 241108.

16 Makino, T., Chia, C.H., Tuan, Nguen T., Segawa, Y., Kawasaki, M., Ohtomo, A., Tamura, K. and Koinuma, H. (2000) *Applied Physics Letters*, **77**, 1632.

17 Ma, D.W., Ye, Z.Z. and Chen, L.L. (2004) *Physica Status Solidi a: Applied Research*, **201**, 2929.

18 Sakurai, K., Takagi, T., Kubo, T., Kajita, D., Tanabe, T., Takasu, H., Fujita, S. and Fujita, S. (2002) *Journal of Crystal Growth*, **237–239**, 514.

19 Gruber, T., Kirchner, C., Kling, R., Reuss, F., Waag, A., Bertram, F., Forster, D., Christen, J. and Schreck, M. (2003) *Applied Physics Letters*, **83**, 3290.

20 Vigil, O., Vaillant, L., Cruz, F., Santana, G., Morales-Acevedo, A. and Contreras-Puente, G. (2000) *Thin Solid Films*, **361–362**, 53.

21 Choi, Y.-S., Lee, C.-C. and Cho, S.M. (1996) *Thin Solid Films*, **289**, 153.

22 Van Vechten, J.A. and Bergstresser, T.K. (1970) *Physical Review B: Condensed Matter*, **1**, 3351.

23 Johnson, P.D. (1954) Some optical properties of MgO in the vacuum ultraviolet. *Physical Review*, **94**, 845.

24 Roessler, D.M. and Walker, W.C. (1967) Electronic spectrum and ultraviolet optical properties of crystalline MgO. *Physical Review*, **159**, 733.

25 Segnit, E.R. and Holland, A.E. (1965) *Journal of the American Ceramic Society*, **48**, 412.

26 Bundesmann, C., Schmidt-Grund, R. and Schubert, M. (2008) Far-infrared to vacuum-ultra-violet optical properties of ZnO: phonons, plasmons, dielectric constants, refractive indices, band-to-band transitions, and excitons, in *Transparent Conductive Zinc Oxide, Springer Series in Materials Science*, Vol. 104 (eds K. Ellmer, A. Klein and B. Rech) Springer, Berlin.

27 Bundesmann, C. (2005) Phonons and plasmons in ZnO-based alloy and doped ZnO thin films studied by infrared spectroscopic ellipsometry and Raman scattering spectroscopy, PhD Thesis, Universität Leipzig (Shaker, Aachen, 2006).

28 Ohtomo, A. and Tsukazaki, A. (2005) Pulsed laser deposition of thin films and superlattices based on ZnO. *Semiconductor Science and Technology*, **20**, S1.

29 Takeuchi, I., Yang, W., Chang, K.S., Aronova, M.A., Venkatesan, T., Vispute, R.D. and Bendersky, L.A. (2003) *Journal of Applied Physics*, **94**, 7336.

30 Chen, J., Shen, W.Z., Chen, N.B., Qiu, D.J. and Wu, H.Z. (2003) *Journal of Physics: Condensed Matter*, **15**, L475.

31 Takagi, T., Tanaka, H., Fujita, S. and Fujita, S. (2003) *Japanese Journal of Applied Physics*, **42**, L401.

32 Sharma, A.K., Narayan, J., Muth, J.F., Teng, C.W., Jin, C., Kvit, A., Kolbas, R.M. and Holland, O. (1999) *Applied Physics Letters*, **75**, 3327.

33 Jaffe, J.E., Pandey, R. and Kunz, A.B. (1991) *Physical Review B: Condensed Matter*, **43**, 14030.

34 Jellison, G.E., Jr, and Boatner, L.A. (1998) *Physical Review B: Condensed Matter*, **58**, 3586.

35 Jellison, G.E., Jr, (2001) *Physical Review B: Condensed Matter*, **65**, 049902.

36 Koike, K., Hama, K., Nakashima, I., Takada, G., Ogatab, K., Sasa, S., Inoue, M. and Yano, M. (2005) *Journal of Crystal Growth*, **278**, 288.

37 Schmidt, R., Rheinlander, B., Schubert, M., Spemann, D., Butz, T., Lenzner, J., Kaidashev, E.M., Lorenz, M., Rahm, A., Semmelhack, H.C. and Grundmann, M. (2003) *Applied Physics Letters*, **82**, 2260.

38 Schmidt-Grund, R., Carstens, A., Rheinländer, B., Spemann, D., Hochmut, H., Lorenz, M., Grundmann, M., Herzinger, C.M. and Schubert, M. (2006) Refractive indices and band-gap properties of rocksalt $Mg_xZn_{1-x}O$ ($0.68 \leq x \leq 1$). *Journal of Applied Physics*, **99**, 123701.

39 Schmidt-Grund, R., Schubert, M., Rheinländer, B., Fritsch, D., Schmidt, H., Kaideshev, E.M., Lorenz, M., Herzinger, C.M. and Grundmann, M. (2005) UV-VUV spectroscopic ellipsometry of ternary $Mg_xZn_{1-x}O$. *Thin Solid Films*, **455–456**, 500.

40 Teng, C.W., Muth, J.F., Özgür, Ü., Bergmann, M.J., Everitt, H.O., Sharma, A.K., Jin, C. and Narayan, J. (2000) *Applied Physics Letters*, **76**, 979.

41 Kang, J.H., Park, Y.R. and Kim, K.J. (2000) *Solid State Communications*, **115**, 127.

42 Zhao, D., Liu, Y., Shen, D., Lu, Y., Zhang, J. and Fan, X. (2002) *Journal of Crystal Growth*, **234**, 427.

43 Kang, T.D., Lee, H., Park, W.-I. and Yib, G.-C. (2004) *Thin Solid Films*, **455–456**, 609.

44 Rigamonti, R. (1946) *Gazzetta Chimica Italiana*, **76**, 474.

45 Sapozhnikov, Y.P. (1961) *Russian Journal of Inorganic Chemistry*, **6**, 1291.

46 Bundesmann, C., Schubert, M., Spemann, D., Butz, T., Lorenz, M., Kaidashev, E.M., Grundmann, M., Ashkenov, N., Neumann, H. and Wagner, G. (2002) *Applied Physics Letters*, **81**, 2376.

47 Zhang, Y.T., Du, G.T., Liu, D., Zhu, H.C., Cui, Y.G., Dong, X. and Yang, S. (2004) *Journal of Crystal Growth*, **268**, 140.

48 Narayan, J., Sharma, A.K., Kvit, A., Jin, C., Muth, J.F. and Holland, O.W. (2002) *Solid State Communications*, **121**, 9.

49 Matsumoto, Y., Murakami, M., Jin, Z.W., Ohtomo, A., Lippmaa, M., Kawasaki, M. and Koinuma, H. (1999) *Japanese Journal of Applied Physics*, **38**, L603.

50 Bundesmann, C., Schubert, M., Rahm, A., Spemann, D., Hochmuth, H., Lorenz, M. and Grundmann, M. (2004) *Applied Physics Letters*, **85**, 905.

51 Chang, I.F. and Mitra, S.S. (1968) *Physical Review*, **172**, 924.

52 Chen, J. and Shen, W.Z. (2003) *Applied Physics Letters*, **83**, 2154.

53 Lucovsky, G., Brodsky, M.H. and Burstein, E. (1970) *Physical Review B: Condensed Matter*, **2**, 3295.

54 Bundesmann, C., Rahm, A., Lorenz, M., Grundmann, M. and Schubert, M. (2006) Infrared optical properties of $Mg_xZn_{1-x}O$ thin film ($0 \leq x \leq 1$): Long-wavelength optical phonons and dielectric constants. *Journal of Applied Physics*, **99**, 113504.

55 Serrano, J., Romero, A.H., Manjon, F.J., Lauck, R., Cardona, M. and Rubio, A. (2004) *Physical Review B: Condensed Matter*, **69**, 094306.

56 Chang, K.J., Froyen, S. and Cohen, M.L. (1983) *Journal of Physics C: Solid State Physics*, **16**, 3475, and references therein.

57 Emeline, A.V., Kataeva, G.V., Ryabchuk, V.K. and Serpone, N. (1999) *The Journal of Physical Chemistry B*, **103**, 9190.

58 Madelung, O. (2003) *Semiconductors: Data Handbook*, 3rd edn, Springer, New York.

59 Ashrafi, A. and Jagadish, C. (2007) *Journal of Applied Physics*, **102**, 071101.

60 Ryu, Y.R., Lee, T.S. and White, H.W. (2004) A technique of hybrid beam deposition for synthesis of ZnO and other metal oxides. *Journal of Crystal Growth*, **261**, 502.

61 Koffyberg, R.P. (1976) *Physical Review B: Condensed Matter*, **13**, 4470.

62 Shigemori, S., Nakamura, A., Ishihara, J., Aoki, T. and Temmyo, J. (2004) *Japanese Journal of Applied Physics*, **43**, L1088.

7
ZnO Nanostructures

One-dimensional semiconductor nanowires and nanorods have attracted increasing attention due to their physical properties arising from quantum confinement (such as electronic quantum transport and enhanced radiative recombination of carriers). However, increased surface-to-volume ratio and the role of nonradiative surface recombination would have to be dealt with. Nanowires could form the fundamental building blocks for applications such as short-wavelength nanolasers, field-effect transistors, ultrasensitive nano-sized gas sensors, nanoresonators, transducers, actuators, nanocantilevers, and field emitters (FEs) [1–4]. These nanostructures are ideal for studying transport mechanisms in one-dimensional systems, which are important not only for understanding the fundamental phenomena in low-dimensional systems, but also for developing new generation nanodevices with high performance. Many nanowires made of materials such as Si, C, InP, GaAs, CdS, SnO_2, GaN, ZnO, and In_2O_3 have been fabricated for different applications using mostly a catalyst-assisted vapor–liquid–solid (VLS) growth method (vapor–solid process if without the catalyst) [1, 2, 5, 6]. Among these materials, ZnO is considered to be the most promising one due to its large exciton binding energy (60 meV), high electromechanical coupling constant, and resistivity to harsh environment as well as the relative ease with which such structures can be produced with ZnO. Therefore, 1D ZnO structures stimulated a good deal of attention, and a large number of publications have appeared lately reporting nanostructures of various shapes (e.g., nanowires, nanobelts, nanorings, nanotubes, nanodonuts, nanopropellers, etc.) grown by different methods [1, 2, 5–25]. In this chapter, synthesis and properties of such nanostructures formed of ZnO are discussed.

7.1
Synthesis of ZnO Nanostructures

7.1.1
Vapor–Liquid–Solid (Vapor Transport) Process

A rich variety of nanostructures can be grown using the vapor transport method, which is based on transport of Zn and O vapor on to a substrate where they react to

form ZnO. The mixture of Zn and O vapor can be produced by decomposition of either ZnO powder, which occurs at relatively high temperatures (~1975 °C is the melting temperature), or ZnO^+ graphite mixture (referred to as the carbothermal method), where graphite lowers the decomposition temperature significantly, or by evaporating Zn metal (~420 °C is the melting point) under oxygen flow, in which case the transport and reaction zones should be separated to avoid Zn and O reaction away from the substrate. The nanostructure formation and its shape depend strongly on the Zn to O vapor pressure ratio. Naturally, the growth of patterned and aligned 1D nanostructures is important for device applications. Although various kinds of nanostructures can be obtained using the catalyst-free vapor–solid process, more control over nanostructure formation (alignment, density, and location) and patterned growth can be achieved via the VLS process with the use of catalysts, which initiate and guide the growth [1].

The VLS processes are usually carried out in a horizontal tube furnace, as shown in Figure 7.1. In this schematic, the carrier gas, Ar, is introduced from the left end of the alumina tube and is pumped out from the right end. The source material is loaded on an alumina boat and positioned at the center of the highest temperature zone in the alumina tube. The substrate temperature usually drops with the distance from the position of the source material(s). The local temperature where the substrate is situated (usually 500–700 °C) determines the type of product that will be obtained. To reduce the decomposition temperature, ZnO powder is usually mixed with graphite powder to form the source mixture. At temperatures 800–1100 °C, graphite reacts with ZnO to form Zn, CO, and CO_2 vapors, which then react on the substrate to form ZnO nanostructures.

In VLS nanowire growth, metals such as Au, Fe, and Sn can be used to act as catalysts and to play a pivotal role in forming liquid alloy droplets with the nanowire reactant components for deposition on the preferred site. For 1D ZnO nanowires grown via the VLS process, the commonly used catalyst is Au. The spatial distribution of the catalyst particles determines the pattern of the nanowires. This step can be achieved using a variety of patterning technologies for producing complex configurations. Or simply, driven by energy minimization, a thin Au film deposited on the

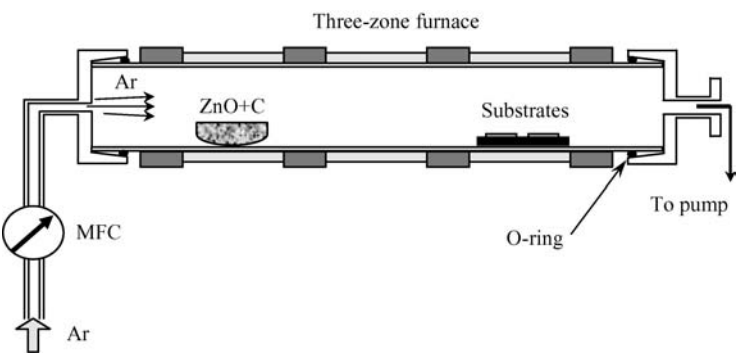

Figure 7.1 A schematic diagram of the horizontal tube furnace for growth of ZnO nanostructures by the solid–vapor phase process.

substrate can be heated so that the continuous Au layer turns into a discontinuous layer of small Au droplets, in which case, the resulting nanowire diameter will be somewhat randomized depending on the size of distribution of the Au droplets. Reactant metal (Zn) forms a liquid alloy with Au and nanowire growth begins in the presence of oxygen after the liquid becomes supersaturated with reactant materials and continues as long as the catalyst alloy remains in the liquid state and the reactants are available. By choosing the optimal match between the substrate lattice and the nanowires, the nature of epitaxial orientation relationship between the nanowire and substrate paves the way for the alignment of nanowires normal to the substrate. The size of the catalyst particles defines the diameter of nanowires. Growth terminates when the temperature is below the eutectic temperature of the catalyst alloy or the reactant is no longer available. As a result, a nanowire obtained from the VLS process typically has a solid catalyst nanoparticle at its tip with a diameter comparable to that of the connected nanowires. Therefore, by confirming the existence of a catalyst at the tip, one can determine if the nanowire growth was governed by a VLS process. Structurally, ZnO has three types of fast growth directions: $\langle 2\,\bar{1}\,\bar{1}\,0\rangle$, $\langle 01\bar{1}0\rangle$, and $\pm[0\,0\,0\,1]$. Together with the polar surfaces due to atomic terminations, ZnO exhibits a wide range of novel structures that can be grown by tuning the growth rates along these directions. Typically, nanowires grow along [0 0 0 1] and their side surfaces are enclosed by $\{2\,\bar{1}\,\bar{1}\,0\}$.

Self-organized [0 0 0 1]-oriented ZnO nanowires have been synthesized on sapphire substrates with a catalyzed VLS process using an Au thin film as the catalyst [6]. As mentioned above, selective nanowire growth could be readily achieved by patterning the Au thin film before growth. Typical scanning electron microscope (SEM) images of nanowire arrays grown on *a*-plane sapphire $(1\,1\,\bar{2}\,0)$ substrates with patterned Au thin film are presented in Figure 7.2. These results confirm that the ZnO nanowires grow only in the Au-coated areas, and each nanowire is capped with Au–Zn alloy clusters on the tip. By adjusting the growth time, nanowires could be grown up to 10 μm in length. The diameters of these wires range from 20 to 150 nm, although more than 95% of them have diameters between 70 and 100 nm. The dispersion in diameter is due to the inhomogeneous sizes of the Au nanocluster catalysts when the substrate is annealed during the growth process. Haupt *et al.* [23] were able to reduce the average diameter of the nanowires below 30 nm by using the VLS technique after premasking the *a*-plane sapphire substrates with self-organizing, gold-loaded diblock copolymers to form quasi-hexagonally ordered Au nanoclusters. The capability of patterned nanowire growth helps to fabricate nanoscale light emitters in a controllable fashion.

Room-temperature photoluminescence (PL) spectra of ZnO nanowires showed a strong band-edge emission at ∼377 nm [6]. In addition, a very weak blue band (440–480 nm) and an almost negligible green band (510–580 nm) were observed. These samples were explored for possible stimulated emission at room temperature by measuring the excitation density-dependent emission with excitation from the fourth harmonic of a Nd:yttrium–aluminum–garnet (Nd:YAG) laser (266 nm, 3 ns pulse width). Light emission was collected in the direction normal to the end surface plane (along the *c*-axis) of the nanowires, and lasing was observed in the absence of any fabricated mirrors with increasing pump power, as shown in Figure 7.3. At

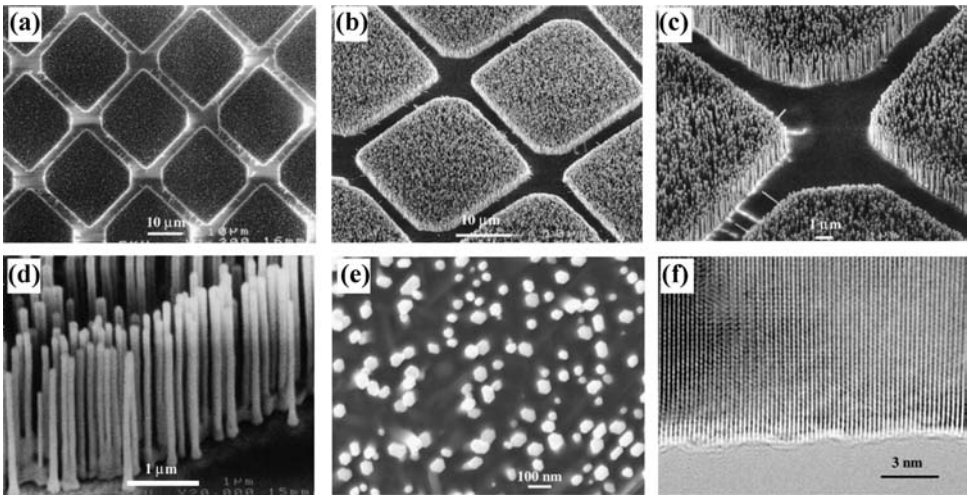

Figure 7.2 Scanning electron microscope images of ZnO nanowire arrays grown on sapphire substrates (a–e). A top view of the well-faceted hexagonal nanowire tips is shown in (e). (f) High-resolution TEM image of an individual ZnO nanowire showing its ⟨0 0 0 1⟩ growth direction. (Courtesy of P. Yang [6].)

low excitation intensities, the spectrum consists of a single broad spontaneous emission peak (Figure 7.3) with a full width at half maximum of 17 nm. When the excitation intensity exceeds a threshold of 40 kW cm^{-2}, sharp peaks emerge in the emission spectra. The linewidth of these peaks is 0.3 nm, which is 50 times smaller than the linewidth of the spontaneous emission peak. Above threshold, the integrated emission intensity increases rapidly with pump power confirming stimulated emission. The observed single or multiple sharp peaks between 370 and 400 nm were attributed to different lasing modes. The lasing action in these nanowire arrays without any fabricated mirrors is possible if one considers these single-crystalline and well-faceted nanowires as natural resonance cavities along the *c*-direction. One end of the nanowire is the epitaxial interface between sapphire and ZnO, whereas the other end is the sharp (0 0 0 1) plane of the ZnO nanocrystals. Both ends serve as good laser cavity mirrors, because the refractive index for ZnO is more than that for sapphire and air (2.45, 1.8, and 1, respectively). This natural cavity or waveguide formation in nanowires provides a simple approach to forming a nanowire laser cavity without cleavage and etching.

Even though as-grown ZnO nanorods are n-type, intentional n-type doping is necessary to increase the carrier concentration required for practical electronic device applications. With the use of In metal acting simultaneously as the catalyst as well as the doping source, VLS growth of ordered and vertically aligned n-type doped ZnO nanorod arrays has been achieved on p-GaN/Al_2O_3 substrates [26]. Figure 7.4 shows the SEM images of the well-ordered n-type ZnO nanorod arrays. The ordering was accomplished by using a 15 nm thick In thin film evaporated onto a self-organized polystyrene nanosphere mask transferred to the substrate. The low-temperature PL

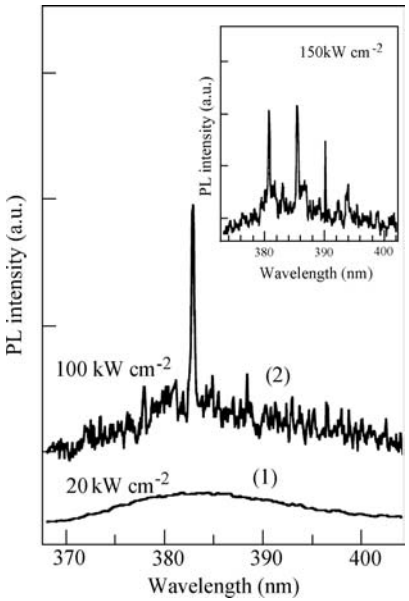

Figure 7.3 Emission spectra from nanowire arrays below (line 1) and above (line 2) the lasing threshold. The pump power levels for these spectra were 20 and 100 kW cm^{-2}, respectively. The spectra are offset for easy comparison. The inset shows the spectrum for 150 kW cm^{-2} excitation density. (Courtesy of P. Yang [6].)

measurements on n-type ZnO nanorod arrays revealed a significantly enhanced In-related donor-bound exciton line (I_9, see Section 3.2.2) when compared to undoped ZnO nanorods, demonstrating incorporation of In. Electrical transport measurements performed on single ZnO nanorods in high vacuum also showed an order of magnitude drop ($2.0 \times 10^{-2}\,\Omega\,cm$) in resistivity with In doping.

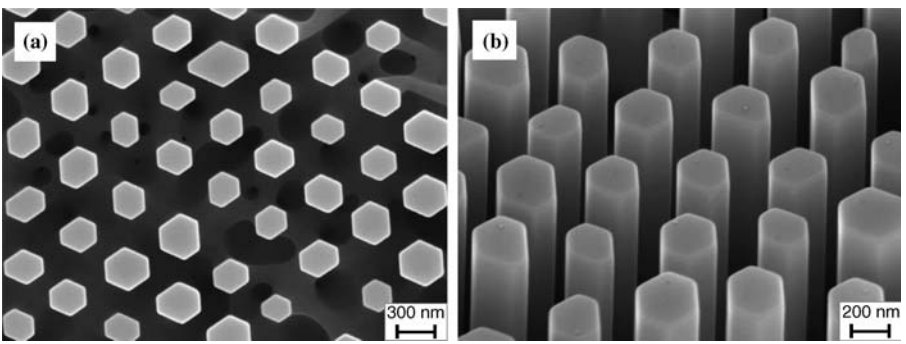

Figure 7.4 (a) Plan-view and (b) angled-view SEM images of In-doped ZnO nanorod arrays grown by the VLS method on patterned In-covered p-GaN/Al_2O_3 substrates. (Courtesy of J. Fallert and C. Klingshirn [26].)

Well-defined lasing modes have been identified under optical excitation of ZnO nanorods grown in a similar fashion using catalyst-assisted VLS technique by employing self-organized polystyrene spheres on GaN substrates as a mask during Au evaporation [27]. Ordered arrays of (0 0 0 1)-oriented ZnO nanorods with 200 nm diameter and 4.7 μm length were obtained with 500 nm rod-to-rod spacing as shown in Figure 7.5a. As alluded earlier, well-aligned ZnO nanorods provide a perfect gain medium as well as act as waveguides and Fabry–Perot resonators with well-defined cavity ends. With increasing optical excitation density, where both the excitation and detection were performed perpendicular to the substrate plane for an individual ZnO nanorod (i.e., along the *c*-axis of the nanorods), sharp emission peaks representing different lasing modes were observed to emerge above different threshold densities. The threshold density increased with the decreasing lasing mode frequency, as shown in Figure 7.5b. The closely spaced lasing modes that had linewidths of ∼0.1 nm are consistent with calculations of the guided modes in ZnO nanorods [28]. As additional lasing modes appeared at lower energies with increasing excitation density, the lower (higher energy) lasing modes saturated and even weakened in intensity due to increased draining sources of electron–hole pairs, as shown in the inset of Figure 7.5b. Time-resolved micro-PL measurements revealed very fast decay times of ∼8 ps for all the lasing modes, characteristic of stimulated emission. These results clearly indicate that ZnO nanorods when appropriately prepared can be used in UV-emitting nanolaser arrays.

Nanobelts are nanowires that have a well-defined geometrical shape and side surfaces and are usually grown by sublimation of ZnO powder without a catalyst [2]. Due to differences in surface energies among the (0 0 0 1), $\{0\,1\,\bar{1}\,0\}$, and $\{2\,\bar{1}\,\bar{1}\,0\}$ planes, freestanding ZnO nanobelts and nanowires are usually dominated by the lower energy nonpolar surfaces such as $\{01\,\bar{1}0\}$ and $\{2\,\bar{1}\,\bar{1}0\}$. When there is no doping, a nanobelt grows along $[01\,\bar{1}0]$, with top and bottom flat surfaces $\pm(2\,\bar{1}\,\bar{1}\,0)$ and side surfaces $\pm(0\,0\,0\,1)$. Pan *et al*. [2] were able to grow nanobelts with each nanobelt having a uniform width along its entire length and the typical widths and thicknesses of the nanobelts were in the range of 50–300 nm and 10–30 nm, respectively. For investigation of quantum confinement effects, ultrasmall nanobelts having good size uniformity with an average diameter of 5.5 nm have been grown using tin as the catalyst [29]. In comparison with the PL from nanobelts of an average width of 200 nm, the 5.5 nm nanobelts exhibited a 14 nm shift (387–373 nm) in the emission peak, indicating quantum confinement.

ZnO nanobelts dominated by (0 0 0 1) polar surfaces could also be grown by introducing In and/or Li doping [30]. In this case, the nanobelts grow along $[2\,\bar{1}\,\bar{1}\,0]$ (the *a*-axis), with their top/bottom large surface $\pm(0\,0\,0\,1)$ and the side surfaces $\pm(0\,1\,\bar{1}\,0)$. These polar nanobelts tend to roll into an enclosed ring or a spiral shape to reduce the electrostatic energy. When the surface charges are not compensated during growth, rolling of the nanobelt to form a circular ring would minimize or neutralize the overall dipole moment, reducing the spontaneous polarization-induced electrostatic energy. The minimization of the total energy, which has contributions from spontaneous polarization and elasticity produced by bending, determines the stable shape of the nanobelt.

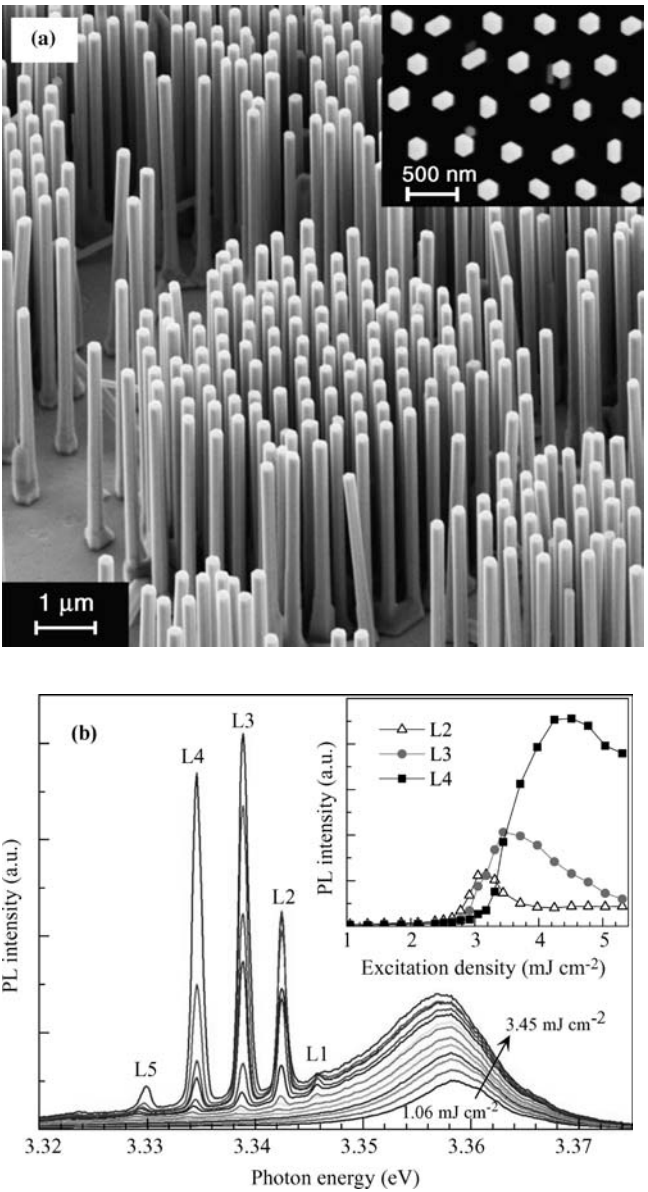

Figure 7.5 (a) 45° side-view SEM image of hexagonally ordered ZnO nanorod arrays grown by the VLS method on patterned Au-covered GaN/Al_2O_3 substrates. The inset is the top view of the nanorod arrays. (b) 10 K emission spectra from a single nanorod pumped by 355 nm excitation from a pulsed Ti:Sapphire laser. The pump power is varied from about 1.0 to 3.5 mJ cm^{-2}. L1 to L5 indicate different lasing modes. (Courtesy of J. Fallert and C. Klingshirn [27].)

As another example of various types of nanostructures, polar surface-dominated ZnO nanopropeller arrays have been synthesized using a two-step high-temperature solid–vapor deposition process by Gao and Wang [18]. The first step involves the growth of the nanopropeller axis that is a straight nanowire along the *c*-axis and enclosed by {2 1 1 0} surfaces. In the second step, the sixfold symmetric nanoblades are formed along the crystallographic equivalent *a*-axis (⟨2 1 1 0⟩) perpendicular to the nanowire, and the array is formed by epitaxial growth of nanoblades on the nanowire. The growth of nanopropeller arrays on polycrystalline Al_2O_3 substrates was conducted at 600–700 °C for 60 min (step I) and then at 800–900 °C for 30 min (step II) under pressure of 200 mbar. Figure 7.6a shows top view of well-aligned ZnO nanopropeller arrays on a polycrystalline Al_2O_3 substrate grown in a relatively high temperature zone (∼680 °C, step I). Each nanopropeller array column consists of six arrays of triangular blades of 4–5 μm in length and propeller arrays of diameter ∼10 μm. Columns of the nanopropellers maintain their sixfold arrays of parallel nanoribbon blades around the central nanowire, as seen in Figure 7.6b. The mor-

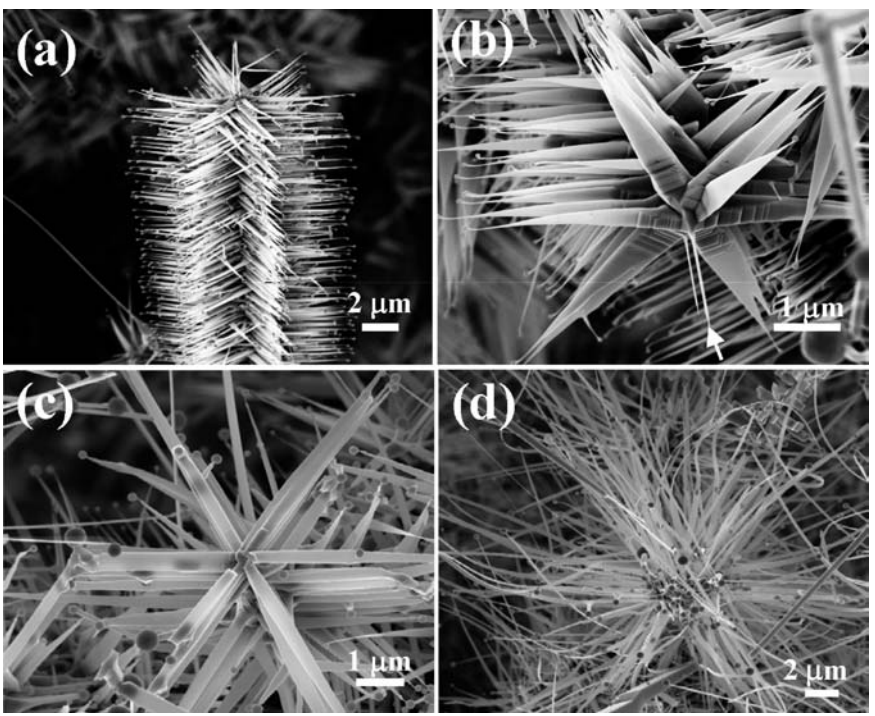

Figure 7.6 SEM images of bunches of ZnO nanopropeller arrays rooted at Al_2O_3 substrate grown at various temperatures: (a) A single column of the as-synthesized ZnO nanopropeller arrays. (b) Front view of a column of ZnO nanopropeller arrays with nanowires at the central axis, which was collected from a lower temperature zone (∼620 °C). (c) A column of ZnO nanopropeller arrays with uniform nanoribbon shape and smoother surface, which was collected from a medium temperature zone (∼650 °C). (d) A column of ZnO nanopropeller arrays with long nanoribbons, which was collected from a higher temperature zone (∼680 °C). (Courtesy of Z.L. Wang [18].)

phology and shape of the nanopropellers were reported to be dependent on the local temperature, surface diffusion rate, and the availability of Zn–O vapor. In the lower temperature region, due to a relatively slower surface diffusion and the decrease in supply of the vapor as more source material is being consumed, a triangular structure was formed. In the medium temperature region, a faster diffusion of the Zn–O vapor and higher surface mobility lead to the formation of uniform and longer nanoblades.

There have also been reports on the growth of ZnO tetrapod structures [19, 20]. In Ref. [20], such structures were prepared either from oxidation of Zn in air or by heating a mixture of ZnO and graphite (1 : 1) at 1100 °C in a tube furnace. Djurišić *et al*. [20] also fabricated ZnO samples by heating a mixture of ZnO, GeO_2, and graphite at 1100 °C and studied the morphology of the fabricated structures as a function of GeO_2 percentage up to 10%. Figure 7.7 shows the representative SEM images of the obtained ZnO structures. Similar tetrapod structures are obtained for both the starting materials (i.e., Zn and ZnO:C). When GeO_2 is added to the starting material (ZnO:C), multipod structures started to form, as illustrated in Figure 7.7c. With increasing GeO_2 concentration in the starting material, a larger amount of multipod structures appeared (for small GeO_2 content, both tetrapods and multipods were formed). It was concluded that Ge enables nucleation of additional legs on the core that would normally develop into a tetrapod.

In a study by Kong *et al*. [7], single-crystal nanorings of ZnO were grown by the solid–vapor process. The raw material was a mixture of ZnO, indium oxide, and lithium carbonate powders at a weight ratio of 20 : 1 : 1, and it was placed in the highest temperature (1400 °C) zone available in a horizontal tube furnace. At such a high temperature and low pressures ($\sim 10^{-3}$ Torr), ZnO decomposes into Zn^{2+} and O^{2-}. This decomposition process is the key step to control the anisotropic growth of the nanobelts. After a few minutes of evaporation and decomposition, the Ar carrier gas was introduced at a flux of 50 standard cubic centimeters per minute. Synthesis was conducted at 1400 °C for 30 min. The condensation products were deposited onto a silicon substrate placed in a temperature zone of 200–400 °C under Ar pressure of 500 Torr. The as-synthesized sample was composed of many freestanding nanorings (20–40 % of the whole product) (Figure 7.8a). The rings had typical diameters of $\sim$1–4 μm and thin, wide shells of $\sim$10–30 nm thick. SEM images recorded at high magnification clearly show the perfect circular shape of the complete rings, with uniform shapes and flat surfaces as recorded in Figure 7.8b. Two types of nanoring structures were found as identified by transmission electron microscopy (TEM) imaging. The type I structure is a single-crystal nanoring with nearly perfect circular shape. However, there is electron diffraction contrast caused by nonuniform deformation along the circumference (not shown). The type II structure is a nanoring with its shell being a uniformly deformed single-crystal ribbon around the circumference (not shown).

7.1.2
Metalorganic Vapor-Phase Epitaxy and Molecular Beam Epitaxy

For device fabrication, heteroepitaxial growth with control over impurities and thickness down to nanometer scale is required. VLS method is limited and cannot

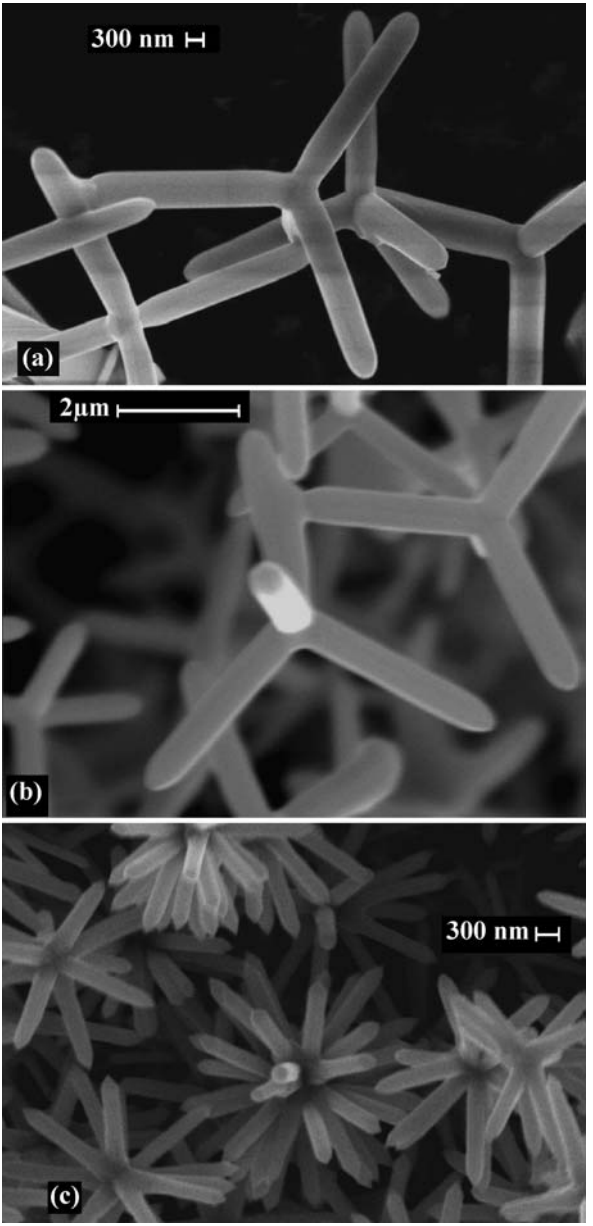

Figure 7.7 Representative SEM images of ZnO nanostructures: (a) ZnO prepared from Zn. (b) ZnO prepared from ZnO:C. (c) ZnO prepared from ZnO:C:GeO_2. (Courtesy of A.B. Djurišić [20].)

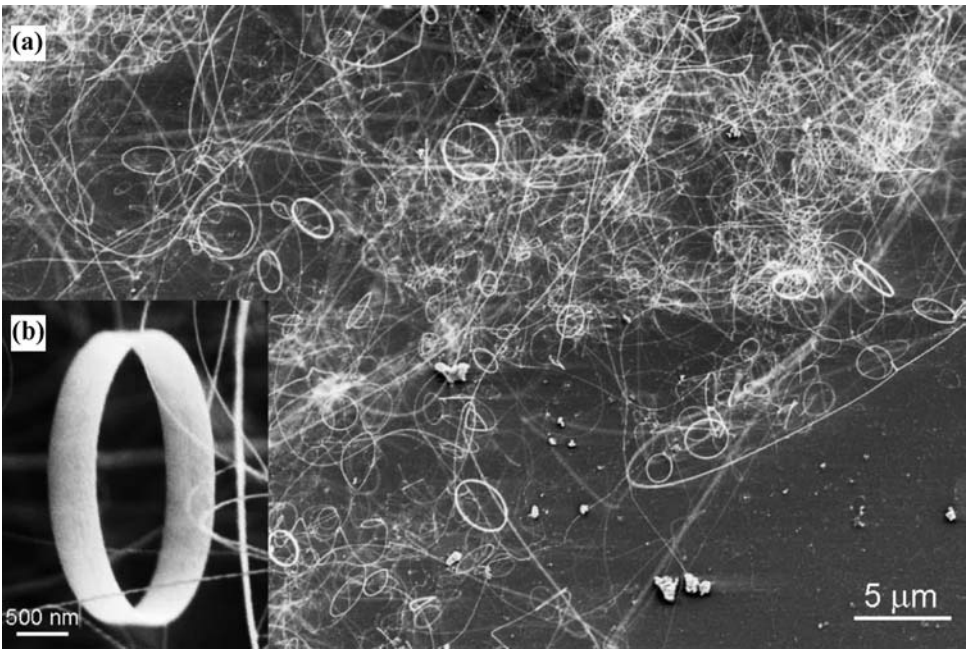

Figure 7.8 (a) Low-magnification SEM image of the as-synthesized ZnO nanorings. (b) High-magnification SEM image of a freestanding single-crystal ZnO nanoring, showing uniform and perfect geometrical shape. The ring diameter is 1–4 μm, the thickness of the ring is 10–30 nm, and the width of the ring shell is 0.2–1 μm. (Courtesy of Z.L. Wang [7].)

meet these requirements. Growth of complex structures for device applications can only be accomplished by advanced epitaxial methods such as metalorganic vapor-phase epitaxy (MOVPE) or metalorganic chemical vapor deposition (MOCVD) and molecular beam epitaxy (MBE). Particularly, MOVPE (or MOCVD) has been proven to be a powerful technique for large-scale production with accurate control over doping and thickness (see Section 2.3.4).

For MOVPE growth of ZnO nanorods, usually diethylzinc and oxygen are employed as the reactants and argon as the carrier gas [15]. N_2O as the oxygen source and nitrogen as the carrier gas have also been used [31]. Typical growth temperatures range from 400 [15] to 1050 °C [31]. The growth occurs without a catalyst, and flat terraces and steps are observed at the nanorod tips resulting from the layer-by-layer growth mode, instead of the metallic nanoparticles characteristic to catalyst-assisted VLS processes.

Figure 7.9 shows ZnO nanorods grown by Park *et al.* [15] using low-pressure MOVPE on Al_2O_3 (0 0 0 1) substrates at 400 °C without any metal catalysts. Very thin ZnO buffer layers were deposited at a low temperature before the nanorod growth. The mean diameter of nanorods obtained by MOVPE was as small as 25 nm, smaller than the typical diameters of 50–100 nm for those prepared by other deposition methods [6]. Furthermore, ZnO nanorods were well aligned vertically, showing uniformity in their diameters, lengths, and densities as revealed from electron

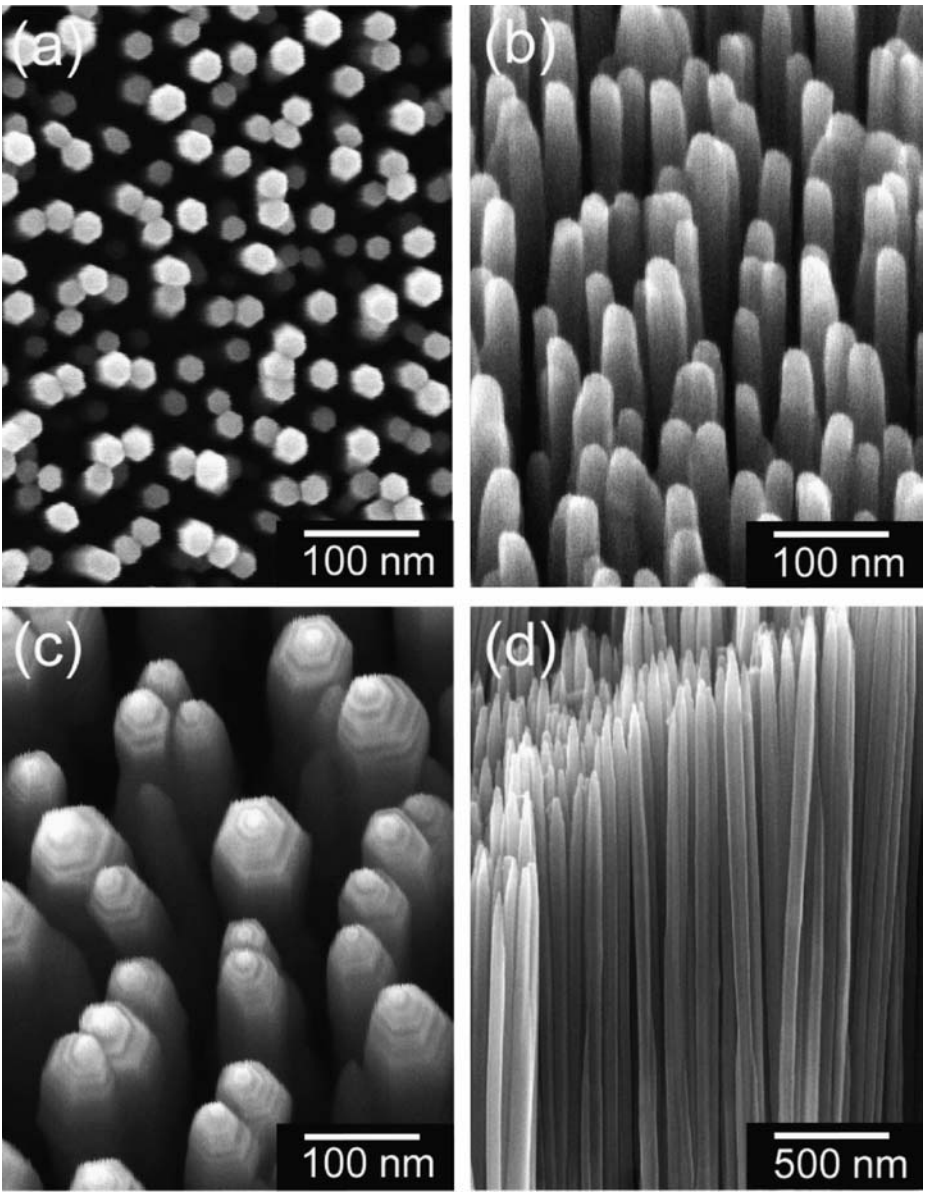

Figure 7.9 Field emission SEM (a) plan-view and (b) tilted images of ZnO nanorods with a mean diameter of 25 nm and (c) tilted and (d) cross-sectional images of ZnO nanorods with a mean diameter of 70 nm. In (c), hexagon-shaped pyramids with flat terraces and steps are seen at the ends of the nanorods. (Courtesy of G.-C. Yi [15].)

microscopy. The results of θ–2θ scan, θ-rocking curve, and ϕ-scan measurements on the nanorods are presented in Figure 7.10. Only the (0 0 2) and (0 0 4) diffraction peaks are visible in the XRD θ–2θ scans shown in Figure 7.10a, and a small full width at half maximum (FWHM) value of 0.6° was obtained from the XRD θ-rocking

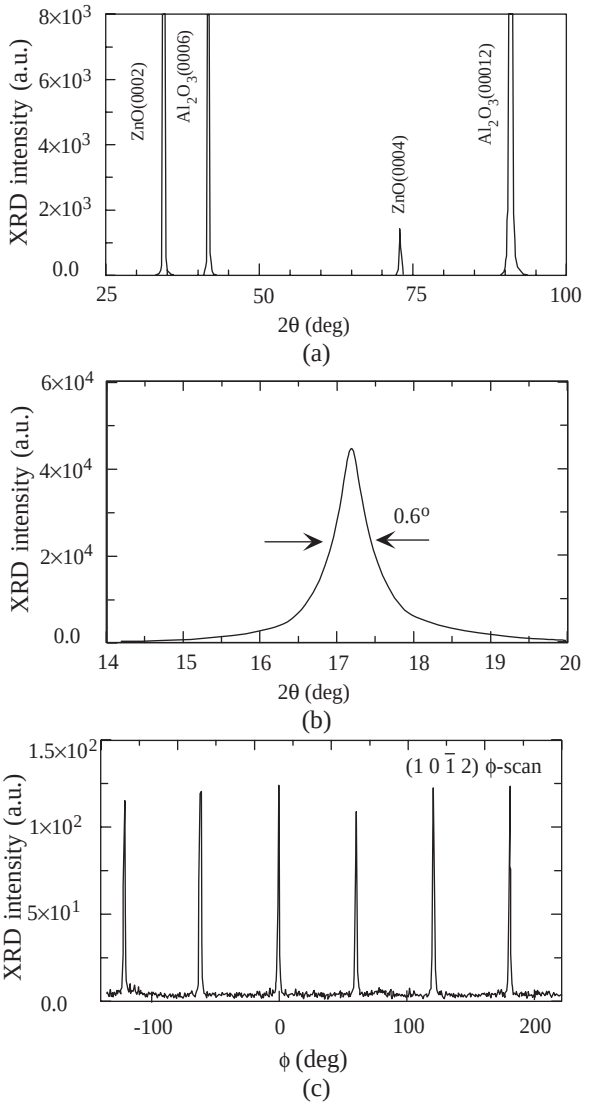

Figure 7.10 XRD (a) θ–2θ scan, (b) rocking curve, and (c) azimuthal (ϕ) scan measurement results of ZnO nanorods. From the XRD θ–2θ scan data, only two peaks are shown at 34.32° and 72.59° corresponding to ZnO (0 0 2) and (0 0 4) peaks, respectively. The rocking curve also shows a FWHM value of 0.6°. A sixfold symmetry in ϕ-scan data is also observed, indicating in-plane alignment of the nanorods. (Courtesy of G.-C. Yi [15].)

curve measurements (Figure 7.10b). Furthermore, Figure 7.10c shows a sixfold rotational symmetry in the azimuthal scan. These results clearly indicate that the ZnO nanorods were epitaxially grown with homogeneous in-plane alignment as well as *c*-axis orientation. The room-temperature PL spectra of the nanorods showed strong and narrow excitonic emission with a dominant peak at 3.29 eV and an extremely weak deep level emission at 2.5 eV, indicating the high optical quality of the nanorods. Free exciton emission lines were still clearly visible at 10 K, and no quantum confinement effect was evident for the nanorods with diameters exceeding 20 nm [32].

For ZnO nanorods grown at relatively higher temperatures (700–1050 °C), vertical alignment of the *c*-axis-oriented nanorods was observed only on *a*-plane sapphire substrates, whereas the use of *c*-plane sapphire, Si (1 1 1), $SrTiO_3$ (1 0 0), and $SrTiO_3$ (1 1 1) substrates resulted in rather random alignment [31]. To test the possibility of a catalyst-assisted process, nanorods were also grown on *a*-plane sapphire substrates partially coated with a thin (1–3 nm) gold layer. Close to 100% vertical orientation of ZnO nanorods with a diameter of 50 ± 5 nm and a length of several micrometers was observed in areas without gold metallization, while growth with no preferential direction occurred in the areas coated with gold, demonstrating that MOVPE growth of ZnO nanorods is different from the VLS process.

Li *et al*. [17] prepared ZnO nanoneedles on silicon through chemical vapor deposition. The diameters of the needle tips were in the range of 20–50 nm. High-resolution transmission electron microscopy revealed that the nanoneedles were single crystals along the [0 0 0 1] direction. They exhibited multiple tip surface perturbations, and were just 1–3 nm in dimension. Field emission measurements showed fairly low turn-on and threshold fields of 2.5 and 4.0 V mm^{-1}, respectively. The nanosize perturbations on the nanoneedle tips have been assumed to be the cause for such excellent field emission performance. High emission current density, high stability, and low turn-on field make ZnO nanoneedle arrays one of the promising candidates for high brightness field emission electron sources and flat panel displays.

Among the various nanostructure types obtained by MOVPE are ZnO tubes [33]. Tube structures were grown epitaxially on sapphire (0 0 0 1) substrates at 350–450 °C with both the ZnO *c*-axis and the growth direction being parallel to the substrate normal. All of the tubes had hexagonal cross sections and the same in-plane orientation. The characteristics of the tubes were found to be strongly dependent on both the growth temperature and reactor pressure. Figure 7.11 shows SEM images of the tubes formed at 400 °C under different reactor pressures. Figure 7.11a indicates that all of the tubes have hexagonal shapes and all the hexagons have the same in-plane orientation. Figure 7.11b–d shows the SEM images taken with an inclination angle of the tubes obtained at 0.3, 0.6, and 1.0 Torr, respectively. The density of the hexagonal ZnO tubes decreased from 4 to 0.6 μm^{-2} with increasing pressure from 0.3 to 3 Torr. The well-defined hexagonal shape is an indication of epitaxial growth and consequently single crystalline nature of the tubes. XRD studies (rocking curve, θ–2θ scan, and ϕ-scan measurements) of the samples showed that the tubes were well aligned both in the growth plane (in-plane) and along the growth

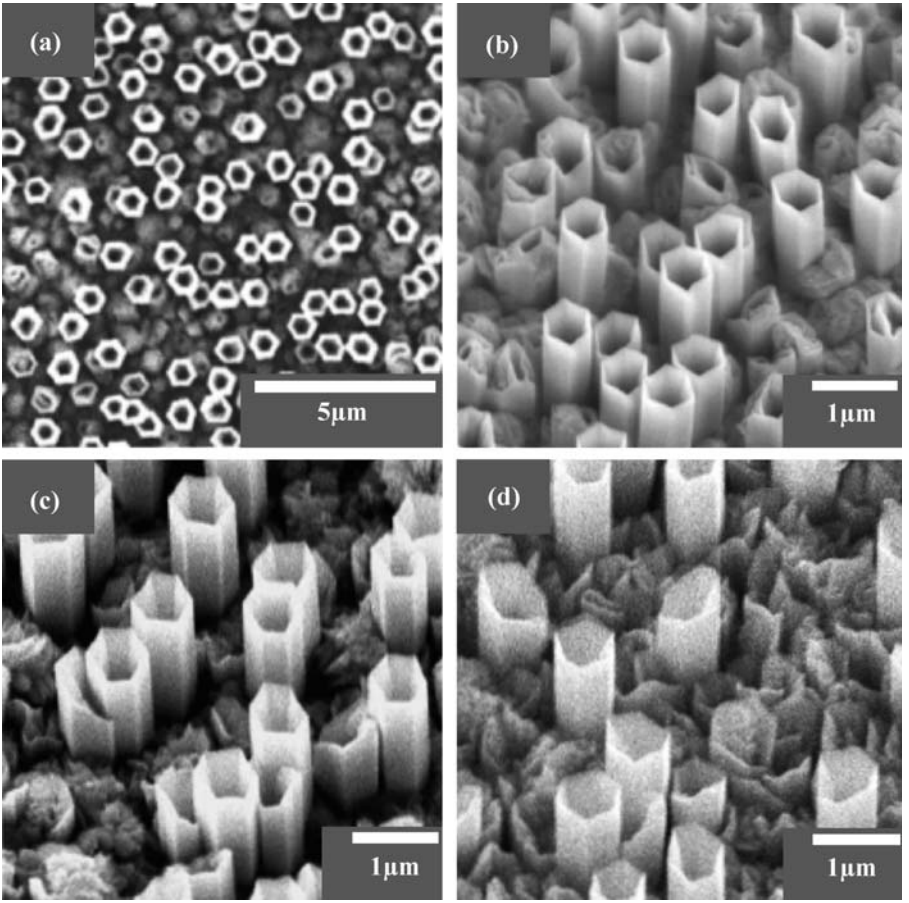

Figure 7.11 SEM images of ZnO tubes formed at 400 °C under different reactor pressures. (a) Top image of the tubes obtained at 0.3 Torr. (b), (c), and (d) SEM images taken with an inclination angle of the tubes obtained at 0.3, 0.6, and 1.0 Torr, respectively. (Courtesy of B.P. Zhang [33].)

direction (out-of-plane). The growth temperature also greatly influenced the tube formation. In the temperature range of 350–450 °C, the density of the tubes increased from 0.04 to 1 μm^{-2} and the outer sizes of the tubes decreased from 1.0 to 0.4 μm with increasing temperature. However, no tubes were obtained at 500 °C. Therefore, the tube density can be modified by changing either the growth temperature or the reactor pressure, and the tube size can be tuned with growth temperature.

To embed heterostructures directly into nanorods, MOVPE growth of ternary ZnMgO nanopillars has also been investigated using a bis(cyclopentadienyl)magnesium ($MeCp_2Mg$) precursor for Mg [31]. For incorporation of Mg into ZnO, the growth temperature had to be reduced from 950 to 700 °C after growth of a ZnO nanorod initiation layer. The resulting ZnMgO nanorods were also *c*-axis oriented

and vertically aligned as the ZnO nanorods. However, they did not show any PL peaks other than those from ZnO due to poor crystallinity and optical quality resulting from lower growth temperature. Therefore, MgZnO-related emission was evident only after annealing at 850 °C for 30 min, with up to 170 meV blueshift with respect to the ZnO band edge, corresponding to a Mg composition of about 9%.

The current–voltage characteristics of single ZnO nanorods grown by catalyst-driven MBE on Au-coated sapphire substrates have been investigated at different temperatures and gas ambients [34]. Individual nanorods were removed from the substrate and placed between ohmic contact pads 3.7 μm apart. The conductivity of the nanorods was increased by a postgrowth anneal in hydrogen gas at 400 °C. In a temperature range from 25 to 150 °C, the resistivity of nanorods treated in H_2 at 400 °C prior to measurement showed an activation energy of 0.089 ± 0.02 eV and was insensitive to the ambient used (C_2H_4,N_2O,O_2 or 10% H_2 in N_2). In sharp contrast, the conductivity of nanorods not treated in H_2 was sensitive to trace concentrations of gases in the measurement ambient even at room temperature, with increased currents in the presence of hydrogen, demonstrating their potential as gas sensors. Similar devices containing multiple nanorods were also shown to have *I–V* characteristics that are sensitive to the presence of ozone (O_3) [35].

Fabrication of single Pt/ZnO nanowire Schottky diodes was also achieved with nanowires grown by site-selective MBE and then transferred to SiO_2-coated Si substrates [36]. The diodes exhibited ideality factors of 1.1 at 25 °C and very low (1.5×10^{-10} A, equivalent to 2.35 A cm^{-2}, at −10 V) reverse currents. A strong photoresponse was also observed, with the current–voltage characteristics becoming ohmic when the diodes were illuminated by 366 nm wavelength light. The on–off current ratio at 0.15−5 V was ∼6. Thermionic emission was suggested to be the dominant current transport mechanism within the nanowire and densities of bulk and surface traps were assumed low.

7.1.3 Other Synthesis Methods

The gas-phase approaches discussed above are dominantly used for growing ZnO-based nanostructures. However, they require expensive equipment, source materials, and substrates and employ relatively high growth temperatures. Other simpler wet-chemical synthesis methods such as sol–gel [37], electrodeposition [38, 39], and aqueous chemical growth [40] have been developed for cost-effective growth of ZnO nanostructures at low temperatures [41–43]. On the other hand, the control of morphology and the positioning of the nanostructures using these techniques is challenging. Postgrowth photolithographic techniques and pregrowth patterning of the substrate using an Ag mask for selective growth have been used to achieve patterned arrays of ZnO nanorods with aqueous chemical growth [40].

In the context of using these simpler and cost-efficient techniques for device applications, Könenkamp *et al.* [39] fabricated vertical LEDs using ZnO nanowires grown by electrodeposition from aqueous solutions on fluorine-doped SnO_2-coated glass substrates. Because during electrodeposition the growth of ZnO columns

(100–200 nm in diameter and 2 μm in length) proceeded under electron injection from the underlying SnO_2 layer, a good electrical contact between SnO_2 and ZnO was assumed. The space between the nanowires was filled with polystyrene and a 0.5–1.5 μm-thick coating of poly(3,4-ethylene-dioxythiophene)(PEDOT)/poly(styrenesulfonate) was applied to establish p-type contact to the nanowire tips. Finally, a 100 nm-thick Au layer was deposited by vacuum evaporation to provide a Schottky barrier-type contact for hole injection. EL was observed from the device at a threshold of 10 V with a current density of $\sim 100\,\mathrm{mA\,cm^{-2}}$ at the nanowire tips. Similar to PL from uncoated nanowires, EL showed a broad defect-related emission centered at 620 nm. A shoulder at 384 nm, an order of magnitude weaker than the UV band-edge emission, was observed. Even though further improvements are needed to enhance UV emission, ZnO nanowire LEDs showed stable operation for $\sim$1 h.

7.2 Applications of ZnO Nanostructures

As already mentioned, intermixed with growth and characterization, ZnO nanostructures are considered for light-emitting applications such as nanolasers and also for field-effect transistors (FETs), gas sensors, nanoactuators, nanocantilevers, and so on. Some of these device applications are discussed in Chapter 8. Like ZnO thin films, ZnO nanorods and nanobelts have also been successfully utilized for FETs [44–48]. For operational principles of FETs, reader is referred to Section 8.5.4. Arnold *et al*. [44] fabricated FETs by depositing dispersed ZnO nanobelts on predefined gold electrode arrays. A SiO_2 gate dielectric of thickness 120 nm and a back gate electrode fabricated by evaporating gold on the p+ Si side of the substrate were used. By forming metal electrode/nanostructure electrical contacts, where electrode gaps were as small as 100 nm and as large as 6 μm, and capacitively coupling the nanostructure to a nearby gate electrode, a nanobelt FET was produced. A typical nanobelt FET showed a gate threshold voltage of −15 V, a switching ratio of nearly 100, and a peak conductivity of $1.25 \times 10^{-3}\,\Omega^{-1}\,\mathrm{cm}^{-1}$, see Ref. [44].

As discussed in Section 8.5.4, n-channel FETs with back gate geometry were also fabricated using e-beam lithography along with high-quality ZnO nanorods prepared by catalyst-free MOVPE [45]. Electron mobility measured for the nanorod FET structure ($75\,\mathrm{cm^2\,V^{-1}\,s^{-1}}$) was higher than that of ZnO thin film transistors [49], presumably due to high purity and low defect concentrations of single-crystal ZnO nanorods as a result of the employed catalyst-free growth method. The device characteristics significantly improved after passivating the nanorod surface with a polyimide thin layer, and electron mobilities higher than $1000\,\mathrm{cm^2\,V^{-1}\,s^{-1}}$ were obtained. As far as the origin of enhanced ZnO nanorod FET characteristics is concerned, studies suggested that polyimide coating suppresses the chemisorption process [50, 51], which decreases the transistor gain, in addition to improved quality. Furthermore, passivation of defects that deteriorate FET characteristics by trapping and scattering carriers [52, 53] and the gate structure being surrounded by polyimide

coating were also listed as possible causes for improved characteristics of ZnO nanorod FETs.

Heo *et al.* [48] fabricated single ZnO nanowire metal-oxide semiconductor field-effect transistors (MOSFETs) on SiO_2-coated Si substrates with top gate electrodes. The separation of the source–drain electrodes was 7 μm, and 50 nm- thick (Ce,Tb) $MgAl_{11}O_{19}$ was used as the gate dielectric. The depletion-mode transistors exhibited good pinchoff and saturation characteristics, a threshold voltage of approximately −3 V and a maximum transconductance of 0.3 mS mm^{-1}. When illuminated with ultraviolet light (366 nm), the drain–source current increased by approximately a factor of 5 and the maximum transconductance was ∼5 mS mm^{-1}. Part of the increase in drain–source current was due to photoconductivity in the portion of the wire uncovered by the gate metal. The estimated channel mobility was ∼3 cm^2 V^{-1} s^{-1} and the on–off ratio at V_g of 0–3 V and V_{ds} of 10 V was ∼25 in the dark and ∼125 under UV illumination.

ZnO nanowire FETs were utilized for O_2 detection [46]. Single-crystal ZnO nanowires synthesized, using a vapor-trapping CVD method, were configured as FETs, and the adsorption of oxygen molecules was shown to cause the depletion of the FET channel. Oxygen is chemisorbed to ZnO surface at vacancy sites, forming O_2^- and resulting in a surface charge depletion layer, thus leading to a reduction in the electrical conductivity. Moreover, the detection sensitivity could be modulated by gate voltage. The sensitivity was shown to increase with decreasing nanowire radius from 270 to 20 nm. The single nanowire photoconductivity spectrum was also measured for these FETs and the transconductance was observed to decrease with illumination. It was demonstrated that nanowire FETs could be reversibly turned on and off by applying a switching illumination. These results indicate the potential of ZnO for nanoscale electronics, optoelectronics, and chemical sensing devices.

ZnO nanobelts were also considered for applications as nanosensors and nanoactuators. The piezoelectric coefficient of a ZnO nanobelt was measured using AFM with a conductive tip [54]. For this purpose, ZnO nanobelts were dispersed on a (1 0 0) Si wafer coated with Pd. The nanobelts were then coated with 5 nm layer of Pd. It was ensured that the top and bottom surfaces of the nanobelts were not short-circuited. The effective piezoelectric coefficient d_{33} for the (0 0 0 1) surface of the nanobelts was measured by piezoresponse force microscopy. The d_{33} coefficient was found to vary from 26.7 to 14.3 pm V^{-1} with increasing frequency from 30 to 150 kHz. These values are considerably larger than that for bulk ZnO (9.9 pm V^{-1}).

ZnO nanostructures as nanocantilever arrays (nanofingers) have also been obtained, as shown in Figure 7.12. During the growth of nanocantilever arrays, the Zn-terminated ZnO (0 0 0 1) polar surface was reported to be chemically active and the oxygen-terminated {0 0 0 1} polar surface to be inert [21]. It should be pointed out that the (0 0 0 1) surface is the Zn polar surface, which upon exposure to O could be O terminated. On the other hand, the $(0\,0\,0\,\bar{1})$ surface is the O polar surface. Caution must be exercised to avoid any confusion. Relatively long and wide "comb-like" nanocantilever arrays have been grown from the (0 0 0 1) Zn surface (Figure 7.12) by a self-catalyzed process due to enrichment of Zn at the growth front [21]. The chemically inactive {0 0 0 1} O surface did not initiate any growth. The (0 0 0 1) Zn surface tended to

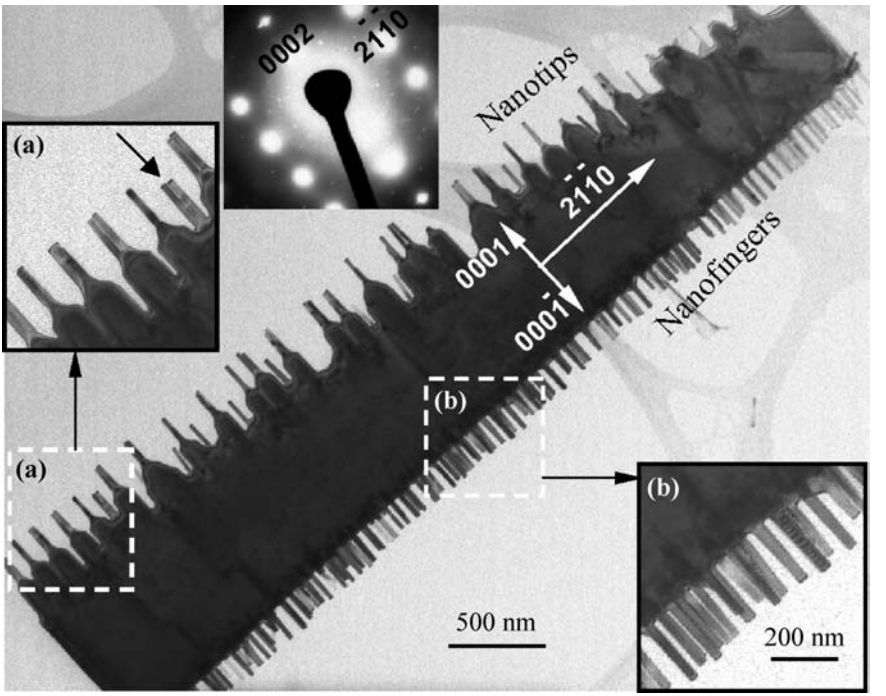

Figure 7.12 Transmission electron microscopy image of a double-sided comb structure, showing the distinct arrays of nanotips and nanofingers on the two sides. The insets are the corresponding electron diffraction pattern and the enlargements of two selected areas, as indicated. (Courtesy of Z.L. Wang [21].)

have small Zn clusters at the growth front, as evidenced by the high-resolution TEM image. The Zn clusters as well as the local enrichment in Zn at the growth front tend to initiate the growth of ZnO analogous to the vapor–liquid–solid growth process. Therefore, the self-catalyzed effect of Zn clusters resulted in fast growth of the nanotips. The $\{0\,0\,0\,1\}$ O-terminated surface, however, is likely to be inert and may not exhibit an effective self-catalyzed effect; thus, the surface may not initiate the growth of nanocantilevers. By changing the growth kinetics so that there is no growth on the $\{0\,0\,0\,1\}$ O-terminated surface, a comb-like structure with long teeth only on one side has been grown, as depicted in Figure 7.12, with the top/bottom surfaces being $\pm(0\,1\,\bar{1}\,0)$ and the side surfaces $\pm(2\,\bar{1}\,\bar{1}\,0)$. It is possible that a change in growth condition results in the disappearance of the $\{0\,0\,0\,1\}$ type of facets; thus, the chemically inert $\{0\,0\,0\,1\}$ surface does not initiate any teeth growth.

Microelectromechanical systems (MEMS) have already transitioned to a new realm with much improved sensitivity and functionality. Further improvements are assumed within reach with nanostructures. For example, by combining MEMS technology with self-assembled nanobelts, cost-effective cantilevers with much improved sensitivity may be produced for a range of devices and applications such as force, pressure, mass, and thermal, biological, and chemical sensors.

Semiconducting nanobelts are ideal candidates for cantilever applications, because they are structurally defect-free single crystals and provide a significant improvement in the cantilever sensitivity due to their reduced dimensions. Individual ZnO nanobelts could be aligned on Si chips to have a range of lengths and therefore resonance frequencies [3].

In conclusion, it is clear that a wide variety of nanostructures can be produced with ZnO using relatively simple synthesis methods. These nanostructures can certainly be used for studying fundamental physics in nanoscale. Even though devices have already been demonstrated using ZnO nanostructures (see also Chapter 8), whether the advancements in technology and materials science will allow their applications to real-life devices is not yet clear. However, it is clear that ZnO is very favorable as compared to other semiconductors in that this material lends itself well to the production of nanostructures from which functional devices have already been fabricated.

References

1 Wang, Z.L. (2004) *Materials Today*, **7**, 26.

2 Pan, Z.W., Dai, Z.R. and Wang, Z.L. (2001) *Science*, **291**, 1947.

3 Wang, Z.L. (2004) *Journal of Physics: Condensed Matter*, **16**, R829.

4 Heo, Y.W., Norton, D.P., Tien, L.C., Kwon, Y., Kang, B.S., Ren, F., Pearton, S.J. and LaRoche, J.R. (2004) *Materials Science & Engineering R-Reports*, **47**, 1.

5 Duan, X., Huang, Y., Cui, Y., Wang, J. and Lieber, C.M. (2001) *Nature*, **409**, 66.

6 Huang, M.H., Mao, S., Feick, H., Yan, H., Wu, Y., Kind, H., Weber, E., Russo, R. and Yang, P. (2001) Room temperature ultraviolet nanowire lasers. *Science*, **292**, 1897.

7 Kong, X.Y., Ding, Y., Yang, R. and Wang, Z.L. (2004) Single-crystal nanorings formed by epitaxial self-cooling of polar nanobelts. *Science*, **303**, 1348.

8 Bai, X.D., Gao, P.X., Wang, Z.L. and Wang, E.G. (2003) *Applied Physics Letters*, **82**, 4806.

9 Roy, V.A.L., Djurisic, A.B., Chan, W.K., Gao, J., Lui, H.F. and Surya, C. (2003) *Applied Physics Letters*, **83**, 141.

10 Yu, S.F., Clement Yuen, Lau, W.I., Park, S.P. and Yi, G.-C. (2004) *Applied Physics Letters*, **84**, 3241.

11 Yatsui, T., Kawazoe, T., Ueda, M., Yamamoto, Y., Kourogi, M. and Ohtsu, M. (2001) *Applied Physics Letters*, **81**, 3651.

12 Qiu, Z., Wong, K.S., Wu, M., Lin, W. and Xu, H. (2004) *Applied Physics Letters*, **84**, 2739.

13 Chik, H., Liang, J., Cloutier, S.G., Kouklin, N. and Xu, J.M. (2004) *Applied Physics Letters*, **84**, 3376.

14 Zhao, Q.X., Willander, M., Morjan, R.E., Hu, Q.-H. and Campbell, E.E.B. (2003) *Applied Physics Letters*, **83**, 165.

15 Park, W.I., Kim, D.H., Jung, S.-W. and Yi, G.-C. (2002) Metalorganic vapor-phase epitaxial growth of vertically well-aligned ZnO nanorods. *Applied Physics Letters*, **80**, 4232.

16 Liu, X., Wu, X., Cao, H. and Chang, R.P.H. (2004) *Journal of Applied Physics*, **96**, 3141.

17 Li, Y.B., Bando, Y. and Golberg, D. (2004) *Applied Physics Letters*, **84**, 3603.

18 Gao, P.X. and Wang, Z.L. (2004) Nanopropeller arrays of ZnO. *Applied Physics Letters*, **84**, 2883.

19 Yu, W.D., Li, X.M. and Gao, X.D. (2004) *Applied Physics Letters*, **84**, 2658.

20 Djurišić, A.B., Leung, Y.H., Choy, W.C.H., Cheah, K.W. and Chan, W.K. (2004) Visible photoluminescence in ZnO tetrapod and

multipod structures. *Applied Physics Letters*, **84**, 2635.

21 Wang, Z.L., Kong, X.Y. and Zuo, J.M. (2003) Induced growth of asymmetric nanocantilever arrays of polar surfaces. *Physical Review Letters*, **91**, 185502.

22 Zhang, B.P., Binh, N.T., Segawa, Y., Kashiwaba, Y. and Haga, K. (2004) Photoluminescence study of ZnO nanorods epitaxially grown on sapphire ($11\bar{2}0$) substrates. *Applied Physics Letters*, **84**, 586.

23 Haupt, M., Ladenburger, A., Sauer, R., Thonke, K., Glass, R., Roos, W., Spatz, J.P., Rauscher, H., Riethmüller, S. and Möller, M. (2003) *Journal of Applied Physics*, **93**, 6252.

24 Ladenburger, A., Haupt, M., Sauer, R., Thonke, K., Xu, H. and Goedel, W.A. (2003) *Physics E*, **17**, 489.

25 Shan, W., Walukiewicz, W., Ager, J.W., III, Yu, K.M., Zhang, Y., Mao, S.S., Kling, R., Kirchner, C. and Waag, A. (2005) *Applied Physics Letters*, **86**, 153117.

26 Zhou, H., Fallert, J., Sartor, J., Dietz, R.J.B., Klingshirn, C., Kalt, H., Weissenberger, D., Gerthsen, D., Zeng, H. and Cai, W. (2008) *Applied Physics Letters*, **92**, 132112.

27 Zhou, H., Wissinger, M., Fallert, J., Hauschield, R., Stelzl, F., Klingshirn, C. and Kalt, H. (2007) *Applied Physics Letters*, **91**, 181112.

28 Hauschild, R. and Kalt, H. (2006) *Applied Physics Letters*, **89**, 123107.

29 Wang, X.D., Ding, Y., Summers, C.J. and Wang, Z.L. (2004) *The Journal of Physical Chemistry B*, **108**, 8773.

30 Kong, X.Y. and Wang, Z.L. (2003) *Nano Letters*, **3**, 1625.

31 Kling, R., Kirchner, C., Gruber, T., Reuss, F. and Waag, A. (2004) *Nanotechnology*, **15**, 1043.

32 Park, W.I., Jun, Y.H., Jung, S.W. and Yi, G.-C. (2003) *Applied Physics Letters*, **82**, 964.

33 Zhang, B.P., Binh, N.T., Wakatsuki, K., Segawa, Y., Yamada, Y., Usami, N., Kawasaki, M. and Koinuma, H. (2004) Formation of highly oriented ZnO tubes on sapphire (0 0 0 1) substrates. *Applied Physics Letters*, **84**, 4098.

34 Heo, Y.W., Tien, L.C., Kwon, Y., Norton, D.P., Pearton, S.J., Kang, B.S., Ren, F., Gila, B.P. and Pearton, S.J. (2004) *Applied Physics Letters*, **85**, 2002.

35 Kang, B.S., Heo, Y.W., Tien, L.C., Norton, D.P., Ren, F., Gila, B.P. and Pearton, S.J. (2005) *Applied Physics A: Materials Science & Processing*, **80**, 1029.

36 Heo, Y.W., Tien, L.C., Kwon, Y., Pearton, S.J., Kang, B.S., Ren, F. and LaRoche, J.R. (2004) *Applied Physics Letters*, **85**, 3107.

37 Lakshmi, B.B., Patrissi, C.J. and Martin, C.R. (1997) *Chemistry of Materials*, **9**, 2544.

38 Li, Y., Cheng, G.S. and Zhang, L.D. (2000) *Journal of Materials Research*, **15**, 2305.

39 Könenkamp, R., Word, R.C. and Schlegel, C. (2004) *Applied Physics Letters*, **85**, 6004.

40 Postels, B., Kreye, M., Wehmann, H.-H., Bakin, A., Boukos, N., Travlos, A. and Waag, A. (2007) *Superlattices and Microstructures*, **42**, 425.

41 Li, Z., Xiong, Y. and Xie, Y. (2003) *Inorganic Chemistry*, **42**, 8105.

42 Liu, B. and Zeng, H.C. (2004) *Langmuir*, **20**, 4196.

43 Mulligan, R.F., Iliadis, A.A. and Kofina, P. (2003) *Journal of Applied Polymer Science*, **89**, 1058.

44 Arnold, M.S., Avouris, P., Pan, Z.W. and Wang, Z.L. (2003) *The Journal of Physical Chemistry. B*, **107**, 659.

45 Park, W.I., Kim, J.S., Yi, G.-C., Bae, M.H. and Lee, H.-J. (2004) Fabrication and electrical characteristics of high-performance ZnO nanorod field effect transistors. *Applied Physics Letters*, **85**, 5052.

46 Fan, Z., Wang, D., Chang, P.-C., Tseng, W.-Y. and Lu, J.G. (2004) *Applied Physics Letters*, **85**, 5923.

47 Fan, Z., Chang, P.-C., Lu, J.G., Walter, E.C., Penner, R.M., Lin, C.-H. and Lee, H.P. (2004) *Applied Physics Letters*, **85**, 6128.

48 Heo, Y.W., Tien, L.C., Kwon, Y., Norton, D.P., Pearton, S.J., Kang, B.S. and Ren, F. (2004) *Applied Physics Letters*, **85**, 2274.

49 Bae, H.S., Yoon, M.H., Kim, J.H. and Im, S. (2003) *Applied Physics Letters*, **82**, 733.

50 Liu, M. and Kim, H.K. (2004) *Applied Physics Letters*, **84**, 173.
51 Lagowski, L., Sproles, E.S., Jr, and Gatos, H.C. (1977) *Journal of Applied Physics*, **48**, 3566.
52 Masum, J., Parmiter, P., Hall, T.J. and Crouch, M. (1996) *IEE Proceedings-G: Circuits. Devices and Systems*, **143**, 307.
53 Xiong, Y.Z., Ng, G.-I., Wang, H. and Fu, J.S. (2001) *IEEE Transactions on Electron Devices*, **48**, 2192.
54 Zhao, M.H., Wang, Z.L. and Mao, S.X. (2004) *Nano Letters*, **4**, 587.

8
Processing, Devices, and Heterostructures

In many respects, ZnO competes with GaN for device applications. However, there is no doubt that GaN device technology is much more mature, as GaN-based very high-performance electronic and optical devices have already been demonstrated. GaN-based power field effect transistors (FETs) are capable of producing over 500 W of CW power in the communication band, light emitting diodes (LEDs) have taken world like a storm with emphasis on the efficiency in performance, while they are already more efficient than the mighty fluorescent bulbs, and blue lasers are already used in game consoles and high-definition video players. The same, however, cannot necessarily be said about ZnO even though its applications overlap a good deal with those of GaN. On the electronic side, the relatively low mobility of ZnO compared to GaN and stronger electron–phonon coupling, together with relatively low-thermal conductivity, are serious shortcomings of ZnO. However, transparent thin-film transistors (TFTs) built in poly-ZnO appear to hold some potential. Furthermore, the worldwide shortage of In in the face of expanding demand for indium tin oxide (ITO) seems to be opening the door for ZnO-based transparent oxides to be explored. If successful, this application area is huge. It remains to be seen, however, as to how competitive ZnO would be with the existing technologies. On the optical device front, ZnO needs desperately to show high p-type conductivity along with hetero-junctions for competitive devices to be built. Again the competition is GaN, which is well on its way to really dominate the optical device development arena for quite sometime. One advantage ZnO has over GaN is that its exciton-binding energy is 60 meV compared to 25 meV for GaN. In addition, ZnO appears to be a more efficient light emitter compared to GaN. If lasers utilizing excitonic transitions were to be built, ZnO would have an advantage over GaN provided p-type conductivity is obtained and other necessary processing capabilities are developed for ZnO. Furthermore, electromechanical coupling of ZnO, particularly along the *c*-direction, is higher than that of GaN, which could pave the way for applications such as acoustic wave devices (to some extent it has already). In addition, ZnO appears to be well suited for producing nanostructures, which may be used for devices. A significant part of the recent research in the field of ZnO-based devices and applications has dealt mostly with ZnO nanostructures (nanowires, nanorods, nanobelts, nanotips) and their integration into the mainstream semiconductor materials – with Si, GaN,

and organic semiconductors. One-dimensional (1D) nanostructures, such as nanowires (NWs), have attracted a great deal of attention due to their advantages, for example, good charge carrier transport properties and high crystalline quality [1–3]. 1D systems have unique properties that make them potentially attractive for nanoscale devices, such as light-emitting diodes, lasers, photodetectors, chemical/biosensors, and surface acoustic wave (SAW) devices, which have been intensively investigated [4–7].

It is imperative that a semiconductor device be connected to the outside world with ideally no adverse change to its current–voltage characteristics and no additional voltage drop. This can be accomplished only through low-resistance ohmic contacts to the semiconductor. An ideal contact is one where, when combined with the semiconductor, there are no barriers to the carrier flow in either the positive or the negative direction. Ideally, this occurs when the semiconductor and the metal work functions are about the same, and there are no appreciable interface states, which tend to pin the Fermi level. Because one cannot just dial up an ideal work function for the semiconductor–metal system under consideration, particularly when the work function of the semiconductor varies with doping, it is not possible to find just the right combination. In the event that the contact is not Ohmic, a Schottky barrier is formed at the semiconductor–metal interface, the height of which is determined by the work functions of the metal and the semiconductor. Schottky contacts are employed for rectifier devices, Schottky diode being the simplest example. Schottky diodes have lower blocking voltages than their p–i–n counterparts but have advantages in terms of switching speed and lower forward voltage drop. In this chapter, Ohmic and Schottky contacts to ZnO are discussed first followed by the device applications of ZnO along with the processing-related issues.

8.1
A Primer to Semiconductor–Metal Contacts

When a metal and a semiconductor (ideally with no surface states) are brought in contact and equilibrium is maintained, their Fermi levels will align. If the Fermi levels of the metal and the semiconductor were the same before contact, then there would be no change in the band structure after contact. Usually, matching the work functions is nearly impossible in part because the Fermi level in the semiconductor, and thus the work function, depends on the carrier concentration.

Let us consider the case of an n-type semiconductor and a metal with a work function that is larger than that of the semiconductor. The alignment of the Fermi levels after contact, brought about by the electron motion from the higher-toward-the-lower-energy side, creates a depletion region in the semiconductor and a barrier at the interface. The barrier height ϕ_B is simply the difference between the metal work function ϕ_m and the electron affinity (χ) in the n-type semiconductor ($\phi_m - \chi$), as shown in Figure 8.1. Similarly, the band diagram for a rectifying metal p-type semiconductor system before and after contact (in equilibrium) is shown in Figure 8.2a and b, respectively. In these ideal pictures, the amount of band bending

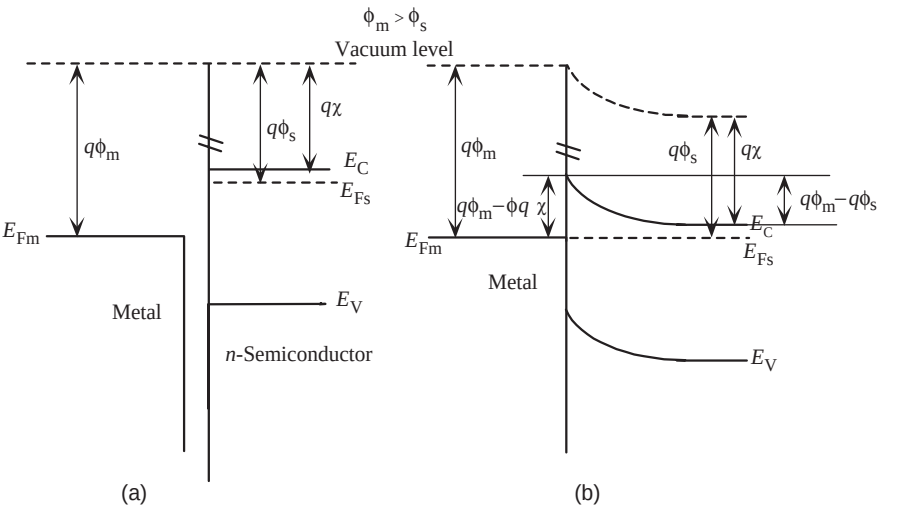

Figure 8.1 A metal n-type semiconductor pair before (a) and after (b) contact with no surface/interface states. The metal work function is greater than that for the semiconductor ($\phi_m > \phi_s$).

in the semiconductor is the difference between the metal work function ϕ_m and semiconductor work function ϕ_s, $(\phi_m - \phi_s)$.

In a metal–semiconductor junction, the electrons approaching the interface also experience an image-force lowering of the barrier. A negative charge at a distance x

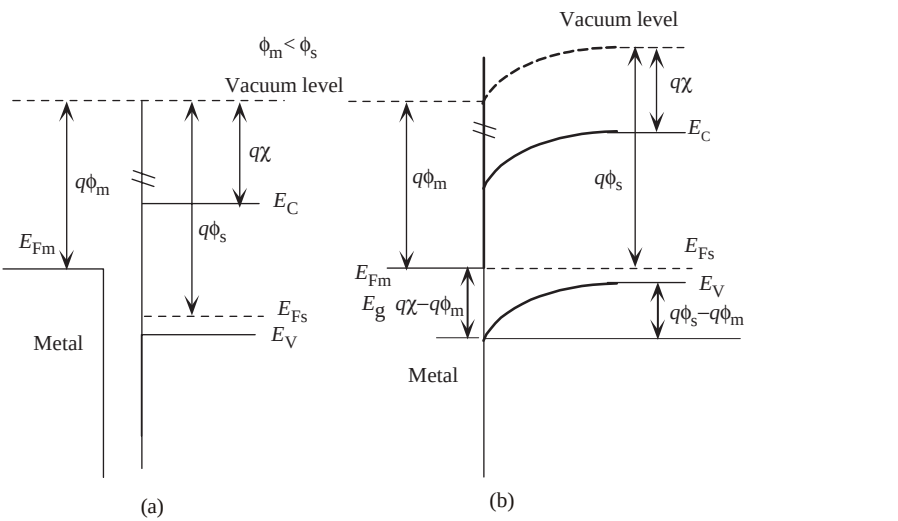

Figure 8.2 A metal p-type semiconductor pair before (a) and after (b) contact with no surface/interface states. The metal work function is greater than that for the semiconductor ($\phi_s > \phi_m$).

from the surface of, say, a metal induces a positive image charge of equal value at a distance $-x$ from the surface (into the metal). The total potential energy resulting from the attractive force between the electron and its positive-charged image separated by $2x$ and the applied electric field can be written as

$$U(x) = -\frac{q^2}{16\pi\varepsilon_0 x} - qEx, \tag{8.1}$$

where E is the net electric field and q is the electron charge. Notice that there is already a built-in electric field normal to the surface at the interface after contact of the metal with the semiconductor due to an alignment of Fermi levels as seen in Figures 8.1 and 8.2. Application of an additional electric field (bias) will contribute to the total electric field appearing in Equation 8.1. The maximum (minimum in the case of p-type semiconductor) of the potential in the semiconductor occurs at a distance x_m from the interface, which is where the derivative of the potential energy in Equation 8.1 goes to zero:

$$x_m = \sqrt{\frac{q}{16\pi\varepsilon_s\varepsilon_0 E}}. \tag{8.2}$$

Here, ε_s is the relative dielectric constant of the semiconductor and ε_0 is the permittivity of free space. Under the influence of the electric field applied normal to the surface, the confining barrier can be lowered, and the magnitude of this image-force lowering of the barrier is given by

$$\Delta\phi_B = \sqrt{\frac{qE}{4\pi\varepsilon_s\varepsilon_0}}. \tag{8.3}$$

Clearly, the image-force lowering increases through a square root dependence with the electric field. The resulting effective barrier for electron escaping the metal can be expressed as

$$\phi_B = q(\phi_m - \chi) - \Delta\phi_B. \tag{8.4}$$

For an ideal but rectifying metal n-type semiconductor contact with image-force lowering, the conduction band energy diagram at the interface is shown in Figure 8.3 for equilibrium, and forward- and reverse-bias cases. In the equilibrium case of Figure 8.3a, no external bias is applied to the metal–semiconductor rectifying contact. Forward bias (negative voltage applied to the n-type semiconductor with respect to the metal) lowers the barrier to the electron flow from the semiconductor side by the amount of the applied bias, as shown in Figure 8.3b, and a reverse bias (positive voltage applied to the n-type semiconductor with respect to the metal) increases the barrier as shown in Figure 8.3c. The barrier to electron flow from the metal to the semiconductor remains almost unchanged except through a change in $\Delta\phi_B$. The net electric field in the semiconductor near the interface is decreased with forward bias and increased with reverse bias. This image-force lowering term increases with increasing electric field due to a reverse bias and decreases with forward bias as described by Equation 8.3. In addition, the position

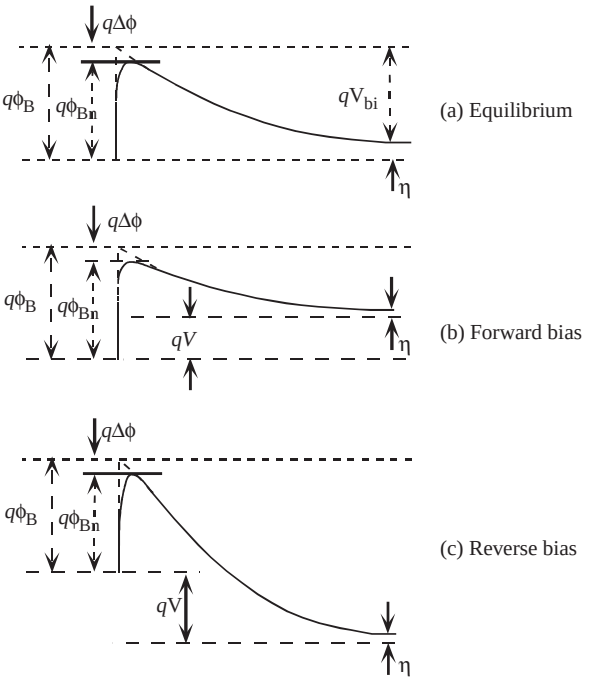

Figure 8.3 Ideal metal n-type semiconductor contacts under (a) equilibrium and (b) forward and (c) reverse biases. Also shown is the image-force lowering of the barrier.

of the peak in the barrier, x_m, moves closer to the metal–semiconductor interface with increasing electric field due to the reverse bias as expected from Equation 8.2. For the metal/p-type semiconductor system, the dependencies of the barrier lowering and the position of the potential maximum on the applied bias are similar to that for n-type semiconductor.

When a bias is applied to the metal–semiconductor system, current flow takes place if the carriers in the metal or in the semiconductor gain sufficient energy, by thermal means or by means of electric field or by both, to overcome the potential barrier. However, when the barrier is sufficiently thin, they can also go through the barrier either by direct tunneling, if the barrier thickness is comparable to the tunneling distance, or by gaining sufficient energy with respect to the Fermi level combined with tunneling at some point in the barrier. The current conduction process over or through a barrier created by a metal semiconductor contact is schematically shown in Figure 8.4. These processes can be circumvented by defects through trap-assisted processes. In cases when defects are not involved, there are three mechanisms [8–10] that govern the current flow in a metal–semiconductor system, namely, thermionic emission (TE), thermionic field emission (TFE), and field emission (FE). A brief review of these mechanisms is given in the following sections.

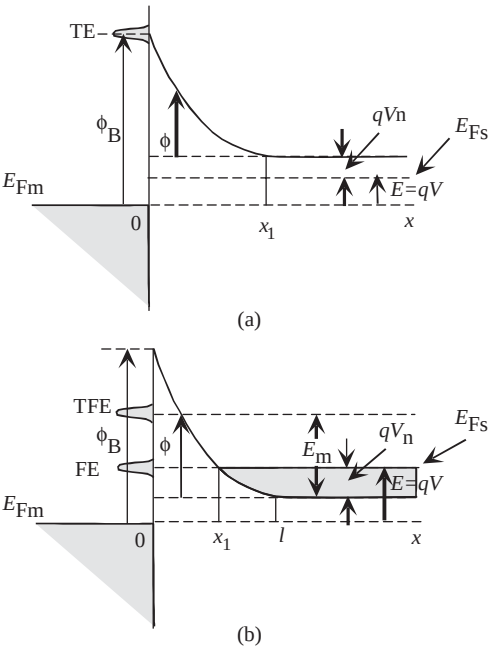

Figure 8.4 Potential energy diagram and current flow mechanisms for a forward-biased Schottky barrier: (a) for the thermionic emission process, which is more likely when the doping level in the semiconductor is relatively low and the Fermi level is below the conduction band, and (b) for the thermionic field emission and direct tunneling, referred to as field emission, which is more likely when the doping level in or on the semiconductor surface is sufficiently high to the extent that the Fermi level may even be in the conduction band as depicted.

8.1.1 Thermionic Emission

For lightly or moderately doped semiconductors, $N_d \lessapprox 10^{17}\,\mathrm{cm}^{-3}$, the depletion region is relatively wide. It is, therefore, nearly impossible for electrons to tunnel through the barrier unless aided by defects, which are considered not to exist in this ideal picture. In a forward-biased junction, however, the electrons can surmount the top of the barrier, which is lowered with respect to the Fermi level in the semiconductor by an amount equal to the applied bias. This thermally activated process is called the thermionic emission as shown in Figure 8.4a and has been treated in many studies and early literature such as the one by Henish [11]. In reverse bias, the barrier for electrons from the semiconductor to the metal is made even larger, and the electron flow from the semiconductor to the metal in this ideal picture is cut off. On the metal side, if the electrons in the metal gain sufficient energy by the applied bias, they too can overcome the barrier, which is the dominant mechanism for the reverse-bias current in an ideal picture. Naturally, an ohmic behavior is not observed. The electron flow from the metal to the semiconductor and from the semiconductor to the

metal must balance for zero bias under steady-state conditions, which ensures zero net current. The thermionic process requires electrons to gain considerable energy for current flow from which it gets its name.

The traditional current–voltage expression representing thermionic emission is given by

$$J_{te} = J_{te0}\left[\exp\left(\frac{qV}{kT}\right) - 1\right] \tag{8.5}$$

with

$$J_{te0} = A^* T^2 \exp\left(\frac{-q\phi_B}{kT}\right), \tag{8.6}$$

where J_{te0} is the saturation value of the current density J_{te}, A^* is the *effective Richardson constant*, ϕ_B is the barrier height including the effect of the image-force barrier lowering $\Delta\phi_B$ as given in Equation 8.4. Equation 8.5 is based on the condition that the series resistance of the circuit is negligibly small. It should be pointed out that the saturation current density is typically designated by J_S instead of J_{te0} in general. As the kT term in the exponent indicates, the slope of J_{te0}/T^2 would vary with temperature with a slope of kT in a semilogarithmic plot. Under the assumption of single-valley conduction bands such as n-type ZnO and single and spherical valence band conduction, the effective Richardson constant is

$$\begin{aligned} A^* &= A^*_{free}\left(\frac{m^*_e}{m_0}\right) \quad \text{(n-type)}, \\ A^* &= A^*_{free}\left(\frac{m^*_{hh}}{m_0}\right) \quad \text{(p-type)}, \end{aligned} \tag{8.7}$$

where $A^*_{free} = 4\pi q k^2 m_0/h^3 = 120\ \text{A cm}^{-2}\ \text{K}^{-2}$ is the Richardson constant for free space. When both heavy- and light-hole bands are occupied or the valence band is degenerate such as in cubic compound semiconductors, the effective Richardson constant for p-type is given by

$$A^* = A^*_{free}\left(\frac{m^*_{hh} + m^*_{lh}}{m_0}\right). \tag{8.8}$$

Equation 8.5 is a representation of the carrier flux from the semiconductor to the metal, with the barrier being voltage (V) dependent, $\phi_B - V$. If from the metal to the semiconductor, with the barrier fixed at ϕ_B, there exists a parasitic resistance in the circuit such as semiconductor resistance (R_s), the thermionic-emission current expression is modified as

$$J_{te} = J_{te0}\left[\exp\left(\frac{q(V - IR_s)}{kT}\right) - \right]1, \tag{8.9}$$

where the current I is determined by the product of the current density J and the area of the structure. Furthermore, because both A^* and $\Delta\phi_B$ are voltage dependent, it is

customary to represent the current–voltage characteristics for applied voltages >3kT/q for simplicity as

$$J_{te} = J_{te0}\left[\exp\left(\frac{qV}{nkT}\right) - \right]1, \tag{8.10}$$

where n denotes the ideality factor and lumping deviations from ideal thermionic emission. The saturation current density J_{te0}, which is given by Equation 8.6, is to a first extent independent of voltage except through any barrier lowering.

In the reverse direction, the barrier lowering becomes more important. In such a case (using J_S instead of J_{te0} for saturation current),

$$J_R \approx J_S = A^* T^2 \exp\left(\frac{-q\phi_B}{kT}\right), \tag{8.11}$$

where the image-force barrier lowering $\Delta\phi_B$ is included in the expression for the net barrier ϕ_B, and the electric field at the metal semiconductor interface is given by

$$E = \sqrt{\frac{2qN_D}{\varepsilon_0\varepsilon_s}\left(-V + V_{bi} - \frac{kT}{q}\right)}. \tag{8.12}$$

Neglecting the image-force lowering, the barrier height and the effective Richardson constant can be experimentally determined by plotting $\ln(J_R/T^2)$ versus $1000/T$ (Richardson plot). Actually, the result would be that of the effective barrier height including the image-force lowering. If the interface electric field can be determined, the image-force lowering can be calculated. Performing the measurements for a range of reverse-bias conditions that would allow the determination of saturation current for that range of biases would allow the determination of the image-force lowering component. The assumption here is that components of the current other than the thermionic emission do not exist or can be separated. Confidence can be gained if the image-force lowering so determined is linearly dependent on the square root of the interface electric field. From an experimental point of view, generation–recombination current would also increase, unless negligible, which would exacerbate the determination of barrier lowering by image force.

The generation–recombination current is given by

$$J_{gr} = \frac{qn_i W}{\tau}\exp\left(\frac{qV}{2kT}\right), \tag{8.13}$$

where n_i is the intrinsic carrier concentration, τ is the effective carrier lifetime, and W is the depletion depth given by

$$W = \sqrt{\frac{2\varepsilon_0\varepsilon_s(V_{bi} - V)}{qN_D}}. \tag{8.14}$$

The contribution by the generation–recombination current to the overall current is negligibly small for ZnO even for very small effective carrier lifetimes, because the intrinsic carrier concentration is nearly zero at room temperature (RT). Even at

elevated temperatures, this remains to be the case because intrinsic concentration at those temperatures remains negligibly small.

8.1.2 Thermionic–Field Emission

For intermediately doped semiconductors, $\approx 10^{17}\,\mathrm{cm}^{-3} < N_\mathrm{d} \lessapprox 10^{18}\,\mathrm{cm}^{-3}$, the depletion region is not sufficiently thin to allow direct tunneling of carriers that are more or less in equilibrium. This process requires some energy gain from the bias sufficient to raise the electron energy to a value E_m where the barrier is sufficiently thin for tunneling, as shown in Figure 8.4b. This process was first discussed by Dolan and Dyke [12] in conjunction with field emission from a metal tip. This process is one that incorporates elements of thermionic emission, in the sense that electrons must be moderately hot or warm, and tunneling that requires penetration through a sufficiently thin barrier.

Thermionic field emission in classical treatments is assumed to be associated with the intermediate temperature range and where the electrons tunnel from the semiconductor to the metal at an energy E_m above the conduction band edge. The component of the current for the TFE process from the semiconductor to the metal for this form of current transport has been expressed by Stratton [13] and Padovani and Stratton [14] as

$$J_\mathrm{tfe} = \frac{A^* T^2}{2\pi kT}\left(\frac{\pi}{f_\mathrm{m}}\right)^{1/2} \exp\left(\frac{qV_\mathrm{n}}{kT} - b_\mathrm{m} - c_\mathrm{m}E_\mathrm{m}\right)\left[1 + \mathrm{erf}\left(E_\mathrm{m} f_\mathrm{m}^{1/2}\right)\right]. \tag{8.15}$$

The constants b_m, c_m, and f_m are the Taylor expansion coefficients for the exponent of the transparency of the barrier around an energy E_m. The energy E_m is chosen to satisfy $c_\mathrm{m}kT = 1$ (This would make $c_\mathrm{m}E_\mathrm{m}$ term in Equation 8.15 E_m/kT).

If the extension of the Fermi level into the conduction band qV_n is taken as positive, b_m, c_m, and f_m constants are defined as

$$b_\mathrm{m} = \left[\frac{q(\phi_\mathrm{B} - V + V_\mathrm{n})^{1/2}(\phi_\mathrm{B} - V + V_\mathrm{n} - E_\mathrm{m}/q)^{1/2} - E_{00}E_\mathrm{m}/kT}{E_{00}}\right], \tag{8.16}$$

$$c_\mathrm{m} = \frac{1}{E_{00}}\log\left[\frac{q^{1/2}(\phi_\mathrm{B} - V + V_\mathrm{n})^{1/2} + (q\phi_\mathrm{B} - qV + qV_\mathrm{n} - E_\mathrm{m})^{1/2}}{E_\mathrm{m}^{1/2}}\right], \quad \text{and} \tag{8.17}$$

$$f_\mathrm{m} = \frac{\cos h^2(E_{00}/kT)}{4E_{00}q(\phi_\mathrm{B} - V + V_\mathrm{n})}, \quad \text{respectively,} \tag{8.18}$$

where

$$E_{00} = \frac{q\hbar}{2}\sqrt{\frac{N_\mathrm{D}}{\varepsilon_\mathrm{s} m^*}}. \tag{8.19}$$

In the case of nondegenerate semiconductors, the sign of the qV_n term would be reversed. The energy E_m at which the electron emission takes place can be found using $c_m KT = 1$ and Equation 8.17 and is given by

$$E_m = \frac{q(\phi_B - V + V_n)}{\cos h^2(E_{00}/kT)}. \tag{8.20}$$

An inspection of Equation 8.15 together with Equations 8.16–8.18 leads to the recognition that the current–voltage characteristics are dominated by the exponential factor, and neglecting the error function term in Equation 8.15, the forward current density due to TFE can be expressed as

$$J_{tfeF} = J_{tfe0}\exp\left(\frac{qV}{E_0}\right), \tag{8.21}$$

where

$$E_0 = E_{00}\cot h\left(\frac{E_{00}}{kT}\right) \tag{8.22}$$

and $J_{tfe0} = J_{SF}$ is the saturation value of the forward current J_{tfeF} expressed by

$$J_{tfe0} = J_{SF} = \frac{A^* T^2\sqrt{\pi q E_{00}(\phi_B - V + V_n)}}{kT\cos h(E_{00}/kT)}\exp\left(\frac{qV_n}{kT} - \frac{q(\phi_B + V_n)}{E_0}\right). \tag{8.23}$$

Considering the electron emission from the metal to the semiconductor at the energy E_m, the total current in the forward direction and neglecting the error function term in Equation 8.15, in the framework of the TFE regime, the forward current can be expressed as

$$J_F = J_{SF}[\exp(qV/n_F kT) - 1] \quad \text{with} \quad n_F = \frac{E_{00}}{kT}\cot h\left(\frac{E_{00}}{kT}\right) = \frac{E_0}{kT}. \tag{8.24}$$

In reverse bias, the metal potential is raised. If the doping level in the semiconductor is low and the barrier width is large (keep in mind that the barrier width becomes smaller for energies above the Fermi level in the metal compared to the forward-bias case), the current flow takes place through thermionic emission, and Equation 8.5 together with Equation 8.6 treats the problem well. However, in cases when the doping level is moderate or high, the dominant current mechanism in the reverse-bias direction also would be TFE in an intermediate temperature range as in the case of forward-bias/under similar conditions but in the low-temperature range, field emission would be dominant as will be discussed later. In the intermediate temperature region for reverse bias, if the electrons are assumed to tunnel at an energy E_m, the parameters b_m, c_m, and f_m can be obtained as

$$b_m = \frac{q(E_m - V - E_{Fm})}{E_{00}}\left[\frac{(q\phi_B - qV)^{1/2}(q\phi_B + E_{Fm} - E_m)^{1/2}}{E_m - E - E_{Fm}} - \log\frac{(q\phi_B - qV)^{1/2} + (q\phi_B + E_{Fm} - E_m)^{1/2}}{(E_m - E - E_{Fm})^{1/2}}\right], \tag{8.25}$$

$$c_{\mathrm{m}} = \frac{1}{E_{00}} \log \left[\frac{(q\phi_{\mathrm{B}} - qV)^{1/2} + (q\phi_{\mathrm{B}} + E_{\mathrm{Fm}} - E_{\mathrm{m}})^{1/2}}{(E_{\mathrm{m}} - qV - E_{\mathrm{Fm}})^{1/2}} \right], \quad \text{and} \tag{8.26}$$

$$f_{\mathrm{m}} = -\frac{1}{4} E_{00} [qV - q\phi_{\mathrm{B}} / \cos h^2 (E_{00}/kT)], \quad \text{respectively,} \tag{8.27}$$

where $E = qV$, with V being the amplitude of the applied reverse bias.

Using $c_{\mathrm{m}} kT = 1$ and Equation 8.26, one can now derive an expression for E_{m}, the energy at which tunneling occurs, as

$$E_{\mathrm{m}} = E_{\mathrm{Fm}} + \frac{q\phi_{\mathrm{B}} - qV \sin h^2 (E_{00}/kT)}{\cos h^2 (E_{00}/kT)}. \tag{8.28}$$

The current–voltage relationship in reverse bias has again an exponential dependence, which can be expressed as

$$J_{\mathrm{tfeR}} = J_{\mathrm{tfe0}} \exp \left(\frac{-qV}{E'} \right), \tag{8.29}$$

where

$$E' = E_{00} \left[\frac{E_{00}}{kT} - \tan h \left(\frac{E_{00}}{kT} \right) \right]^{-1}, \tag{8.30}$$

and the saturation value is

$$J_{\mathrm{tfe}} = J_{\mathrm{SR}} = \frac{AT^2 \sqrt{\pi q E_{00} (\phi_{\mathrm{B}} - V \cos h^2 (E_{00}/kT))}}{kT \cos h (E_{00}/kT)} \exp \left(-\frac{q\phi_{\mathrm{B}}}{E_0} \right), \tag{8.31}$$

with A now being the Richardson constant of the metal.

As in the case of forward bias, considering the electron emission from the semiconductor to the metal, the reverse current–voltage characteristics for the thermionic field emission can be expressed in terms of more familiar parameters as

$$J_{\mathrm{m} \to \mathrm{s}} = -\frac{A^* T}{k} \int_0^{q\phi_{\mathrm{Bn}}} f_{\mathrm{m}} T(\xi)(1 - f_{\mathrm{s}}) \mathrm{d}\xi \quad \text{with} \quad n_{\mathrm{R}} = \frac{E_{00}}{kT} \left[\frac{E_{00}}{kT} - \tan h \left(\frac{E_{00}}{kT} \right) \right]^{-1}. \tag{8.32}$$

These relations provide a smooth transition from the TFE regime to the field emission regime as the temperature is lowered, which hampers the thermionic emission. A unique property here is that the sum of the inverse of the forward and reverse ideality factors adds up to 1:

$$n_{\mathrm{F}}^{-1} + n_{\mathrm{R}}^{-1} = 1. \tag{8.33}$$

8.1.3 Field Emission

In heavily doped semiconductors, $N_d \gtrapprox 10^{18}\,cm^{-3}$, the depletion region is narrow even for cold and cool electrons at the bottom of the conduction band or at the Fermi level, the latter is for degenerate semiconductors, and direct electron tunneling from the semiconductor to the metal is allowed as shown in Figure 8.4b. In the absence of a good match between the metal and the semiconductor work functions, which is generally the case, this is the best approach to pursue ohmic contacts provided very large doping concentrations can be attained.

The density of current flowing from the semiconductor to the metal is proportional to the product of the transmission coefficient $T(\xi)$, the occupation probability in the semiconductor f_s, and the unoccupation probability in the metal, $1-f_m$:[1)]

$$J_{s\to m} = \frac{A^* T}{k}\int_0^{q\phi_B} f_s T(\xi)(1-f_m)d\xi. \tag{8.34}$$

For low temperatures and/or high doping levels, $T(\xi) \approx \exp(-q\phi_B/E_{00})$. Similarly, the density of current flowing from the metal to the semiconductor is proportional to the product of the transmission coefficient, the unoccupation probability in the semiconductor, and the occupation probability in the metal:

$$J_{m\to s} = -\frac{A^* T}{k}\int_0^{q\phi_B} f_m T(\xi)(1-f_s)d\xi. \tag{8.35}$$

The total density of current is simply the sum of the density of current flowing in both directions and can be approximated by

$$J_{fe} \approx \exp\left(\frac{-q\phi_B}{E_{00}}\right). \tag{8.36}$$

For the forward-bias case, the parameters b_m, c_m, and f_m of Equation 8.15 are now for the field emission current defined as

$$b_m = \frac{q\phi_B - qV}{E_{00}}, \tag{8.37}$$

$$c_m = \frac{1}{2E_{00}}[\log(4(\phi_B - V)/V_n)], \quad \text{and} \tag{8.38}$$

$$f_m = \frac{1}{4}E_{00} q V_n, \quad \text{respectively.} \tag{8.39}$$

1) The occupation probability depicts the likelihood of a state being occupied by an electron, and one minus the occupation probability exhibits that to be free of electrons.

Padovani and Stratton [14] presented an analytical expression for the forward current for direct tunneling as

$$J_{\mathrm{fe}} = J_{\mathrm{fe0}} \exp\left(\frac{qV}{E_{00}}\right) \tag{8.40}$$

and

$$J_{\mathrm{fe0}} = J_{\mathrm{SF}} = \frac{2\pi A^* T^2 E_{00}}{kT\left[\log\left\{2\left(\frac{\phi_{\mathrm{B}}-V}{V_{\mathrm{n}}}\right)\right\}\right]\sin\left[\frac{\pi kT}{2E_{00}}\log\left\{2\left(\frac{\phi_{\mathrm{B}}-V}{V_{\mathrm{n}}}\right)\right\}\right]} \exp\left(\frac{-q\phi_{\mathrm{B}}}{kT}\right). \tag{8.41}$$

For the reverse-bias case, the parameters b_{m}, c_{m}, and f_{m} are defined as

$$b_{\mathrm{m}} = \frac{1}{E_{00}}\left[\sqrt{q\phi_{\mathrm{B}}(q\phi_{\mathrm{B}}-qV)} + qV\log\frac{\sqrt{q\phi_{\mathrm{B}}}+\sqrt{(q\phi_{\mathrm{B}}-qV)}}{\sqrt{-qV}}\right], \tag{8.42}$$

$$c_{\mathrm{m}} = \frac{1}{E_{00}}\log\frac{\sqrt{q\phi_{\mathrm{B}}}+\sqrt{(q\phi_{\mathrm{B}}-qV)}}{\sqrt{-qV}}, \quad \text{and} \tag{8.43}$$

$$f_{\mathrm{m}} = -\frac{1}{4}E_{00}E. \tag{8.44}$$

The above parameters, however, are not easily traceable in terms of experiments. By assuming that the reverse-bias voltage is larger than the barrier height, Padovani and Stratton further simplified Equations 8.42 and 8.43 to

$$b_{\mathrm{m}} = \frac{2\phi_{\mathrm{B}}^{3/2}}{3E_{00}\sqrt{q\phi_{\mathrm{B}}-qV}} \quad \text{and} \quad c_{\mathrm{m}} = \frac{\phi_{\mathrm{B}}^{1/2}}{E_{00}\sqrt{q\phi_{\mathrm{B}}-qV}}. \tag{8.45}$$

The resultant current density is then

$$J_{\mathrm{FER}} = \frac{\pi A E_{00} T^2}{kT\left[\sqrt{\frac{\phi_{\mathrm{B}}}{\phi_{\mathrm{B}}-V}}\right]\sin\left\{\frac{\pi kT}{E_{00}}\sqrt{\frac{\phi_{\mathrm{B}}}{\phi_{\mathrm{B}}-V}}\right\}} \exp(-2(q\phi_{\mathrm{B}})^{3/2}/3E_{00}\sqrt{q\phi_{\mathrm{B}}-qV}), \tag{8.46}$$

where A is the Richardson constant of the metal. In the limit of zero temperature, Equation 8.46 further reduces to

$$J_{\mathrm{FER}} = AT^2\left(\frac{E_{00}}{kT}\right)^2 \frac{\phi_{\mathrm{B}}-V}{\phi_{\mathrm{B}}} \exp(-2(q\phi_{\mathrm{B}})^{3/2}/3E_{00}\sqrt{q\phi_{\mathrm{B}}-qV}). \tag{8.47}$$

Equation 8.47 shows that a plot of the $\ln J_{\mathrm{FER}}/q(\phi_{\mathrm{B}}-V)$ as a function of $\sqrt{q\phi_{\mathrm{B}}-qV}$ would yield a straight line with a slope of $2(\phi_{\mathrm{B}})^{3/2}/3E_{00}$.

A plot of the natural logarithm of the current given in Equation 8.40 versus voltage would yield a slope of q/E_{00} regardless of the temperature, which is a characteristic of direct tunneling current. The coefficient in front of Equation 8.40 (the saturation current), which is expanded in Equation 8.41, clearly indicates that the lower the

barrier ϕ_B, and the higher the doping level, which increases E_{00} through Equation 8.19, the higher the saturation current and thus the higher the current. This explicitly implies that the resistance is low. The key for a good ohmic contact and high current is then to find a metal with a small barrier, which calls for a metal with a work function equal to or smaller than that of the semiconductor for the n-type case. For the p-type case, the same implies in the sense that the work function of the metal needs to be equal to or larger than that of the semiconductor, which is very hard to do for wide bandgap semiconductors. Additionally, the situation is exacerbated by the large-hole mass, which tends to decrease the E_{00} term and thus increase the resistance.

8.1.4 Leakage Current

In addition to thermionic emission, thermionic field emission, and field emission (tunneling) currents, other currents such as defect-assisted tunneling, which may have a quasiohmic nature, can be lumped into what is called the leakage current of more or less unknown origin that can be expressed as

$$I_{lk} = \frac{V - IR_s}{R_t}. \tag{8.48}$$

R_t is considered to be a fitting parameter that represents defects and inhomogeneities at the metal–semiconductor interface and R_s is the semiconductor resistance introduced in Equation 8.9. In semiconductors with less than ideal interfaces, a tunneling barrier E_0 may not be predicted, in which case it should be considered as another fitting parameter. In practice, the terms I_{te0} and I_{tfe0} are also considered to be fitting parameters that represent the magnitude of the contributions to the current from thermionic emission and thermionic field emission, respectively.

The current–voltage characteristics deviate substantially from the aforementioned treatment and the role that surfaces and defects play must be taken into consideration. However, this is nearly impossible to model, as the nature of the defects germane to this problem is not known. With improvements in the quality of p–n or metal–semiconductor junctions, one can extract the leakage component from temperature-dependent current measurements with the help of the current conduction models discussed above. Surface- and defect-related currents have a bearing on the I–V characteristics in both forward- and reverse-bias directions but could be the dominating component in reverse bias. This takes on a special meaning in Schottky detectors where the reverse bias leakage goes toward the dark current and adversely affects the detectivity of the device.

A scenario where defects are responsible for tunneling through a metal–semiconductor interface is schematically depicted in Figure 8.5. Following the initial application of a small external bias, electrons may tunnel from the Schottky barrier to an interfacial state in the barrier. After this point, two or more paths become available, namely, tunneling through the remaining barrier or thermal excitation through a set of deep states. Participation by defects introduces memory effects due to time

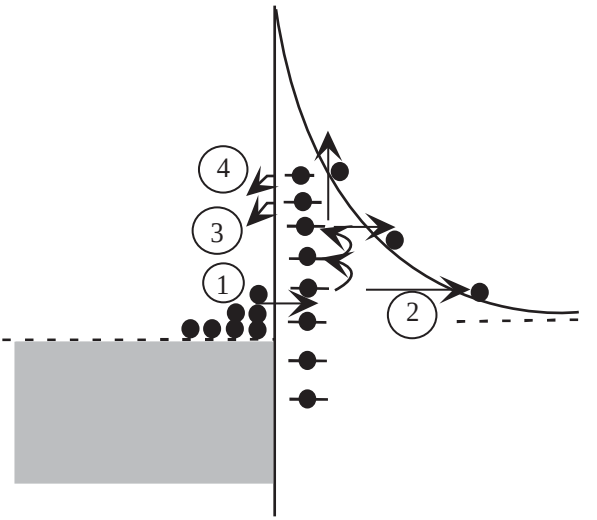

Figure 8.5 Band diagram of a Schottky diode interface illustrating specific defect-assisted tunneling processes proposed for explaining the large leakage at low-bias voltages.

constants involved in that trap filling and ionization with their characteristic time constant are involved. This manifests itself as unstable current–voltage characteristics as the voltage across the device is swept. For example, the completion of the first voltage sweep would cause for most of the available defect states to be filled. This leaves just a few empty states available for deep-level assisted tunneling. Therefore, the second voltage sweep would show a current–voltage characteristic with lower leakage current, albeit unstable. However, once the filled state population reaches equilibrium, the current–voltage characteristic becomes stable. It is also plausible to release trapped electrons, by tunneling back to the Schottky metal. This would give rise to excess leakage current at low bias voltages. Some of the detrapping processes may be initiated by illumination. Light excitation frees defect states and results in increased leakage current when dark current measurements are made following illumination in Schottky barrier detector structures.

8.2
Ohmic Contacts to ZnO

An ohmic contact can simply be defined as having a linear and symmetric current–voltage relationship for both positive and negative voltages and is important for carrying electrical current into and out of the semiconductor, ideally with no parasitic resistance. It is well known that parasitic resistance, in the form of contact resistance, is one of the major obstacles in realizing long-lifetime operation of optical and electrical devices due to excess power disspitation. A major loss of device performance is often caused by high-resistance metal–semiconductor ohmic

contacts through thermal stress and/or contact failure due to, for example, Joule heating [15]. Thus, to attain high-performance ZnO-based optical and electrical devices, ohmic contacts that are thermally stable and reliable and have low resistance are imperative. This can be achieved either by performing surface preparation to reduce the metal semiconductor barrier height, which would increase carrier tunneling probability, or by increasing the effective carrier concentration near the surface perhaps taking advantage of the oxygen loss [16–19].

Low-resistance ohmic contacts are one of the main vehicles in improving device performance [17]. Although a low-resistance ohmic contact on n-type wide bandgap semiconductors can be obtained by thermal annealing, surface roughness and structural degradation of the interface can be induced during thermal annealing [20, 21], resulting in poor device performance and reliability [22]. Therefore, it may in some instances be preferable to develop low-resistance ohmic contacts that do not rely on the use of thermal annealing. For this reason, nonalloyed ohmic contacts with low specific contact resistance are preferred [19, 23–25], particularly for shallow junction and low-voltage devices because they provide smooth metal–semiconductor interfaces resulting from the limited interface reaction. Against this background, it is fair to state that the contact metallization technology in ZnO has not been explored extensively.

Lee *et al*. [25] have achieved low-resistance and nonalloyed ohmic contacts to epitaxially grown n-ZnO formed by exposing n-ZnO to an inductively coupled hydrogen and argon plasma. The specific contact resistivity [26] of the resulting ohmic contacts was shown to drastically decrease from 7.3×10^{-3} to $4.3 \times 10^{-5}\,\Omega$ cm^2 by hydrogen plasma treatment of Ti/Au metallization. The specific contact resistivity of the Ar-plasma-treated sample has also decreased to $5.0 \times 10^{-4}\,\Omega\,\text{cm}^2$, which is lower by an order of magnitude compared to that of the as-grown sample, and this decrease has been attributed to the formation of a shallow donor by ion bombardment leading to oxygen vacancies on the ZnO surface. This result is comparable to that reported by Kim *et al*. [20], using the same metallization scheme after annealing at 300 °C. The specific contact resistance was measured to be $2 \times 10^{-2}\,\Omega\,\text{cm}^2$ for the as-deposited contact, and 2×10^{-4} and $1 \times 10^{-3}\,\Omega\,\text{cm}^2$ for the contacts annealed at 300 and 500 °C, respectively [20]. Annealing at 300 °C for 1 min resulted in high-quality ohmic contacts leading to a reduction by two orders of magnitude in specific contact resistance compared to as-deposited contacts. This enhancement has been attributed to the combined effects of the increases in the carrier concentration near the ZnO layer surface and the contact area.

Kim *et al*. [23] have investigated nonalloyed Al and Al/Pt ohmic contacts on n-type ZnO and found that the *I*–*V* characteristics of as-deposited Al and Al/Pt contacts on n-type ZnO reveal a linear behavior with a specific contact resistivity of 8.0×10^{-4} and $1.2 \times 10^{-5}\,\Omega\,\text{cm}^2$, respectively. Pt overlayer on Al contact, compared to the case without the overlayer, has resulted in a large reduction in the specific contact resistivity on n-type ZnO. This reduction has been attributed to the prevention of surface oxide layer (Al–O) by the Pt metal, which is similar to the case of GaN. A nonalloyed In-based ohmic contact, formed on a hydrothermally grown n-type ZnO substrate by KrF excimer laser irradiation with $0.3\,\text{J}\,\text{cm}^{-2}$ and metal deposition

without any impurity doping, has been investigated by Akane *et al.* [24]. An In-deposited laser-irradiated sample exhibited ohmic behavior with a resistivity of $7 \times 10^{-1}\,\Omega\,cm^2$. The same, however, was not the case for nonradiated samples with and without the contact metal, which indicates that laser irradiation enables current conduction into the n-type ZnO substrate. A decrease in the current density was also observed 5 min after annealing at 300 °C, which resulted in the degradation of the electrical properties. In addition, Ti/Au contacts showed thermal degradation after annealing at temperatures more than 300 °C [20], and the same behavior was observed by Akane *et al.* [24] for In ohmic contacts annealed at 300 °C for 5 min. Kim *et al.* [27] have investigated Ru ohmic contacts to n-type ZnO. In spite of the fact that the as-deposited Ru contact yielded a specific contact resistivity of $2.1 \times 10^{-3}\,\Omega\,cm^2$, the contact annealed at 700 °C for 1 min yielded a specific contact resistance of $3.2 \times 10^{-5}\,\Omega\,cm^2$, about two orders of magnitude smaller compared to the as-deposited one without showing any electrical and thermal degradation observed in the case of Ti/Au and In contacts. It was also shown that prolonged annealing (10 min) at the same temperature caused no significant electrical and surface morphology degradation indicating that Ru is suitable for high-temperature ZnO devices [27]. The surface modification (by means of applying a high-energy beam of Ga ions before the metal deposition) and Pt direct-write metal deposition approaches have been applied to unintentionally doped n-type ZnO films and linear ohmic contact characteristics have been achieved [17, 28]. The specific contact resistivity values for surface modification doses $D_{s1} = 1 \times 10^{17}\,cm^{-2}$, $D_{s2} = 3 \times 10^{17}\,cm^{-2}$, and $D_{s3} = 3 \times 10^{16}\,cm^{-2}$ have been obtained as 3.1, 3.3, and $3.7 \times 10^{-4}\,\Omega\,cm^2$, respectively. These values are one order of magnitude lower than the lowest specific contact resistance ($4.1 \times 10^{-3}\,\Omega\,cm^2$) for Pt direct-write without surface-modified contacts [17, 28].

Sheng *et al.* [19] have fabricated Al/Au nonalloyed ohmic contacts on epitaxial $Mg_xZ_{1-x}O$ ($0 \leq \times \leq 0.34$) using the low barrier height of Al on ZnO [29]. The specific contact resistance has been investigated as a function of Mg composition in ZnO films and it has been shown that with increasing Mg composition (increasing bandgap) the specific contact resistance increased from 2.5×10^{-5} to $9.1 \times 10^{-3}\,\Omega\,cm^2$. This represents an increase of more than two orders of magnitude compared to a ZnO sample with an electron concentration of $1.6 \times 10^{17}\,cm^{-3}$. The experimental specific contact resistances as a function of temperature for unintentionally and heavily Ga-doped ZnO are given in Figure 8.6. It has been shown that if the electron concentrations were increased (e.g., by Ga-doping during growth), specific contact resistivity would decrease because of increased tunneling. Another observation was that, even if the specific contact resistivity did not change as a function of temperature, heavily doped ZnO showed lower specific contact resistivity than that of the unintentionally doped ZnO, as one would expect [19].

Ip *et al.* [30] could obtain a minimum specific contact resistance of $6 \times 10^{-4}\,\Omega\,cm^2$ for Ti/Al/Pt/Au contacts on undoped ($n = 10^{17}\,cm^{-3}$) bulk ZnO. The contacts did not show ohmic behavior in the as-deposited state and reached their minimum resistance after 250 °C annealing. This value was essentially independent of the surface cleaning procedure employed, including sequential solvent cleaning or H_2 plasma

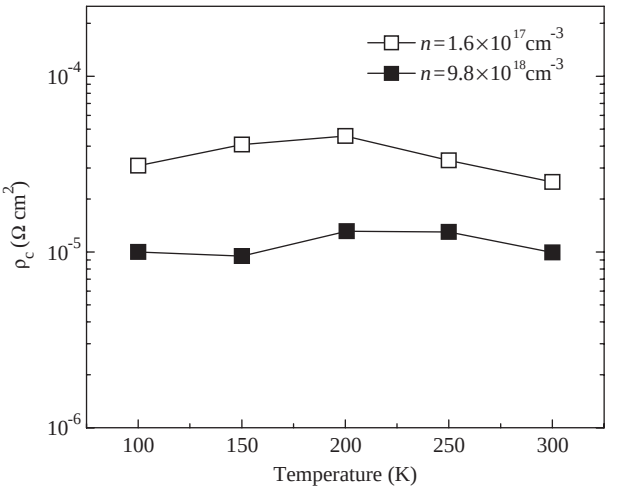

Figure 8.6 Experimental specific contact resistances as a function of temperature for unintentionally doped (open squares) and heavily Ga-doped (solid squares) ZnO. (After Ref. [19].)

exposure. Higher annealing temperatures degraded the specific contact resistance, and Auger electron spectroscopy depth profiling revealed increasing intermixing of the metal layers and reaction of Ti with ZnO. Al was observed to outdiffuse to the surface at temperatures as low as 350 °C, and the contact metallization was almost completely intermixed by 600 °C.

The dependence of Ti/Al/Pt/Au ohmic contact resistance on carrier concentration in P-doped n-type ZnO thin films (7.5×10^{15}–1.5×10^{20} cm^{-3}) has also been reported [31, 32] (P doping has been reported to result in p-type doping as well). Even in the as-deposited state, low specific contact resistances ranging from 3×10^{-4} to 8×10^{-7} Ω cm^2 were observed. The lowest specific contact resistance of 8×10^{-7} Ω cm^2 for nonalloyed ohmic contacts was achieved in the sample with carrier concentration of 1.5×10^{20} cm^{-3} when measured at 30 °C. In the annealed samples, minimum specific contact resistances of 3.9×10^{-7} and 2.2×10^{-8} Ω cm^2 were obtained in samples with carrier concentrations of 6.0×10^{19} cm^{-3} measured at 30 °C and 2.4×10^{18} cm^{-3} measured at 200 °C, respectively. Figure 8.7 shows the dependence of specific contact resistance on carrier concentration for the as-deposited and annealed contacts. Temperature-dependent measurements showed that the dominant transport mechanisms were tunneling in the contacts for the most highly doped films and thermionic emission for the films with lower doping. As in the case of bulk ZnO, Auger electron spectroscopy detected Ti–O interfacial reaction and intermixing between Al and Pt at 200 °C. The significant changes in morphology even for low-temperature (200 °C) anneals suggest that thermally more stable contact schemes should be explored.

Some of the various ohmic contact metallization approaches on n-type ZnO are summarized in Table 8.1 together with carrier concentration, specific contact resistance, and method used to measure the specific contact resistivity. Al [33–35],

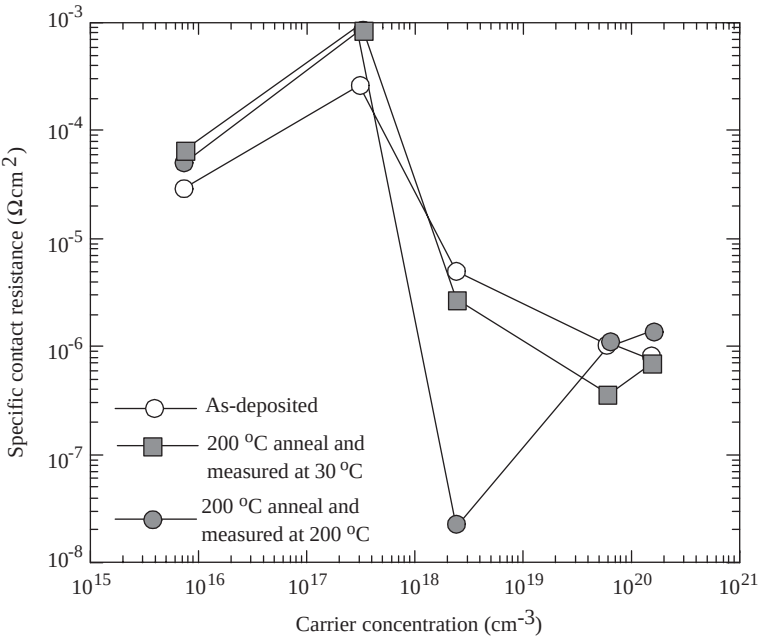

Figure 8.7 Specific contact resistance versus carrier concentration of the as-deposited ohmic contact measured at 30 °C and at 30 and 200 °C after annealing at 200 °C for 1 min (After Ref. [31].)

Al/Au [36], Ti [37], In [38], and InGa [39] metallizations were also used to obtain ohmic contacts. Despite some progress in ZnO-based devices, difficulties remain in the reproducible growth of p-type ZnO and thus very limited information exists on ohmic contacts to p-type ZnO material [40–42]. For that reason, the ohmic contact to the p-type ZnO material will not be discussed here.

Conversion from ohmic behavior to rectifying behavior following exposure of the sample to remote oxygen plasma at room temperature has been observed [43]. The conversion is also accompanied by a reduction of the green hydrogen donor-bound exaction luminescence intensities and a 0.75 eV increase in the n-type band bending observed by X-ray photoemission spectroscopy (XPS).

8.3 Schottky Contacts to ZnO

In spite of the fact that high-quality Schottky contacts are critical for ZnO device applications, there is little information about the Schottky contacts on ZnO to date. The chemical reactions between the metal and the semiconductor, the surface states, the contaminants, the defects in the surface layer, and the diffusion of the metal into the semiconductor are well known problems in the formation of Schottky contacts. In the case of ZnO, for instance, Al is expected to produce the most

Table 8.1 Ohmic contacts to n-type ZnO for various metallization schemes.

Metallization	Type	Annealing conditions	Carrier concentration (cm^{-3})	ρ_c at RT ($\Omega\,cm^2$)	Method of ρ_c measurement	Reference
Al/Au	n	—	1.6×10^{17}	2.5×10^{-5} for ZnO 9.1×10^{-5} for $Mg_{0.34}Zn_{0.66}O$	TLM	[19]
Ti/Au	n (Al-doped)	As-grown 300 °C for 1 min 500 °C for 1 min	2×10^{17}	2.0×10^{-2} as-deposited 2.0×10^{-4} annealed at 300 °C 1.0×10^{-3} annealed at 500 °C	*c*-TLM	[20]
Al	n (Al-doped)	Nonannealed	2×10^{18}	8.0×10^{-4}	*c*-TLM	[23]
Al/Pt	n (Al-doped)	Nonannealed	2×10^{18}	1.2×10^{-5}	*c*-TLM	[23]
In	n	Nonannealed 300 °C for 5 min	Unintentionally doped	7.0×10^{-1} as-deposited (KrF pre-irradiation) 7.3×10^{-1} annealed at 300 °C	TLM	[24]
Ti/Au	n (Al-doped)	—	7×10^{17}	7.3×10^{-3} as-deposited 4.3×10^{-5} H_2 plasma, 5.0×10^{-4} Ar plasma	TLM	[25]
Ru	n	As-grown 700 °C for 1 min	3×10^{18}	2.1×10^{-3} as-deposited 3.2×10^{-5} annealed at 700 °C	*c*-TLM	[27]
Pt-Ga	n	—	Unintentionally doped	4.1×10^{-3} w/o surface modification 3.1×10^{-4} for dose of $D_{s1}=1\times10^{17}\,cm^{-2}$ 3.3×10^{-4} for dose of $D_{s2}=3\times10^{17}\,cm^{-2}$ 3.7×10−4 for dose of $D_{s3}=3\times10^{6}\,cm^{-2}$	TLM	[17, 28]
Ti/Al/Pt/Au	n	250 °C	Unintentionally doped (10^{17})	6×10−4	*c*-TLM	[30]
Ti/Al/Pt/Au	n (P-doped)	As-grown 200 °C	1.5×10^{20} 6.0×10^{19}	8.0×10^{-7} 3.9×10^{-7}	TLM	[31, 32]
Re/Ti/Au	n (Al-doped)	As-grown 700 °C	2×10^{18}	2.1×10^{-4} 1.7×10^{-7}	*c*-TLM	[44]

c-TLM stands for circular transmission line method.

dissociated cations (Zn) in ZnO because of its strong reaction with anions (O) in ZnO. This results in low barrier height and leakage current.

To create Schottky barrier with undoped ZnO, a high work function can be applied to the surface of a ZnO crystal. Although many publications [39, 45] show that Au has some serious problems at high temperatures (>340 K), it has widely been applied to ZnO to form Schottky barriers [37–39, 45–47]. Other metals used for the same purpose are Ag [33–35, 38, 45, 46], Pd [47, 48], and Pt [49–52]. It has been found that all these reactive metals form relatively high Schottky barriers of 0.6–0.84 eV to n-type ZnO.

Although Schottky barrier heights were first reported by Mead [46] for various metal contacts on vacuum-cleaved n-type ZnO surfaces in 1965, the thermal stability of the Schottky diodes fabricated on ZnO has not been extensively studied. It was observed that Au Schottky contacts resulted in poor current–voltage characteristics and degraded easily with thermal cycling of the samples [35]. This was the first study of its kind showing that the thermal stability of Ag Schottky contacts was better than that of the Au Schottky contacts. Mead [46] measured barrier heights for Ag and Au Schottky contacts as 0.68 and 0.65 eV, respectively. Neville and Mead [47] investigated surface barrier systems consisting of Au and Pd on bulk ZnO, which were chemically prepared by concentrated phosphoric acid, concentrated HCl, and organic solvents, and showed an ideality factor very close to unity (1.05). Koppa *et al.* [37] have investigated Au Schottky contacts on n-type ZnO wafers, which were clean, stoichiometric, highly ordered, and smooth after exposure to O_2/He plasma. Significant improvement in the *I–V* characteristics of as-deposited Au Schottky contacts was observed relative to those characteristics measured for similar contacts deposited on the same surfaces of as-received wafers. Compared to the contacts on the as-received material, which showed microampere level leakage currents and ideality factors of $n > 2$, contacts on plasma-cleaned wafers cooled in vacuum showed leakage current of about 36 nA at -4 V, a barrier height of 0.67 eV, and an ideality factor of 1.86. Furthermore, contacts on plasma-cleaned wafers cooled in unignited plasma gas followed by a 30 s exposure to plasma at room temperature showed a leakage current of about 20 pA at -7 V, a barrier height of 0.60 eV, and an ideality factor of 1.03 [37].

Au and Ag Schottky contacts on epiready (0 0 0 1) Zn surface of undoped n-ZnO samples have been investigated by Polyakov *et al.* [45], comparing their barrier heights and thermal stabilities. Schottky barrier heights of 0.65–0.69 eV and diode ideality factors of 1.6–1.8 have been obtained by capacitance–voltage and current–voltage measurements, respectively. The ideality factor had a value close to 2 for almost all the samples studied due to an increase of the tunneling current through the junction [8]. Both the Au and the Ag Schottky diodes have shown degradation, but with different degradation characteristics, after heating in vacuum at temperatures as low as 365 K. Sheng *et al.* [34] have fabricated Ag Schottky contacts on the $(1\,1\,\bar{2}\,0)$*a*-surface of an epitaxial ZnO film grown by OMVPE. The Schottky barrier height at room temperature was determined to be 0.69 eV by thermionic emission using *I–V*-T measurements. The ideality factor decreased from 1.37 to 1.29 as the temperature was increased from 265 to 340 K. The reason for the high-ideality factor

of 1.33 obtained by fitting the thermionic emission theory to the experimental forward *I–V* curve at room temperature could most probably be due to the existence of an interfacial layer and surface states [34]. For nonideal Schottky diodes, the flat band barrier height, which is obtained by modifying the measured one, is more meaningful. By doing so, the flat band barrier heights were determined from *I–V* and *C–V* measurement to be 0.89 and 0.92 eV, respectively [34].

Au and Ag Schottky contacts have been prepared by vacuum evaporation onto the $(0\,0\,0\,\bar{1})$ O-terminated surface of the ZnO crystal and characterized by measuring the *I–V* and *C–V* relationships in a temperature range of 90–300 K by Ohashi *et al.* [38]. A barrier height 0.5 eV was obtained for the Au Schottky contact, which is lower than that reported for the same contact by others [45–47]. In this case, the low value of the barrier height was attributed to the high donor density. The greater-than-unity ideality factors (1.3–1.6) obtained for the Schottky contacts were most probably due to relatively high carrier concentration leading to the increase of tunneling current through the junction.

Ip *et al.* [52] obtained the annealing and the temperature dependence of Schottky barrier height of Pt contacts on P-doped n-type $(n = 10^{16}\mathrm{cm}^{-3})$ thin-film ZnO deposited by pulsed laser deposition (PLD). The carrier concentration in the films was $7.5 \times 10^{15}\,\mathrm{cm}^{-3}$ with a corresponding mobility of $6\,\mathrm{cm}^2\,\mathrm{V}^{-1}\,\mathrm{s}^{-1}$. For the unannealed samples, the barrier height ranged from 0.61 ± 0.04 eV at 30 °C to 0.46 ± 0.06 eV at 200 °C with saturation current densities ranging from $1.5 \times 10^{-4}\,\mathrm{A\,cm}^{-2}$ (30 °C) to $6.0 \times 10^{-2}\,\mathrm{A\,cm}^{-2}$ (100 °C), respectively. The ideality factors increased from 1.70 at 30 °C to 3.43 at 200 °C. The measured barrier height for Pt on ZnO is similar to the value reported for both Au and Ag rectifying contacts on the material mentioned above. The barrier height reduced significantly to 0.42 eV after annealing at 300 °C (1 min.) and the reverse current was larger than predicted by thermionic emission alone in both as-deposited and annealed contacts.

Table 8.2 summarizes the common Schottky metals for n-type ZnO. As can be seen from this table, the ideality factor for ZnO Schottky contacts is higher than unity in the majority of the studies. This has been explained by different mechanisms such as the prevalence of tunneling [8], the presence of an interface layer, surface states [34], increased surface conductivity [37], and/or the influence of deep recombination centers [45].

8.4 Etching of ZnO

For successful device fabrication, controllable and high-resolution etching of ZnO is necessary. The possibility of wet chemical etching is a fundamental advantage of ZnO, which is readily etched in many acid solutions including NH_4Cl, HNO_3/HCl, HF/HNO_3, and $H_3PO_4/HAc/H_2O$ [25, 53–60]. ZnO reacts in acid solution producing a zinc salt, which dissolves in water, to form the etched pattern. This reaction in most cases limits etching and has activation energies of $\sim$6 kCal mol^{-1} [61]. Etching of the ZnO strongly depends on the material quality and also the surface polarity [62]. The

Table 8.2 Schottky contacts to n-type ZnO.

Metal	Deposition method	ϕ_B (eV)	Method of ϕ_B measurement	Ideality factor (n)	Method of n measurement	Reference
Ag	Electron beam	0.84		1.5	I–V	[33]
Ag	Electron beam	0.69	C–V, I–V	1.37 at 265 K, 1.33 at RT, 1.29 at 340 K	I–V	[34]
Au	Electron beam	—		>2 as-received	I–V	[37]
		0.67		1.86 (plasma cleaned)		
		0.60		1.03 (unignited plasma, 30 s plasma)		
Au	Vacuum	0.50	I–V	1.3–1.6	I–V	[38]
Au	—	—	—	1.19	I–V	[39]
Au	Vacuum	0.65	C–V	1.6–1.8	I–V	[45]
Ag	Vacuum	0.69	C–V	1.6–1.8	I–V	[45]
Au	Thermal	0.71	Photoresponse	—		[46]
Ag	Thermal	0.68	Photoresponse	—		[46]
Au	Thermal	0.66	C–V, I–V, photoresponse	1.05	I–V	[47]
Pt	Electron beam	0.89	I–V	1.15 (hydrogen peroxide-cleaned)	I–V	[49]
		0.93	C–V			
Pt	Electron beam	0.7	I–V	1.5 (ozone cleaned)	I–V	[50, 51]
W	Sputtering	0.49	I–V	2 (ozone cleaned)	I–V	[50, 51]
Pt	Electron beam	As-deposited	I–V	As-deposited	I–V	[52]
		0.61 (303 K)		1.70 (303 K)		
		0.46 (473 K)		3.43 (473 K)		
		Annealed		Annealed (1 min at 300 °C)		
		0.42 (303 K)		4.29 (303 K)		
		0.40 (473 K)		4.78 (473 K)		

oxygen-terminated surface of ZnO etches much faster than the zinc-terminated ZnO [63]. Furthermore, etching of zinc- and oxygen-terminated surfaces of ZnO bulk wafers results in different surface morphologies [64]. Etch pits appear on the zinc-terminated surface, providing estimates for the density of threading dislocations on zinc face. In contrast, hillocks form on the oxygen terminated surface of ZnO after etching.

Etching rate for ZnO in most single acids, mixed acids, and alkalis is very fast, irreproducible, and nonuniform, unless the solution concentration is drastically reduced by diluting it with water [61]. For example, the room-temperature etch rates of ZnO grown on sapphire by PLD have been measured as ~100 and ~500 nm min^{-1} in 0.24M HCl and 0.06M H_3PO_4, respectively, with photoresist providing a stable mask for pattern transfer [61]. The etch rates were significantly higher for $Mg_{0.1}Zn_{0.9}O$, >300 nm min^{-1} in 0.024M H_3PO_4 and >400 nm min^{-1} in 0.024M HCl [61]. A controllable and moderate etching rate (~20 nm min^{-1}) was also obtained with aqueous NH_4Cl solution (15%). However, the surface morphologies of the etched films became rougher with increasing etching time, and the band edge (defect) luminescence intensity decreased (increased) [65]. In general, wet etch processes are isotropic, therefore, result in undercuts and cannot produce vertical profiles. Dry etching methods possess several advantages over conventional wet etching processes, including high resolution and easy process automation. Ar/Cl_2 and $Ar/CH_4/H_2$ and BCl_3/Ar plasma chemistries have been shown to be capable of etching ZnO at slow (< 0.4 μm min^{-1}) but practical etch rates at room temperature [66–71]. The near-surface stoichiometry of ZnO was shown to be unaffected after etching using BCl_3 [68] and $Ar/CH_4/H_2$ [72], indicating equirate removal of the Zn and O etch products. As a consequence of this and the ion-assisted nature of dry etching, a smooth and anisotropic pattern transfer was obtained using a Ni/Cr mask [72].

Among the above-mentioned plasma chemistries, $CH_4/H_2/Ar$ is very attractive because it is noncorrosive and relatively insensitive to the amount of residual water vapor in the etching chamber. Substitution of C_2H_6 for CH_4 has been shown to lower the threshold ion energy for initiation of etching and increase the etch rate of bulk single-crystal ZnO by a factor of ~2 in inductively coupled plasmas (ICPs) [73]. The etch rates in $CH_4/H_2/Ar$ plasma has been shown to decrease significantly when ZnO was doped increasingly by Li, Al, and Ag, presumably due to lower volatility of reaction byproducts of Li, Ag, and Al doped ZnO [74]. A disadvantage of the $CH_4/H_2/Ar$ chemistry for ZnO dry etching is that excessive deposition of a-C:H (amorphous hydrogenated carbon) films on the surface of ZnO film can impede continuous etching reaction.

The effect of the introduction of interhalogens such as ICl, IBr, BI_3, and BBr_3 to Ar plasma has been investigated as interhalogen discharges have high reactive neutral density even at moderate power levels [75]. Addition of interhalogens led to relatively low etch-induced damage, while some trenches were observed near the sidewalls of etched patterns when $CH_4/H_2/Ar$ plasma was used. However, etch rates achieved in plasmas with interhalogens were too low (< 15 nm min^{-1}) for efficient pattern transfer.

Table 8.3 Some of the reported etching rates and conditions using various chemistries [76].

Chemistry	Etch rate (nm min^{-1})	ICP power (W)	RF power (W)	Bias (–V)	Temperature	Reference
Cl_2/H_2	20	1500	100		20	[78]
Cl_2/Ar	120–300	500	250		50–300	[67]
CH_4/H_2	120	1500	100		20	[78]
$CH_4/H_2/Ar$	10–300	500	50–300	91–294		[66]
BCl_3	128–150	900	140		20–250	[68]
$BCl_3/Cl_2/Ar$	9–98	900	140		20	[69]
$BCl_3/CH_4/H_2$	220–310	1200		250–350	20	[77]

Table 8.3 lists the etch rates obtained for various dry etching chemistries [76]. The highest dry etching rates were achieved with $BCl_3/CH_4/H_2$ (310 nm min^{-1}) [77], $CH_4/H_2/Ar$ (300 nm min^{-1}) [57], and Cl_2/Ar (300 nm min^{-1}) plasmas [67].

8.5 Heterostructure Devices

To reiterate, ZnO is considered a potentially attractive material for fabricating devices emitting light in the UV region because of its large exciton-binding energy (60 meV). As discussed in Section 4.2, reproducible p-type ZnO has not yet been developed and therefore a widespread fabrication of ZnO p–n homojunction-based LEDs has not been possible. In the interim, n-type ZnO growth on other available and comparable p-type materials was used as a short-term pathway for at least investigating the particulars of junctions participated by ZnO. This subject has received a great deal of attention, and heterojunctions of good quality have been realized by using various p-type materials such as Si [79–81], GaN [82, 83], AlGaN [84], $SrCu_2O_2$ [85, 86], NiO [87], ZnTe [88], Cu_2O [89, 90], CdTe [91], SiC [92, 93], diamond [94], $ZnRh_2O_4$ [95], and ZnO/GaAs [96]. Some details of these heterostructures concerning their growth and properties can be found in review studies [97, 98]. Suffice it to say only in a few cases was electroluminescence (EL) under forward bias was observed [79, 82–89]. In other cases, the p–n heterojunctions were considered for uses as ultraviolet photodetectors (PDs), and their photoresponse properties were studied. A very attractive device application of ZnO, where ZnO is not part of the active device, is that among the transparent conductive oxide (TCO) materials available, ZnO is very promising for its high-conductivity and transparency. In PDs, for example, ZnO is gaining a good deal of attention as a transparent contact material due to its good electrical and optical properties in addition to its low cost (needs to be lowered further), nontoxicity, and relatively low deposition temperature. If one study on radiation hardness of ZnO holds true, ZnO-based PDs in and of themselves could have superior resistance to ionizing radiation and high-energy particles. In general, PDs based on other semiconductors with ZnO transparent window layers would have a significant

advantage over the indium tin oxide window varieties because the transparency of ITO at 450 nm is about 80%, and ZnO is expected to be much better in this context as well as offering lower resistance. As for ZnO being used for the active region of PDs, there have been a number of reports on photoresponse properties of ZnO-based PDs [80, 81, 87, 92, 95, 96]. In the following section, light emitters followed by photodetectors are discussed.

8.5.1 Light-Emitting Devices

One of the first, if not the first, ZnO-based hybrid heterostructure LEDs was fabricated by Drapak [89] in 1967 who used Cu_2O as a p-type layer that was obtained by thermal oxidation of a Cu metal layer deposited on vapor phase grown ZnO substrates. The fabricated LED structures revealed electroluminescence in both forward and reverse biases, and broad spectra with maxima at 540 nm were observed. Again in the realm of hybrid LEDs, Tsurkan *et al.* [88] grew p-ZnTe on n-ZnO substrates. They fabricated two sets of heterostructures with different carrier concentrations in both p-ZnTe and n-ZnO: Heterostructure hole and electron concentrations in the first type (set I) and in the second type (set II) were 9×10^{17} and 2×10^{17} and 5×10^{14} and 8×10^{18} cm^{-3}, respectively. For both types, intense EL was observed under forward bias; however, spectra obtained from set I and set II heterostructures were different as shown in Figure 8.8. In set I, the EL spectrum was dominated by a broad yellow band with maxima at 2.0 and 2.22 eV at 300 and 77 K, respectively. On the contrary, the spectra in set II consisted of an intense narrow band in the violet region with a maximum at 3.02 eV and a set of much weaker bands peaking at 2.8 and 2.34 eV as seen in Figure 8.8. A yellow band in set I p-ZnTe/n-ZnO heterostructures was, as the authors explained, a result of electron injection from low-resistive n-ZnO into high-resistive p-ZnTe. In set II heterostructures, violet emission at 3.02 eV was attributed to hole injection from low-resistive p-ZnTe into higher resistive n-ZnO, and EL emission was purported to have resulted from donor–acceptor recombination.

Ohta *et al.* [85] fabricated p-$SrCu_2O_2$/n-ZnO-type heterostructures. A Y_2O_3-stabilized ZrO_2 (YSZ) single crystal (1 1 1) with an extremely flat surface was used as substrate. An ITO epilayer, used as transparent n-electrode, was grown on the substrate by PLD. Then, n-ZnO and p-$SrCu_2O_2$ layers were successively deposited in the same PLD chamber. By controlling the deposition atmosphere, n-type ZnO conductivity was achieved. The p-type conductivity was controlled by substituting K^+ ions for Sr^{2+} sites in $SrCu_2O_2$. The *I–V* characteristics had a diode-like behavior with a turn-on voltage of ~3 V. At room temperature and under forward-biased conditions, the band-edge UV emission had a maximum at 382 nm. The EL spectra at various injection currents are shown in Figure 8.9. An abrupt increase in the EL intensity with increasing injection current was observed without a significant change in the spectral shape or the peak energy. However, the external quantum efficiency of the diode was very low (< 0.001%) because of what was termed to be the interface nonuniformity. The 3 V turn-on voltage is in good agreement with the bandgap energy of ZnO. The

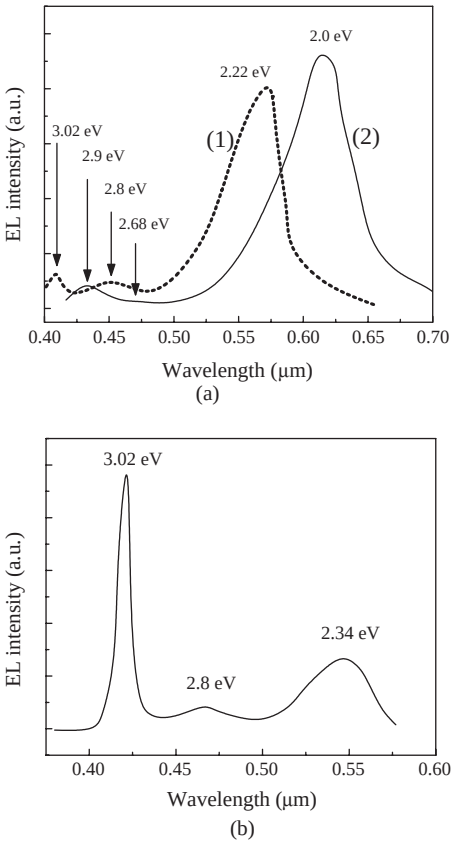

Figure 8.8 Spectral characteristics of type-I [(a) curve 1 at 77 K, curve 2 at 300 K] and type II [(b) 77 K] p-ZnTe/n-ZnO heterostructures. (After Ref. [88].)

authors attributed the observed UV emission to transitions associated with electron–-hole plasma in ZnO.

The most important factor in realizing high-quality heterostructure devices is the structural relationship between the semiconductors forming the heterojunctions, because the lattice mismatch causes extended defects with detrimental effects such as creation of nonradiative centers. For this reason, using materials with close lattice parameters is essential for fabricating high-quality heterostructure devices. As listed in Table 2.3, among all the non-ZnO-related semiconductors, semiconductor GaN is one that has a very close in-plane lattice parameter to ZnO, with a lattice mismatch of 1.8%. Therefore, in the absence of p-type ZnO, fabricating heterostructures using p-type GaN and n-type ZnO is promising. There have been several reports on such heterostructures [82–84].

Alivov *et al*. [82] have reported growth, processing, and fabrication of n-ZnO/p-GaN heterojunction LED devices, where the 1 μm thick CVD-grown n-ZnO (Ga-doped)

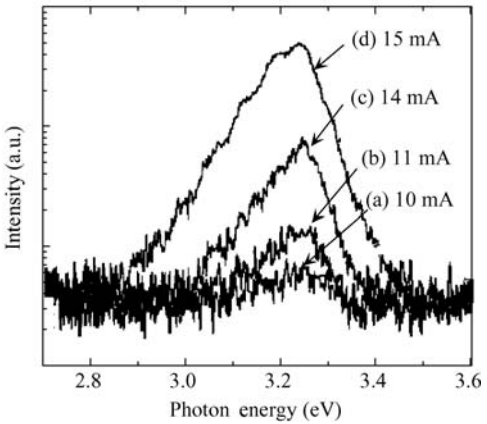

Figure 8.9 Emission spectra of the p-$SrCu_2O_2$/n-ZnO p–n junction LED for several currents. Electric currents were (a) 10 mA, (b) 11 mA, (c) 14 mA, and (d) 15 mA, respectively. (After Ref. [95].)

and the molecular beam epitaxy (MBE)-grown p-GaN (Mg-doped) layers had carrier concentrations of $4.5 \times ^{18}$ and $3 \times 10^{17}\,\mathrm{cm}^{-3}$, respectively. Cathodoluminescence measurements have shown two sets of peaks appearing at 390 and 510 nm, and 383 and 430 nm for ZnO and GaN, respectively. Electroluminescence was observed under forward bias and the spectrum consisted of a band with a maximum at 430 nm. Moreover, it has been pointed out that EL emerges from p-GaN, where the radiative recombination occurs, because the probable band alignment favors electron injection from n-ZnO to p-GaN in addition to high symmetry between n-doping and p-doping in favor of n-doping. The quantum efficiency is very low in these structures because Mg-doped GaN, which is where the luminescence emanates, suffers from low efficiency.

To favor hole injection into ZnO thereby promote emission in that material, Alivov *et al*. [84] fabricated n-ZnO (Ga-doped)/p-$Al_{0.12}Ga_{0.88}N$ (Mg-doped) heterojunction LEDs on 6H-SiC substrates, a schematic depiction of which is shown in the inset of Figure 8.10. Diode-like, rectifying *I*–*V* characteristics with a turn-on voltage of ∼3.2 V and a low reverse-leakage current of $\sim 10^{-7}$ A were observed at room temperature. As shown in Figure 8.10, an intense 389 nm UV emission, which was stable at temperatures up to 500 K, is observed when the diode is forward biased. It was also shown that this emission originated from the excitonic recombination within the ZnO layer. The energy diagram for this heterostructure obtained from the Anderson model [99], albeit too simplistic, shows a higher barrier for electrons than that for holes (valence and conduction band offsets of 0.11 and 0.45 eV, respectively). Therefore, hole injection from the wider bandgap $Al_{0.12}Ga_{0.88}N$ side ($E_g \sim 3.64$ eV) into the ZnO side ($E_g \sim 3.3$ eV) of the heterojunction is much more likely and is responsible for recombination emission in ZnO as opposed to the p-GaN/n-ZnO case where the electron injection from ZnO to GaN with a concomitant emission in GaN dominates the spectrum. It should be pointed out, of course, that the Anderson

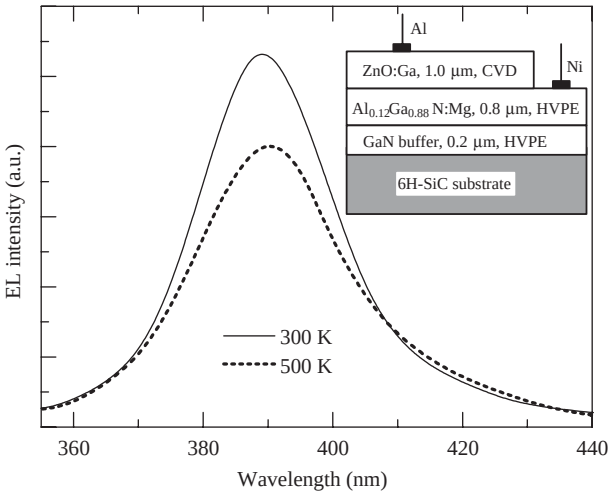

Figure 8.10 Electroluminescence spectra of an n-ZnO/p-$Al_{0.12}Ga_{0.88}N$ heterostructure light-emitting diode at 300 and 500 K. Inset shows the schematic diagram of the structure. (After Ref. [84].)

model describes the band diagram for the ideal case where there is no lattice mismatch between contacting materials and there are no imperfections at the interface. In spite of this it allows sketching of the most probable heterojunction band alignment.

Similar results were obtained from n-$Mg_{0.1}Zn_{0.9}O$/n-ZnO/p-$Al_{0.16}Ga_{0.84}N$/p-GaN triple heterostructure LEDs fabricated by Osinsky *et al.* [100]. The strong electroluminescence at 390 nm, observed under forward bias, was attributed to excitonic recombination in the ZnO layer. These results show that p-AlGaN is a good candidate for fabricating efficient heterostructure LEDs with ZnO active layers.

For potential ZnO-based laser diodes, lasing would occur due to excitonic UV transitions and would therefore lead to much lower threshold currents compared to other materials. It is well known that employing a p–n–n (or n–p–p) type double heterostructure (DH), a quantum well (QW) straddled by larger bandgap barrier layers, is a very effective means of achieving low-threshold laser diodes owing to better carrier and optical confinement that provides higher internal quantum efficiencies, lower diffraction losses, superinjection, and weaker temperature dependence. The carrier confinement, resulting from the potential barriers at both sides of the heterojunctions, increases the carrier density in the recombination region and practically eliminates the spread of the injected carriers beyond the active region. Consequently, growth of ZnO-based DH placing ZnO between wider bandgap p- and n-type materials (for example, GaN, ZnMgO, and AlGaN) could pave the way for fabrication of laser diodes with ZnO as the active layer. Alivov *et al.* [101] demonstrated high-quality p-GaN/n-ZnO/n-GaN DH with good *I*–*V* and EL characteristics. A 0.7 μm thick Mg-doped p-type GaN layer was deposited first on a

c-plane sapphire substrate by OMVPE. On this composite, an unintentionally doped 0.4 µm thick n-type ZnO layer was grown by plasma-assisted MBE at a substrate temperature of 600 °C. Finally, a 0.4 µm thick n-GaN layer was grown at 550 °C on the n-ZnO layer by plasma-assisted MBE. Scanning electron microscopy (SEM) of this n-GaN/n-ZnO/p-GaN double heterostructure is presented in Figure 8.11a, indicating sharp interfaces to the extent discernable by SEM. Fabricated diode structure exhibited rectifying diode-like behavior with low-leakage current of 4.4×10^{-7} A and a breakdown voltage of 12 V. At room temperature, EL was observed under forward bias that blue-shifted with increasing bias, as shown in Figure 8.11b. From a comparison of EL with the photoluminescence (PL) spectra of n-ZnO and p-GaN it

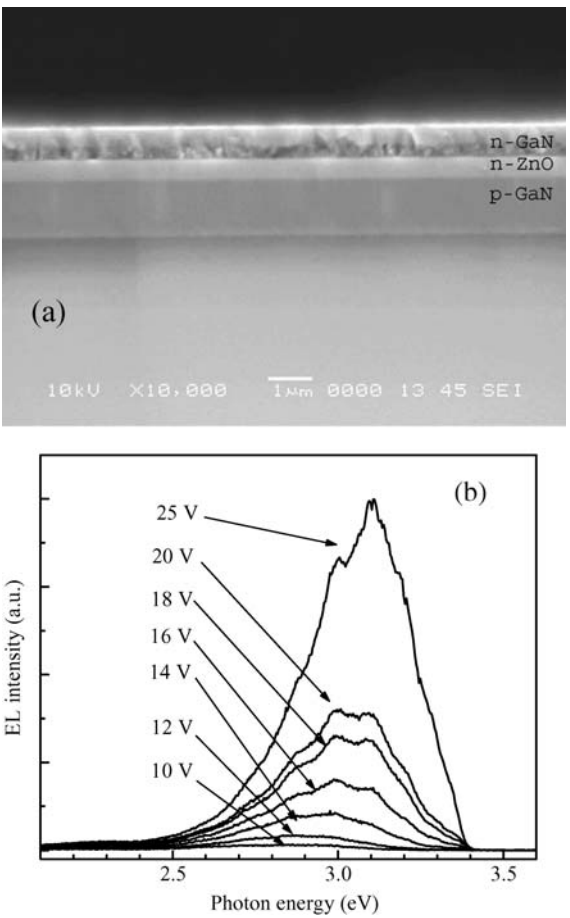

Figure 8.11 (a) Scanning electron microscope image of an n-GaN/n-ZnO/p-GaN double heterostructure. (b) Electroluminescence spectra at various forward biases. (After Ref. [101].)

was concluded that the emission is primarily from the ZnO region of the DH. Because DH lasers greatly depend on physical properties of the well layer and its thickness, which in this case is ZnO, by modifying these parameters the quality of such DH could be significantly improved.

All ZnO-based light-emitting devices have also been reported [102, 103] as p-type doping thought to become available. However, p-doping concentration obtained by N-doping in this particular case is relatively low as compared to the adjoining n-type ZnO helping compose the p–n junction. Therefore, injection from the highly doped n-type ZnO into the lightly doped p-type ZnO is dominant, and the recombination takes place primarily in the p-type ZnO, as shown in Figure 8.12. This degrades the recombination efficiency as the quality of the p-type material is inferior. PL and absorption (transmission) measurements performed in the same structure indicate the EL emission to coincide with the PL band at 440 nm, which is thought to represent the donor–acceptor pair recombination in p-type ZnO. To circumvent this problem, the p-doping level must be increased and/or heterojunction wherein the recombination occurs irrespective of the relative doping levels should be controlled.

Near-band-edge electroluminescence has also been observed from ZnO homojunction LED structures fabricated using 0.4 μm thick phosphorous-doped p-ZnO on gallium-doped n-ZnO grown by RF sputtering on *c*-sapphire [104]. The p-ZnO layer was reported to have a hole concentration of $1.0 \times 10^{19}\,\mathrm{cm}^{-3}$ and a mobility of $1\,\mathrm{cm}^2\,\mathrm{V}^{-1}\,\mathrm{s}^{-1}$ after rapid thermal annealing at 800 °C in N_2 ambient for 5 min. A clear rectifying behavior was observed with a threshold voltage of 3.2 V, and a UV emission was evident at 380 nm at room temperature. By inserting 40 nm thick $Mg_{0.1}Zn_{0.9}O$ barrier layers with a 40 nm thick n-ZnO layer near the p–n junction, the carrier recombination was confined in the n-type ZnO, which resulted in the suppression of the defect-related broad band centered at ~650 nm and enhancement of the band-edge emission by 55% when compared to the sample with no $Mg_{0.1}Zn_{0.9}O$ barriers (see Figure 8.13).

ZnO-based LEDs were also fabricated using p-type arsenic-doped BeZnO and ZnO layers grown by hybrid beam deposition [105]. The hole concentrations in the p-type layers were reported to range from high $10^{16}\,\mathrm{cm}^{-3}$ for BeZnO to mid $-10^{17}\,\mathrm{cm}^{-3}$ for ZnO. The active region was composed of seven undoped $Be_{0.2}Zn_{0.8}O$ (7 nm)/ZnO (4 nm) QWs. The turn on voltage was above 10 V, and UV electroluminescence peaks were observed at 363 and 388 nm at room temperature as shown in Figure 8.14, which were attributed to localized excitons (LEs) in the QWs and donor- or acceptor-bound excitons, respectively. The green band (GB) centered at ~550 nm blueshifted with increasing current injection. The peak at 363 nm was the dominant spectral feature at current injection levels above 20 mA. Similar active regions were used to fabricate laser structures with $Be_{0.3}Zn_{0.7}O$ cladding layers [106]. Under pulsed current injection, sharp Fabry–Pérot oscillations were observed over the 3.21 eV emission peak, above a threshold current density of $\sim 420\,\mathrm{A\,cm}^{-2}$. However, no further analysis of the cavity resonance mode separation was reported.

In terms of nanostructure devices, p–n junctions formed between n-ZnO nanotips and p-GaN films have been investigated [107]. The diodes demonstrated threshold

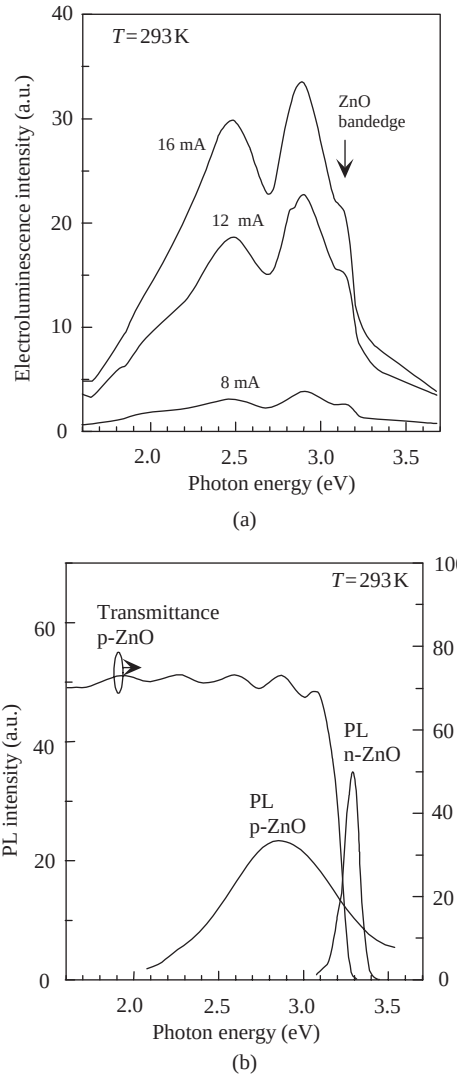

Figure 8.12 (a) Electroluminescence spectra of all ZnO p–n junction recorded at 293 K for DC forward-bias currents of 8, 12, and 16 mA. The arrow indicates the absorption edge of p-type ZnO top layer. (b) PL spectra at 293 K of undoped and p-type ZnO layers (dotted lines) and transmission spectrum (broken line) of p-type ZnO layer. The EL emission is redshifted (440 nm) with respect to the band edge and occurs where the PL emission is detected and is most likely associated with donor–acceptor pair (DAP) transitions in the p-type ZnO layer. Thickness of the undoped and p-type films is 1 μm and 500 nm, respectively. (Courtesy of M. Kawasaki [103].)

and breakdown voltages of ∼3 V and ∼−8 V, respectively, with a reverse-leakage current of ∼54 μA at −5 V. Blue light emission was observed under forward bias with a dominant EL wavelength at 406 nm and attributed to electron injection from ZnO nanotips into p-GaN, where the emission took place, because n-doping in ZnO is

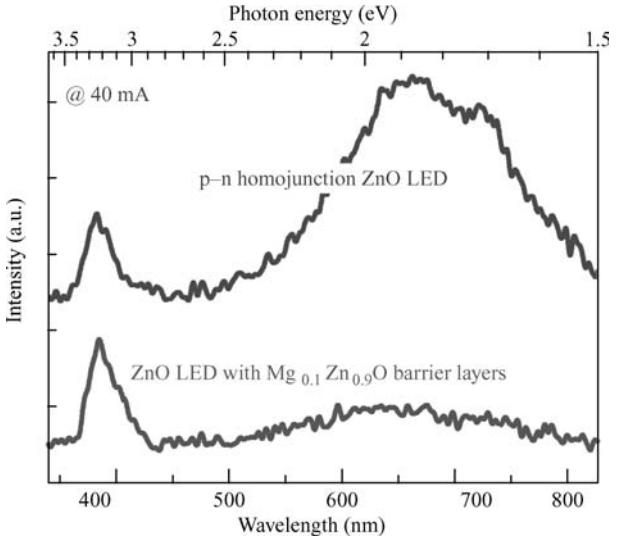

Figure 8.13 Electroluminescence spectra from ZnO-based LEDs grown by RF sputtering with and without $Mg_{0.1}Zn_{0.9}O$ barrier layers measured at an operating current of 40 mA. (After Ref. [104].)

higher than p-doping in GaN. N-ZnO nanotip/p-Si p–n diodes were also fabricated by the same group with low-threshold voltage (< 2 V), sharp breakdown at ~ -17 V, and a relatively small reverse-leakage current, $\sim 50\,\mu$A at -10 V. Such type of p–n diodes are thought to have potential applications in Si IC interconnects.

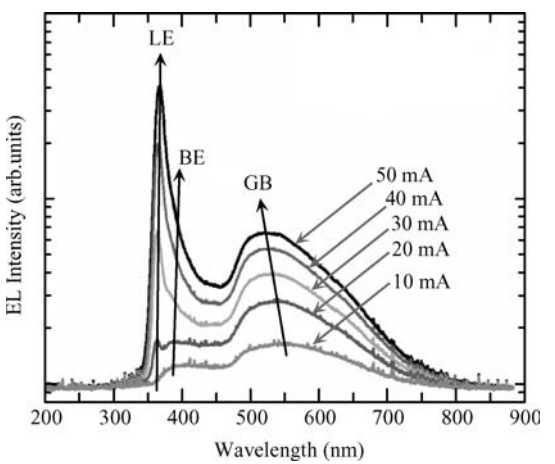

Figure 8.14 Electroluminescence spectrum measured at room temperature for ZnO-based LED having 7 BeZnO/ZnO QWs in the active layer. The primary spectral emission peak is located near 363 nm and arises from localized-exciton (LE) emissions in the QWs, while the secondary peak centered near 388 nm is from impurity-bound exciton emissions in ZnO. The green band (GB) blueshifts with increasing current injection. (After Ryu *et al.*)

ZnO nanotips have also been used to increase radiation outcoupling in the form of an improved passive light extraction layer in GaN light emitters [108]. The cross-sectional schematic of an integrated ZnO nanotip/GZO/GaN LED is shown in Figure 8.15a. InGaN/GaN multiple quantum well LED structures were grown on *c*-plane sapphire by MOCVD. The Ga-doped ZnO (GZO) layer, which has the dual role of contact to p-GaN and optically transparent window, was deposited on top of these conventional GaN LED structures. Then ZnO nanotips were grown on GZO-coated GaN as a light extraction layer. In comparison with a conventional Ni/Au p-electrode GaN LED, the light emission efficiency enhanced by a factor of ~1.7 (Figure 8.15b).

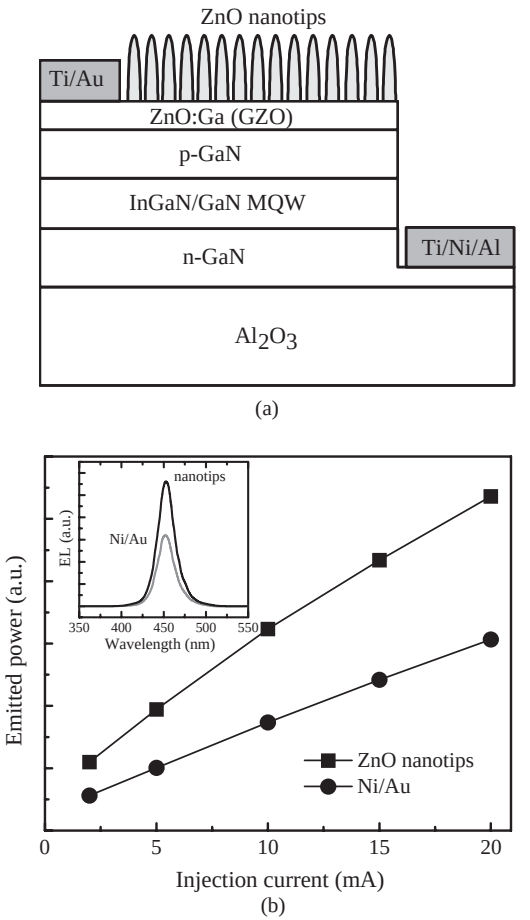

Figure 8.15 (a) Schematic diagram of an integrated ZnO nanotip/GZO/GaN LED. (b) Light output power versus forward injection current for Ni/Au and ZnO nanotip/GZO/GaN LED; inset compares the EL spectra of Ni/Au p-contact GaN LED and ZnO nanotip/GZO/GaN LED at a forward current of 20 mA. (After Ref. [108].)

Enhancement in light extraction efficiency was explained by the interaction between the spontaneous emission from the GaN LED and the spontaneous emission from the ZnO nanostructures. With an optimized GZO layer on p-GaN significantly higher light emission efficiencies are expected from the integrated ZnO nanotip/GZO/GaN LED structure. The results represent one of the low-cost and large-scale fabrication methods for the integration of ZnO nanotips with GaN-based optoelectronic devices using epitaxial growth technologies without the need for e-beam lithography or etching. Even without the nanotips, GZO or Al-doped ZnO (AZO)-coated GaN in place of ITO, which is used in all GaN-based LEDs, might turn out to be very lucrative in part fuelled by worldwide shortage of In. Transparent oxides based on ZnO are discussed in Section 8.5.5.

8.5.1.1 Microcavity Devices

Planar semiconductor microcavities (MCs) [109] in strong coupling regime have attracted a good deal of attention owing to their potential to enhance and control the interaction between photons and excitons, which could pave the way for cavity polaritons (see Section 3.2.1 for a discussion of bulk polaritons in ZnO). Cleaved and/or etched facets are not applicable to microcavities, which are basically vertical cavity structures. Instead, reflectors made of either heterostructures composed of materials with similar lattice structure but dissimilar indices of refraction (the more dissimilar the less the number of pairs needed and the wider the blocking wavelength band) or dielectric stacks are employed. Two of these reflectors are required, one for the bottom and the other for the top. Due to epitaxial growth requirements, the bottom reflector stack is usually made of the semiconductor variety, while the top can be depending on the mode of pumping. A typical microcavity is composed of a semiconductor cavity material of optical length $m\lambda/2$, where m is an integer and λ is the wavelength of emission, sandwiched between top and bottom reflectors such as distributed Bragg reflectors (DBRs). The spectral overlap of the high-reflectivity region (stop band) of the reflectors and the luminescence emission spectrum from the active QW region should be maximized. For a significant interaction between the cavity mode and excitonic states needed for reducing lasing threshold, the exciton energy should be at or close to the resonance frequency of the cavity mode. In the case of quantum wells embedded in the cavity, the optical field amplitude at the QW position (spatial) should be maximized by placing the QWs at the cavity standing wave antinodes.

DBRs are formed of dielectric stacks with alternating low- and high-refractive index layers both having $\lambda/4$ thickness ($\lambda = \lambda_{air}/n$ is the design wavelength, with n being the refractive index at the wavelength of particular interest). This gives rise to a stop band (wider with increasing refractive index contrast, which is desirable) with high reflectivity centered at λ_{air} and oscillating side-lobes on both sides. In the stop band, the mirror reflectivity is given by

$$R = \left(\frac{1-(n_{ext}/n_c)(n_L/n_H)^{2N}}{1+(n_{ext}/n_c)(n_L/n_H)^{2N}} \right)^2, \tag{8.49}$$

which for a large number of mirror pairs, N can be approximated by [110]

$$R = 1 - 4\left(\frac{n_{ext}}{n_c}\right)\left(\frac{n_L}{n_H}\right)^{2N}, \tag{8.50}$$

where and n_L, n_H, n_c, and n_{ext} are the refractive indices of the low- and high-refractive index layers, the cavity material, and the external medium, respectively. Obviously, a large number of pairs are needed for high reflectivity if the refractive index contrast between the layers of the DBR is small.

A semiconductor MC is very similar to a simple Fabry–Pérot resonator with planar mirrors. However, due to the penetration of the cavity field into DBRs, the depth is given by [110]

$$L_{DBR} = \frac{\lambda}{2n_c}\frac{n_L n_H}{n_H - n_L}, \tag{8.51}$$

the effective Fabry–Pérot cavity length L_{eff} is larger than the cavity layer thickness L_c ($L_{eff} = L_c + L_{DBR}$) and should be designed to be an integer multiple of $\lambda/2$. The cavity mode frequency is then given by

$$\omega_m = \frac{L_c\omega_c + L_{DBR}\omega_s}{L_{eff}}, \tag{8.52}$$

where ω_c is the Fabry–Perot frequency defined by the cavity length and ω_s is the center frequency of the DBR stop band.

In vertical cavity devices, because the gain region is short and thus the gain is low, the reflectivity of the top and bottom reflectors must be high for lasing, in the high 90% range, to overcome optical losses. The light is usually extracted from the top; therefore, the reflectivity of the bottom DBR should be as close to 100% as possible while that of the top can be made slightly less depending on the desired output optical power. Naturally, the reflector stacks should be made of materials that have no loss at the operation wavelengths. Even small errors in the thickness of each layer in the DBR can easily lead to large deviations from the desired central wavelength of the reflection band. It should be noted that the required thickness control for high-reflectivity DBRs scale with the wavelength exacerbating the situation for short wavelengths.

For the more matured GaN-based vertical cavity structures, AlGaN/GaN DBRs are usually the natural choice for simplicity of integration even though they require a large number of pairs (>30) for high reflectivity due to small refractive index contrast (~0.1) and current conduction through them is very difficult. In addition, Al-containing nitride heterostructures with increasing thickness suffer from cracks induced by lattice mismatch. Consequently, the quality of the QWs grown on such DBRs deteriorates, which would increase the lasing threshold. The cracks may also result in the formation of undesirable accidental in-plane resonators [111]. To overcome the cracking problem, lattice-matched $Al_{0.82}In_{0.18}N$/GaN DBRs has been applied [112–116]. Peak reflectivities higher than 99% have been reported for nitride DBRs [113–115, 117–119]. Patterned growth can also be used to accommodate strain better, in part eliminating the tendency to crack.

Compared to semiconductor DBRs, dielectric DBRs possess a number of advantages such as high-refractive index mismatch (e.g., ~0.6 at 400 nm for SiO_2/SiN_x

DBRs). For example, Chichibu *et al.* [120] reported high reflectivity (>99%) and wide stop band (~82 nm) SiO_2/ZrO_2 DBRs (eight pairs) for ZnO-based MCs owing to a large refractive index contrast between SiO_2 and ZrO_2. Growth of the dielectric DBRs as the top reflectors is straightforward as they do not need to be grown epitaxially on the cavity. All dielectric DBRs as the bottom reflectors, however, have been possible only after removal of the substrate [121–127], which require cumbersome processing steps.

Shown in Figure 8.16 are the reflectivity spectra calculated using the transfer matrix method [128] for a 10-pair SiO_2/Si_3N_4 DBR and a 30-pair $Al_{0.38}Ga_{0.62}N/GaN$ DBR, both designed for a central wavelength of 380 nm. Refractive indices used in these calculations for 380 nm wavelength were 1.46, 2.05, 2.41, and 2.67 for SiO_2, Si_3N_4, $Al_{0.38}Ga_{0.62}N$, and GaN, respectively. Note that a better contrast in refractive indices provided by the SiO_2/Si_3N_4 stack even with fewer pairs results in higher reflectivity and wider stop band compared to the $Al_{0.38}Ga_{0.62}N/GaN$ quarter wave stack. The inset in Figure 8.16 shows the measured reflectivity spectrum for a 26.5-pair $Al_{0.5}Ga_{0.5}N/Al_{0.15}Ga_{0.85}N$ DBR.

A planar cavity provides no in-plane confinement (perpendicular to the growth axis) and just as for electronic states in QWs photons have only in-plane dispersion. Photons are quantized along the cavity as the mirrors force the axial wave vector k_z in the medium to be $2\pi/L_c$. Hence the cavity photon energy is approximately

$$E = \frac{\hbar c}{n_c} k = \frac{\hbar c}{n_c}\left[\left(\frac{2\pi}{L_c}\right)^2 + k_{//}^2\right]^{1/2}. \tag{8.53}$$

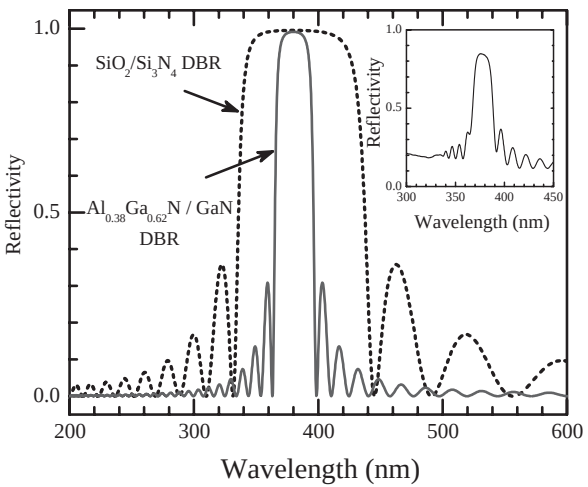

Figure 8.16 Calculated reflection spectra of (a) a 10-pair SiO_2/Si_3N_4 quarter wave reflector and (b) 30-pair $Al_{0.38}Ga_{0.62}N/GaN$ quarter wave stack designed for a central wavelength of 380 nm and (c) experimentally obtained reflectivity in an MBE grown 26.5-pair $Al_{0.5}Ga_{0.5}N/Al_{0.15}Ga_{0.85}N$ DBR. (Courtesy of R. Shimada and J. Xie, Virginia Commonwealth University.)

For small $k_{//}$, the in-plane dispersion is parabolic (as depicted in the above equation) and therefore it can be described by a cavity photon effective mass $M = 2\pi^2 h n_c / c L_c$. This effective mass is very small, $\sim 10^{-5} m_e$, and the dispersion can be measured directly in angle-resolved experiments allowed by the introduction of an in-plane component to the photon wave vector. Experiments involving off-normal incidence can also be modeled by including an appropriate *in-plane* wave vector for the field.

In addition to improved extraction efficiency and narrower and more directional emission, MCs allow strong coupling between excitons and cavity photons resulting in the formation of cavity polaritons that are quasiparticles whose genesis lies in the superposition of excitons and cavity photons having the same energy and momentum. In contrast to polaritons in the bulk material, where the photon dispersion is linear ($\omega = kc/n_c$), cavity polariton has a quasi-two-dimensional nature with a finite energy at zero wave vector, $\boldsymbol{k} = 0$, and is characterized by a very small in-plane effective mass as mentioned above, which gives rise to narrowing of the linewidth. This feature is due to the half-photon and half-exciton character of the polaritons, the photon fraction having very strong dispersion. In bulk materials, it is difficult to probe the properties of exciton-polaritons due to the photon-polariton conversion process at the air–semiconductor interface (semiconductor surface). However, in MCs propagation to the surface is not required and the polaritons are converted directly into external photons as a result of the finite lifetime of their photon component within the cavity. Moreover, since the wave vector perpendicular to the sample surface is quantized, the complications due to spatial dispersion along the growth direction are eliminated and there is a one-to-one correspondence between the internal polariton states and the external photons, which allows measurement of polariton dispersion curves in reflectivity or PL experiments.

At resonance, two polariton modes arise from symmetric and antisymmetric combinations of the exciton and cavity modes. Only the cavity mode couples directly to the external photons away from resonance, and the excitonic mode becomes weak. When the Rabi splitting ($\hbar\Omega_{Rabi}$), the minimum energy splitting between the upper and the lower polariton branches, is larger than both the exciton and the cavity linewidths, the system is in the strong coupling regime. The splitting can then be measured in the optical spectrum where the two modes anticross. Figure 8.17 shows a typical anticrossing behavior. This strong coupling regime is completely different from that for excitons in isolated QWs not embedded in an MC. In the case of QWs without the MC, excitons decay irreversibly into the continuum of photon states along the growth direction due to the discontinuity of translational symmetry along the growth direction. Thus excitons in QWs would have a finite lifetime ($\sim$20 ps) [129]. The photon states in MCs, which are quantized along the growth direction (along the cavity), and each of the in-plane exciton states can only couple to one external photon state. Quasistationary eigenstates exist as the cavity polaritons, and the irreversible exciton decay does not arise. In the time domain, excitations oscillate between the two modes on a subpicosecond timescale with a period h/Ω_i before the leakage of photons from the cavity takes place.

The Rabi splitting in MCs is enhanced significantly compared to that in bulk making it easier to achieve the desired coupling at practical temperatures. The cavity polaritons feature large and unique optical nonlinearities not achievable in a bulk

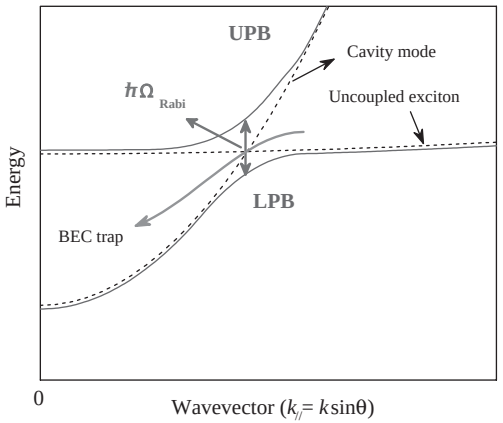

Figure 8.17 A simple sketch of the cavity polariton dispersion. θ is measured from the surface normal.

material caused by their bosonic nature, which when combined with their low density of states (low effective mass on the order of $10^{-5}m_e$ at $k = 0$) could allow the formation of a dynamical Bose–Einstein condensate (BEC) [130, 131] in the trap states defined by the lower polariton branch (LPB) at $k = 0$ as shown in Figure 8.17. Recombination from this state in the BEC[2)] regime is coherent, monochromatic, and sharply directed, which bodes well for laser emission. The relaxation of polaritons into the $\boldsymbol{k} = 0$ state is stimulated if the population of the final state is more than one [132]. When the relaxation to the ground state of the trap is faster than the radiative recombination from this state, optical amplification occurs.

Attaining the strong coupling regime in semiconductor MCs, however, requires structures and materials in which excitons are robust at the operating temperature. In principle, increasing the exciton oscillator strength can further increase the coupling strength and permit a large Rabi splitting, that is, deeper trap states, more resistant to exciton density and temperature broadening. A large exciton-binding energy will prevent dissociation of polaritons or excitons into free carriers. The large oscillator strength and binding energy of excitons in ZnO make the ZnO-based MCs excellent candidates for achieving a higher exciton–photon-coupling regime, thus lasing, at operating temperature. This feature is markedly different from those governing conventional lasers. Lasing in conventional lasers is predicated upon population inversion that requires substantial pumping/carrier injection. In a microcavity structure, however, the lasing condition is uniquely dependent only on the lifetime of lower polariton ground state. This is expected to lead to extremely low-threshold polariton lasers ideal for, and saviors of, vertical cavity surface emitting laser (VCSEL).

Polariton lasing is prevented in the popular GaAs-based MCs (VCSEL structures) because of the slow relaxation of photoexcited polaritons down to the bottom of the

2) Using the atom metaphore, a Bose–Einstein condensate is a state of matter confined in an external potential and cooled to temperatures very near to absolute zero. Under such conditions, a large fraction of atoms collapse into the lowest quantum state of the external potential, at which point quantum effects become apparent on a macroscopic scale.

lower polariton branch. Moreover, the needed strong coupling regime is not sustained at room temperature in the GaAs system due to small exciton-binding energy. Consequently, wide-bandgap semiconductors such as GaN and ZnO with their large exciton-binding energies must be considered for room temperature polariton devices. Several groups have already reported polariton luminescence at RT from bulk [133, 134] and QW [135] GaN-based MCs with vacuum Rabi splittings as high as 43 meV. Even room temperature polariton lasing has been observed under nonresonant pulsed optical pumping in bulk GaN-based MCs [136].

Due to its larger exciton-binding energy, ZnO supports stronger exciton–photon interaction than GaN. Accordingly, the vacuum Rabi splitting for cavity polaritons in a ZnO MC sandwiched between $Mg_xZn_{1-x}O$/ZnO DBRs has been calculated to be as large as $\Omega_i \sim 120$ meV [137], which was later modified to a record value of Ω_i at ~ 191 meV [138]. ZnO-based planar resonators, which consist of a ZnO cavity layer surrounded by ZrO_2/MgO DBRs, were grown by pulsed laser deposition and were found to exhibit $\Omega_i \sim 50$ meV [139]. A vacuum Rabi splitting of the same order (50 meV) was also observed in ZnO-based hybrid MCs using 29-pair AlGaN/GaN bottom and 8-pair SiO_2/Si_3N_4 top DBRs [140]. Figure 8.18a shows the angle-resolved PL spectra at room temperature up to 40° from the surface normal. It is clear that the lower polariton mode gets closer to the uncoupled exciton mode, and the upper polariton mode is dispersed from the exciton mode to the cavity mode with increasing collection angle (i.e., polariton wave vector). The experimental cavity polariton dispersion curve shown in Figure 8.18b exhibits a typical anticrossing behavior between the

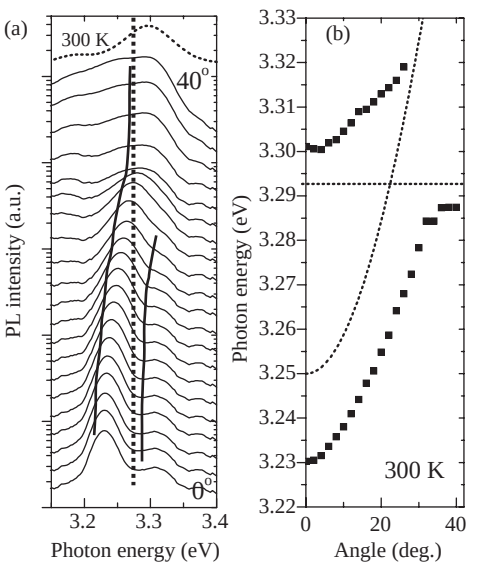

Figure 8.18 (a) Angle-resolved PL spectra at RT in the range of 0°–40° for a λ-thick ZnO hybrid MC. The dotted line is the exciton mode. The solid lines are guides to the eye. (b) Experimental cavity polariton dispersion curve. The dashed lines represent the cavity and exciton modes. (Courtesy of R. Shimada [140].)

cavity mode and the exciton mode when the cavity mode energy crosses the exciton mode. These results are promising for the realization of room-temperature ZnO-based polariton devices. ZnO-based electrical injection lasers may also be realizable in the near future when reproducible and reliable p-type conductivity in ZnO is achieved.

8.5.1.2 **Optically Pumped Lasers**

Fundamentals of stimulated emission and lasing are discussed in Section 3.5. Specific to ZnO, there are plenty of reports on UV lasing from ZnO-based materials and devices under optical pumping, for example, lasing from ZnO photonic crystals [141, 142] and random lasing from ZnO powder under certain pumping conditions [143]. A ZnO-based optically pumped third-order distributed feedback (DFB) laser has also been reported [144]. A single longitudinal mode was observed between 10 and 270 K. Mode selection was accomplished via a third-order diffraction grating. As seen from Figure 8.19, the DFB laser had a spectral linewidth of 0.5 nm, a pump threshold intensity of 0.12 MW cm^{-2}, and a peak output power of 14 mW. The temperature tuning coefficient of ZnO refractive index was deduced to be 9×10^{-5} K^{-1} from wavelength versus temperature measurements. However, none of these methods is promising for any practical device applications that demand high power output and low excitation threshold.

Unavailability of reliable p-type conductivity prevents ZnO from competing with GaN for optoelectronic applications to a first extent. There are of course continuing developments in the GaN industry to satisfy the increasing demands for larger data

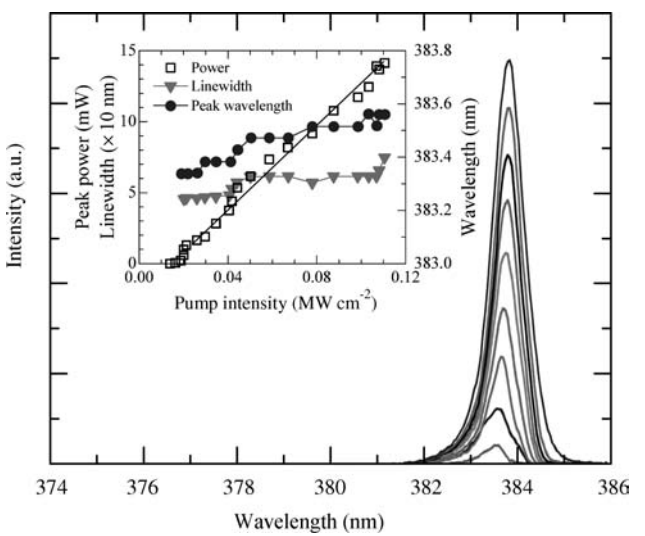

Figure 8.19 Emission spectra of a ZnO-based DFB laser as a function of optical pump power measured at 0.15, 0.25, 0.35, 0.45, 0.6, 0.8, 0.9, 1.0, and 1.1 MW cm^{-2}. The inset shows peak power (triangles, left *y*-axis), emission wavelength (squares, right *y*-axis), and linewidth (circles, left *y*-axis, 10×) versus pump intensity curves. (Courtesy of D. Hofstetter [144].)

storage capacity by developing short-wavelength emitters of high efficiency, such as high-coherence and low-threshold UV/violet lasers. ZnO-based low-threshold or nearly thresholdless lasers, especially those based on polariton lasing in ZnO, will also have applications in ever increasing telecommunications and optical storage, in addition to being possible strong light pump sources for white light generation. Therefore, further attention needs to be paid to the development of reliable p-type ZnO that will allow demonstration of high-efficiency ZnO light sources.

8.5.2 Photodiodes

There have been many reports regarding photoresponse properties of the ZnO-based heterojunctions [80, 81, 87, 92, 95, 96]. For example, Jeong *et al.* [80] reported on the photoelectric properties of n-ZnO/p-Si PDs, which detect UV photons in the depleted n-ZnO and simultaneously detect visible photons in the depleted p-Si by employing two related photoelectric mechanisms. The *I–V* measurements obtained while the photodiodes are exposed to radiation in a wavelength range of 310–650 nm showed a linear increase in photocurrent with reverse bias. In the visible range, the photocurrent rose rapidly with bias but saturated beyond a critical voltage. The diodes exhibited high responsivities of 0.5 and 0.3 $A W^{-1}$ for UV (310 nm) and red (650 nm) photons, respectively, under a 30 V bias with a minimum near 380 nm that corresponds to the bandgap of ZnO.

Transparent window p-NiO/n-ZnO PDs were heteroepitaxially grown by Ohta *et al.* [87] on a Y_2O_3-stabilized ZrO_2 (1 1 1) substrate by PLD combined with a solid-phase epitaxy technique. The fabricated diodes exhibited clear rectifying *I–V* characteristics with an ideality factor of ∼2 and a forward turn-on voltage of ∼1 V. Spectral responsivity measurements were performed via photoexcitation from the substrate side by using a monochromated Xe lamplight under several reverse-bias conditions. A photoresponsivity as high as ∼0.28 $A W^{-1}$ was achieved at 6 V reverse bias under irradiation by 360 nm light that corresponds to an energy slightly over the ZnO energy gap (3.30 eV). Spectral response of the p-NiO/n-Zno diode reported by Ohta *et al.* [87] at several reverse-bias voltages are shown in Figure 8.20 along with the device structure depicted in the inset.

Ohta *et al.* [95] also reported on transparent p–n heterojunctions composed of p-$ZnRh_2O_4$ and n-ZnO thin layers grown by reactive solid-phase epitaxy technique. Polycrystalline $ZnRh_2O_4$ was deposited on a ZnO epitaxial layer at room temperature. Thermal annealing of the bilayer sample at 950 °C in air converted the polycrystalline $ZnRh_2O_4$ layer to what was reported to be an epitaxial single-crystalline layer. The resultant p–n heterojunctions had an abrupt interface and exhibited distinct rectifying *I–V* characteristics with a threshold voltage of ∼2 V that is in agreement with the bandgap energy of $ZnRh_2O_4$. The photovoltage originating mainly from the n-ZnO layer was also observed.

As discussed above, the critical factor influencing the properties of heterostructures is the similarity of the lattice parameters. In this respect, 6H-SiC seems to be a good candidate because it has a relatively small lattice mismatch with ZnO (∼3.5%,

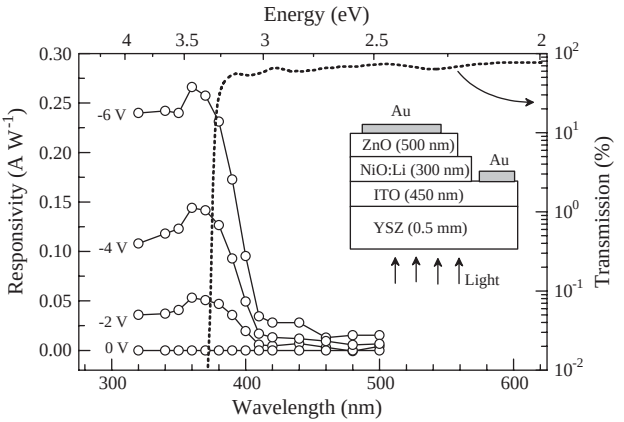

Figure 8.20 Spectral response of the p-NiO/n-ZnO diode at several reverse-bias voltages. The device structure is also shown in the inset. (After Ref. [87])

see Table 2.3), and p-6H-SiC substrates are commercially available. Alivov *et al.* [92, 93] demonstrated n-ZnO/p-6H-SiC type PDs using 0.5 μm thick n-ZnO layers on p-type 6H-SiC substrates grown at 600 °C by plasma-assisted MBE. Ohmic contacts to the 250 μm diameter mesastructures were made by vacuum evaporation of 300/1000 Å thick Au/Al and Au/Ni metal layers to n-ZnO and p-SiC layers, respectively. The *I–V* characteristics of the n-ZnO/p-SiC heterostructures shown in the inset of Figure 8.21 reveal a diode-like behavior with turn-on and soft breakdown voltages of ∼5 and −23 V, respectively, and somewhat low-leakage current of $\sim 10^{-7}$ A

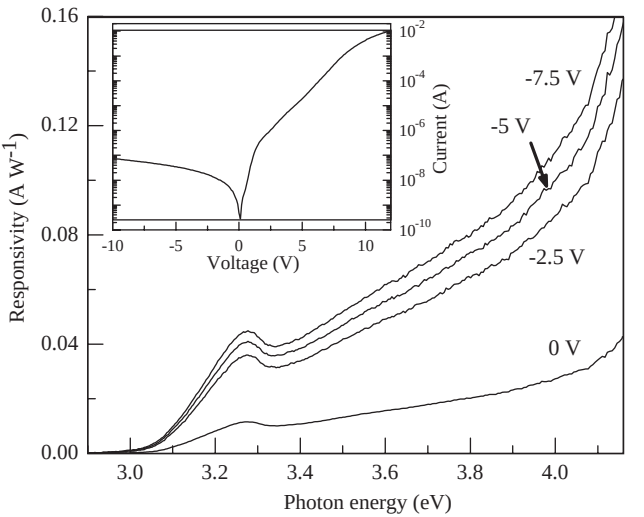

Figure 8.21 Spectral photoresponse of the n-ZnO/p-SiC photodiode structure at various reverse biases ranging from 0 to −7.5 V. The inset shows the room-temperature *I–V* characteristics of n-ZnO/p-SiC heterojunctions. (After Ref. [92].)

under −10 V reverse bias. When illuminated from the ZnO side of the heterostructure, the n-ZnO/p-6H-SiC structures exhibited quite good photosensitivity to UV radiation with a maximum at ∼3.283 eV, as illustrated in Figure 8.21. A photoresponse as high as 0.045 A W^{-1} at −7.5 V reverse bias was observed.

8.5.3
Metal–Insulator–Semiconductor Diodes

In the absence of p–n junctions, electroluminescence properties of ZnO could be exploited by fabricating metal–insulator–semiconductor (MIS) structures that do not require p-type ZnO. In spite of this, there have been only a few reports on such MIS structures [145–147]. Shimizu *et al.* [146] demonstrated an MIS diode with an insulating ZnO layer obtained by keeping the ZnO crystal in a 30% solution of H_2O_2. At room temperature, this diode emitted in the defect-related green region of the spectrum with a peak at 2.5 eV. Minami *et al.* [145] used an insulating SiO layer deposited by thermal evaporation, and under forward bias the device emitted in the UV region (3.13 eV) at 300 K. The current–voltage characteristics of the diodes showed a typical nonlinear behavior.

In a follow-up work by Alivov *et al.* [147] ion implantation was employed to produce an insulating ZnO layer. In this work, 2 μm thick ZnO:Ga films were implanted with 180 keV N^+ ions to a dose of 1.2×10^{14} cm^{-2} at a sample temperature of 773 K. The penetration depth at the ion energy of 180 keV, calculated by a TRIM (Transport of ions in matter) program, was about 0.25 μm, which sets the thickness of the insulating layer to 0.25 μm. MIS diodes were fabricated by first masking the surface and then using a 10% HNO_3 aqueous solution to remove part of the upper (insulating) ZnO layer for gaining access to the conducting ZnO layer below for ohmic-contact formation. The top Au metal layer, deposited thermally onto the insulating layer (i-layer), was 1.8 mm in diameter. Ohmic contact to the lower conducting layer was made by indium evaporation. *I–V* characteristics of a typical diode obtained by Alivov *et al.* [147] are shown in Figure 8.22. This figure shows a quite good and rectifying behavior of the MIS diode with a threshold voltage near 3 V and a reverse current of about 10^{-6} A (or current density 3.93×10^{-5} A cm^{-2}). Under forward bias (metal at positive terminal), UV light emission was observed at RT with a maximum at ∼388 nm (3.197 eV) and an FWHM of 128 meV. The EL spectrum of the LED was very similar to the CL spectrum of the ZnO layer. From the foregoing discussion, it can be concluded that the radiation mechanisms in both cases are similar that is very probably excitonic in nature. No EL emission was observed under reverse-bias conditions either for MIS structure or for that without an insulating layer. It is known that the properties of the MIS diodes depend strongly on the quality of the isolation layer and its thickness and electrical properties. Creating an MIS diode in this manner, therefore, is of special interest because ion implantation is a very controllable technology and suitable for the fabrication of various microelectronic structures. Moreover, diodes of this type are of interest not only in the design of light emitters but also in the development of transparent transistors.

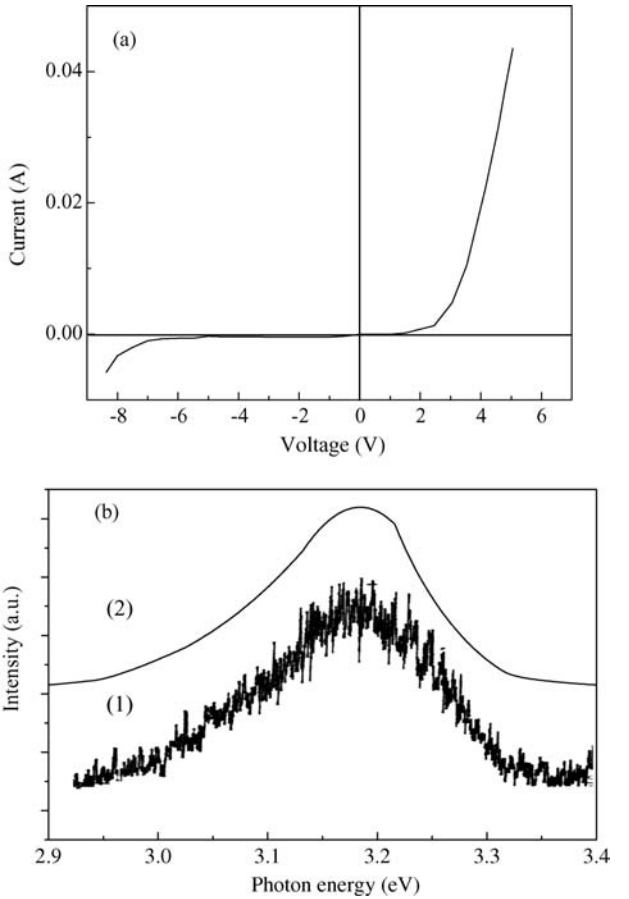

Figure 8.22 (a) Current–voltage characteristics of a ZnO MIS diode. (b) Room-temperature (1) EL and (2) CL spectra of the MIS diode and ZnO layer, respectively. (After Ref. [147].)

8.5.4
Field Effect Transistors

Motivation for ZnO-based FETs are availability of bulk growth capability (although high resistivity is needed, which has not yet been demonstrated), amenability to conventional chemical etching, relatively low growth temperature (which may or may not have much effect on FET technology), and high radiation hardness (which remains to be seen in functional devices) [148]. We should mention that the effective mass and the thermal conductivity in ZnO are larger relative to GaN, its presumed competitor that has made great strides, which does not bode well for ZnO-based FETs. For completeness, however, a short discussion of the developments in this subfield is given here.

The simplest form of FETs is what is dubbed as the thin-film transistor. TFTs have simpler growth and processing technologies compared to heterostruture FETs and therefore have lower manufacturing cost. They usually contain polycrystalline active channels that are grown on amorphous substrates, which results in a limited device performance. Even though the first conceptualization of TFTs dates back to 1930s, significant advances in the development of TFTs occurred with the relatively recent rapid growth of the active-matrix liquid crystal display industry [149, 150]. Si has shown its supremacy also in the TFT technology where amorphous Si (a-Si) and polycrystalline Si (poly-Si) currently dominate the field. Naturally, alternative materials are constantly being explored to compete with the Si-based TFTs, with unique characteristics and niche target applications. The most striking advantage of ZnO for TFTs is its transparency to visible light, as discussed in Section 8.5.5. In many applications, TFTs are used as voltage-controlled switches. The most important electrical parameters in quantifying TFT performance are the active channel mobility, turn-on gate voltage, and the drain current on-to-off ratio [151, 163]. Except being transparent, ZnO-based TFTs have been shown to exhibit higher channel mobilities and on-to-off ratios compared to their Si counterparts as discussed below.

Let us give a brief analytical treatment of FET current–voltage characteristics. Because the only purpose of the oxide is to reduce the leakage current and is void of carriers, its effect on the gate voltage can be treated as a constant capacitance (i.e., voltage independent) in series with the depletion capacitance (i.e., voltage dependent). Doing so would allow one to initially utilize the expressions developed for metal–semiconductor field effect transistors (MESFETs) followed by correction for the oxide capacitance. Furthermore, the long-channel lengths prevailing in thin-film transistors would allow the use of the expressions developed for long-channel MESFETs, that is, expressions developed under the constant mobility assumption.

The current–voltage relationships can be found in the literature, for example, Lehovec and Zuleeg [152] and in many elementary device texts. However, for completeness, the essential derivations are provided here. For a long-channel MESFET, we will make use of the long-channel depletion approximation schematically depicted in Figure 8.23 where the depletion under the gate due to gate bias and drain bias is shown. Note that the access regions, and therefore their resistances on the gate and drain sides of the channel, have been eliminated for simplicity.

The depletion depth under the gate is expressed as

$$W = \sqrt{\frac{2\varepsilon_s(V_{bi} - V_a)}{qN_D}}, \tag{8.54}$$

where ε_s, V_{bi}, V_a, and N_D represent the semiconductor permittivity, Schottky metal built-in voltage, effective applied gate bias, and donor concentration in the channel, respectively. The effective gate bias on the source and drain sides are given by

$$V_a = -V_g\big|_{y=0} \quad \text{and} \quad V_a = -(V_g + V_D)\big|_{y=L}, \tag{8.55}$$

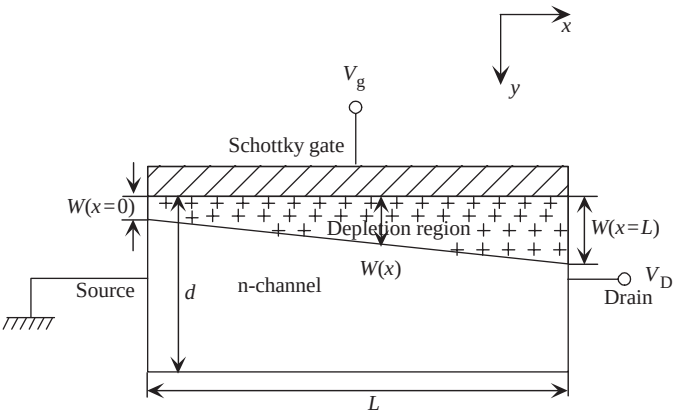

Figure 8.23 Depletion region formed under the gate of a MESFET in the long-channel approximation with source and drain access regions omitted.

respectively, where V_g is the gate voltage, V_D is the drain voltage, and L represents the channel length. The depletion region depth on the source and drain sides of the gate, therefore, can be expressed as

$$W(x=0)=\sqrt{\frac{2\varepsilon_s(|V_g|+V_{bi})}{qN_D}} \quad \text{and} \quad W(x=L)=\sqrt{\frac{2\varepsilon_s(|V_g|+V_D+V_{bi})}{qN_D}}. \tag{8.56}$$

If the channel thickness is d, the total voltage V_p required to deplete the channel at $x=x_2$ ($W(x_2)=d$) equals to

$$W(x_2)=d=\sqrt{\frac{2\varepsilon_s(V_{bi}-V_g+V_D)}{qN_D}} \rightarrow V_{bi}-(V_g-V_D)=\frac{qN_D}{2\varepsilon_s}d^2,$$
$$V_p=\frac{qN_D}{2\varepsilon_s}d^2. \tag{8.57}$$

Note that V_g is negative and V_D is positive for an n-channel depletion mode device. Having the dependence of the depletion depth on the gate and drain biases, and thus the open channel that is the channel thickness d minus the depletion depth, we can now begin developing the expressions for current–voltage characteristics. The current along the channel can be written as

$$J=\sigma(x)E(x), \tag{8.58}$$

where $\sigma(x)$ and $E(x)$ represent the position-dependent channel conductivity and lateral electric field. In the constant mobility assumption, channel conductivity is field and therefore position independent and is given by

$$\sigma(x)=q\mu_n N_D, \tag{8.59}$$

The cross-sectional area of the device, normal to the plane of the paper in Figure 8.23, is

$$A = (d-W)Z, \tag{8.60}$$

where Z represents the channel width, dimension normal to the plane of paper in Figure 8.23. The drain current can then be expressed as

$$I_D = qN_D\mu_n(d-W)Z\frac{dV(x)}{dx}, \tag{8.61}$$

where dV/dx represents the electric field at point x along the channel. Rearranging Equation 8.61 we have

$$I_D dx = qN_D\mu_n(d-W)Z dV(x). \tag{8.62}$$

Rewriting Equation 8.57 at an arbitrary position x along the channel

$$W(x) = \sqrt{\frac{2\varepsilon_s(V_{bi}+V_x-V_g)}{qN_D}} \quad \text{or} \quad [W(x)]^2 = \frac{2\varepsilon_s(V_{bi}+V_x-V_g)}{qN_D} \tag{8.63}$$

and taking the derivative

$$W(x)dW = \frac{\varepsilon_s dV(x)}{qN_D} \rightarrow dV(x) = \frac{qN_D}{\varepsilon_s}W(x)dW, \tag{8.64}$$

which when substituted into Equations 8.61 or 8.62 leads to the current expression:

$$I_D dx = qN_D\mu_n(d-W)Z\frac{qN_D}{\varepsilon_s}W(x)dW. \tag{8.65}$$

Integrating under the gate, we obtain

$$\int_{x_1}^{x_2} I_D dx = \int_{W_1}^{W_2} qN_D\mu_n(d-W)Z\frac{qN_D}{\varepsilon_s}W(x)dW. \tag{8.66}$$

We can continue to perform the integration while noting that the drain current is independent of position:

$$\begin{aligned}
\int_{x_1}^{x_2} I_D dx &= \int_{W_1}^{W_2} qN_D\mu_n(d-W)Z\frac{qN_D}{\varepsilon_s}W(x)dW,\\
I_D L &= \int_{W_1}^{W_2} \frac{q^2N_D^2}{\varepsilon_s}\mu_n(d-W)ZW(x)dW,\\
I_D &= \frac{q^2\mu_n N_D^2 Z}{\varepsilon_s L}\int_{W_1}^{W_2}(d-W)W(x)dW,\\
I_D &= \frac{q^2\mu_n N_D^2 Z d^3}{6\varepsilon_s L}\left[\frac{3}{d^2}\left(W_2^2-W_1^2\right)-\frac{2}{d^3}\left(W_2^3-W_1^3\right)\right].
\end{aligned} \tag{8.67}$$

Defining the current under the condition wherein the depletion region at the drain end of the channel penetrates through the entire thickness of the channel as the saturation current or the current at the drain pinch-off condition (I_p):

$$I_p = \frac{q^2 \mu_n N_D^2 Z d^3}{6\varepsilon_s L}.$$

Then the drain current expression becomes

$$I_D = I_p \left[\frac{3}{d^2}\left(W_2^2 - W_1^2\right) - \frac{2}{d^3}\left(W_2^3 - W_1^3\right) \right], \tag{8.68}$$

where W_1 and W_2 represent the depletion depths under the source and drain sides of the gate, respectively.

Converting to reduced voltages through

$$\begin{aligned} u(x) &\equiv \frac{W}{d} = \sqrt{\frac{V_{bi} + V(x) + |V_g|}{V_p}}, \\ u_1(x) &\equiv \frac{W_1}{d} = \sqrt{\frac{V_{bi} + |V_g|}{V_p}}, \\ u_2(x) &\equiv \frac{W_2}{d} = \sqrt{\frac{V_{bi} + V_D + |V_g|}{V_p}}. \end{aligned} \tag{8.69}$$

Equation 8.68 can be written as

$$I_D = I_p \left[3\left(u_2^2 - u_1^2\right) - 2\left(u_2^3 - u_1^3\right) \right].$$

Substituting Equation 8.69 into Equation 8.68, we obtain for the drain current

$$I_D = I_p \left\{ 3\frac{V_D}{V_p} - 2\left[\left(\frac{V_{bi} + |V_g| + V_D}{V_p} \right)^{3/2} - \left(\frac{V_{bi} + |V_g|}{V_p} \right)^{3/2} \right] \right\}. \tag{8.70}$$

At the saturation point on the drain side, the drain voltage equals the pinch-off voltage, which implies

$$u_2(x) \equiv \frac{W_2}{d} = \sqrt{\frac{V_{bi} + V_D + |V_g|}{V_p}} = 1. \tag{8.71}$$

Using Equation 8.71 in Equation 8.70, we obtain for the drain saturation current

$$\begin{aligned} I_{Dsat} &= I_p \left[1 - 3u_1^2 + 2u_1^3 \right] \\ &= I_p \left[1 - 3\left(\frac{V_{bi} + |V_g|}{V_p} \right) + 2\left(\frac{V_{bi} + |V_g|}{V_p} \right)^{3/2} \right]. \end{aligned} \tag{8.72}$$

The drain voltage at saturation is expressed as

$$V_{Dsat} = V_p - V_g - V_{bi} = \frac{qN_D d^2}{2\varepsilon_s} - V_g - V_{bi}. \tag{8.73}$$

The transconductance is given by

$$g_m = \left.\frac{\partial I_D}{\partial V_g}\right|_{V_D=\text{constant}} = \frac{2qZ\mu_n N_D}{L}[u_2 - u_1]. \tag{8.74}$$

The drain conductance in the saturation regime is given by

$$g_D = \left.\frac{\partial I_D}{\partial V_D}\right|_{V_g=\text{constant}} = \frac{2qZ\mu_n N_D}{L}[d - u_2]. \tag{8.75}$$

For comparison, one can write the drain conductance in the linear region as

$$g_{D0}(V_D \to 0) = g_{max}\left[1 - \sqrt{\frac{V_g + V_{bi}}{V_p}}\right], \tag{8.76}$$

where $g_{max} = 2qZ\mu_n N_D/L$.

The transconductance in the saturation regime is expressed as

$$g_{mSat} = \left.\frac{\partial I_{Dsat}}{\partial V_g}\right|_{V_{DS}=\text{constant}} = g_{max}[1 - u_1] = g_{max}\left[1 - \sqrt{\frac{V_g + V_{bi}}{V_p}}\right]. \tag{8.77}$$

The drain current–voltage characteristics for an arbitrary MESFET with an external pinch-off voltage of −2 V (when added to the built-in voltage in terms of amplitude equals to V_p) is shown in Figure 8.24.

The basic TFT structure involves a channel layer such as Si or ZnO between source and drain electrodes and a gate electrode that is separated from the channel, source,

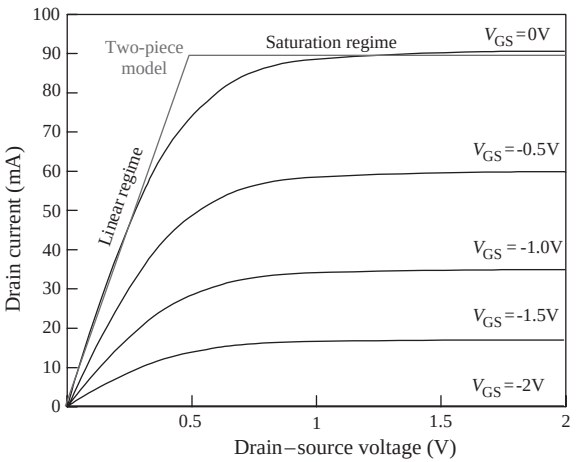

Figure 8.24 Typical output current–voltage characteristics of an arbitrary MESFET with an external pinch-off voltage of −2 V. In two-piece models applicable to the cases where velocity saturation occurs, it is assumed that the mobility is constant in certain region of the channel under the gate toward the source and velocity is saturated in the rest. The boundary depends on the drain voltage and the gate dimension.

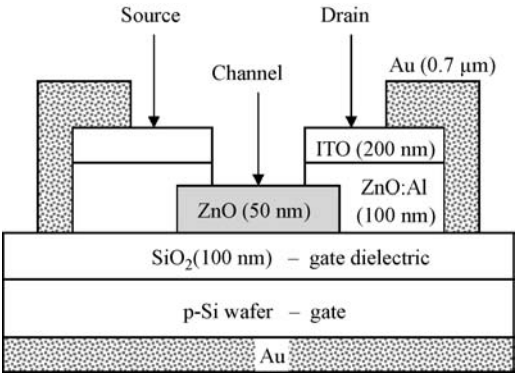

Figure 8.25 Schematic representation of a typical ZnO channel TFT structure. (After Ref. [153].)

and drain by a thin-gate dielectric. A typical TFT structure based on a ZnO channel is shown in Figure 8.25 [153]. In this case where an insulator (oxide) is placed between the gate metal and the semiconductor (metal oxide semiconductor or MOS structure), the gate voltage in the above expressions should be modified. The gate voltage in this case may be denoted by V'_g, which is now equal to

$$V'_g = V_g + V_{ox}, \tag{8.78}$$

where V_{ox} is the voltage drop across the oxide. The equations derived for a MESFET above can be generalized for a MOS structure by finding the relationship between V'_g and V_g. The gate capacitance may now be considered to be formed of two series capacitances, one the depletion capacitance of the semiconductor ($C_s = \varepsilon_s W^{-1}$ per unit area) and the other the capacitance of the gate insulator (C_{ox}). It should be noted that C_{ox} is constant but the charge, therefore, the voltage drop across its gate, is voltage dependent. The total capacitance is

$$C^{-1} = C_{ox}^{-1} + C_s^{-1} \Rightarrow C = \frac{C_{ox}C_s}{C_{ox} + C_s}. \tag{8.79}$$

The total charge can be written as

$$CV'_g = C_{ox}V_{ox} + qN_D W, \tag{8.80}$$

where W is still given by Equation 8.54. Substituting Equation 8.79 into Equation 8.80 leads to

$$V_{ox} = \frac{1}{C_{ox}}\left(\frac{C_{ox}C_s}{C_{ox} + C_s}V'_g - qN_D W\right). \tag{8.81}$$

From Equations 8.78 and 8.81 one easily obtains

$$V_g = \left(\frac{C_{ox}}{C_{ox} + \varepsilon_s/W}V'_g + \frac{1}{C_{ox}}qN_D W\right). \tag{8.82}$$

By using this relationship, V_g can be obtained from V_g' and substituted into the equations derived for a MESFET to obtain the solutions for MOSFET structures involving an insulator under the gate.

After gaining some understanding of the analytical treatment of the current–voltage characteristics in a nominal FET, let us now return to the discussion of ZnO-based transistors. For the device configuration shown in Figure 8.25, ZnO channel and ZnO:Al and ITO contact layers were deposited on thermally oxidized p-Si wafers by RF sputtering. For these ZnO TFT structures with p-Si gate, SiO_2 gate dielectric, a channel length of 200 μm, and a width-to-length ratio of 9 : 1, a channel mobility as high as 25 $cm^2 V^{-1}$ and an on-to-off ratio above 7×10^8 were reported after a 600 °C postdeposition annealing of the whole structure and under high gate voltage bias of 70 V across the 100 nm SiO_2. The turn-on voltage, defined as the gate voltage required to fully "turn off" the transistor, was identified as −2 V, and the gate leakage was relatively low as seen from Figure 8.26b (10^{-8} A at 70 V). Although high mobilities and on-to-off ratios were attained at high gate voltages, the results indicate that ZnO-channel TFTs may compete with amorphous and polycrystalline Si TFTs in terms of performance. With further improvements in the channel and dielectric layer quality and consequently by reducing the gate dielectric thickness, similar performance may be expected at much lower gate voltages. Reduction of the processing temperature is also critical to demonstrate the practicability of ZnO TFTs. Accordingly, Nishii *et al.* [154] reported ZnO TFTs, using amorphous SiN_x gate dielectric and a $CaHfO_x$ buffer layer between SiN_x and the ZnO channel, with mobilities as high as 7 $cm^2 V^{-1} s^{-1}$ at a 30 V gate voltage. The maximum process temperature was also reduced to 300 °C.

It should be noted that when the TFT is in "off" state, the leakage can have two components: source-to-drain leakage and gate-to-channel leakage. With decreasing channel length the former increases and the latter decreases. Therefore, the off current is dominated by the gate dielectric leakage for large channel devices. The results of Hoffman [153] mentioned above (on-to-off ratio of 7×10^8 and gate leakage current of 10^{-8} A) indicate that the gate dielectric leakage can be effectively controlled. Same is true for the source-to-drain leakage, which is dominant for small channel lengths. For example, Carcia *et al.* [165] fabricated ZnO TFTs with smaller channel lengths (20 μm) by RF magnetron sputtering on heavily doped n-type Si substrates held near room temperature. In this structure, the substrate was coated with a 100 nm thick thermal oxide layer, and more than 200 μm wide Ti–Au (10 nm/100 nm) source and drain electrodes with a 20 μm gap (channel length) were deposited and patterned directly on the thermal silicon oxide layer. The gate electrode was also formed of Ti–Au deposited on the back of the Si-substrate. A ZnO film about 100 nm thick was then sputtered between the source and the drain electrodes using a shadow mask. The best devices exhibited field-effect mobility of more than 2 $cm^2 V^{-1} s^{-1}$ and an on–off ratio of more than 10^6, without any postdeposition annealing (nearly room-temperature processing). ZnO TFTs with even reduced channel lengths of 5 μm have been shown to exhibit very low off-currents of ∼1 pA and on-to-off ratios of $\sim 10^7$, showing that the source-to-drain leakage current can be significantly decreased [154].

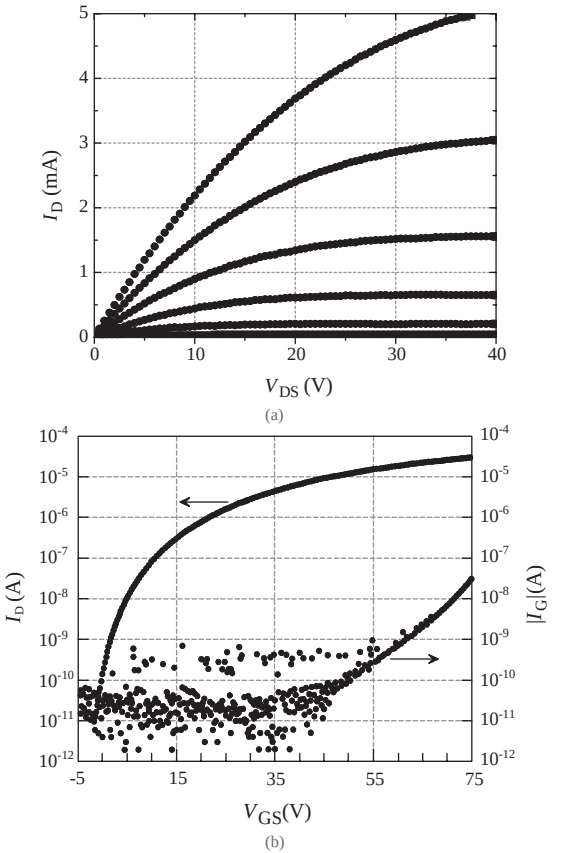

Figure 8.26 Electrical characteristics of a ZnO channel TFT: (a) drain current–drain voltage (I_D–V_{DS}) characteristics with the gate voltage, V_{GS}, from 0 to 70 V in 10 V increments; (b) transfer characteristics and gate leakage current I_G for $V_{DS} = 100$ mV. (Courtesy of R.L. Hoffman [153].)

FETs with single-crystalline ZnO channels consisting of high-quality epitaxial films grown on lattice-matched (0 0 0 1) $ScAlMgO_4$ substrates by laser molecular beam epitaxy have been reported [155]. An amorphous alumina gate insulator was deposited for gate oxide by using either RF magnetron sputtering or electron beam evaporation to avoid excessive gate leakage. The drift mobilities of the device with an electron-beam-deposited gate dielectric are as high as $40\,cm^2\,V^{-1}\,s^{-1}$. However, hysteresis appears in transfer characteristics, which can be eliminated by thermal annealing of the entire device in air. The much larger hysteresis and lower mobilities were observed for devices with sputtered gate insulators. This is presumably due to large surface/interface states created by ion or electron bombardment during the sputtering. Similar improvement in the mobility was observed for nanocrystalline ZnO channel TFTs fabricated on Si-substrates with Al_2O_3 gate dielectric layers

deposited either by electron beam evaporation or atomic layer deposition (ALD), with values ranging between 2 and 42 $cm^2 V^{-1} s^{-1}$ [156].

In another report, Yano *et al.* [148] discussed the $Mg_{0.3}Zn_{0.7}O$/ZnO HFET structure grown by MBE on *a*-plane sapphire substrate and its performance. A low-temperature initiation layer was annealed at 750 °C followed by the deposition at 350 °C of a 400 nm thick bottom $Mg_{0.3}Zn_{0.7}O$ barrier layer, a 20 nm thick ZnO active layer where the transport is to take place, a 30 nm thick top $Mg_{0.3}Zn_{0.7}O$ barrier layer, and a 20 nm thick MgO gate insulation layer (due to Schottky barriers on ZnO being leaky in general). The bandgap of the $Mg_{0.3}Zn_{0.7}O$ barrier layer was estimated to be ~4.1 eV layer at room temperature. Utilizing the reported [157] ratio of $\Delta E_C/\Delta E_V \sim 9$, the band-edge discontinuities at heterointerface were roughly estimated to be $\Delta E_C \sim 0.7$ eV for conduction band and $\Delta E_V \sim 0.08$ eV for valence band, favoring electron confinement. Although wet chemical etching potential is touted as a good deal, dry etching with ECR-assisted etching using a gas mixture of CF_4 and CH_4 (2 : 3) was employed to remove the top heterojunction layer for ohmic contacts. An Au/In (200/20 nm in thickness) bilayer metal was evaporated on the ZnO-recessed regions and alloyed at 400 °C for 5 min to obtain the ohmic contacts for source and drain electrodes. An Au/Ti (70 nm 20 nm^{-1}) bilayer metal was evaporated on the MgO surface layer to attain the Schottky contact for gate electrode. Hall bridge measurements led to a sheet electron density of $\sim 6 \times 10^{12}$ cm^{-2} and a high Hall mobility (μ_{Hall}) of 130 $cm^2 V^{-1} s^{-1}$, which is typical of ZnO epitaxial layers at room temperature. Nonsaturating FET output characteristics were observed with associated transconductances typically more than 1 mS mm^{-1} and drain currents of about 2 mA mm^{-1}. Tremendous improvements are needed to be considered really competitive with other available technologies.

Nanowires are often configured also as FET structures with a back gate for current transport studies (see Figure 8.27). Employing the coupled piezoelectric and semiconducting properties of ZnO piezoelectric field-effect transistors (PEFETs) composed of a ZnO nanowire bridging across two ohmic contacts were demonstrated by Wang *et al.* [158] for measuring forces in the nanonewton range. In such PEFETs, the source-to-drain current is controlled by the bending of the NW. The mechanism for the PEFET operation has been attributed to the carrier trapping effect and the creation of a charge depletion region under elastic deformation. The linear relationship between the bending force and the conductance was found at small bent regions, demonstrating the principle of nanowire-based nanoforce and nanopressure sensors. To improve the electrical characteristics of ZnO nanorod FETs, different treatments were employed. Park *et al.* [2] reported significant improvement by coating ZnO nanorods with polyimide. The ZnO nanorods prepared by catalyst-free MOVPE were dispersed on SiO_2/Si substrates where 250 nm thick SiO_2 was used as the gate dielectric and the heavily doped n-Si acted as the back gate. The Au/Ti electrodes were placed with a separation of 2–5 μm only on the nanaowire ends using e-beam lithography. The typical nanowire FETs exhibited transconductance and mobility values of 140 nS and 75 $cm^2 V^{-1} s^{-1}$, respectively, at room temperature for a gate bias of 2.4 V. After coating the nanorod surface with a polyimide thin layer, the drain current–gate voltage (I_{sd}–V_g) characteristics showed a turn-off at $V_g = -5$ V, a

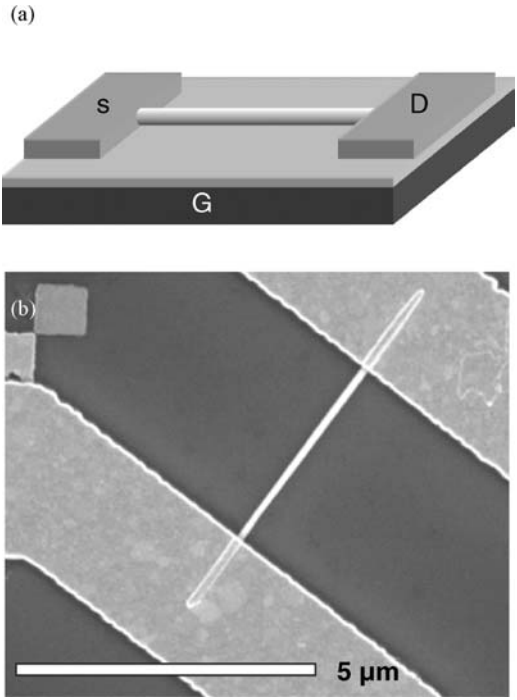

Figure 8.27 (a) Schematic side view and (b) field-emission–scanning electron microscopy image of a ZnO nanorod FET device. (Courtesy of G.-C. Yi. [2].)

large current on–off ratio of 10^4–10^5, and a transconductance as high as 1.9 μS at $V_g = 2.3$ V (when $V_{sd} = 1.0$ V) that is an order of magnitude higher than that for as-grown ZnO nanorod FETs without a polyimide coating (see Figure 8.28). The electron mobility estimated from the transconductance had a maximum value of 1000–1200 $cm^2 V^{-1} s^{-1}$. A significant improvement of ZnO nanowire FET device performance was also observed in another report [1] after surface passivation.

8.5.5
Transparent Conducting Oxides and Thin-Film Transistors

Although Si has shown its supremacy in the field of TFT technology with amorphous Si and polycrystalline Si, an interest is developing for the optically transparent analogue, the transparent thin-film transistor (TTFT) technology [151, 159, 160]. Unlike conventional FET or TFT structures, TTFTs require all device components (channel, gate, electrodes, and substrate) to be transparent. Such invisible TTFTs can be used in a wide range of applications where transparency is required for some commercial and military applications. For instance, if used in automobile windshields, they could transmit visual information, making glass also serve as an electronic device to improve security systems. The interest is in part because it is

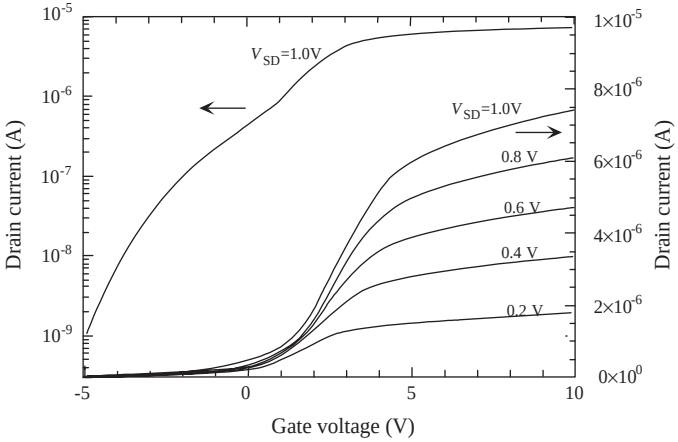

Figure 8.28 Source–drain current–gate voltage (I_{sd}–V_g) curves (solid lines) at different source–drain voltages (V_{sd}) and log scale plot (open circles) of I_{sd}–V_g ($V_{sd} = 1.0$ V) for a ZnO single nanorod FET after polyimide coating on the device. (Courtesy of G.-C. Yi [2].)

expected that the characteristics of TTFT will not degrade on exposure to visible light due to the wide bandgap of its active channel layer, whereas the characteristics of amorphous or poly-Si TFT do degrade. Therefore, measures would not be required in this case to shield the active channel layer from visible light, unlike the commercial amorphous silicon transistors in which visible light generates excess carriers and therefore must be shielded. In addition, it should be noted that such invisible thin-film transistors using ZnO as an active channel achieve much higher field-effect mobility than do amorphous silicon transistors (0.5 $cm^2 V^{-1} s^{-1}$), the major material of today's FET technology. Besides, high-quality crystalline ZnO films can be grown at relatively low deposition temperatures on various substrates including amorphous glasses. In this vein, a number of reports are already available on ZnO-based TTFT [151, 153, 159–170] using various methods for ZnO growth.

Before delving into the discussion of transistor structures, a brief review of the transparent oxides based on ZnO on their own merits is warranted. In most optoelectronic devices such as flat panel displays, LEDs, and solar cells, it is essential to use a transparent electrode such as a thin-film transparent conducting oxide (TCO). Although tin-doped ITO thin films deposited by magnetron sputtering are widely used today for most transparent electrode applications, there are many reports on other TCO semiconductors such as AZO, GZO, indium zinc oxide (IZO), tin zinc oxide (TZO) in large part due to the expected worldwide shortage of In. The growing demand for ITO thin-film transparent electrodes is the impetus for looking at alternative TCO materials since a stable supply of ITO may be difficult to achieve for the expanding market because of the cost and, as mentioned, limited amount of indium available. ZnO-based TCOs have attracted significant attention due to their good conductivity, high optical transparency (in the 90% range), excellent surface

Table 8.4 Minimum resistivity and maximum carrier concentration obtained for ZnO films doped with various impurities.

Dopant	Dopant content (wt%)	Resistivity ($\times 10^{-4}\,\Omega$ cm)	Carrier concentration ($\times 10^{20}$ cm^{-3})
Al_2O_3	1–2	0.85	15.4
Ga_2O_3	2–7	1.2	14.5
B_2O_3	2	2.0	5.4
Sc_2O_3	2	3.1	6.7
SiO_2	6	4.8	8.8
V_2O_5	0.5–3	5.0	4.9
F	0.5	4.0	5.0
Undoped	0	4.5	2.0

(After Minami [175].)

smoothness, low deposition temperature, good etchability for patterning, and good reproducibility [171–173]. Candidates for transparent amorphous oxides having large electron mobilities must be constituted of heavy posttransition metal cations with an electronic configuration $(n-1)d^{10}ns^0$, where $n \geq 5$ [174]. Oxide semiconductor XZO films, where X = Al, Ga, In, Sn, are prepared from a target made of homogeneous $Al_2O_3(ZnO)_n$, $Ga_2O_3(ZnO)_n$, $In_2O_3(ZnO)_n$, or $SnO_2(ZnO)_n$ compounds. Although various dopants have been used to achieve ZnO TCO films, low resistivity (below $2 \times 10^{-4}\,\Omega$ cm) and high carrier concentration (above 10^{21} cm^{-3}) have been obtained only in AZO and GZO films, as can be seen from Table 8.4 [175]. For example, resistivities as low as 0.85×10^{-4} and $0.81 \times 10^{-4}\,\Omega$ cm have been obtained for ZnO:Al [176] and ZnO:Ga [177] thin films grown by pulsed laser deposition, comparable to values obtained for ITO (e.g., $0.72 \times 10^{-4}\,\Omega$ cm [178]). In general, the electrical properties of the TCO films strongly depend on the deposition methods and conditions. AZO and GZO films with resistivities on the order of $10^{-5}\,\Omega$ cm have been achieved by PLD, but preparing films on large substrates with high deposition rates still remains as challenging.

As in the case of overall renewal of interest in ZnO, interest in TTFT technology was reborn owing to reports of p-type conductivity in several wide bandgap oxide semiconductors [179, 180]. These wide bandgap oxides in combination with known n-type transparent semiconductors such as ZnO, SnO_2, Ga_2O_3, and In_2O_3 [160] paved the way for the fabrication of optically transparent oxide based p–n junction diodes, UV-emitters, as we have been discussing [85, 95, 181–183].

A typical schematic representation of a ZnO-based bottom-gate-type TTFT structure reported to have an optical transmission (including substrate) of ~75% for visible light is shown in Figure 8.29 [163]. A glass substrate was blanket coated with a 200 nm thick layer of sputtered indium tin oxide to serve as the gate and a 220 nm thick layer of aluminum–titanium oxide (ATO) deposited by atomic layer deposition to serve as the gate insulator. After deposition of the ZnO layer by ion beam sputtering, a rapid thermal anneal, typically at 600–800 °C in O_2, was employed to

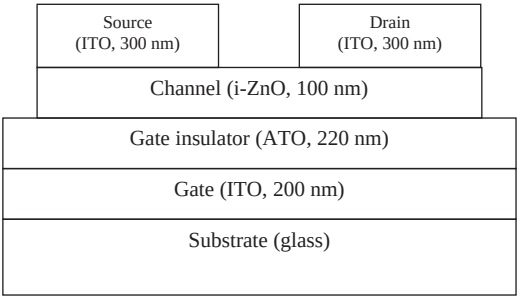

Figure 8.29 Schematic representation of a typical ZnO channel enhancement mode TTFT structure. (After Ref. [163].)

increase the ZnO channel resistivity to improve the electrical quality of the ATO/ZnO interface and to enhance the crystallinity of the ZnO layer. After the deposition of the ITO source/drain electrodes, a 300 °C rapid thermal annealing in O_2 was performed to improve the transparency of the ITO layer. Figure 8.30 displays DC electrical characteristics involving the drain current I_D, gate current I_G, gate voltage V_{GS}, and the drain voltage V_{DS} for a ZnO channel TTFT having a channel length and width-to-length ratio of 1500 μm and 10 : 1, respectively. These curves indicate an n-channel, enhancement-mode TFT operation with excellent drain current saturation and a maximum drain current on-to-off ratio of $\sim 10^7$. The effective channel mobility and the turn-on gate voltage were found to be 0.35–0.45 $cm^2 V^{-1} s^{-1}$ and −12 V, respectively.

Song *et al.* [172] reported on TTFTs using amorphous ZnO:In (IZO) for the active channel layer and gate–source–drain electrodes fabricated by RF magnetron sputtering on glass substrates at room temperature while amorphous AlO_x served as the gate dielectric. The devices exhibited threshold voltages of 1.1 V, on–off ratios of $\sim 10^6$, saturation currents of 1.41 μA at 5 V, and optical transmittance of 80% (including the substrate) in the visible range. Nomura *et al.* [184] proposed a novel semiconducting material, amorphous oxide semiconductor In-Ga-Zn-O (a-IGZO), for the active channel in TTFTs. To their proposal in effect, they deposited a-IGZO on polyethylene terephthalate (PET) at room temperature that exhibited a Hall effect mobility more than 10 $cm^2 V^{-1} s^{-1}$. TTFTs fabricated on such PET sheets showed saturation mobilities of 6–9 $cm^2 V^{-1} s^{-1}$, and device characteristics were stable during repetitive bending of the TTFT sheet. The transfer characteristics showed a low off-current, on the order of 10^{-7} A, and a $\sim 10^3$ on-to-off current ratio. Studies on the effect of bending on the TTFT characteristics showed that the performance of the TTFT after repetitive bending remained unaffected. Only a slight decrease in the saturation current was observed. The TTFT was stable at temperatures up to 120 °C but inoperative at higher temperatures, probably owing to the softening of the PET substrate.

Another key issue for ZnO TFTs is the selection of the gate insulator. Various gate dielectric materials have been tested for ZnO-based TFTs, such as SiO_2 [162], HfO_2 [169], PbZrTiO [185], ZnMgO [186], and Y_2O_3 [184]. As an example, TTFTs with transparent oxide semiconductor ZnO serving as the electron channel and

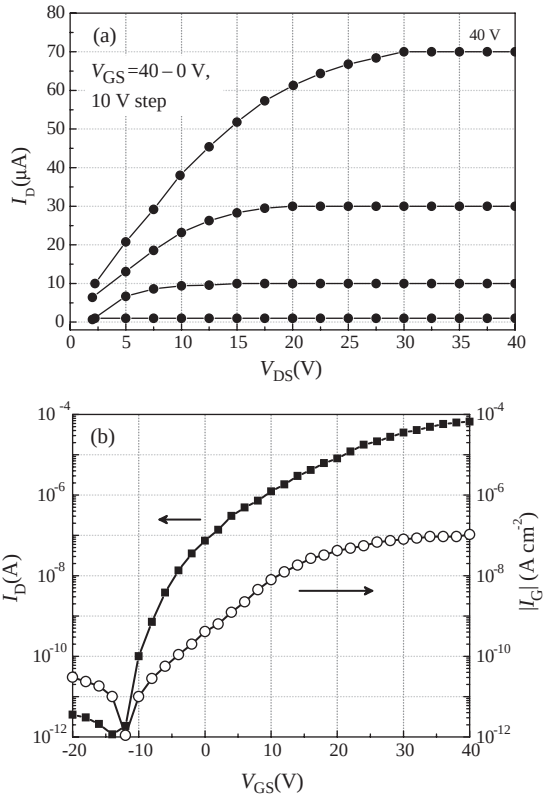

Figure 8.30 Electrical characteristics of a ZnO channel TTFT: (a) drain current–drain voltage (I_D–V_{DS}) characteristics with the gate voltage V_{GS}, from 0 to 40 V in 10 V increments; (b) transfer characteristics and gate leakage current for $V_{DS} = 10$ V. (After Ref. [163].)

200 nm thick high dielectric constant $Bi_{1.5}Zn_{1.0}Nb_{1.5}O_7$ (BZN) as the gate insulator have been reported [187]. The devices were shown to have very low operation voltages (< 4 V) afforded by the high capacitance of the BZN dielectric. At an operating voltage of 4 V the devices exhibited a field-effect mobility (drift mobility) and a current on–off ratio of 0.024 cm^2 V^{-1} s^{-1} and 2×10^4, respectively, and the threshold voltage was 2 V. High optical transparency (>80% for wavelengths above 400 nm), low-temperature processing, and low operation voltage of ZnO-based thin-film transistors with integrated BZN dielectric are promising for transparent device technology. Masuda *et al.* [162] fabricated n-channel depletion-mode TTFTs with undoped ZnO grown by PLD on glass for the channel and a double-layer gate insulator consisting of SiN_x (250 nm) and SiO_2 (50 nm) to suppress the leakage current, where ITO was used as the gate electrode and IZO as the source and drain electrodes. Even though the TFTs operated successfully with an optical transmittance of more than 80%, the on-to-off ratio was only $\sim 10^5$.

Lowering the carrier concentration in a TFT channel is crucial for reducing the leakage current. This can be achieved by compensating the n-type carriers by acceptor doping. High performance thin TTFTs with nitrogen-doped ZnO as the channel grown by atomic layer deposition on glass substrates have been demonstrated by Lim *et al.* [188]. The entire TFT fabrication process was carried out below 150 °C including the Al_2O_3 gate insulator deposition before the ZnO channel growth. By nitrogen doping the electron concentration in ZnO was lowered to $6 \times 10^{14}\,cm^{-3}$. Consequently, the enhancement-mode TFT devices (40 μm channel width, 20 μm channel length) exhibited off-currents as low as 2 pA, with a threshold (turn-on) voltage of 4.7 V, an on-to-off drain current ratio of 9.5×10^7, and a saturation mobility of $6.7\,cm^2\,V^{-1}\,s^{-1}$ at 35 V drain bias. The devices with undoped ALD-grown ZnO channels did not show any pinch-off and depletion as the electron concentrations in the channel were up to $5 \times 10^{19}\,cm^{-3}$.

Enhancement-mode MgZnO-based field-effect transistors utilizing HfO_2 as gate dielectric and ITO-coated glass substrates have also been reported [169]. A polycrystalline ZnO channel doped with Mg (10%) and P (2%, assuming that it serves as p-type compensating center) was used to decrease the electron carrier concentration. Mg doping increases the bandgap and therefore increases the activation energy for defect-related donors, helping the compensation of n-type carriers together with P doping. In these devices, an on–off ratio of 10^3 and channel mobility on the order of $5\,cm^2\,V^{-1}\,s^{-1}$ were obtained. Another report [189] compared ZnO thin-film metal–semiconductor field effect transistors and metal–oxide semiconductor field-effect transistors with either P-doped (2%) or undoped ZnO channels and gate lengths as small as 1.5 μm. Growth of a ~0.8–0.9 μm thick ZnO buffer on the sapphire or glass substrate was deemed necessary prior to depositing the active layers to reduce gate leakage current. As would be expected due to the relatively low barrier height of metals on n-type ZnO (0.6–0.8 eV), the MOS structure with 50 nm thick (Ce,Tb)$MgAl_{11}O_{19}$ gate dielectric showed an order of magnitude lower gate leakage current than the MESFET. The MOS gate structures using P-doped ZnO channels showed good depletion-mode conductance modulation with a field-effect mobility of $5.32\,cm^2\,V^{-1}\,s^{-1}$, compared to the very poor modulation by the metal structures.

Transparent nature of ZnO, potential achievement of low-cost polycrystalline ZnO, and fabrication technologies that are amenable to thin-film transistor production appear to suggest that ZnO may find a niche application in transparent thin-film technologies with added features over the Si-based varieties.

8.6 Piezoelectric Devices

As discussed in Section 1.4 ZnO is piezoelectric, and the piezoelectric coefficients along with the stiffness coefficients are listed in Table 1.6. Piezoelectric devices are based on electromechanical coupling that converts the mechanical energy into electrical energy and vice versa. When the piezoelectric material is strained, an electrical polarization is generated, or it is strained when an electric field is applied to

it. Due to its moderately high (very high for a semiconductor) electromechanical coupling coefficients, ZnO has been successfully used in thin-film piezoelectric devices such as bulk acoustic wave and surface acoustic wave resonators, filters, sensors, and microelectromechanical systems (MEMSs), the most common application being the SAW filter that has been an important component in mass consumer items such as TV filters and wireless communication systems. Successful development of sputtering of high-quality ZnO thin films on Si has been a breakthrough in the SAW device field as it allowed integration of ultrasonics with Si electronics for the first time, liberating device design from bulk piezoelectric substrates. For implementing acoustic wave devices, piezoelectric ZnO thin films grown on nonpiezoelectric substrates having high acoustic velocity and low propagation loss (diamond, sapphire), weakly piezoelectric materials such as quartz, amorphous substrates such as glass, and other semiconductors (Si, GaAs, InP, etc.) have been used.

To reiterate, the most widely used acoustic wave devices are the SAW devices that involve piezoelectric materials to convert electrical signals into mechanical waves in the launching transducers, and after some propagation, convert mechanical waves back into electrical signals at the receiving transducers. SAW resonators, delay lines, and filters are widely used in communication systems due to their low power consumption and ease of fabrication. They are especially useful in chemical and biochemical sensing applications as surface acoustic waves are strongly affected by changes in the surface properties.

A simple schematic of a SAW delay line is shown in Figure 8.31. The interdigital transducer (IDT) electrodes on the transmitter and the receiver sides represent a sampled data structure in real space, and time information is determined by the sound velocity. The mechanical wave is generated at the transmitter by applying an AC voltage across the input IDT fingers, which induces lattice vibrations. The generated acoustic wave propagates at the sound velocity defined by the device structure and the crystallographic directions of the constituent layers. The acoustic wave propagation polarizes the lattice cells along its way generating an electric field, and therefore induces a potential difference across the fingers of the output IDT when it reaches the receiver. The SAW devices may operate at frequencies from tens of MHz to 10GHz. The center frequency of the SAW device is determined by the SAW velocity of the substrate v_s, and the periodicity of the IDT (i.e., the wavelength at the central frequency, λ_0) through $f_0 = v_s/\lambda_0$. The number of electrodes in the IDTs, N, determines the bandwidth, $BW_{3dB} = 90/N$.

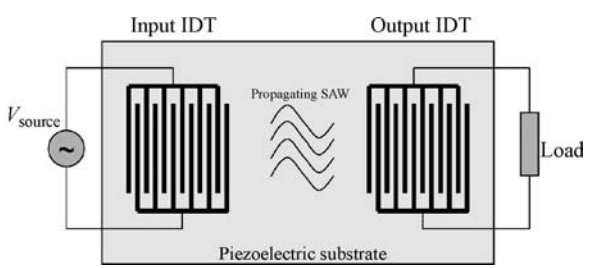

Figure 8.31 Schematic representation (top view) of a SAW delay line device.

The performance of a SAW device depends mainly on the acoustic wave velocity v_s, and the electromechanical coupling coefficient K^2, both of which depend on the material, direction of propagation, and the surface orientation. The electromechanical coupling coefficient that describes the efficiency of conversion between the mechanical energy and electrical energy, that is, the piezoelectric coupling strength of the piezoelectric material, is given by

$$K^2 = \frac{e^2}{C\varepsilon}, \tag{8.83}$$

where e, C, and ε are the piezoelectric, elastic, and dielectric constants along the acoustic wave propagation direction of interest. The effective elastic stiffness of a medium that increases due to piezoelectric stiffening is described by

$$C_s = C(1 + K^2). \tag{8.84}$$

The sound velocity is therefore increased by the increase of the stiffening, as it is given in terms of the elastic stiffness coeffcients. For example, remember from Section 1.4 that the sound velocity in a wurtzite structure along the c-axis is given by

$$v_s = \sqrt{\frac{C_{33}}{\rho}}, \tag{8.85}$$

where C_{33} is the appropriate stiffness coefficient for propagation along the c-axis, and ρ is the mass density.

SAW devices have been implemented with ZnO thin films grown on various substrates such as Si, GaAs, quartz, sapphire, SiC, diamond, GaN, and AlN. The resulting multilayer structures offer some flexibility over single layers as the sound velocity and the electromechanical coupling depend on the ZnO film thickness (h) to SAW wavelength (λ) ratio, h/λ (this ratio can instead be expressed as the thickness–frequency product hf). The energy of the surface acoustic wave is confined mostly near the surface (within one wavelength) and decays exponentially with depth. When the thin film is grown on a substrate with higher acoustic velocity, for almost all the acoustic energy to be confined in the film, the h/λ ratio should be much larger than 1. If h/λ is much smaller than 1, the acoustic wave mostly propagates in the substrate with a velocity slightly smaller than that in the substrate alone. Simply put, with increasing h/λ more and more acoustic energy is transported in the thin film and the velocity approaches increasingly to that in the thin film alone.

In a layered SAW structure involving a thin film grown on a substrate, different guided acoustic modes can be excited, namely, Rayleigh waves (also called SAW waves) along the surface and Love waves, which are modified shear horizontal (SH) plate waves [190]. Rayleigh waves have longitudinal and sheer vertical (SV) components that are coupled and travel at the same velocity, which is between 0.87 and 0.95 times the substrate transverse wave velocity (unlike the longitudinal and shear bulk acoustic waves which propagate independently with different velocities). They are confined to within a few wavelengths of the surface. Love waves, on the other hand, have SH component instead of the SV components and differ from the SH modes on

a free plate in that they exist in a layer on a semiinfinite substrate and can leak into the substrate. With increasing h/λ ratio, higher order modes are excited. The first higher order Rayleigh mode is called the Sezawa mode. For example, in an *a*-plane ZnO layer grown on *r*-plane sapphire, the *c*-axis lies in the thin-film plane, resulting in an in-plane acoustic anisotropy. The electromechanical coupling is maximum for the Rayleigh-type waves for propagation parallel to the *c*-axis of the film, while the Love-type waves have zero coupling for such propagation. Instead, the electromechanical coupling is maximum for the Love-type waves for propagation perpendicular to the *c*-axis, for which Rayleigh-type waves have now zero coupling. In other directions of propagation, the propagating wave is said to be the generalized SAW wave [191]. The anisotropy simply results in one type of wave having maximum electromechanical coupling while the other one has zero coupling.

Figure 8.32 shows the S_{21} scattering parameter (ratio of the transmitted signal amplitude to the incident signal amplitude) of from a 10 μm wavelength (IDT periodicity) SAW device fabricated on a 1.5 μm thick *a*-plane ZnO film grown on *r*-plane sapphire [192]. The central frequency is at ~420MHz (Rayleigh wave), which gives a sound velocity of 4200 m s^{-1} using $\lambda_0 = 10\,\mu m$. To reduce the conductivity and achieve piezoelectricity, the as-grown n-type ZnO films were compensated by Li doping during MOCVD growth. As mentioned above, the efficiency of the electromechanical coupling is at maximum along the [0 0 0 1] *c*-direction for the Rayleigh wave and along the $[1\ \bar{1}\ 0\ 0]$*m*-direction for the Love wave. Furthermore, the phase velocity of the Rayleigh wave is higher than that of the Love wave; and therefore, the IDTs were placed along the *c*-axis of the ZnO film to obtain a higher frequency SAW response. The acoustic velocity in sapphire (Al_2O_3) is higher than that in ZnO. Consequently, the acoustic velocity in the SAW device will decrease as the h/λ ratio increases, that is, as the ZnO film thickness increases. Therefore, for high frequency SAW filters, the ZnO film also has to be as thin as possible. However, reducing the film thickness reduces the efficiency of the electromechanical coupling. This

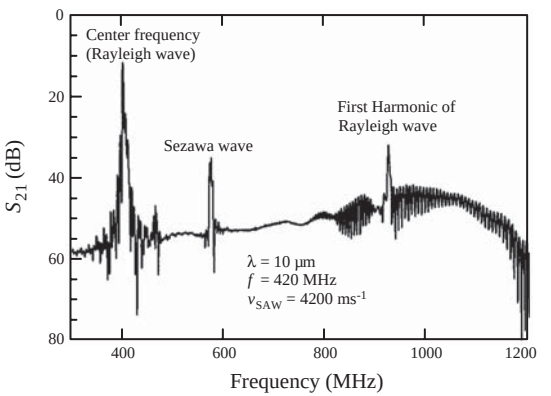

Figure 8.32 Frequency response of a 10 μm wavelength SAW device on a 1.5 μm thick ZnO film. (After Ref. [192].)

trade-off between the operating frequency and the coupling coefficient has to be taken into account in SAW device design.

The effective electromechanical coupling coefficient K^2_{eff}, is usually obtained by fitting the measured frequency spectrum via simulations combining the effective permittivity approach and the coupling of the modes model [193, 194]. K^2_{eff} values as high as 6% were obtained for SAW devices with 1.5 μm thick ZnO thin films on *r*-sapphire designed for a wavelength of 10 μm (h/λ ratio of 0.15), and a corresponding acoustic velocity of ~4200 m s^{-1} [192]. As seen from Figure 8.32 the insertion loss was as low as 11 dB, which includes the 6 dB loss related to device design. As expected, the acoustic velocity increased (~5700 m s^{-1} for $h/\lambda = 0.05$) and K^2_{eff} reduced (to less than 1% for $h/\lambda = 0.05$) with decreasing h/λ ratio. A slightly higher maximum coupling was calculated for the Love wave mode (6.46% for $hf = 870$ m s^{-1}), but at a smaller acoustic velocity (~3800 m s^{-1}), therefore, lower frequency [191].

SAW properties of $Mg_xZn_{1-x}O$ on *r*-sapphire have also been investigated [195]. With increasing Mg content, the acoustic velocity increases, but the electromechanical coupling efficiency drops. The Sezawa wave has a velocity of ~3450 m s^{-1} in ZnO/Al_2O_3 with a coupling coefficient of ~6% ($hf = 1500$ m s^{-1}) and ~4700 m s^{-1} in $Mg_{0.3}Zn_{0.7}O/Al_2O_3$ with a coupling coefficient of only ~0.76% ($hf = 3255$ m s^{-1}). The piezoelectric properties may be tailored further by the use of $Mg_{0.3}Zn_{0.7}O/ZnO$ multilayer structures.

For SAW devices using ZnO thin films grown on Si, electromechanical coupling coefficients up to 1.9% for the Sezawa wave have been reported ($h/\lambda = 0.26$) [196]. The propagation loss on thin-film ZnO devices on Si was measured to be relatively low (7 dB cm^{-1}, for $h/\lambda = 0.04$). SAW devices have also been fabricated using ZnO layers deposited on GaAs substrates for the possibility of monolithic integration with GaAs electronics, with K^2_{eff} values as high as 1.5% at $hf \sim 1500$ m s^{-1} [197]. For applications requiring good thermal stability, SAW devices have been developed on ZnO thin films deposited on quartz substrates. Even though these devices do not exhibit electromechanical coupling coefficients larger than those on other substrates ($K^2_{\text{eff}} = 1.1\%$) [198], their temperature coefficient of frequency (TCD) values are extremely small ($\Delta f/f = 0.37$ ppm °C^{-1}) [199].

To explore higher frequency capability, ZnO thin films have been prepared on high acoustic velocity materials such as SiC and AlN. SAW devices fabricated using 400 nm thick ZnO thin films deposited on commercial SiC substrates have shown generalized SAW modes with acoustic velocities of 7000 m s^{-1} and pseudo SAW modes with acoustic velocities of 12 500 m s^{-1} [200]. An electromechanical coupling coefficient of 5.2% was predicted for the generalized SAW mode when the IDT was placed at the ZnO/SiC interface and the top surface was metallized. ZnO thin films grown on GaN, AlN, and AlGaN templates on sapphire also provide advantages such as supporting higher order modes with higher acoustic velocity. The maximum coupling coefficient for the second-order wave mode was estimated as 4.3% for $ZnO/GaN/c\text{-}Al_2O_3$ (for $hf \sim 3000$ m s^{-1}, h here is the sum of ZnO and GaN thicknesses) and 3.8% for $ZnO/AlN/c\text{-}Al_2O_3$ (for $hf \sim 3000$–6000 m s^{-1}) [201]. For the ZnO thin films on $Al_xGa_{1-x}N/c\text{-}Al_2O_3$ alloy, the bandwidth (within ±0.3% of the

maximum K_{eff}^2) of the second order wave mode was found to increase with increasing Al content (x) up to $3620hf$ for $x = 1$ [201]. ZnO thin films deposited on diamond that has the highest acoustic velocities among all materials have shown to exhibit SAW velocities as large as 11 600 m s^{-1} with coupling coefficients up to 1.1% [202]. Using 0.65 μm wide electrode devices with a center frequency of 10GHz, a coupling coefficient of 1.5% was also demonstrated on such structures for the fifth harmonic of the second Sezawa mode [203]. All the abovementioned results show that ZnO thin films on various substrates can be successfully implemented into efficient SAW devices. Even though piezoelectric materials such as $LiNbO_3$ and $LiTaO_3$ have larger electromechanical coupling coefficients, as high as 38 and 14%, respectively [204, 205], ZnO is promising for applications that require electro-acoustic modulation and monolithic integration with other semiconductor technologies.

ZnO-based SAW devices have been used for UV photodetection [206, 207] and for gas [208–210] and biochemical [211] sensing. The SAW UV photodetector is based on the acousto-electric interaction. The photogenerated carriers increase the conductivity in the material, which in turn increases the attenuation and decreases the SAW velocity, and therefore, the SAW frequency. The change in the velocity Δv, in a semiconductor/piezoelectric material bilayer due to acousto-electric interaction is given by [212]

$$\frac{\Delta v}{v_0} = \frac{K_{\text{eff}}^2}{2} \frac{1}{1 + (\sigma/\sigma_{\text{m}})^2}, \tag{8.86}$$

where v_0 is the SAW velocity on free surface for zero conductance, σ is the semiconducting layer's sheet conductivity, and σ_{m} is the characteristic conductivity at which maximum loss occurs, $\sigma_{\text{m}} = v_0 (\varepsilon_1 + \varepsilon_2)$, with ε_1 and ε_2 being the dielectric constants of the semiconducting and piezoelectric layers, respectively. The perturbation in SAW velocity results in a phase shift across the device:

$$\Delta\Phi = 2\pi \frac{L}{\lambda} \frac{\Delta v}{v_0}, \tag{8.87}$$

where L is the length of the region in between the transmitter and receiver IDTs covered by the semiconducting layer.

Using a 200 nm thick polycrystalline ZnO film on $LiNbO_3$, a hybrid SAW UV detector with a central frequency of 37MHz has been demonstrated [206]. The ZnO thin film in between the IDTs acted as the UV absorbing medium and $LiNbO_3$ as the piezoelectric layer. Under illumination by 365 nm light with 40 mW cm^{-2} intensity, a frequency shift of $\Delta f = 170$kHz was observed, and the sensitivity was better than 10 μW cm^{-2}. SAW UV detectors with ZnO piezoelectric layers (highly compensated by Li doping with resistivity above 10^7 Ω cm) have also been demonstrated [207]. The semiconducting ZnO absorber layer was grown on Li-doped ZnO on *r*-sapphire by MOCVD with a thin $Mg_{0.2}Zn_{0.8}O$ buffer layer in between for isolation and as a diffusion barrier for Li. The IDTs were placed on the piezoelectric layer with the ZnO UV absorbing layer in between the transmitter and receiver IDTs. A frequency shift up to 11MHz and an insertion loss increase of ~23 dB were observed in the central Sezawa mode frequency (711MHz) when the device was illuminated with 365 nm

light of intensity 2.32 mW cm^{-2}. The corresponding maximum phase shift was measured at 365 nm as 107°. ZnO SAW UV detectors with such performance were proposed for use as passive zero-power remote wireless sensors [207].

8.7
Sensors and Solar Cells Based on ZnO Nanostructures

ZnO nanorod FET sensors may open up opportunities for highly sensitive and selective real-time detection of a wide variety of gas and bio molecules. The principle of gas sensor operation depends on the nature of gas molecules and is based on the modification of NW FET channel conductivity. Oxygen vacancies in ZnO function as n-type donors on oxide surfaces and are electrically and chemically active. Upon adsorption of charge-accepting gas molecules, for example, NO_2 and O_2, electrons are depleted from the conduction band resulting in a reduced conductivity of the n-type oxide. On the other hand, molecules that chemically react with surface oxygen (e.g., CO and H_2) interact with surface-adsorbed oxygen on ZnO and remove it leading to an increase in conductivity. ZnO exhibits strong adsorption of molecules on the surface, which affects the electrical characteristics of ZnO-based devices, dependent on surface-mediated phenomena. Thanks to the large surface-to-volume ratio of the nanostructures, the detection sensitivity of FET biosensors may be increased to a single-molecular detection level by measuring the small conductance changes caused by binding of biomolecular species on a nanorod conduction channel.

8.7.1
Gas Sensors

There is a strong interest in the development of lightweight gas sensors capable of ppm range sensitivity and extended operation at low-power levels. All experimental results demonstrate that ZnO nanowires, owing to the large surface area, have a potential for detecting NO_2 [213, 214], NH_3 [215], NH_4 [216], CO [216], H_2 [217–219] H_2O [220], O_3 [219, 221, 222], H_2S [223], and C_2H_5OH [224]. Detection of gas molecules is usually achieved by measuring the resistivity change of either the nanocrystalline ZnO films or the nanowire channel of an FET.

Cho *et al.* [213] reported a 1.8-fold decrease in resistance of well-dispersed ZnO nanorods at 1 ppm NO_2, while there was no significant change in resistance at 50 ppm CO. Sputtered nanocrystallite Cu-doped ZnO films of columnar structure with an average grain size of 5 nm exhibited very high sensitivity (2.7–20 ppm) to CO at 350 °C [216]. A substantial change in resistance of the ZnO films was also observed at a low operating temperature of 150 °C when the sensor was exposed to 6 ppm CO. The sensitivity for room-temperature detection of hydrogen by ZnO nanorods was shown to be greatly enhanced by sputter-depositing clusters of Pd on the surface [218]. An increase in the resistivity by a factor of 5 was observed upon exposure to hydrogen concentrations of 10–500 ppm compared to that without Pd. Pd-coated ZnO nanorods showed sensitivities lower than 10 ppm, with 95% recovery of the initial conductance after 20 s.

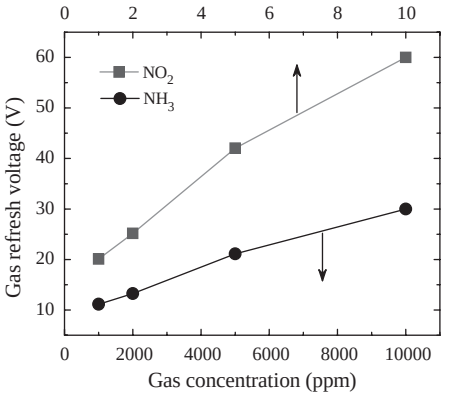

Figure 8.33 Gate refresh voltages of a ZnO nanowire FET for NH_3 and NO_2 gas molecules as a function of gas concentration. (After Ref. [225].)

ZnO nanorods are also promising candidates for detecting extremely low concentrations of H_2S. High response and good selectivity of ZnO nanorods to low concentrations of H_2S was observed by Wang *et al.* [223]. The ratio of the electrical resistance in air to that in 0.05 ppm H_2S was measured to be 1.7 at room temperature. One of the most important parameters of gas sensors is their selectivity. The selectivity is achieved by applying different voltages to the gate of a nanowire FET or by performing measurements at different temperatures since different gas molecules have different activation energies. Figure 8.33 shows an example of such selectivity for NH_3 and NO_2 gas molecules, where the refresh (erase) voltages, negative gate voltages required for electrical desorption of adsorbed gas molecules, for the two gas molecules are significantly different making it possible to distinguish different gas species [225].

8.7.2 Bio Sensors

The potential of ZnO nanostructures as nanosized biosensors has also been explored for detecting different biological molecules. Development of 1D ZnO nanostructures as bio sensors is in the state of infancy and only a limited number of reports are available [226–231]. The 1D ZnO biosensors have advantages such as stability in air, nontoxicity, chemical stability, electrochemical activity, ease of synthesis, and bio-safe characteristics. As in the case of gas sensors, the principle of operation is that the conductance of ZnO nanorod FETs drastically changes when biomolecules are adsorbed.

The key factor in most biological processes is the need for a small change of the pH concentration created by the release of H^+ ions during biochemical reactions. Therefore, determination of pH is a prerequisite for many processes. The sensing mechanism for pH is the polarization-induced bound surface charge by interaction with the polar molecules in the liquids. Application of ZnO nanorods as pH sensors

for intracellular chemical sensing is under development and a room-temperature sensitivity (change in surface potential) as high as ~59 mV per decade change in the pH value has been reported [231].

Kim *et al.* [226] reported on fabrication of electrical biosensors based on functionalized ZnO nanorod surfaces with *biotin*, a water soluble B-complex vitamin, for highly sensitive detection of biomolecule "streptavidin" that has an extraordinarily strong affinity for biotin. The biotin-modified ZnO nanorod FET exhibited drastic conductance increase to 17 μS after exposition to a 250 nm streptavidin solution, presumably due to the biotin–streptavidin binding.

8.7.3 Solar Cells

Solar cells represent a very promising renewable energy technology because they provide clean (beyond manufacturing) and renewable energy reducing our dependence on fossil oil and our impact on the environment. Dye-sensitized solar cells (DSSCs), using inorganic semiconductors, are being studied for very efficient, inexpensive, and large-scale solar energy conversion. DSSCs have been explored as possible substitutes for conventional silicon cells, but they suffer from possible dye agglomeration or electrolyte leakage [232–236]. During its traversal to the photoelectrode, an electron in a polycrystalline solar cell usually crosses about 10^3–10^6 nanoparticles, and the disordered structure of the nanoparticles film leads to enhanced scattering of free electrons, thus reducing the electron mobility and increasing electron recombination rate. Replacement of the nanoparticle film with an array of oriented single-crystalline nanorods must result in the rapid collection of carriers generated throughout the device as the nanorods provide a direct path from the point of photogeneration to the conducting substrate, thus effectively reducing the electron recombination losses. Moreover, electron transport in the single crystalline rod is expected to be several orders of magnitude faster than that in a random polycrystalline network. However, increased surface area by nanorods, as compared to thin films, also increases the surface recombination causing reduction in efficiency. As shown in Figure 8.34, a DSSC has three main components: (i) a thick (~10 μm) film of wide bandgap semiconductor nanostructures (TiO_2, SnO_2, or ZnO), (ii) a monolayer of organic dye molecules absorbed into the semiconductor nanostructures, and (iii) a liquid electrolyte containing the redox couple I^-/I_3^- that penetrates in between the dye-coated nanostructures.

ZnO is obviously one of the best candidates among semiconductors for DSSC applications as it can be synthesized easily and inexpensively into different shapes and sizes using various methods, and is environment friendly and stable indefinitely. Photovoltage and photocurrent measurements using modulated illumination on dye-sensitized ZnO solar cells have shown tens to hundreds of times faster electron transport in nanorod array electrodes compared to nanocrystalline particulate electrodes assembled from colloidal nanoparticles, with the electron lifetimes being only slightly smaller [237].

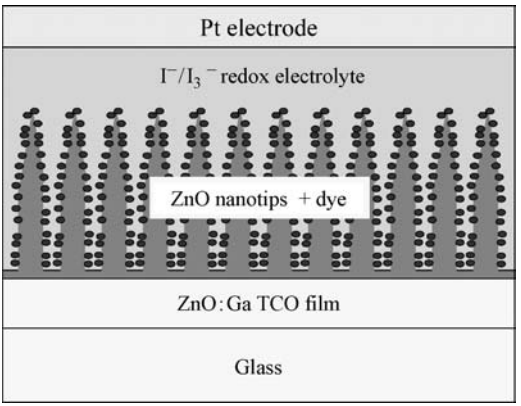

Figure 8.34 A schematic diagram of nanotip ZnO-based DSSCs. (Courtesy of Y. Lu [107].)

8.8 Concluding Remarks

ZnO offers some potential in providing electronic, photonic, and spin-based devices, and encouraging progress has been made in the research phase. Despite this progress, there are still a number of important issues that needs to be further investigated before this material can be transitioned to commercial use for the stated applications. The task is made more difficult by the highly successful GaN that competes for similar applications. However, there are some niche applications of ZnO, which are not addressed by GaN which if explored fully might pave the way for ZnO. Transparent thin-film transistors, ZnO-based transparent oxides, laser structures exploiting the large exciton-binding energy of ZnO (see Section 8.5.1.1 on lasers wherein ZnO active layers are explored for potential polariton lasers) are among these applications.

In the case of TTFTs, the critical issues are the mobility in noncrystalline or polycrystalline ZnO, and the choice of gate oxide, substrate, and the methods to deal with high electron concentrations encountered in ZnO channel layers. For electrical characteristics, the on-to-off ratio as well as the transconductance is important to hone in on.

ZnO also lends itself to applications in sensing, in part, due to the ease with which ZnO can be produced in the form of nanostructures. There is still much to be understood in terms of the mechanism of ZnO gas and bio-sensors. Although a number of ZnO sensors have been reported on detecting different gas and bio molecules, the selectivity (not unique to ZnO) remains to be the main issue since identification of the nature of the absorbed molecules is very important. Although several approaches have been proposed, which employ different activation energies of different gas molecules, this field is still in a state of infancy and much more effort is needed to pave the way for improved selectivity of ZnO sensors and to increase the lifetime of the devices.

Regarding the solar sells that received some attention despite very stiff competition, further studies are required to improve the current density and efficiency. This could be achieved by the application of various electrolytes and doping the ZnO films to improve its conductivity. There is also the control of the properties of individual building blocks, which at this point is inadequate, and the device-to-device reproducibility is low.

As for the nanostructures, ZnO nanostructures (nanowires, nanorods, etc.) provide a path to a new generation of devices, but a deliberate effort has to be made for ZnO nanostructures to be taken seriously for large-scale device applications, and to achieving high device density with accessibility to individual nanodevices. Reliable methods for assembling and integrating building blocks into circuits need to be developed.

Finally, ZnO as a semiconductor is facing very stiff competition from GaN that is much more mature in terms of devices (also has acceptable p-type dopant unlike the case with ZnO). Lack of a credible p-type doping hampers the thought of widespread optical emitters in ZnO. Furthermore, highly ionic nature of ZnO with large electron–phonon coupling and low thermal conductivity do not bode well for ZnO-based electronic devices. Nanostructures seem a little easier to produce with ZnO, but it remains to be seen whether nanostructures, in general, as hyped would really make inroads in the area of devices.

References

1 Chang, P.C., Fan, Zh., Chien, Ch.J., Stichtenoth, D., Ronning, C. and Lu, J.G. (2006) High-performance ZnO nanowire field effect transistors. *Applied Physics Letters*, **89**, 133113.

2 Park, W., Kim, J.S., Yi, G.C., Bae, M.H. and Le, H.-J. (2006) Fabrication and electrical characteristics of high-performance ZnO nanorod field-effect transistors. *Applied Physics Letters*, **85**, 5052.

3 Fan, Zh. and Jia, G.Lu. (2005) Electrical properties of ZnO nanowire field effect transistors characterized with scanning probes. *Applied Physics Letters*, **86**, 032111.

4 Yang, P., Yan, H., Mao, S., Russo, R., Johnson, J., Saykally, R., Morris, N., Pham, J., He, R. and Choi, H.-J. (2002) Controlled growth of ZnO nanowires and their optical properties. *Advanced Functional Materials*, **12**, 323.

5 Wan, Q., Li, Q.H., Chen, Y.J., Wang, T.H., He, X.L., Li, J.P. and Lin, C.L. (2004) Fabrication and ethanol sensing characteristics of ZnO nanowire gas sensors. *Applied Physics Letters*, **84**, 3654.

6 Liu, C.H., Zapien, J.A., Yao, Y., Meng, X.M., Lee, C.S., Fan, S.S., Lifshitz, Y. and Lee, S.T. (2003) High-density ordered ultraviolet light-emitting ZnO nanowire arrays. *Advanced Materials*, **15**, 838.

7 Kind, H., Yan, H., Messer, B., Law, M. and Yang, P. (2002) Nanowire ultraviolet photodetectors and optical switches. *Advanced Materials*, **14**, 158.

8 Sze, S.M. (1981) *Physics of Semiconductor Devices*, Wiley-VCH Verlag GmbH, New York. Ch. 5.

9 Rhoderick, E.H. and William, E.H. (1988) *Metal Semiconductor Contacts*, Clarendon Press, Oxford.

10 Stratton, R. (1969) Tunneling in schottky barrier rectifiers, in *Tunneling Phenomena in Solids, 1967 NATO Advanced Study Institute at Riső Denmark* (eds E. Burstein

and S. Lundqvist), Plenum Press, New York.

11 Henish, H.K. (1957) *Rectifying Semi-Conductor Contacts*, Clarendon Press, Oxford.

12 Dolan, W.W. and Dyke, W.P. (1942) *Physical Review*, **61**, 339.

13 Stratton, R. (1962) Theory of field emission from semiconductors. *Physical Review*, **125**, 67.

14 Padovani, F.A. and Stratton, R. (1966) Field and thermionic–field emission in Schottky barriers. *Solid-State Electronics*, **9**, 695.

15 Lin, M.E., Ma, Z., Huang, F.Y., Fan, Z.F., Allen, L.H. and Morkoç, H. (1994) *Applied Physics Letters*, **64**, 1003.

16 Hoppe, V., Stachel, D. and Beyer, D. (1994) *Physica Scripta*, **T57**, 122.

17 Iliadis, A.A., Vispute, R.D., Venkatesan, T. and Jones, K.A. (2002) *Thin Solid Films*, **420–421**, 478.

18 Ishikawa, H., Tsukui, K., Koide, Y., Teraguchi, N., Tomomura, Y., Suzuki, A. and Murakami, M. (1996) *Journal of Vacuum Science & Technology B*, **14**, 1812.

19 Sheng, H., Emanetoglu, N.W., Muthukumar, S., Feng, S. and Lu, Y. (2002) *Journal of Electronic Materials*, **31**, 811.

20 Kim, H.K., Han, S.H., Seong, T.Y. and Choi, W.K. (2000) *Applied Physics Letters*, **77**, 1647.

21 Kim, H.K., Han, S.H., Seong, T.Y. and Choi, W.K. (2001) *Journal of the Electrochemical Society*, **148**, G114.

22 Lin, Y.J. and Lee, C.T. (2000) *Applied Physics Letters*, **77**, 3986.

23 Kim, H.K., Kim, K.K., Park, S.J., Seong, T.Y. and Adesida, I. (2003) *Journal of Applied Physics*, **94**, 4225.

24 Akane, T., Sugioka, K. and Midorikawa, K. (2000) *Journal of Vacuum Science & Technology B*, **18**, 1406.

25 Lee, J.M., Kim, K.K., Park, S.J. and Choi, W.K. (2001) *Applied Physics Letters*, **78**, 3842.

26 Marlow, G.S. and Das, M.B. (1982) *Solid-State Electronics*, **25**, 91.

27 Kim, H.K., Kim, K.K., Park, S.J., Seong, T.Y. and Yoon, Y.S. (2002) *Japanese Journal of Applied Physics, Part 2: Letters*, **41**, L546.

28 Inumpudi, A., Iliadis, A.A., Krishnamoorthy, S., Choopun, S., Vispute, R.D. and Venkatesan, T. (2002) *Solid-State Electronics*, **46**, 1665.

29 Brillson, L.J. (1978) *Journal of Vacuum Science & Technology*, **15**, 1378.

30 Ip, K., Baik, K., Heo, Y., Norton, D., Pearton, S.J., LaRoche, J., Luo, B., Ren, F. and Zavada, J.M. (2003) *Journal of Vacuum Science & Technology B*, **21**, 2378.

31 Ip, K., Heo, Y., Baik, K., Norton, D.P., Pearton, S.J. and Ren, F. (2004) *Applied Physics Letters*, **84**, 544.

32 Ip, K., Heo, Y., Baik, K., Norton, D.P., Pearton, S.J. and Ren, F. (2004) *Journal of Vacuum Science & Technology B*, **22**, 171.

33 Liang, S., Sheng, H., Liu, Y., Huo, Z., Lu, Y. and Shen, H. (2001) *Journal of Crystal Growth*, **225**, 110.

34 Sheng, H., Muthukumar, S., Emanetoglu, N.W. and Lu, Y. (2002) *Applied Physics Letters*, **80**, 2132.

35 Simpson, J.C. and Cordora, J.F. (1988) *Journal of Applied Physics*, **63**, 1781.

36 Xiong, G., Wilkinson, J., Mischuck, M., Tuzemen, S., Ucer, K.B. and Williams, R.T. (2002) *Applied Physics Letters*, **80**, 1195.

37 Koppa, B.J., Davis, R.F. and Nemanich, R.J. (2003) *Applied Physics Letters*, **82**, 400.

38 Ohashi, N., Tanaka, J., Ohgaki, T., Haneda, H., Ozawa, M. and Tsurumi, T. (2002) *Journal of Materials Research*, **17**, 1529.

39 Auret, F.D., Goodman, S.A., Hayes, M., Legodi, M.J., van Laarhoven, H.A. and Look, D.C. (2001) *Applied Physics Letters*, **79**, 3074.

40 Heo, Y.W., Kwon, Y.W., Li, Y., Pearton, S.J. and Norton, D.P. (2004) *Applied Physics Letters*, **84**, 3474.

41 Kim, S., Kang, B., Ren, F., Heo, Y., Ip, K., Norton, D.P. and Pearton, S.J. (2004) *Applied Physics Letters*, **84**, 1904.

42 Lim, J.H., Kim, K.K., Hwang, D.K., Kim, H.K., Oh, J.H. and Park, S.J. (2005)

Journal of the Electrochemical Society, **152**, G179.

43 Mosbacker, H.L., Strzhemechny, Y.M., White, B.D., Smith, P.E., Look, D.C., Reynolds, D.C., Litton, C.W. and Brillson, L.J. (2005) Role of near-surface states in ohmic-schottky barrier formation of gold contacts to ZnO. *Applied Physics Letters*, **87**, 012102.

44 Kim, S.H., Kim, K.K., Park, S.J. and Seong, T.Y. (2005) *Journal of the Electrochemical Society*, **152**, G169.

45 Polyakov, A.Y., Smirnov, N.B., Kozhukhova, E.A., Vdodin, V.I., Ip, K., Heo, Y.W., Norton, D.P., and Pearton, S. J. (2003) *Applied Physics Letters*, **83**, 1575.

46 Mead, C.A. (1965) *Physics Letters*, **18**, 218.

47 Neville, R.C. and Mead, C.A. (1970) *Journal of Applied Physics*, **41**, 3795.

48 Slobodchikov, S.V., Salikhov, Kh.M. Russu, E.V. and Malinin, Yu.G. (2001) *Semiconductors*, **35**, 464.

49 Kim, S.-H., Kim, H.-K. and Seong, T.-Y. (2005) *Applied Physics Letters*, **86**, 112101.

50 Ip, K., Gilla, B.P., Onstine, A.H., Lambers, E.S., Heo, Y.W., Baik, K.H., Norton, D.P., Pearton, S.J., Kim, S., LaRoche, J.R. and Ren, F. (2004) *Applied Physics Letters*, **84**, 5133.

51 Ip, K., Gila, B.P., Onstine, A.H., Lambers, E.S., Heo, Y.W., Baik, K.H., Norton, D.P., Pearton, S.J., Kim, S., LaRoche, J.R. and Ren, F. (2004) *Applied Surface Science*, **236**, 387.

52 Ip, K., Heo, Y.W., Baik, K.H., Norton, D.P., Pearton, S.J., Kim, S., LaRoche, J.R. and Ren, F. (2004) *Applied Physics Letters*, **84**, 2835.

53 Shinoda, M., Nishide, T., Sawada, Y., Hosaka, M. and Matsumoto, T. (1993) *Japanese Journal of Applied Physics, Part 2: Letters*, **32**, L1565.

54 Li, Y., Tompa, G.S., Liang, S., Gorla, C., Lu, Y. and Doyle, J. (1997) *Journal of Vacuum Science & Technology A: Vacuum Surfaces and Films*, **15**, 1063.

55 Gardeniers, J.G.E., Rittersma, Z.M. and Burger, G.J. (1998) *Journal of Applied Physics*, **83**, 7844.

56 Hiramatsu, M., Imaeda, K., Horio, N. and Nawata, M. (1998) *Journal of Vacuum Science & Technology A: Vacuum Surfaces and Films*, **16**, 669.

57 Lee, J.-M., Chang, K.-M., Kim, K.-K., Choi, W.-K. and Park, S.J. (2001) *Journal of the Electrochemical Society*, **148**, G1.

58 Maki, H., Ikoma, T., Sakaguchi, I., Ohashi, N., Haneda, H., Tanaka, J. and Ichinose, N. (2002) *Thin Solid Films*, **411**, 91.

59 Fryar, J., McGlymn, E., Henry, M.O., Cafolla, A.A. and Hanson, C.J., (2003) *Physica B*, **340–342**, 210.

60 Zhu, J., Emanetoglu, N.W., Chen, Y., Yakshinskiy, B.V. and Lu, Y. (2004) *Journal of Electronic Materials*, **33**, 556.

61 Chen, J.-J., Jang, S., Ren, F., Li, Y., Kim, H.-S., Norton, D.P., Pearton, S.J., Osinsky, A., Chu, S.N.G. and Weawer, J.F. (2006) *Journal of Electronic Materials*, **35**, 516.

62 Petukhov, V., Bakin, A., El-Shaer, A.-H., Mofor, A.-C. and Waag, A. (2007) *Electrochemical and Solid-State Letters*, **10**, H357.

63 Iwanaga, H. and Shibata, N. (1967) *Japanese Journal of Applied Physics*, **6**, 415.

64 Mariano, A.N. and Hanneman, R.E. (1963) *Journal of Applied Physics*, **34**, 384.

65 Sun, J., Bian, J., Liang, H., Zhao, J., Hu, L., Zhao, Z., Liu, W. and Du, G. (2007) *Applied Surface Science*, **253**, 5161.

66 Ip, K., Baik, K.H., Overberg, M.E., Lambers, E.S., Heo, Y.W., Norton, D.P., Pearton, S.J., Ren, F. and Zavada, J.M. (2002) *Applied Physics Letters*, **81**, 3546.

67 Lim, W.T., Baek, I.K., Lee, J.W., Lee, E.S., Jeon, M.H., Cho, G.S., Heo, Y.W., Norton, D.P. and Pearton, S.J. (2003) *Applied Physics Letters*, **83**, 3105.

68 Ip, K., Overberg, M.E., Baik, K.W., Wilson, R.G., Kucheyev, S.O., Williams, J.S., Jagadish, C., Ren, F., Heo, Y.W., Norton, D.P., Zavada, J.M. and Pearton, S.J. (2003) *Solid-State Electronics*, **47**, 2289.

69 Kim, H.-K., Bae, J.W., Kim, T.-K., Kim, K.-K., Seong, T.-Y. and Adesida, I. (2003)

Journal of Vacuum Science & Technology B, **21**, 1273.

70 Stafford, L., Margot, J., Chaker, M. and Pearton, S.J. (2005) *Applied Physics Letters*, **87**, 071502.

71 Na, S.W., Shin, M.H., Chung, Y.M., Han, J.G. and Lee, N.E. (2005) *Journal of Vacuum Science & Technology A: Vacuum Surfaces and Films*, **23**, 898.

72 Pearton, S.J., Norton, D.P., Ip, K., Heo, Y.W. and Steiner, T. (2005) *Progress in Materials Science*, **50**, 293.

73 Lim, W., Voss, L., Khanna, R., Gila, B.P., Norton, D.P., Pearton, S.J. and Ren, F. (2006) *Applied Surface Science*, **253**, 1269.

74 Shin, M.H., Park, M.S., Jung, S.H., Boo, J.H. and Lee, N.-E. (2007) *Thin Solid Films*, **515**, 4950.

75 Lim, W.T., Stafford, L., Wright, J.S., Vossa, L.F., Khanna, R., Song, J.-I., Park, J.-S., Heo, Y.W., Lee, J.-H., Kim, J.-J., Norton, D.P. and Pearton, S.J. (2007) *Applied Surface Science*, **253**, 9228.

76 Hwang, Dae-Kue, Oh, Min-Suk, Lim, Jae-Hong and Park, Seong-Ju, (2007) *Journal of Physics D: Applied Physics*, **40**, R387.

77 Bae, J.-W., Jeong, C.-H., Kim, H.-K., Kim, K.-K., Cho, N.-G., Seong, T.-Y., Park, S.-J., Adesida, I. and Yeom, G.-Y. (2003) *Japanese Journal of Applied Physics*, **42**, L535.

78 Kim, H.-K., Bae, J.W., Kim, K.-K., Park, S.-J., Seong, T.-Y. and Adesida, I. (2004) *Thin Solid Films*, **447**, 90.

79 Xiong, G., Wilkinson, J., Tüzemen, S., Ucer, K.B. and Williams, R.T. (2002) *Proceedings of SPIE*, **256**, 4644.

80 Jeong, I.-S., Kim, J.-H. and Im, S. (2003) *Applied Physics Letters*, **83**, 2946.

81 Nikitin, S.E., Nikolaev, Yu.A., Polushina, I.K., Rud, V.Yu., Rud, Yu.V. and Terukov, E.I. (2003) *Semiconductors*, **37**, 1329.

82 Alivov, Ya.I., Van Nostrand, J.E., Look, D.C., Chukichev, M.V. and Ataev, B.M. (2003) *Applied Physics Letters*, **83**, 2943.

83 Yu, Q.-X., Xu, B., Wu, Q.-H., Liao, Y., Wang, G.-Z., Fang, R.-C., Lee, H.-Y. and Lee, C.-T. (2003) *Applied Physics Letters*, **83**, 4713.

84 Alivov, Ya.I., Kalinina, E.V., Cherenkov, A.E., Look, D.C., Ataev, B.M., Omaev, A.K., Chukichev, M.V. and Bagnall, D.M. (2003) Fabrication and characterization of n-ZnO/p-AlGaN heterojunction light-emitting diodes on 6H-SiC substrates. *Applied Physics Letters*, **83**, 4719.

85 Ohta, H., Kawamura, K., Orita, M., Hirano, M., Sarukura, N. and Hosono, H. (2000) Current injection emission from a transparent p–n junction composed of p-$SrCu_2O_2$/n-ZnO. *Applied Physics Letters*, **77**, 475.

86 Kudo, A., Yanagi, H., Ueda, K., Hosono, H., Kawazoe, K. and Yano, Y. (1999) *Applied Physics Letters*, **75**, 2851.

87 Ohta, H., Hirano, M., Nakahara, K., Maruta, H., Tanabe, T., Kamiya, M., Kamiya, T. and Hosono, H. (2003) *Applied Physics Letters*, **83**, 1029.

88 Tsurkan, A.E., Fedotova, N.D., Kicherman, L.V. and Pasko, P.G. (1975) *Semiconductors*, **6**, 1183.

89 Drapak, I.T. (1968) *Semiconductors*, **2**, 624.

90 Ishizuka, S., Suzuki, K., Okamoto, Y., Yanagita, M., Sakurai, T., Akimoto, K., Fujiwara, N., Kobayashi, H., Matsubara, K. and Niki, S. (2004) *Physica Status Solidi c*, **1**, 1067.

91 Aranovich, J.A., Golmayo, D., Fahrenbruch, A.L. and Bube, R.H. (1980) *Journal of Applied Physics*, **51**, 4260.

92 Alivov, Ya.I., Özgür, Ü., Doğan, S., Johnstone, D., Avrutin, V., Onojima, N., Liu, C., Xie, J., Fan, Q. and Morkoç, H. (2005) *Applied Physics Letters*, **86**, 241108.

93 Alivov, Ya.I., Johnstone, D., Özgür, Ü., Avrutin, V., Fan, Q., Akarca-Biyikli, S.S. and Morkoç, H. (2005) *Japanese Journal of Applied Physics, Part 1: Regular Papers, Short Notes & Review Papers*, **44**, 7281.

94 Wang, C.-X., Yang, G.-W., Liu, H.-W., Han, Y.-H., Luo, J.-F., Gao, C.-X. and Zou, G.-T. (2004) *Applied Physics Letters*, **84**, 2427.

95 Ohta, H., Mizoguchi, H., Hirano, M., Narushima, S., Kamiya, T. and Hosono, H. (2003) *Applied Physics Letters*, **82**, 823.

96 Nikitin, S.E., Nikolaev, Yu.A., Rud, V.Yu., Rud, Yu.V., Terukov, E.I., Fernelius, N. and Goldstein, J. (2004) *Semiconductors*, **38**, 393.

97 Özgür, Ü., Alivov, Ya.I., Liu, C., Teke, A., Reshchikov, M., Doğan, S., Avrutin, V., Cho, S.-J. and Morkoç, H. (2005) *Journal of Applied Physics Reviews*, **98**, 04301.

98 Look, D.C. and Claflin, B., (2004) *Physica Status Solidi b: Basic Research*, **241**, 624.

99 Milnes, A.G. and Feucht, D.L. (1972) *Heterojunctions and Metal–Semiconductor Junctions*, Academic Press, New York.

100 Osinsky, A., Dong, J.W., Kauser, M.Z., Hertog, B., Dabiran, A.M., Chow, P.P., Pearton, S.J., Lopatiuk, O. and Chernyak, L. (2004) MgZnO/AlGaN heterostructure light emitting diodes. *Applied Physics Letters*, **85**, 4272.

101 Alivov, Ya.I., Özgür, Ü., Doğan, S., Liu, C., Moon, Y., Gu, X., Avrutin, V. and Morkoç, H. (2005) *Solid-State Electronics*, **49**, 1693.

102 Tsukazaki, A., Ohtomo, A., Onuma, T., Ohtani, M., Makino, T., Sumiya, M., Ohtani, K., Chichibu, S.F., Fuke, S., Segawa, Y., Ohno, H., Koinuma, H. and Kawasaki, M. (2005) *Nature Materials*, **4**, 42.

103 Tsukazaki, A., Kubota, M., Ohtomo, A., Onuma, T., Ohtani, K., Ohno, H., Chichibu, S.F. and Kawasaki, M. (2005) Blue light-emitting diode based on ZnO. *Japanese Journal of Applied Physics*, **44**, L643.

104 Lim, J.H., Kang, C.K., Kim, K.K., Park, I.K., Hwang, D.K. and Park, S.J. (2006) *Advanced Materials*, **18**, 2720.

105 Ryu, Y.R., Lee, T.S., Lubguban, J.A., White, H.W., Kim, B.J., Park, Y.S. and Youn, C.J. (2006) *Applied Physics Letters*, **88**, 241108.

106 Ryu, Y.R., Lubguban, J.A., Lee, T.S., White, H.W., Jeong, T.S., Youn, C.J. and Kim, B.J. (2007) Excitonic ultraviolet lasing in ZnO-based light emitting devices. *Applied Physics Letters*, **90**, 131115.

107 Lu, Y. (2007) Presented at Challenges Facing ZnO and GaN: Facts and Myths, Virginia Crossing Resort, October 18–19, Richmond, VA, USA.

108 Zhong, J., Chen, H., Saraf, G., Lu, Y., Choi, C.K. and Song, J.J. (2007) Integrated ZnO nanotips on GaN light emitting diodes for enhanced emission efficiency. *Applied Physics Letters*, **90**, 203515.

109 Skolnick, M.S., Fisher, T.A. and Whittaker, D.M. (1998) Strong coupling phenomena in quantum microcavity structures. *Semiconductor Science and Technology*, **13**, 645.

110 Savona, V., Andreani, L.C., Schwendimann, P. and Quattropani, A. (1995) Quantum well excitons in semiconductor microcavities; unified treatment of weak and strong coupling regimes. *Solid State Communications*, **93**, 733.

111 Nurmikko, A.V. and Song, Y.K. (2000) Gain spectroscopy and vertical cavity devices in wide-gap semiconductors. *Journal of Luminescence*, **87–89**, 145.

112 Dorsaz, J., Carlin, J.-F., Zellweger, C.M., Gradecak, S. and Ilegems, M. (2004) InGaN/GaN resonant-cavity LED including an AlInN/GaN Bragg mirror. *Physica Status Solidi a: Applied Research*, **201**, 2675.

113 Carlin, J.-F., Dorsaz, J., Feltin, E., Butté, R., Grandjean, N., Ilegems, M. and Laügt, M. (2005) Crack-free fully epitaxial nitride microcavity using highly reflective AlInN/GaN Bragg mirrors. *Applied Physics Letters*, **86**, 031107.

114 Dorsaz, J., Carlin, J.-F., Gradecak, S. and Ilegems, M. (2005) Progress in AlInN–GaN Bragg reflectors: application to a microcavity light emitting diode. *Journal of Applied Physics*, **97**, 084505.

115 Feltin, E., Butté, R., Carlin, J.-F., Dorsaz, J., Grandjean, N. and Ilegems, M. (2005) Lattice-matched distributed Bragg reflectors for nitride-based vertical cavity surface emitting lasers. *Electronics Letters*, **41**, 94.

116 Feltin, E., Carlin, J.-F., Dorsaz, J., Christmann, G., Butté, R., Laügt, M.,

Ilegems, M. and Grandjean, N. (2006) Crack-free highly reflective AlInN/AlGaN Bragg mirrors for UV applications. *Applied Physics Letters*, **88**, 051108.

117 Waldrip, K.E., Han, J., Figiel, J.J., Zhou, H., Makarona, E. and Nurmikko, A.V. (2001) Stress engineering during metalorganic chemical vapor deposition of AlGaN/GaN distributed Bragg reflectors. *Applied Physics Letters*, **78**, 3205.

118 Ng, H.M., Moustakas, T.D. and Chu, S.N.G. (2000) High reflectivity and broad bandwidth AlN/GaN distributed Bragg reflectors grown by molecular-beam epitaxy. *Applied Physics Letters*, **76**, 2818.

119 Mitrofanov, O., Schmult, S., Manfra, M.J., Siegrist, T., Weimann, N.G., Sergent, A.M. and Molnar, R.J. (2006) High-reflectivity ultraviolet AlGaN/AlGaN distributed Bragg reflectors. *Applied Physics Letters*, **88**, 171101.

120 Chichibu, S.F., Ohmori, T., Shibat, N. and Koyama, T. (2006) Dielectric SiO_2/ZrO_2 distributed Bragg reflectors for ZnO microcavities prepared by the reactive helicon-wave-excited-plasma sputtering method. *Applied Physics Letters*, **88**, 161914.

121 Song, Y.-K., Zhou, H., Diagne, M., Ozden, I., Vertikov, A., Nurmikko, A.V., Carter-Coman, C., Kern, R.S., Kish, F.A. and Krames, M.R. (1999) A vertical cavity light emitting InGaN quantum well heterostructure. *Applied Physics Letters*, **74**, 3441.

122 Song, Y.-K., Zhou, H., Diagne, M., Nurmikko, A.V., Schneider, R.P., Jr, Kuo, C.P., Krames, M.R., Kern, R.S., Carter-Coman, C. and Kish, F.A. (2000) A quasicontinuous wave, optically pumped violet vertical cavity surface emitting laser. *Applied Physics Letters*, **76**, 1662.

123 Martin, R.W., Edwards, P.R., Kim, H.-S., Kim, K.-S., Kim, T., Watson, I.M., Dawson, M.D., Cho, Y., Sands, T. and Cheung, N.W. (2001) Optical spectroscopy of GaN microcavities with thicknesses controlled using a plasma etchback. *Applied Physics Letters*, **79**, 3029.

124 Tawara, T., Gotoh, H., Akasaka, T., Kobayashi, N. and Saitoh, T. (2003) Low-threshold lasing of InGaN vertical-cavity surface-emitting lasers with dielectric distributed Bragg reflectors. *Applied Physics Letters*, **83**, 830.

125 Semond, F., Sellers, I.R., Natali, F., Byme, D., Leroux, M., Massies, J., Ollier, N., Leymarie, J., Disseix, P. and Vasson, A. (2005) Strong light-matter coupling at room temperature in simple geometry GaN microcavities grown on silicon. *Applied Physics Letters*, **87**, 021102.

126 Kim, T.K., Yang, S.S., Son, J.K., Hong, Y.G. and Yang, G.M. (2006) GaN microcavity structure with dielectric distributed Bragg reflectors fabricated by using a wet-chemical etching of a (1 1 1) Si substrate. *Applied Physics Letters*, **89**, 041129.

127 Chu, J.-T., Lu, T.-C., You, M., Su, B.-J., Kao, C.-C., Kuo, H.-C. and Wang, S.-C. (2006) Emission characteristics of optically pumped GaN-based vertical-cavity surface-emitting lasers. *Applied Physics Letters*, **89**, 121112.

128 Born, M. and Wolf, E. (1999) *Principles of Optics*, 7th edn, Cambridge University Press, Cambridge, UK.

129 Andreani, L.C., Tassone, F. and Bassani, F. (1991) Radiative lifetime of free excitons in quantum wells. *Solid State Communications*, **77**, 641.

130 Bose, S.N. (1924) *Zeitschrift Fur Physik*, **26**, 178.

131 Einstein, A. (1925) *Sitz Ber Preuss Akad Wiss (Berlin)*, **1**, 3.

132 Savvidis, P.G., Baumberg, J.J., Stevenson, R.M., Skolnick, M.S., Whittaker, D.W. and Roberts, J.S. (2000) Angle-resonant stimulated polariton amplifier. *Physical Review Letters*, **84**, 1547.

133 Butté, R., Christmann, G., Feltin, E., Carlin, J.-F., Mosca, M., Ilegems, M. and Grandjean, N. (2006) Room-temperature polariton luminescence from a bulk

microcavity. *Physical Review B: Condensed Matter*, **73**, 033315.

134 Alyamani, A., Sanvitto, D., Khalifa, A.A., Skolnick, M.S., Wang, T., Ranalli, F., Parbrook, P.J., Tahraoui, A. and Airey, R. (2007) GaN hybrid microcavities in the strong coupling regime grown by metal-organic chemical vapor deposition on sapphire substrates. *Journal of Applied Physics*, **101**, 093110.

135 Feltin, E., Christmann, G., Butté, R., Carlin, J.-F., Mosca, M. and Grandjean, N. (2006) Room temperature polariton luminescence from a GaN/AlGaN quantum well microcavity. *Applied Physics Letters*, **89**, 071107.

136 Christopoulos, S., Baldassarri Höger von Högersthal, G., Grundy, A.J.D., Lagoudakis, P.G., Kavokin, A.V., Baumberg, J.J., Christmann, G., Butté, R., Feltin, E., Carlin, J.-F. and Grandjean, N. (2007) Room-temperature polariton lasing in semiconductor microcavities. *Physical Review Letters*, **98**, 126405.

137 Zamfirescu, M., Kavokin, A., Gil, B., Malpuech, G. and Kaliteevski, M. (2002) ZnO as a material mostly adapted for the realization of room-temperature polariton lasers. *Physical Review B: Condensed Matter*, **65**, 161205.

138 Chichibu, S.F., Uedono, A., Tsukazaki, A., Onuma, T., Zamfirescu, M., Ohtomo, A., Kavokin, A., Cantwell, G., Litton, C.W., Sota, T. and Kawasaki, M. (2005) Exciton-polariton spectra and limiting factors for the room-temperature photoluminescence efficiency in ZnO. *Semiconductor Science and Technology*, **20**, S67.

139 Schmidt-Grund, R., Rheinländer, B., Czekalla, C., Benndorf, G., Hochmut, H., Rahm, A., Lorenz, M. and Grundmann, M. (2007) ZnO based planar and micropillar resonators. *Superlattices and Mmicrostructures*, **41**, 360.

140 Shimada, R., Xie, J., Avrutin, V., Özgür, Ü. and Morkoç, H. (2008) Cavity polaritons in ZnO-based hybrid microcavities. *Applied Physics Letters*, **92**, 011127.

141 Wu, X., Yamilov, A., Liu, X., Li, S., Dravid, V.P., Chang, R.P.H. and Cao, H. (2004) Ultraviolet photonic crystal laser. *Applied Physics Letters*, **85**, 3657.

142 Scharrer, M., Yamilov, A., Wu, X., Cao, H. and Chang, R.P.H. (2006) Ultraviolet lasing in high-order bands of three dimentional ZnO photonic crystals. *Applied Physics Letters*, **88**, 201103.

143 Cao, H., Zhao, Y.G., Ho, S.T., Seeling, E.W., Wang, Q.H. and Chang, R.P.H. (1999) Random laser action in semiconductor powder. *Physical Review Letters*, **82**, 2278.

144 Hofstetter, D., Bonetti, Y., Giorgetta, F.R., El-Chaer, A.-H., Bakin, A., Waag, A., Schmidt-Grund, R., Schubert, M. and Grundmann, M. (2007) Demonstration of an ultraviolet ZnO-based optically pumped third order distributed feedback laser. *Applied Physics Letters*, **91**, 111108.

145 Minami, T., Tanigava, M., Yamanishi, M. and Kawamura, T. (1974) *Japanese Journal of Applied Physics*, **13**, 1475.

146 Shimizu, A., Kanbara, M., Hada, M. and Kasuga, M. (1978) *Japanese Journal of Applied Physics*, **17**, 1435.

147 Alivov, Ya.I., Look, D.C., Ataev, B.M., Chukichev, M.V., Mamedov, V.V., Zinenko, V.I., Agafonov, Yu.A. and Pustovit, A.N. (2004) Fabrication of ZnO-based metal-insulator-semiconductor diode by ion implantation. *Solid-State Electronics*, **48**, 2343.

148 Yano, M., Koike, K., Sasa, S. and Inoue, M. (2006) ZnO/ZnMgO heterojunction FETs, in *Zinc Oxide Bulk, Thin Films and Nanostructures: Processing, Properties and Applications* (eds C. Jagadish and S.J. Pearton), Elsevier, Oxford.

149 Kagan, Cherie R. and Paul, Andry(eds) (2003) *Thin-Film Transistors*, Marcel Dekker, New York.

150 Yue Kuo(ed.) (2004) *Thin Film Transistors Materials and Processes, Volume 1: Amorphous Silicon Thin Film Transistors*, Kluwer Academic Publishers, Boston.

151 Hoffman, R. (2006) ZnO thin-film transistors, in *Zinc Oxide Bulk, Thin Films and Nanostructures: Processing, Properties and Applications* (eds C. Jagadish and S.J. Pearton), Elsevier, Oxford.

152 Lehovec, K. and Zuleeg, R. (1970) Voltage–current characteristics of GaAs JFETs in the hot electron range. *Solid-State Electronics*, **13**, 1415.

153 Hoffman, R.L. (2004) *Journal of Applied Physics*, **95**, 5813.

154 Nishii, J., Hossain, F.M., Takagi, S., Aita, T., Saikusa, K., Ohmaki, Y., Ohkubo, I., Kishimoto, S., Ohtomo, A., Fukumura, T., Matsukura, F., Ohno, Y., Koinuma, H., Ohno, H. and Kawasaki, M. (2003) High mobility thin film transistors with transparent ZnO channels. *Japanese Journal of Applied Physics, Part 2: Letters*, **42**, L347.

155 Nishii, J., Ohtomo, A., Ohtani, K., Ohno, H. and Kawasaki, M. (2005) High-mobility field-effect transistors based on single-crystalline ZnO channels. *Japanese Journal of Applied Physics*, **44**, L1193.

156 Carcia, P.F., McLean, R.S. and Reilly, M.H. (2005) Oxide engineering of ZnO thin-film transistors for flexible electronics. *Journal of the Society for Information Display*, **13**, 547.

157 Makino, T., Chia, C.H., Tuan, N.T., Sun, H.D., Segawa, Y., Kawasaki, M., Ohtomo, A., Tamura, K. and Koinuma, H. (2000) *Applied Physics Letters*, **77**, 975.

158 Wang, X.D., Zhou, J., Song, J.H., Liu, J., Xu, N.S. and Wang, Z.L. (2006) Piezoelectric field effect transistor and nanoforce sensor based on a single ZnO nanowire. *Nano Letters*, **6**, 2768.

159 Wager, J.F. (2003) *Science*, **300**, 1245.

160 Ohta, H. and Hosono, H. (2004) Transparent oxide optoelectronics. *Materials Today*, **7**, 42.

161 Ohya, Y., Niwa, T., Ban, T. and Takahashi, Y. (2001) Thin film transistor of ZnO fabricated by chemical solution deposition. *Japanese Journal of Applied Physics, Part 1: Regular Papers, Short Notes & Review Papers*, **40**, 297.

162 Masuda, S., Kitamura, K., Okumura, Y., Miyatake, S., Tabata, H. and Kawai, T. (2003) Transparent thin film transistors using ZnO as an active channel layer and their electrical properties. *Journal of Applied Physics*, **93**, 1624.

163 Hoffman, R.L., Norris, B.J. and Wager, J.F. (2003) ZnO-based transparent thin-film transistors. *Applied Physics Letters*, **82**, 733.

164 Hossain, F.M., Nishii, J., Takagi, S., Ohtomo, A., Fukumura, T., Fujioka, H., Ohno, H., Koinuma, H. and Kawasaki, M. (2003) *Journal of Applied Physics*, **94**, 7768.

165 Carcia, P.F., McLean, R.S., Reilly, M.H. and Nunes, G. Jr. (2003) Transparent ZnO thin-film transistor fabricated by RF magnetron sputtering. *Applied Physics Letters*, **82**, 1117.

166 Ohtomo, A. and Kawasaki, M. (2000) IEICE (the Institute of Electronics, Information and Communication Engineers, Japan). *Transactions on Electron*, **E83-C**, 1614.

167 Kawasaki, M., Tamura, K., Saikusa, K., Aita, T., Tsukazaki, A., Ohtomo, A., Jin, Z.G., Matsumoto, Y., Fukumura, T., Koinuma, H., Ohmaki, Y., Kishimoto, S., Ohno, Y., Matsukura, F., Ohno, H., Makino, T., Tuan, N.T., Sun, H.D., Chia, C.H., Segawa, Y., Tang, Z.K. and Wang, G.K.L. (2000) Extended Abstracts of the 2000 International Conference on Solid-State Devices and Materials, 128.

168 Sasa, S., Ozaki, M., Koike, K., Yano, M. and Inoue, M. (2006) *Applied Physics Letters*, **89**, 053502.

169 Kwon, Y., Li, Y., Heo, Y.W., Jones, M., Holloway, P.H., Norton, D.P., Park, Z.V. and Li, S. (2004) Enhancement-mode thin-film field-effect transistor using phosphorus-doped (Zn,Mg)O channel. *Applied Physics Letters*, **84**, 2685.

170 Heo, Y.W., Tien, L.C., Kwon, Y., Norton, D.P., Pearton, S.J., Kang, B.S. and Ren, F. (2004) *Applied Physics Letters*, **85**, 2274.

171 Dehuff, N.L., Kettenring, E.S., Hong, D., Chiang, H.Q., Wager, J.F., Hoffman, R.L., Park, C.-H. and Keszler, D.A. (2005)

Transparent thin-film transistors with zinc indium oxide channel layer. *Journal of Applied Physics*, **97**, 064505.

172 Song, Ju-Il, Park, Jae-Soung, Kim, Howoon, Heo, Young-Woo, Lee, Joon-Hyung, Kim, Jeong-Joo and Choi, Byeong Dae (2007) Transparent amorphous indium zinc oxide thin-film transistors fabricated at room temperature. *Applied Physics Letters*, **90**, 022106.

173 Ito, N., Sato, Y., Song, P.K., Kaijio, A., Inoue, K. and Shigesato, Y. (2006) *Thin Solid Films*, **496**, 99.

174 Hosono, Hideo, (2006) Ionic amorphous oxide semiconductors: material design, carrier transport, and device application. *Journal of Non-Crystalline Solids*, **352**, 851.

175 Minami, T. (2005) Transparent conducting oxide semiconductors for transparent electrodes. *Semiconductor Science and Technology*, **20**, S35.

176 Agura, H., Suzuki, A., Matsushita, T., Aoki, T. and Okuda, M. (2003) Low resistivity transparent conducting Al-doped ZnO films prepared by pulsed laser deposition. *Thin Solid Films*, **445**, 263.

177 Park, S.-M., Ikegami, T. and Ebihara, K. (2006) Effects of substrate temperature on the properties of Ga-doped ZnO by pulsed laser deposition. *Thin Solid Films*, **513**, 90.

178 Suzuki, A., Matsushita, T., Aoki, T. and Yoneyama, Y. (2001) Pulsed laser deposition of transparent conducting indium tin oxide films in magnetic field perpendicular to plume. *Japanese Journal of Applied Physics*, **40**, L401.

179 Kawazoe, H., Yasukawa, M., Hyodo, H., Kurita, M., Yanagi, H. and Hosono, H. (1997) *Nature*, **389**, 939.

180 Kudo, A., Yanagi, H., Hosono, H. and Kawazoe, H. (1998) *Applied Physics Letters*, **73**, 220.

181 Kawazeo, H., Yanagi, H., Ueda, K. and Hosono, H. (2000) *MRS Bulletin*, **25**, 28.

182 Yanagi, H., Ueda, K., Ohta, H., Orita, M., Hirano, M. and Hosono, H. (2002) *Solid-State Communications*, **121**, 15.

183 Look, D.C., Claflin, B., Alivov, Y.I. and Park, S.J. (2004) *Physica Status Solidi a: Applied Research*, **201**, 2203.

184 Nomura, K., Ohta, H., Takagi, A., Kamiya, T., Hirano, M. and Hosono, H. (2004) Room-temperature fabrication of transparent flexible thin-film transistors using amorphous oxide semiconductors. *Nature*, **432**, 488.

185 Izyumskaya, N., Alivov, Y.I., Lee, H., Kang, Y.-S., Cho, S.-J. and Morkoç, H. (2007) Multi-functional perovskite oxides and their applications: the case of PZT. *Critical Reviews in Solid State and Materials Sciences*, **32**, 111.

186 Wu, H., Liang, J., Jin, G., Lao, Y. and Xu, T. (2007) Transparent Thin-Film Transistors Using ZnMgO as Dielectrics and Channel. *IEEE Transactions on Electron Devices*, **54**, 2856.

187 Kim, Il-Doo, Choi, YongWoo and Tuller, Harry L. (2005) Low-voltage ZnO thin-film transistors with high-κ $Bi_{1.5}Zn_{1.0}Nb_{1.5}O_7$ gate insulator for transparent and flexible electronics. *Applied Physics Letters*, **87**, 043509.

188 Lim, S.J., Kwon, Soon-ju, Kim, Hyungjun and Park, Jin-Seong, (2007) High performance thin film transistor with low temperature atomic layer deposition nitrogen-doped ZnO. *Applied Physics Letters*, **91**, 183517.

189 Kao, C.J., Kwon, Yong Wook, Heo, Y.W., Norton, D.P., Pearton, S.J., Ren, F. and Chi, G.C. (2005) Comparison of ZnO metal-oxide-semiconductor field effect transistor and metal-semiconductor field effect transistor structures grown on sapphire by pulsed laser deposition. *Journal of Vacuum Science & Technology B*, **23**, 1024.

190 Cheeke, J.D.N. (2002) *Fundamentals and Applications of Ultrasonic Waves*, CRC Press, Boca Raton.

191 Lu,Y., Emanetoglu, N.W. and Chen, Y. (2006) ZnO piezoelectric devices, in *Zinc Oxide Bulk, Thin Films and Nanostructures: Processing, Properties and Applications* (eds C. Jagadish and S.J. Pearton) Elsevier, Amsterdam.

192 Gorla, C.R., Emanetoglu, N.W., Liang, S., Mayo, W.E., Lu, Y., Wraback, M. and Shen, H. (1999) Structural, optical, and surface acoustic wave properties of epitaxial ZnO films grown on $(0\,1\,\bar{1}\,2)$ sapphire by metalorganic chemical vapor deposition. *Journal of Applied Physics*, **85**, 2595.

193 Chen, Y.Y., Wu, T.T. and Chou, T.T. (2004) Analysis of the frequency response of a dispersive IDT/ZnO/sapphire SAW filter using effective permittivity and the coupling of modes model. *Journal of Physics D: Applied Physics*, **37**, 120.

194 Wu, T.-T. and Wang, W.-S. (2004) An experimental study on the ZnO/sapphire layered surface acoustic wave device. *Journal of Applied Physics*, **96**, 5249.

195 Emanetoglu, N.W., Muthukumar, S., Wu, P., Wittstruck, R., Chen, Y. and Lu, Y. (2003) $Mg_xZn_{1-x}O$: A new piezoelectric material. *IEEE Transactions on Ultrasonics Ferroelectrics and Frequency Control*, **50**, 537.

196 Weber, A.H., Weiss, G. and Hunklinger, S. (1991) Comparison of Rayleigh and Sezawa wave modes in ZnO-SiO_2-Si structures. *Proceedings of the IEEE Ultrasonic Symposium*, **1**, 363.

197 Zhang, V.Y., Lefebvre, J.Z. and Gryba, T. (2001) SAW characteristics in a layered ZnO/GaAs structure for design of integrated SAW filters. *Proceedings of the IEEE Ultrasonic Symposium*, **1**, 261.

198 Tomar, M., Gupta, V. and Sreenivas, K. (2003) Improvements in the temperature stability of an IDT/ZnO/fused-quartz thin film SAW device with ZnO over-layer. *Proceedings of the IEEE Ultrasonic Symposium*, **1**, 901.

199 Kadota, M. and Kando, H. (2004) Small and low-loss IF SAW filters using zinc oxide film on quartz substrate. *IEEE Transactions on Ultrasonics Ferroelectrics and Frequency Control*, **51**, 464.

200 Didenko, I.S., Hickernell, F.S. and Naumenko, N.F. (2000) The experimental and theoretical characterization of the SAW propagation properties for zinc oxide films on silicon carbide. *IEEE Transactions on Ultrasonics Ferroelectrics and Frequency Control*, **47**, 179.

201 Chen, Y., Emanetoglu, N.W., Saraf, G., Wu, P. and Lu, Y. (2005) Analysis of SAW properties in ZnO/$Al_xGa_{1-x}N$/c-Al_2O_3 structures. *IEEE Transactions on Ultrasonics Ferroelectrics and Frequency Control*, **52**, 1161.

202 Higaki, K., Nakahata, H., Kitabayashi, H., Fujii, S., Tanabe, K., Seki, Y. and Shikata, S. (1997) High frequency SAW filter on diamond. *IEEE MTT-S Digest*, **2**, 829.

203 Nakahata, H., Hachigo, A., Itakura, K. and Shikata, S. (2000) Fabrication of high frequency SAW filters from 5 to 10GHz using SiO_2/ZnO/diamond structure. *Proceedings of the IEEE Ultrasonic Symposium*, **1**, 349.

204 Kuznetsova, I.E., Zaitsev, B.D., Joshi, S.G. and Borodina, I.A. (2001) Investigation of acoustic waves in thin plates of lithium niobate and lithium tantalate. *IEEE Transactions on Ultrasonics Ferroelectrics and Frequency Control*, **48**, 322.

205 Adler, E.L. (1989) Electromechanical coupling to Lamb and shear-horizontal modes in piezoelectric plates. *IEEE Transactions on Ultrasonics Ferroelectrics and Frequency Control*, **36**, 223.

206 Sharma, P. and Sreenivas, K. (2003) Highly sensitive ultraviolet detector based on ZnO/$LiNbO_3$ hybrid surface acoustic wave filter. *Applied Physics Letters*, **83**, 3617.

207 Emanetoglu, N.W., Zhu, J., Chen, Y., Zhong, J., Chen, Y., Lu, Y. (2004) Surface acoustic wave ultraviolet photodetectors using epitaxial ZnO multilayers grown on *r*-plane sapphire. *Applied Physics Letters*, **85**, 3702.

208 Anisimkin, V.I., Penza, M., Valentini, A., Quaranta, F. and Vasanelli, L. (1995) Detection of combustible gases by means of a ZnO-on-Si surface acoustic wave (SAW) delay line. *Sensors and Actuators B: Chemical*, **23**, 197.

209 Ippolito, S.J., Kandasamy, S., Kalantar-zadeh, K., Wlodarski, W., Galatsis, K.,

Kiriakidis, G., Katsarakis, N. and Suchea, M. (2005) Highly sensitive layered ZnO/$LiNbO_3$ SAW device with InO_x selective layer for NO_2 and H_2 gas sensing. *Sensors and Actuators B: Chemical*, **111–112**, 207.

210 Ahmadi, S., Hassani, F., Tigli, O., Ahmadi, S., Korman, C. and Zaghloul, M. (2003) Integrated CMOS surface acoustic wave gas sensor: design and characteristics. *Proceedings of IEEE Sensors*, **2**, 1199.

211 Zhang, Z., Emanetoglu, N.W., Saraf, G., Chen, Y., Wu, P., Zhong, J., Lu, Y., Chen, J., Mirochnitchenko, O. and Inouye, M. (2006) DNA immobilization and SAW response in ZnO nanotips grown on $LiNbO_3$ substrates. *IEEE Transactions on Ultrasonics Ferroelectrics and Frequency Control*, **53**, 786.

212 Wixforth, A., Scriba, J., Wassermeier, M., Kotthaus, J.P., Weimann, G. and Schlapp, W. (1989) Surface acoustic waves on $GaAs/Al_xGa_{1-x}$ as heterostructures. *Physical Review B: Condensed Matter*, **40**, 7874.

213 Cho, P.S., Kim, K.W. and Lee, J.H. (2006) NO_2 sensing characteristics of ZnO nanorods prepared by hydrothermal method. *Journal of Electroceramics*, **17**, 975.

214 Baratto, C., Sberveglieri, G., Onischuk, A., Caruso, B. and Stasio, S. (2004) Low temperature selective NO_2 sensors by nanostructured fibers of ZnO. *Sensors and Actuators B: Chemical*, **100**, 261.

215 Devi, G.S., Subrahmanyam, V.B., Gadkari, S.C. and Gupta, S.K. (2006) NH_3 gas sensing properties of nanocrystalline ZnO based thick films. *Analytica Chimica Acta*, **568**, 41.

216 Gong, H., Hu, J.Q., Wang, J.H., Ong, C.H. and Zhu, F.R. (2006) Nano-crystalline Cu-doped ZnO thin film gas sensor for CO. *Sensors and Actuators B: Chemical*, **115**, 247.

217 Rout, C.S., Raju, A.R., Govindaraj, A. and Rao, C.N.R. (2006) Hydrogen sensors based on ZnO nanoparticles. *Solid State Communications*, **138**, 136.

218 Wang, H.T., Kang, B.S., Ren, F., Tien, L.C., Sadik, P.W., Norton, D.P., Pearton, S.J. and Lin, J. (2005) Hydrogen-selective sensing at room temperature with ZnO nanorods. *Applied Physics Letters*, **86**, 243503.

219 Kang, B.S., Heo, Y.W., Tien, L.C., Norton, D.P., Ren, F., Gila, B.P. and Pearton, S.J. (2005) Hydrogen and ozone gas sensing using multiple ZnO nanorods. *Applied Physics A: Materials Science & Procedures*, **80**, 1029.

220 Wang, X.H., Ding, Y.F., Zhang, J., Zhu, Z.Q., You, S.Z., Chen, S.Q. and Zhu, J.Z. (2006) Humidity sensitive properties of ZnO nanotetrapods investigated by a quartz crystal microbalance. *Sensors and Actuators B: Chemical*, **115**, 421.

221 Christoulakis, S., Suchea, M., Koudoumas, E., Katharakis, M., Katsarakis, N. and Kiriakidis, G. (2006) Thickness influence on surface morphology and ozone sensing properties of nanostructured ZnO transparent thin films grown by PLD. *Applied Surface Science*, **252**, 5351.

222 Martins, R., Fortunato, E., Nunes, P., Ferreira, I., Marques, A., Bender, M., Katsarakis, N., Cimalla, V. and Kiriakidis, G. (2004) Zinc oxide as an ozone sensor. *Journal of Applied Physics*, **96**, 1398.

223 Wang, C.H., Chu, X.F. and Wu, M.W. (2006) Detection of H_2S down to ppb levels at room temperature using sensors based on ZnO nanorods. *Sensors and Actuators B: Chemical*, **113**, 320.

224 Xue, T.F., Hu, J.F., Qin, H.W., Zhou, Y., An, K., Zhang, L., Han, T. and Li, Y.X. (2004) Sensing properties of the ZnO based composite oxide (Al,Sb)/ZnO to C_2H_5OH gas. *Rare Metal Materials and Engineering*, **33**, 1006.

225 Fan, Z. and Lu, J.G. (2005) *Applied Physics Letters*, **86**, 123510.

226 Kim, J.S., Park, W.I., Lee, C.-H. and Yi, G.-C. (2006) ZnO Nanorod Biosensor for Highly Sensitive Detection of Specific Protein Binding. *Journal of Korean Physical Society*, **49**, 1635.

227 Batista, P.D. and Mulato, M. (2005) ZnO extended-gate field-effect transistors as pH sensors. *Applied Physics Letters*, **87**, 143508.

228 Kang, B.S., Ren, F., Heo, Y.W., Tien, L.C., Norton, D.P. and Pearton, S.J. (2005) pH measurements with single ZnO nanorods integrated with a microchannel. *Applied Physics Letters*, **86**, 112105.

229 Dulub, O., Meyer, B. and Diebold, U. (2005) Observation of the dynamical change in a water monolayer adsorbed on a ZnO surface. *Physical Review Letters*, **95**, 136101.

230 Al-Hillia, S.M., Willander, M., Öst, A. and Strålfors, P. (2007) ZnO nanorods as an intracellular sensor for pH measurements. *Journal of Applied Physics*, **102**, 084304.

231 Al-Hilli, S.M., Al-Mofarji, R.T. and Willander, M. (2006) Zinc oxide nanorod for intracellular pH sensing. *Applied Physics Letters*, **89**, 173119.

232 Beek, W.J.E., Wienk, M.M. and Janssen, R.A.J. (2004) Efficient hybrid solar cell from zinc oxide nanoparticles and a conjugated polymer. *Advanced Materials*, **16**, 1009.

233 Law, M., Greene, L., Johnson, J.C., Saykally, R. and Yang, P. (2005) Nanowire dye-sensitized solar cells. *Nature*, **4**, 455.

234 Du Pasquier, A., Chen, H. and Lu, Y. (2006) Dye sensitized solar cells using well-aligned zinc oxide nanotip arrays. *Applied Physics Letters*, **89**, 253513.

235 Baxter, J.B. and Aydil, E.S. (2005) Nanowire-based dye-sensitized solar cells. *Applied Physics Letters*, **86**, 053114.

236 Jiang, C.Y., Sun, X.W., Lo, G.Q., Kwong, D.L. and Wang, J.X. (2007) Improved dye-sensitized solar cells with a ZnO-nanoflower photoanode. *Applied Physics Letters*, **90**, 263501.

237 Martinson, A.B.F., McGarrah, J.E., Parpia, M.O.K. and Hupp, J.T. (2006) *Physical Chemistry Chemical Physics*, **8**, 4655.

Index